

DOT/FAA/AR-xx/xx

Air Traffic Organization
NextGen & Operations Planning
Office of Research and
Technology Development
Washington, DC 20591



Volume III – UAS Airborne Collision Severity Evaluation – Fixed-Wing

July 2017

Final Report

This document is available to the U.S. public through the National Technical Information Services (NTIS), Springfield, Virginia 22161.

This document is also available from the Federal Aviation Administration William J. Hughes Technical Center at actlibrary.tc.faa.gov.



U.S. Department of Transportation
Federal Aviation Administration

NOTICE

This document is disseminated under the sponsorship of the U.S. Department of Transportation in the interest of information exchange. The U.S. Government assumes no liability for the contents or use thereof. The U.S. Government does not endorse products or manufacturers. Trade or manufacturers' names appear herein solely because they are considered essential to the objective of this report. The findings and conclusions in this report are those of the author(s) and do not necessarily represent the views of the funding agency. This document does not constitute FAA policy. Consult the FAA sponsoring organization listed on the Technical Documentation page as to its use.

This report is available at the Federal Aviation Administration William J. Hughes Technical Center's Full-Text Technical Reports page: actlibrary.tc.faa.gov in Adobe Acrobat portable document format (PDF).

Legal Disclaimer: The information provided herein may include content supplied by third parties. Although the data and information contained herein has been produced or processed from sources believed to be reliable, the Federal Aviation Administration makes no warranty, expressed or implied, regarding the accuracy, adequacy, completeness, legality, reliability or usefulness of any information, conclusions or recommendations provided herein. Distribution of the information contained herein does not constitute an endorsement or warranty of the data or information provided herein by the Federal Aviation Administration or the U.S. Department of Transportation. Neither the Federal Aviation Administration nor the U.S. Department of Transportation shall be held liable for any improper or incorrect use of the information contained herein and assumes no responsibility for anyone's use of the information. The Federal Aviation Administration and U.S. Department of Transportation shall not be liable for any claim for any loss, harm, or other damages arising from access to or use of data or information, including without limitation any direct, indirect, incidental, exemplary, special or consequential damages, even if advised of the possibility of such damages. The Federal Aviation Administration shall not be liable to anyone for any decision made or action taken, or not taken, in reliance on the information contained herein.

Technical Report Documentation Page

1. Report No. DOT/FAA/AR-xx/xx		2. Government Accession No.		3. Recipient's Catalog No.	
4. Title and Subtitle Volume III – UAS Airborne Collision Severity Evaluation – Fixed-Wing Fixed-wing projectile development, simulation protocols, target development, testing and results.				5. Report Date July 2017	
				6. Performing Organization Code	
7. Author(s) Gerardo Olivares, Thomas Lacy, Luis Gomez, Jaime Espinosa de los Monteros, Russel J. Baldrige, Chandresh Zinzuwadia, Tom Aldag, Kalyan Raj Kota, Trent Ricks, Nimesh Jayakody				8. Performing Organization Report No.	
9. Performing Organization Name and Address National Institute for Aviation Research Wichita State University 1845 Fairmount Wichita, KS 67260-0093 Department of Aerospace Engineering Mississippi State University PO Box A Mississippi State, MS 39762				10. Work Unit No. (TRAIS)	
				11. Contract or Grant No.	
12. Sponsoring Agency Name and Address U.S. Department of Transportation Federal Aviation Administration Office of Aviation Research Washington, DC 20591				13. Type of Report and Period Covered	
				14. Sponsoring Agency Code	
15. Supplementary Notes					
16. Abstract					
17. Key Words Crashworthiness, Airborne Collision, UAS, National Institute for Aviation Research, NIAR			18. Distribution Statement This document is available to the U.S. public through the National Technical Information Service (NTIS), Springfield, Virginia 22161. This document is also available from the Federal Aviation Administration William J. Hughes Technical Center at actlibrary.tc.faa.gov .		
19. Security Classif. (of this report) Unclassified		20. Security Classif. (of this page) Unclassified		21. No. of Pages	
				22. Price	

REVISION HISTORY

Revision	Description of Modifications	Release Date
-	Initial release	21 Dec 2017
1	<ul style="list-style-type: none"> - Page 7 – added paragraph to specify the project will not assess already certified products. - Page 12 – added paragraph explaining differences between quadcopter and fixed-wing UASs. - Page 96 – added figures 115 and 116 with diagram showing materials in both manned aircraft. - Page 97 – added figures 117 and 118 with diagram showing gage thicknesses of main components of both aircraft. - Page 99 – extended explanation of impact velocity selection. - Page 104 – removed paragraph relating level 4 with catastrophic events. - Page 171 – added paragraph to specify the project will not assess already certified products. - Page 174 – removed paragraph relating level 4 with catastrophic events. - Page 184 – added recommendation: analyze more velocities and masses to be able to establish thresholds. - Page A-8-9 – added table 44 with comparison of relevant specifications of the fixed-wing and quadcopter UASs. - Appendix F – added appendix to describe data processing methods used in physical testing. 	18 Jul 2017

ACKNOWLEDGEMENTS

The authors would like to thank all the Federal Aviation Administration (FAA) personnel that has been involved in this research project. In particular, the authors would like to thank Sabrina Saunders-Hodge, Bill Oehlschlager, Paul Rumberger, and Paul Campbell for all their contributions and their valuable input throughout the research.

The authors would also like to thank General Jim Poss and Colonel Stephen P. Luxion from the FAA's Center of Excellence for Unmanned Aircraft Systems (ASSURE) for supporting this research.

The authors also acknowledge the contributions of the graduate research assistants from the National Institute for Aviation Research (NIAR) Computational Mechanics Laboratory: Armando Barriga, Hoa Ly, Rodrigo Marco, Sameer Naukudkar, and Nathaniel J. Baum; researchers from the NIAR Crash Dynamics Laboratory: Robert Huculak and Andy Mackey; and Mississippi State University (MSU) graduate researcher Prateek Jolly.

Last, but not least, thanks to all the industry participants that helped throughout the research.

TABLE OF CONTENTS

Chapter	Page
TABLE OF CONTENTS	VII
LIST OF FIGURES	XII
LIST OF ACRONYMS	XXXV
EXECUTIVE SUMMARY	XXXVI
1. INTRODUCTION	1
1.1 Background	1
1.1.1 Unmanned Aircraft Systems Categories	1
1.1.2 Unmanned Aircraft Systems Market Size	2
1.1.3 Unmanned Aircraft Systems Impact Severity Classification	4
1.2 Project Scope	6
2. FIXED-WING UAS PROJECTILE DEFINITION	8
2.1 Fixed-wing UAS Geometry and Specifications	8
2.2 Fixed-wing UAS Reverse Engineering	12
2.2.1 Data Collection	12
2.2.2 Material Designation	13
2.2.3 CAD Modeling	14
2.3 Finite Element Model	17
2.3.1 Discretization	17
2.3.2 Material Definitions	20
2.3.3 Connections	21
2.3.4 Contact Modeling	23
2.3.5 Fixed-Wing UAS Component Mass Check	25
2.4 UAS Component Level Tests and Verification	25
2.4.1 Ballistic Component Level Tests	26

2.4.2 Selection of Components for Ballistic Tests	26
2.4.3 Ballistic Test Setup	26
2.4.4 Ballistic Test Equipment	27
2.4.5 Test Matrix	29
2.4.6 Impact Test Results	32
2.4.7 Fixed-Wing UAS Component FE Models	36
2.4.8 Fixed-Wing UAS Component FE Model Verification	38
2.5 Fixed-wing FE Model Limitations	51
3. TARGET DEFINITION - COMMERCIAL TRANSPORT & BUSINESS JETS	52
3.1 Rationale for Selection of Targets and Impact Areas	54
3.1.1 Commercial Transport Jet	54
3.1.2 Business Jet	56
3.1.3 Aircraft Impact Areas	57
3.2 CAD Reverse Engineering	61
3.2.1 Commercial Transport Jet	62
3.2.2 Business Jet	68
3.3 Target Finite Element Model	73
3.3.1 Mesh Sensitivity Study	73
3.3.2 Mesh Quality Criteria	77
3.3.3 Discretization	78
3.3.4 Connections	87
3.3.5 Materials	89
3.3.6 Contacts	99
4. UAS – COLLISION ANALYSIS	100
4.1 Selection of Impact Conditions	100
4.1.1 Impact Velocity	100
4.1.2 Impact Conditions	101
4.1.3 Load Case Name Convention	104
4.1.4 Simulation Matrix	104
4.2 Damage Category Definition	105
4.2.1 Damage Levels	105

4.2.2 Fire Risk	106
4.3 Commercial Transport Jet Airborne Collision Studies	107
4.3.1 Vertical Stabilizer	108
4.3.2 Horizontal Stabilizer	112
4.3.3 Wing Leading Edge	116
4.3.4 Windshield	120
4.4 Business Jet Airborne Collision Studies	124
4.4.1 Vertical Stabilizer	125
4.4.2 Horizontal Stabilizer	129
4.4.3 Wing Leading Edge	133
4.4.4 Windshield	137
4.5 Conclusions	141
5. KINETIC ENERGY PARAMETRIC STUDIES	144
5.1 Introduction	144
5.1.1 Load Case Name Convention	144
5.2 Mass Sensitivity Study	145
5.2.1 UAS Scaling Methodology	145
5.2.2 Simulation Results	147
5.3 Velocity Parametric Study	149
5.3.1 Velocity Determination	150
5.3.2 Simulation Results	151
5.4 Conclusions	153
5.4.1 Mass	154
5.4.2 Velocity	154
5.4.3 Future Work	154
6. UAS IMPACT COMPARISON TO EQUIVALENT BIRD STRIKES	155
6.1 Bird Strike Requirements	155
6.2 Comparison Study	155
6.2.1 1.8 kg (4.0 lb) Bird – Simulation Results	156
6.2.2 3.6 kg (8.0 lb) Bird – Simulation Results	161
6.3 Conclusions	163

6.3.1 Summary	163
6.3.2 Future Work	163
7. COMPARISON BETWEEN BIRD, QUADCOPTER/FIXED-WING UAS IMPACTS	164
7.1 UAS Configuration Comparison	164
7.2 Comparison Study	164
7.2.1 Simulation Results –Bird and Quadcopter/Fixed-Wing UASs	166
7.2.2 Comparison of UAS Architectures – Quadcopter and Fixed-Wing	169
7.3 Conclusions	170
7.3.1 Future Work	170
8. CONCLUSIONS AND FUTURE WORK	172
8.1 Technical Approach	172
8.1.1 Building Block Approach FE Model Development and Validation	173
8.1.2 Verification and Validation FEA Models: Coupon to Sub-Assembly Level Testing	173
8.1.3 Selected Impact Conditions	174
8.1.4 Proposed Evaluation Criteria for Airborne Collisions	174
8.2 Airborne Collision severity evaluation	176
8.2.1 Unmanned Aircraft Systems Impact Severity Classification	176
8.2.2 Commercial Transport Jet Airborne Collisions	177
8.2.3 Business Jet Airborne Collision	179
8.2.4 Airborne Collision Impact Severity Study Conclusions	181
8.3 Impact Kinetic Energy and UAS Architecture Parametric Analyses	184
8.3.1 Mass	184
8.3.2 Impact Velocity	184
8.3.3 Conclusions Velocity and Mass Influence on Impact Damage	185
8.4 UAS Impact Comparisons to Equivalent Bird Impacts	186
8.4.1 Bird Strike – UAS Strike Comparison Conclusions	187
8.5 UAS System Architecture	188
8.6 Future Work	189
8.6.1 UAS Airborne Collision R&D Roadmap	189
8.6.2 Airborne Collision Studies Phase II: General Aviation and Rotorcraft	189

8.6.3 Airborne Collision Standard: Development of an Unmanned Aircraft Systems Mid-Air-Collisions Equivalent Level of Safety	190
8.6.4 UAS Certification by Analysis Protocol Development	190
8.6.5 Mass, Impact Velocity and Architecture Risk Classification	191
9. REFERENCES	192
APPENDIX A – FIXED-WING UAS MODEL DETAILS	A-1
APPENDIX B – IDENTIFICATION OF UAS CRITICAL COMPONENTS	B-1
APPENDIX C – AIRBORNE COLLISION ANALYSIS REPORT	C-1
APPENDIX D – MASS SENSITIVITY STUDY	D-1
APPENDIX E – VELOCITY SENSITIVITY STUDY	E-1
APPENDIX F – BIRD STRIKE COMPARISON	F-1
APPENDIX G – DATA PROCESSING METHODS	G-1

LIST OF FIGURES

Figure	Page
1. Top five sUAS markets [7]	4
2. sUAS fleet [7]	4
3. The Precision Hawk Lancaster Hawkeye Mark III	8
4. (A) Fixed-wing UAS fuselage subassembly and (B) Solder joint connecting transverse PCBs to the sidewalls	10
5. Plan view of the starboard wing of the fixed-wing UAS	10
6. Fixed-wing UAS tail subassembly	11
7. Fixed-wing UAS (A) Motor subassembly and (B) Motor components	12
8. Fixed-wing UAS battery (left) and payload (right) subassemblies	12
9. Fixed-wing UAS CAD model: (A) Front view, (B) Side view, and (C) Isometric view	14
10. CAD model of the fixed-wing UAS motor subassembly	15
11. CAD model of the fixed-wing UAS fuselage subassembly	15
12. CAD model of the fixed-wing UAS wing subassembly	15
13. CAD model of the fixed-wing UAS tail subassembly	16
14. CAD model of the fixed-wing UAS battery subassembly	16
15. CAD model of the fixed-wing UAS payload subassembly	16
16. Fixed-wing UAS parts modeled with shell elements	19
17. Fixed-wing UAS parts modeled with solid elements	19
18. Fixed-wing UAS fuselage and battery subassembly PCBs connected using a beam FE and rigid connectors	22
19. Fixed-wing UAS tail subassembly PCB supported by four zip ties	22
20. (A) Mounting bracket and (B) FE idealization	23
21. (A) Solder connection between PCBs and (B) FE idealization	25
22. Test frame setup for ballistic component level tests (LC = load cell)	27
23. Typical sabots for the fixed-wing UAS motor (left) and battery (right) subassembly	27
24. PCB Piezotronics load cell used in ballistic component level tests	28
25. Strain gages on test frame for ballistic component level tests	28
26. Measurement of the (A) Yaw and (B) Pitch angles at impact from a battery subassembly impact test	32
27. Deformation and fracture of target panel (2-5695) impacted with motor at 127.56 m/s: (A) Impact side (B) Back side	33

28.	Deformation and perforation of test panel impacted with motor at 65.2 m/s: (A) Impact side (B) Back side	34
29.	Motor (A) Before and (B) After 65.2 m/s impact test	34
30.	Permanent deformation of target panel 2-5693 impacted with battery subassembly at 120.09 m/s: (A) Impact side (B) Back side	35
31.	(A) Battery subassembly impact debris inside the target chamber and (B) Unfolding of the battery cell ribbon assembly	36
32.	(A) Fixed-wing UAS motor and (B) FE idealization	36
33.	(A) Fixed-wing UAS battery subassembly and (B) FE idealization	37
34.	(Left) Typical target panel and test frame assembly and (Right) FE idealization	38
35.	(Left) Typical target panel with strain gages and (Right) FE idealization	38
36.	Target panel strain gage and load cell locations	39
37.	Predicted motor contact reaction force with the target panel (impact velocity, 128.6 m/s)	39
38.	Measured and predicted target panel extensional strain in x -direction at a (A) Near-field (SG1) and (B) Far-field (SG3) strain gage for a motor impact at 128.6 m/s nominal velocity	40
39.	Measured and predicted force in the top left load cell for a motor impact at nominal velocity of 128.6 m/s	41
40.	High-speed images of a fixed-wing UAS motor impact (test 2-5695) at 127.56 m/s and a corresponding simulated nominal impact at four times: (A) $t = 0.0$ ms, (B) $t = 0.2$ ms, (C) $t = 0.4$ ms, and (D) $t = 0.6$ ms	42
41.	(A) Actual (target panel 2-5695) and (B) Simulated target panel after fixed-wing UAS motor impact at a 128.6 m/s nominal velocity	43
42.	(A) Actual (target panel 2-5700) and (B) Simulated target panel after an oblique fixed-wing UAS motor impact at a 130.61 m/s velocity	43
43.	Measured and predicted target panel extensional strain in the x -direction at a (A) near-field (SG1) and (B) Far-field (SG6) strain gage for a motor impact at a 65.2 m/s velocity	44
44.	High-speed images of a fixed-wing UAS motor impact (test 2-5699) at 65.2 m/s and a corresponding simulated nominal impact at four times: (A) $t = 0.0$ ms, (B) $t = 0.2$ ms, (C) $t = 0.5$ ms, and (D) $t = 0.7$ ms	45
45.	(A) actual (target panel 2-5699) and (B) simulated target panel after fixed-wing UAS motor impact at a 65.2 m/s impact velocity	46
46.	Measured and predicted target panel extensional strain in the x -direction at a (A) Near-field (SG1) and (B) Far-field (SG3) strain gage for a battery subassembly impact at a 128.6 m/s nominal velocity	47

47. (A) Measured (test 2-5693) and (B) Simulated target panel extensional strain in the x -direction at 1.5 ms during a fixed-wing UAS battery subassembly impact at a 128.6 m/s nominal velocity.	48
48. Measured and predicted force in the top left load cell for a battery subassembly impact at a nominal velocity of 128.6 m/s	49
49. Measured and predicted target panel out-of-plane displacement for the battery subassembly at a nominal impact velocity of 128.6 m/s	49
50. High-speed images of a fixed-wing UAS battery subassembly impact (test 2-5693) at 120.09 m/s and a corresponding simulated nominal impact at four times: (A) $t = 0$ ms, (B) $t = 1$ ms, (C) $t = 2$ ms, and (D) $t = 4$ ms	50
51. NIAR narrow body aircraft model developed for crashworthiness research	53
52. NIAR business jet aircraft model developed for crashworthiness research	53
53. Building block approach for the NIAR narrow body aircraft model	54
54. Current market outlook published by Boeing and Airbus (2014 to 2034) [48] [49]	55
55. Numerical proportion of civil aircraft components reported as being impacted and damaged by birds in the USA, 1990–2014 [55]	60
56. Civil aircraft components reported as being impacted and damaged by wildlife in the USA, 1990–2014 [55]	60
57. CFD flow analysis on the commercial transport jet model	61
58. Commercial transport jet overall dimensions	62
59. Commercial transport jet horizontal stabilizer	63
60. Commercial transport jet horizontal stabilizer CAD model	63
61. Commercial transport jet vertical stabilizer	64
62. Commercial transport jet vertical stabilizer CAD model	64
63. Commercial transport jet forward fuselage CAD construction	65
64. Commercial transport jet windshield	65
65. Commercial transport jet windshield cross-section	66
66. Commercial transport jet wing layout and selected area for UAS impacts	66
67. Commercial transport jet wing – leading edge CAD model	67
68. Commercial transport jet wing CAD model	67
69. Business jet dimensions	68
70. Business jet horizontal stabilizer	69
71. Business jet horizontal stabilizer CAD model and dimensions	69
72. Business jet vertical stabilizer	70
73. Business jet vertical stabilizer CAD model and dimensions	70

74. Business jet forward fuselage	71
75. Business jet windshield CAD model	71
76. Business jet windshield cross-section	71
77. Business jet wing	72
78. Business jet wing CAD model	72
79. Mesh sensitivity study flat plate FE model	74
80. Illustration of mesh size compared for mesh sensitivity study	75
81. Damage and effective plastic strain comparison for mesh sensitivity study	75
82. Reaction force time history for mesh sensitivity study	76
83. Peak reaction forces for different element lengths on flat plate impacted by a sphere.	76
84. Computational time comparison for mesh sensitivity study	76
85. Mesh size validation on motor component level test.	77
86. Commercial transport jet horizontal stabilizer - Geometry and mesh	79
87. Commercial transport jet horizontal stabilizer - Internal structure geometry and mesh	80
88. Commercial transport jet horizontal stabilizer - Mesh size	80
89. Commercial transport jet vertical stabilizer - Geometry and mesh	81
90. Commercial transport jet vertical stabilizer - Internal structure geometry and mesh	81
91. Commercial transport jet vertical stabilizer - Mesh size	82
92. Commercial transport jet windshield - Geometry and mesh	82
93. Commercial transport jet windshield - Mesh size	83
94. Commercial transport jet wing - Geometry and mesh	83
95. Commercial transport jet wing - Internal frames	83
96. Business jet horizontal stabilizer - Geometry and mesh	84
97. Business jet horizontal stabilizer - Mesh size	84
98. Business jet vertical stabilizer - Geometry and mesh	85
99. Business jet vertical stabilizer - Mesh size	85
100. Business jet front section - Geometry and mesh	86
101. Business jet front section - Mesh size	86
102. Business jet wing - Geometry and mesh	87
103. Business jet wing - Mesh size	87
104. Spot-weld beam connection	88
105. Nodal rigid body	88
106. Commercial transport jet front section and vertical stabilizer connections.	88

107. Material sensitivity study FE model set-up	90
108. Damage and failure comparison of different LS-DYNA material models on a generic leading edge impacted by a quadcopter UAS model	91
109. Stress strain curve for bi-linear elastic plastic [68]	92
110. MMPDS data for Aluminum 6061-T6 [67]	92
111. FE model of coupon for material verification	93
112. MMPDS Aluminum 6061-T6 material verification	93
113. Leading edge impact area	94
114. Windshield impact area	94
115. Commercial transport jet airframe materials of the subassemblies subject to study.	97
116. Business jet airframe materials of the subassemblies subject to study.	97
117. Commercial transport jet airframe gage thicknesses of metallic components.	98
118. Business jet airframe gage thicknesses of metallic components subject to study.	98
119. National Airspace System classifications [73]	101
120. UAS impact location parametric study setup	102
121. Kinematics of an UAS collision for impact location parametric study at 128.6 m/s	103
122. Commercial transport jet airborne collision simulation – Energy summary	108
123. UAS impact locations – Commercial jet vertical stabilizer	108
124. Energy distribution for commercial transport jet vertical stabilizer cases	109
125. Kinematics of the impact between a commercial transport jet vertical stabilizer and a 1.8 kg (4.0 lb) UAS at location 1 at 128.6 m/s (250 knots)	110
126. External/internal damage sustained by a commercial transport jet vertical stabilizer impacted at location 1 with a 1.8 kg (4.0 lb) UAS at 128.6 m/s (250 knots)	110
127. Impulse and energy balance of the impact between a commercial transport jet vertical stabilizer and a 1.8 kg (4.0 lb) fixed-wing UAS at location 1 at 128.6 m/s (250 knots)	111
128. Internal energy per component of the impact between a commercial transport jet vertical stabilizer and a 1.8 kg (4.0 lb) fixed-wing UAS at location 1 at 128.6 m/s (250 knots)	111
129. UAS impact locations – Commercial jet horizontal stabilizer	112
130. Energy distribution for commercial transport jet horizontal stabilizer cases	113
131. Kinematics of the impact between a commercial transport jet horizontal stabilizer and a 1.8 kg (4.0 lb) fixed-wing UAS at location 2 at 128.6 m/s (250 knots)	114
132. External/internal damage sustained by a commercial transport jet horizontal stabilizer impacted at location 2 with 1.8 kg (4.0 lb) fixed-wing UAS at 128.6 m/s (250 knots)	114

133. Impulse and energy balance of the impact between a commercial transport jet horizontal stabilizer and a 1.8 kg (4.0 lb) fixed-wing UAS at 128.6 m/s (250 knots)	115
134. Internal energy per component of the impact between a commercial transport jet horizontal stabilizer at location 2 and a 1.8 kg (4.0 lb) fixed-wing UAS at 128.6 m/s (250 knots)	115
135. UAS impact locations – Commercial jet wing	116
136. Energy distribution for commercial transport jet wing cases	117
137. Kinematics of the impact between a commercial transport jet wing at location 3 and a 1.8 kg (4.0 lb) fixed-wing UAS at 128.6 m/s (250 knots)	118
138. External/internal damage sustained by a commercial transport jet wing impacted at location 3 with a 1.8 kg (4.0 lb) fixed-wing UAS at 128.6 m/s (250 knots)	118
139. Impulse and energy balance of the impact between a commercial transport jet wing and a 1.8 kg (4.0 lb) fixed-wing UAS at 128.6 m/s (250 knots)	119
140. Internal energy per component of the impact between a commercial transport jet wing and a 1.8 kg (4.0 lb) fixed-wing UAS at 128.6 m/s (250 knots)	119
141. UAS impact locations – Commercial jet windshield	120
142. Energy distribution for commercial transport jet windshield cases	121
143. Kinematics of the impact between a commercial transport jet windshield at location 1 and a 1.8 kg (4.0 lb) fixed-wing UAS at 128.6 m/s (250 knots).	122
144. External/internal damage sustained by a commercial transport jet windshield impacted at location 1 with a 1.8 kg (4.0 lb) fixed-wing UAS at 128.6 m/s (250 knots)	122
145. Impulse and energy balance of the impact between a commercial transport jet windshield and a 1.8 kg (4.0 lb) fixed-wing UAS at 128.6 m/s (250 knots)	123
146. Internal energy per component of the impact between a commercial transport jet windshield and a 1.8 kg (4.0 lb) fixed-wing UAS at 128.6 m/s (250 knots)	123
147. Business jet airborne collision simulation – Energy summary	125
148. UAS impact locations – Business jet vertical stabilizer	125
149. Energy distribution for business jet vertical stabilizer cases	126
150. Kinematics of the impact between a business jet vertical stabilizer at location 1 and a 1.8 kg (4.0 lb) fixed-wing UAS at 128.6 m/s (250 knots)	127
151. External/internal damage sustained by a business jet vertical stabilizer impacted at location 1 with a 1.8 kg (4.0 lb) fixed-wing UAS at 128.6 m/s (250 knots)	127
152. Impulse and energy balance of the impact between a business jet vertical stabilizer at location 1 and a 1.8 kg (4.0 lb) fixed-wing UAS at 128.6 m/s (250 knots)	128
153. Internal energy per component of the impact between a business jet vertical stabilizer at location 1 and a 1.8 kg (4.0 lb) fixed-wing UAS at 128.6 m/s (250 knots)	128
154. UAS impact locations – business jet horizontal stabilizer	129

155. Energy distribution for business jet horizontal stabilizer cases	130
156. Kinematics of the impact between a business jet horizontal stabilizer at location 1 and a 1.8 kg (4.0 lb) fixed-wing UAS at 128.6 m/s (250 knots)	131
157. External/internal damage sustained by a business jet horizontal stabilizer impacted at location 1 with a 1.8 kg (4.0 lb) fixed-wing UAS at 128.6 m/s (250 knots)	131
158. Impulse and energy balance of the impact between a business jet horizontal stabilizer and a 1.8 kg (4.0 lb) fixed-wing UAS at 128.6 m/s (250 knots)	132
159. Internal energy per component of the impact between a business jet horizontal stabilizer and a 1.8 kg (4.0 lb) fixed-wing UAS at 128.6 m/s (250 knots)	132
160. UAS impact locations – business jet wing leading edge	133
161. Energy distribution for business jet wing cases	134
162. Kinematics of the impact between a business jet wing at location 2 and a 1.8 kg (4.0 lb) fixed-wing UAS at 128.6 m/s (250 knots)	135
163. External/internal damage sustained by a business jet wing impacted at location 2 with a 1.8 kg (4.0 lb) fixed-wing UAS at 128.6 m/s (250 knots)	135
164. Impulse and energy balance of the impact between a business jet wing and a 1.8 kg (4.0 lb) fixed-wing UAS at 128.6 m/s (250 knots)	136
165. Internal energy per component of the impact between a business jet wing and a 1.8 kg (4.0 lb) fixed-wing UAS at 128.6 m/s (250 knots)	136
166. UAS impact locations – Business jet cockpit windshield	137
167. Energy distribution for of business jet horizontal stabilizer cases	138
168. Kinematics of the impact between the business jet windshield and a 1.8 kg (4.0 lb) fixed-wing UAS at 128.6 m/s (250 knots)	139
169. External/internal damage sustained by the business jet windshield impacted at location 1 with a 1.8 kg (4.0 lb) fixed-wing UAS at 128.6 m/s (250 knots)	139
170. Impulse and energy balance of the impact between a business jet windshield and a 1.8 kg (4.0 lb) fixed-wing UAS at 128.6 m/s (250 knots)	140
171. Internal energy per component of the impact between a business jet windshield and a 1.8 kg (4.0 lb) fixed-wing UAS at 128.6 m/s (250 knots)	140
172. Summary of collision severity levels on commercial transport jet	142
173. Summary of collision severity levels on business jet	143
174. 1.0 scale and 1.3 scale fixed-wing UAS FE models: (a) front view and (b) side view	146
175. Comparison of skin and internal damage produced by a 1.8/3.6 kg (4.0/8.0 lb) UAS after impact with a commercial transport jet horizontal stabilizer	148
176. Comparison of the effective plastic deformation sustained by the inner layer of the commercial transport jet transparency after impact with a 1.8/3.6 kg (4.0/8.0 lb) UAS	148

177. Damage comparison in business jet vertical stabilizer on impact with 1.8/3.6 kg UAS	149
178. Comparison of windshield damage for CFCL1, CFC1, and CFCC1 – 56.7/128.6/187.8 m/s (110/250/365 knots)	152
179. Comparison of wing leading edge damage for CFWL3, CFW3, and CFWC3 – 56.7/128.6/187.8 m/s (110/250/365 knots)	152
180. Comparison of horizontal stabilizer damage for BFHL1, BFH1, and BFHC1 – 44.8/128.6/167.2 m/s (87/250/325 knots)	153
181. Kinematics of a commercial transport jet horizontal stabilizer impacted by an UAS (top) and a bird (bottom), of 1.8 kg (4.0 lb) – CFH2 vs. CB4H2	158
182. Comparison of damage on a commercial transport jet horizontal stabilizer, produced by a 1.8 kg (4.0 lb) UAS (left) and bird (right) impact at 128.6 m/s (250 knots)	158
183. Comparison of skin and internal damage produced by a 1.8 kg (4.0 lb) UAS and Bird after impact with a commercial transport jet wing leading edge	159
184. Comparison of skin and internal damage produced by a 1.8 kg (4.0 lb) UAS and Bird - business jet vertical stabilizer	160
185. Comparison of skin and internal damage produced by a 1.8 kg (4.0 lb) UAS and Bird after impact with a business jet wing leading edge	160
186. Comparison of skin and internal damage produced by a 3.6 kg (8.0 lb) UAS and Bird after impact with a commercial transport jet horizontal stabilizer	162
187. Comparison of skin and internal damage produced by a 3.6 kg (8.0 lb) UAS and Bird after impact with a business jet vertical stabilizer	162
188. Quadcopter UAS CAD model isometric view	164
189. UAS impact location – business jet vertical stabilizer	165
190. Comparison of impact kinematics for 1.8 kg (4.0 lb) projectiles: bird (top), quadcopter UAS (middle), and fixed-wing UAS (bottom)	167
191. Comparison of skin and internal damage produced by 1.8 kg (4.0 lb) projectiles: bird (left), quadcopter UAS (middle), and fixed-wing UAS (right)	167
192. Comparison of skin and internal damage produced by 1.8 kg (4.0 lb) projectiles: bird (left), quadcopter UAS (middle), fixed-wing UAS (right)	168
193. Contact force and impulse plots produced by 1.8 kg (4.0 lb) projectiles: bird, quadcopter, UAS, and fixed-wing UAS	168
194. Normalized energy balance plots produced by 1.8 kg (4.0 lb) projectiles: bird, quadcopter UAS, and fixed-wing UAS	169
195. Commercial transport jet airborne collision impact locations	177
196. Commercial transport jet airborne collision – Energy summary	178
197. Business jet airborne collision impact locations	180
198. Business jet airborne collision – Energy summary	181

199. Summary of collision severity levels on commercial transport jet	182
200. Summary of collision severity levels on business jet	183
201. Comparison of damage after impact of a 1.8 kg (4.0 lb) fixed-wing UAS/Bird into a business jet horizontal stabilizer	187
202. Comparison of damage after impact of 1.8 kg (4.0 lb) quadcopter (left) and fixed-wing (right) UASs into a business jet vertical stabilizer	189
203. Target panel strain gage and load cell locations	A-10
204. Measured and predicted target panel extensional strain in the x -direction at strain gages SG1-SG6 for a motor impact at 128.6 m/s nominal velocity	A-11
205. Measured and predicted target panel extensional strain in the y -direction at strain gages SG9-SG11 for a motor impact at 128.6 m/s nominal velocity	A-12
206. Measured and predicted target panel extensional strain at strain gages SG7, SG8, SG12 and SG13 for a motor impact at 128.6 m/s nominal velocity	A-13
207. Measured and predicted force in all four load cells for a motor impact at a nominal velocity of 128.6 m/s	A-14
208. Measured and predicted target panel extensional strain in the x -direction at strain gages SG1-SG6 for a motor impact at a 65.2 m/s velocity	A-15
209. Measured and predicted target panel extensional strain in the y -direction at strain gages SG9-SG11 for a motor impact at a 65.2 m/s velocity	A-16
210. Measured and predicted target panel extensional strain at strain gages SG7, SG8, SG12, and SG13 for a motor impact at a 65.2 m/s velocity	A-17
211. Measured and predicted force in all four load cells for a motor impact at a velocity of 65.2 m/s	A-18
212. Measured and predicted target panel extensional strain in the x -direction at strain gages SG1-SG6 for a battery subassembly impact at a 128.6 m/s nominal velocity	A-19
213. Measured and predicted target panel extensional strain in the y -direction at strain gages SG9-SG11 for a battery subassembly impact at a 128.6 m/s nominal velocity	A-20
214. Measured and predicted target panel extensional strain at strain gages SG7, SG8, SG12, and SG13 for a battery subassembly impact at a 128.6 m/s nominal velocity	A-21
215. Measured and predicted force in all four load cells for a battery subassembly impact at a nominal velocity of 128.6 m/s	A-22
216. Predicted total, kinetic, internal, hourglass, and contact energies for a 128.6 m/s fixed-wing UAS impact into the NIAR test frame	A-24
217. Predicted energy ratio for a 128.6 m/s fixed-wing UAS impact into the NIAR test frame	A-24
218. Isometric views of the predicted fixed-wing UAS impact at 128.6 m/s to the NIAR test frame at three times: (A) $t = 0$ ms, (B) $t = 2.5$ ms, and (C) $t = 5$ ms	A-25

219. Predicted fixed-wing UAS impact at 128.6 m/s to NIAR test frame at six times: (A) $t = 0$ ms, (B) $t = 1$ ms, (C) $t = 2$ ms, (D) $t = 3$ ms, (E) $t = 4$ ms, and (F) $t = 5$ ms	A-26
220. Predicted total, kinetic, internal, hourglass, and contact energies for a 128.6 m/s fixed-wing UAS impact into a rigid NIAR test frame	A-27
221. Predicted energy ratio for the fixed-wing UAS impact to a rigid NIAR test frame at 128.6 m/s	A-28
222. Schematic of the fixed-wing UAS rigid knife-edge impact (vertical sidewall not shown) at 128.6 m/s	A-28
223. Predicted total, kinetic, internal, hourglass, and contact energies for the rigid knife-edge impact of the fixed-wing UAS at 128.6 m/s	A-29
224. Predicted energy ratio for the rigid knife-edge impact of the fixed-wing UAS at 128.6 m/s	A-29
225. Material study setup	B-1
226. Material study results – effective plastic strain	B-2
227. Material study results – energy transfer	B-2
228. Mass distribution study setup	B-3
229. Mass distribution study results – effective plastic strain	B-4
230. Mass distribution study results – energy transfer	B-4
231. Comparison with hail impact setup	B-5
232. Comparison with hail impact results – effective plastic strain at 180 m/s (350 knots)	B-6
233. Comparison with hail impact results – contact loads and permanent deformation at 180 m/s (350 knots)	B-6
234. Kinematics of the impact between a commercial transport jet vertical stabilizer and a 1.8 kg (4.0 lb) UAS at location 2 at 128.6 m/s (250 knots)	C-1
235. External/internal damage sustained by a commercial transport jet vertical stabilizer impacted at location 2 with a 1.8 kg (4.0 lb) UAS at 128.6 m/s (250 knots)	C-2
236. Impulse and energy balance of the impact between a commercial transport jet vertical stabilizer and a 1.8 kg (4.0 lb) UAS at location 2 at 128.6 m/s (250 knots)	C-2
237. Internal energy per component of the impact between a commercial transport jet vertical stabilizer and a 1.8 kg (4.0 lb) UAS at location 2 at 128.6 m/s (250 knots)	C-3
238. Kinematics of the impact between a commercial transport jet vertical stabilizer and a 1.8 kg (4.0 lb) UAS at location 3 at 128.6 m/s (250 knots)	C-4
239. External/internal damage sustained by a commercial transport jet vertical stabilizer impacted at location 3 with a 1.8 kg (4.0 lb) UAS at 128.6 m/s (250 knots)	C-4
240. Impulse and energy balance of the impact between a commercial transport jet vertical stabilizer and a 1.8 kg (4.0 lb) UAS at location 3 at 128.6 m/s (250 knots)	C-5

241. Internal energy per component of the impact between a commercial transport jet vertical stabilizer and a 1.8 kg (4.0 lb) UAS at location 3 at 128.6 m/s (250 knots) C-5
242. Kinematics of the impact between a commercial transport jet vertical stabilizer and a 1.8 kg (4.0 lb) UAS at location 4 at 128.6 m/s (250 knots) C-6
243. External/internal damage sustained by a commercial transport jet vertical stabilizer impacted at location 4 with a 1.8 kg (4.0 lb) UAS at 128.6 m/s (250 knots) C-6
244. Impulse and energy balance of the impact between a commercial transport jet vertical stabilizer and a 1.8 kg (4.0 lb) UAS at location 4 at 128.6 m/s (250 knots) C-7
245. Internal energy per component of the impact between a commercial transport jet vertical stabilizer and a 1.8 kg (4.0 lb) UAS at location 4 at 128.6 m/s (250 knots) C-7
246. Kinematics of the impact between a commercial transport jet horizontal stabilizer and a 1.8 kg (4.0 lb) UAS at location 1 at 128.6 m/s (250 knots) C-8
247. External/internal damage sustained by a commercial transport jet horizontal stabilizer impacted at location 1 with a 1.8 kg (4.0 lb) UAS at 128.6 m/s (250 knots) C-9
248. Impulse and energy balance of the impact between a commercial transport jet horizontal stabilizer and a 1.8 kg (4.0 lb) UAS at location 1 at 128.6 m/s (250 knots) C-9
249. Internal energy per component of the impact between commercial transport jet horizontal stabilizer and 1.8 kg (4.0 lb) UAS at location 1 at 128.6 m/s (250 knots) C-10
250. Kinematics of the impact between a commercial transport jet horizontal stabilizer and a 1.8 kg (4.0 lb) UAS at location 3 at 128.6 m/s (250 knots) C-11
251. External/internal damage sustained by a commercial transport jet horizontal stabilizer impacted at location 3 with 1.8 kg (4.0 lb) UAS at 128.6 m/s (250 knots) C-11
252. Impulse and energy balance of the impact between a commercial transport jet horizontal stabilizer and a 1.8 kg (4.0 lb) UAS at location 3 at 128.6 m/s (250 knots) C-12
253. Internal energy per component of the impact between commercial transport jet horizontal stabilizer and 1.8 kg (4.0 lb) UAS at location 3 at 128.6 m/s (250 knots) C-12
254. Kinematics of the impact between a commercial transport jet horizontal stabilizer and a 1.8 kg (4.0 lb) UAS at location 4 at 128.6 m/s (250 knots) C-13
255. External/internal damage sustained by a commercial transport jet horizontal stabilizer impacted at location 4 with a 1.8 kg (4.0 lb) UAS at 128.6 m/s (250 knots) C-13
256. Impulse and energy balance of the impact between a commercial transport jet horizontal stabilizer and a 1.8 kg (4.0 lb) UAS at location 4 at 128.6 m/s (250 knots) C-14
257. Internal energy per component of the impact between commercial transport jet horizontal stabilizer and 1.8 kg (4.0 lb) UAS at location 4 at 128.6 m/s (250 knots) C-14
258. Kinematics of the impact between a commercial transport jet horizontal stabilizer and a 1.8 kg (4.0 lb) UAS at location 5 at 128.6 m/s (250 knots) C-15
259. External/internal damage sustained by a commercial transport jet horizontal stabilizer impacted at location 5 with a 1.8 kg (4.0 lb) UAS at 128.6 m/s (250 knots) C-16

260. Impulse and energy balance of the impact between a commercial transport jet horizontal stabilizer and a 1.8 kg (4.0 lb) UAS at location 5 at 128.6 m/s (250 knots) C-16
261. Internal energy per component of the impact between commercial transport jet horizontal stabilizer and 1.8 kg (4.0 lb) UAS at location 5 at 128.6 m/s (250 knots) C-17
262. Kinematics of the impact between a commercial transport jet wing and a 1.8 kg (4.0 lb) UAS at location 1 at 128.6 m/s (250 knots) C-18
263. External/internal damage sustained by a commercial transport jet wing impacted at location 1 with a 1.8 kg (4.0 lb) UAS at 128.6 m/s (250 knots) C-18
264. Impulse and energy balance of the impact between a commercial transport jet wing and a 1.8 kg (4.0 lb) UAS at location 1 at 128.6 m/s (250 knots) C-19
265. Internal energy per component of the impact between a commercial transport jet wing and a 1.8 kg (4.0 lb) UAS at location 1 at 128.6 m/s (250 knots) C-19
266. Kinematics of the impact between a commercial transport jet wing and a 1.8 kg (4.0 lb) UAS at location 2 at 128.6 m/s (250 knots) C-20
267. External/internal damage sustained by a commercial transport jet wing impacted at location 2 with a 1.8 kg (4.0 lb) UAS at 128.6 m/s (250 knots) C-20
268. Impulse and energy balance of the impact between a commercial transport jet wing and a 1.8 kg (4.0 lb) UAS at location 2 at 128.6 m/s (250 knots) C-21
269. Internal energy per component of the impact between a commercial transport jet wing and a 1.8 kg (4.0 lb) UAS at location 2 at 128.6 m/s (250 knots) C-21
270. Kinematics of the impact between a commercial transport jet wing and a 1.8 kg (4.0 lb) UAS at location 4 at 128.6 m/s (250 knots) C-22
271. External/internal damage sustained by a commercial transport jet wing impacted at location 4 with a 1.8 kg (4.0 lb) UAS at 128.6 m/s (250 knots) C-23
272. Impulse and energy balance of the impact between a commercial transport jet wing and a 1.8 kg (4.0 lb) UAS at location 4 at 128.6 m/s (250 knots) C-23
273. Internal energy per component of the impact between a commercial transport jet wing and a 1.8 kg (4.0 lb) UAS at location 4 at 128.6 m/s (250 knots) C-24
274. Kinematics of the impact between a commercial transport jet windshield and a 1.8 kg (4.0 lb) UAS at location 2 at 128.6 m/s (250 knots) C-25
275. External/internal damage sustained by a commercial transport jet windshield impacted at location 2 with a 1.8 kg (4.0 lb) UAS at 128.6 m/s (250 knots) C-25
276. Impulse and energy balance of the impact between a commercial transport jet windshield and a 1.8 kg (4.0 lb) UAS at location 2 at 128.6 m/s (250 knots) C-26
277. Internal energy per component of the impact between a commercial transport jet windshield and a 1.8 kg (4.0 lb) UAS at location 2 at 128.6 m/s (250 knots) C-26
278. Kinematics of the impact between a commercial transport jet windshield and a 1.8 kg (4.0 lb) UAS at location 3 at 128.6 m/s (250 knots) C-27

279. External/internal damage sustained by a commercial transport jet windshield impacted at location 3 with a 1.8 kg (4.0 lb) UAS at 128.6 m/s (250 knots) C-27
280. Impulse and energy balance of the impact between a commercial transport jet windshield and a 1.8 kg (4.0 lb) UAS at location 3 at 128.6 m/s (250 knots) C-28
281. Internal energy per component of the impact between a commercial transport jet windshield and a 1.8 kg (4.0 lb) UAS at location 3 at 128.6 m/s (250 knots) C-28
282. Kinematics of the impact between a business jet vertical stabilizer and a 1.8 kg (4.0 lb) UAS at location 2 at 128.6 m/s (250 knots) C-30
283. External/internal damage sustained by a business jet vertical stabilizer impacted at location 2 with a 1.8 kg (4.0 lb) UAS at 128.6 m/s (250 knots) C-31
284. Impulse and energy balance of the impact between a business jet vertical stabilizer and a 1.8 kg (4.0 lb) UAS at location 2 at 128.6 m/s (250 knots) C-31
285. Internal energy per component of the impact between a business jet vertical stabilizer and a 1.8 kg (4.0 lb) UAS at location 2 at 128.6 m/s (250 knots) C-32
286. Kinematics of the impact between a business jet vertical stabilizer and a 1.8 kg (4.0 lb) UAS at location 3 at 128.6 m/s (250 knots) C-33
287. External/internal damage sustained by a business jet vertical stabilizer impacted at location 3 with a 1.8 kg (4.0 lb) UAS at 128.6 m/s (250 knots) C-33
288. Impulse and energy balance of the impact between a business jet vertical stabilizer and a 1.8 kg (4.0 lb) UAS at location 3 at 128.6 m/s (250 knots) C-34
289. Internal energy per component of the impact between a business jet vertical stabilizer and a 1.8 kg (4.0 lb) UAS at location 3 at 128.6 m/s (250 knots) C-34
290. Kinematics of the impact between a business jet horizontal stabilizer and a 1.8 kg (4.0 lb) UAS at location 2 at 128.6 m/s (250 knots) C-35
291. External/internal damage sustained by a business jet horizontal stabilizer impacted at location 2 with a 1.8 kg (4.0 lb) UAS at 128.6 m/s (250 knots) C-35
292. Impulse and energy balance of the impact between a business jet horizontal stabilizer and a 1.8 kg (4.0 lb) UAS at location 2 at 128.6 m/s (250 knots) C-36
293. Internal energy per component of the impact between a business jet horizontal stabilizer and a 1.8 kg (4.0 lb) UAS at location 2 at 128.6 m/s (250 knots) C-36
294. Kinematics of the impact between a business jet horizontal stabilizer and a 1.8 kg (4.0 lb) UAS at location 3 at 128.6 m/s (250 knots) C-37
295. External/internal damage sustained by a business jet horizontal stabilizer impacted at location 3 with a 1.8 kg (4.0 lb) UAS at 128.6 m/s (250 knots) C-38
296. Impulse and energy balance of the impact between a business jet horizontal stabilizer and a 1.8 kg (4.0 lb) UAS at location 3 at 128.6 m/s (250 knots) C-38
297. Internal energy per component of the impact between a business jet horizontal stabilizer and a 1.8 kg (4.0 lb) UAS at location 3 at 128.6 m/s (250 knots) C-39

298. Kinematics of the impact between a business jet wing and a 1.8 kg (4.0 lb) UAS at location 1 at 128.6 m/s (250 knots) C-40
299. External/internal damage sustained by a business jet wing impacted at location 1 with a 1.8 kg (4.0 lb) UAS at 128.6 m/s (250 knots) C-40
300. Impulse and energy balance of the impact between a business jet wing and a 1.8 kg (4.0 lb) UAS at location 1 at 128.6 m/s (250 knots) C-41
301. Internal energy per component of the impact between a business jet wing and a 1.8 kg (4.0 lb) UAS at location 1 at 128.6 m/s (250 knots) C-41
302. Kinematics of the impact between a business jet wing and a 1.8 kg (4.0 lb) UAS at location 3 at 128.6 m/s (250 knots) C-42
303. External/internal damage sustained by a business jet wing impacted at location 3 with a 1.8 kg (4.0 lb) UAS at 128.6 m/s (250 knots) C-42
304. Impulse and energy balance of the impact between a business jet wing and a 1.8 kg (4.0 lb) UAS at location 3 at 128.6 m/s (250 knots) C-43
305. Internal energy per component of the impact between a business jet wing and a 1.8 kg (4.0 lb) UAS at location 3 at 128.6 m/s (250 knots) C-43
306. Kinematics of the impact between a business jet windshield and a 1.8 kg (4.0 lb) UAS at location 2 at 128.6 m/s (250 knots) C-44
307. External/internal damage sustained by a business jet windshield impacted at location 2 with a 1.8 kg (4.0 lb) UAS at 128.6 m/s (250 knots) C-45
308. Impulse and energy balance of the impact between a business jet windshield and a 1.8 kg (4.0 lb) UAS at location 2 at 128.6 m/s (250 knots) C-45
309. Internal energy per component of the impact between a business jet windshield and a 1.8 kg (4.0 lb) UAS at location 2 at 128.6 m/s (250 knots) C-46
310. Kinematics of the impact between a business jet windshield and a 1.8 kg (4.0 lb) UAS at location 3 at 128.6 m/s (250 knots) C-46
311. External/internal damage sustained by a business jet windshield impacted at location 3 with a 1.8 kg (4.0 lb) UAS at 128.6 m/s (250 knots) C-47
312. Impulse and energy balance of the impact between a business jet windshield and a 1.8 kg (4.0 lb) UAS at location 3 at 128.6 m/s (250 knots) C-48
313. Internal energy per component of the impact between a business jet windshield and a 1.8 kg (4.0 lb) UAS at location 3 at 128.6 m/s (250 knots) C-48
314. Comparison of the impact kinematics between a commercial transport jet vertical stabilizer and a 1.8/3.6 kg (4.0/8.0 lb) UAS at 128.6 m/s (250 knots) D-1
315. Comparison of external/internal damage sustained by a commercial transport jet vertical stabilizer impacted with a 1.8/3.6 kg (4.0/8.0 lb) UAS at 128.6 m/s (250 knots) D-2
316. Comparison of the contact force and impulse of the impact between a commercial transport jet vertical stabilizer and a 1.8/3.6 kg (4.0/8.0 lb) UAS at 128.6 m/s (250 knots) D-2

317. Comparison of the energy balance of the impact between a commercial transport jet vertical stabilizer and a 1.8/3.6 kg (4.0/8.0 lb) UAS at 128.6 m/s (250 knots) D-3
318. Comparison of the impact kinematics between a commercial transport jet horizontal stabilizer and a 1.8/3.6 kg (4.0/8.0 lb) UAS at 128.6 m/s (250 knots) D-4
319. Comparison of external/internal damage sustained by a commercial transport jet horizontal stabilizer impacted with a 1.8/3.6 kg (4.0/8.0 lb) UAS at 128.6 m/s (250 knots) D-4
320. Comparison of the contact force and impulse of the impact between a commercial transport jet horizontal stabilizer and a 1.8/3.6 kg (4.0/8.0 lb) UAS at 128.6 m/s (250 knots) D-5
321. Comparison of the energy balance of the impact between a commercial transport jet horizontal stabilizer and a 1.8/3.6 kg (4.0/8.0 lb) UAS at 128.6 m/s (250 knots) D-5
322. Comparison of the impact kinematics between a commercial transport jet wing and a 1.8/3.6 kg (4.0/8.0 lb) UAS at 128.6 m/s (250 knots) D-6
323. Comparison of external/internal damage sustained by a commercial transport jet wing impacted with a 1.8/3.6 kg (4.0/8.0 lb) UAS at 128.6 m/s (250 knots) D-6
324. Comparison of the contact force and impulse of the impact between a commercial transport jet wing and a 1.8/3.6 kg (4.0/8.0 lb) UAS at 128.6 m/s (250 knots) D-7
325. Comparison of the energy balance of the impact between a commercial transport jet wing and a 1.8/3.6 kg (4.0/8.0 lb) UAS at 128.6 m/s (250 knots) D-7
326. Comparison of the impact kinematics between a commercial transport jet windshield and a 1.8/3.6 kg (4.0/8.0 lb) UAS at 128.6 m/s (250 knots) D-8
327. Comparison of external/internal damage sustained by a commercial transport jet windshield impacted with a 1.8/3.6 kg (4.0/8.0 lb) UAS at 128.6 m/s (250 knots) D-9
328. Comparison of the contact force and impulse of the impact between a commercial transport jet windshield and a 1.8/3.6 kg (4.0/8.0 lb) UAS at 128.6 m/s (250 knots) D-9
329. Comparison of the energy balance of the impact between a commercial transport jet windshield and a 1.8/3.6 kg (4.0/8.0 lb) UAS at 128.6 m/s (250 knots) D-10
330. Comparison of the impact kinematics between a business jet vertical stabilizer and a 1.8/3.6 kg (4.0/8.0 lb) UAS at 128.6 m/s (250 knots) D-11
331. Comparison of external/internal damage sustained by a business jet vertical stabilizer impacted with a 1.8/3.6 kg (4.0/8.0 lb) UAS at 128.6 m/s (250 knots) D-11
332. Comparison of the contact force and impulse of the impact between a business jet vertical stabilizer and a 1.8/3.6 kg (4.0/8.0 lb) UAS at 128.6 m/s (250 knots) D-12
333. Comparison of the energy balance of the impact between a business jet vertical stabilizer and a 1.8/3.6 kg (4.0/8.0 lb) UAS at 128.6 m/s (250 knots) D-12
334. Comparison of the impact kinematics between a business jet horizontal stabilizer and a 1.8/3.6 kg (4.0/8.0 lb) UAS at 128.6 m/s (250 knots) D-13

335. Comparison of external/internal damage sustained by a business jet horizontal stabilizer impacted with a 1.8/3.6 kg (4.0/8.0 lb) UAS at 128.6 m/s (250 knots) D-13
336. Comparison of the contact force and impulse of the impact between a business jet horizontal stabilizer and a 1.8/3.6 kg (4.0/8.0 lb) UAS at 128.6 m/s (250 knots) D-14
337. Comparison of the energy balance of the impact between a business jet horizontal stabilizer and a 1.8/3.6 kg (4.0/8.0 lb) UAS at 128.6 m/s (250 knots) D-14
338. Comparison of the impact kinematics between a business jet wing and a 1.8/3.6 kg (4.0/8.0 lb) UAS at 128.6 m/s (250 knots) D-15
339. Comparison of external/internal damage sustained by a business jet wing impacted with a 1.8/3.6 kg (4.0/8.0 lb) UAS at 128.6 m/s (250 knots) D-16
340. Comparison of the contact force and impulse of the impact between a business jet wing and a 1.8/3.6 kg (4.0/8.0 lb) UAS at 128.6 m/s (250 knots) D-16
341. Comparison of the energy balance of the impact between a business jet wing and a 1.8/3.6 kg (4.0/8.0 lb) UAS at 128.6 m/s (250 knots) D-17
342. Comparison of the impact kinematics between a business jet windshield and a 1.8/3.6 kg (4.0/8.0 lb) UAS at 128.6 m/s (250 knots) D-17
343. Comparison of external/internal damage sustained by a business jet windshield impacted with a 1.8/3.6 kg (4.0/8.0 lb) UAS at 128.6 m/s (250 knots) D-18
344. Comparison of the contact force and impulse of the impact between a business jet windshield and a 1.8/3.6 kg (4.0/8.0 lb) UAS at 128.6 m/s (250 knots) D-19
345. Comparison of the energy balance of the impact between a business jet windshield and a 1.8/3.6 kg (4.0/8.0 lb) UAS at 128.6 m/s (250 knots) D-19
346. Comparison of the impact kinematics between a commercial transport jet vertical stabilizer and a 1.81 kg UAS at 56.7/128.6/187.8 m/s (110/250/365 knots) E-1
347. Comparison of external/internal damage sustained by a commercial transport jet vertical stabilizer impacted with a 1.81 kg UAS at 56.7/128.6/187.8 m/s (110/250/365 knots) E-2
348. Comparison of the contact force and impulse of the impact between a commercial transport jet vertical stabilizer and a 1.81 kg UAS at 56.7/128.6/187.8 m/s (110/250/365 knots) E-2
349. Comparison of the normalized energy balance of the impact between a commercial transport jet vertical stabilizer and a 1.81 kg UAS at 56.7/128.6/187.8 m/s (110/250/365 knots) E-3
350. Comparison of the impact kinematics between a commercial transport jet horizontal stabilizer and a 1.81 kg UAS at 56.7/128.6/187.8 m/s (110/250/365 knots) E-3
351. Comparison of external/internal damage sustained by a commercial transport jet horizontal stabilizer impacted with a 1.81 kg UAS at 56.7/128.6/187.8 m/s (110/250/365 knots) E-4

352. Comparison of the contact force and impulse of the impact between a commercial transport jet horizontal stabilizer and a 1.81 kg UAS at 56.7/128.6/187.8 m/s (110/250/365 knots) E-4
353. Comparison of the normalized energy balance of the impact between a commercial transport jet horizontal stabilizer and a 1.81 kg UAS at 56.7/128.6/187.8 m/s (110/250/365 knots) E-5
354. Comparison of the impact kinematics between a commercial transport jet wing and a 1.81 kg UAS at 56.7/128.6/187.8 m/s (110/250/365 knots) E-6
355. Comparison of external/internal damage sustained by a commercial transport jet wing impacted with a 1.81 kg UAS at 56.7/128.6/187.8 m/s (110/250/365 knots) E-6
356. Comparison of the contact force and impulse of the impact between a commercial transport jet wing and a 1.81 kg UAS at 56.7/128.6/187.8 m/s (110/250/365 knots) E-7
357. Comparison of the normalized energy balance of the impact between a commercial transport jet wing and a 1.81 kg UAS at 56.7/128.6/187.8 m/s (110/250/365 knots) E-7
358. Comparison of the impact kinematics between a commercial transport jet windshield and a 1.81 kg UAS at 56.7/128.6/187.8 m/s (110/250/365 knots) E-8
359. Comparison of external/internal damage sustained by a commercial transport jet windshield impacted with a 1.81 kg UAS at 56.7/128.6/187.8 m/s (110/250/365 knots) E-8
360. Comparison of the contact force and impulse of the impact between a commercial transport jet windshield and a 1.81 kg UAS at 56.7/128.6/187.8 m/s (110/250/365 knots) E-9
361. Comparison of the normalized energy balance of the impact between a commercial transport jet windshield and a 1.81 kg UAS at 56.7/128.6/187.8 m/s (110/250/365 knots) E-9
362. Comparison of the impact kinematics between a business jet vertical stabilizer and a 1.81 kg UAS at 44.7/128.6/167.2 m/s (87/250/325 knots) E-10
363. Comparison of external/internal damage sustained by a business jet vertical stabilizer impacted with a 1.81 kg UAS at 44.7/128.6/167.2 m/s (87/250/325 knots) E-11
364. Comparison of the contact force and impulse of the impact between a business jet vertical stabilizer and a 1.81 kg UAS at 44.7/128.6/167.2 m/s (87/250/325 knots) E-11
365. Comparison of the normalized energy balance of the impact between a business jet vertical stabilizer and a 1.81 kg UAS at 44.7/128.6/167.2 m/s (87/250/325 knots) E-12
366. Comparison of the impact kinematics between a business jet horizontal stabilizer and a 1.81 kg UAS at 44.7/128.6/167.2 m/s (87/250/325 knots) E-12
367. Comparison of external/internal damage sustained by a business jet horizontal stabilizer impacted with a 1.81 kg UAS at 44.7/128.6/167.2 m/s (87/250/325 knots) E-13
368. Comparison of the contact force and impulse of the impact between business jet horizontal stabilizer and 1.81 kg UAS at 44.7/128.6/167.2 m/s (87/250/325 knots) E-13

369. Comparison of the normalized energy balance of the impact between business jet horizontal stabilizer and 1.81 kg UAS at 44.7/128.6/167.2 m/s (87/250/325 knots) E-14
370. Comparison of the impact kinematics between a business jet wing and a 1.81 kg UAS at 44.7/128.6/167.2 m/s (87/250/325 knots) E-14
371. Comparison of external/internal damage sustained by a business jet wing impacted with a 1.81 kg UAS at 44.7/128.6/167.2 m/s (87/250/325 knots) E-15
372. Comparison of the contact force and impulse of the impact between a business jet wing and a 1.81 kg UAS at 44.7/128.6/167.2 m/s (87/250/325 knots) E-15
373. Comparison of the normalized energy balance of the impact between a business jet wing and a 1.81 kg UAS at 44.7/128.6/167.2 m/s (87/250/325 knots) E-16
374. Comparison of the impact kinematics between a business jet windshield and a 1.81 kg UAS at 44.7/128.6/167.2 m/s (87/250/325 knots) E-16
375. Comparison of external/internal damage sustained by a business jet windshield impacted with a 1.81 kg UAS at 44.7/128.6/167.2 m/s (87/250/325 knots) E-17
376. Comparison of the contact force and impulse of the impact between a business jet windshield and a 1.81 kg UAS at 44.7/128.6/167.2 m/s (87/250/325 knots) E-17
377. Comparison of the normalized energy balance of the impact between a business jet windshield and a 1.81 kg UAS at 44.7/128.6/167.2 m/s (87/250/325 knots) E-18
378. Comparison of the kinematics of impact between a commercial transport jet vertical stabilizer and a 1.8 kg (4.0 lb) UAS/Bird at 128.6 m/s (250 knots) F-1
379. Comparison of external/internal damage sustained by a commercial transport jet vertical stabilizer impacted with a 1.8 kg (4.0 lb) UAS/Bird at 128.6 m/s (250 knots) F-2
380. Comparison of the energy balance of the impact between a commercial transport jet vertical stabilizer and a 1.8 kg (4.0 lb) UAS/bird at 128.6 m/s (250 knots) F-2
381. Comparison of the kinematics of impact between a commercial transport jet horizontal stabilizer and a 1.8 kg (4.0 lb) UAS/Bird at 128.6 m/s (250 knots) F-3
382. Comparison of external/internal damage sustained by a commercial transport jet horizontal stabilizer impacted with a 1.8 kg (4.0 lb) UAS/Bird at 128.6 m/s (250 knots) F-4
383. Comparison of the contact force and impulse of the impact between a commercial transport jet horizontal stabilizer and a 1.8 kg (4.0 lb) UAS/bird at 128.6 m/s (250 knots) F-4
384. Comparison of the energy balance of the impact between a commercial transport jet horizontal stabilizer and a 1.8 kg (4.0 lb) UAS/bird at 128.6 m/s (250 knots) F-5
385. Comparison of the kinematics of impact between a commercial transport jet wing and a 1.8 kg (4.0 lb) UAS/Bird at 128.6 m/s (250 knots) F-6
386. Comparison of external/internal damage sustained by a commercial transport jet wing impacted with a 1.8 kg (4.0 lb) UAS/Bird at 128.6 m/s (250 knots) F-6

387. Comparison of the contact force and impulse of the impact between a commercial transport jet wing and a 1.8 kg (4.0 lb) UAS/bird at 128.6 m/s (250 knots) F-7
388. Comparison of the energy balance of the impact between a commercial transport jet wing and a 1.8 kg (4.0 lb) UAS/bird at 128.6 m/s (250 knots) F-7
389. Comparison of the kinematics of impact between a commercial transport jet windshield and a 1.8 kg (4.0 lb) UAS/Bird at 128.6 m/s (250 knots) F-8
390. Comparison of external/internal damage sustained by a commercial transport jet windshield impacted with a 1.8 kg (4.0 lb) UAS/Bird at 128.6 m/s (250 knots) F-8
391. Comparison of the contact force and impulse of the impact between a commercial transport jet windshield and a 1.8 kg (4.0 lb) UAS/bird at 128.6 m/s (250 knots) F-9
392. Comparison of the energy balance of the impact between a commercial transport jet windshield and a 1.8 kg (4.0 lb) UAS/bird at 128.6 m/s (250 knots) F-9
393. Comparison of the kinematics of impact between a business jet vertical stabilizer and a 1.8 kg (4.0 lb) UAS/Bird at 128.6 m/s (250 knots) F-10
394. Comparison of external/internal damage sustained by a business jet vertical stabilizer impacted with a 1.8 kg (4.0 lb) UAS/Bird at 128.6 m/s (250 knots) F-11
395. Comparison of the contact force and impulse of the impact between a business jet vertical stabilizer and a 1.8 kg (4.0 lb) UAS/bird at 128.6 m/s (250 knots) F-11
396. Comparison of the energy balance of the impact between a business jet vertical stabilizer and a 1.8 kg (4.0 lb) UAS/bird at 128.6 m/s (250 knots) F-12
397. Comparison of the kinematics of impact between a business jet horizontal stabilizer and a 1.8 kg (4.0 lb) UAS/Bird at 128.6 m/s (250 knots) F-12
398. Comparison of external/internal damage sustained by a business jet horizontal stabilizer impacted with a 1.8 kg (4.0 lb) UAS/Bird at 128.6 m/s (250 knots) F-13
399. Comparison of the contact force and impulse of the impact between a business jet horizontal stabilizer and a 1.8 kg (4.0 lb) UAS/bird at 128.6 m/s (250 knots) F-13
400. Comparison of the energy balance of the impact between a business jet horizontal stabilizer and a 1.8 kg (4.0 lb) UAS/bird at 128.6 m/s (250 knots) F-14
401. Comparison of the kinematics of impact between a business jet wing and a 1.8 kg (4.0 lb) UAS/bird at 128.6 m/s (250 knots) F-15
402. Comparison of external/internal damage sustained by a business jet wing impacted with a 1.8 kg (4.0 lb) UAS/bird at 128.6 m/s (250 knots) F-15
403. Comparison of the contact force and impulse of the impact between a business jet wing and a 1.8 kg (4.0 lb) UAS/bird at 128.6 m/s (250 knots) F-16
404. Comparison of the energy balance of the impact between a business jet wing and a 1.8 kg (4.0 lb) UAS/bird at 128.6 m/s (250 knots) F-16
405. Comparison of the kinematics of impact between a business jet windshield and a 1.8 kg (4.0 lb) UAS/Bird at 128.6 m/s (250 knots) F-17

406. Comparison of external/internal damage sustained by a business jet windshield impacted with a 1.8 kg (4.0 lb) UAS/Bird at 128.6 m/s (250 knots) F-17
407. Comparison of the contact force and impulse of the impact between a business jet windshield and a 1.8 kg (4.0 lb) UAS/bird at 128.6 m/s (250 knots) F-18
408. Comparison of the energy balance of the impact between a business jet windshield and a 1.8 kg (4.0 lb) UAS/bird at 128.6 m/s (250 knots) F-18
409. Comparison of the kinematics of impact between a commercial transport jet vertical stabilizer and a 3.6 kg (8.0 lb) UAS/Bird at 128.6 m/s (250 knots) F-19
410. Comparison of external/internal damage sustained by a commercial transport jet vertical stabilizer impacted with a 3.6 kg (8.0 lb) UAS/Bird at 128.6 m/s (250 knots) F-20
411. Comparison of the contact force and impulse of the impact between a commercial transport jet vertical stabilizer and a 3.6 kg (8.0 lb) UAS/bird at 128.6 m/s (250 knots) F-20
412. Comparison of the energy balance of the impact between a commercial transport jet vertical stabilizer and a 3.6 kg (8.0 lb) UAS/bird at 128.6 m/s (250 knots) F-21
413. Comparison of the kinematics of impact between a commercial transport jet horizontal stabilizer and a 3.6 kg (8.0 lb) UAS/Bird at 128.6 m/s (250 knots) F-22
414. Comparison of external/internal damage sustained by a commercial transport jet horizontal stabilizer impacted with a 3.6 kg (8.0 lb) UAS/Bird at 128.6 m/s (250 knots) F-22
415. Comparison of the contact force and impulse of the impact between a commercial transport jet horizontal stabilizer and a 3.6 kg (8.0 lb) UAS/bird at 128.6 m/s (250 knots) F-23
416. Comparison of the energy balance of the impact between a commercial transport jet horizontal stabilizer and a 3.6 kg (8.0 lb) UAS/bird at 128.6 m/s (250 knots) F-23
417. Comparison of the kinematics of impact between a business jet vertical stabilizer and a 3.6 kg (8.0 lb) UAS/Bird at 128.6 m/s (250 knots) F-24
418. Comparison of external/internal damage sustained by a business jet vertical stabilizer impacted with a 3.6 kg (8.0 lb) UAS/Bird at 128.6 m/s (250 knots) F-25
419. Comparison of the contact force and impulse of the impact between a business jet vertical stabilizer and a 3.6 kg (8.0 lb) UAS/bird at 128.6 m/s (250 knots) F-25
420. Comparison of the energy balance of the impact between a business jet vertical stabilizer and a 3.6 kg (8.0 lb) UAS/bird at 128.6 m/s (250 knots) F-26
421. Comparison of the kinematics of impact between a business jet horizontal stabilizer and a 3.6 kg (8.0 lb) UAS/Bird at 128.6 m/s (250 knots) F-26
422. Comparison of external/internal damage sustained by a business jet horizontal stabilizer impacted with a 3.6 kg (8.0 lb) UAS/Bird at 128.6 m/s (250 knots) F-27
423. Comparison of the contact force and impulse of the impact between a business jet horizontal stabilizer and a 3.6 kg (8.0 lb) UAS/bird at 128.6 m/s (250 knots) F-27

424. Comparison of the energy balance of the impact between a business jet horizontal stabilizer and a 3.6 kg (8.0 lb) UAS/bird at 128.6 m/s (250 knots)	F-28
425. Quadcopter UAS component level test 1, strain gage 4, raw data.	G-1
426. Quadcopter UAS component level test 1-5660, strain gage 4, comparison filtered/unfiltered.	G-2
427. Quadcopter UAS component level test 1-5669, strain gage 4, comparison filtered/unfiltered	G-2
428. Quadcopter UAS component level test 1 simulation, strain gage 4, comparison filtered/unfiltered.	G-3

LIST OF TABLES

Table	Page
1. Sales forecast summary (million sUAS units) [7]	3
2. Relevant specifications for the Precision Hawk Lancaster Hawkeye Mark III	9
3. Fixed-wing UAS component material designation	13
4. Numbering criteria used in the projectile FE model	17
5. Meshing criteria for shell and solid finite elements	17
6. Strain gage specifications for component level tests	29
7. Component test matrix with results	31
8. Boeing and Airbus aircraft deliveries summary (up to May 2016) [50] [51]	55
9. Boeing 737, A320 and NIAR commercial transport jet model specifications [52]	56
10. Learjet 31A and NIAR business jet model specifications [53][54]	57
11. Bird strike related regulations [56][57]	58
12. Mesh quality criteria for target impact area.	78
13. Mesh elements quantity	79
14. Target connections summary.	89
15. LS-DYNA material models compared	91
16. Airframe materials at impact areas	95
17. Simulation matrix of commercial transport jet airborne collision	104
18. Simulation matrix of business jet airborne collision	104
19. Damage level categories	105
20. Risk of battery fire	106
21. Commercial transport jet airborne collision simulation – Severity levels and fire risk	107
22. Business jet airborne collision simulation – Severity levels and fire risk	124
23. Load case definition	145
24. Mass scaled impact simulation results	147
25. Commercial transport jet velocity variation load cases	150
26. Business jet velocity variation load cases	150
27. Velocity Impact Simulation Results	151
28. Load case definition	156
29. UAS and bird impact simulation results	157

30. Scaled-up UAS and bird impact simulation results	161
31. Load case definitions for bird/UAS impact comparisons	165
32. Bird and UAS impact simulation results	166
33. Scaled-up quadcopter and fixed-wing UAS simulation results – comparison at identical impact locations	170
34. Damage level categories	175
35. Risk of battery fire	176
36. Commercial transport jet airborne collision simulation results – Severity levels and risk of battery fire	178
37. Business jet airborne collision simulation results – Severity levels	180
38. Mass scaled fixed-wing UAS impact simulation results	184
39. Velocity impact simulation results	185
40. UAS and bird impact simulation results	186
41. Quadcopter and fixed-wing UAS impact simulation results - comparison at identical impact locations	188
42. Measured Precision Hawk subassemblies/components masses	A-1
43. Fixed-wing FE model material models and FE types	A-3
44. Summary of the key differences between the quadcopter [2] and fixed-wing UAS finite element models	A-8

LIST OF ACRONYMS

ABS	Acrylonitrile Butadiene Styrene
ARC	Aviation Rulemaking Committee
BBA	Building Block Approach
CAD	Computer-Aided Design
CFD	Computational Fluid Dynamics
CFR	Code of Federal Regulations
CG	Center of Gravity
DIC	Digital Image Correlation
ELOS	Equivalent Level of Safety
FAA	Federal Aviation Administration
FE	Finite Element
FEA	Finite Element Analysis
GA	General Aviation
GRI	Geoscience Research Institute
LiPo	Lithium Polymer
MSU	Mississippi State University
MTOW	Maximum Take-Off Weight
NAS	National Airspace System
NIAR	National Institute for Aviation Research
NPRM	Notice of Proposed Rulemaking
NTSB	National Transportation Safety Board
OEM	Original Equipment Manufacturer
PCB	Printed Circuit Board
RTCA	Radio Technical Commission for Aeronautics
SPH	Smoothed-Particle Hydrodynamics
sUAS	Small Unmanned Aircraft System
UAS	Unmanned Aircraft System
WP	Working Package

EXECUTIVE SUMMARY

According to the latest industry forecast studies, the Unmanned Aircraft Systems (UASs) market volume is expected to reach 4.7 million units by 2020 [1]. Nonetheless, safety, regulatory, social and technical challenges need to be addressed before the sight of an unmanned aircraft in the sky becomes as common and accepted by the public as its manned counterparts. The effect of an airborne collision between an UAS and a manned aircraft is a concern to the public and government officials at all levels. The primary goal of regulating UAS operations into the National Airspace System (NAS) is to ensure an appropriate level of safety. Research is needed to define airborne hazard severity thresholds for collisions between unmanned and manned aircraft, or collisions with people on the ground.

The results presented in this report focus the initial effort on analyzing a small fixed-wing UAS configuration impacting on a typical commercial transport jet and a typical business jet aircraft. This research will help determine airworthiness requirements for unmanned aircraft based on their potential hazard severity to other airspace users in the NAS. The resulting severity thresholds will be based on UAS characteristics (kinetic energy, structure, shape, materials, etc.) under credible encounter scenarios and will provide for test criteria used to evaluate applicable operational and airworthiness standards. UAS that meet test criteria based on thresholds for these characteristics may be approved for operations over or near people on the ground and may be certified as airworthy under different criteria than other UAS [19]. Due to the complexity of the problem, full-scale test article availability, time and budget constraints, it was decided to conduct the R&D effort by using National Institute for Aviation Research (NIAR) physics based Finite Element (FE) modeling techniques based on the Building Block Approach. Conducting these type of impact studies by analysis provides better insight into the crashworthiness response of the target and the projectile. Damage evaluation criteria are proposed to quantify aircraft damage to the different impact scenarios summarized in this report.

Studies were conducted to analyze the damage level to different areas in the aircraft structure for both the commercial and business jet aircraft configurations. According to the simulations presented in this report, an airborne collision between a commercial transport jet and a 1.8 kg (4.0 lb) fixed-wing UAS at 128.6 m/s (250 knots) may result in a damage severity level of medium-high (3-4) in the horizontal and vertical stabilizer, medium (3) in the leading edge of the wing and medium-low (2) in the windshield. Equally, an airborne collision between a business jet and a 1.8 kg (4.0 lb) fixed-wing UAS may result in a damage severity level of high (4) in the horizontal and vertical stabilizer, medium (2-3) in the leading edge of the wing and high (4) in the windshield.

Correspondingly to what was observed in component level physical testing, the simulations carried out in Chapter 4 predicted that most of the damage is produced by relatively dense and stiffer parts (motor, battery, etc.) of the UAS. Additional parametric studies were conducted to analyze the effect of the projectile mass, impact velocity and UAS architecture.

It can be concluded from this study that UAS impacts are likely to cause more damage than bird strikes for an equivalent initial kinetic energy. The UAS impacts were generally associated with greater damage levels due to the hard-bodied mechanical construction of the UAS, its components made of dense, rigid materials and its discrete distribution of masses. Therefore, a 4 lb bird and a 4 lb UAS will introduce different levels of damage to the aircraft.

1. INTRODUCTION

Unmanned Aircraft Systems (UASs) is the fastest growing sector of the aviation industry today, according to The Association for Unmanned Vehicles International (AUVSI), the largest trade group around UASs, estimates that by 2019 more than 70,000 jobs will be created in the US with an economic impact of more than \$13.6B.[1]. Globally, UAS market volume is expected to reach 4.7 million units by 2020 [1]. Nonetheless, safety, regulatory, social and technical challenges need to be addressed before the sight of an unmanned aircraft in the sky becomes as common and accepted by the public as its manned counterparts.

The effect of an airborne collision between an UAS and a manned aircraft is a concern to the public and government officials at all levels. The primary goal of regulating UAS operations into the National Airspace System (NAS) is to assure an appropriate level of safety. While the effects of bird impacts on airplanes are well documented, little is known about the effects of more rigid and higher mass UASs on aircraft structures and propulsion systems. This research evaluates the severity of small UAS (sUAS) (under 55 lb, as defined in the Small Unmanned Aircraft Rule (Part 107)) collisions on commercial and business jet airframes and propulsion systems.

Findings from this research can be used to help define airborne hazard severity thresholds for collisions between unmanned and manned aircraft. The results presented in this report will focus on small fixed-wing UAS configuration impacting on a typical commercial transport aircraft and a typical business jet. A second report will document a quadcopter UAS configuration impacting on the same aircraft structures [2], and the third report will focus on the effects of UAS engine ingestion [3]. Further research will be conducted in the near future to analyze the UAS airborne collision severity level with general aviation (GA) aircraft and rotorcraft.

1.1 BACKGROUND

1.1.1 Unmanned Aircraft Systems Categories

An UAS is an unmanned aircraft and the equipment necessary for the safe and efficient operation of that aircraft. Therefore, an unmanned aircraft is a component of an UAS. It is defined by statute as an aircraft that is operated without the possibility of direct human intervention from within or on the aircraft [4].

Currently there is no standard when it comes to the classification of UASs. Defense agencies have their own standard, and civilian agencies worldwide have their ever-evolving categories definitions for UASs. Currently the Federal Aviation Administration (FAA) classifies UASs into the following categories:

- **Small Unmanned Aircraft Rule (Part 107) [5]:** The proposed rule does not cover the full spectrum of UAS types or weights. The FAA acknowledges that the rulemaking is an incremental stage of adding UASs into the NAS. The small non-hobby or non-recreational UASs must be operated in accordance with the following limitations:
 - Unmanned aircraft must weigh less than 25 kg (55 lb).
 - Cannot be flown faster than a groundspeed of 87 knots (100 mph);
 - Cannot be flown higher than ≈ 122 m (400 ft) above ground level (AGL), unless flown within a 400 ft radius of a structure and does not fly higher than 400 ft above the structure's immediate uppermost limit;

- Minimum visibility, as observed from the location of the control station, may not be less than 3 statute miles (sm); and
 - Minimum distance from clouds being no less than ≈ 152 m (500 ft) below a cloud and no less than ≈ 610 m (2,000 ft) horizontally from the cloud.
- **Micro-UAS:** The Aviation Rulemaking Committee (ARC) was focused on flight over people, and in furtherance of that goal, identified four sUAS categories, defined primarily by level of risk of injury posed, for operations over people. For each category, the ARC recommends a risk threshold that correlates to either a weight or an impact energy equivalent and, to the extent necessary to minimize the risks associated with that category, additional performance standards and operational restrictions. The following is a summary of the category recommendations [6]:
- For Category 1, a sUAS may operate over people if the mass (including accessories/payload, e.g., cameras) is 250 g (0.55 lb) or less.
 - Under Categories 2, 3, and 4, a sUAS may operate over people if it does not exceed the impact energy threshold specified for each category, as certified by the manufacturer using industry consensus test methods, and if its operator complies with operational restrictions specified for each category.

1.1.2 Unmanned Aircraft Systems Market Size

The UAS market is divided into two groups: Hobbyist and Commercial.

1.1.2.1 Hobbyist UAS Forecast

In order to operate in the NAS, the FAA must ensure that aircraft operators are not only aware of the system in which they are operating, but that the agency also has a means to identify owners. One means to accomplish this is through aircraft registration and marking. On December 14, 2015, the FAA issued a rule requiring all UAS weighing more than 250 g (0.55 lb) and less than 24.9 kg (55 lb) to be registered using a new on-line system (UAS weighing more than 55 lb must be registered using the existing Aircraft Registration Process). This registration rule will aid in investigations and allow the FAA to gather data about UAS use.

As of mid-March 2016, there have been over 408,000 registrations. As shown in Table 1, a sales forecast was developed for the sUAS registration rule, which included very small units below the registration size cutoff of 250 g. For this interim final rule, in 2016, the forecast is of 1.9 million potential annual sales, which could increase to 4.3 million units sold annually by 2020. As shown in the first row of Table 1, this would represent the upper bound of the potential number of sUAS operated as model or hobby aircraft [7].

Table 1. Sales forecast summary (million sUAS units) [7]

	2016	2017	2018	2019	2020
Hobbyist (model aircraft)	1.9	2.3	2.9	3.5	4.3
Commercial (non-model aircraft)	0.6	2.5	2.6	2.6	2.7
TOTAL UASs	2.5	4.8	5.5	6.1	7.0

1.1.2.2 Commercial UAS Forecast

In 2015, in support of the sUAS registration rule, a sales forecast for commercial sUASs was developed to derive the potential demand for the new on-line registration system. That forecast represents the high end of the sUAS commercial fleet. As summarized in the second row of Table 1, for 2016, the potential sales of commercial sUASs requiring registration was forecast to be over 600,000, growing to 2.7 million by 2020 [7].

On February 23, 2015, the FAA issued the Operation and Certification of sUASs Notice of Proposed Rulemaking (NPRM) proposing to amend its regulations to adopt specific rules for the operation of sUASs in the NAS. More information on the derivation and assumptions behind this forecast will be provided in the Regulatory Impact Assessment accompanying the final rule publication. [7]

The FAA is working with the Teal Group Corporation, an industry expert in UAS forecasting, to develop a commercial forecast for sUAS operations described in the NPRM. The civil and commercial UAS market will take time to develop and the size of the market will directly relate to the specific requirements developed along with airspace accessibility. The Teal Group has provided the FAA with a forecast for small commercial unmanned aircraft. This forecast analyzes the market demand for different sectors within the regulatory environment.

As shown in Figure 1, it is expected that, once the final sUAS rule is implemented, two different categories of sUAS will emerge. Higher end sUASs will have an average sales price of \$40,000 per unit, while lower end units will have an average price of \$2,500. Over a five-year period, Teal Group forecasts the sUAS fleet to be approximately 542,500. Of this estimated fleet, it is expected that roughly 90% of the demand will be satisfied by the lower end units. The number of sUASs forecasted is highly uncertain and is dependent on the regulatory structure ultimately adopted. Once a final rule for sUASs is published, they will become more commercially viable than they are today. The total fleet shown in Figure 2 is expected to satisfy the market for the top five industries (Figure 1) that will employ the use of sUASs [7].

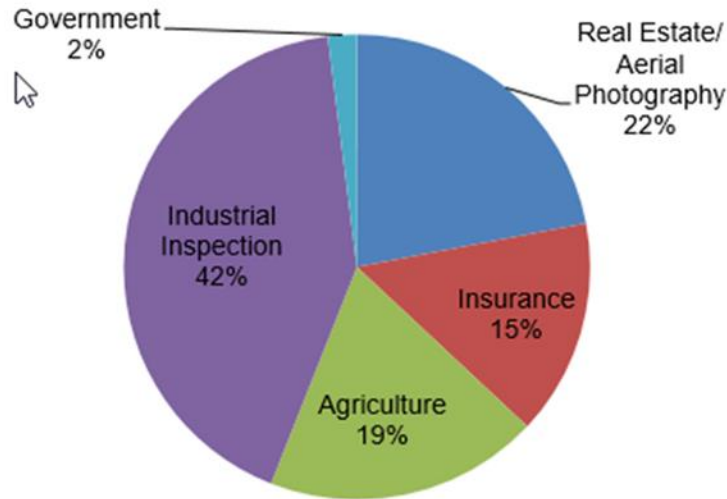


Figure 1. Top five sUAS markets [7]

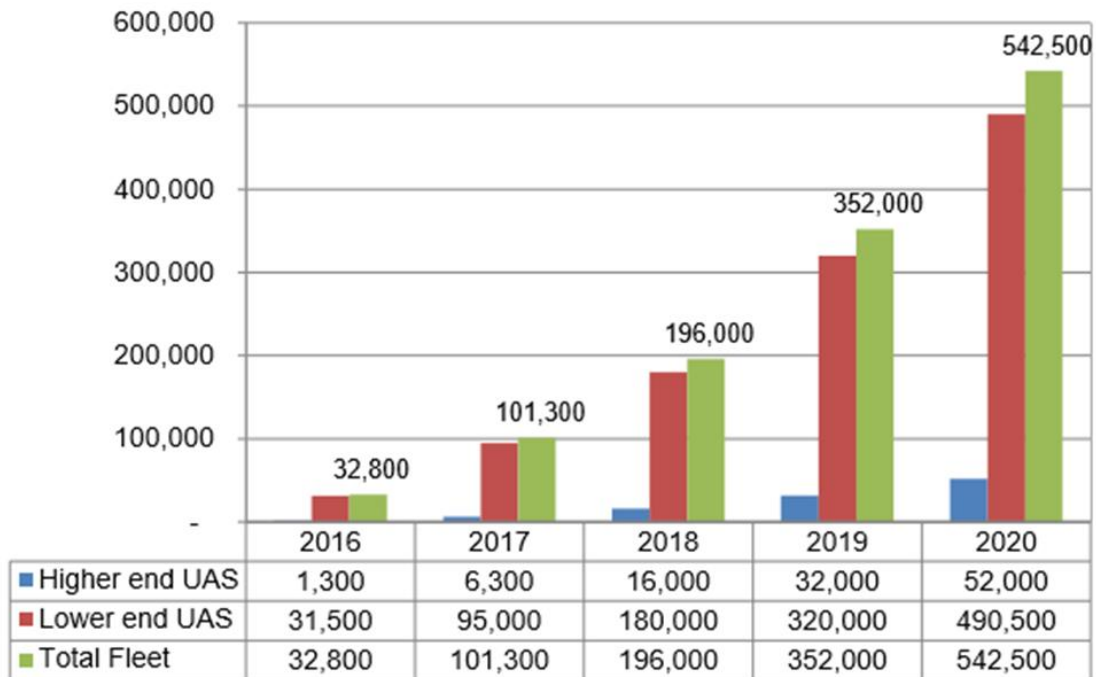


Figure 2. sUAS fleet [7]

1.1.3 Unmanned Aircraft Systems Impact Severity Classification

Conventional Code of Federal Regulations Title 14 (*14 CFR*) system safety analyses include hazards to flight crew and occupants that may not be applicable to unmanned aircraft. However, UAS operations may pose unique hazards to other aircraft and people on the ground. It is necessary to determine hazard severity thresholds for UASs using safety characteristic factors that affect the potential severity of UASs in collisions with other aircraft on the ground or in airborne encounters

as well as collisions with people on the ground. The factors that determine the outcome of an airborne collision are numerous and complex and are highly dependent on the structural design and materials used for the construction of the UAS.

1.1.3.1 Unmanned Aircraft Systems Mid-Air Collisions Equivalent Level of Safety

The primary goal of regulating UAS operations in the NAS is to assure an appropriate level of safety. This goal is quantified by national aviation agencies as an “Equivalent Level of Safety” (ELOS) with that of manned aviation. There are major key differences between manned and unmanned aviation that do not only lay in the separation of the pilot from the cockpit and the level of automation introduced but also in the variety of architectures and materials used for the construction of UASs. These differences could introduce new failure modes, and, as a result, an increased perceived risk that needs to be evaluated [8].

In order to have an equivalent level of safety, according to the definition of the Range Commanders Council in its guidance on UAS operations it states that any UAS operation or test must show a level of risk to human life no greater than that for an operation or test of a piloted aircraft [9].

Although current manned aviation regulations do not impose limits on fatality rates, a statistical analysis of historical data can provide valuable insight on the collision and fatality rates of manned aviation and could be used to define the basis for the ELOS for UASs.

In order for an ELOS to be derived, accident statistics involving mid-air collisions are required. The National Transportation Safety Board (NTSB) has defined two categories of relevant collision accident scenarios: *i*) in-flight collisions with obstacles such as birds, trees, power lines and *ii*) mid-air collisions with other aircraft that could be used to define the UAS requirements. Data pertaining this approach is presented in reference [8] for NTSB data compiled between 1983-2006. If this approach is used, in the future as a reference metrics to define the ELOS, it is recommended to conduct further studies that include NTSB data available to date.

Once the ELOS is defined based on historical data from manned aviation, the next step is to develop a method to estimate the probability of mid-air collisions between UASs and manned aircraft. Several authors have published methodologies on how to evaluate the risk of mid-air collisions between manned aircraft and UASs [10] [11]; some of the midair collision models are based on a theory originally developed to predict the collision frequency of gas molecules [12]. This theory was similarly applied to air traffic in prior literature [13] [14]. The collision frequency between a single UAS and transient air traffic is a product of the transient aircraft density, the combined frontal areas and the relative closing velocity between the colliding manned and unmanned aircraft [10].

The aforementioned metrics provide statistical probabilities of UAS mid-air collisions according to specific parameters defined for the evaluation. It should be noted that not all collisions could lead to catastrophic accidents. The large variability of UAS sizes and the fact that not all the aircraft systems are critical for remaining airborne means that the aircraft involved may survive certain collisions.

The risk assessment to develop an Airborne Collision UAS Impact Severity Classification can be divided into three elements:

- **Estimation of the probability of mid-air collision** between UASs and manned aircraft. This will be a function of the operating airspace, aircraft operated within the airspace and

the UAS configurations operating within the shared airspace. Methods to estimate the probability of impact are presented in references [10] [11].

- **Evaluation of damage potential for typical UASs** (classes based on weight, architecture, operational characteristics [altitude, velocity] mid-air collisions scenarios per manned aircraft class (commercial, general aviation, rotorcraft, etc.) in order to assess the damage severity to manned aircraft. Several groups advocate to use simplified ballistic penetration models [15], similarity principles to existing bird strike requirements or kinetic energy thresholds [16] [17] [18]. The objective of this project is to evaluate the severity of a typical quadcopter [2] or fixed-wing UAS airborne collision with detailed Finite Element (FE) models of the UASs and the target aircraft. These results will be compared with current proposed penetration mechanics and energy based criteria.
- Once the probability of an airborne collision is determined, **the damage models obtained through the research presented in this study can be combined with the probabilistic collision models to define appropriate ELOS criteria.**

1.2 PROJECT SCOPE

Research is needed to establish airborne hazard severity thresholds for collisions between unmanned aircraft, manned-aircraft, or collisions with people on the ground. This research project will help determine airworthiness requirements for unmanned aircraft based on their potential hazard severity to other airspace users and third parties on the ground. The resulting severity thresholds will be based on UAS characteristics (kinetic energy, structure, shape, materials, etc.) under credible encounter scenarios and will provide for test criteria used to evaluate applicable operational and airworthiness standards. UASs that meet test criteria based on thresholds for these characteristics may be approved for operations over or near people on the ground and may be certified as airworthy under different criteria than other UASs [19].

The main research questions being answered through this research are [19]:

- What are the hazard severity criteria for an UAS collision (weight, kinetic energy, etc.)?
- What is the severity of an UAS collision with an aircraft in the air?
- Can an UAS impact be classified similar to a bird strike?
- Will an UAS impacting an engine be similar to a bird engine ingestion?
- What are the characteristics of an UAS where it will not be a risk to an aircraft collision in the air?
- Can the severity of an UAS mid-air collision with an aircraft be characterized into categories based on the UAS, and what would those categories look like?

Using the approved hazard severity characteristics and approved method(s), comprehensive lists of lethality characteristics thresholds will be developed using data and analysis from proposed methods and UAS system safety definitions provided by the Radio Technical Commission for Aeronautics (RTCA) for airborne collision with other UAS and commercial aircraft. Scenarios should involve impacts with representative commercial aircraft structures, control surfaces, propellers and engines, as well as representative sUASs. The scenarios should include analyses similar to bird strike methods of impacts on windshields, as well as an engine ingesting a sUAS. The analyses should include minimum characteristic thresholds for which there is no relevant risk of damage from a collision. In order to answer the aforementioned items the National Institute for Aviation Research (NIAR) proposes the following research approach:

- Working Package (WP) I – Projectile Definition: Definition UAS Classes based on: Gross Take-Off Weight (GTOW), Speed, Altitude, Power-plant, Material Construction, Geometry
- WP II – Target Definition: Business Jet and Commercial Transport Jet
- WP III – UAS Projectile Model Development: Computer-Assisted Design (CAD), and FE models
- WP IV – Aircraft Target Development: CAD, and FE models
- WP V – Safety Evaluation UAS to Aircraft
- WP VI – Aircraft Susceptibility Evaluation: Definition surrogate projectile and test Condition
- WP VII – UAS Susceptibility Evaluation: Definition UAS Crashworthiness Evaluation Method

This research project will utilize a proven simulation technique, the Building Block Approach (BBA) to analyze the outcome and severity of typical impact scenarios. The numerical models will be verified with experimental data at the coupon, and component levels in order to predict the full-scale UAS response under impact. Due to the high level of concern related to this topic, initial simulation analyses will be focused on providing a rough order of magnitude severity evaluation of a fixed-wing UAS with commercial and business jet airframes.

It is important to emphasize that the intent of this research project was not to do an assessment of already certified products (*e.g. Part 23/25/27/29/33*). The investigation was focused on understanding the physics of airborne collisions between UASs and manned aircraft, and identifying characteristics of the UAS that may influence post-impact damage on the manned aircraft.

2. FIXED-WING UAS PROJECTILE DEFINITION

In order to evaluate the severity of an airborne collision between an UAS and a general aviation/commercial aircraft, the FAA has prioritized research and development aimed at characterizing the risk and severity of UAS impacts to aircraft. This overarching research is aimed at addressing the severity of an UAS mid-air collision with another aircraft. Some key challenges include establishment of hazard severity criteria and UAS design guidelines to minimize the potential damage to manned aircraft. The Alliance for System Safety of UAS through Research Excellence (ASSURE) was established in part to address the significant issues associated with integrating UASs into the NAS [20]. This study highlights some of the potential threats fixed-wing UASs pose to general aviation and commercial aircraft.

Fixed-wing UAS airborne collisions represent a significant potential danger to manned aircraft. Additionally, fixed-wing UAS impact scenarios are distinct from those of rotorcraft-based UASs (*e.g.*, differences in geometries, relative velocities, mass distribution, and total mass). For this reason, it was decided to consider fixed-wing UAS for the airborne collision studies along with the quadcopter. In Phase I of this project, Montana State University [21] selected the Precision Hawk as representative of the fixed-wing sUASs being used under Section 333 of the FAA [22]. The Precision Hawk is currently part of the FAA's Pathfinder Program aimed at extending the use of UASs beyond visual line of sight.

Mississippi State University (MSU) was responsible for developing the fixed-wing UAS FE model. A similar study involving quadcopter UAS impacts was performed by the NIAR [2]. In this chapter, the development of verified FE models of an idealized Precision Hawk Lancaster Hawkeye Mark III fixed-wing UAS and its critical components are presented. Structurally complete Precision Hawk UAS models will later be used to assess the impact threat posed to general aviation, business and commercial transport jets and rotorcraft.

2.1 FIXED-WING UAS GEOMETRY AND SPECIFICATIONS

The Precision Hawk Lancaster Hawkeye Mark III is a lightweight fixed-wing UAS with a maximum take-off weight (MTOW) of 2,495 g. Figure 3 shows an image of the UAS modeled for this project. Table 2 presents the most relevant specifications of the fixed-wing UAS.

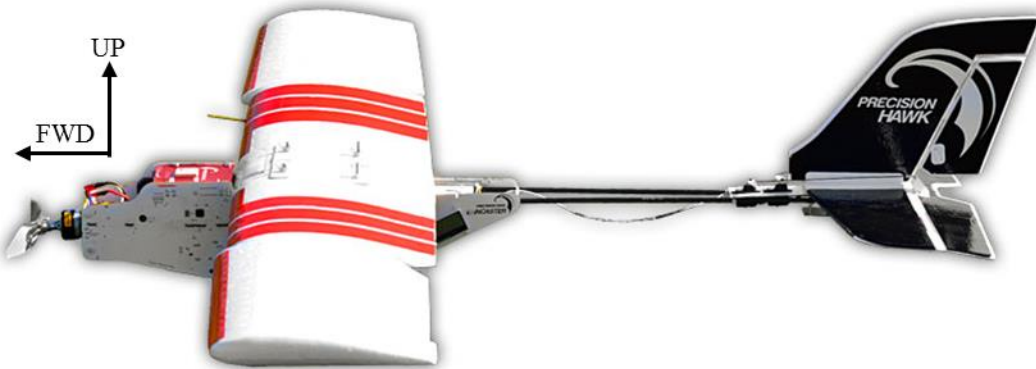


Figure 3. The Precision Hawk Lancaster Hawkeye Mark III

Table 2. Relevant specifications for the Precision Hawk Lancaster Hawkeye Mark III

Mass (MTOW)	2,495 g	5.5 lb
Wingspan	1,500 mm	4 ft 11 in
Length	800 mm	2 ft 7.5 in
Max. Horizontal Speed	19.5 m/s	38 knots
Max. Service Ceiling	4,000 m	13,120 ft

The fixed-wing UAS has an airframe length of 0.8 m and wingspan of 1.5 m. A single Lithium Polymer (LiPo) battery pack is used to maintain a maximum total flight duration of 45 min. It can operate at a maximum speed of 70 km/h (38 knots) and has a maximum operating altitude of 4,000 m (13,120 ft). The fixed-wing UAS consists of a forward fuselage structure comprised of printed circuit boards (PCBs); expanded polystyrene wings, vertical tail, and horizontal stabilizer; and carbon/epoxy composite wing spars and tail booms. The PCBs are used as multifunctional structural elements to provide structural integrity and reduce the amount of electrical wiring necessary to operate the fixed-wing UAS.

The fixed-wing UAS fuselage subassembly (total mass, 487 g) consists of interconnected, multifunctional PCBs as shown in Figure 4 (A). The two PCB vertical sidewalls are connected by multiple transverse PCBs and are tapered at the forward and aft ends for better aerodynamic performance. The sidewalls also contain and protect the fixed-wing UAS payload modules and avionics. Electrical components are attached to the portside (left) sidewall and used to provide the necessary flight controls and diagnostics. A liquid crystal display (LCD) on the aft port side (see Figure 4 (A)) is used to relay information to the operator upon startup. The starboard sidewall also contains a variety of soldered circuits and smaller electronic components.

Multiple PCBs are mounted between the sidewalls to provide structural rigidity and strength and to connect the electronics necessary to control and monitor the fixed-wing UAS. A number of electrical components are soldered to the transverse PCBs. These electrical components are necessary to provide power, network connectivity, and global positioning system (GPS) location capability. A thicker PCB that connects the two sidewalls is used both as a motor subassembly support and firewall. The firewall is attached to the sidewalls via four steel screws and threaded fasteners at the forward end of the fuselage. A tapered power board mounted horizontally behind the firewall board functions as an electrical bus between the port and starboard electronics. The tapered nose of the fuselage ensures that the sidewalls maintain the desired aerodynamic geometry. The GPS board and attached GPS unit are mounted horizontally above the power board. A network board is mounted horizontally aft of the GPS board and directly above the payload bay. It connects the computer module units to Ethernet components.

An additional four PCBs (float struts) are mounted transversely in pairs between the sidewalls on the fore and aft side of the payload bay. These float struts are used to increase the torsional rigidity of the fuselage. Stubs from transverse PCBs are fitted tightly into mating slots in the sidewalls and soldered as show in Figure 4 (B) (such joints are similar to Mortise and Tenon joints commonly

used in woodworking). Unless otherwise stated, all interconnections between PCBs in the fixed-wing UAS are soldered.

The wing subassembly (total mass, 412 g) contains two symmetric expanded polystyrene wings and their supporting structures. The starboard (right) wing is shown in Figure 5. A portion of each wing is sectioned into a flap with an actuator placed beneath it. Each wing has two spars: a tubular carbon/epoxy main spar and a rectangular PCB aft spar. A separate hollow, cylindrical carbon/epoxy tube fits snugly inside both main spars and forms the carry-through structure between the two wings. Each wing also has structural PCBs attached to the upper and lower wing surfaces. These PCBs provide additional structural reinforcement for the easily crushable polystyrene wings at the wing/fuselage interconnection and electrically connect the wing sensors and actuators to the appropriate electrical components in the fuselage subassembly. The wing subassembly is attached to the fuselage subassembly by four screws (Figure 4 (A)) that are attached to four mounting brackets. Two mounting brackets are soldered to each fuselage sidewall.

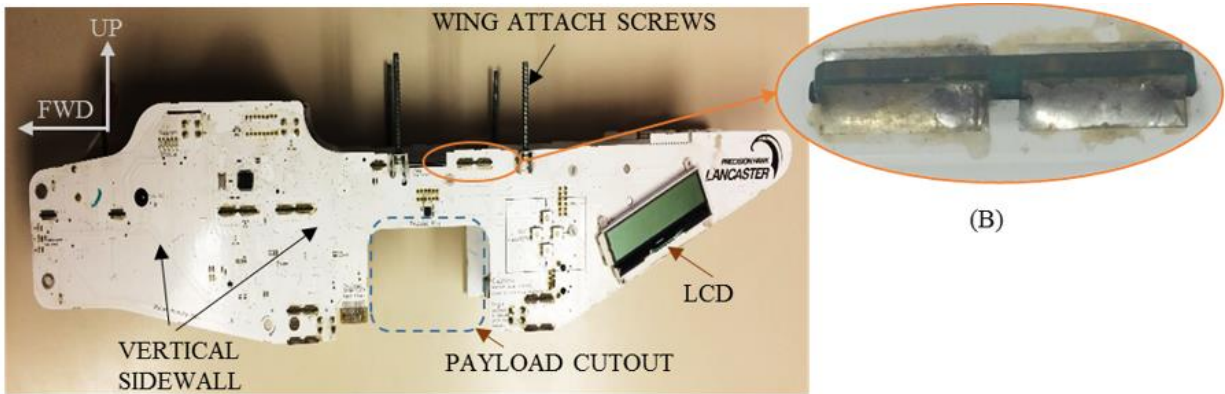


Figure 4. (A) Fixed-wing UAS fuselage subassembly and (B) Solder joint connecting transverse PCBs to the sidewalls

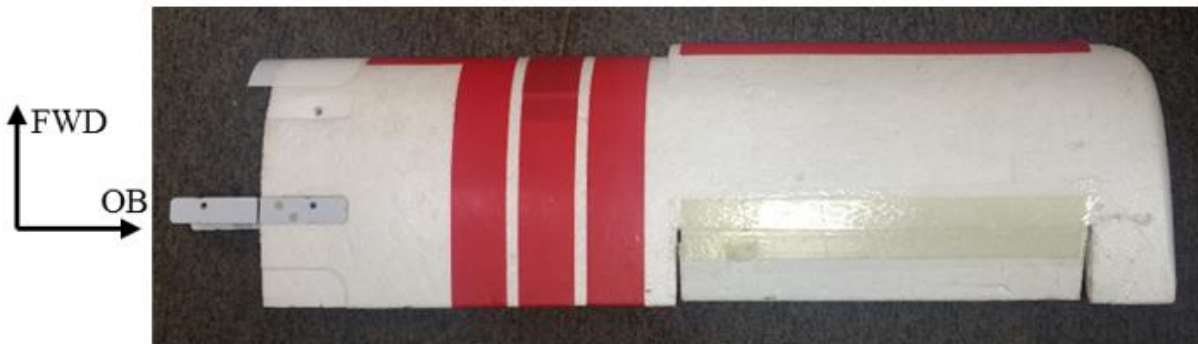


Figure 5. Plan view of the starboard wing of the fixed-wing UAS

The aft portion of the fuselage subassembly (total mass, 250 g) is comprised of a pair of hollow cylindrical carbon/epoxy tail booms that connect the vertical and horizontal stabilizers to the fuselage as shown in Figure 6. Four interconnected PCBs attach the tail booms to the fuselage. These structural PCBs are not soldered and are secured to the booms by four Nylon 6 zip ties. A separate structural PCB is located midway along the tail booms and contains an antenna used to relay data between the fixed-wing UAS and the ground during flight. This PCB is also attached to the tail booms by four Nylon 6 zip ties. Polystyrene vertical and horizontal stabilizers are mounted onto

an Acrylonitrile Butadiene Styrene (ABS) plastic mount at the aft end of the tail booms. The vertical and horizontal stabilizers are sectioned to form the rudder and elevator, respectively. Four structural PCBs are mounted on the aft section of tail booms to structurally support the stabilizers and two servomechanisms motors are used to control the rudder and elevator. These PCBs are soldered to each other and secured to the tail booms by zip ties.

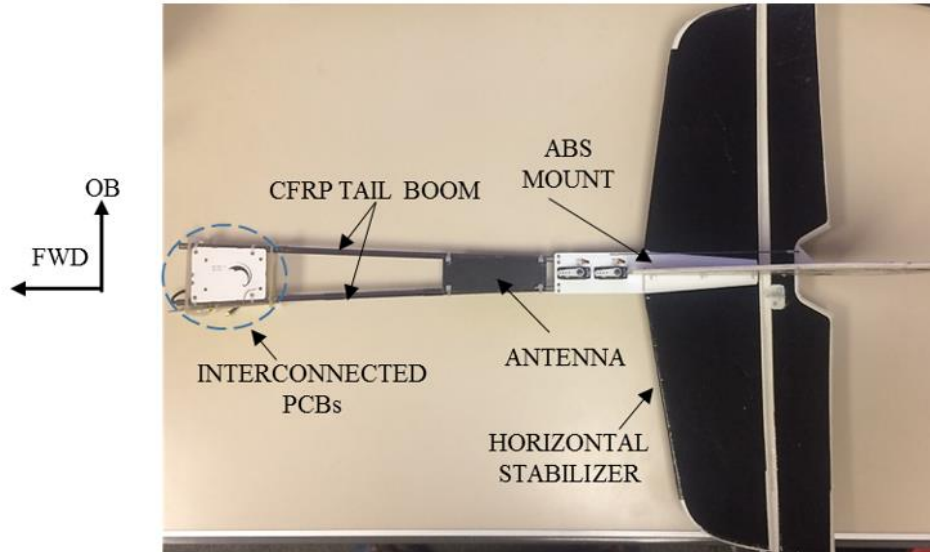


Figure 6. Fixed-wing UAS tail subassembly

The motor subassembly (total mass, 135 g; *cf.*, Figure 7 (A)) is mounted onto the firewall PCB and forms the nose of the fixed-wing UAS. It is comprised of a Park 480 brushless outrunner motor and an APC glass-reinforced nylon 11X8F propeller. Since the fixed-wing UAS does not have any landing gear (*i.e.*, it performs belly landings), folding propeller blades are attached to the motor to reduce the likelihood of blade breakage upon landing. A threaded conical nozzle (not shown in Figure 7 (A)) secures the propeller to the motor. The brushless motor shown in Figure 7 (B) consists of four steel components: a stator, rotor, retainer, and shaft. The rotor and retainer are attached to the shaft with setscrews. The rotor part of the brushless motor is a permanent magnet synchronous motor, which rotates around a fixed armature.

The battery subassembly (total mass, 335 g) shown in Figure 8 is primarily comprised of a LiPo battery enclosed within a housing formed by four PCBs. Two Nylon 6 zip ties and small expanded polystyrene blocks are used to hold the battery in place within the housing. A thin and flexible PCB mounted horizontally under the battery is used to support the battery. This PCB also protects the other internal electrical components from dirt and debris upon landing. A Thunder Power 3S 3900 mAh capacity LiPo battery, comprised of three pouch-type cells, is used to power the motor. Layered folded ribbons are used as ionically conductive separators and are coated with intermittent active material on both sides. A cell is formed by sealing the assemblage inside a flexible, thin aluminum plastic laminate. Each cell is then shrink-wrapped with in a soft plastic pouch.

The payload subassembly, shown in Figure 8, is designed to accommodate various configured payload modules. Note that the total weight of the UAS can vary as a result. For this study, a 394 g camera module is loaded into the payload bay and coupled to various onboard electronic components using an edge connector. This payload subassembly is comprised of a Nikon 1 J3 digital camera supported by six PCBs.

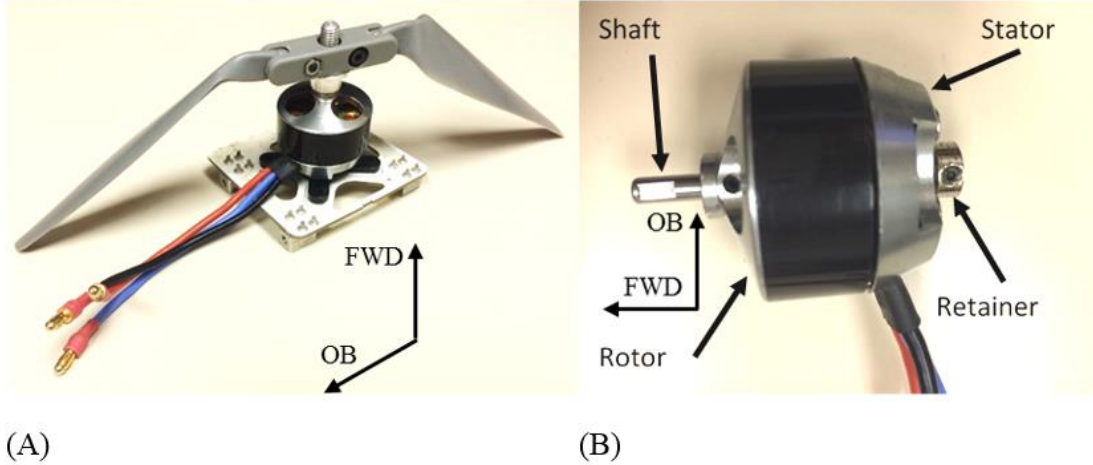


Figure 7. Fixed-wing UAS (A) Motor subassembly and (B) Motor components

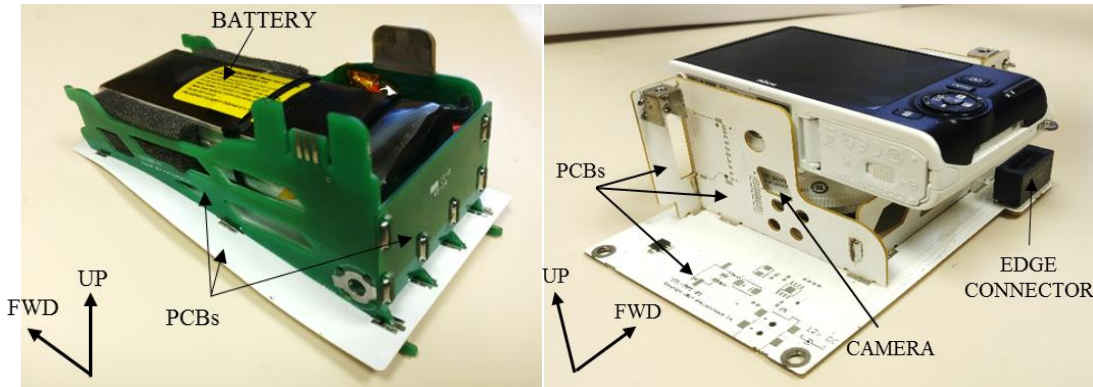


Figure 8. Fixed-wing UAS battery (left) and payload (right) subassemblies

It should be noted that the motor (135 g), battery (335 g), and payload (394 g) subassemblies represent approximately one third of the overall mass (2,015 g) of the fixed-wing UAS. Since these relatively high-density components are arranged roughly in-line and in close proximity with one another in the fixed-wing UAS forward fuselage, they can have a profound effect on the severity of air-air and air-ground collisions.

The fixed-wing UAS (Precision Hawk) differs from the quadcopter UAS (DJI) in terms of basic construction, mass, dimensions, flight specifications, and materials. A summary of the key differences between the quadcopter [2] and fixed-wing UAS finite element models is presented in Table 44 in Appendix A.

2.2 FIXED-WING UAS REVERSE ENGINEERING

Reverse engineering is a technique used to analyze and extract design information from a product and replicate it physically or in the form of a virtual CAD model. The details of the reverse engineering process used for this project are described in the following subsections.

2.2.1 Data Collection

The FE model of the fixed-wing UAS was developed by reverse engineering a 2015 g Precision Hawk Lancaster Hawkeye Mark III obtained from the MSU Geoscience Research Institute (GRI).

As previously mentioned, the fixed-wing UAS was split into six subassemblies for modeling purposes: fuselage, wings, tail, motor, battery, and payload. Each component of the fixed-wing UAS was measured and weighed separately. Since most of the PCBs are soldered together, individual PCB weights were assumed based on single PCB density measurements while ensuring that the total component weight and center of gravity did not significantly differ. The weight of significant electrical components was determined in a similar fashion. Table 42 in APPENDIX A contains a summary of fixed-wing UAS subassembly and component masses.

2.2.2 Material Designation

Identifying the specific material composition of each fixed-wing UAS component was a key challenge associated with reverse engineering the fixed-wing UAS. Specific metal alloys, composite materials, and polymers were assigned to fixed-wing UAS components based upon information from the vendor or from well-accepted sources from the literature. Table 3 details each assumed material and its associated fixed-wing UAS components.

Table 3. Fixed-wing UAS component material designation

Material	Components
Steel 4340	Screws, Mounting Brackets, Motor Components
Aluminum 2024 T-351	Motor
Aluminum Foil	Battery Pouch
Aluminum 2024 T-6	Camera Case, Cylindrical Lens Housing
Carbon/Epoxy Composite	Wing Spars/Carry-through Structure, Tail Booms
FR4 Glass/Epoxy Composite	PCBs
Glass-Reinforced Nylon 6	Propeller
Expanded Polystyrene	Wings, Vertical Tail, Horizontal Stabilizer, Battery Support
Nylon 6	Propeller Support, Zip Ties
ABS	Tail Flanges, Screws, Servos, Connectors, Autopilot, LCD Component

A significant amount of engineering judgement was used in identifying the composition and properties of individual components; this was particularly true for non-structural electrical components. For example, the majority of LCD and autopilot parts were idealized to be fabricated entirely from

ABS. Similarly, the intricate camera lens structure and camera battery housing were idealized using a simplified thin-walled aluminum construction while maintaining the same mass properties of the actual camera structure.

2.2.3 CAD Modeling

A CAD model of the fixed-wing UAS was generated using the CATIA v5 platform [23] and is shown in Figure 9. Individual parts were created using the “*part design*” feature in CATIA and were assembled into their respective subassemblies using the “*assembly*” feature. All six subassemblies were then assembled to create a complete CAD model.

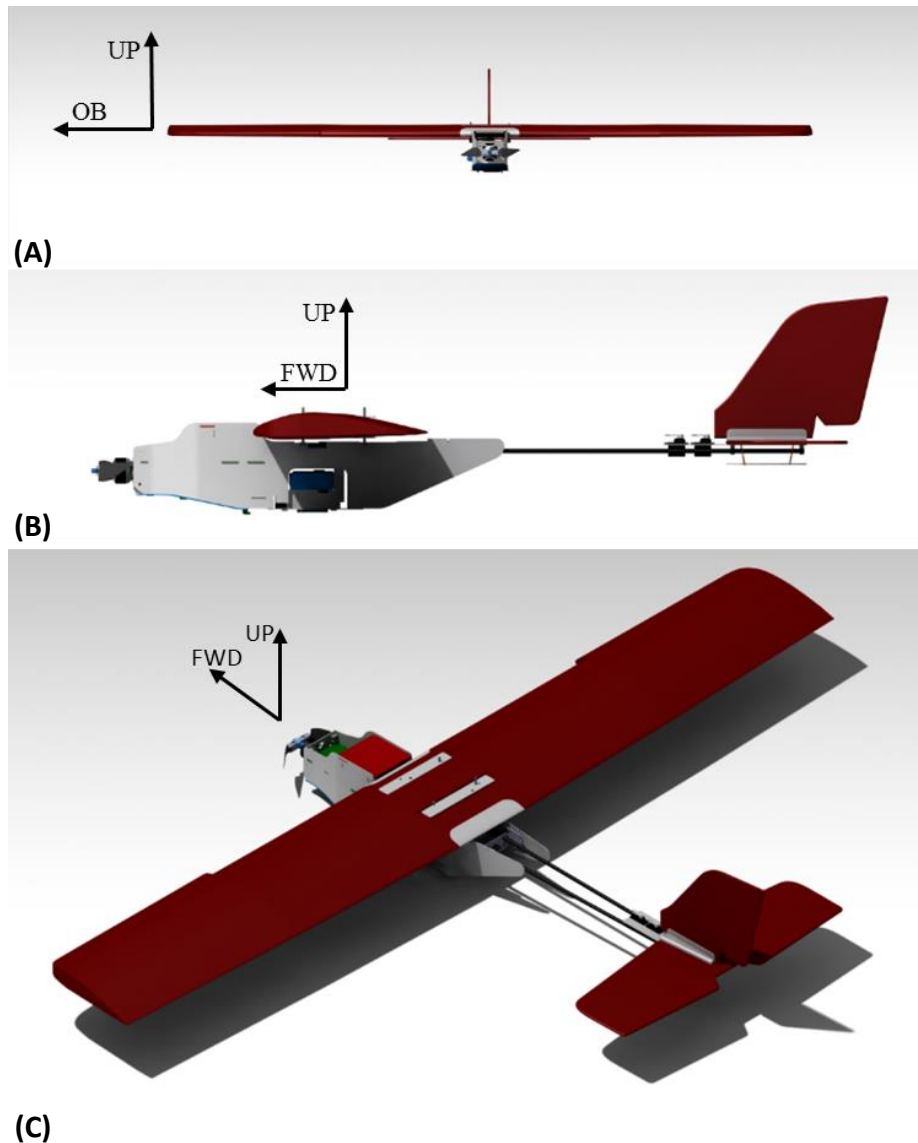


Figure 9. Fixed-wing UAS CAD model: (A) Front view, (B) Side view, and (C) Isometric view

The CAD models of the motor, fuselage, wing, tail, battery, and payload subassemblies, are shown in Figures 10 to 15, respectively. Minor geometric features in the fixed-wing UAS (*e.g.*, nonstructural soldered joints, decorative parts, tiny pass-through holes, and electronic chips) were not included in the CAD model. Special care was used to precisely model the relatively high-density motor, battery, and payload subassemblies since they represent a significant fraction of the fixed-wing UAS's total weight. Such high-density components are likely to be particularly damaging during fixed-wing UAS mid-air impacts to manned aircraft.

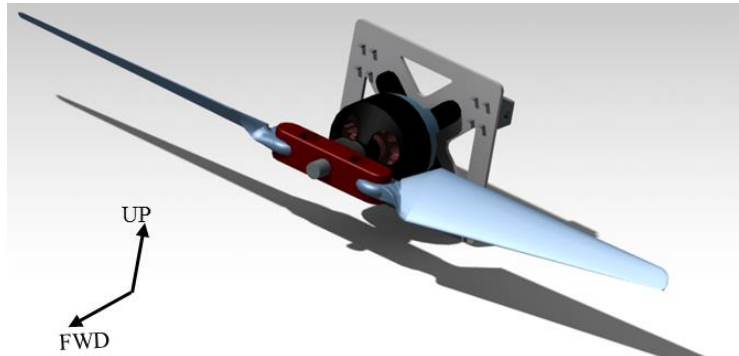


Figure 10. CAD model of the fixed-wing UAS motor subassembly

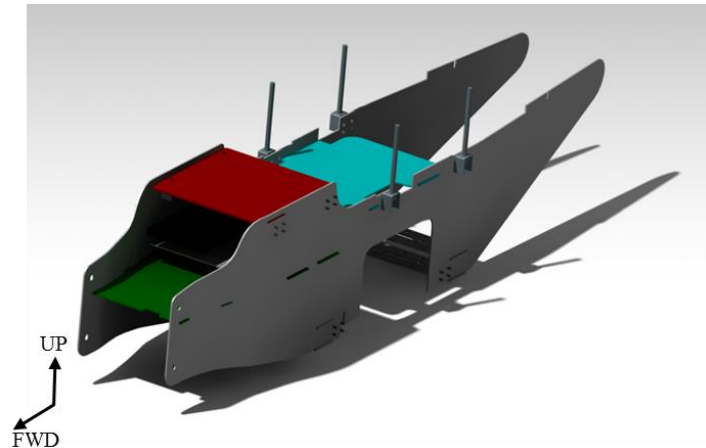


Figure 11. CAD model of the fixed-wing UAS fuselage subassembly

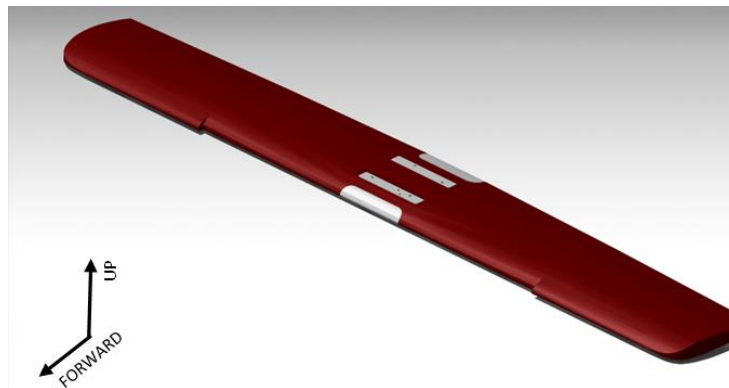


Figure 12. CAD model of the fixed-wing UAS wing subassembly

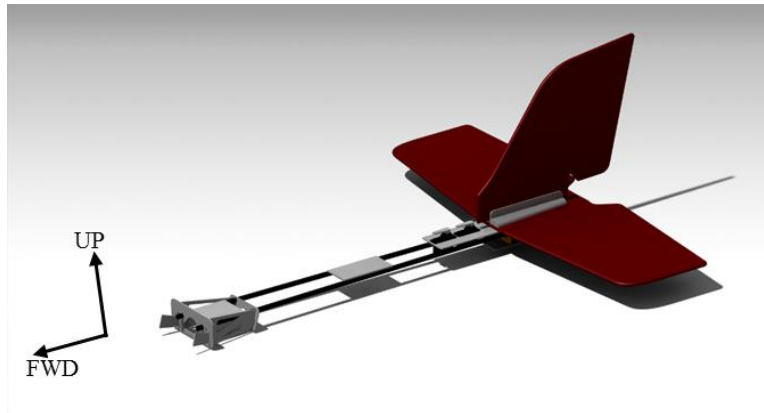


Figure 13. CAD model of the fixed-wing UAS tail subassembly

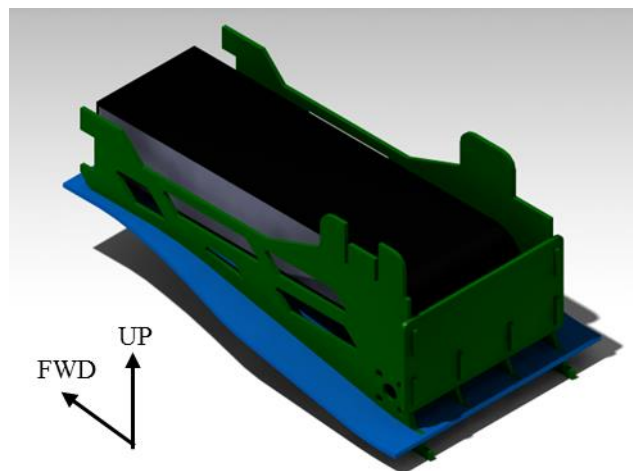


Figure 14. CAD model of the fixed-wing UAS battery subassembly

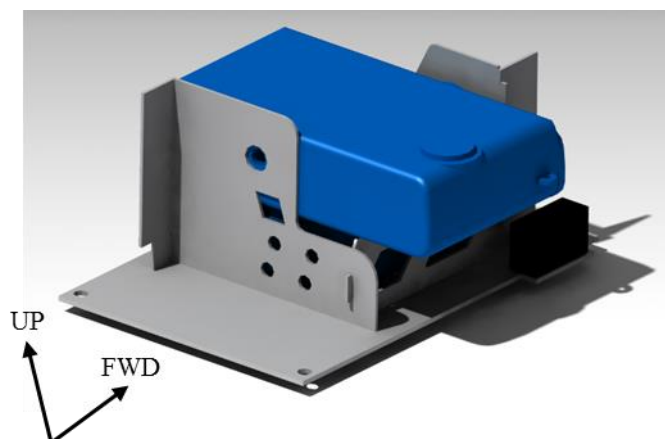


Figure 15. CAD model of the fixed-wing UAS payload subassembly

2.3 FINITE ELEMENT MODEL

A detailed fixed-wing FE model was developed for the solver LS-DYNA smp s R8.0.0. The desired FE discretization was performed using a commercial meshing platform (HyperMesh). Additional details regarding the fixed-wing UAS FE model development and Verification is included in APPENDIX A.

2.3.1 Discretization

The fixed-wing FE model is comprised of 119 parts. Each part was assigned a unique identification number based on its corresponding subassembly. Connections, materials, section properties, nodes, and FEs were numbered in a similar fashion. The numbering scheme implemented for the fixed-wing model is listed in Table 4.

Table 4. Numbering criteria used in the projectile FE model

Subassembly/Group	Numbering Ranges for Each Category	
	ID Number	Node/Element Numbers
Fuselage	20,001-21,000	60,000,001-61,000,000
Wings	21,001-22,000	61,000,001-62,000,000
Tail	22,001-23,000	62,000,001-63,000,000
Engine	23,001-24,000	63,000,001-64,000,000
Battery	24,001-25,000	64,000,001-65,000,000
Payload	25,001-26,000	65,000,001-66,000,000
Connections	26,001-26,100	66,000,001-67,000,000
Materials/Section Properties	26,100-27,000	

The fixed-wing FE model was discretized in accordance with the mesh quality criteria (shown in Table 5) adopted by NIAR.

Table 5. Meshing criteria for shell and solid finite elements

Quality Parameter	Allowable Value	
	Shell Elements	Solid Elements
Minimum Side Length	1 mm	1 mm
Maximum Aspect Ratio	5	5
Minimum Quad Angle	45°	-
Maximum Quad Angle	140°	-
Minimum Tria Angle	30°	-
Maximum Tria Angle	120°	-
Maximum Warp Angle	15°	15°
Minimum Jacobian	0.7	0.5

Separate mesh size restrictions were specified for shell (triangular and quadrilateral) and solid (hexahedral) FEs. For shell elements, the mesh quality parameters were the minimum FE side length, maximum FE aspect ratio, minimum/maximum quadrilateral angles, minimum/maximum triangular angles, maximum warp angle, and minimum Jacobian. For solid elements, the parameters were the minimum side length, maximum aspect ratio, maximum warp angle, and minimum Jacobian. The minimum side length for all FEs was set to 1 mm. Since many non-structural geometric features (*e.g.*, small solder joints, electrical circuit wiring) of the fixed-wing FE model have a characteristic dimension below this threshold, such features were not included in the model. No FE size restrictions were placed on the definition of beam elements used to model fasteners and other interconnections.

A combination of shell, solid, and beam elements were used to mesh the fixed-wing model components. In general, the mesh size should be sufficiently fine in order to permit local buckling, crushing, and large deformations in explicit dynamic FE analyses. The 1 mm minimum FE side length was selected to ensure model fidelity while not significantly increasing computational run times.

Additionally, the stable time step for an explicit FE analysis is determined based on the time required for a sound wave to traverse the smallest element (proportional to dimensions) [24]. The target minimum time step for this model is 0.1 μ s. The fixed-wing FE model has 132,924 nodes and 99,089 FEs; this includes 68,621 solid, 30,334 shell, and 134 beam FEs. The following sections detail the specific parameters set for each FE type. A static assessment of the model was performed prior to running it in LS-DYNA using the preprocessing software HyperMesh. This software tools allow the user to efficiently generate a FE mesh, evaluate FE quality, eliminate any undesirable FE interpenetrations, verify connections, and perform other routine model validation functions.

2.3.1.1 Shell Finite Element

Relatively thin fixed-wing UAS parts such as the PCBs, carbon/epoxy tubes, battery pouches, zip ties, LCD panel, camera casing, and servomechanisms were modeled using fully integrated shell FEs with five through-thickness integration points or reduced-integration shell FEs with the Belytschko–Tsay FE formulation (*ELFORM* = 2 in the LS-DYNA keyword file) (Figure 16). Seventeen different shell element sections were created to account for the various part thicknesses in the associated fixed-wing UAS components. The Belytschko–Tsay formulation was used for most shell FEs in order to yield acceptable computational times. This reduced-integration element can lead to the occurrence of zero-energy hourglass modes, a common FE computational instability [25]. Hourglass type 4 behavior with an hourglass coefficient of 0.05 was selected for all reduced-integration shell FEs to minimize the likelihood of hourglass modes. Shell thinning options were turned off in order to avoid any numerical instabilities [25]. The numerical stability of shell FEs, especially in dynamic buckling and compressive modes, were further improved by enabling bulk viscosity for each shell FE formulation (*BULK VISCOSITY TYPE* = -2) [25], [27]. The shell normal update option for Belytschko–Tsay FEs was set to its recommended value (*IRNXX*=1) in order to avoid any numerical instabilities caused by initially warped elements [25].

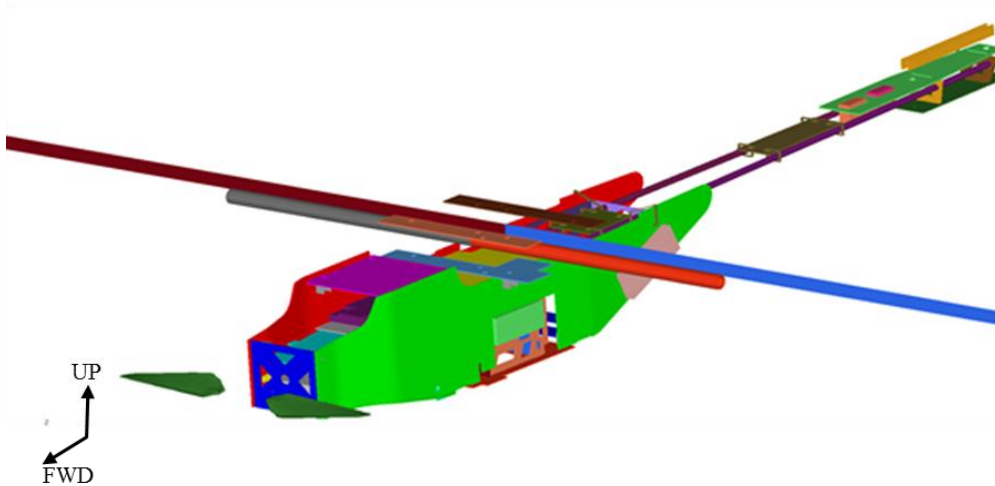


Figure 16. Fixed-wing UAS parts modeled with shell elements

2.3.1.2 Solid Finite Element

The wings, tail mount, vertical tail, horizontal stabilizer, motor, propeller hub, nozzle, and battery cells as well as foam blocks in the battery subassembly, camera lens, camera battery, and electric connectors were modeled as solid FEs (Figure 17). A reduced-integration solid formulation ($ELFORM = 1$) was used with the exception of the battery which uses a fully integrated solid formulation ($ELFORM = 2$). An hourglass type 6 behavior with an hourglass coefficient of 0.1 was assigned to all of the under-integrated solid FEs. When using solid FEs, hexahedral FEs are generally preferred over tetrahedral FEs and other solid FE types [25]. As mentioned previously, only hexahedral FEs were used in the fixed-wing FE model.

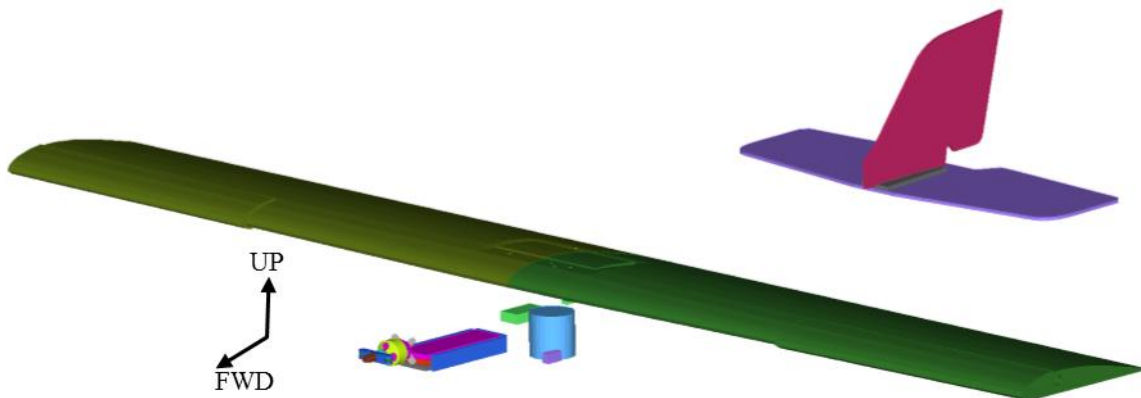


Figure 17. Fixed-wing UAS parts modeled with solid elements

2.3.1.3 Beam Finite Elements

Beam FEs are efficient for modeling simple axial/bending members such as stringers, columns, and bars. The fixed-wing FE model is comprised of a number of bolts and screws that connect the different components. All of these bolts and screws in the fixed-wing FE model were idealized using beam FEs. Uniform circular cross-section areas were assigned to each beam FE with an appropriate diameter based on the specific bolt/screw geometry. A computationally efficient and

robust Hughes-Lui FE formulation [26] with cross-section integration ($ELFORM = 1$) was used for each beam FE.

2.3.2 Material Definitions

The fixed-wing FE model is comprised of 13 unique materials. Five separate LS-DYNA library material models [27] were used represent these materials. Each material was grouped into one of three categories depending on its classification: (1) metals, (2) laminated composites, and (3) polymeric materials. Table 43 contains the material models used for each of the 119 LS-DYNA parts and is included in APPENDIX A.

2.3.2.1 Metals

The fixed-wing UAS motor, mounting brackets, and steel screws were assigned Steel 4340 properties. Material properties and damage parameters were obtained from Quan *et al.* [28]. The steel motor and mounting brackets were idealized using a Johnson-Cook plasticity material model (MAT_015). A Mie-Gruneisen equation of state was specified for solid FEs by specifying the $EOS_GRUNEISEN$ card in the LS-DYNA keyword file [26]; parameters were obtained from Shivpuri *et al.* [29]. A tabulated Johnson Cook elastic-viscoplastic material model (MAT_224) for Aluminum 2024-T351 [30] was obtained from the LS-DYNA Aerospace Working Group and used to model several parts in the motor subassembly.

A simple piecewise linear plasticity model (MAT_024) was used to model the material behavior of the steel screws using the Steel 4340 material parameters from Quan *et al.* [28]. A 50% effective plastic strain to failure was assumed for the screw failure criterion. The idealized outer camera shell and cylindrical lens housing were also modeled with MAT_024 using Aluminum 6061-T6 material properties [31]. Similarly, each thin aluminum plastic laminate pouch enclosing the cells of the fixed-wing UAS battery was modeled with MAT_024 using aluminum plastic laminate material properties [32].

2.3.2.2 Laminated Composites

The fixed-wing UAS laminated composite components are comprised of either quasi-isotropic carbon/epoxy composites or quasi-isotropic PCBs fabricated using FR4 glass-fiber reinforced epoxy. Carbon/epoxy composites are used for the wing spars, wing carry-through structure, and the tail booms. The fuselage subassembly as well as and select payload, motor, wing, and tail components are fabricated from PCBs. All laminated composite components were simulated using the Enhanced Composite Damage material model ($MAT_054-055$) using properties from [33] and [34]. Individual plies were assumed to be locally orthotropic. As an aside, quasi-isotropic PCBs are generally composed of multiple layers of woven glass fiber-reinforced epoxy substrates sandwiched between thin layers of copper foil. Electronic components, connectors, sockets and lead wires are typically attached to PCBs via through-hole connections or soldering joints. The minor reinforcing effect due to the outer layer of copper clad on the PCBs was neglected. Similarly, tiny pass-through holes and non-structural solder joints were not included in the PCB models.

The maximum allowable in-plane tensile, compressive, and shearing ply-stresses and ply-strains were defined in the fiber and transverse directions for each material (carbon/epoxy and FR4) [33] [34]. In general, individual ply failure was simulated as follows. The Chang-Chang interactive

failure criteria [27] was used to account for local tensile and compressive fiber failure under combined loading. Once fiber failure occurred, the lamina stress-strain response in the local fiber direction was assumed to be perfectly-plastic until the total strain in the fiber direction reached the maximum allowable strain. Similarly, in-plane transverse matrix failure (orthogonal to the fiber direction) was predicted using the Tsai-Wu interactive failure criterion [27]. Once the criterion was satisfied, the transverse lamina response was assumed to be perfectly-plastic until reaching the maximum allowable transverse strain. Once the strain in the fiber or transverse direction exceeded the maximum allowable strain value, then the element was deleted accordingly.

2.3.2.3 Polymeric Materials

2.3.2.3.1 Foam Materials

The fixed-wing UAS battery is composed of three prismatic pouched LiPo battery cells. Sahraei *et al.* [32] analyzed the mechanical behavior of a prismatic lithium ion battery and identified that the out-of-plane stress/strain relationship closely resembled that of foam materials [32]. The battery cells were then simulated in LS-DYNA [32] using a crushable foam model (*MAT_063*). The fixed-wing UAS battery and camera battery were similarly modeled using material properties from Sahraei *et al.* [32]. Additionally, each fixed-wing UAS battery cell was modeled as a stack of ten individual layers of solid FEs in order to better simulate battery cell micro-buckling. In general, LiPo batteries do not experience significant tensile loads. However, in complex impact loading conditions, local tensile stresses could become significant. The *MAT_ADD_EROSION* [27] card was enabled in the simulations to prevent unrealistic deformation under local tensile stresses. A maximum principal and volumetric strain at failure were set to 7% and 100%, respectively. Since the camera battery occupies a much smaller volume than the fixed-wing UAS battery, and is enclosed in the relatively rigid camera housing, it was modeled as a single block of solid FEs.

The wings, vertical tail, horizontal stabilizer, and foam used to position the fixed-wing UAS battery in its housing were assumed to be fabricated from expanded polystyrene. A crushable foam model (*MAT_063*) was used to simulate the expanded polystyrene with an assumed 1 MPa tensile cutoff stress. Similar to the battery cell model, the *MAT_ADD_EROSION* card was enabled, and the maximum principal and volumetric strains at failure were set to 7% and 100%, respectively.

2.3.2.3.2 Thermoplastics

As previously mentioned, various connectors and other components were assumed to be fabricated from thermoplastic materials including ABS and Nylon 6. Both materials were simulated using separate LS-DYNA piecewise linear plasticity material models (*MAT_024*). Strain rate dependent material properties were obtained for ABS from [35]. Nylon 6 was assumed to exhibit elastic-perfectly-plastic material behavior; material properties were obtained from [36] and [37]. Glass fiber reinforced Nylon 6 material properties were obtained from [37] and [38].

2.3.3 Connections

2.3.3.1 Bolts/Screws

All bolts/screws in the fixed-wing FE model were modeled using beam FEs. A single beam FE was used to represent a bolt regardless of its length, and a uniform cross-section area was assumed. Special care was taken to ensure that each beam FE was connected to any surrounding part(s) in

an appropriate manner. Rigid connectors were used to attach the beam FE nodes to surrounding nodes from other part(s) using multipoint constraint equations between master (beam FE) and slave (surrounding) nodes. In this model, the displacements and rotations from the slave nodes are identical to those of the master node. Such an idealization is shown in Figure 18 for a typical assembly held together by a bolt/screw. In the figure, the fixed-wing UAS fuselage sidewall and battery subassembly are held together by a bolt. A single beam FE (*i.e.*, bolt) was aligned along the hole axis. At each node of the beam FE, rigid connectors are used to constrain the motion of the surrounding nodes from an adjacent PCB. Shear and tensile failure modes were enabled for each beam FE based on the bolt's material model.

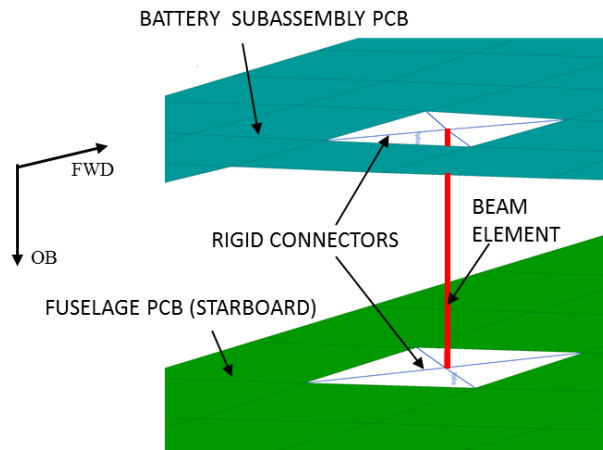


Figure 18. Fixed-wing UAS fuselage and battery subassembly PCBs connected using a beam FE and rigid connectors

2.3.3.2 Nylon 6 Zip Ties

Several parts in the fixed-wing FE model are joined together with Nylon 6 zip ties. Eight zip ties are located in the tail subassembly, two connect the tail subassembly to the fuselage subassembly, and two secure the battery to its PCB enclosure. All twelve zip ties were modeled with using shell FEs and are allowed to fail. For example, a PCB in the tail subassembly is secured to the tail booms using four zip ties as shown in Figure 19. Note that this modeling strategy allows some relative movement between the connected parts. Upon zip tie failure, the parts can become detached and separate as needed.

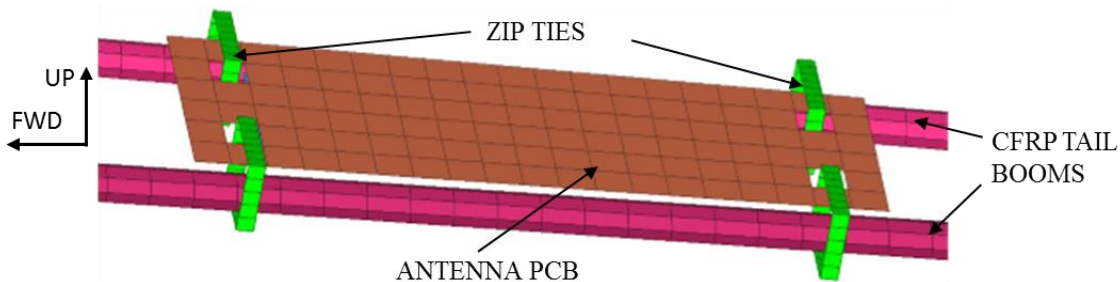


Figure 19. Fixed-wing UAS tail subassembly PCB supported by four zip ties

2.3.3.3 Mounting Brackets

The fixed-wing FE model contains 16 mounting brackets that are permanently attached to PCBs via solder joints. These brackets are used to secure the wings, payload, firewall, and GPS PCB to the fuselage via a screw or bolt connection. An example of a mounting bracket is shown in Figure 20 (A). This particular bracket is used to secure the wings to the fuselage via a screw. Each bracket was modeled using shell FEs. The FE representation of the bracket (with an attached screw) is shown in Figure 20 (B). Note that rigid connectors are used to attach the bolt to the mounting bracket.

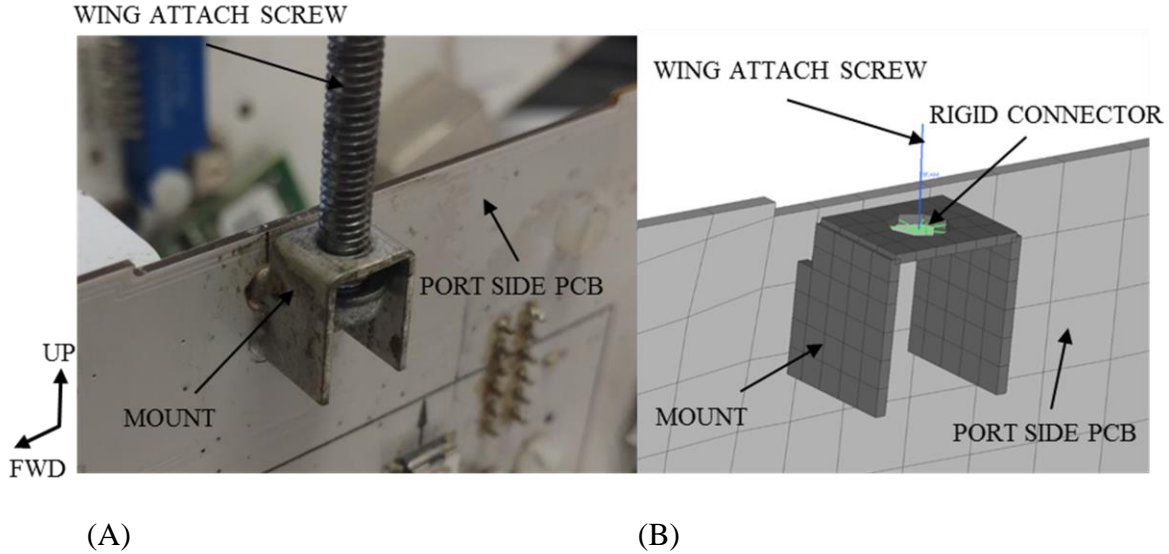


Figure 20. (A) Mounting bracket and (B) FE idealization

2.3.4 Contact Modeling

LS-DYNA provides a wide variety of techniques for simulating surface contact behavior [26]. The FE surface contact definitions used in the fixed-wing UAS model are outlined as follows. Four distinct contact types were used to define the contact behavior among individual fixed-wing UAS parts; these generally involved establishing contact laws and failure criteria between master surfaces/nodes and corresponding slave surfaces/nodes. These baseline contact definitions were shown to sufficiently simulate the impact behavior of the fixed-wing model without incurring any significant numerical instabilities across a wide range of target models. Note that the contact definitions are highly problem specific and depend on the structural geometry, morphology, and material properties of a given target. For example, simulated UAS impacts to targets with sharp “knife-edge” geometries may require different contact definitions to ensure numerical stability than impacts to targets with large contact surface areas (*i.e.*, flat plates). Slight modifications to the baseline contact definitions may be required depending on the nature of the impact scenario and target under consideration.

In LS-DYNA, the *CONTROL_CONTACT* card can be specified to overwrite individual default contact parameters globally as required [26]. For example, shell thickness offsets during contact were considered (*SHLTHK* = 1). For tied contact behavior where slave nodes are constrained to move with a master surface, the slave nodes are projected onto the master surface by default. This

option was disabled in the fixed-wing model (*TIEDPRJ* = 1). Penetrations encountered during the first timestep were permitted (*IGNORE* = 1). In the fixed-wing FE model, a global surface contact definition was used to specify the contact behavior among the vast majority of parts. In addition, three separate contact definitions were used to characterize the structural interconnections at solder joints in the fixed-wing UAS FE model.

2.3.4.1 Global Surface Contact

A single global surface contact definition was adopted to describe the majority of possible contact scenarios during component impacts using the *AUTOMATIC_SINGLE_SURFACE* card [26]. Static and dynamic friction coefficients between contacting surfaces were assumed 0.2. Segment-based contact (*i.e.*, over a viable FE surface/edge) was assumed (*SOFT* = 2), and warped segment checking was enabled (*SBOPT* = 3). Additionally, surface penetrations were assessed at nodes and FE edges to improve the accuracy of the simulated contact behavior (*DEPTH* = 13).

2.3.4.2 Solder Joints

The fixed-wing FE model consists of a number of solder joints, which connect PCBs, electrical connectors, and electronic components to each other. Figure 21(A) shows a picture of two actual solder joints connecting two PCBs to one of the fuselage vertical sidewalls. Solder joints are modeled by creating one of three contact definitions depending on the type of joint. It was assumed that the static and dynamic friction coefficients between two relatively smooth surfaces were appropriately small (*i.e.*, 0.01-0.05).

Surface contact between two soldered PCBs was simulated by defining the *CONTACT_TIED_SHELL_EDGE_TO_SURFACE* card in the LS-DYNA keyword file [26]. Recall that a stub from one PCB is fitted tightly into a corresponding slot in a mating PCB and soldered. The *BEAM_OFFSET* option was enabled to transfer force/moment resultants between the master surface and slave nodes along a shell FE edge using beam-like springs. The FE representation of this contact type is shown in Figure 21(B). Contact is defined between slave nodes along one PCB edge (stub) and shell FEs (master surfaces) corresponding to the location of the PCB slot. The static and dynamic friction coefficients between the two connecting parts were set to 0.01.

Solid FEs were connected to shell FEs by defining the *CONTACT_TIED_NODES_TO_SURFACE* card [26]. This definition was necessary to simulate the surface contact between soldered electrical connectors and components. Discrete springs were used to transfer force/moment resultants between the master surface and slave nodes by enabling the *OFFSET* option. The static and dynamic friction coefficients between solid and shell FEs in contact were each set to 0.05. Slave (*SST*) and/or master (*MST*) thickness parameters were specified in both the *TIED_SHELL_EDGE_TO_SURFACE* and the *TIED_NODES_TO_SURFACE* contact cards, if applicable, in order to better define the location of the contact surface. The actual fixed-wing UAS camera battery was soldered to a PCB within the camera housing. Since such PCBs were not explicitly simulated, a separate surface contact (*CONTACT_TIEBREAK_NODES_TO_SURFACE*) was defined to support the battery within the camera housing during impact.

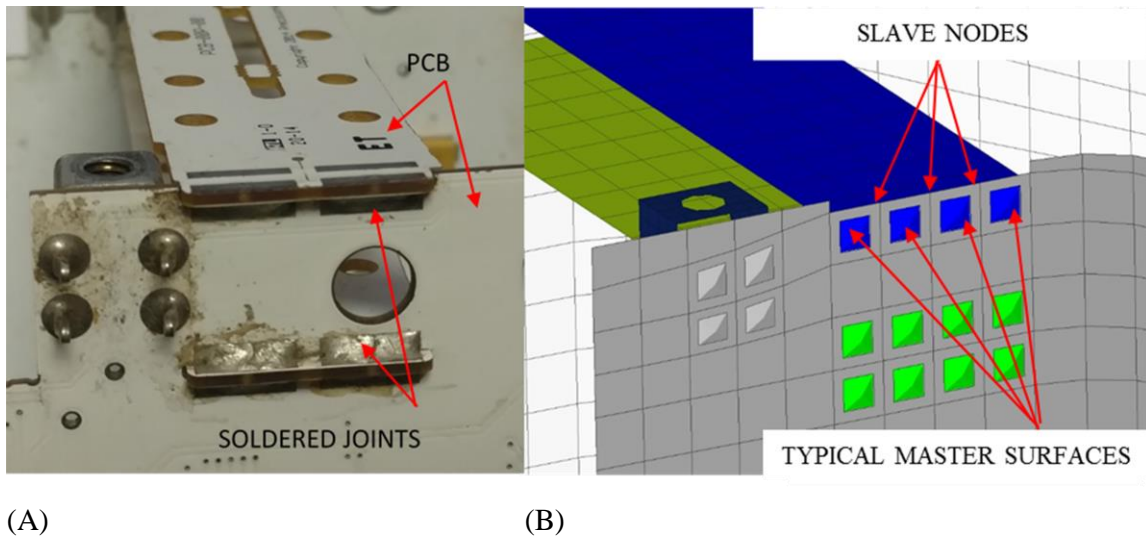


Figure 21. (A) Solder connection between PCBs and (B) FE idealization

2.3.5 Fixed-Wing UAS Component Mass Check

As suggested previously, the fixed-wing UAS components and/or subassemblies were weighed individually. Since the motor and battery subassemblies were used in ballistic component level tests (see section 2.4), special care was taken to ensure that the simulated mass properties of these components were within a fraction of a percent of the measured values. Similarly, the mass of the simulated payload (camera) was within a fraction of a percent of the actual value. Again, the relatively high-density motor, battery, and payload subassemblies represent a significant fraction of the fixed-wing UAS's total weight and are likely to be particularly damaging during mid-air impacts to manned aircraft. The PCB density used in the simulations was based upon measurements from a representative PCB sample; the assumed density did not account for embedded copper circuitry, solder joints, small pass-through holes, and other minor features. The actual fixed-wing UAS PCB fuselage and support structures contained large numbers of small computer chips, hundreds of electronic connector pins and/or solder connections, Ethernet ports, card readers, electrical wires, and other non-structural features that were not explicitly modeled. The mass of such components can be accounted for by the inclusion of non-structural point masses in the FE model. As an aside, the number and distribution of point masses employed in the idealized UAS model can be tailored to precisely match the mass of the actual UAS, or to slightly modify the overall UAS mass properties in order to coincide with some reference projectile (*i.e.*, 4.0 lb bird).

2.4 UAS COMPONENT LEVEL TESTS AND VERIFICATION

This section presents a description of the various component level tests performed as well as a description of the procedure followed to verify the FE model by correlation to the physical testing. For each of the tests, a simulation was set up with the same conditions (initial conditions, boundary conditions, etc.) as the physical test and the same parameters were output for comparison and correlation with test results.

2.4.1 Ballistic Component Level Tests

Multiple fixed-wing UAS component-level impact tests were performed. The fixed-wing UAS contains three significant high-density components: the motor, battery, and camera. In order to verify the component-level FE models, the impact behaviors of the motor (without the firewall and propeller) and the battery subassembly were characterized. Three motors and one battery subassemblies were supplied to MSU by Precision Hawk In addition, one battery was supplied by MSU GRI. The impact behavior of the camera was not characterized as part of this work.

2.4.2 Selection of Components for Ballistic Tests

A set of three complementary studies were carried out by the NIAR to understand which factors influence a midair collision with an UAS. A detailed description of these studies can be found in APPENDIX B.

In the first study, four 1.81 kg (4.0 lb) projectiles comprised of typical UAS materials or materials combinations (steel, aluminum, plastic, LiPo battery) were compared with a bird of the same mass. The projectiles were impacted into a flat aluminum plate at 169.8 m/s (330 knots), and the projectile material behavior and the load transfer to the target was compared. It was identified that the components with greater strength and stiffness induced greater damage and higher loads.

In a different study, four spherical 34 g projectiles, comprised of the same UAS materials as in the first study, were compared with an ice projectile of equivalent mass at velocities ranging from 56.6-180 m/s (110-350 knots). The study's objective was to compare projectile impacts involving UAS materials to hail impacts. Projectiles comprised of higher stiffness/strength, more dense materials (*i.e.*, steel or aluminum) produced aluminum target panel perforations at impact speeds above 102.9 m/s (200 knots), while projectiles comprised of less dense, more compliant materials failed to penetrate the target panels at velocities up to 180 m/s (350 knots). These results suggest that hard UAS components, such as motors, can be particularly damaging during high-speed impacts, which would later prove to be correct with physical testing.

Finally, the influence of mass concentration on the damage introduced into a structure during impact was investigated. Impact simulation results obtained using a single 1.81 kg (4.0 lb) spherical steel projectile were compared to results obtained using either 2, 4, 6, or 8 independent spherical projectiles with the same overall mass. Distributing the overall mass between multiple, not connected, projectiles increased the internal energy absorbed by the impacted structure and caused the masses to more rapidly decelerate than for the case of a single projectile. Therefore less damage was created.

From these three studies, it was concluded that UAS components with a higher mass, stiffness, and/or strength pose a greater threat to a given target structure. Therefore, the fixed-wing UAS motor, battery, and camera were selected as critical projectiles in component level ballistic testing. The fixed-wing UAS camera was unable to be tested as part of this study since it exceeded the maximum compressed gas gun projectile size.

2.4.3 Ballistic Test Setup

The target frame for the ballistic impact test consisted of two square steel frames bolted together, sandwiching about a flat aluminum test panel. The frame was bolted in all four corners to the

anchor frame, through the load cells. The test frame assembled in the testing rig as well as the positions of the load cells is shown in Figure 22.

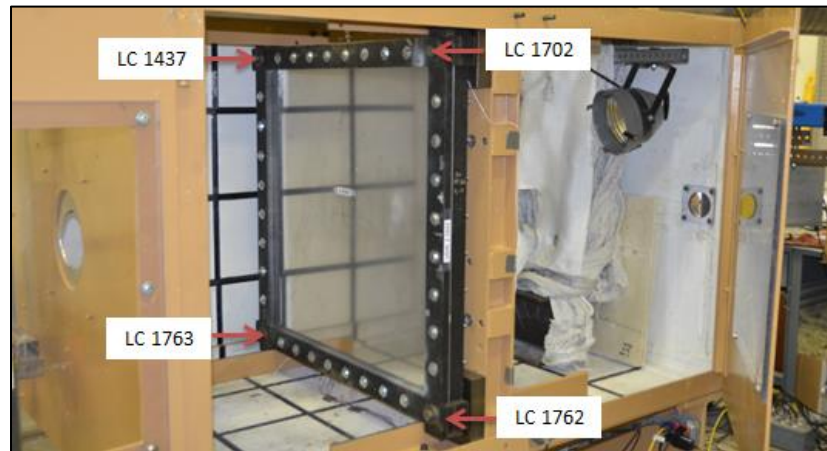


Figure 22. Test frame setup for ballistic component level tests (LC = load cell)

2.4.4 Ballistic Test Equipment

The following instruments were used to conduct the ballistic tests and record all of the necessary data.

I. Compressed Gas Gun System:

A compressed gas gun system was used to accelerate the projectiles (UAS motors, batteries) up to velocities of 128.6 m/s (250 knots) and impact precisely the center of the panel specimen. Tolerances of 5% in the velocity and 5° deviation in the perpendicularity of the impact were desired.

II. Projectile Sabot:

Custom-designed polystyrene foam sabots were used to support each type of projectile in the compressed gas gun and to provide a uniform loading surface during launch. Additional low-density foam blocks were placed around the projectiles to support and position them in the center of each sabot. Typical sabot configurations for the fixed-wing UAS motor and battery subassembly are shown in Figure 23.

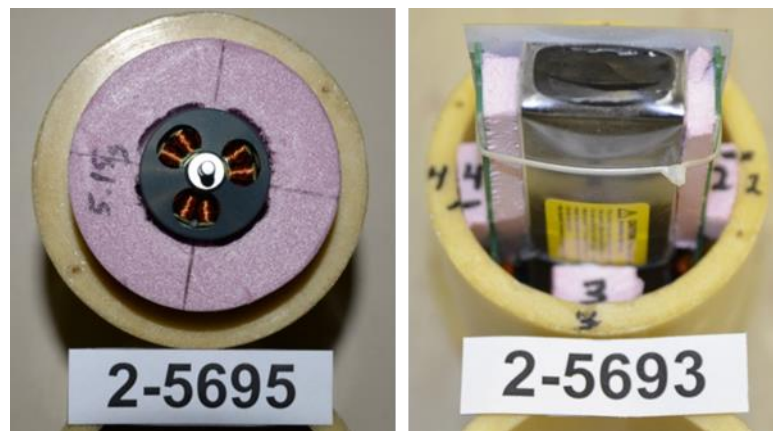


Figure 23. Typical sabots for the fixed-wing UAS motor (left) and battery (right) subassembly

III. Load Cells:

Four uniaxial load cells from PCB Piezotronics were located at the corners of the test specimen mounting frame and were used to record the force transferred to the test fixture base. The load cell force gages had a 266,893 N (60,000 lbf) capacity and had a sampling rate of 1 MHz. All load cells were calibrated to within 1.1% linearity with $\pm 1\%$ of uncertainty. Figure 24 and Figure 22 show the load cell and their positions for the test setup, respectively.



Figure 24. PCB Piezotronics load cell used in ballistic component level tests

IV. Strain Gages:

Thirteen linear, $\frac{1}{4}$ in grid, 350 Ω standard elongation strain gages from Vishay were installed at selected locations on the panel specimens at the NIAR. The data acquisition system sampled results at a rate of 1 MHz. The locations where the uniaxial strain gages were installed on the panel are shown in Figure 25; specifications are shown in Table 5.

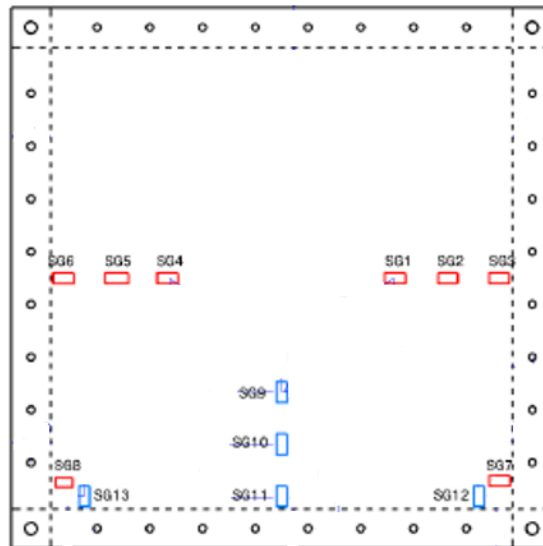


Figure 25. Strain gages on test frame for ballistic component level tests

Table 6. Strain gage specifications for component level tests

Gage ID	K-216.31-2041
Gage Resistance	$350 \pm 0.3\% \Omega$
Gage Factor	$2.02 \pm 1.0\%$
Transverse Sensitivity	0.00%
Adhesive	AE-10
Post Curve	N/A

V. High-Speed Video Cameras:

Three high-speed video cameras were used to record the projectile impacts at 10,000 frames per second from three different viewing angles. Camera 1 was positioned perpendicular to the shot line, camera 2 was positioned in front of the plate at an oblique angle and camera 3 recorded the impact from the top.

VI. 3D Digital Image Correlation (DIC) system:

A Vision Research high-speed camera capable of data acquisition rate of 10 kHz was used for the digital image correlation setup. A 1 ft x 1 ft portion at the center on the rear side of the panel was painted white and a random black speckle pattern was applied using spray paint. The camera setup was pointed at this speckled patch. The DIC software was able to capture the 3D displacements and in-plane strains induced in the panel during impact.

VII. Projectile Velocity Measurement:

Projectile velocity measurements were obtained using two lasers placed perpendicular to the projectile's trajectory as it exited the barrel. The distance between the lasers was known and allowed for automated velocity calculation based on the time difference from the projectile sequentially interrupting the laser beams.

In addition, digital camera still images of the test setup and the test articles were taken before and after each test.

2.4.5 Test Matrix

Three motor and two battery subassembly impact tests were performed using the compressed-gas gun launcher described in section 2.4.3 . The test matrix for the five tests is shown in Table 7.

Two motor impact tests were performed at a nominal impact velocity of 128.6 m/s (250 knots) and one was performed at 64.3 m/s (125 knots). Such velocities are consistent with the relative velocities between arbitrary fixed-wing UASs and manned aircraft operating at altitudes less than 4,000 m (13,120 ft). Each component was impacted onto a 1.59 mm (0.0625 in, *i.e.*, a typical aircraft Aluminum skin thickness [39][40]) thick instrumented Aluminum 2024-T3 flat panel secured within the NIAR test frame (section 2.4.2). Preliminary FE analyses suggested that the motor would completely penetrate the instrumented aluminum panel at an impact velocity of 128.6 m/s. The lower motor impact velocity was selected in order to minimize the likelihood of motor penetration.

The impact behavior of the battery subassembly was evaluated at a nominal impact velocity of 128.6 m/s (250 knots). Preliminary FE models of battery subassembly impact tests suggested that

for an impact velocity of 128.6 m/s, the battery subassembly would not penetrate the instrumented aluminum panel. One concern regarding UAS impacts to aircraft structures is the likelihood of a charged battery ignition/explosion. Accordingly, one of the battery subassembly impact tests was performed with a partially (50%) charged battery. The remaining impact test involved a fully discharged battery.

Table 7. Component test matrix with results

Test Number	Shot Number	Panel Type	Projectile Type	Projectile Weight (g)	Pitch (Deg.)	Yaw (Deg.)	Impact Velocity (knots)	Impact Velocity	Deviation from nominal velocity	Impact Energy (J)	Panel Penetration (Y/N)	Rebound Velocity (m/s)	Residual Velocity (m/s)	Peak Load (N)	Permanent Deformation (mm)	Max Deflection (mm)
MOTOR																
1	2-5695	0.063" Al	Motor	75.89	1.8° D	1.5° L	247.95	127.56	-0.8%	617.49	Y	n/a	93.57	15,160	n/a	n/a
	2-5700	0.063" Al	Motor	76.83	4.3° D	30.8° L	253.88	130.61	1.5%	655.37	Y	n/a	99.06	14,160	n/a	n/a
2	2-5699	0.063" Al	Motor	77.36	0.9° U	7.1° L	126.8	65.23	-1.4%	164.59	N	7.92	n/a	30,590	n/a	24.89
BATTERY																
3	2-5693	0.063" Al	Battery (Discharged)	329.73	10.8° U	11.5° L	233.43	120.09	-6.6%	2377.97	N	n/a	n/a	93,380	19.23	42.16
4	2-5694	0.063" Al	Battery (50% Charged)	340.25	3.2° D	7.6° L	255.95	131.67	2.4%	2949.99	N	n/a	n/a	117,530	24.21	46.23

2.4.6 Impact Test Results

For each impact test, the projectile impact velocity, impact energy, and pitch and yaw impact angles were determined. In addition, the peak load, permanent through-thickness deflection, and maximum deflection were determined if possible. Projectile rebound and residual velocities were determined, if applicable. Images acquired from high-speed cameras were used to calculate the projectile orientation at impact. A global Cartesian coordinate system was defined relative to the gas gun. The flight path of a projectile corresponded to the positive z -axis, and the target was located in the xy plane. The x - and y -axes were located in the horizontal and vertical directions, respectively. Ideally, the projectile centerline at impact would correspond to the z -axis. The actual pitch and yaw angles of a given projectile at impact, however, were determined relative to the projectile's centerline. The definitions of positive pitch and yaw angles relative to the global coordinate system are graphically presented in Figure 26. The roll angle could not be accurately determined based on the experimental setup.

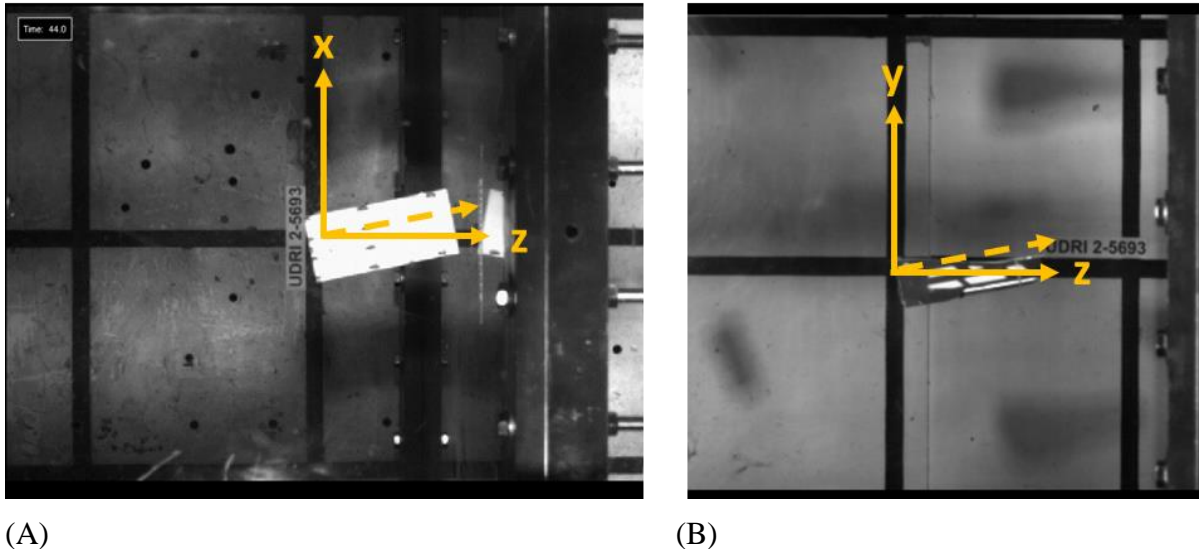


Figure 26. Measurement of the (A) Yaw and (B) Pitch angles at impact from a battery subassembly impact test

2.4.6.1 Motor Impact Tests

As previously mentioned, three fixed-wing UAS motors were tested with no propeller assembly attached. The motor is the densest component on the fixed-wing UAS and poses one of the most significant threats in an airborne collision. The measured pitch/yaw angles, impact velocity, impact energy, projectile rebound/residual velocities, peak load, permanent through-thickness plate displacement, and maximum plate deflection are included in

Table 7. All three impact velocities closely matched the desired velocities. Minor pitch and yaw angles were observed for two of the tests ($<7.1^\circ$) resulting from complex sabot/projectile interactions that commonly occur during the sabot separation phase after launch. One of the motors tested at a 128.6 m/s nominal impact velocity (target panel 2-5700) struck the target at a high yaw angle (30.8°).

No significant differences in the impact results for the two 128.6 m/s nominal impact velocity tests

Test Number	Shot Number	Panel Type	Projectile Type	Projectile Weight (g)	Pitch (Deg.)	Yaw (Deg.)	Impact Velocity (knots)	Impact Velocity	Deviation from nominal velocity	Impact Energy (J)	Panel Penetration (Y/N)	Rebound Velocity (m/s)
MOTOR												
1	2-5695	0.063" Al	Motor	75.89	1.8° D	1.5° L	247.95	127.56	-0.8%	617.49	Y	n/a
	2-5700	0.063" Al	Motor	76.83	4.3° D	30.8° L	253.88	130.61	1.5%	655.37	Y	n/a
2	2-5699	0.063" Al	Motor	77.36	0.9° U	7.1° L	126.8	65.23	-1.4%	164.59	N	7.9
BATTERY												
3	2-5693	0.063" Al	Battery (Discharged)	329.73	10.8° U	11.5° L	233.43	120.09	-6.6%	2377.97	N	n/a
4	2-5694	0.063" Al	Battery (50% Charged)	340.25	3.2° D	7.6° L	255.95	131.67	2.4%	2949.99	N	n/a

were observed, with the exception of the higher yaw angle for target panel 2-5700. Both motors penetrated the target panels. As a result, the rebound velocities, permanent plate displacement at the center of impact, and maximum deflections were not determined. Similar impact energies (617.49 N-m/655.37 N-m) and peak loads (15.16 kN/14.16 kN) were observed for the two tests. The residual velocities were 93.57 m/s and 99.06 m/s. All of these results indicate that the high yaw angle for one motor had a negligible influence on the impact behavior. The impact damage (petaling) to the target was consistent with a sharp object impact and is shown in Figure 27 for target panel 2-5695. No evidence of damage or permanent deformation in both motors was observed after testing.

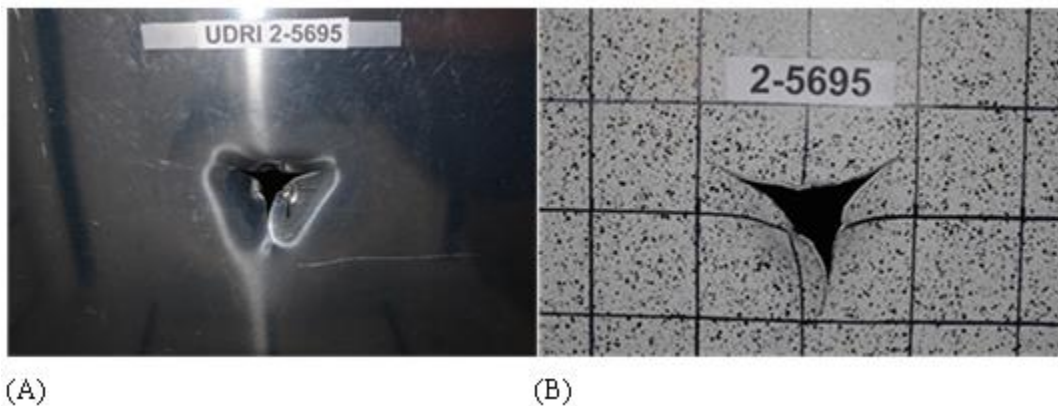


Figure 27 Deformation and fracture of target panel (2-5695) impacted with motor at 127.56 m/s:
(A) Impact side (B) Back side

A third motor impact test was performed at a lower nominal impact velocity of 64.3 m/s (125 knots). The motor perforated but did not completely penetrate the target panel 2-5699 (Figure 28). A rebound velocity of 7.9 m/s was measured, indicating that a significant amount of the impact

energy (164.59 N-m) was absorbed by the motor and panel. As an aside, the motor shaft slid back through the rotor without damaging any other parts of the motor as shown in Figure 29. No permanent deformation of the motor was observed. A maximum through-thickness plate deflection of 24.89 mm was measured at the center of impact using the DIC system. Additionally, the peak load during the impact test was 30.59 kN. Note that this force is significantly higher than the peak forces observed from the 128.6 m/s nominal impact velocity tests. This makes sense since the kinetic energy absorbed by the plate is greater for the non-penetrating impact.

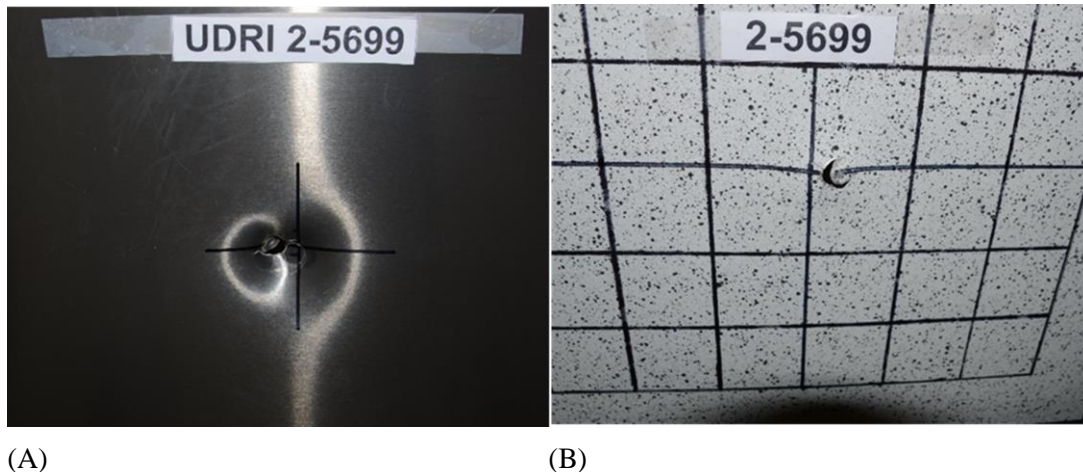


Figure 28. Deformation and perforation of test panel impacted with motor at 65.2 m/s: (A) Impact side (B) Back side

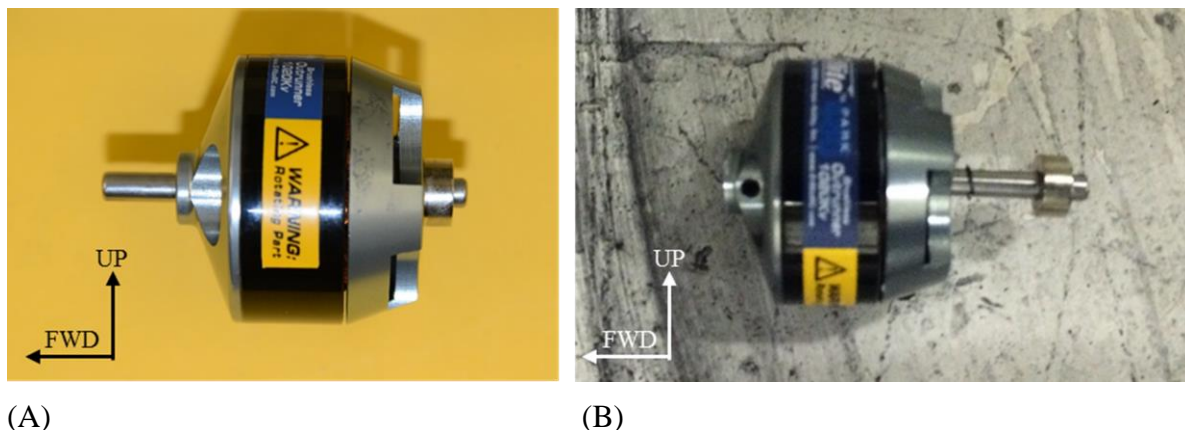


Figure 29. Motor (A) Before and (B) After 65.2 m/s impact test

2.4.6.2 Battery Impact Tests

Two battery subassemblies were impact tested with a measured impact velocity for each battery subassembly within 6% of the desired 128.6 m/s (250 knots) velocity (

Table 7). Some variation in the projectile pitch and yaw angles at impact was observed ($<12^\circ$). The two battery subassemblies did not penetrate the panel. Maximum through-thickness plate deflections of 42.16 mm and 46.23 mm were measured by the DIC system. Permanent through-thickness plate deflections of 19.23 mm and 24.21 mm were observed for both tests. The permanent deflection from target panel 2-5693 (

Table 7) caused by the battery subassembly impact is shown in Figure 30. The peak impact loads

Test Number	Shot Number	Panel Type	Projectile Type	Projectile Weight (g)	Pitch (Deg.)	Yaw (Deg.)	Impact Velocity (knots)	Impact Velocity	Deviation from nominal velocity	Impact Energy (J)	Panel Penetration (Y/N)	Rebound Velocity (m/s)
MOTOR												
1	2-5695	0.063" Al	Motor	75.89	1.8° D	1.5° L	247.95	127.56	-0.8%	617.49	Y	n/a
	2-5700	0.063" Al	Motor	76.83	4.3° D	30.8° L	253.88	130.61	1.5%	655.37	Y	n/a
2	2-5699	0.063" Al	Motor	77.36	0.9° U	7.1° L	126.8	65.23	-1.4%	164.59	N	7.9
BATTERY												
3	2-5693	0.063" Al	Battery (Discharged)	329.73	10.8° U	11.5° L	233.43	120.09	-6.6%	2377.97	N	n/a
4	2-5694	0.063" Al	Battery (50% Charged)	340.25	3.2° D	7.6° L	255.95	131.67	2.4%	2949.99	N	n/a

(93.38 kN/117.53 kN) and impact energies (2,377.97 N-m/2,949.99 N-m) were similar for both tests.

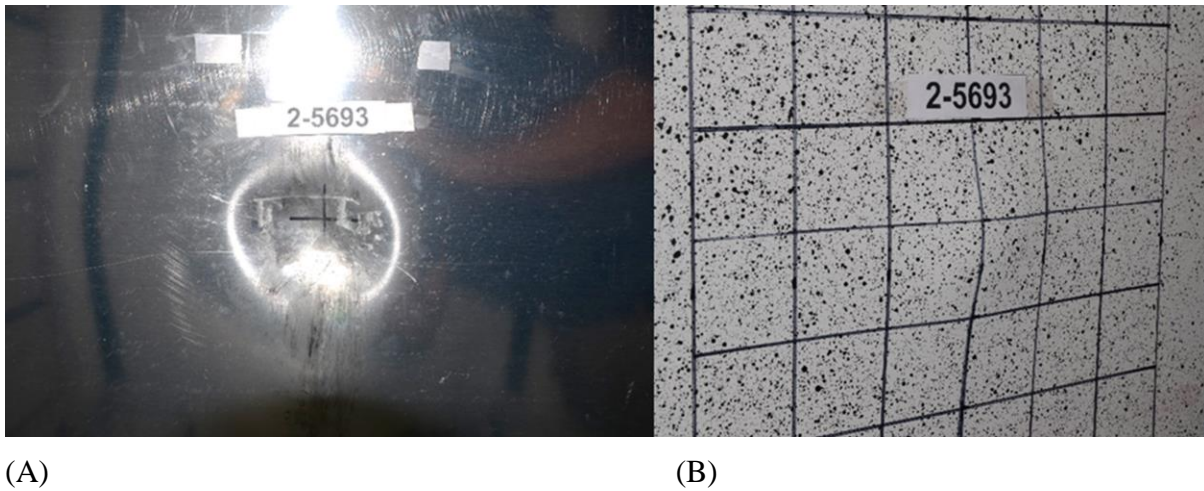
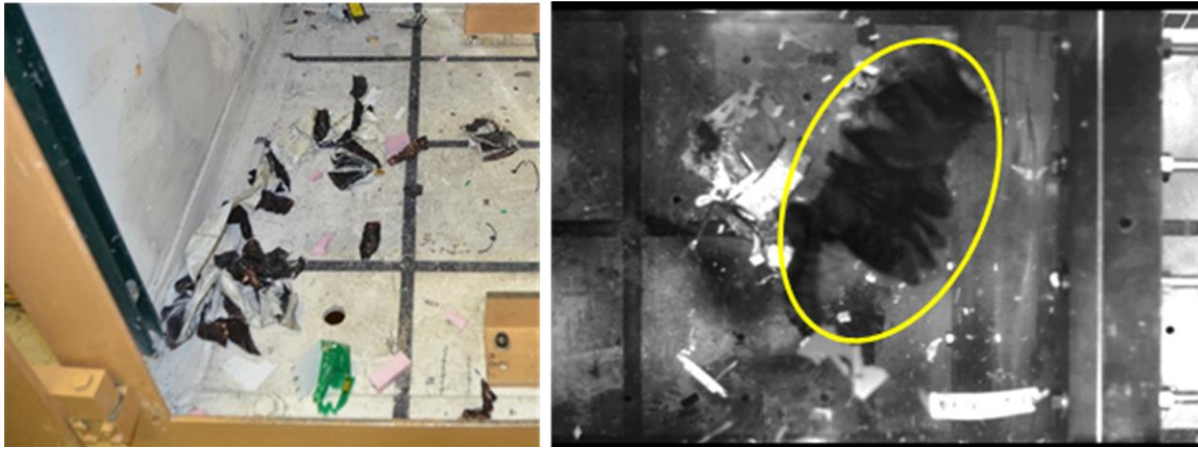


Figure 30. Permanent deformation of target panel 2-5693 impacted with battery subassembly at 120.09 m/s: (A) Impact side (B) Back side

Upon impact, both battery subassemblies were completely destroyed. Hence, it was not possible to determine the rebound velocity. Although one battery was partially charged, no signs of battery ignition/explosion due to the impact were observed. It is unclear if partially intact batteries would pose a fire hazard to aircraft. Figure 31 (A) shows the battery subassembly debris in the target chamber after a 120.09 m/s impact to the target panel (target panel 2-5693). Upon impact, the PCB

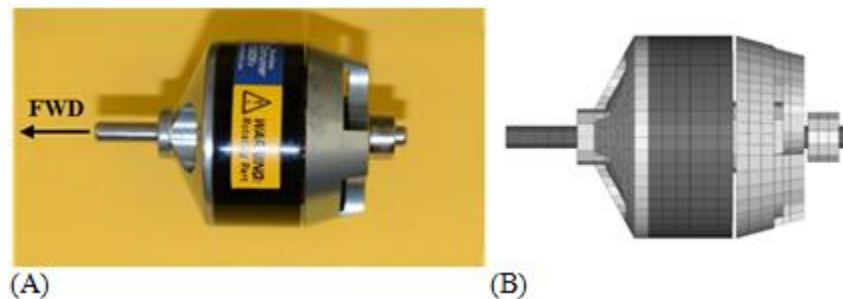
battery enclosure was shattered, and the battery cell ribbon assemblies rapidly unfolded as shown in Figure 31 (B).



(A) (B)
Figure 31. (A) Battery subassembly impact debris inside the target chamber and (B) Unfolding of the battery cell ribbon assembly

2.4.7 Fixed-Wing UAS Component FE Models

FE simulations of fixed-wing UAS battery subassembly and motor component tests were performed in order to facilitate Verification of the complete fixed-wing UAS model. High fidelity FE models of the motor (Figure 32), battery subassembly (Figure 33), Aluminum 2024-T3 target panel/steel test frame assembly (Figure 34) were developed. The steel motor model (Figure 32) was comprised of solid FEs. The battery subassembly model (Figure 33) was constructed as follows. Shell FEs were used to simulate the FR4 PCB housing, aluminum battery pouch, and Nylon 6 zip ties. The LiPo battery cells and foam supporting blocks were modeled using solid FEs. The motor and battery subassembly FE models were identical to those included in the complete fixed-wing FE model (*cf.*, Section 2.3).



(A) (B)
Figure 32. (A) Fixed-wing UAS motor and (B) FE idealization

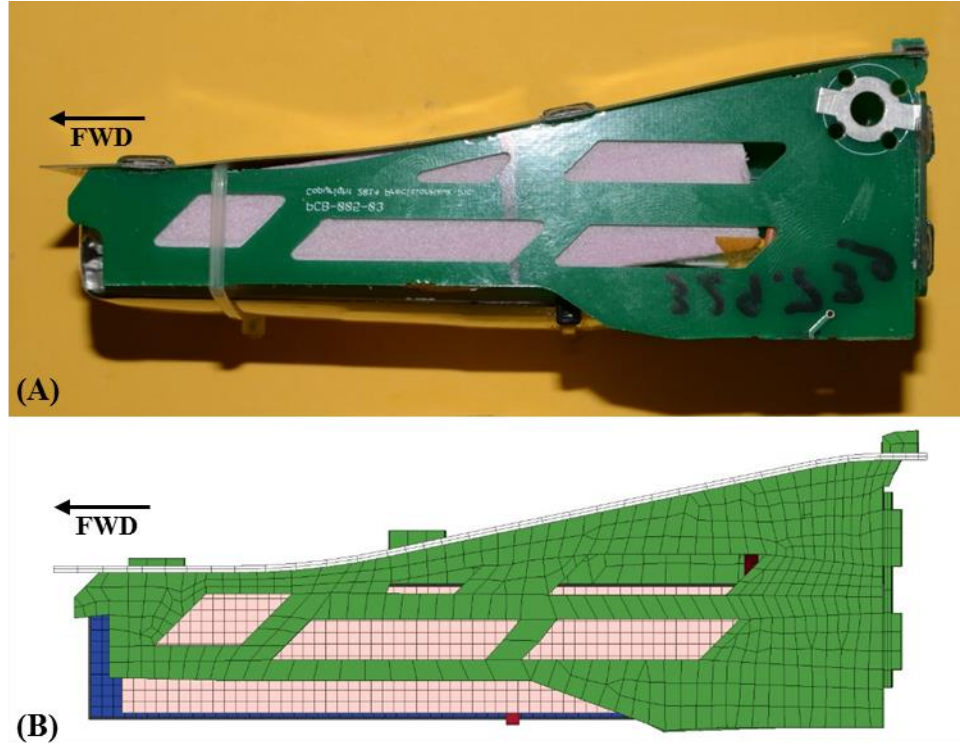


Figure 33. (A) Fixed-wing UAS battery subassembly and
(B) FE idealization

The FE model of the target (*i.e.*, target panel and steel test frame assembly) was developed previously by the NIAR [41]. It consists of a 1041.4 mm x 1041.4 mm aluminum target panel sandwiched between two steel frames as shown in Figure 34. The corners of the steel frames were bolted to an underlying steel support structure through four cylindrical load cell assemblies.

The 1.59 mm thick aluminum panel was discretized with fully integrated quadrilateral shell FEs ($ELFORM = 16$, $SHRF = 0.833$) using five through-thickness integration points. The Johnson-Cook material model (MAT_15) for the Aluminum 2024-T3 target panel was defined. Beam FEs were used to connect (“bolt”) the perimeter of the target panel to the steel frame assembly. The steel frame assembly was discretized with fully integrated ($ELFORM = 2$) hexahedral solid FEs. A piecewise linear plasticity model (MAT_024) was used to simulate the Steel 4340 test frame.

In the target panel FE model, element sets were defined corresponding to nominal strain gage locations (shown in green in Figures 34 (right) and 35 (right)) on the backside of the actual target panel. Calculated strains averaged over each element set were compared to measured strains at these locations. The four corner load cells (shown in blue in Figure 35) were modeled using solid FEs. Forces were calculated over a load cell cross-section and compared to the measured load-time history from the impact tests.

For each FE analysis, the *CONTACT_ERODING_SINGLE_SURFACE* contact algorithm [27] was used to characterize the surface contact between the fixed-wing UAS components and the target. A static and dynamic friction coefficient of 0.2 was assumed between each component (projectile) and target.

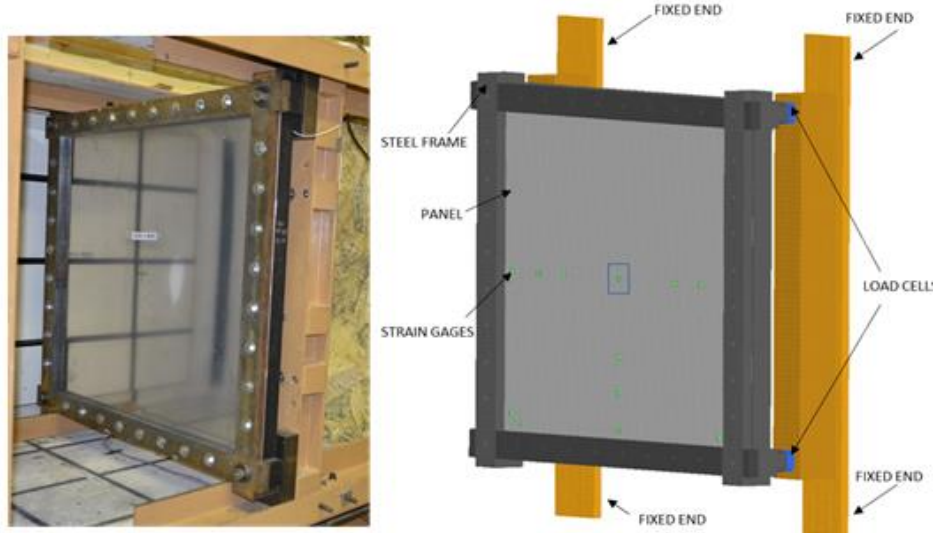


Figure 34. (Left) Typical target panel and test frame assembly and (Right) FE idealization

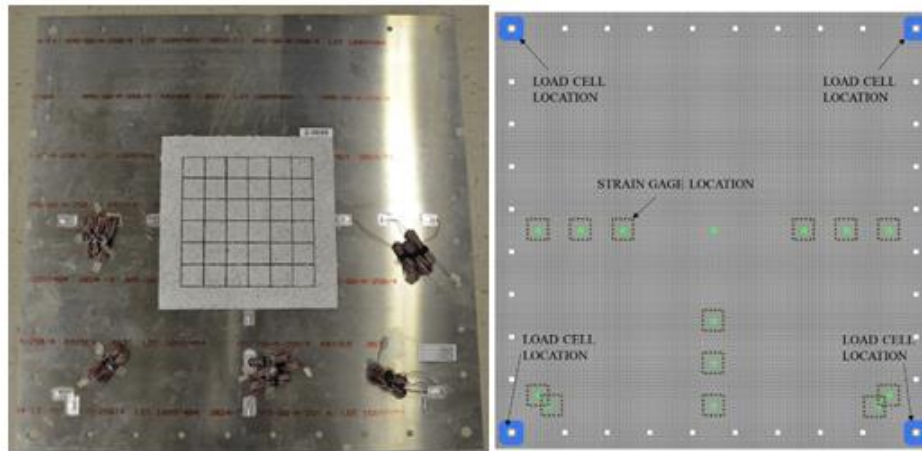


Figure 35. (Left) Typical target panel with strain gages and (Right) FE idealization

2.4.8 Fixed-Wing UAS Component FE Model Verification

Various motor and battery subassembly FE model analysis results were compared to experimental test data. FE estimates of the target panel backside strains were evaluated against actual strains measured at thirteen strain gage locations (SG1-SG13, *cf.*, Figure 36). Similarly, force-time histories were calculated in the FE model at the four load cells and compared to experimentally measured values. In all simulations, it was assumed that the projectiles struck the geometric center of the target panels. A 15 kHz low-pass filter was applied to the strain and load cell data for both the FE simulations and experiments in order to reduce high frequency oscillations in the data. A detailed procedure on the data processing is included in Appendix G. The experimental data were given a time offset to match the simulated first point of contact. The same offset was used for all plots within each test case.

In the FE simulations, the contact reaction force between projectile (*i.e.*, motor or battery subassembly) and target panel was used to define the end of contact. For example, Figure 37 shows the predicted contact reaction force between projectile and target from a motor impact simulation conducted at a nominal impact velocity of 128.6 m/s. As can be seen in the figure, the contact force rapidly increases with time and then drops as the projectile penetrates the target. Once the predicted contact force reached zero (either due to projectile penetration or rebound), the projectile and target were assumed to be no longer in contact.

A series of stability checks were performed for all component-level simulations. The nature and type of the stability checks will be discussed in detail for the full fixed-wing UAS impact simulations in APPENDIX A.

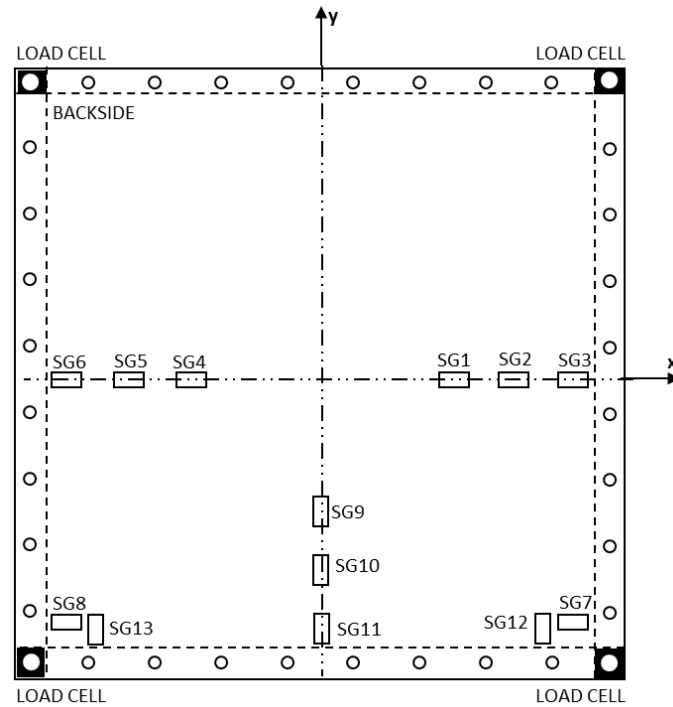


Figure 36. Target panel strain gage and load cell locations

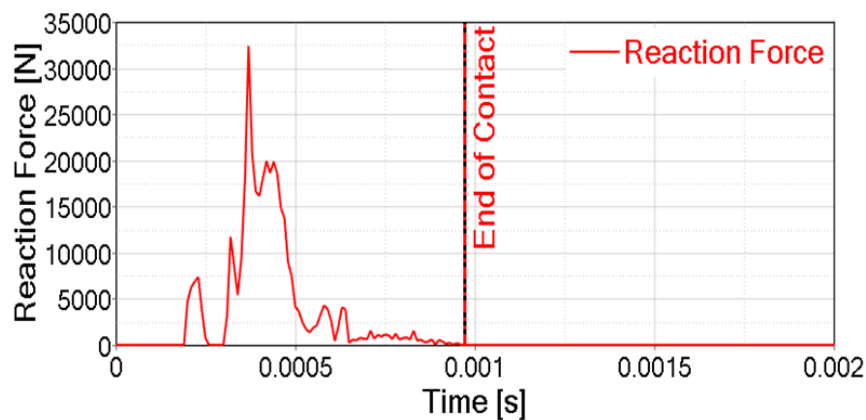


Figure 37. Predicted motor contact reaction force with the target panel (impact velocity, 128.6 m/s)

2.4.8.1 Fixed-Wing UAS Motor FE Model Verification

Calculated strain-time histories at each target panel strain gage location (SG1-SG13) were compared to measured histories from two motor impact tests conducted at a nominal velocity of 128.6 m/s (250 knots) and one motor test conducted at a 65.2 m/s (126.7 knots) impact velocity. For the two higher velocity motor impact tests, there were minor differences in the measured strain-time histories for each test due to subtle differences in measured velocity as well as pitch and yaw angles. For these two tests, a single simulation was performed for a normal impact at a nominal velocity of 128.6 m/s.

In the FE simulation of the lower speed motor impact test, the actual measured impact velocity and pitch/yaw angles were modeled. In general, the predicted strain-time histories at all thirteen strain gage locations reasonably matched measured results for all three tests. This is particularly impressive since all three motor impact tests involved complete or partial penetration of the target panels. For example, the calculated/measured extensional strains in the x -direction at one near-field (SG1) and one far-field (SG3) strain gage location are shown in Figure 38 (A) and Figure 38 (B), respectively, for the two tests (target panels 2-5695, 2-5700) conducted at a nominal impact velocity of 128.6 m/s. The calculated near-field and far-field strain-time histories accurately captured both the primary peaks and the essential character of the measured strains throughout the impact duration. Similar results were obtained at the remaining strain gage locations for these two tests; measured/calculated strain-time histories at all strain gage locations are included in APPENDIX A.

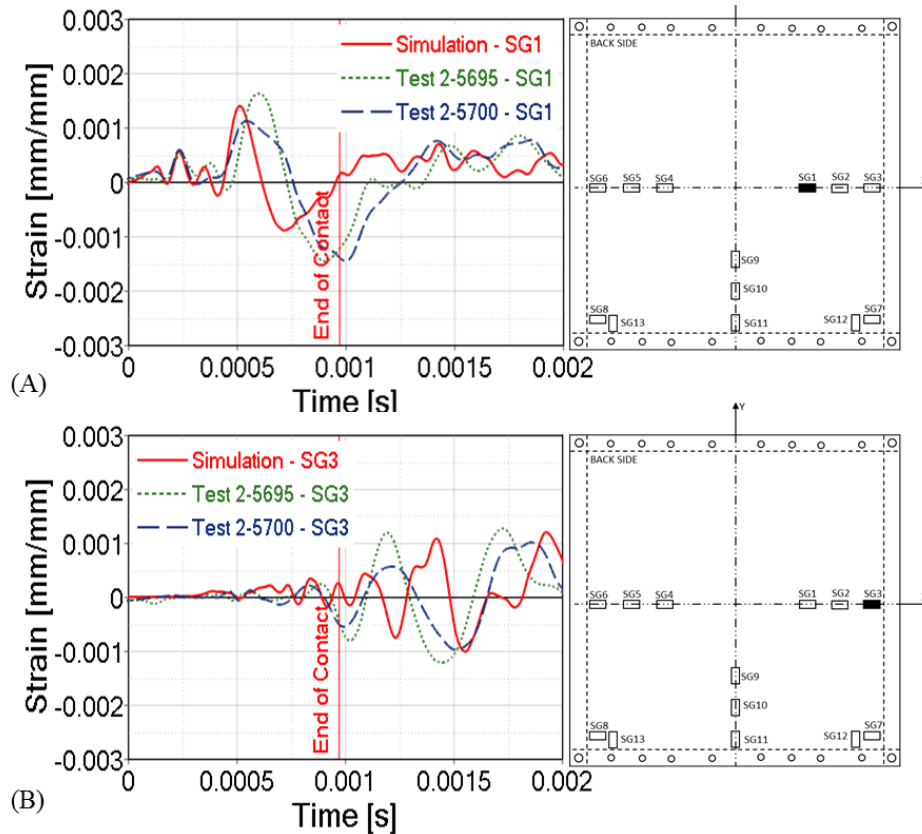


Figure 38. Measured and predicted target panel extensional strain in x -direction at a (A) Near-field (SG1) and (B) Far-field (SG3) strain gage for a motor impact at 128.6 m/s nominal velocity

In addition, simulated full-field strain components and peak plate deflections closely matched measured strains obtained from a DIC system up until the point of projectile penetration. Prior to penetration, the estimated strain field captured the essential character of the local field in the vicinity of the impact site. After penetration, the high-speed DIC images became obscured by DIC speckle paint delamination from the target plate surface, impact debris, target petaling that changed the orientation of the plate surface, and the motor itself. Hence, DIC measurements could not be used to characterize the peak deflection after penetration.

Calculated load-time histories at each load cell were compared to measured histories from the two motor impact tests (target panels 2-5695, 2-5700) conducted at a nominal velocity of 128.6 m/s (250 knots). In general, the predicted load-time histories at all four load cells reasonably matched measured results. The simulated and measured load-time histories at a typical load cell are shown in Figure 39. Load-time histories for the remaining load cells demonstrated a similar level of correlation; load-time histories for all four load cells are included in APPENDIX A.

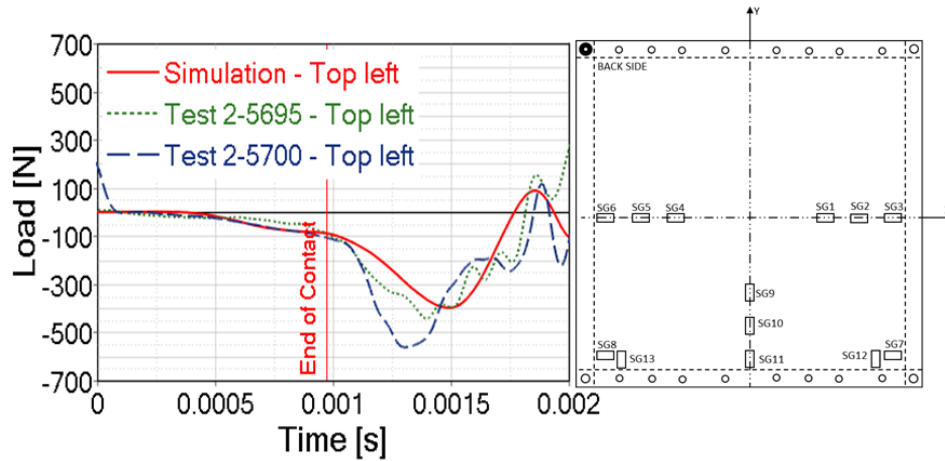


Figure 39. Measured and predicted force in the top left load cell for a motor impact at nominal velocity of 128.6 m/s

High-speed images of the higher velocity motor impacts were qualitatively compared to a simulated nominal impact. For example, Figure 40 shows a series of experimental images from the onset of impact for target panel 2-5695 until the end of contact. The figure also includes images of the simulated impact at the same moments in time. The motor is shown at the center of the target panel in Figure 40 (A) just prior to impact. Shortly after impact, the motor began to perforate the panel as shown in Figure 40 (B). The target panel started petaling as the motor continued in the impact direction (Figure 40 (C)). The motor completely penetrated through the panel at the end of contact (Figure 40 (D)).

The FE simulation results reasonably matched the observed penetration behavior throughout the impact event. Figure 41 contains an image of the actual penetrated target panel (target panel 2-5695) as well as an image of the failed target panel from the nominal impact simulation. Both the actual and simulated panel demonstrated petaling deformation consistent with sharp projectile penetrations. While the target and simulated panels displayed three and four distinct petals, respectively, the size and shape of the penetration domains were very similar. Since petaling in real materials is a stochastic process, the number of actual petals will vary from one test to another. As an aside, target panel 2-5700 involved a relatively large yaw angle (+30.8°).

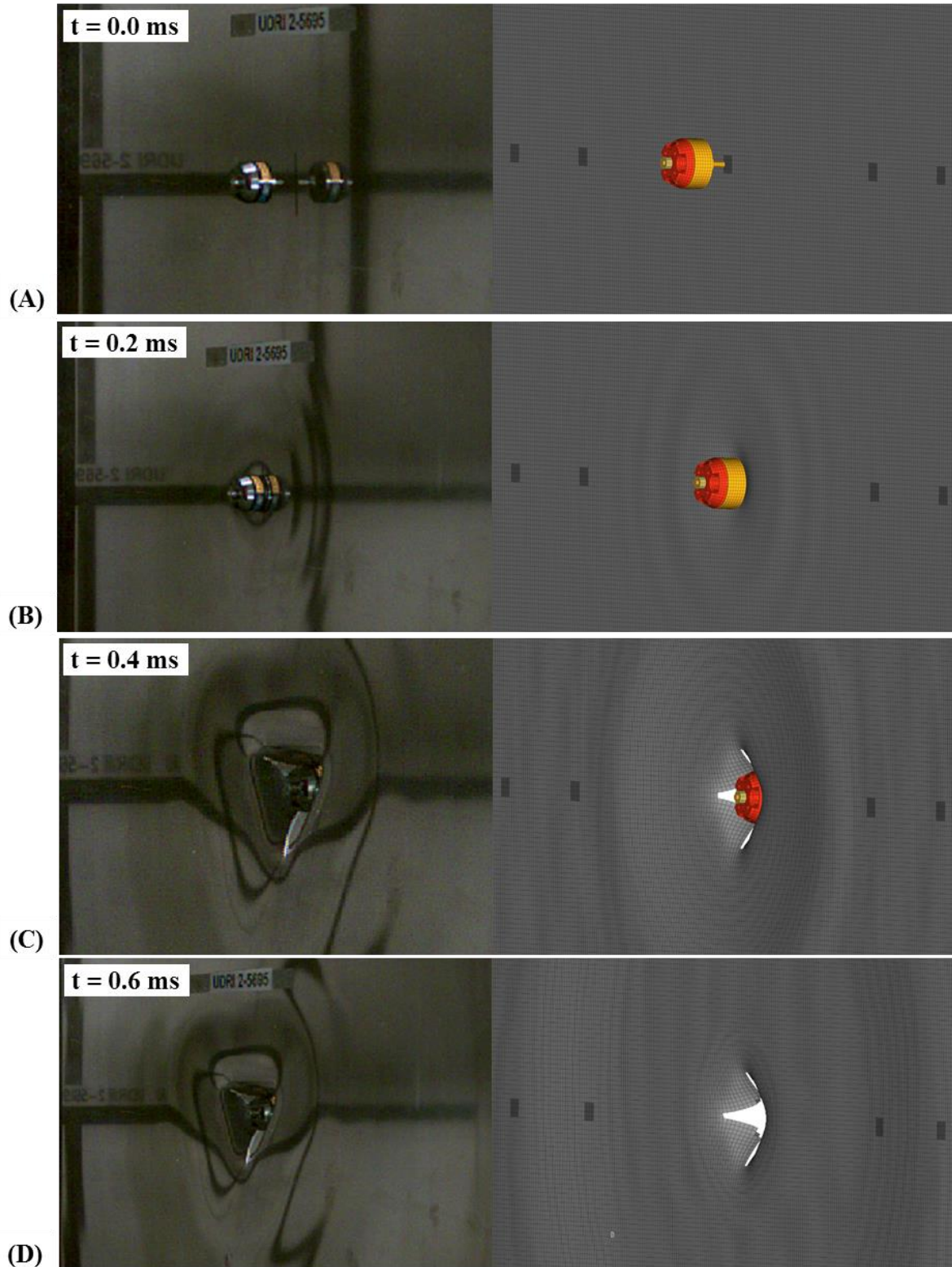


Figure 40. High-speed images of a fixed-wing UAS motor impact (test 2-5695) at 127.56 m/s and a corresponding simulated nominal impact at four times: (A) $t = 0.0$ ms, (B) $t = 0.2$ ms, (C) $t = 0.4$ ms, and (D) $t = 0.6$ ms

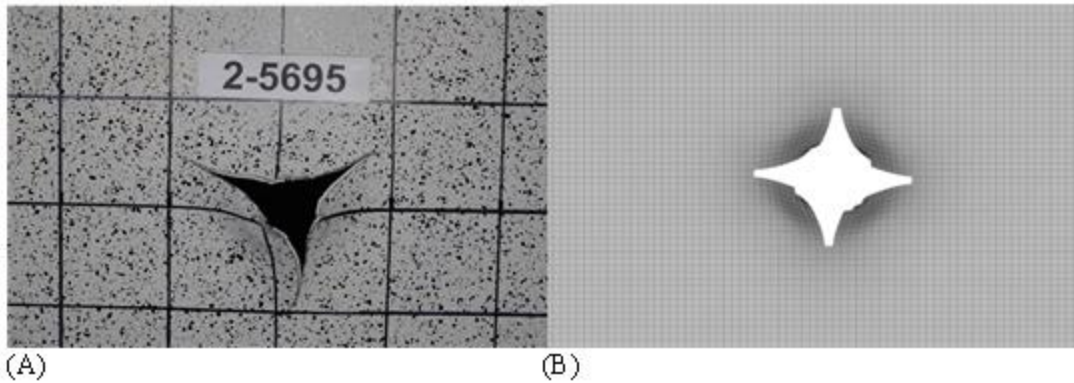


Figure 41. (A) Actual (target panel 2-5695) and (B) Simulated target panel after fixed-wing UAS motor impact at a 128.6 m/s nominal velocity

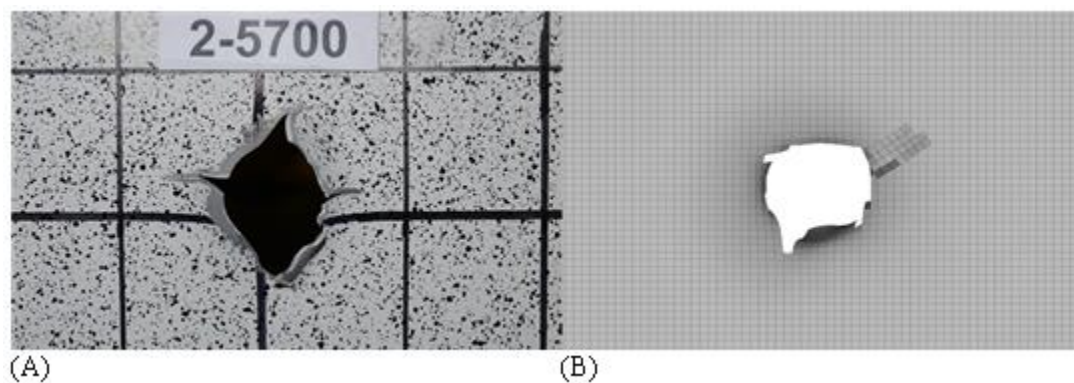


Figure 42. (A) Actual (target panel 2-5700) and (B) Simulated target panel after an oblique fixed-wing UAS motor impact at a 130.61 m/s velocity

An additional FE simulation was performed using the actual pitch/yaw angles and the measured impact velocity from target panel 2-5700. Figure 42 contains images of the actual and simulated target panel after penetration. The actual oblique motor impact resulted in a semicircular penetration with a lower degree of petaling. The essential features of the penetration region were well characterized by the FE model.

A similar comparison of the actual (target panel 2-5699) and simulated impact behavior between the motor and target panel was performed for the lower 65.2 m/s (126.7 knots) impact velocity. The calculated/measured extensional strains in the x -direction at one near-field (SG1) and one far-field (SG6) strain gage location are shown in Figure 43 (A) and Figure 43 (B), respectively.

Similar to the high velocity tests, the calculated strain-time histories accurately captured the essential character of the measured local strains. Similar results were obtained at the remaining strain gage locations for the low velocity test; measured/calculated strain-time histories at all strain gage locations are included in APPENDIX A. Analogously, the calculated load-time histories at each load cell reasonably matched measured values. Load-time histories for all four load cells are included in APPENDIX A.

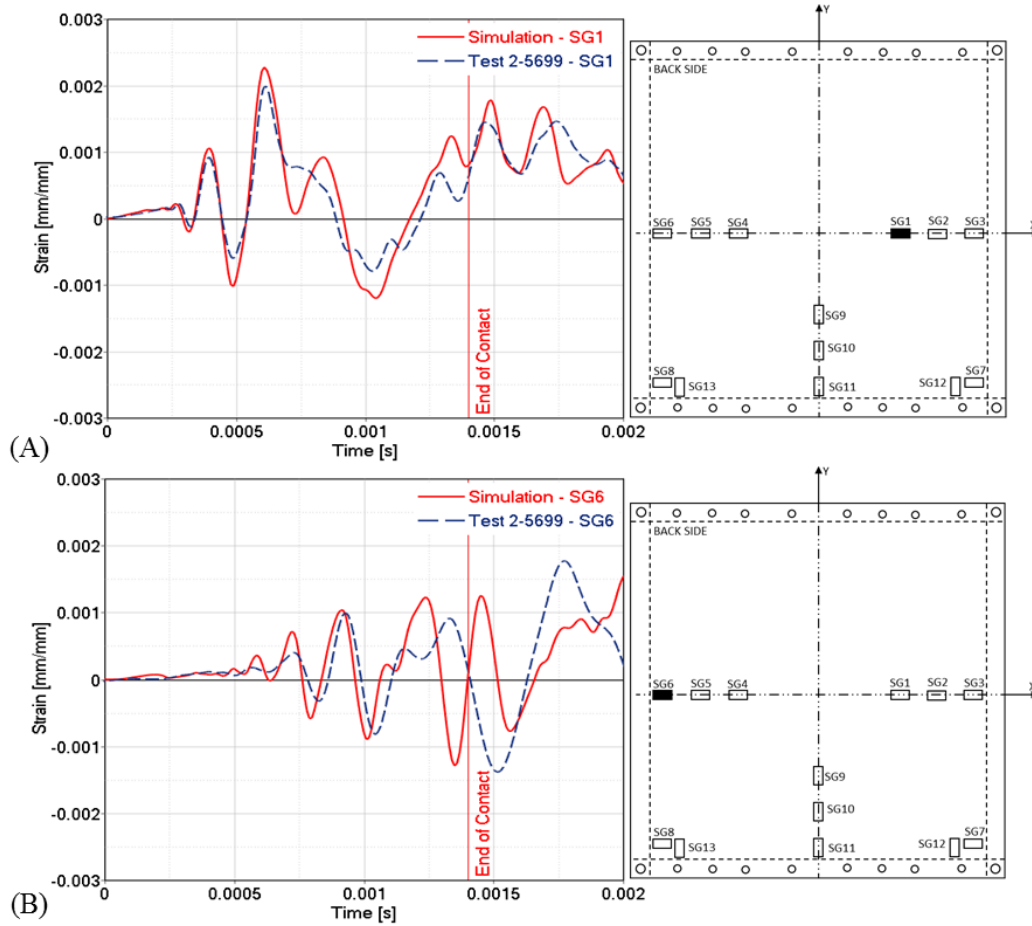


Figure 43. Measured and predicted target panel extensional strain in the x -direction at a (A) near-field (SG1) and (B) Far-field (SG6) strain gage for a motor impact at a 65.2 m/s velocity

High-speed images of the lower velocity motor impact test were compared to images from the simulated impact. Figure 44 shows a series of images from the observed (target panel 2-5699) and simulated impacts. The motor is shown at the center of the target panel in Figure 44 (A) just prior to impact. Shortly after impact, the motor shaft perforated the panel as shown in Figure 44 (B). After partial penetration, the motor began to rebound from the target panel (Figure 44 (C)). The motor completely rebounded from the panel at the end of contact (Figure 44 (D)).

Again, the FE simulation results successfully matched the observed impact behavior. Figure 45 contains an image of the actual perforated target panel (target panel 2-5699) as well as an image of the simulated target panel. Both the actual and simulated panels demonstrated a semicircular puncture with a small degree of petaling. Similar to the higher velocity impact simulations, the FE model was able to capture the size, shape and characteristic features of the perforation.

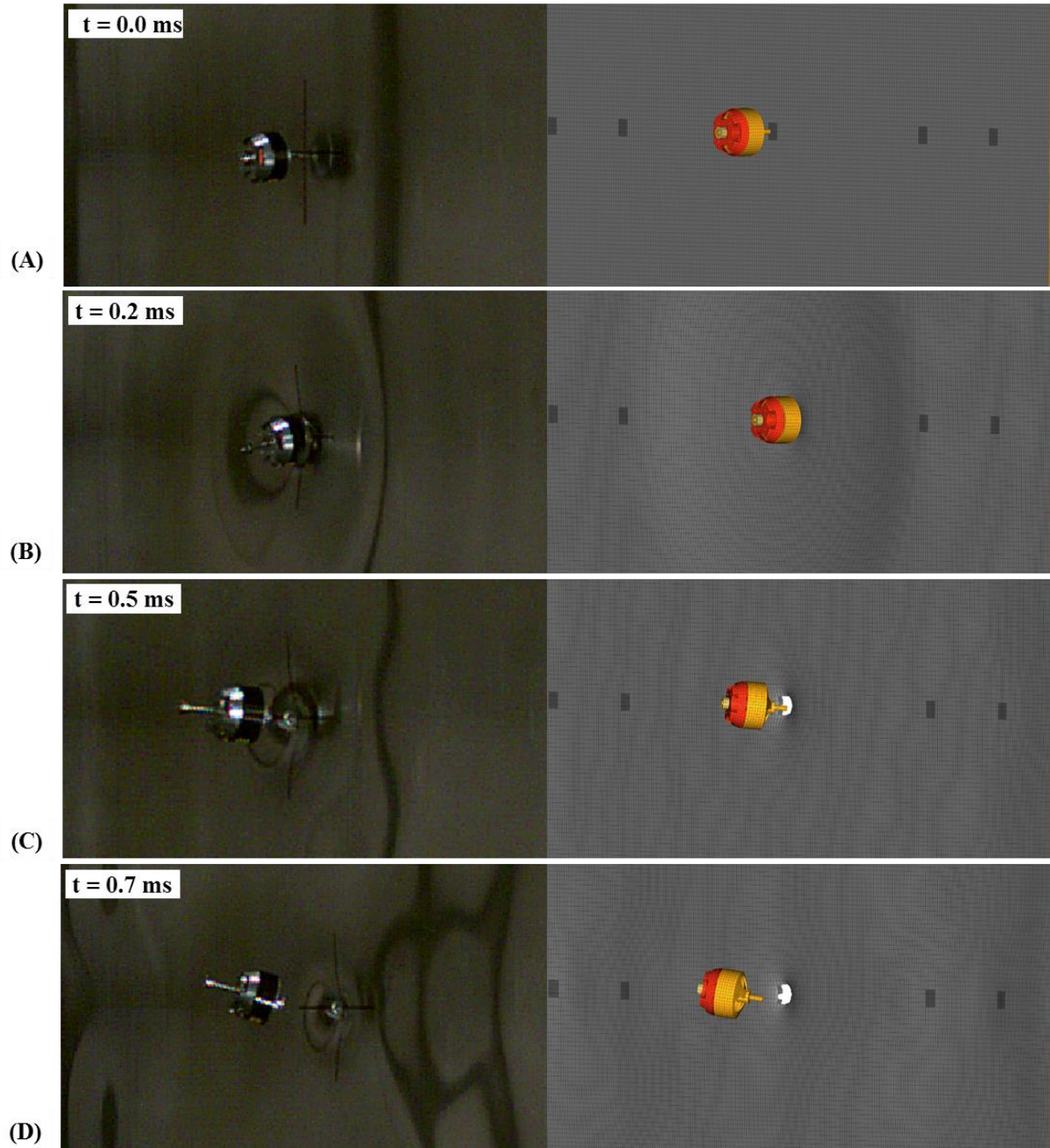


Figure 44. High-speed images of a fixed-wing UAS motor impact (test 2-5699) at 65.2 m/s and a corresponding simulated nominal impact at four times: (A) $t = 0.0$ ms, (B) $t = 0.2$ ms, (C) $t = 0.5$ ms, and (D) $t = 0.7$ ms

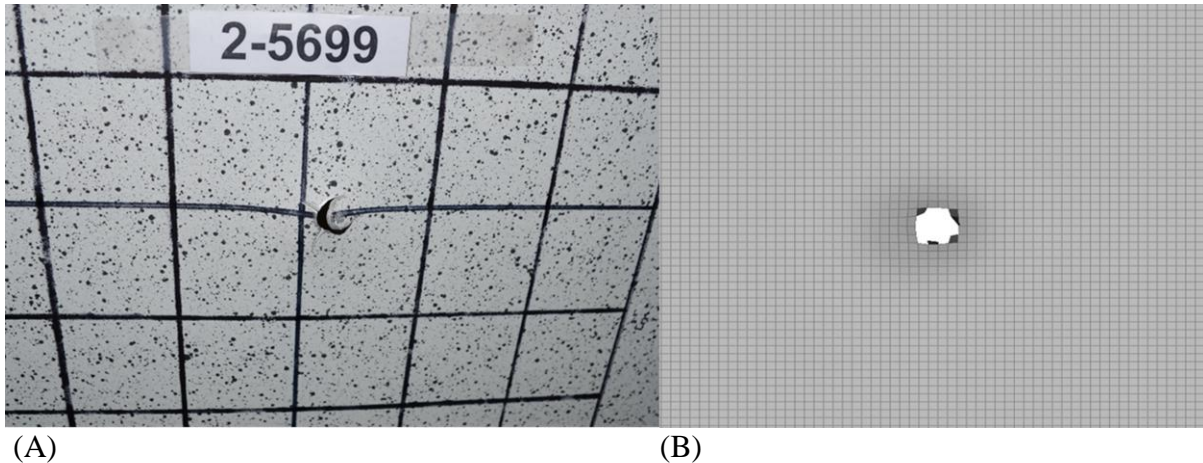


Figure 45. (A) actual (target panel 2-5699) and (B) simulated target panel after fixed-wing UAS motor impact at a 65.2 m/s impact velocity

2.4.8.2 Fixed-Wing UAS Battery Subassembly FE Model Verification

Predicted strain-time histories at each target panel strain gage location (SG1-SG13) were compared to measured histories from the two battery subassembly impact tests (target panels 2-5693, 2-5694) conducted at a nominal velocity of 128.6 m/s (250 knots). In these two impact tests, there were minor differences in the measured strain-time histories due to subtle differences in measured velocity, subassembly mass, and pitch/yaw angles.

For these two tests, a single simulation was performed for a normal impact at a nominal velocity of 128.6 m/s. In general, the predicted strain-time histories at all thirteen strain gage locations closely matched measured results. The calculated/measured strains at one near-field (SG1) and one far-field (SG3) strain gage location are shown in Figure 46 (A) and Figure 46 (B), respectively. Similar to the motor impact tests, the calculated strain-time histories accurately captured both the initial peaks and the essential character of the measured strains up until the end of contact. Comparable results were obtained at the remaining strain gage locations; measured/calculated strain-time histories at all strain gage locations are included in APPENDIX A.

In addition, simulated full-field strain components closely matched measured strains obtained from a DIC system. For example, Figure 47 contains plots of the calculated/measured extensional strain in the x -direction at 1.5 ms. The magnitude and gradient in the predicted strain field reasonably matched the local field near the impact site. Such results are typical for all strain components over the duration of impact.

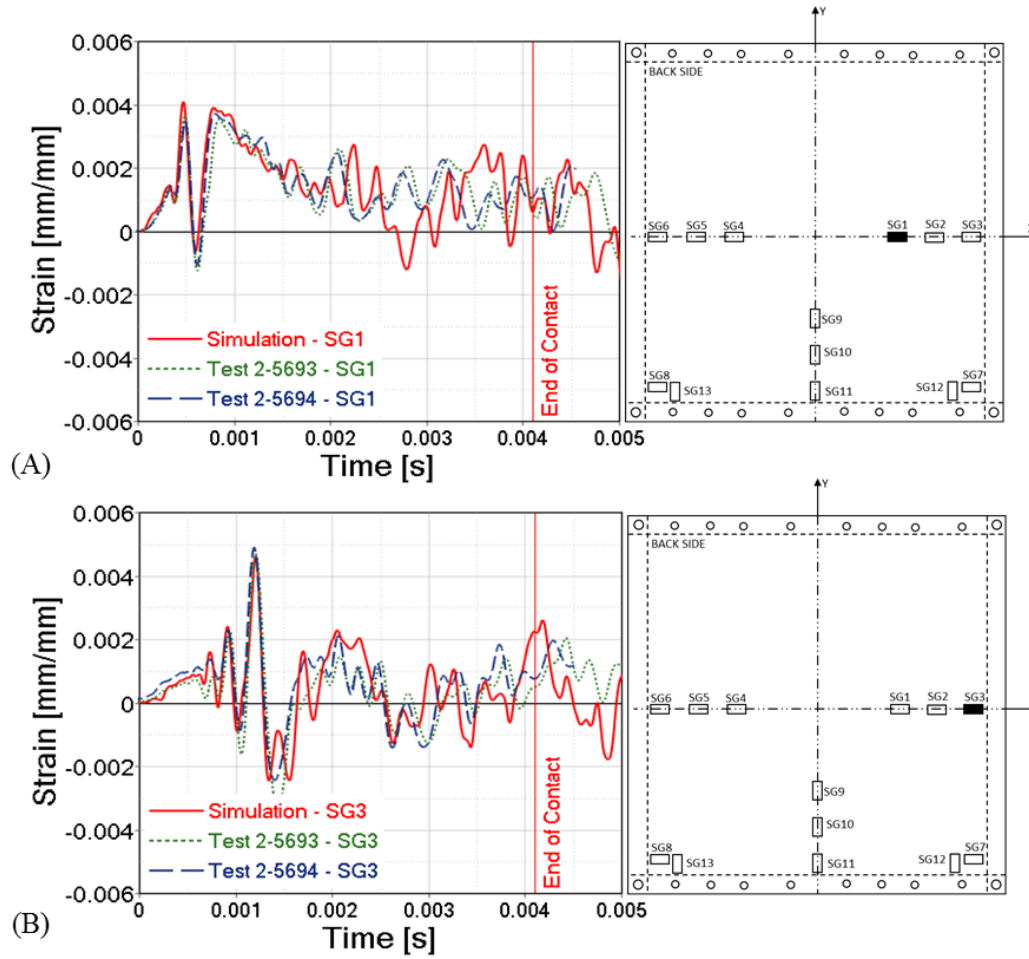


Figure 46. Measured and predicted target panel extensional strain in the x -direction at a (A) Near-field (SG1) and (B) Far-field (SG3) strain gage for a battery subassembly impact at a 128.6 m/s nominal velocity

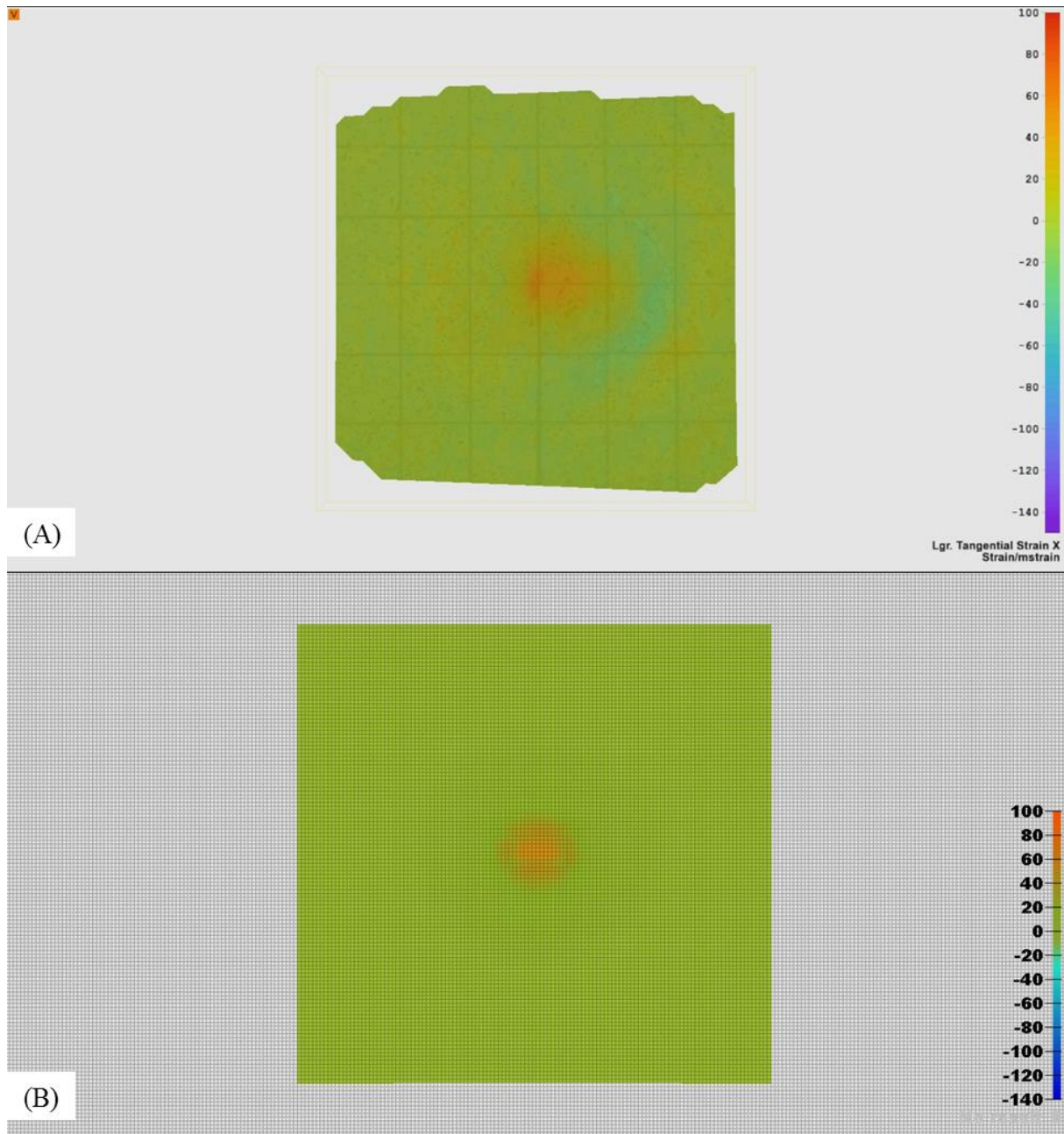


Figure 47. (A) Measured (test 2-5693) and (B) Simulated target panel extensional strain in the x -direction at 1.5 ms during a fixed-wing UAS battery subassembly impact at a 128.6 m/s nominal velocity.

The predicted load-time history at each load cell was compared to measured histories from the two battery subassembly impact tests. The simulated and measured load-time history at the top left load cell accurately matched the initial force peaks (Figure 48). Load-time histories for the remaining load cells demonstrated a similar level of correlation; load-time histories for all four load cells are included in APPENDIX A.

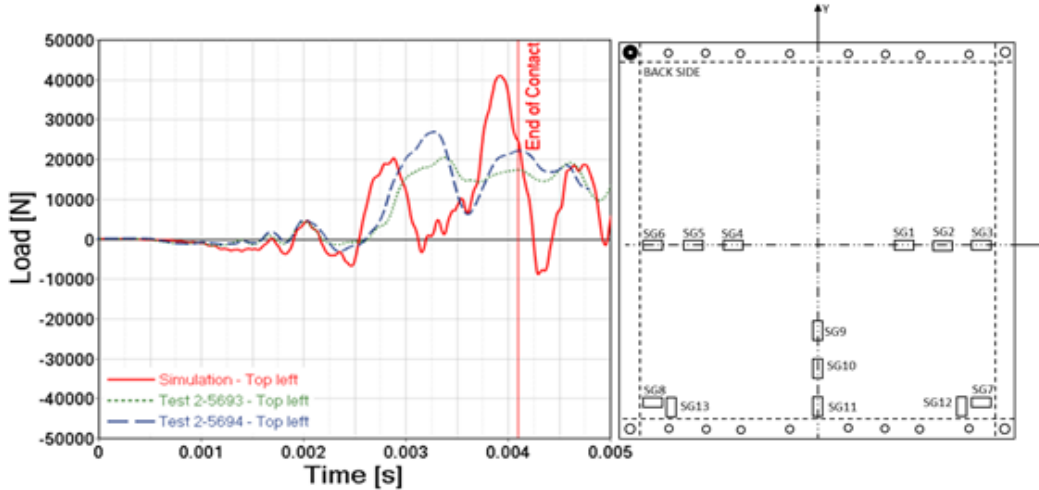


Figure 48. Measured and predicted force in the top left load cell for a battery subassembly impact at a nominal velocity of 128.6 m/s

The calculated out-of-plane z -displacement at the target panel impact location was compared to measured values from the two battery subassembly impact tests (target panels 2-5693, 2-5694) as shown in Figure 49. The measured displacements increased rapidly until reaching a local maximum at around 2 ms and then decreased slightly until the end of contact. The simulated displacement closely matched the experimentally measured values.

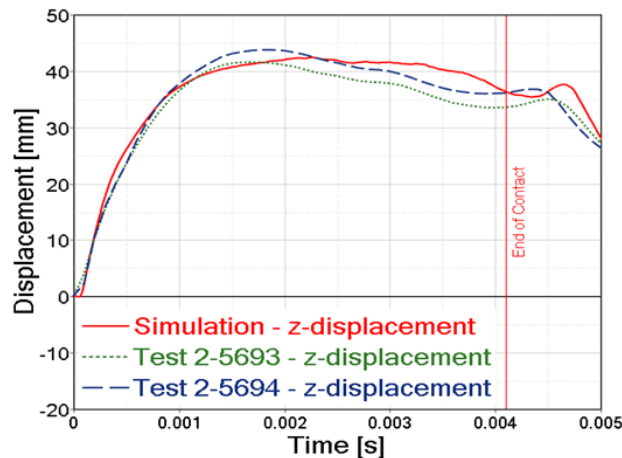


Figure 49. Measured and predicted target panel out-of-plane displacement for the battery subassembly at a nominal impact velocity of 128.6 m/s

High-speed images of battery subassembly impacts were qualitatively compared to the simulated nominal impact. For example, Figure 50 shows a series of images from the onset of impact until the end of contact from target panel 2-5693 along with simulation results at the same moments in time. The battery subassembly is shown at the center of the target panel in Figure 50 (A) just prior to impact. Shortly after impact, the battery subassembly began to crumple as shown in Figure 50 (B). Large PCB sections became increasingly detached, and the battery cell assembly began to unfold (Figure 50 (C)). At the end of contact, the actual battery subassembly was significantly fragmented (Figure 50 (D)). The FE simulation results reasonably matched the observed failure throughout the impact event. Since FE deletion was employed to ensure numerical stability, it is

difficult to directly compare the degree of observed and predicted fragmentation of the battery subassembly. Nonetheless, the battery subassembly model appears to closely match the physics of impact of the actual subassembly. Similar results were observed for the other impact test.

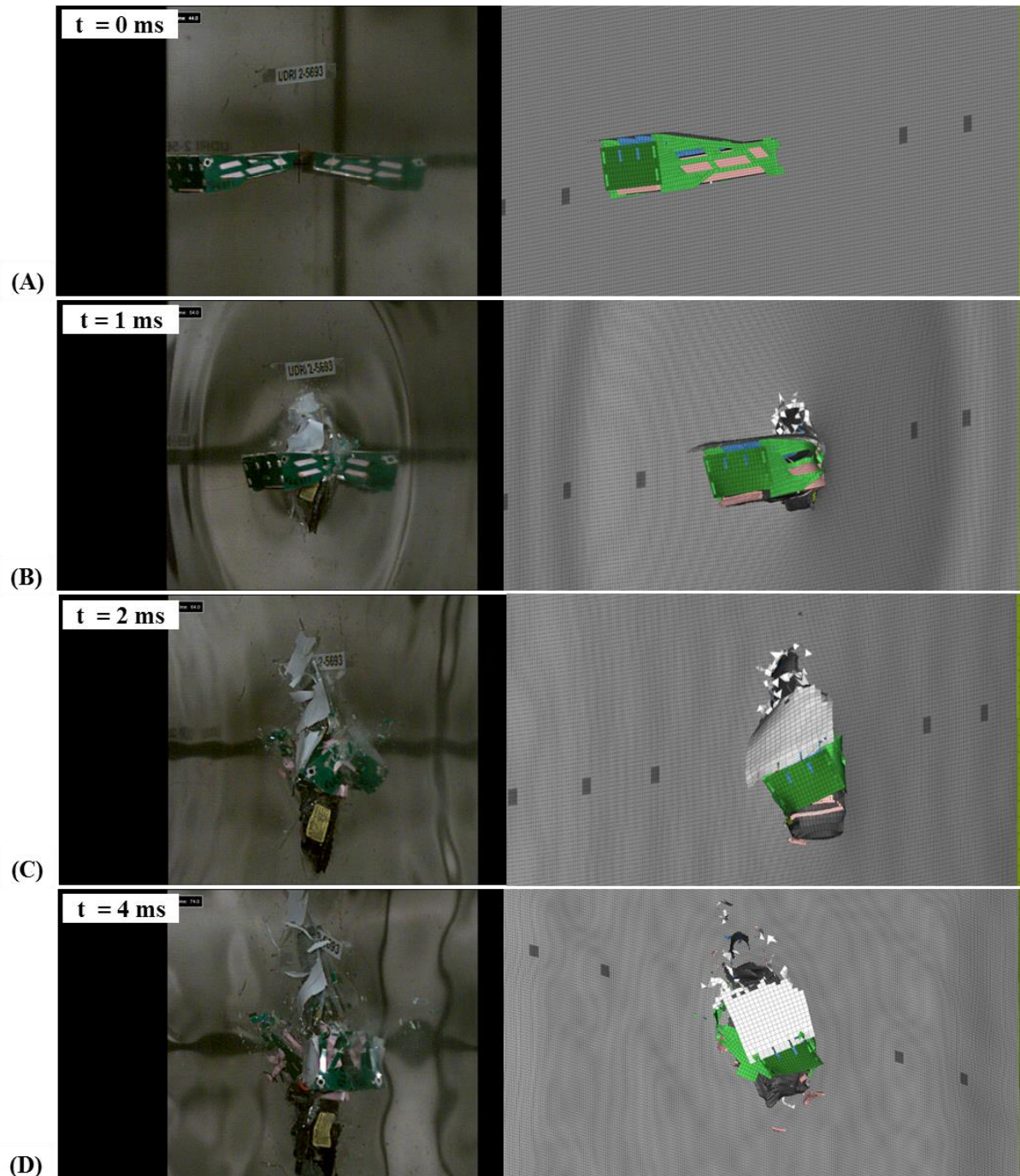


Figure 50. High-speed images of a fixed-wing UAS battery subassembly impact (test 2-5693) at 120.09 m/s and a corresponding simulated nominal impact at four times: (A) $t = 0$ ms, (B) $t = 1$ ms, (C) $t = 2$ ms, and (D) $t = 4$ ms

2.5 FIXED-WING FE MODEL LIMITATIONS

Chapter 2 has presented the FE model of a fixed-wing UAS that was designed for crashworthiness collision simulations in LS-DYNA software. It was verified with component level tests to ensure good correlation with physics within the envelope of conditions tested.

The model is intended to be used for assessing impact dynamics with aircraft structures to simulate mid-air collisions. It is recommended to limit the applications to impact velocities in range of 64.3-128.6 m/s (125-250 knots), for which component level tests verified the behavior of the main components of the UAS.

Further work will have to be conducted to verify the model for lower impact velocities and ground collisions.

3. TARGET DEFINITION - COMMERCIAL TRANSPORT & BUSINESS JETS

This chapter covers the modeling of targets subjected to UAS impact. The UAS airborne collision hazard severity evaluation was conducted through several WPs as defined in the project scope in section 1.2. The following WPs pertain to target modeling.

- *WP II. Target Definition:* Conduct a study to classify aircraft type and select a representative commercial transport jet, business jet and general aviation aircraft.
- *WP IV(a). Aircraft Target Commercial Jet:* Use the NIAR Aircraft FE analysis (FEA) library to define representative Part 25 Commercial Transport Jet components that can be subjected to UAS Impact.
- *WP IV(b). Aircraft Target Business Jet:* Use the NIAR Aircraft FEA library to define representative Part 23 Business Jet components that can be subjected to UAS Impact.

A FE modeling (FEM) approach was used to answer several research questions for evaluating UAS airborne collision hazard severity. This was the only feasible option available to answer the questions in detail within the time frame and budget set for this research project. Fortunately, through several years of research, the NIAR has developed a library of full aircraft models for ongoing crashworthiness research projects. These models have been created using a Physics Based Modeling approach for obtaining high fidelity models that can be used for a wide range of applications such as ditching, bird strike and crashworthiness research. Figure 51 and Figure 52 show the global aircraft models created by the NIAR for crashworthiness research. The availability of these aircraft models enabled us to select the areas and components of interest for this research program and refine them with the necessary details. The fact that these models were readily available resulted in great time and cost reductions allowing additional studies to be performed (different targets and projectiles) to provide better conclusions. If these models would have not been available, the majority of time and cost would have been spent developing a single target and only limited results would have been obtained.

In order to build these FE models, the NIAR followed a Physics Based Modeling approach that takes advantage of advances in computational power, the latest computational tools, years of research in understanding the fundamental physics of the crashworthiness event, generated test-to-test variability data, and verified & validated (V&V) modeling methodologies. This approach uses the Building Block Approach as illustrated in Figure 53. The building block approach is the incremental development of analysis and supporting tests where typically there is an increase in size and complexity of the test article and a decrease in the number of supporting tests. In order to develop this method it is necessary to have a good understanding of the underlying physics and corresponding test variability from the coupon to the system level. The definition of the numerical model is not driven by system level test results; it is driven by a predefined, V&V building block modeling methodology. Using this approach, simulations should be able to predict the system level test results within an acceptable scatter band. An objective validation criteria based on an understanding of the test-to-test variability is used to evaluate the numerical models.

At the coupon level, FE methodologies were defined for material characterization as part of an internal research project [43]. An example of material model validation is shown in section 3.3.5.2. Different joint modeling techniques were evaluated through various research projects and applied to the development of the full aircraft models as well as the targets under consideration [45]. Joint and connection details are documented in section 3.3.4. A fuselage drop test performed by the FAA [46] was used to evaluate the FE model of the aircraft at the sub-assembly level by extracting

the same section out of the NIAR model [47]. By validating multiple sub-assembly level models, the complete full aircraft model was developed and validated [44]. The same approach and lessons learned were applied to create the NIAR Business Jet model.

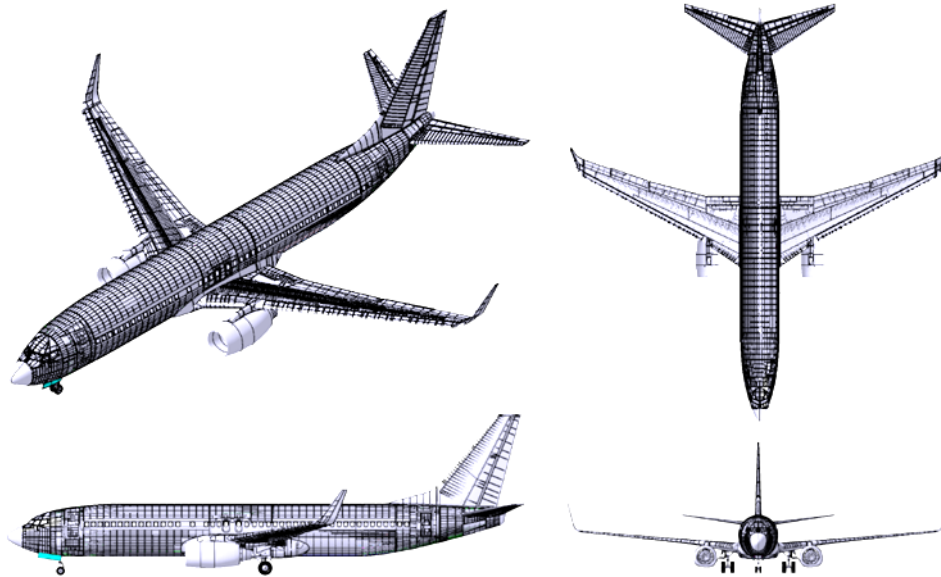


Figure 51. NIAR narrow body aircraft model developed for crashworthiness research

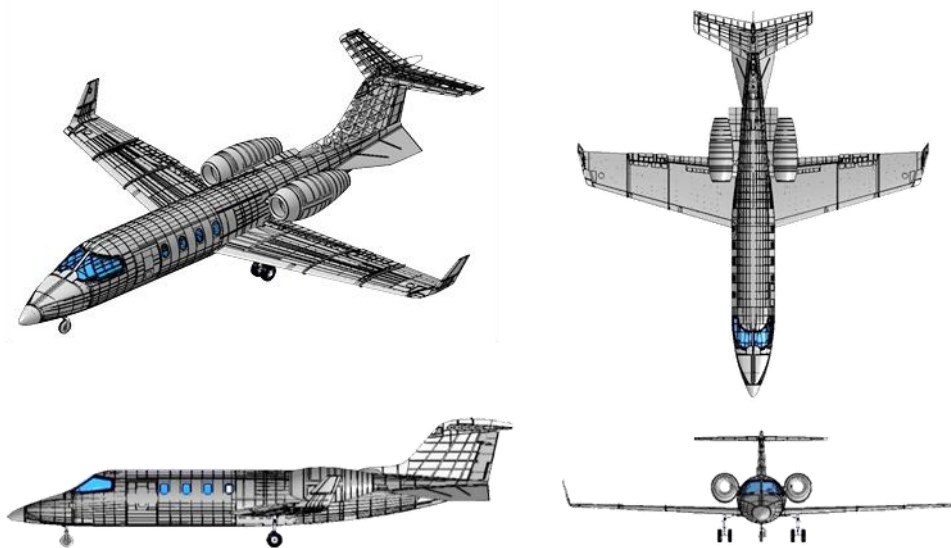


Figure 52. NIAR business jet aircraft model developed for crashworthiness research

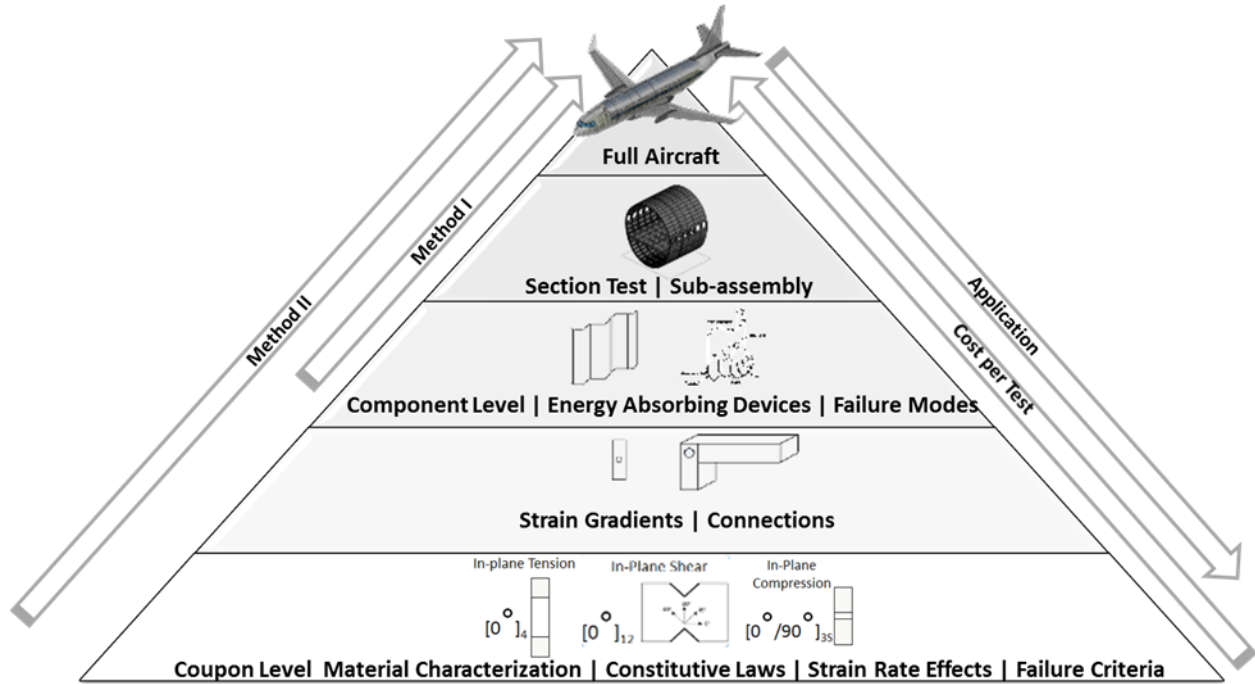


Figure 53. Building block approach for the NIAR narrow body aircraft model

3.1 RATIONALE FOR SELECTION OF TARGETS AND IMPACT AREAS

A review of the airspace usage was conducted to select a representative commercial transport jet and business jet. A summary of the justification for selection of representative aircraft models is provided in this section. Further information can also be found in the research conducted by Montana State University [21] as part of work for WP II.

3.1.1 Commercial Transport Jet

In the recent years, intercontinental travel in developing countries is increasing at a high rate and the future market demand for narrow-body aircraft is predicted to be the highest of all configurations. Figure 54 shows the prediction made by The Boeing Company [48] and Airbus Group [49] of the number of airplanes, which will enter service in a given twenty year period (2014 to 2034). Based on these predictions, single-aisle aircrafts are, and will continue to be, the most popular transport jet model in the market. Single-aisle or narrow body commercial transport jets typical seat 5-6 passengers per row. In addition, the number of passengers that these airliners can transport varies between 130 and 240. Therefore, potential mid-air collisions between a single-aisle aircraft and an UAS are important to study for ensuring occupant safety.

Moreover, as it can be seen in the Table 8, both the Boeing 737 and Airbus A320 families are the best-selling aircraft, having by far the highest numbers of deliveries. Table 8 summarizes the deliveries of single-aisle aircraft by Boeing [50] and Airbus [51].

Therefore, the narrow-body single-aisle aircraft, similar to Boeing 737 and Airbus A320, are the most popular transport jets in the world. Thus, a generic model of the narrow-body single-aisle

aircraft configuration was reverse engineered and will be referred to as commercial transport jet in this report.

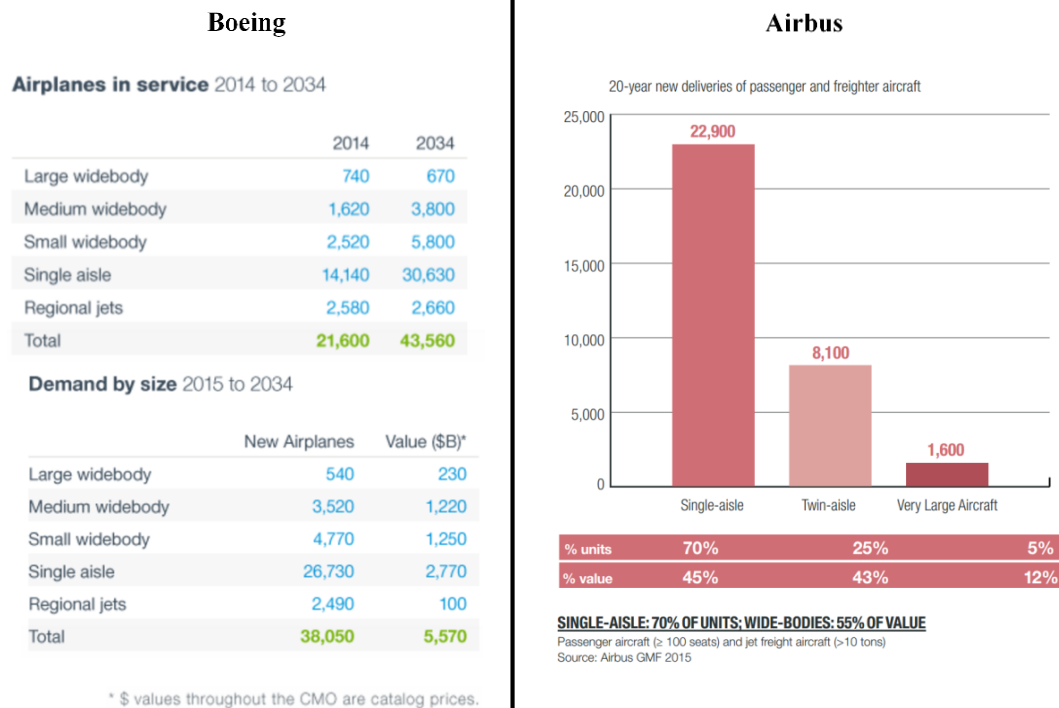


Figure 54. Current market outlook published by Boeing and Airbus (2014 to 2034) [48] [49]

Table 8. Boeing and Airbus aircraft deliveries summary (up to May 2016) [50] [51]

	Boeing						Airbus			
Aircraft Type	737	747	757	767	777	787	A300/A310	A320	A330/A340/A350	A380
Total Deliveries	9048	1521	1049	1085	1041	417	816	7068	1680	190

3.1.1.1 Commercial Transport Jet Specifications

Table 9 shows specifications of the Boeing 737-800, Airbus A320, and commercial transport jet models developed by the NIAR. The specifications provide insight into the size and scale of the aircraft when compared to the UAS and the cruise and approach velocities. These velocities were the basis for selecting velocities for UAS impact studies.

Table 9. Boeing 737, A320 and NIAR commercial transport jet model specifications [52]

	B737-800		A320		NIAR model	
MTOW	79,015 kg	174,200 lb	77,000 kg	169,755 lb	79,000 kg	174,165 lb
Wing span	35.79 m	117 ft 5 in	34.09 m	111 ft 9 in	35.84 m	117 ft 7 in
Horizontal stabilizer span	14.35 m	47 ft 1 in	12.45 m	40 ft 10 in	14.27 m	46 ft 10 in
Vertical stabilizer span	7.06 m	23 ft 2 in	5.87 m	19.26 ft	7.21 m	23 ft 8 in
Fuselage length	38.02 m	124 ft 9 in	37.57 m	123 ft 3 in	37.97 m	124 ft 7 in
Cruise Altitude	10,955 m	35,940 ft	11,280 m	37,000 ft	11,000 m	36,089 ft
Max cruise speed (Mach)	0.82		0.82		0.82	
Cruising speed (Mach)	0.78		0.78		0.78	
Minimum landing speed	55.0 m/s	107 knots	N/A	N/A	56.6 m/s	110 knots

3.1.2 Business Jet

Similarly, the Learjet 31A model was selected as a representative aircraft for the business jet category. Although this aircraft is not the most registered by the FAA, it has similar dimensions and specifications in comparison to many other business jets [53]. Thus, a generic model of similar size as the Learjet 31A was developed and will be referred to as business jet in this report.

3.1.2.1 Business Jet Specifications

The specifications for the Learjet 31A and the NIAR model are presented in Table 10. The velocities selected for UAS impact studies are explained in subsequent chapters.

Table 10. Learjet 31A and NIAR business jet model specifications [53][54]

	Learjet31A		NIAR model	
MTOW	7,711 kg	17,000 lb	7,711 kg	17,000 lb
Wing Span	13.35 m	43 ft 9 in	13.28 m	43 ft 7 in
Horizontal Stabilizer Span	4.48 m	14 ft 8 in	4.47 m	14 ft 8 in
Vertical Stabilizer Span	1.68 m	5 ft 6 in	2.67 m	8 ft 9 in
Length Overall	14.83 m	48 ft 8 in	14.71 m	48 ft 3 in
Cruise Altitude	13,105 m	43,000 ft	13,105 m	43,000 ft
Max Cruise Speed (Mach)	0.83		0.83	
Cruising Speed (Mach)	0.79		0.79	
Minimum Landing Speed	44 m/s	87 knots	44 m/s	87 knots

3.1.3 Aircraft Impact Areas

One of the main goals of this UAS impact research was to compare UAS impacts to bird strike impacts for which extensive regulations already exist for certification of aircraft. Thus, an important part of this research was to assess if UAS impacts on aircraft are analogous to those from bird strikes. The selection of components of the aircraft for UAS impact was largely based on the Part 25 requirements for bird impacts. The regulations for bird strike impact were reviewed thoroughly and are summarized in Table 11. Based on the review, the empennage of Part 25 aircraft must withstand 8 lb bird impacts while the rest of the structure, including windshields, must withstand 4 lb bird impacts.

A survey of reported bird impacts on aircraft, between 1990 and 2014 in the United States of America (USA), was conducted by the FAA and a summary of the areas of aircraft impacted was documented [55]. Two pie charts indicating the location and severity of bird strike cases and a summary table as presented in the report are shown in Figure 55 and Figure 56, respectively. The largest percentage of strikes occurred on the windshield, nose, wing/rotor, engine, and fuselage. Figure 55 and Figure 56 also indicate that the components most damaged due to bird impact were the wing/rotor and engines. If the probability of impact with an UAS into a certain area of the aircraft is assumed similar to a bird strike, two areas of interest can be noted: airframe and powerplants.

The structural evaluation of UAS impacts to aircraft structures is covered in this report. Therefore based on the Part 25 requirements and bird strike impact survey, the components selected for bird strike impact are the windshield, wing leading edge, horizontal stabilizer leading edge and vertical stabilizer leading edge. A separate report to evaluate UAS ingestion and impact on engine components was performed by Ohio State University (OSU) [3].

Another consideration of UAS impacts was how the UAS would be affected by the airflow characteristics over selected components of the aircraft. The argument is that turbulence and flow patterns may diminish the effects of a UAS impact or cause the UAS to completely avoid an impact. Therefore, the selection of localized areas for UAS impact was based on some preliminary Computational Fluid Dynamics (CFD) analyses using the aircraft Outer Mold Line (OML). Flow patterns, shown in Figure 57, were studied and the areas on the wing and stabilizers showing turbulent flow patterns were ignored. Thus, based on the information presented in this section, the selected components and impact areas were modeled with more detail necessary for obtaining accurate UAS impact FEA results. Details of the CAD and FEM of these components are presented in subsequent sections.

Table 11. Bird strike related regulations [56][57]

Category	Chapter	Aircraft Component/ Bird Mass	Regulation
Part 23	<i>14 CFR 23.775</i> Windshield and Windows	Windshield 0.907 kg (2 lb)	Windshield panes directly in front of the pilots in the normal conduct of their duties, and the supporting structures for these panes, must withstand, without penetration, the impact of a two-pound bird when the velocity of the airplane (relative to the bird along the airplane's flight path) is equal to the airplane's maximum approach flap speed.
Part 25	<i>14 CFR 25.631</i> Bird Strike Damage	Empennage 3.63 kg (8 lb)	The empennage structure must be designed to assure capability of continued safe flight and landing of the airplane after impact with an 8 lb bird when the velocity of the airplane is equal to V_C at sea level.
	<i>14 CFR 25.775</i> Windshield and Windows	Windshield 1.81 kg (4 lb)	Windshield panes directly in front of the pilots in the normal conduct of their duties, and the supporting structures for these panes, must withstand, without penetration, the impact of a 4lb bird when the velocity of the airplane is equal to the value of V_C , at sea level.

Table 14 Continuation. Bird strike related regulations [56][57]

Part 25	14 CFR 25.571 Damage tolerance and fatigue evaluation of structure	Aircraft structure 1.81 kg (4 lb)	<ul style="list-style-type: none"> - Impact with a 4 lb bird when the velocity of the airplane is equal to V_C at sea level or $0.85 V_C$ at 8,000 ft, whichever is more critical. - The damaged structure must be able to withstand the static loads (considered as ultimate loads) which are reasonably expected to occur on the flight. Dynamic effects on these static loads need not be considered. Corrective action to be taken by the pilot following the incident must be considered. If significant changes in structural stiffness or geometry, or both, follow from a structural failure or partial failure, the effect on damage tolerance must be further investigated.
Part 29	14 CFR 29.631 Bird Strike	Rotorcraft Structure 1 kg (2.2 lb)	The rotorcraft must be designed to ensure capability of continued safe flight and landing (for Category A) or safe landing (for Category B) after impact with a 2.2 lb (1.0 kg) bird when the velocity of the rotorcraft (relative to the bird along the flight path of the rotorcraft) is equal to V_{NE} or V_H (whichever is the lesser) at altitudes up to 8,000 ft. Compliance must be shown by tests or by analysis based on tests carried out on sufficiently representative structures of similar design.

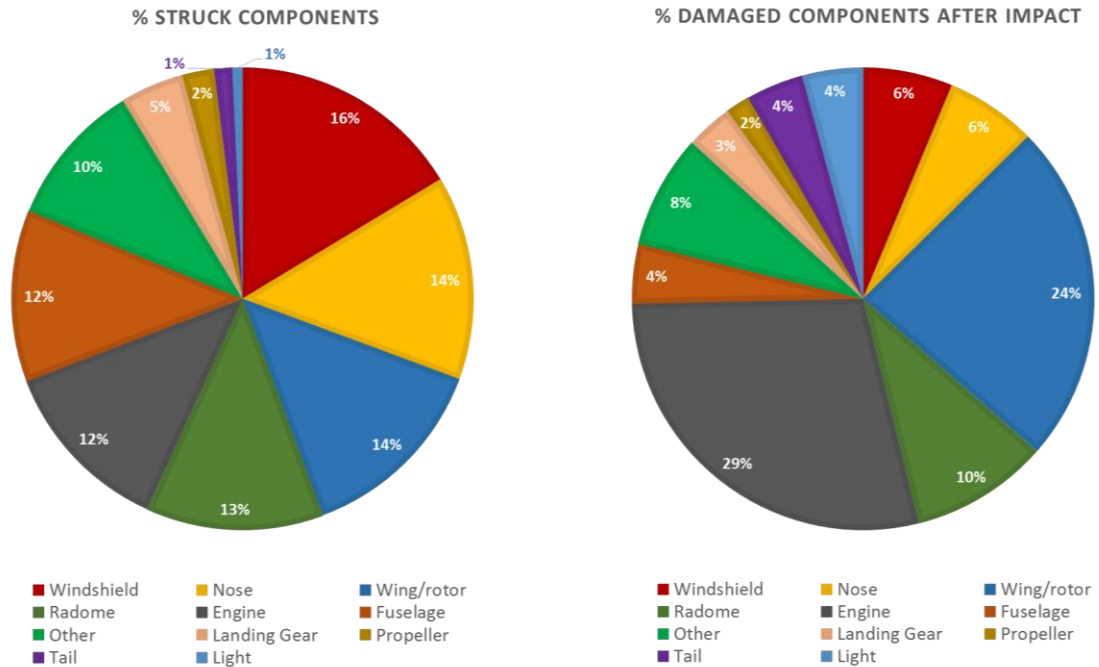


Figure 55. Numerical proportion of civil aircraft components reported as being impacted and damaged by birds in the USA, 1990–2014 [55]

Aircraft component	Birds (25-year total)			
	Number struck	% of total	Number damaged	% of total
Windshield	21,937	16	971	6
Nose	19,133	14	984	6
Wing/rotor	18,332	14	3,683	24
Radome	16,638	12	1,497	10
Engine(s) ¹	16,636	12	4,417	29
Fuselage	16,107	12	643	4
Other	13,574	10	1,227	8
Landing gear	5,979	4	508	3
Propeller	2,953	2	265	2
Tail	1,740	1	621	4
Light	911	1	656	4
Total²	133,940	100	15,472	100

Figure 56. Civil aircraft components reported as being impacted and damaged by wildlife in the USA, 1990–2014 [55]

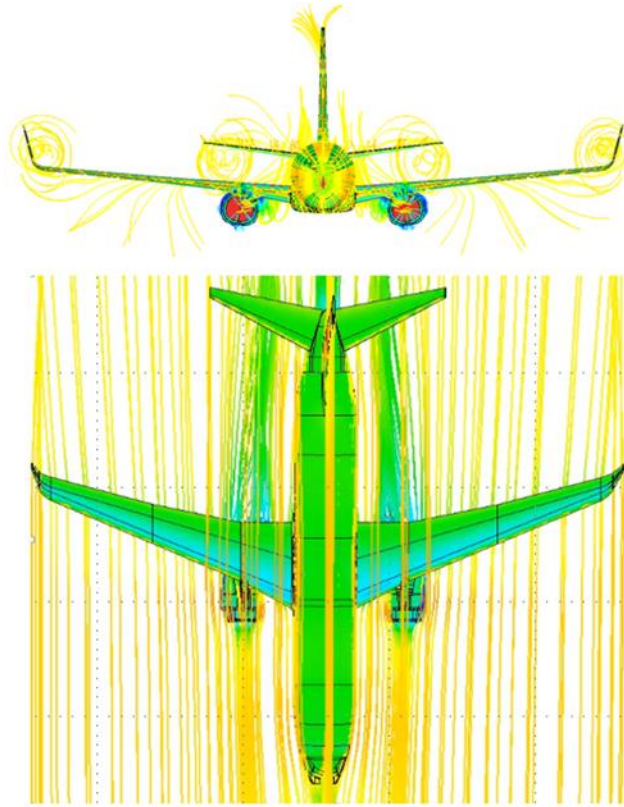


Figure 57. CFD flow analysis on the commercial transport jet model

3.2 CAD REVERSE ENGINEERING

CAD models for target areas were generated by the NIAR for UAS impact studies. Since the actual aircraft drawings were not available, the target areas were reverse engineered based on information available in technical manuals [58][59], books [60] and other online resources. Input from design engineers and Original Equipment Manufacturers (OEMs) helped in refining the models and verifying the fidelity of the structure.

Due to the unavailability of the proprietary aircraft drawings, some structural modeling assumptions were made in accordance with the information found in the literature. While for each aircraft category some specific simplifications were made, the following are a few common simplifications applicable to both the commercial transport jet model and the business jet model:

- Avionics and wires were not modeled.
- Fastener diameter and spacing were determined by means of repair specifications [58].
- Lightening holes and wire harnesses holes were modeled based on available data.

These simplifications would not significantly affect the predicted failure of the airframe primary structure and provide a reasonable stiffness when compared to the actual airframe, especially in the designated impact areas.

3.2.1 Commercial Transport Jet

The wing, windshield, and horizontal and vertical stabilizers similar to a commercial transport jet were modeled for UAS impact. Details of these models are presented in this section. Figure 58 shows the overall dimensions of the commercial transport jet developed by the NIAR.

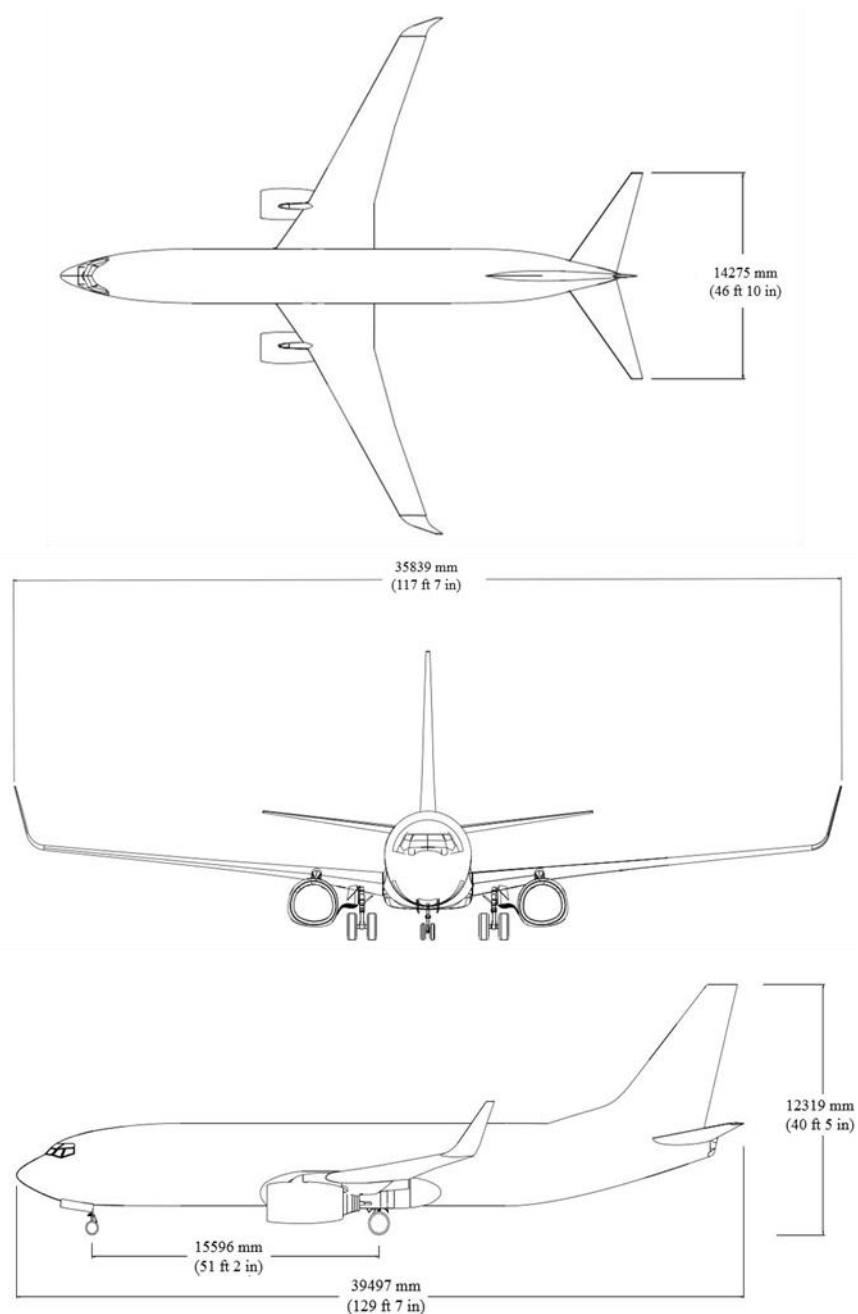


Figure 58. Commercial transport jet overall dimensions

3.2.1.1 Horizontal Stabilizer

Figure 59 shows the horizontal stabilizer CAD model. A planview including the overall dimensions is included on the right of the figure. The internal structure of the horizontal stabilizer model is presented in Figure 60. The leading edge was refined in order to more accurately capture the stiffness characteristics of this target structure at the point of impact. The anti-icing systems, wires, access panels, and certain lightening holes were not accounted for in the geometry.

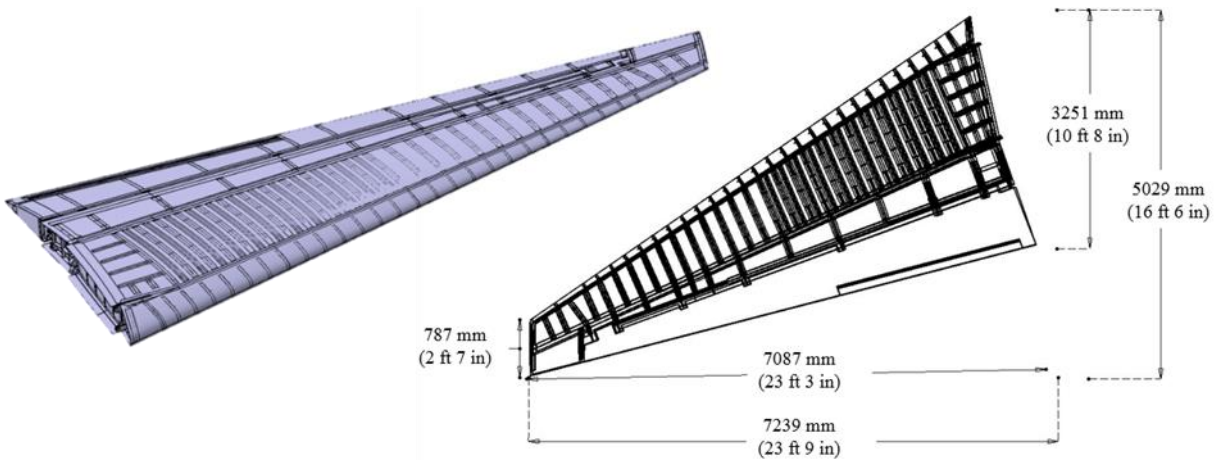


Figure 59. Commercial transport jet horizontal stabilizer

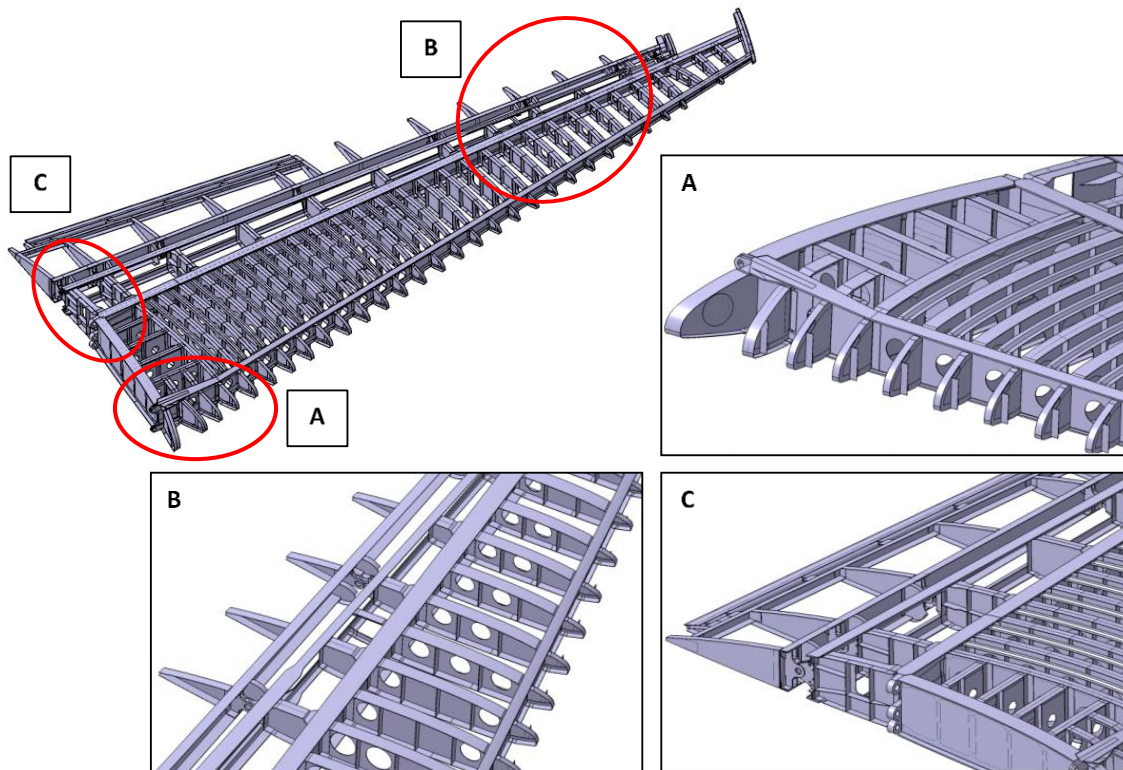


Figure 60. Commercial transport jet horizontal stabilizer CAD model

3.2.1.2 Vertical Stabilizer

The CAD model of the vertical stabilizer and a planview including the overall dimensions are shown in Figure 61. Figure 62 shows detailed views of the construction of the vertical stabilizer. The leading edge was refined in order to more accurately capture the stiffness characteristics of the vertical stabilizer at the point of impact. The same assumptions made for the horizontal stabilizer were applied to the vertical stabilizer.

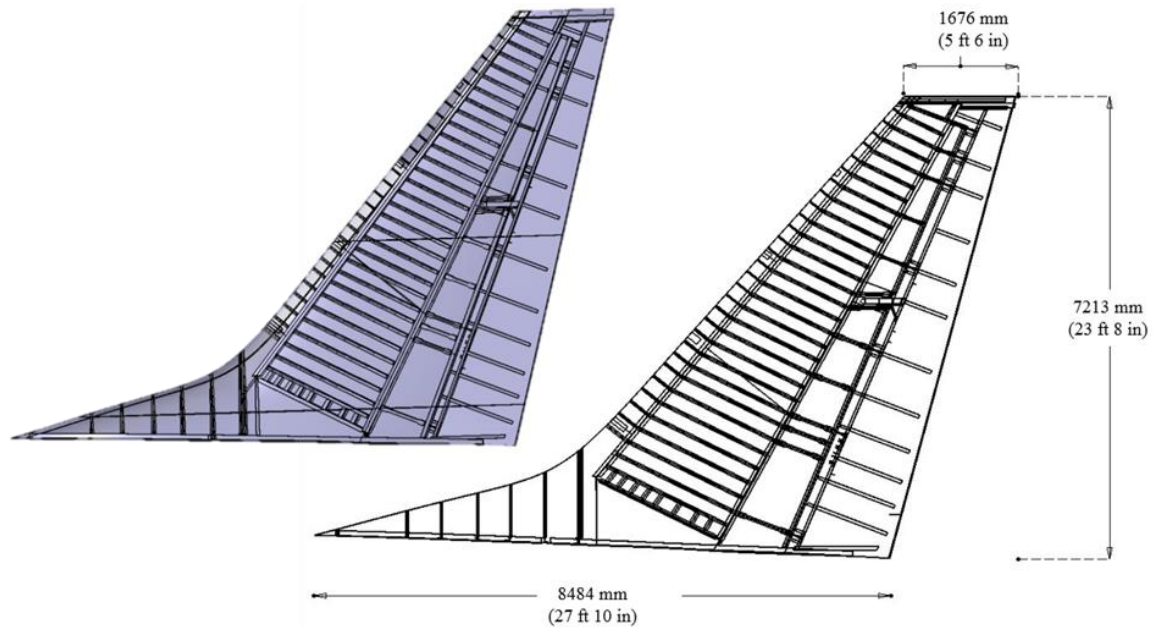


Figure 61. Commercial transport jet vertical stabilizer

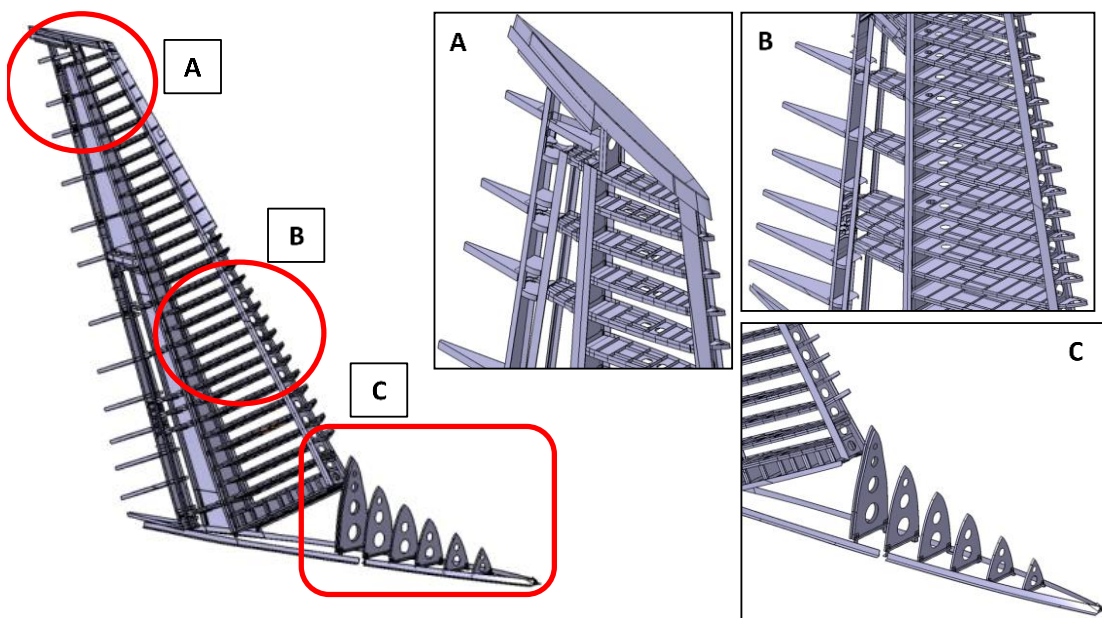


Figure 62. Commercial transport jet vertical stabilizer CAD model

3.2.1.3 Windshield

Figure 63 shows the complete commercial transport jet forward fuselage CAD model. Figure 64 shows an isolated view of the windshield. Similar to the horizontal and vertical stabilizers, the windshield and surrounding structure were refined. Details of the windshield construction were obtained from a PPG technical data sheet [61]. Features of the windshield such as the silicon gasket, metal inserts, and edge fillers were not modeled. Figure 65 includes detailed images of the windshield cross-section.

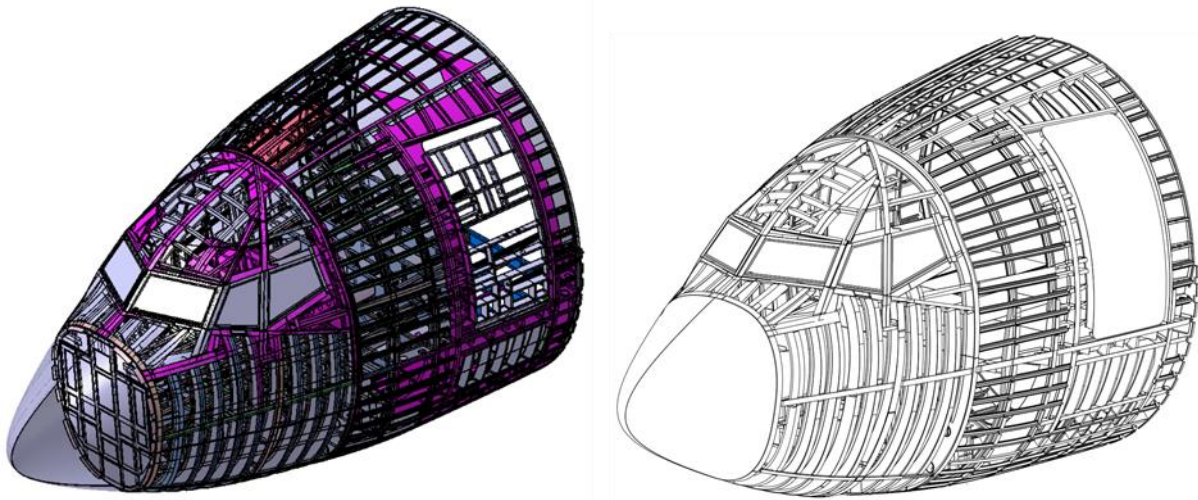


Figure 63. Commercial transport jet forward fuselage CAD construction

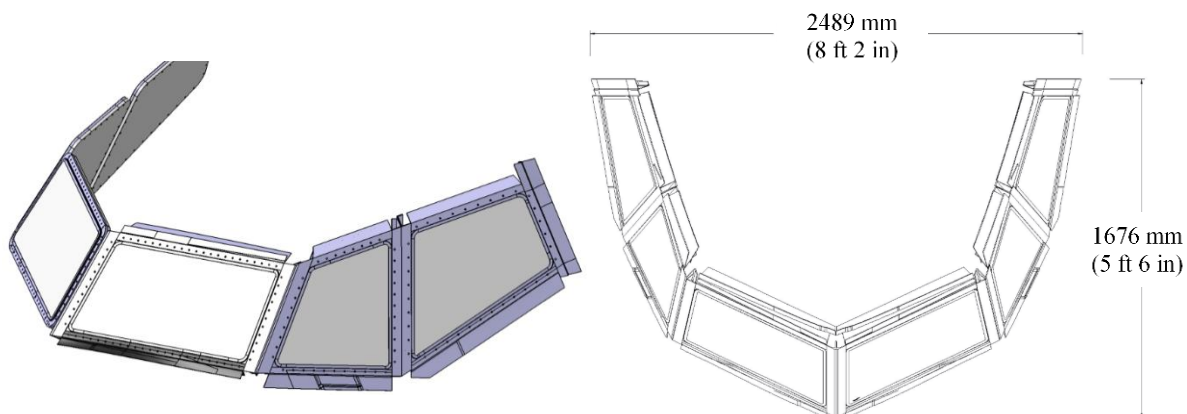


Figure 64. Commercial transport jet windshield

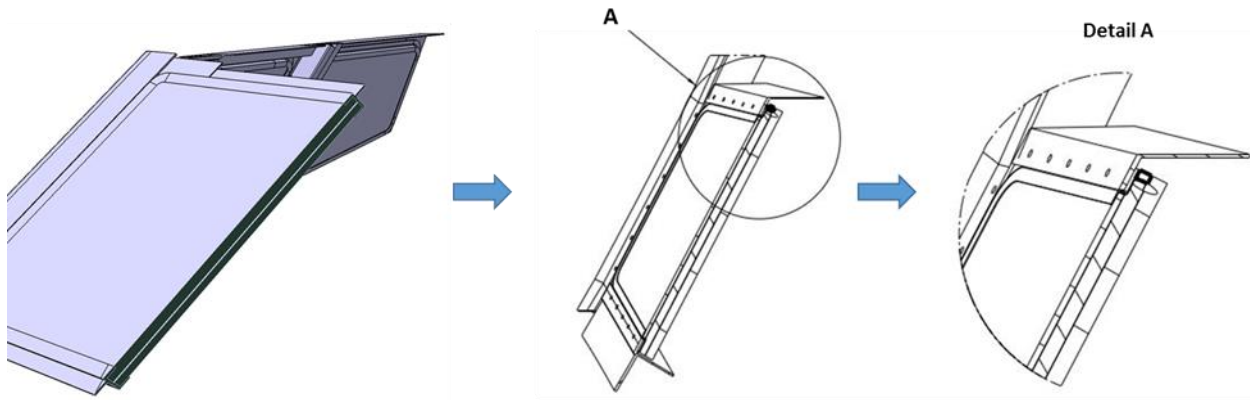


Figure 65. Commercial transport jet windshield cross-section

3.2.1.4 Wing

Figure 66 shows the commercial transport jet wing layout and the selected area for UAS impact studies. A leading edge of this size jet is typically made out of two main components: the fixed-wing and the slats. For this study, only the fixed leading edge of the wing was modeled. The slats were not modeled because if the fixed leading edge can withstand the UAS impact without great damage, then the leading edge with the slat should perform even better from the crashworthiness perspective. The effect of the UAS impacting on the actual slat will be considered in future studies.

The specific wing area selected for the UAS impact was the fixed-wing part spanning Slat 3 and part of Slat 2. The selection of Slat 3 was based on preliminary CFD analyses as discussed in section 3.1.3 . These analyses were used to identify areas with laminar flow around the wing leading edge in order to reduce the possibility of the UAS being redirected due to turbulent flow. In addition, because the fixed-wing structure under Slat 2 is different from that found on Slat 3, a section of the Slat 2 was included in the numerical model for evaluation purposes. At the same time, impacts to this Slat 2 section can be used to evaluate the possibility of wing spar rupture close to the fuel tank.

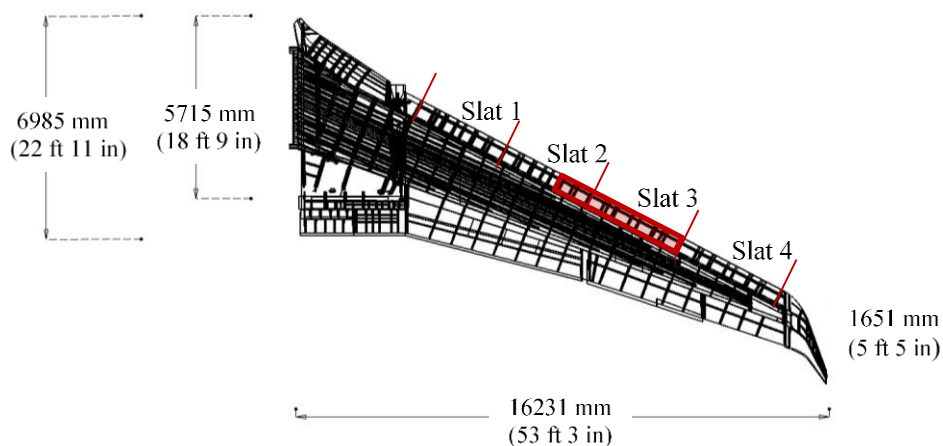


Figure 66. Commercial transport jet wing layout and selected area for UAS impacts

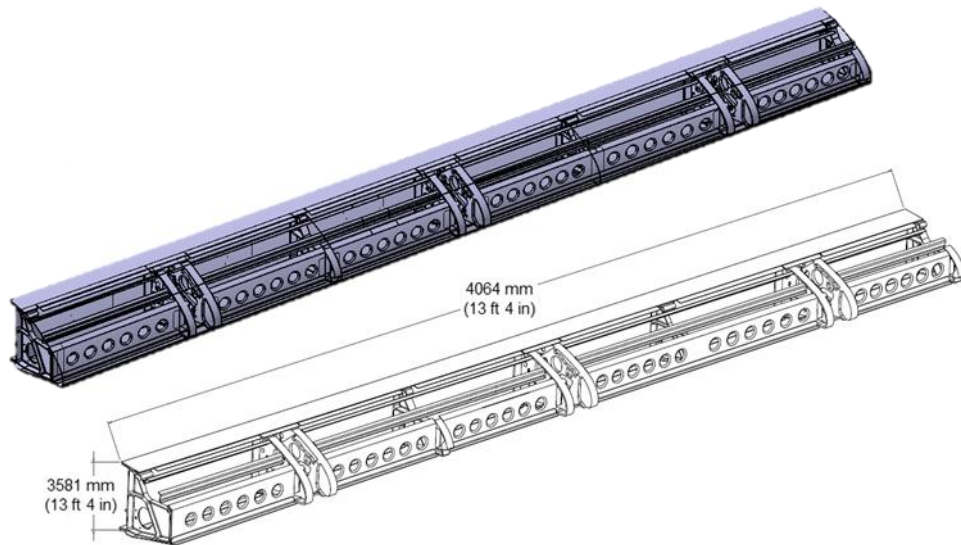


Figure 67. Commercial transport jet wing – leading edge CAD model

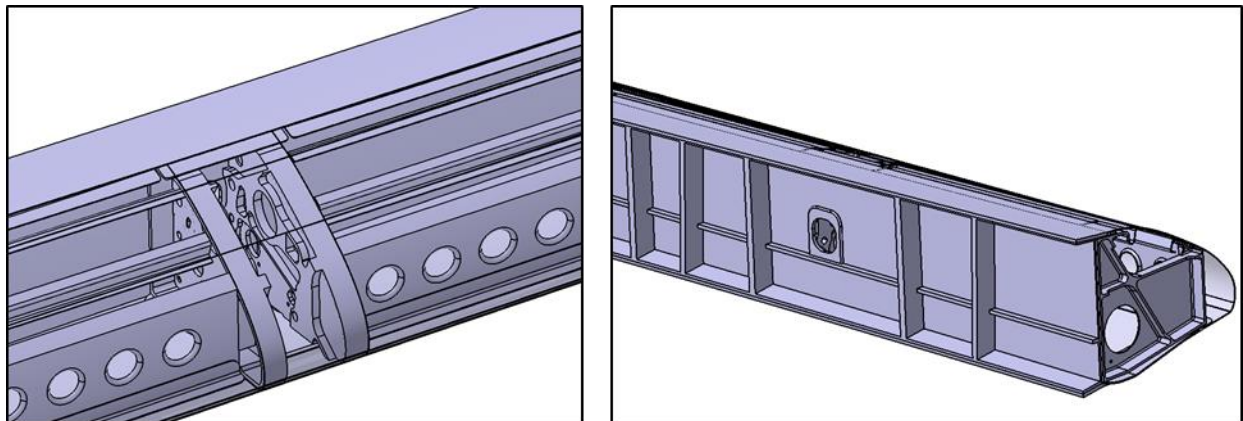


Figure 68. Commercial transport jet wing CAD model

3.2.2 Business Jet

The business jet model was developed following the same procedures as the commercial transport jet. Repair manuals and other technical sources provided most of the information needed to build the CAD model [59]. Figure 69 provides the overall dimensions of the business jet model. The following subsections present the construction details of the components of the business jet selected for collision studies.

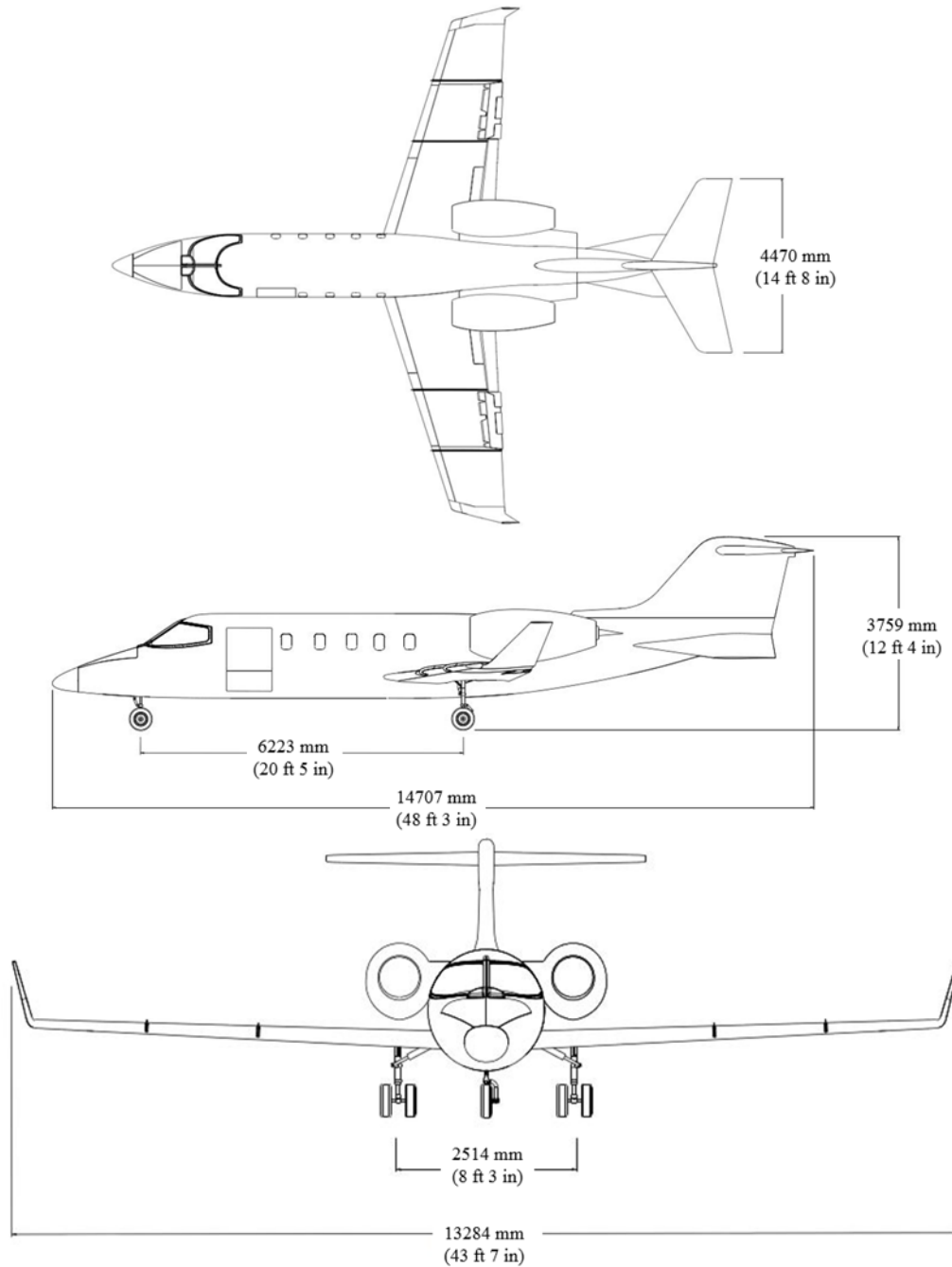


Figure 69. Business jet dimensions

3.2.2.1 Horizontal Stabilizer

Figure 70 shows the horizontal stabilizer CAD model. Figure 71 presents a top view of the internal structure and the overall dimensions of the business jet horizontal stabilizer. Leading edge ribs lightening holes were modeled to scale based on the available information. Anti-icing tubes and wiring were not modeled for the horizontal stabilizer.

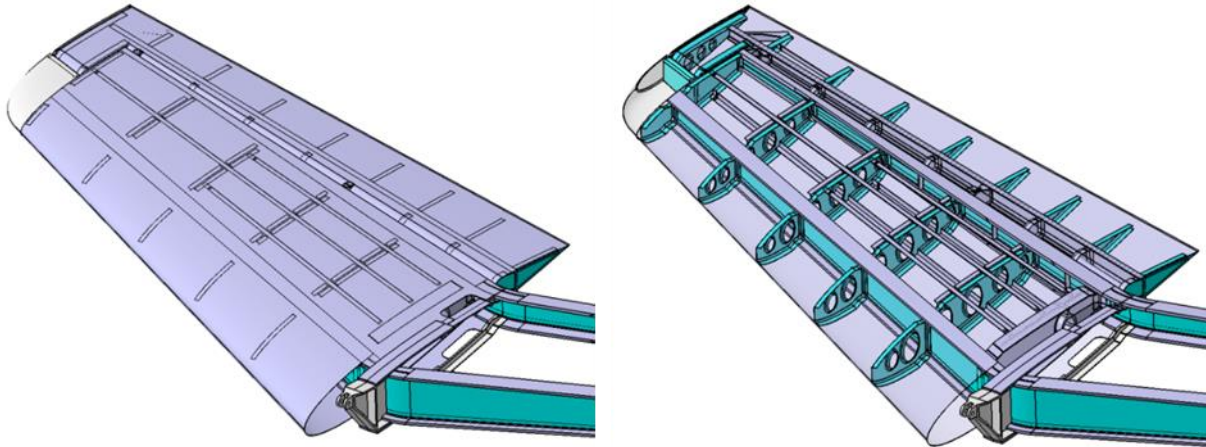


Figure 70. Business jet horizontal stabilizer

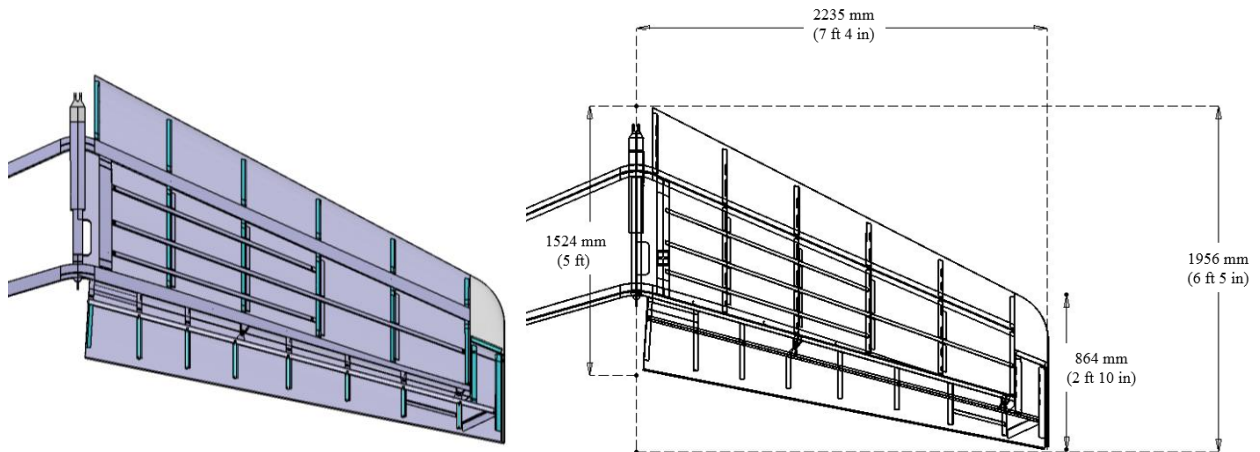


Figure 71. Business jet horizontal stabilizer CAD model and dimensions

3.2.2.2 Vertical Stabilizer

Figure 72 shows the internal structure of the business jet vertical stabilizer. Since the light (located on the tip) is not a critical structural component, this component was highly simplified and was considered to be part of the aluminum skin. Figure 73 presents a side view of the vertical stabilizer and a sketch with the main dimensions. The same assumptions for the horizontal stabilizer were made for the vertical stabilizer.

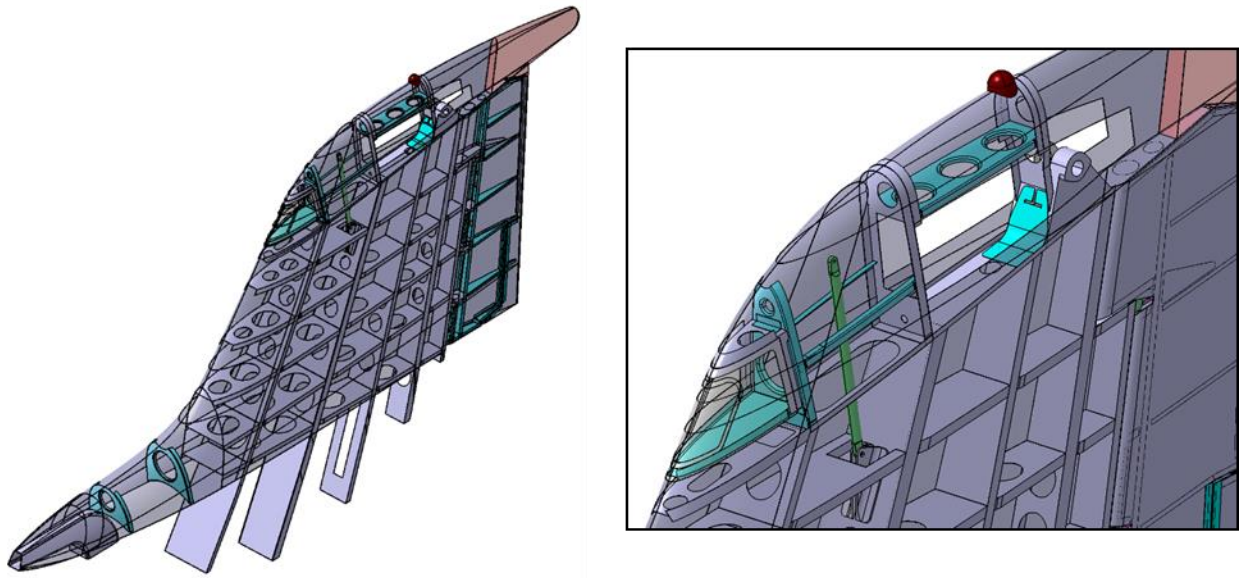


Figure 72. Business jet vertical stabilizer

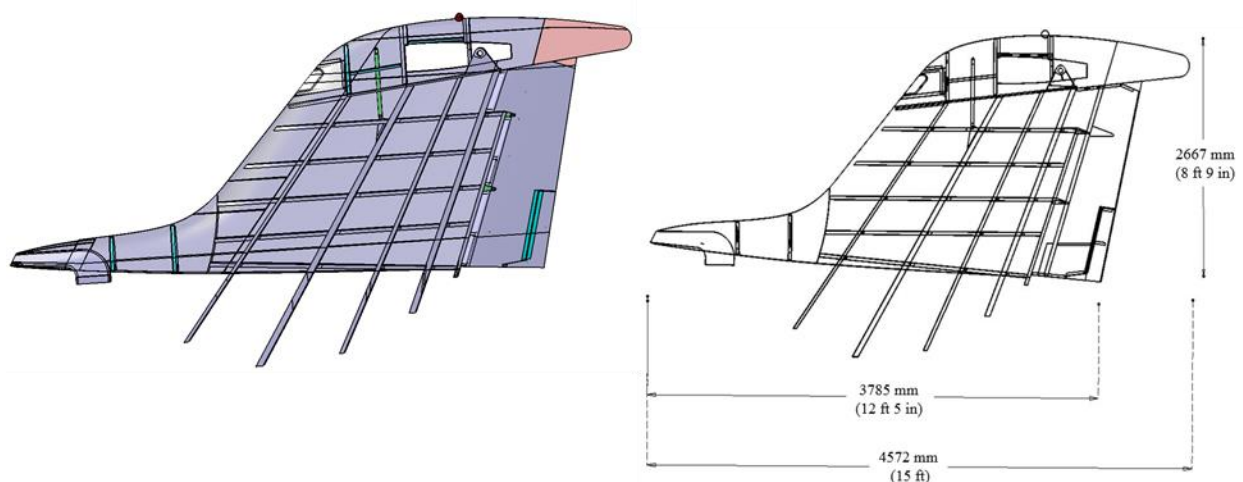


Figure 73. Business jet vertical stabilizer CAD model and dimensions

3.2.2.3 Windshield

Figure 74 shows the detailed business jet forward fuselage CAD model. Figure 75 shows a detailed view of the business jet windshield and a sketch including the overall dimensions. Windshield details were obtained from a repair manual [59]. Parts such as the silicone gasket and inserts were not modeled. A detailed view of the windshield cross-section is shown in Figure 76.

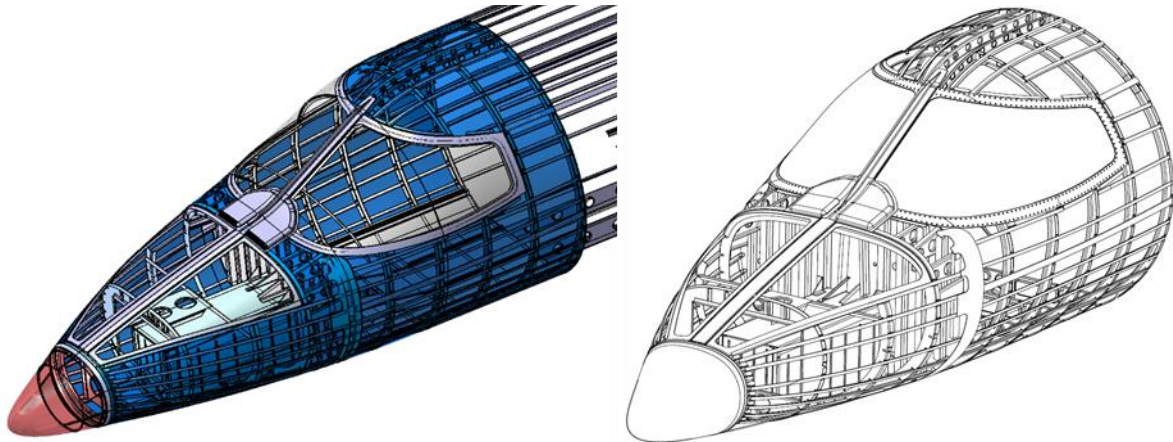


Figure 74. Business jet forward fuselage

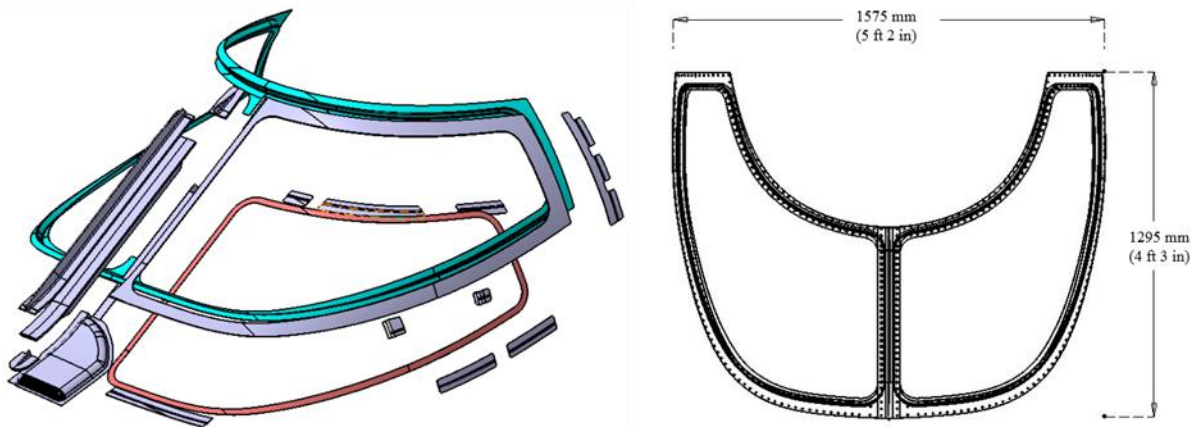


Figure 75. Business jet windshield CAD model

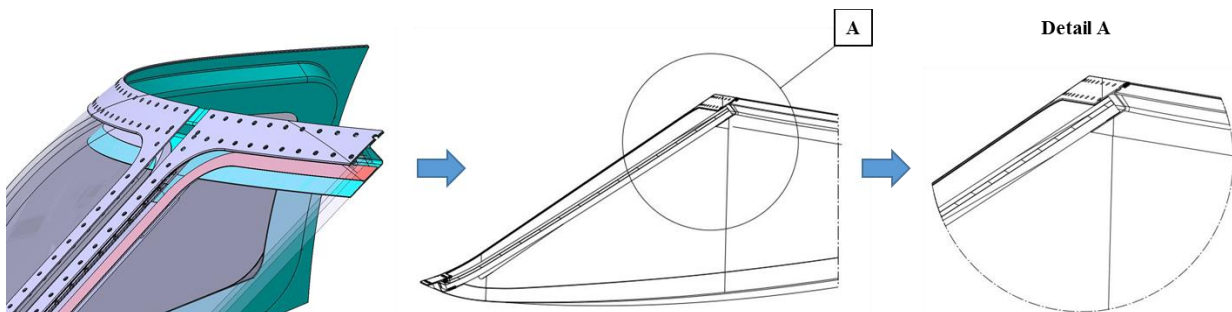


Figure 76. Business jet windshield cross-section

3.2.2.4 Wing

Figure 77 shows the business jet wing CAD model. Based on the available data, there were a smaller number of nose ribs along the leading edge than in the stabilizers. Relevant details such as the leading edge anti-icing pipe were modeled to keep an accurate leading edge stiffness. Figure 78 presents a top view of the business jet wing and a sketch with the principal dimensions of the wing. Internal wiring and access panels were not modeled. The control surfaces were fixed in place and the corresponding actuators were not modeled.

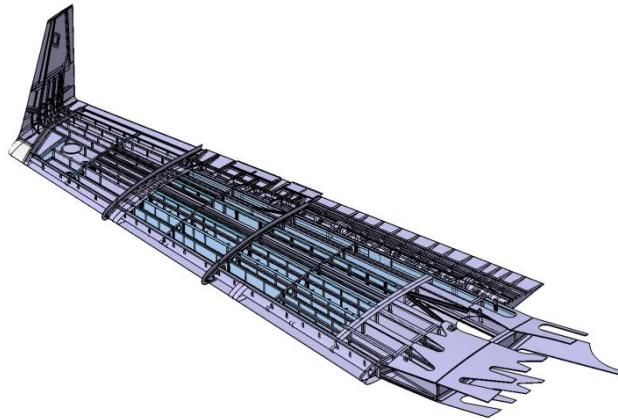


Figure 77 Business jet wing

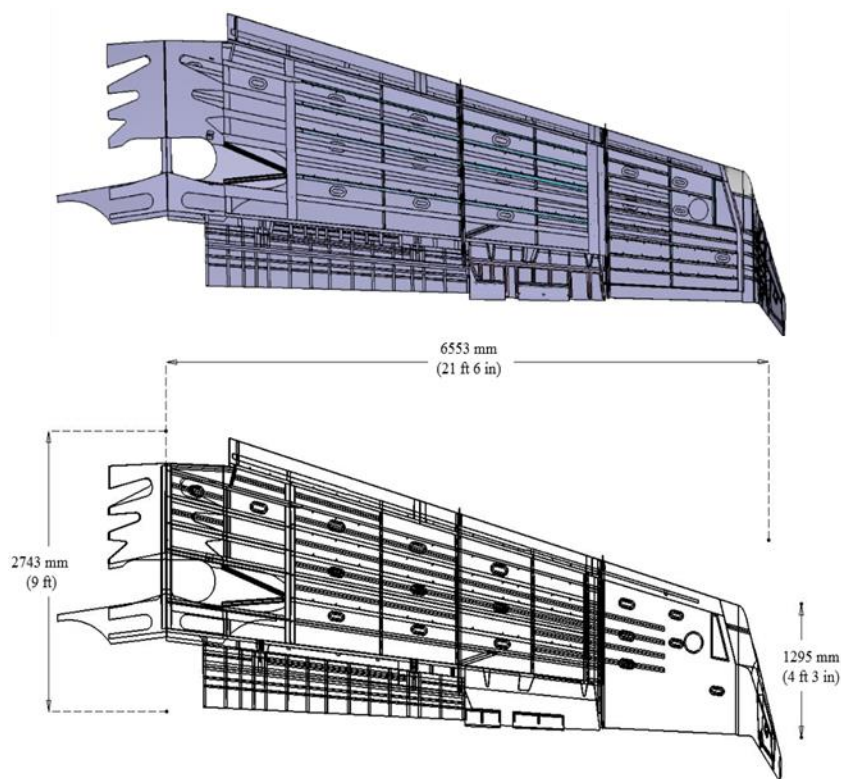


Figure 78. Business jet wing CAD model

3.3 TARGET FINITE ELEMENT MODEL

This section explains the process followed to develop the FE model of the commercial transport jet and the business jet components. The following procedure was carried out to create the FE model:

- Obtain CAD data (STP format) for each model.
- Clean up geometry prior to meshing (split surfaces where symmetric, defeature small details, etc.).
- Select element type for each part depending on geometry and element size constraints.
- Discretize the geometry (meshing).
- Check quality criteria.
- Assign section properties: shell thicknesses and beam cross section.
- Assemble FE meshed parts.
- Check models for non-desired entities (free nodes, free edges, mesh overlap, duplicate elements, non-aligned element normal, etc.).
- Assign appropriate material properties.
- Add non-structural mass to nodes wherever necessary.
- Perform a mass check.
- Renumber model components to avoid clashes between the UAS and the target FE models.

A series of sensitivity studies were conducted in order to define the discretization (mesh) criteria, as well as the material models, that will be used for full-scale analyses. The accuracy of the FEA results largely depends on correct input and on a comprehensive understanding of parameters used in defining the numerical models. The results of these sensitivity studies and other FE model parameters selected for developing the target FE models are documented in subsequent sections.

3.3.1 Mesh Sensitivity Study

The computational cost of explicit dynamic analyses is driven by the minimum element length [25]. In addition, the deformations, loads, and failure modes are also influenced by element size. As a result, a mesh sensitivity study was performed to select an element size for FE discretization of targets so that a balance could be obtained between result accuracy and computational efficiency.

3.3.1.1 Mesh Sensitivity Study with Generic Motor Model and Flat Plate

To perform the study, a validated FE model of a 3.175 mm (0.125 in) flat plate was used [41]. A 3.2 mm element length was selected as a baseline for comparison to other element lengths. A FE model of a 34.2 g steel sphere with similar dimensions as a motor of an UAS was created. The simulated spherical projectile was impacted to the flat plate FE model at a velocity of 128.6 m/s (250 knots). A schematic of the FE models is shown in Figure 79 and is similar to the setup used in previous simulations (section 2.4.7). Six different element lengths were compared as illustrated in Figure 80: 1.6 mm, 3.2 mm (baseline), 6.35 mm, 12.7 mm, 25.4 mm, and 50.8 mm. Preliminary analyses indicated that a 6.35 mm element length correlated well with the 3.2 mm baseline. Therefore, a 5 mm element length was also evaluated to further understand the mesh sensitivity.

FE results for multiple element lengths were evaluated based on several different factors. The first factors studied were the damage and failure mode. Figure 81 illustrates the damage and effective plastic strain for different element lengths. Perforation was observed for all models up to a 6.35 mm element length. FE results for larger element lengths showed no damage. However, with a 6.35 mm element length, the failure modes were different from what was observed with the baseline model. Therefore, an intermediate 5 mm element size was considered.

Figure 82 shows the time history of reaction forces. Peak reaction forces are plotted in Figure 83. As the element size was decreased, the reaction force converged as would be expected. There was a clear improvement in the performance of the FE model with the 5 mm element length. Additionally, the computational runtime for each FE model was compared and is shown in Figure 84. The computational runtime increases as the element size decreases as would be expected. As previously mentioned, the computational cost of explicit dynamic analyses is driven by the minimum element length [25]. While lower FE lengths give more accurate results, for this study, any element size lower than the baseline was considered to be undesirable. The runtime for the FE model with the 5 mm element length was not significantly different than the baseline.

Thus, based on the mesh sensitivity analysis performed, a 5 mm element length used for discretizing the impacted area of every target FE model described in Chapter 3. This element length provides a good balance between computational time and accuracy of results (stress gradients, failure prediction and reaction forces). Verification of the mesh sensitivity study was achieved during the motor component level test (section 2.4.8.1) when the simulation predicted the experimentally observed panel failure behavior. This test showed a petaling failure mode on the panel.

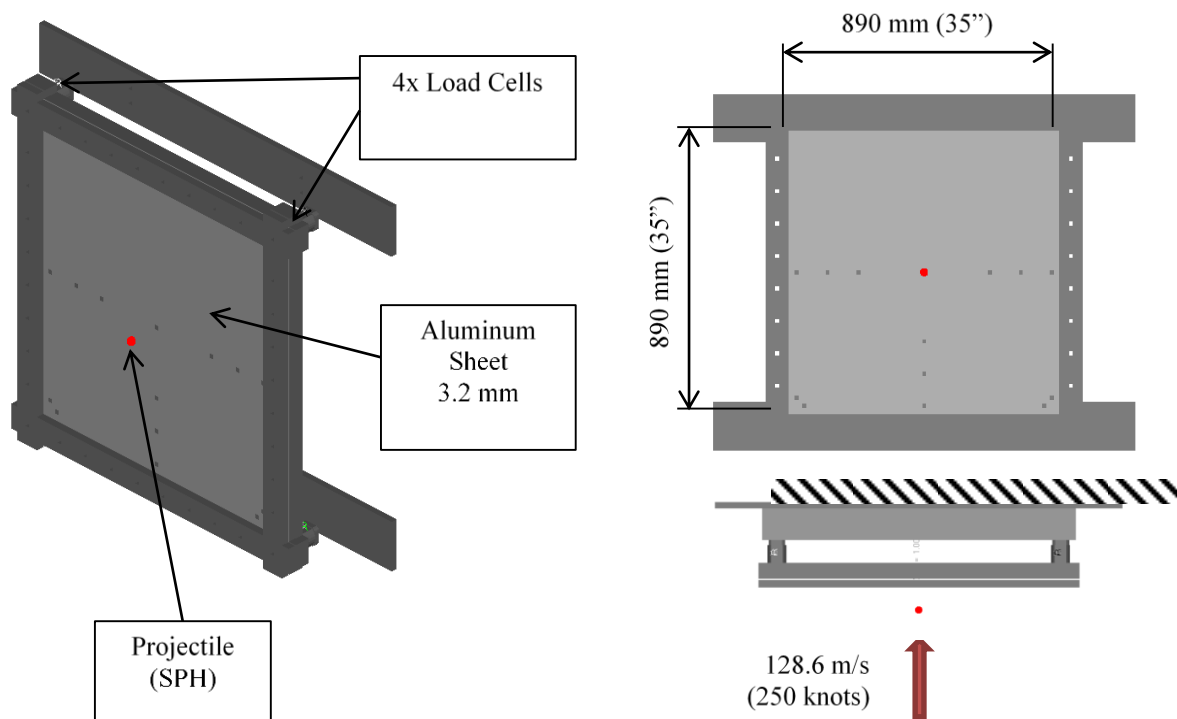


Figure 79. Mesh sensitivity study flat plate FE model

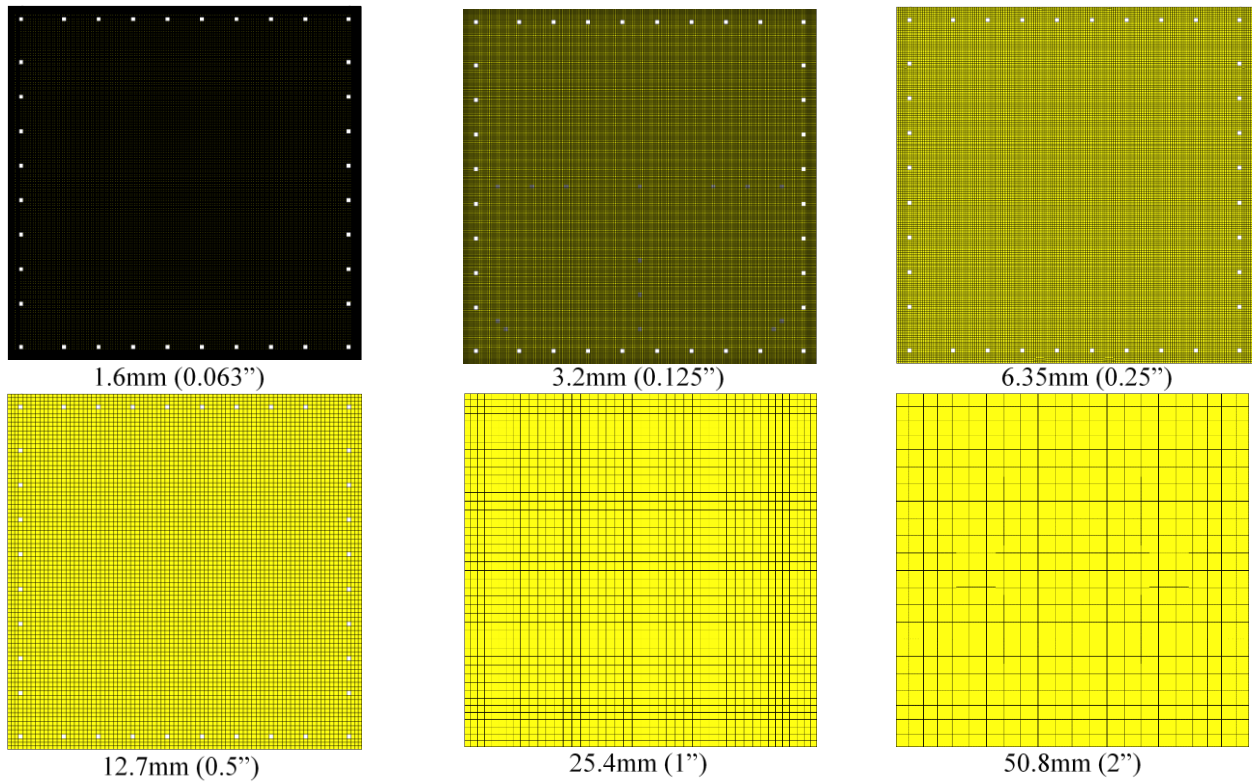


Figure 80. Illustration of mesh size compared for mesh sensitivity study

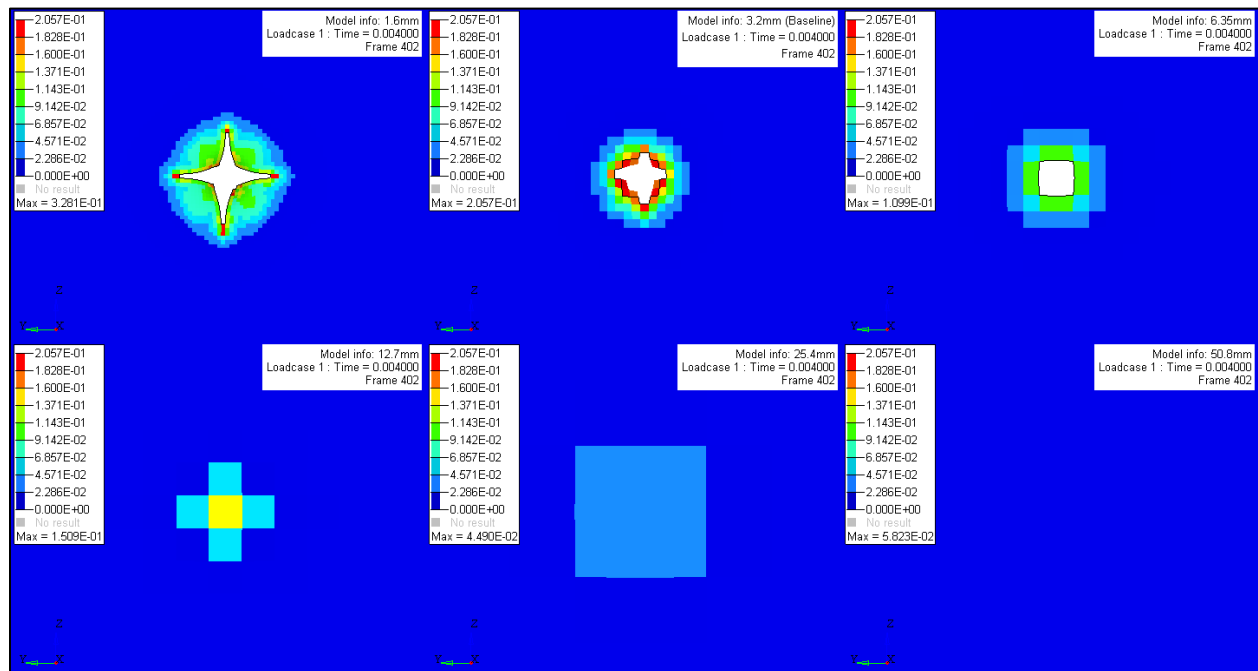


Figure 81. Damage and effective plastic strain comparison for mesh sensitivity study

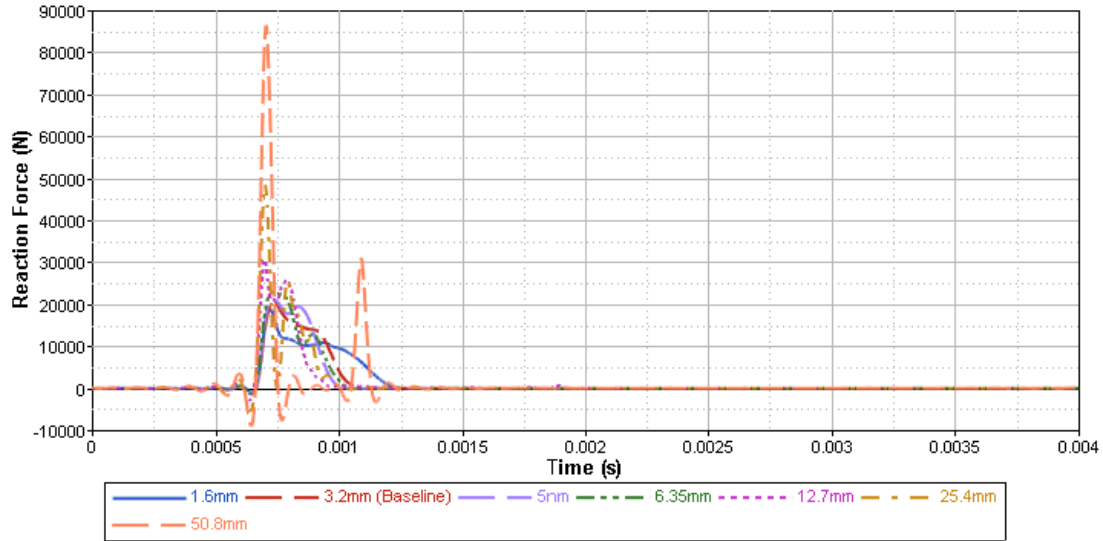


Figure 82. Reaction force time history for mesh sensitivity study

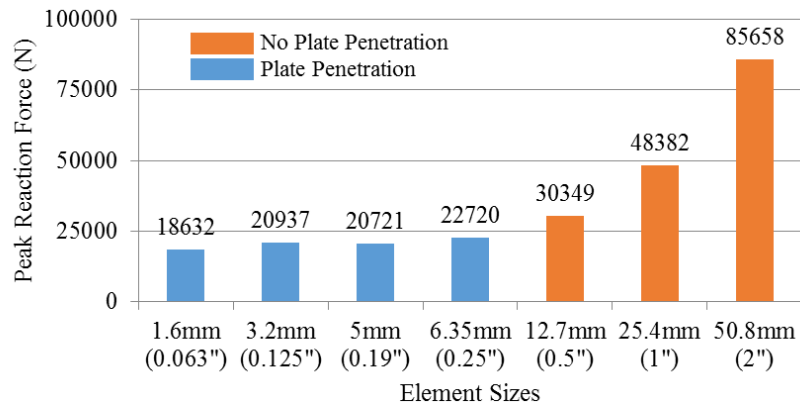


Figure 83. Peak reaction forces for different element lengths on flat plate impacted by a sphere.

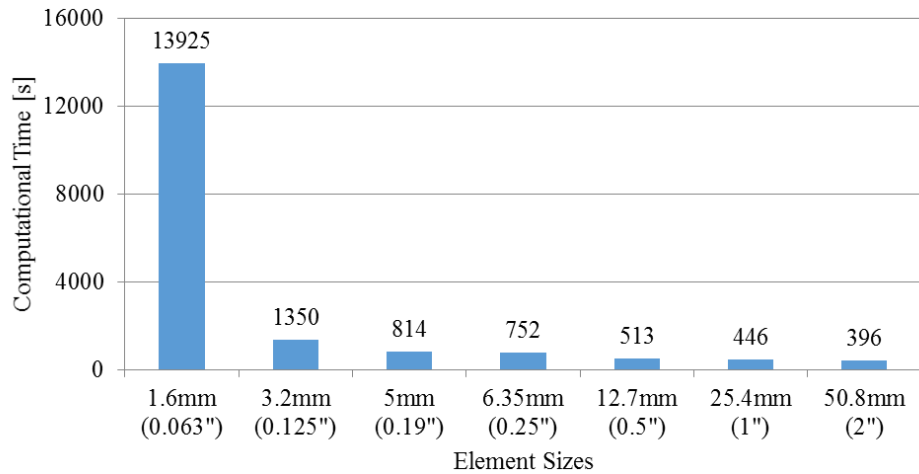


Figure 84. Computational time comparison for mesh sensitivity study

3.3.1.2 Verification of Selected Mesh Size

As detailed in section 2.4.1 of the quadcopter report [2], ballistic tests were conducted on the flat plate FE models described in section 3.3.1.1 using motor components of the quadcopter UAS to help validate the corresponding FE model. Note that the size and mass of the motor for the quadcopter is similar to that of the fixed-wing UAS. A 5 mm mesh size was used to discretize the flat plate for the motor verification study. Figure 85 shows the comparison of the test to the FE analysis. The results show good correlation in damage prediction.

Thus, the mesh sensitivity study follows the philosophy of the building block approach, and the component level correlation to test helps define FE model parameters such as mesh size that would produce accurate results. This provides confidence in the possible damage prediction of the aircraft targets by using the mesh size documented on the previous section.

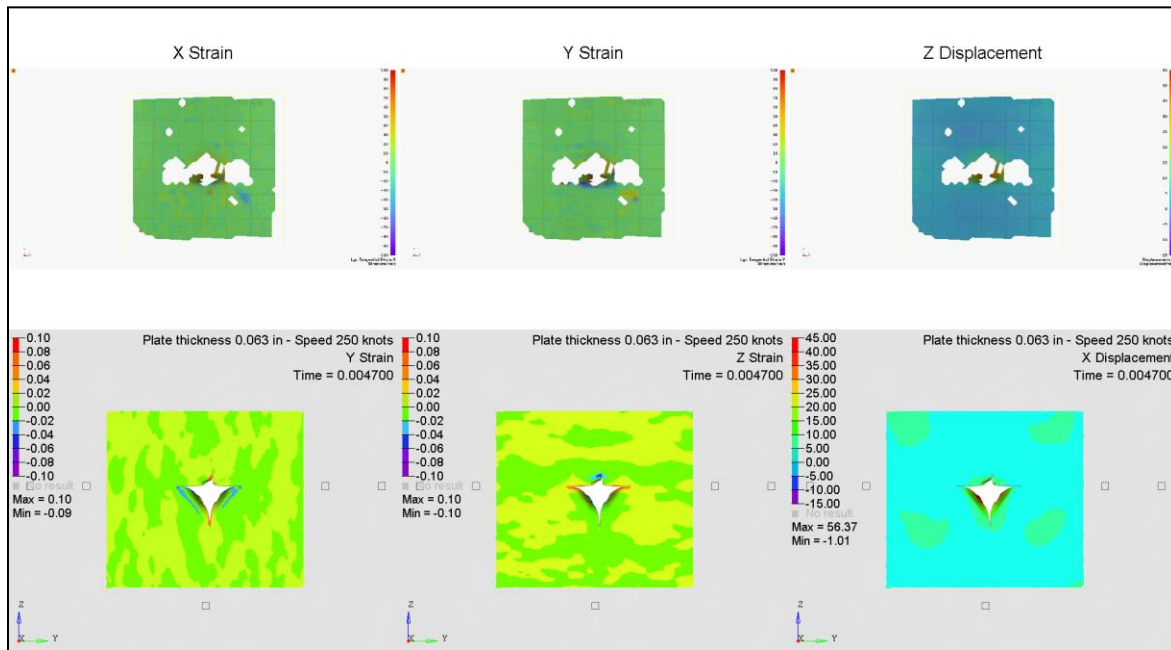


Figure 85. Mesh size validation on motor component level test.

3.3.2 Mesh Quality Criteria

Table 12 contains the criteria used to discretize the target areas of components of the commercial transport and business jet models. The quality criteria are based on recommended practices for crash analysis [62][63] and on the mesh sensitivity study detailed in section 3.3.1 .

The quality parameters are defined in section 2.3 . Larger element lengths were used for areas that were not directly impacted in order to reduce the element count and create more computationally efficient models.

Table 12. Mesh quality criteria for target impact area.

Quality Parameter	Allowable Min.	Allowable Max.
Element Size	5 mm	8 mm
Aspect Ratio	-	5
Quad Angle	45°	140°
Tria Angle	30°	120°
Warp Angle	-	15°
Jacobian	0.7	-

Some decisions and assumptions were made while meshing in order to generate a good quality mesh for the crash analyses:

- Small fillets were defeatured and meshed with sharp edges.
- A minimum of two elements were kept on stiffeners to maintain the correct stiffness of the part.
- All sheet metal parts were meshed at the mid-surface using shell elements.
- Whenever possible, at least three through-thickness elements were used when meshing with solid elements. If it was not feasible due to the element size constraint, a fully integrated formulation was used instead.
- The total number of trias in the model was limited to 5%, and any concentration of tria elements was avoided to maintain a homogeneous stress distribution.

3.3.3 Discretization

This section details the results of the discretization process applied to the geometry of the horizontal stabilizer, vertical stabilizer, wing, and forward fuselage of both aircraft models. The element types used for generating the FE model are detailed in section 2.3.1 .

Table 13 summarizes the type and quantity of elements in each target model after the discretization process.

Table 13. Mesh elements quantity

		1D elements	2D elements	3D elements
NIAR Commercial Transport Jet	Front Section	32,473	798,264	349,779
	Horizontal Stab.	12,858	288,520	-
	Vertical Stab.	15,568	582,705	288
	Wing	1,371	302,070	-
NIAR Business Jet	Front Section	8,149	394,344	228,688
	Horizontal Stab.	2,548	124,518	-
	Vertical Stab.	2,901	158,433	122
	Wing	15,271	544,503	-

3.3.3.1 Commercial Transport Jet

The discretized target components of the commercial transport jet are shown from Figure 86 to Figure 95. The discretized FE model is compared against the CAD models.

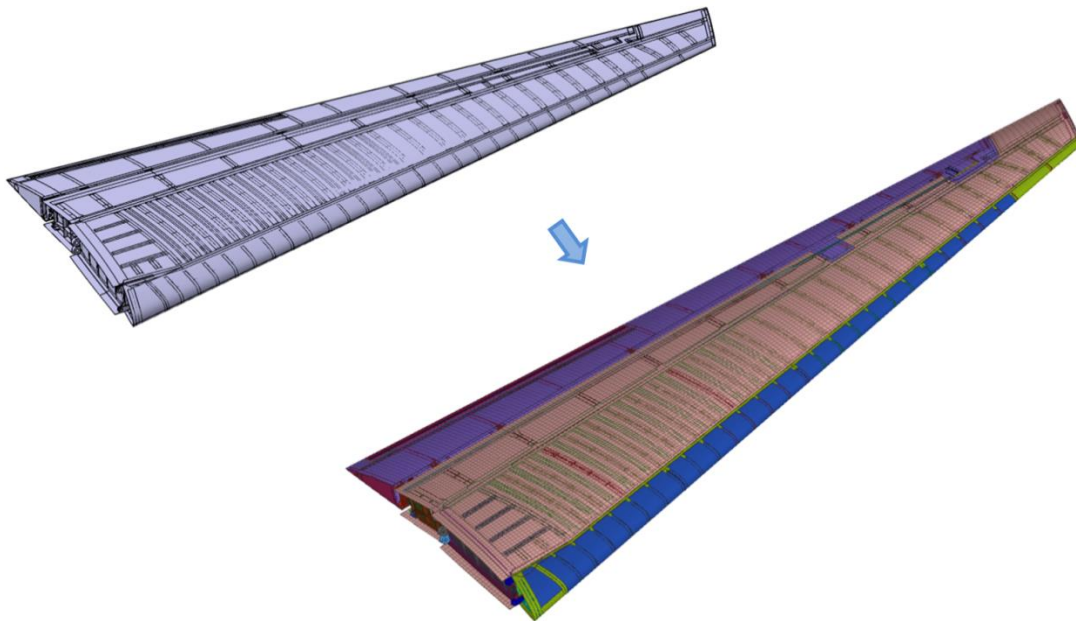


Figure 86. Commercial transport jet horizontal stabilizer - Geometry and mesh

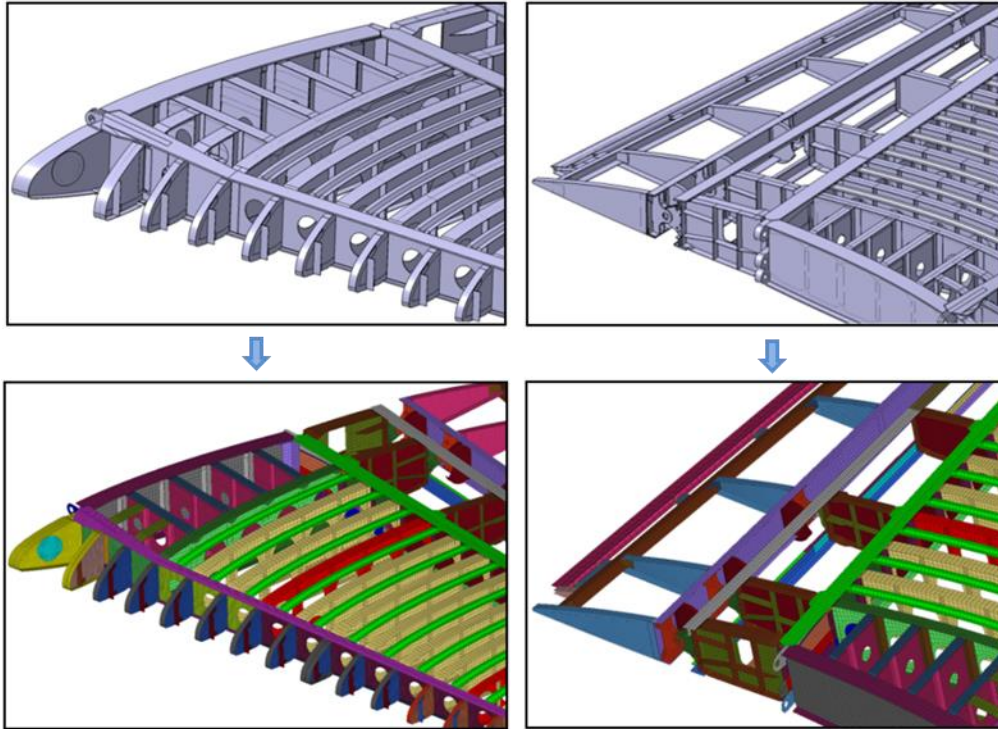


Figure 87. Commercial transport jet horizontal stabilizer - Internal structure geometry and mesh

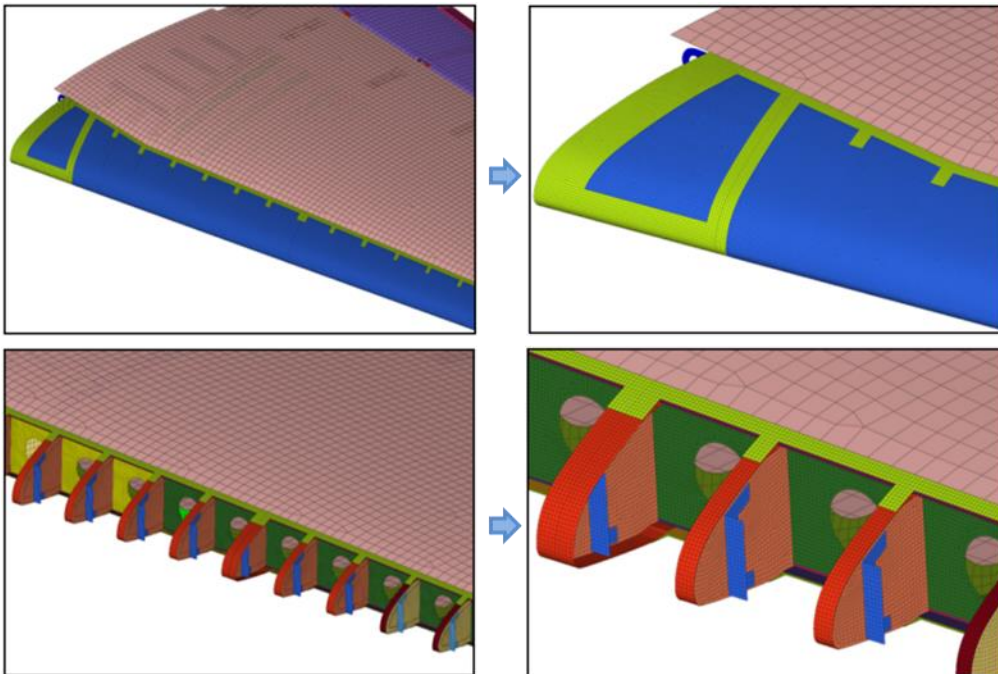


Figure 88. Commercial transport jet horizontal stabilizer - Mesh size

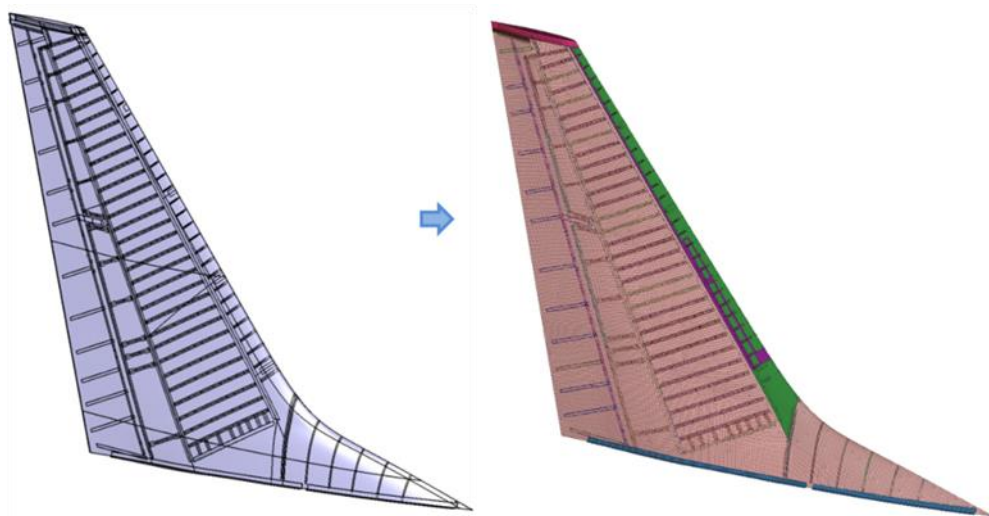


Figure 89. Commercial transport jet vertical stabilizer - Geometry and mesh

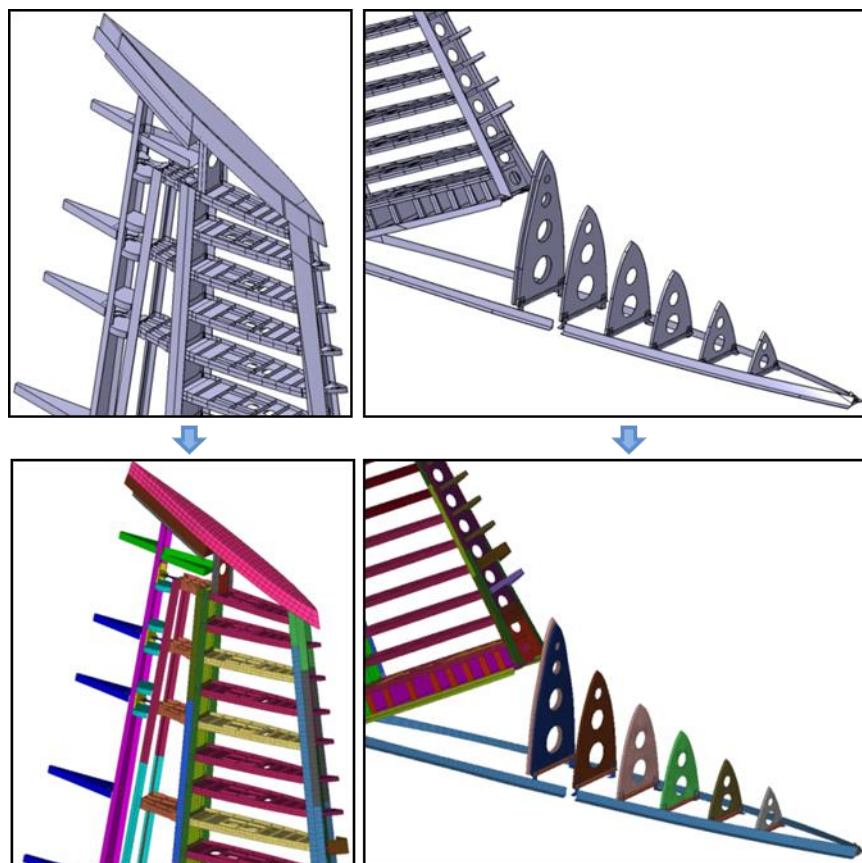


Figure 90. Commercial transport jet vertical stabilizer - Internal structure geometry and mesh

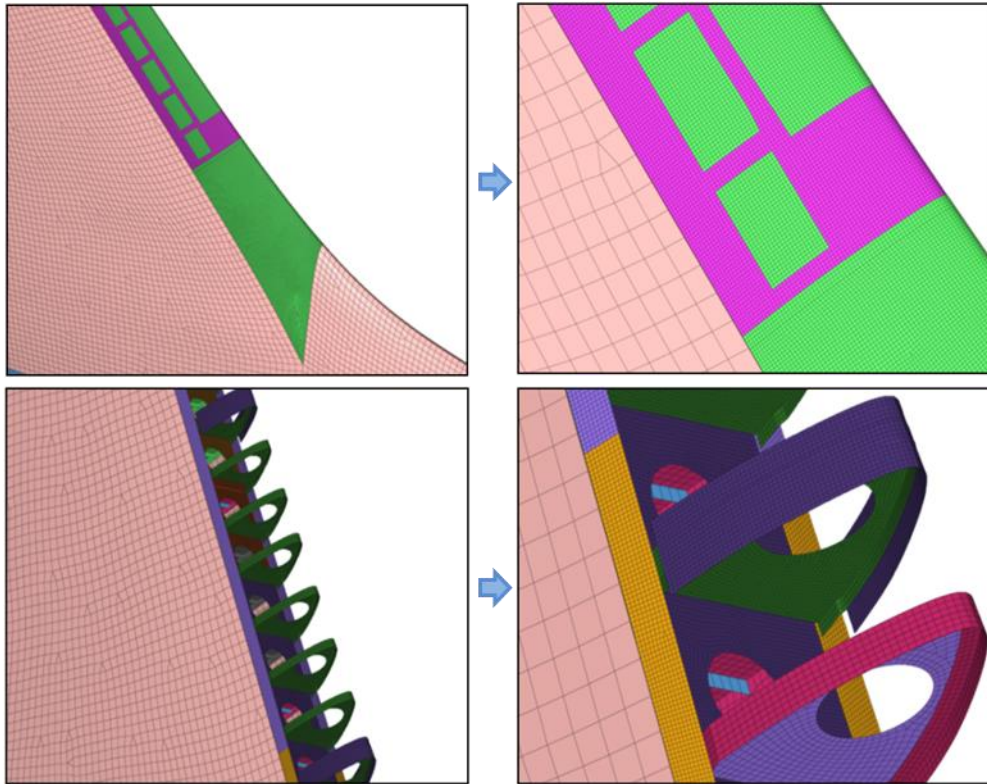


Figure 91. Commercial transport jet vertical stabilizer - Mesh size

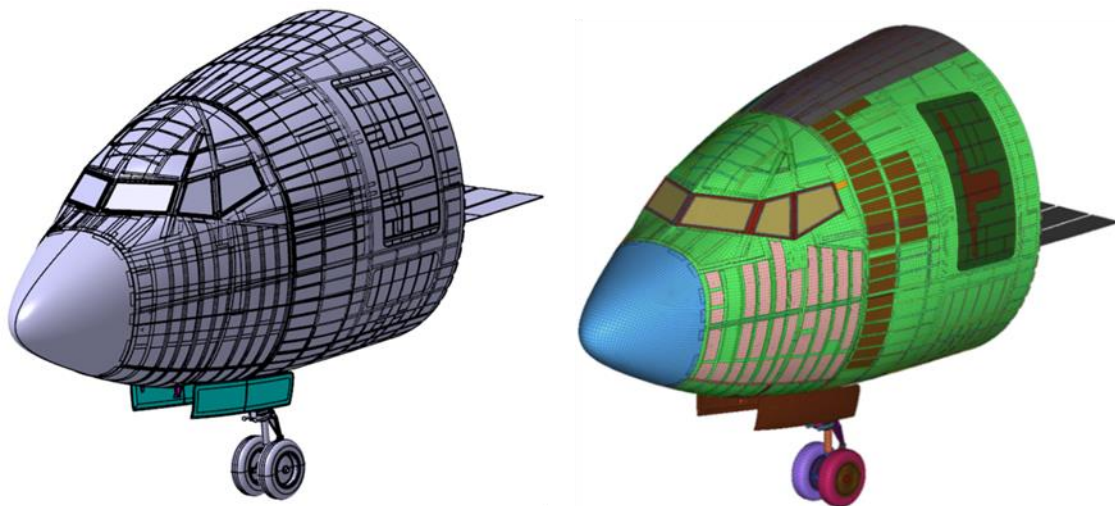


Figure 92. Commercial transport jet windshield - Geometry and mesh

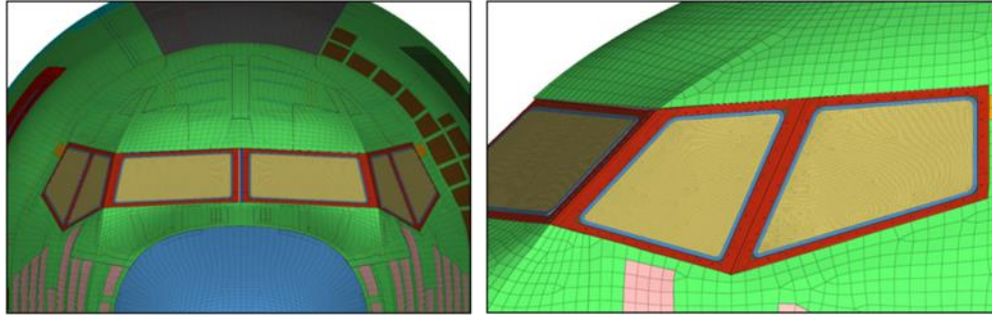


Figure 93. Commercial transport jet windshield - Mesh size

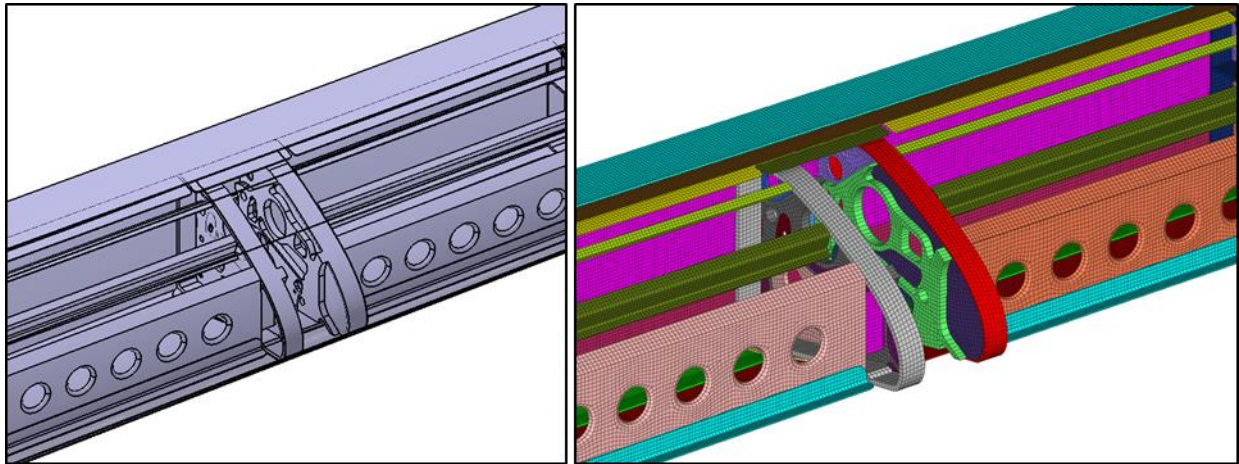


Figure 94. Commercial transport jet wing - Geometry and mesh

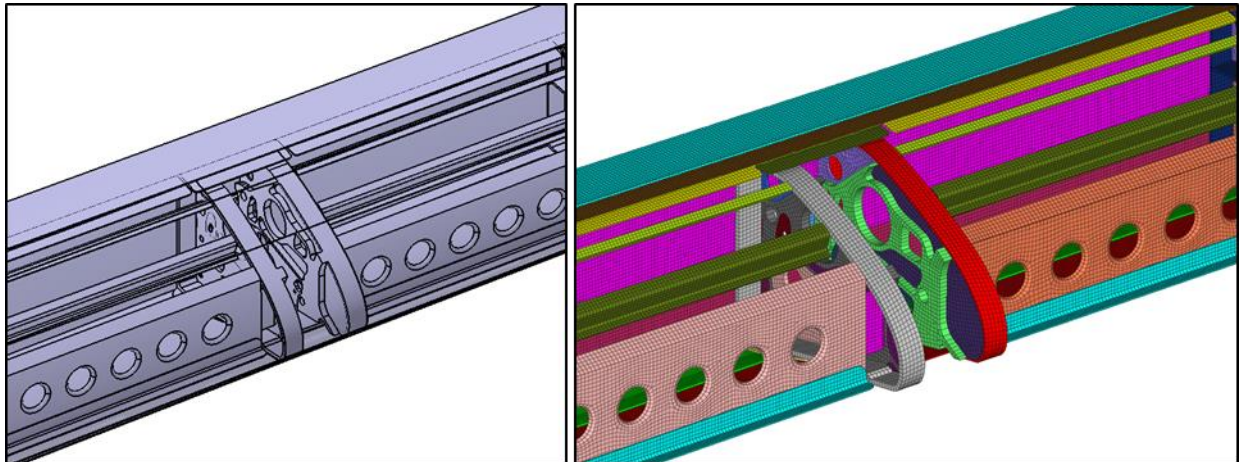


Figure 95. Commercial transport jet wing - Internal frames

3.3.3.2 Business Jet

The discretized target components of the business jet are shown from Figure 96 to Figure 103. The discretized FE model is compared against the CAD models.

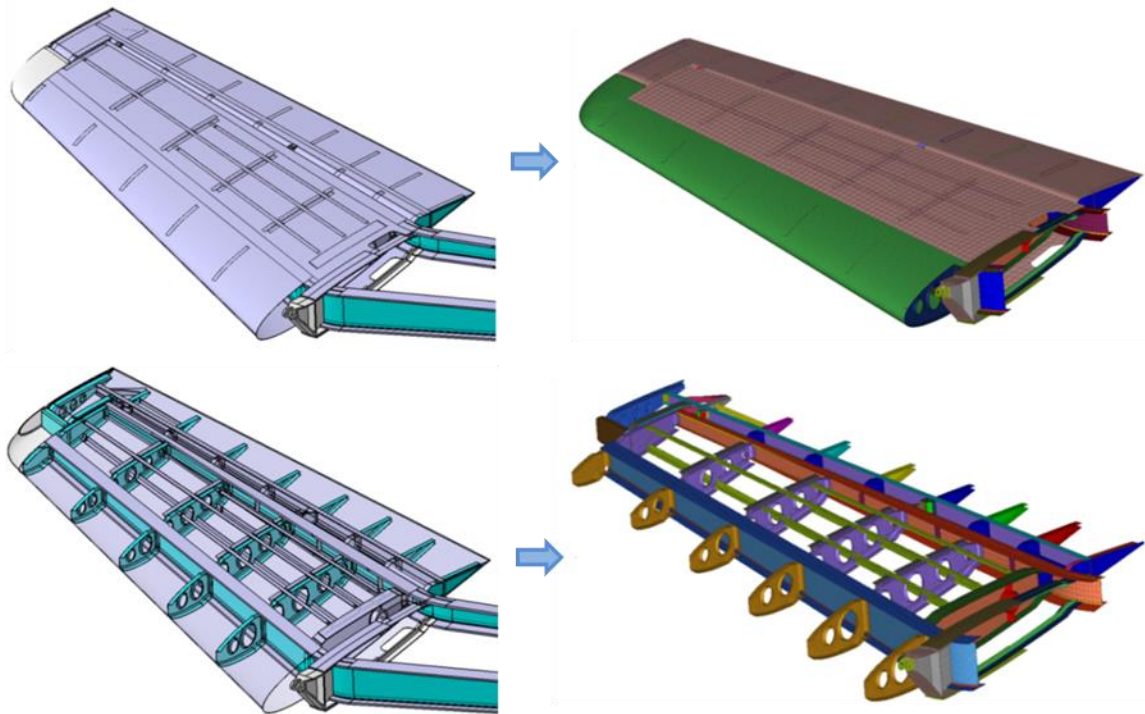


Figure 96. Business jet horizontal stabilizer - Geometry and mesh

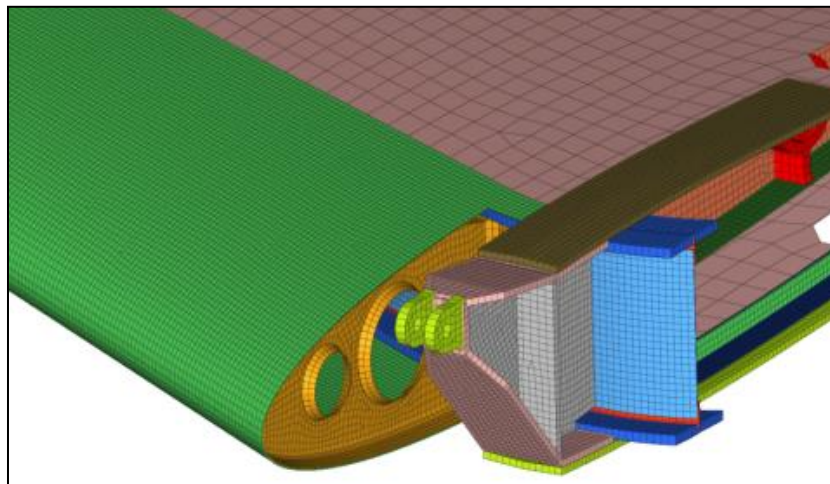


Figure 97. Business jet horizontal stabilizer - Mesh size

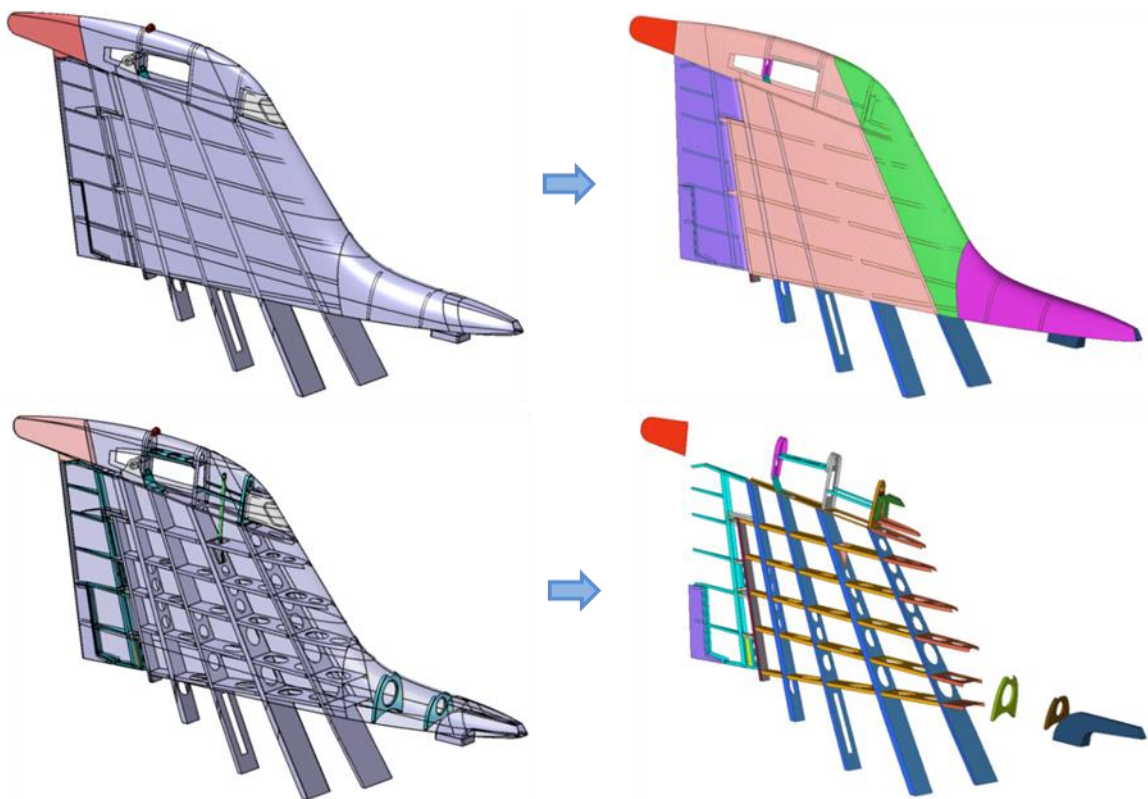


Figure 98. Business jet vertical stabilizer - Geometry and mesh

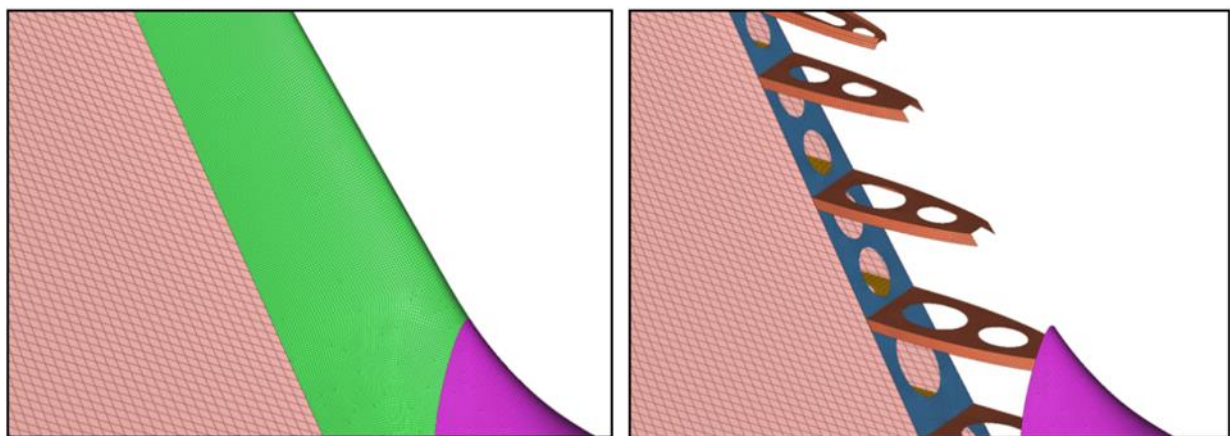


Figure 99. Business jet vertical stabilizer - Mesh size

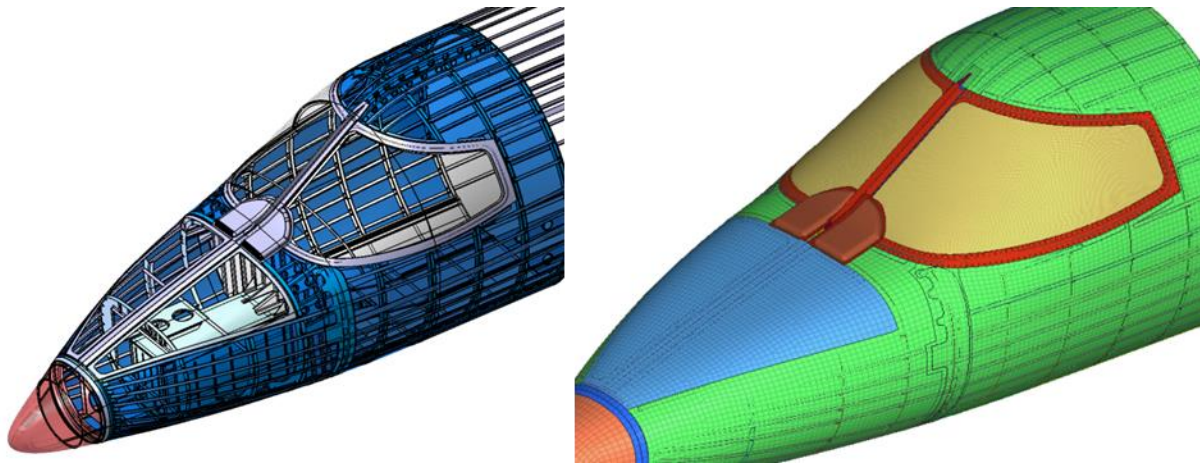


Figure 100. Business jet front section - Geometry and mesh

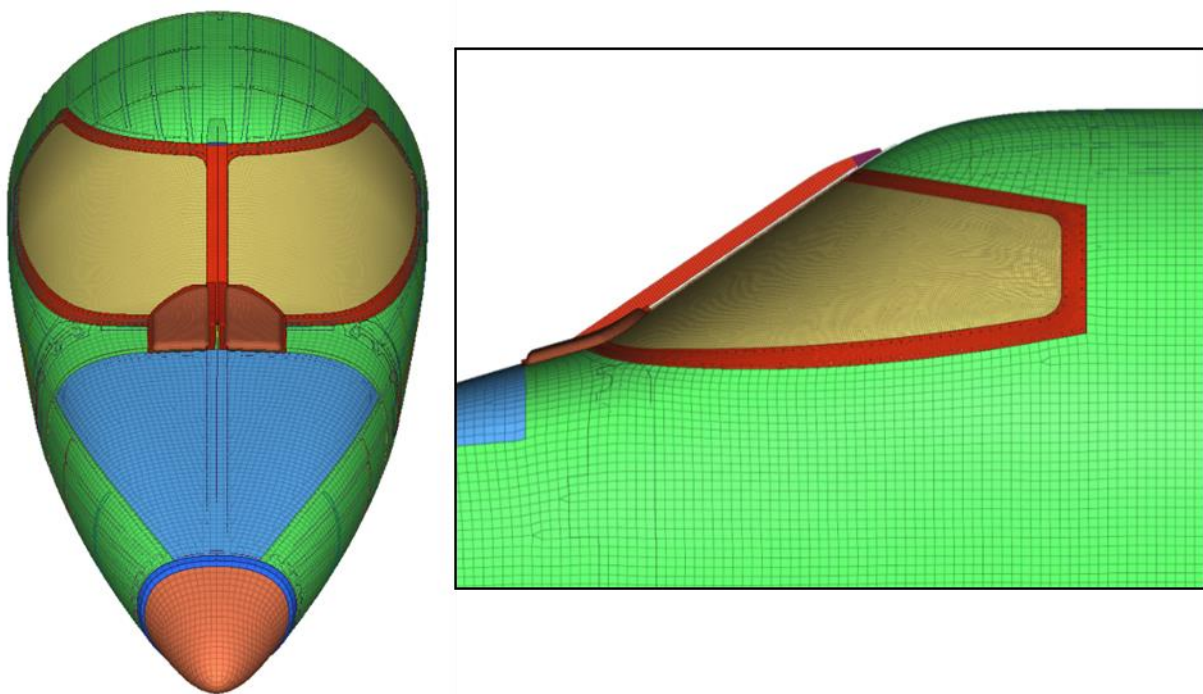


Figure 101. Business jet front section - Mesh size

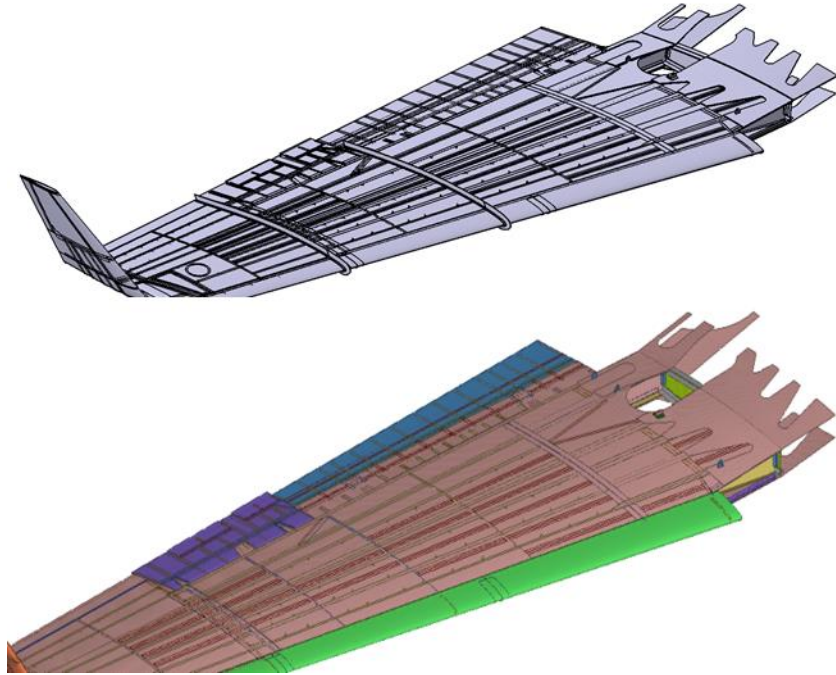


Figure 102. Business jet wing - Geometry and mesh

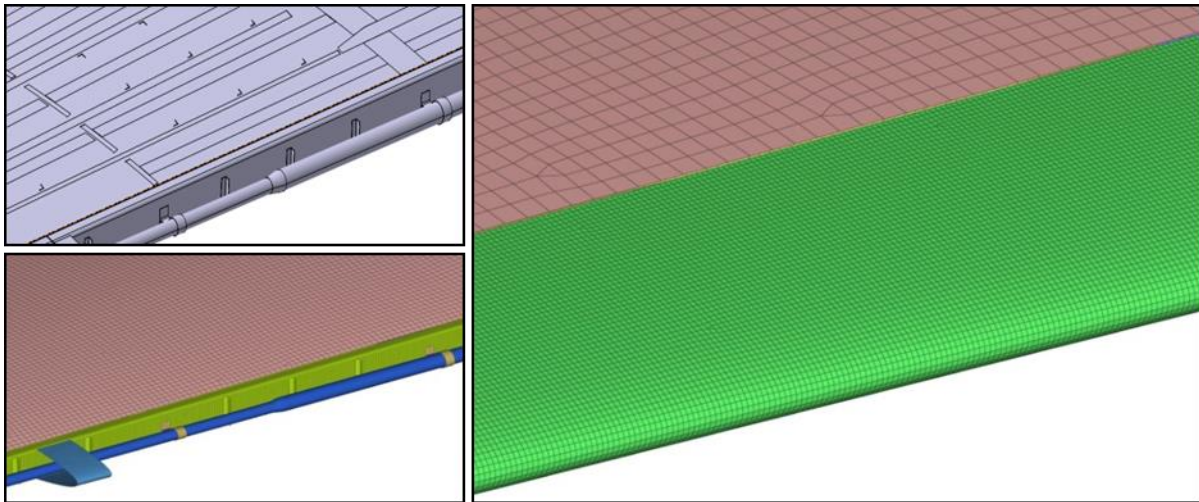


Figure 103. Business jet wing - Mesh size

3.3.4 Connections

The discretized models were connected using two connection types:

- Mesh independent spot-weld beam element: this is one of several options used to model fasteners in FE models. This connection is practical for large models because it is possible to automate the connection process. An example of a spot-weld beam connection between the front spar and the front web is shown in Figure 104.

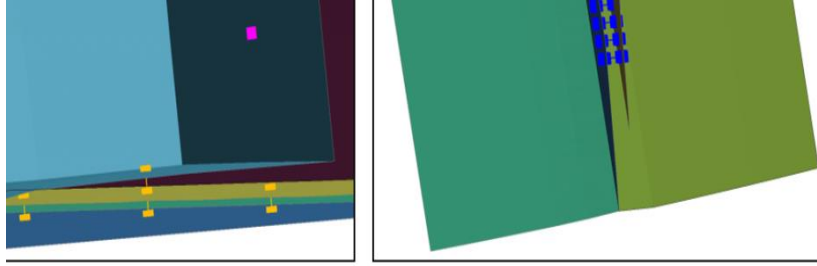


Figure 104. Spot-weld beam connection

- Nodal Rigid Body (NRB): the selected set of nodes are constrained to only allow rigid body motion. Figure 105 shows a NRB around a hole.

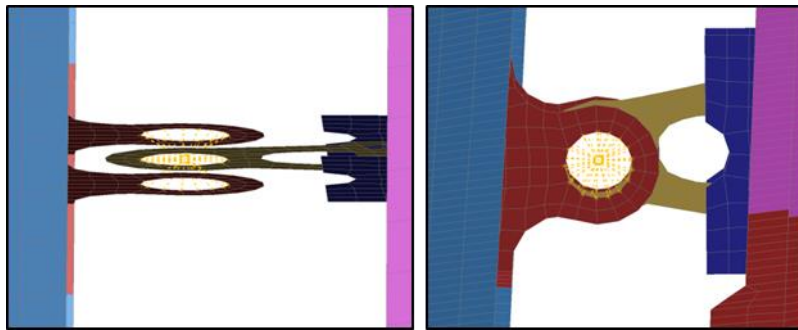


Figure 105. Nodal rigid body

Fastener locations on the target models were established using technical manuals [58][59] and using repair guidelines specified by the FAA Advisory Circular AC 43.13-1B [64]. Two examples of the final FE model are shown in Figure 106. Connections are highlighted in different colors based on fastener diameter. The same procedure was followed for the rest of the target models. A summary of the total number of connections for the different target models is provided in Table 14.

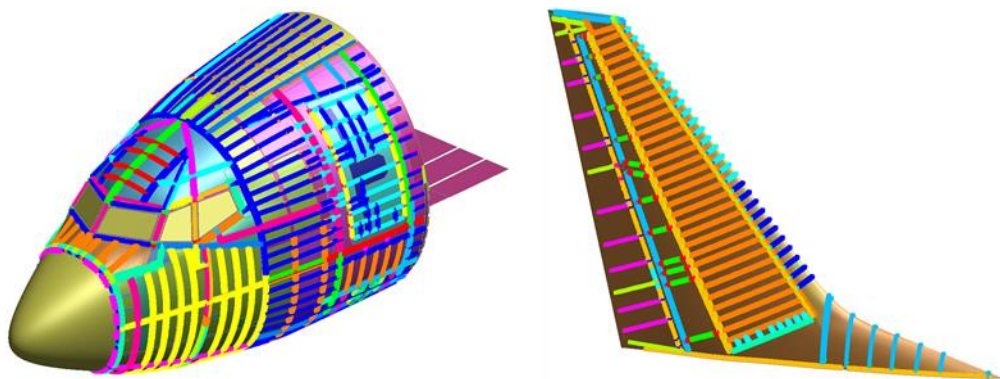


Figure 106. Commercial transport jet front section and vertical stabilizer connections.

Table 14. Target connections summary.

		Spot-weld beam	NRB
Commercial Transport Jet	Front Section	32473	402
	Horizontal Stab.	12858	34
	Vertical Stab.	15568	22
	Wing	1371	-
Business Jet	Front Section	8149	503
	Horizontal Stab.	2548	2
	Vertical Stab.	2901	2
	Wing	15271	36

3.3.5 Materials

LS-DYNA offers several ways to model the material response [27]. There are basic material cards, requiring minimal input as well as complex ones, which capture the effects of strain rate, temperature, and triaxiality. Numerous plasticity models are also available. The correct material model definition is critical for accurate responses of the FE model.

Following the building block approach, validation studies were performed at the coupon level to gain confidence in material modeling for FE analyses.

3.3.5.1 Material Sensitivity Study

In the absence of test data, it is desirable for FE model crashworthiness predictions to be slightly conservative. Therefore, a material sensitivity study was performed to understand the response and to select a FE material model for the targets.

It is also important to note that extensive coupon level testing is required to populate the parameters in the more advanced material models in LS-DYNA [27]. Due to the variety of target materials, parameters for advanced material models were not available for all target components. For this study, the major source for material data was the MMPDS [67]. MMPDS data generally provides enough information to populate the *MAT_024* or **MAT_PIECEWISE_LINEAR_PLASTICITY* material card. This material model captures plasticity and failure and was used for most of the components [67]. Based on research for developing target models, it was found that most skins, especially for the leading edge of the commercial transport jet, are constructed using 2024-T3 clad aluminum. Fortunately, extensive research has been performed by the FAA [65][66] for populating

and validating two different LS-DYNA material models. These are *MAT_015* or **MAT_JOHNSON_COOK* and *MAT_224* or **MAT_TABULATED_JOHNSON_COOK*. These three material models are defined in the LS-DYNA manuals [27].

For conducting the material sensitivity study, a preliminary quadcopter UAS model was impacted on a generic leading edge model at 102.9 m/s (200 knots). The skin of the leading edge model was modeled using 2024-T3 clad aluminum with a gage thickness of 0.063 in (1.6 mm). A schematic for the FE model setup for this study is shown in Figure 107. Three different LS-DYNA material models

Table 15 were used for the skin (first target component impacted) as shown in Table 14. The key independent variables governing the response of the selected materials are also summarized in the table.

The damage and failure modes observed for the FE model results are presented in Figure 108. Based on research performed by the FAA [65], the high fidelity *MAT_015* material model has been validated against several component level tests and articles from aircraft structures. Therefore, *MAT_015* was used as the baseline model for comparison of damage. The FE model using *MAT_224* showed similar damage characteristics as *MAT_015* results while the FE model results based on *MAT_024* exhibited extensive damage on the leading edge. Due to the lack of material model parameters for the various target leading edge materials, the validated *MAT_015* model for 2024-T3 clad aluminum [65], was used to model the leading edge skins for all the targets. All the remaining components of the targets were modeled using *MAT_024* since that data was readily available from MMPDS [67].

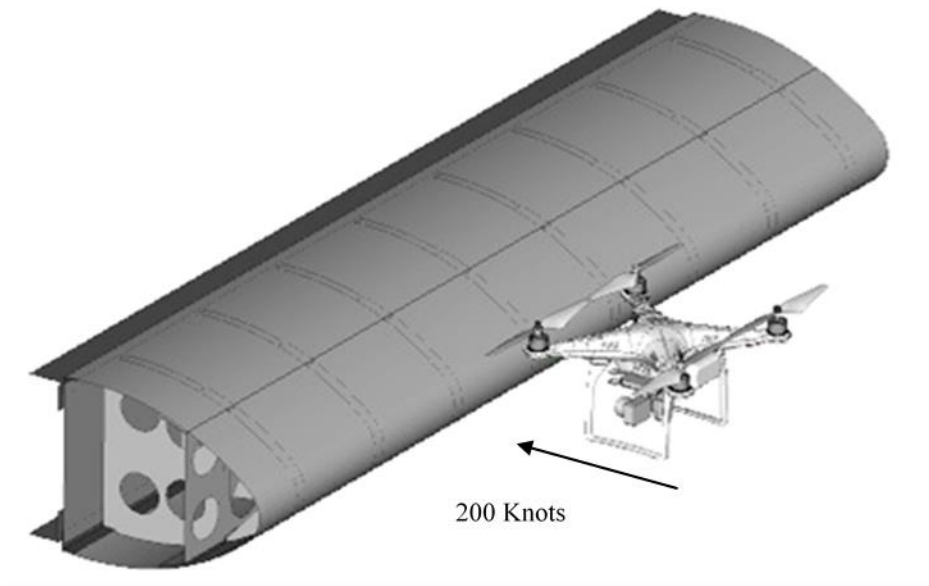


Figure 107. Material sensitivity study FE model set-up

Table 15. LS-DYNA material models compared

Model	LS-DYNA Material Model	Input Data Reference	Temperature Dependence	Strain-Rate Parameters	Triaxiality & Lode Surface	Plasticity*
1	15	DOT/FAA/AR-03/57 [65]	YES	YES	NO	YES
2	224	DOT/FAA/TC-13/25 [66]	YES	YES	YES	YES
3	24	MMPDS-09 [67]	NO	NO	NO	YES*

*Plasticity is represented by tangent modulus not full range curve.

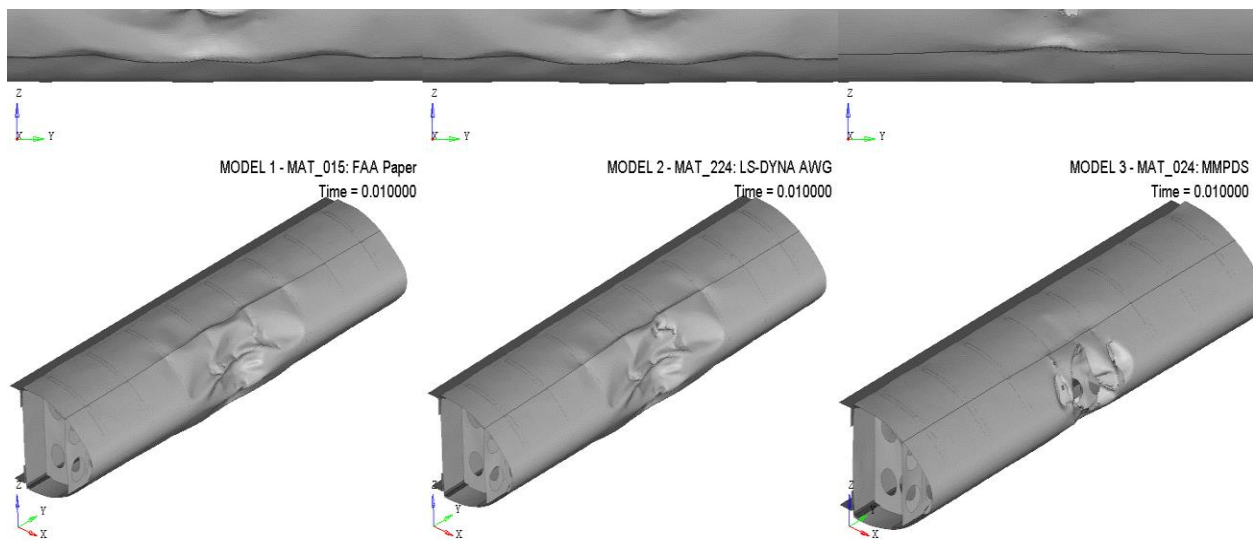


Figure 108. Damage and failure comparison of different LS-DYNA material models on a generic leading edge impacted by a quadcopter UAS model

The evaluation of material modeling at the component level is part of the building block approach. The validation at the component level provides assurance that the target model results are accurate.

3.3.5.2 Material Verification Methodology

Since test data for some structural materials were not available, a conservative approach using material data from the MMPDS were used. The data from MMPDS provided sufficient information to populate the *MAT_024* material card [67]. *MAT_024* is an elastic-plastic material with an option to define an arbitrary stress/strain curve and arbitrary strain rate dependency [27]. For some cases, the full range stress/strain curves were not available in MMPDS and therefore the

materials were modeled as bi-linear elastic plastic where the stress strain behavior was approximated as straight lines using the Young's modulus and tangent modulus as shown in Figure 109.

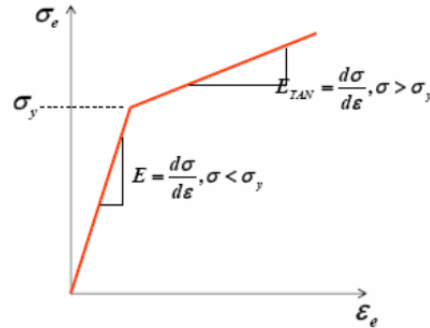


Figure 109. Stress strain curve for bi-linear elastic plastic [68]

The material verification study is performed using a FE model of a test coupon. As an example consider the Aluminum 6061-T6 data shown in Figure 110.

MMPDS-09
1 April 2014

Table 3.6.2.0(g). Design Mechanical and Physical Properties of 6061 Aluminum Alloy Extruded Rod, Bar, and Shapes

Specification	AMS 4161, AMS 4172, & AMS-QQ-A-200/8*	AMS-QQ-A-200/8*	AMS 4160 & AMS-QQ-A-200/8*	AMS 4150, AMS 4173 & AMS-QQ-A-200/8*			
Form	Extruded rod, bar, and shapes						
Temper	T4, T4510, and T4511	T42 ^b	T62 ^b	T6, T6510, and T6511			
Cross-sectional area, in. ²	≤ 32		
Thickness, in.	≤ 3.000	All	All	≥ 0.250	≤ 1.000	1.001-6.500	
Basis	S	S	S	S	A	B	A
Mechanical Properties:							
F_u , ksi:							
L	26	26	38	38	38	41	38
LT	37	40	33
F_y , ksi:							
L	16	12	35	35	35	38	35
LT	33	36	28
$F_{0.2}$, ksi:							
L	14	34	37	34
LT	35	38	30
$F_{0.2}$, ksi:							
L	16	26	28	19
F_{br} , ksi:							
(e D = 1.5)	42	64	69	52
(e D = 2.0)	55	82	88	69
F_{br} , ksi:							
(e D = 1.5)	22	54	58	42
(e D = 2.0)	26	60	65	50
ϵ , percent (S-Basis):							
L	16	16	10*	10	10*	...	10
E , 10 ³ ksi	9.9						
E_c , 10 ³ ksi	10.1						
G , 10 ³ ksi	3.8						
μ	0.33						
Physical Properties:							
α , lb/in. ³	0.098						
C, K, and α	See Figure 3.6.2.0						

Last Revision: Apr 2012, MMPDS-07, Item 11-62.

a Mechanical properties were established under QQ-A-200/8.

b Design allowables were based upon data obtained from testing samples of material, supplied in the O to F temper, which were heat treated to demonstrate response to heat treatment by suppliers. Properties obtained by the user, however, may be lower than those listed if the material has been formed or otherwise cold- or hot-worked, particularly in the annealed temper, prior to solution heat treatment.

c The mechanical properties are to be based upon the thickness at the time of quench.

d Bearing values are "dry pin" values per Section 1.4.7.1.

e For thicknesses ≤ 0.249 inch, $\epsilon = 8\%$.

Figure 110. MMPDS data for Aluminum 6061-T6 [67]

The set-up of the FE model of the coupon is shown in Figure 111. The stress/strain results of the FE analysis of the coupon are compared against the MMPDS data to verify the performance of the material as shown in Figure 112.

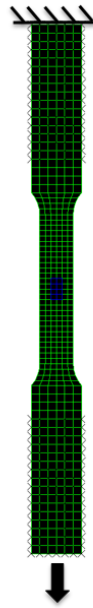


Figure 111. FE model of coupon for material verification

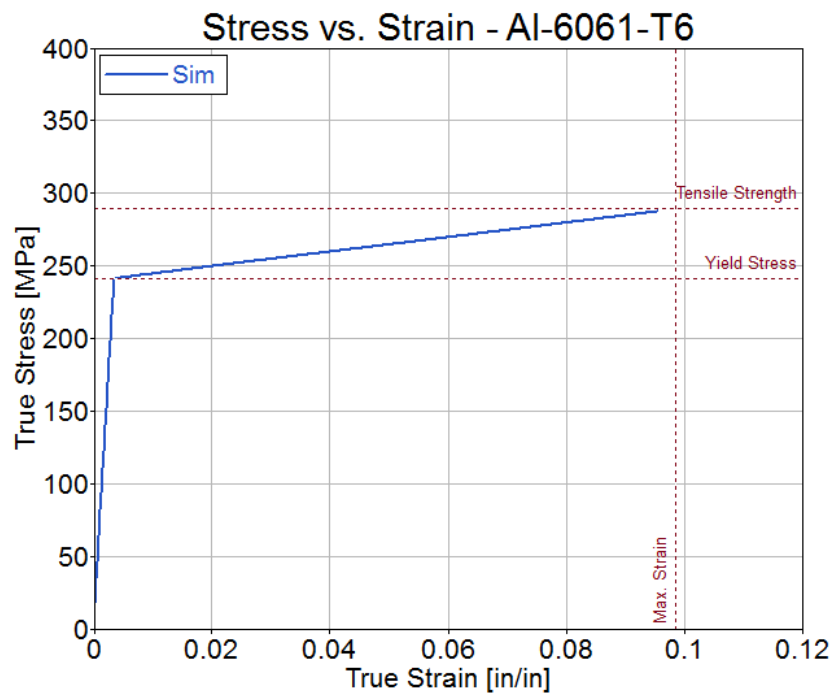


Figure 112. MMPDS Aluminum 6061-T6 material verification

3.3.5.3 Material Definition

This section presents the materials used for the target models. Figure 113 and Figure 114 point out the impact areas of interest for a typical leading edge and windshield model. Table 16 summarizes the materials used for different target components, the LS-DYNA material card used for defining those materials and the source for material input data.

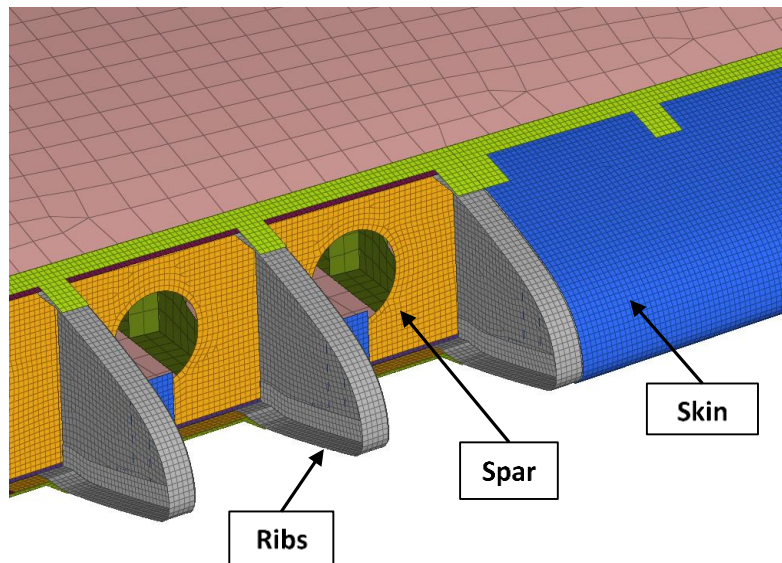


Figure 113. Leading edge impact area

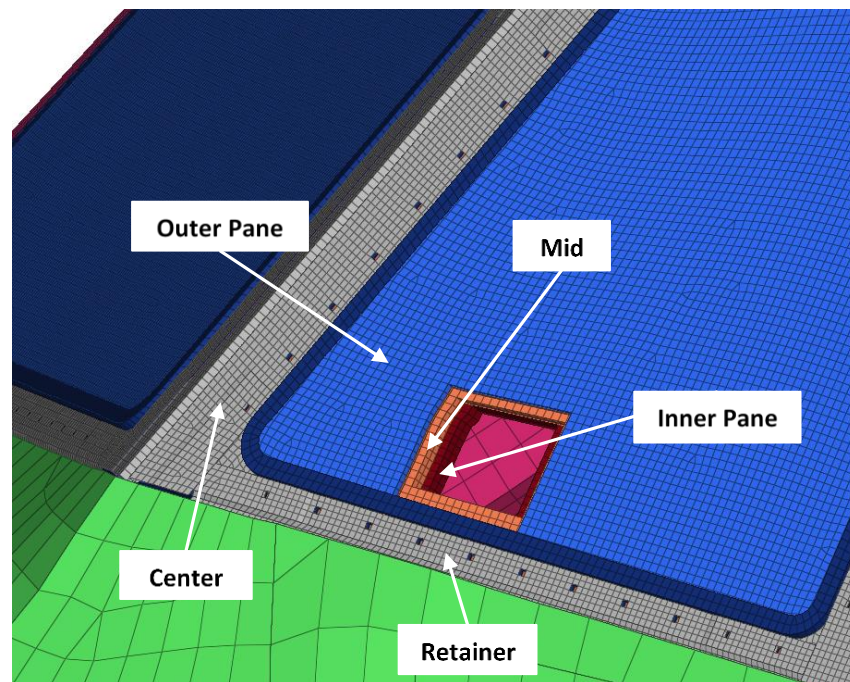


Figure 114. Windshield impact area

Table 16. Airframe materials at impact areas

		Part	Material	LS-DYNA MAT card	Reference
Commercial Transport Jet	Horizontal Stabilizer	Skin	2024-T3 Al	<i>MAT_015</i>	DOT/FAA/AR-03/57 [65]
		Ribs	2024-T42 Clad Al	<i>MAT_024</i>	MMPDS-09 [67]
		Front spar	7075-T6 Al	<i>MAT_024</i>	MMPDS-09 [67]
	Vertical Stabilizer	Skin	2024-T3 Al	<i>MAT_015</i>	DOT/FAA/AR-03/57 [65]
		Ribs	2024-T42 Clad Al	<i>MAT_024</i>	MMPDS-09 [67]
		Front spar	7075-T6 Al	<i>MAT_024</i>	MMPDS-09 [67]
	Wing	Skin	2024-T3 Al	<i>MAT_015</i>	DOT/FAA/AR-03/57 [65]
		Ribs	7050-T7451 Al	<i>MAT_024</i>	MMPDS-09 [67]
		Front spar	7050-T7451 Al	<i>MAT_024</i>	MMPDS-09 [67]
	Front Section	Outer pane	PMMA	<i>MAT_024</i>	Hidallana-Gamage [70]
		Mid layer	PVB	<i>MAT_024</i>	Wang. [69]
		Inner pane	MIL-PRF-25690	<i>MAT_124</i>	MIL-HDBK-17A [71]
		Center post	7050-T7452 Al	<i>MAT_024</i>	MMPDS-09 [67]
		Retainer	7075-T6 Al	<i>MAT_024</i>	MMPDS-09 [67]

Business Jet	Horizontal Stabilizer	Skin	2024-T3 Al	<i>MAT_015</i>	DOT/FAA/AR-03/57 [65]
		Ribs	2024-T42 Clad Al	<i>MAT_024</i>	MMPDS-09 [67]
		Front spar	2024-T3 Clad Al	<i>MAT_024</i>	MMPDS-09 [67]
	Vertical Stabilizer	Skin	2024-T3 Al	<i>MAT_015</i>	DOT/FAA/AR-03/57 [65]
		Ribs	2024-T3 Al	<i>MAT_024</i>	MMPDS-09 [67]
		Front spar	2024-T3 Al	<i>MAT_024</i>	MMPDS-09 [67]
	Wing	Skin	2024-T3 Al	<i>MAT_015</i>	DOT/FAA/AR-03/57 [65]
		Ribs	2024-T3 Al	<i>MAT_015</i>	DOT/FAA/AR-03/57 [65]
		Front spar	2024-T3 Al	<i>MAT_015</i>	DOT/FAA/AR-03/57 [65]
	Front Section	Outer pane	MIL-PRF-25690	<i>MAT_124</i>	MIL-HDBK-17A [71]
		Mid layer	MIL-PRF-5425	<i>MAT_124</i>	MIL-HDBK-17A [71]
		Inner pane	MIL-PRF-25690	<i>MAT_124</i>	MIL-HDBK-17A [71]
		Center post	2024-T3511 Al	<i>MAT_024</i>	MMPDS-09 [67]
		Retainer	2024-T3 Al	<i>MAT_024</i>	MMPDS-09 [67]

Figure 115 and Figure 116 illustrate the materials that conform the different components of the commercial transport and business jets respectively.

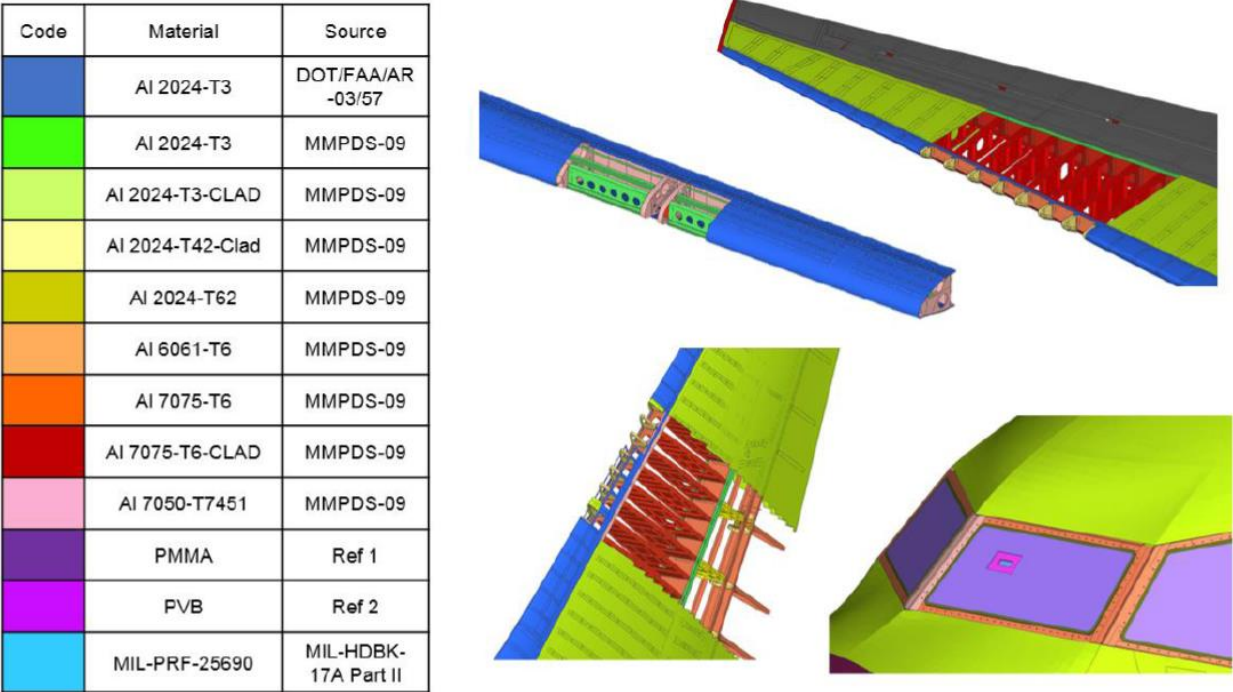


Figure 115. Commercial transport jet airframe materials of the subassemblies subject to study.

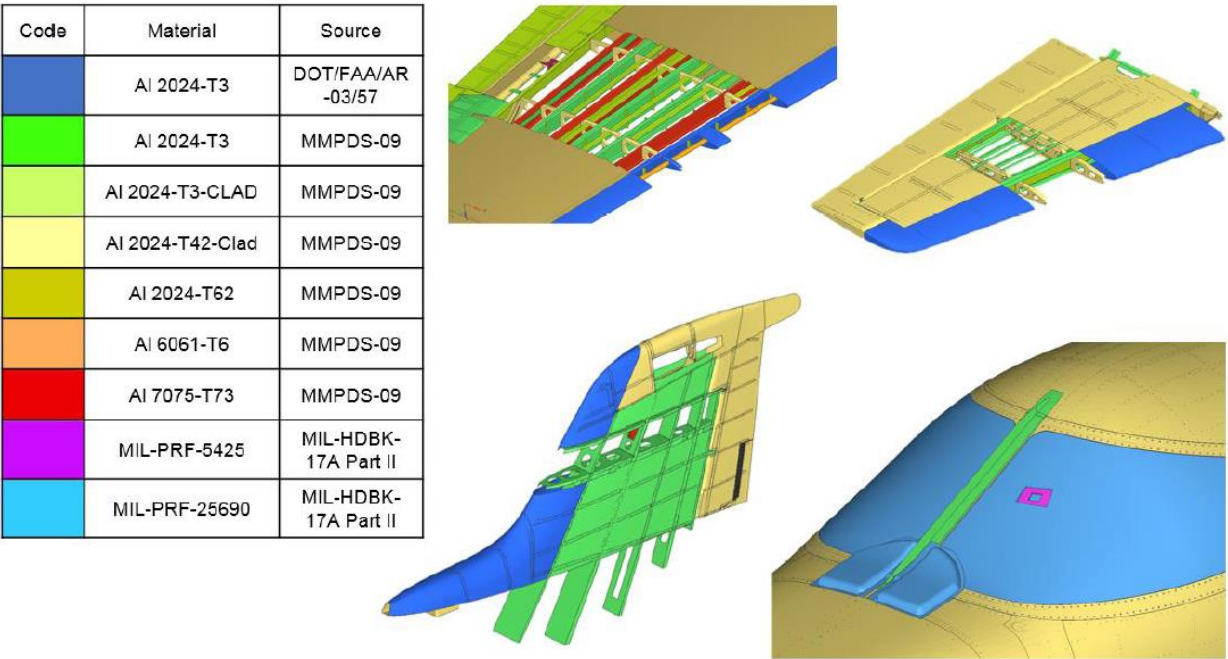


Figure 116. Business jet airframe materials of the subassemblies subject to study.

Similarly, Figure 117 and Figure 118 illustrate gage thicknesses of the metallic parts in the different subassemblies being studied for both commercial and business jets respectively.

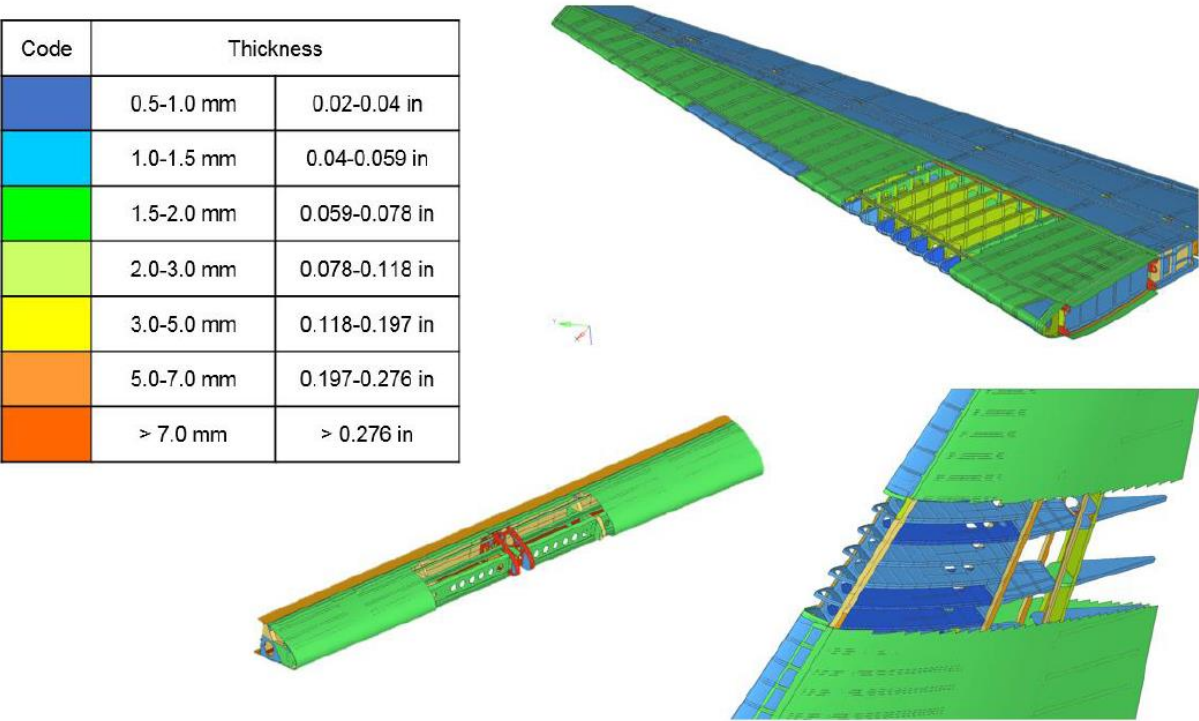


Figure 117. Commercial transport jet airframe gage thicknesses of metallic components.

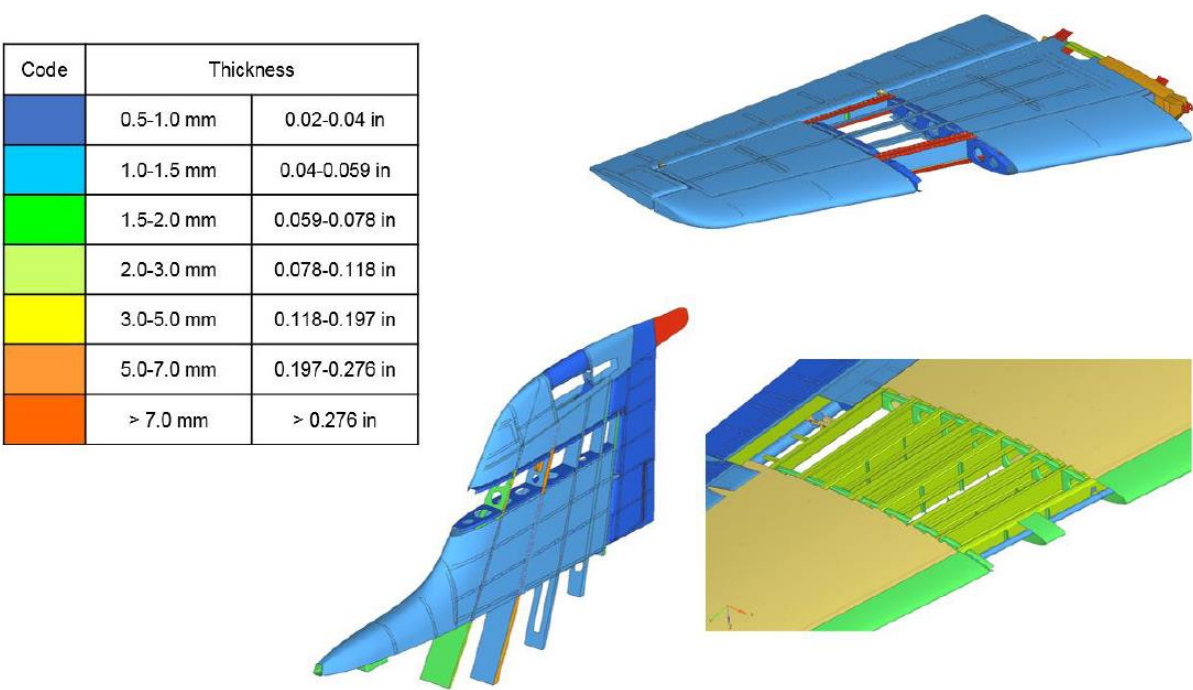


Figure 118. Business jet airframe gage thicknesses of metallic components subject to study.

3.3.5.4 Material Model Limitations

The selection of the material card for the different components was made based on the experimental data available and the sensitivity analysis conducted. In general, *MAT_024* provides conservative results due to its limitations. Some of these limitations are:

- Stress failure in the material card is defined for uniaxial tension conditions. Shear, compression or mixed stress states will also fail at the same uniaxial tension value leading to more conservative results.
- Input data coming from MMPDS-09 [67] contains material properties for quasi-static conditions. The results subjected to these values led to a conservative approach from a failure perspective. Note that this is not a limitation of the material card itself, but a simplification in the procedure of obtaining the data with lack of rate-dependency.

The limitations presented above supported the decision of applying *MAT_015* where the impact area properties allowed it, reducing the conservatism of the target model and providing results that are more realistic.

3.3.6 Contacts

For the general assembly of all target models, the **CONTACT_AUTOMATIC_SINGLE_SURFACE* contact card was used. **CONTACT_SPOTWELD* was also used to capture the contact between the spot-weld elements and the remaining 2D and 3D target elements.

4. UAS – COLLISION ANALYSIS

Once the FE models of both UASs and the commercial transport and business jets were completed, a series of impact scenarios were set up by NIAR with the objective of characterizing the dynamic event of a midair collision.

This chapter provides, first, a justification of the impact boundary conditions (velocity, UAS impact locations, etc.) selected for these baseline simulations. Second, a classification of the different levels of aircraft damage severity is presented. Subsequently, the baseline (worst-case) simulations for both commercial transport and business jets, are described and summarized. All supplementary simulation results are available in APPENDIX C. Finally, conclusions are reached on whether a midair collision with a 1.8 kg (4.0 lb) fixed-wing UAS is severe and the damage levels are presented.

The simulations presented in this chapter established a baseline to select the worst case scenarios to be used in further studies as reference for comparison of different parameters (mass, velocity) or situations (bird strike), presented in Chapters 5. and 6.

4.1 SELECTION OF IMPACT CONDITIONS

4.1.1 Impact Velocity

FAA General Operating and Flight Rules (*14 CFR Part 91*) [72] airworthiness requirements set the limits of operating speeds at different altitudes. The requirements are as follows:

- *91.817*: Mach 1 over land (with a few exceptions that are noted in Appendix B to 91.817)
- *91.117(a)*: 250 KIAS below 10,000 ft MSL
- *91.117(b)*: 200 KIAS below 2,500 ft within 4NM of the primary airport for Class C and D airspace (unless within Class B airspace)
- *91.117(c)*: 200 KIAS under the shelf of Class B airspace
- *91.117(c)*: 200 KIAS in a VFR corridor through Class B airspace

The Aeronautical Information Manual paragraph *5-7-2-j.2(b)* indicates the following holding speeds:

- 200 KIAS below 6,000 ft.
- 230 KIAS from 6,001 to 14,000 ft.
- 265 KIAS above 14,000 ft.

It was assumed that the most probable high velocity impact scenario was either at landing/take-off or at holding flight phase. Consequently, the holding speed was selected as the baseline velocity for the aircraft: a maximum of 200 KIAS, as defined in *14 CFR Part 91.117(b)*, which at 2,500 ft is equivalent to approximately 208 knots (107 m/s) true airspeed (TAS). Figure 119 presents a schematic of the NAS classifications from the FAA.

The specifications of the fixed-wing UAS selected for this study, see section 2.1 , provide the maximum velocity (19.5 m/s, 38 knots) and service ceiling (4,000 m, 13,120 ft).

Therefore, to account for the relative velocities of a frontal impact (plus a small margin), a velocity of 128.6 m/s (250 knots) was selected as the baseline for the study presented in this chapter. A broader range of velocities, from minimum landing to cruise speed, was investigated in a parametric study that is presented in Chapter 5.

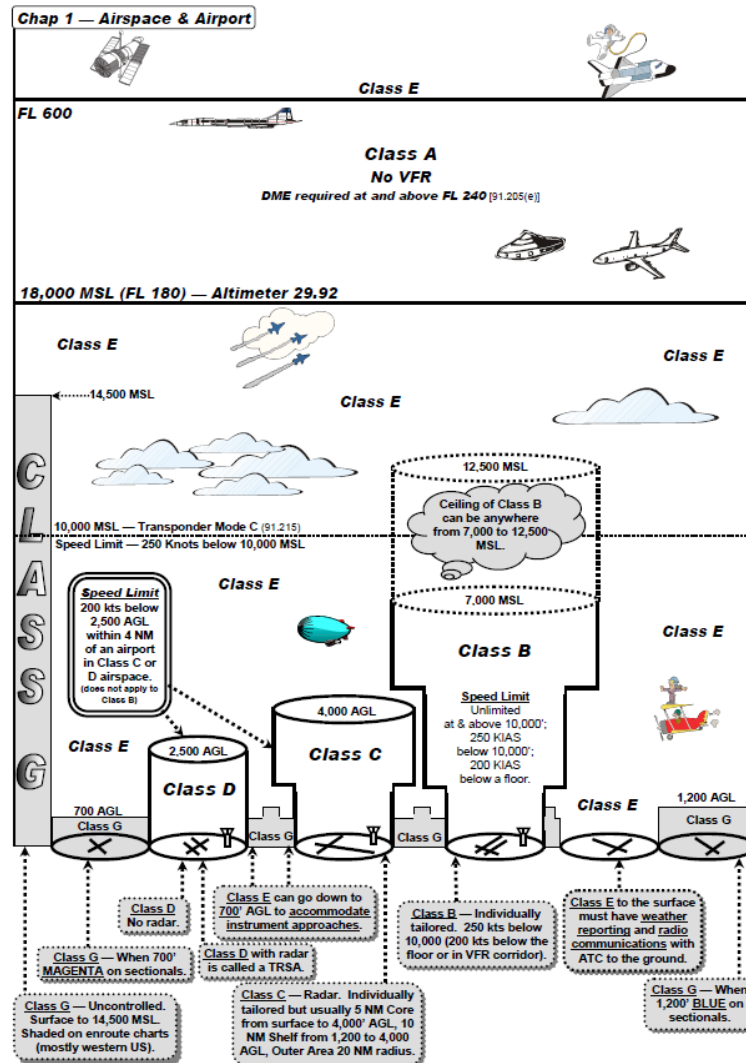


Figure 119. National Airspace System classifications [73]

4.1.2 Impact Conditions

In preliminary simulations, it was observed that small variations in the vertical or horizontal position of the UAS with respect to the aircraft or in the angle of impact significantly altered the levels of damage after impact. Consequently, boundary and initial conditions were of extreme importance for simulating midair collision events. Fortunately, FE simulation possesses a great advantage over physical testing, allowing full control over the boundary and initial conditions of the simulation.

In contrast, physical testing would require multiple and costly repetitions to arrive at the worst-case scenario.

Accordingly, a parametric study was completed with the objective of identifying the most critical local impact conditions to reduce the number of simulations to be run for each of the impacted aircraft subassemblies. To achieve this, the UAS FE model was impacted into a wing leading edge FE model, developed and validated through simulation and testing by the NIAR in a previous project for bird strike [41]. The leading edge assembly was constructed from 2024-T3 aluminum alloy with a skin thickness of 1.22 mm. Several parameters were investigated, which are presented in the following sections. The criteria to select the worst case were based on the amount of damage introduced into the structure. Note that the UAS model used in this study is a quadcopter configuration, discussed in [2], which was used to correlate damage severity to impact location. This trend is a function of the aircraft structure's receptiveness to damage and is therefore applicable to the fixed-wing UAS.

4.1.2.1 Impact Location

To determine the influence of the impact location along the leading edge, two sets of impact locations were defined. Three centered impact locations were selected along the horizontal direction as it shown on the top of Figure 120. These locations were positioned in front of a nose rib (front rib), at a $\frac{1}{4}$ rib-to-rib distance from the center of the nose rib, and in the middle location between two nose ribs. The second set had the aim of investigating the impact severity of three different vertical positions, which were vertically aligned with the mid-bay centered position.

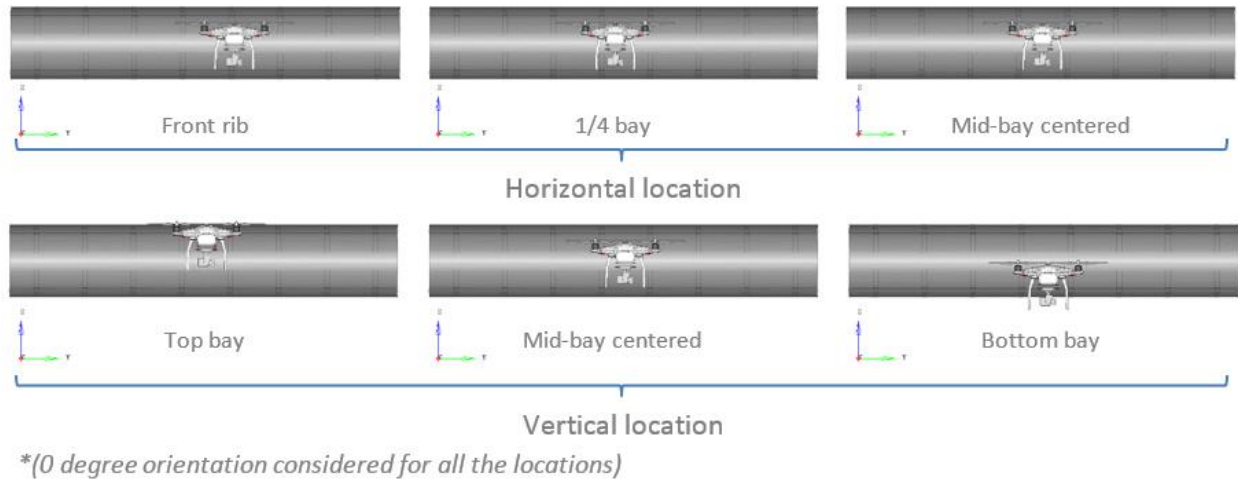


Figure 120. UAS impact location parametric study setup

Figure 121 presents the kinematics for the two sets of impact locations studied. The bottom center image shows the centered case, the left and right images show the upper and lower vertical impact, respectively, and the top image shows a direct impact to the rib.

It was observed that when impacting close to the rib, most of the internal energy was absorbed by the UAS, and the target structure mostly received damage to the rib and little penetration into the airframe. In contrast, when the impact was centered between ribs, the skin of the airfoil absorbed

most of the internal energy. In this case, the UAS perforated the skin and penetrated into the airframe severely damaging the spar. Similarly, the vertical sensitivity study indicated that whenever the UAS impacted off-center with respect to the leading edge, a considerable part of the UAS was deflected, as it is illustrated in both bottom left and right images of Figure 121. It was concluded that the highest level of damage occurred when the UAS center of gravity (CG) was aligned with the leading edge of the airfoil and the UAS impacted at the center between two ribs.

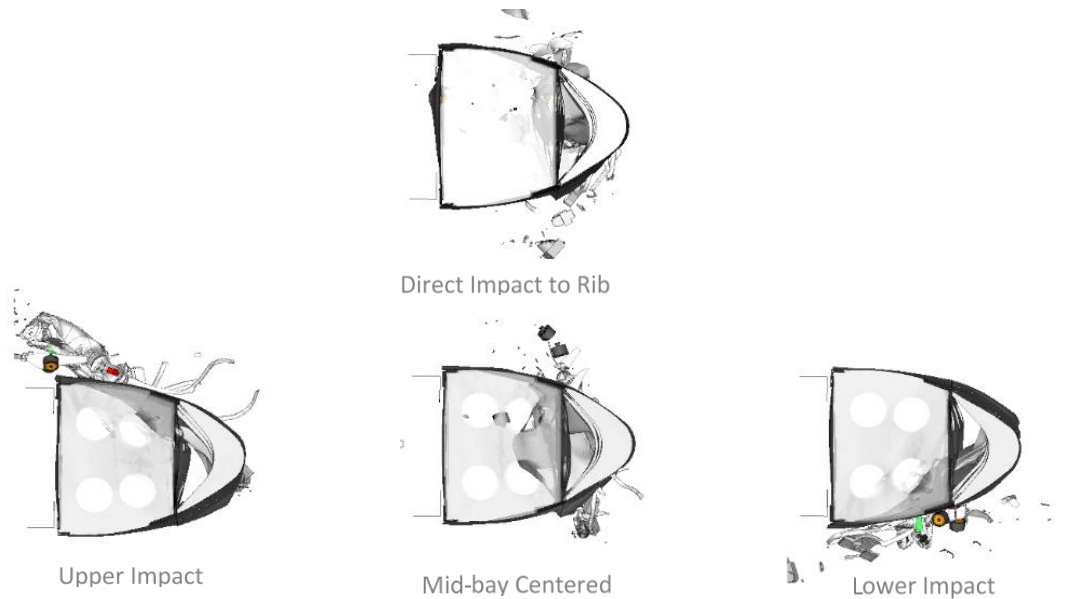


Figure 121. Kinematics of an UAS collision for impact location parametric study at 128.6 m/s

4.1.2.2 Conclusions of Parametric Study

The results of all the iterations for both parametric studies (location and orientation) are presented in [2] for the quadcopter UAS. Damage was assessed based on the integrity of the inner structure after the collision as well as considering if the UAS penetrated into the airframe.

Based on the results obtained in the two parametric studies, a head-on impact of a fixed-wing UAS between the two closest ribs of the target with the CG aligned with the leading edge of the target was chosen as the most severe impact condition. It was consequently selected as baseline for the initial conditions of the collision study against the leading edges of the commercial and business jet targets.

This study also highlighted the extreme importance of defining initial conditions that lead to the worst case levels of damage. Small deviations in the impact location might underpredict the severity of the event.

4.1.3 Load Case Name Convention

In order to provide a brief label that accurately describes each combination of UAS, aircraft type, target component, and local impact position the following convention is used to name each load case presented in this chapter:

Every impact condition will be coded using four characters (ABCD):

- A – Distinguishes between Commercial (C) and Business Jet Airplanes (B)
- B – Distinguishes between UAS Type:
 - 2.7 lb. Quadcopter (Q)
 - 4.0 lb. Fixed-Wing (F)
- C – Distinguishes between impact area:
 - Vertical Stabilizer (V)
 - Horizontal Stabilizer (H)
 - Wing (W)
 - Cockpit Windshield (C)
- D – Distinguishes between impact location (1 through 5)

Example CFV4

- Commercial
- Fixed-Wing
- Vertical Stabilizer
- Impact Location #4

4.1.4 Simulation Matrix

Table 17 and Table 18 present the full simulation matrix performed for this chapter of the project.

Table 17. Simulation matrix of commercial transport jet airborne collision

Commercial Transport Jet															
Vertical Stabilizer				Horizontal Stabilizer					Wing				Windshield		
CFV1	CFV2	CFV3	CFV4	CFH1	CFH2	CFH3	CFH4	CFH5	CFW1	CFW2	CFW3	CFW4	CFC1	CFC2	CFC3

Table 18. Simulation matrix of business jet airborne collision

Business Jet											
Vertical Stabilizer			Horizontal Stabilizer			Wing			Windshield		
BFV1	BFV2	BFV3	BFH1	BFH2	BFH3	BFW1	BFW2	BFW3	BFC1	BFC2	BFC3

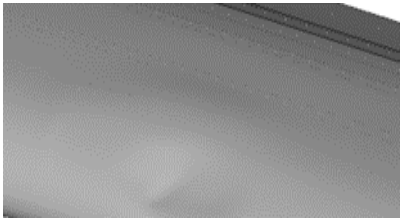
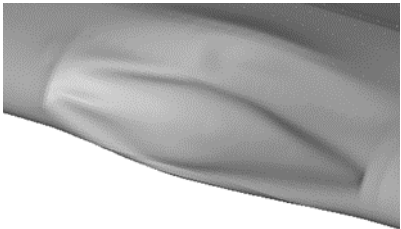
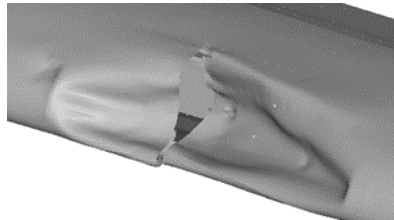
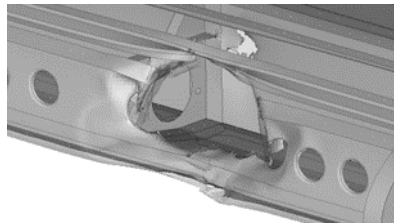
4.2 DAMAGE CATEGORY DEFINITION

4.2.1 Damage Levels

Over 70 impact scenarios were analyzed as part of this study. In order to categorize the results of each scenario relative to one another, a set of criteria were defined as shown in Table 19.

The lowest damage category, Level 1, generally corresponds to a minimal amount of localized damage. The next category, Level 2, represents significant visible damage to the external surface of the aircraft with some internal component damage but with no appreciable skin rupture. The third category, Level 3, describes impact events where the outer surface of the aircraft is compromised in a way that could allow ingress of foreign objects into the airframe, with some damage to substructure. Finally, Level 4 indicates damage that includes all of the preceding aspects as well as extensive damage to internal components and possibly compromising the primary structure.

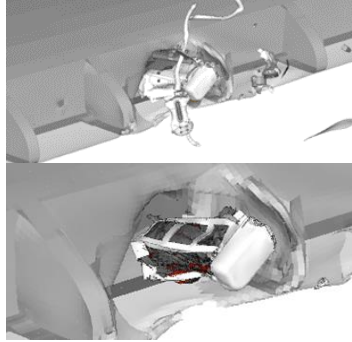
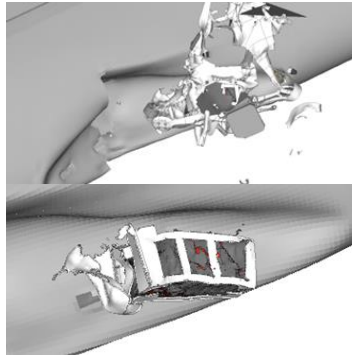
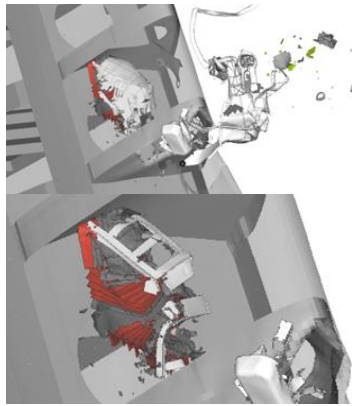
Table 19. Damage level categories

Severity	Description	Example
Level 1	<ul style="list-style-type: none">• Airframe undamaged.• Small deformations.	
Level 2	<ul style="list-style-type: none">• Extensive permanent deformation on external surfaces.• Some deformation in internal structure.• No failure of skin.	
Level 3	<ul style="list-style-type: none">• Skin fracture.• Penetration of at least one component into the airframe.	
Level 4	<ul style="list-style-type: none">• Penetration of UAS into airframe.• Failure of primary structure.	

4.2.2 Fire Risk

The risk of fire associated with damaged LiPo batteries was addressed for each simulation based on the trends observed during component level ballistic testing [2], and the particular kinematics of a given impact scenario. Table 20 presents the criteria used in this study.

Table 20. Risk of battery fire

Fire Risk	Description	Example
Yes	<ul style="list-style-type: none"> UAS (including the battery) penetrates the airframe. Battery deforms but stays undamaged. Verification tests showed that partly damaged batteries created heat and sparks. 	
No	<ul style="list-style-type: none"> The UAS does not penetrate the airframe. 	
No	<ul style="list-style-type: none"> UAS (including the battery) penetrates the airframe. The battery sustains great damage, destroying its cells. Verification tests showed that completely damaged batteries did not create heat and sparks. 	

Note that the label of “Fire Risk” indicates a potential outcome rather than an impending event due to the qualitative nature of the assessment. Further studies and physical testing into this phenomenon would be required in order to determine any additional severity. During preliminary component level testing, the fire risk appeared inversely proportional to impact velocity. Higher velocities caused the battery to disintegrate, reducing the heat generated after impact, while lower

velocities allowed the battery pack to remain consolidated, increasing the post-impact heat generation.

4.3 COMMERCIAL TRANSPORT JET AIRBORNE COLLISION STUDIES

As introduced in section 3.1.3, the target areas for impact on the NIAR commercial transport jet are vertical stabilizer (section 4.3.1), horizontal stabilizer (section 4.3.2), wing leading edge (section 4.3.3), and windshield (section 4.3.4). This section presents the results of explicit dynamic simulations of impacts of the 1.8 kg (4.0 lb) fixed-wing UAS into the commercial transport jet. Table 21 and Figure 122 summarize the results of the collision studies on the commercial transport jet. This section will describe in detail the results in each of the four subassemblies.

Table 21. Commercial transport jet airborne collision simulation – Severity levels and fire risk

Case	Commercial Transport Jet															
	Vertical Stabilizer				Horizontal Stabilizer					Wing				Windshield		
	CFV1	CFV2	CFV3	CFV4	CFH1	CFH2	CFH3	CFH4	CFH5	CFW1	CFW2	CFW3	CFW4	CFC1	CFC2	CFC3
Severity	Level 4	Level 3	Level 4	Level 4	Level 4	Level 4	Level 4	Level 4	Level 4	Level 3	Level 3	Level 3	Level 3	Level 2	Level 2	Level 2
Fire Risk	No	No	No	No	No	No	No	No	No	No	No	No	No	No	No	No

As shown in Figure 122, for each one of the impact conditions we can quantify how the initial kinetic energy of the UAS prior to impact is transformed into aircraft and UAS internal energies through the structural deformations introduced during impact, a residual UAS kinetic energy that is a function of the UAS post-impact debris mass moving at a post-impact residual velocity, friction energy which is a function of the sliding contact energy between the UAS and the aircraft structure, and eroded energy from the mass of the UAS and aircraft eroded elements used to increase the stability of the calculation.

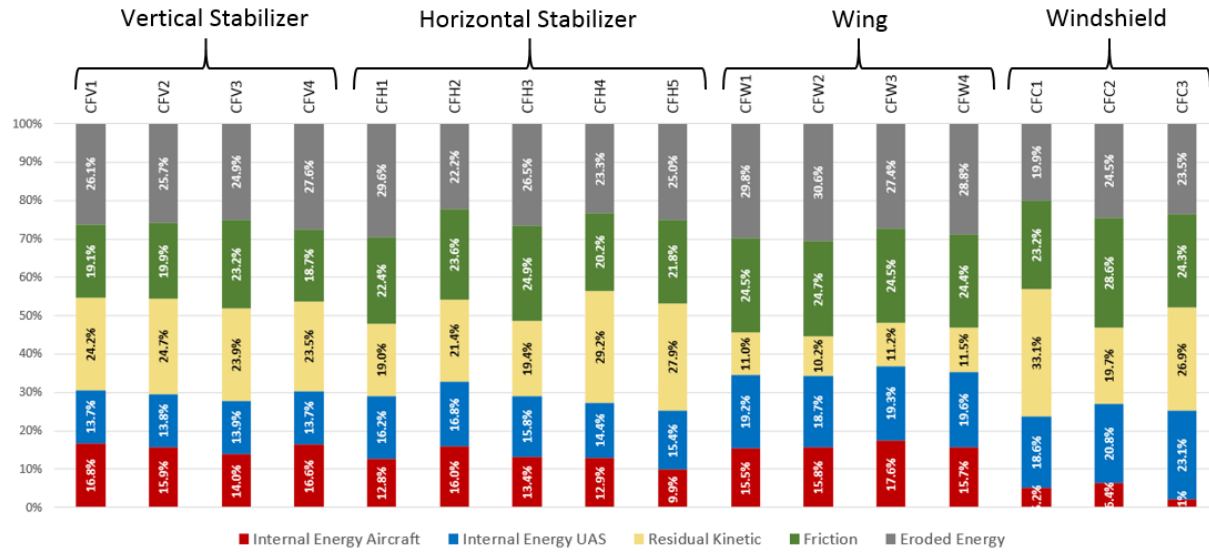


Figure 122. Commercial transport jet airborne collision simulation – Energy summary

4.3.1 Vertical Stabilizer

The vertical stabilizer of the commercial transport jet was subjected to impact at four different locations that were selected based on the criteria described in Section 4.1.2 . The diagram in Figure 123 illustrates the positions being impacted and the naming assigned to each of the cases. The UAS was assigned an initial speed of 128.6 m/s (250 knots) in the local x -axis of the aircraft. Fixed boundary conditions of the vertical stabilizer were considered at the root of both front and rear spars.

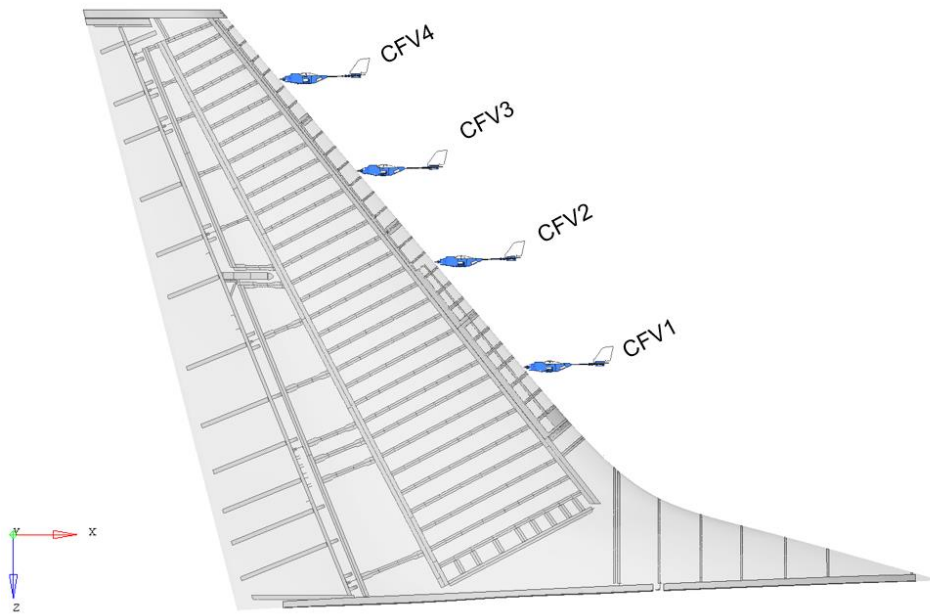


Figure 123. UAS impact locations – Commercial jet vertical stabilizer

4.3.1.1 Summary of Results – Commercial Transport Jet Vertical Stabilizer

A summary of the results for all four cases is presented in Figure 124. For each case, the left bar represents a summation of all the different energies involved in the impact event, measured at 15 ms after initial contact and normalized with the total energy at time zero. The percentage of the total energy for the each respective type of energy is shown. The right bar specifies the severity level (1-4), as described in section 4.2.1 .

Consistent levels of damage were observed for each impact target component (Figure 124) indicating that the impact behavior of the UAS for a given target structure was generally not affected by local features in the structure. The energy level of the impact was such that localized discrepancies did not significantly increase or decrease the overall damage level. It is worth noting that none of the cases showed situations where the battery penetrated the airframe, and therefore none of them can be considered with potential risk for fire.

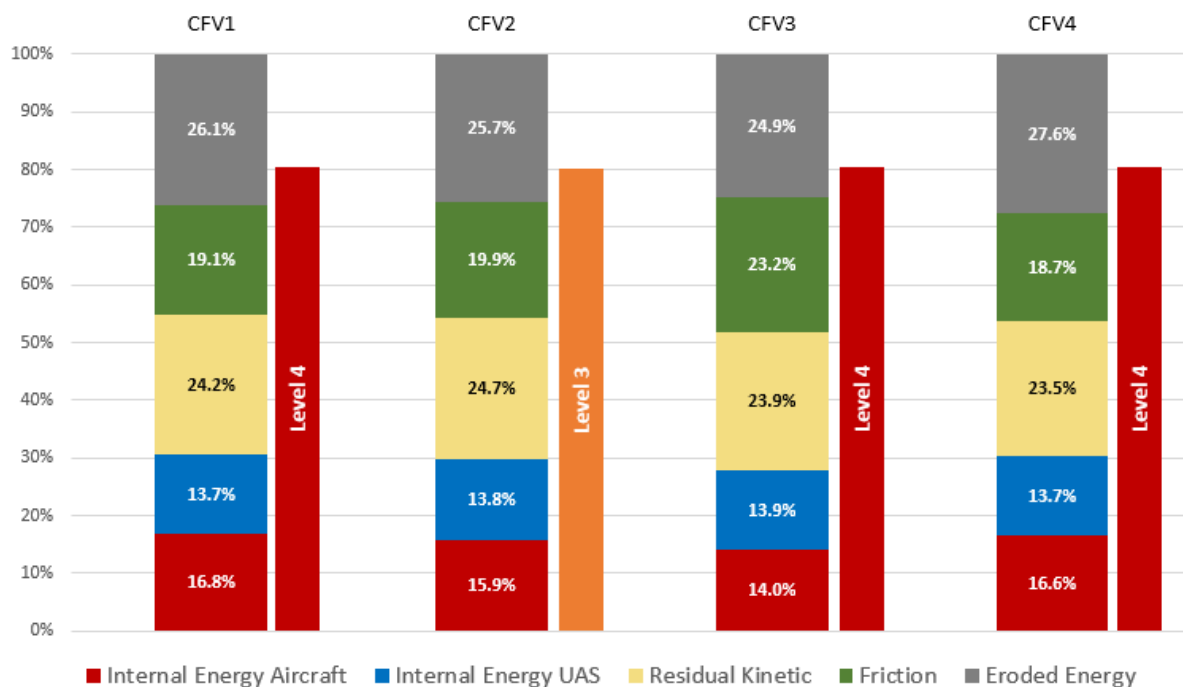


Figure 124. Energy distribution for commercial transport jet vertical stabilizer cases

The nose rib pitch commercial transport jet varies along the span, leaving the spar more exposed to a direct hit of the UAS if it penetrates the skin. For inner locations of the span, the rib pitch is small enough so that the web of the rib can interfere with the trajectory of the UAS and therefore protect the front spar. Moreover, the distance between the leading edge and the front spar is greater closer to the root. This allows a greater deformation of the skin, which is translated into a greater amount of internal energy being absorbed. This decelerates the UAS more than at outboard locations prior to impact with the front spar. Additionally, it was observed that the severity of the impact caused the battery to be fully destroyed in every case, minimizing the potential for fire risk.

4.3.1.2 Critical Case – CFV1

The UAS was impacted against the vertical stabilizer at 128.6 m/s (250 knots) along the local x -axis direction of the aircraft. The impact location selected was at approximately 40% of the vertical stabilizer span, with the CG of the UAS aligned with the leading edge, at the midpoint between ribs 6 and 7. Figure 125 depicts the kinematics of the event. Figure 126 shows the damage caused to the skin and inner structure of the vertical stabilizer.

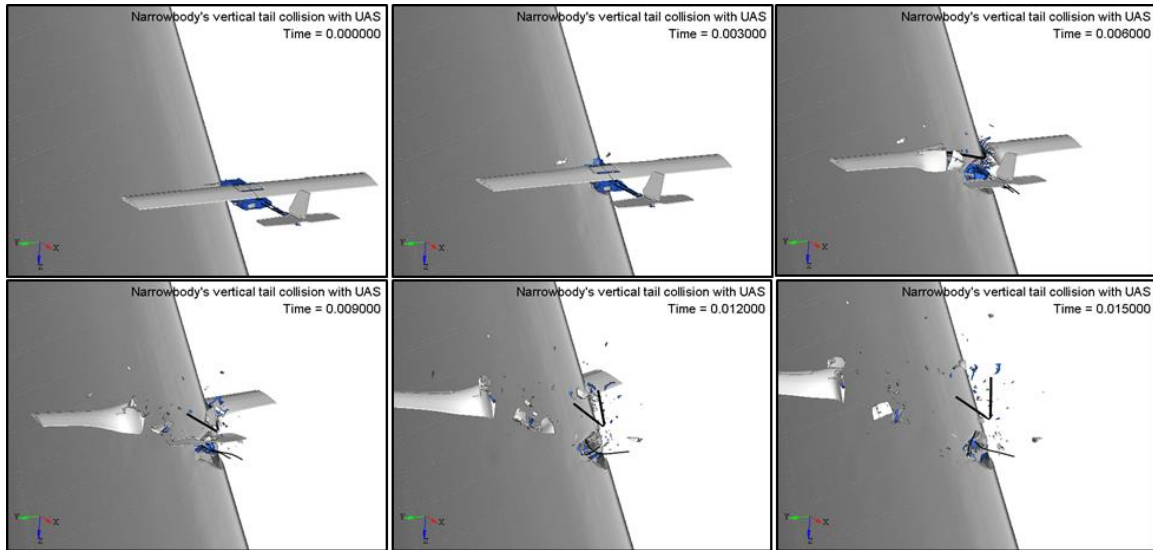


Figure 125. Kinematics of the impact between a commercial transport jet vertical stabilizer and a 1.8 kg (4.0 lb) UAS at location 1 at 128.6 m/s (250 knots)

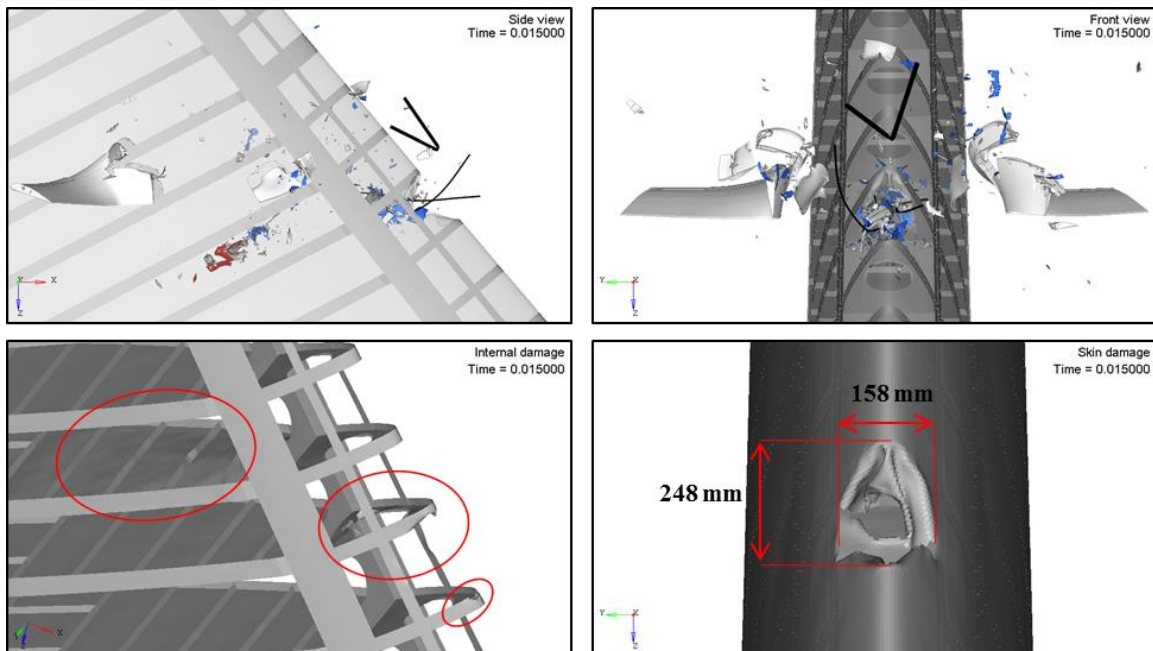


Figure 126. External/internal damage sustained by a commercial transport jet vertical stabilizer impacted at location 1 with a 1.8 kg (4.0 lb) UAS at 128.6 m/s (250 knots)

The UAS damaged the skin and the upper and lower ribs, creating a 158 x 248 mm² damage zone (*i.e.*, puncture, large scale petaling, and inelastic deformation) on the skin surface and allowing some fragments of UAS components to penetrate into airframe. The permanent deformation in the ribs can be perceived in the bottom left image of Figure 126. The front spar did not sustain any visible damage. The damage introduced by the UAS involved penetration of the skin but no damage to the front spar, and consequently the severity was classified as Level 3.

Figure 127 shows the impulse due to the contact force between UAS and vertical stabilizer, as well as the energy balance for both of them. Figure 128 shows the internal energies of UAS and vertical stabilizer parts directly involved in the impact.

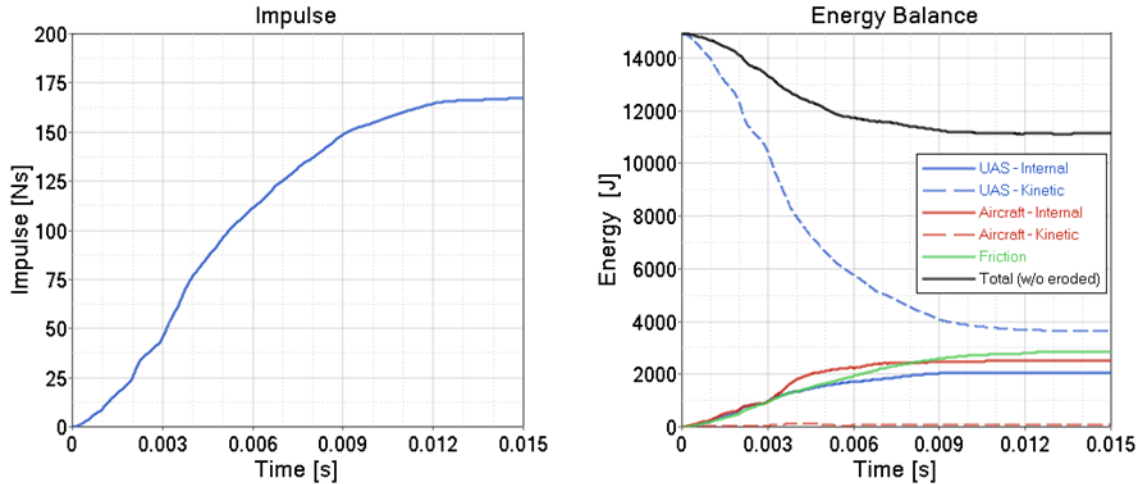


Figure 127. Impulse and energy balance of the impact between a commercial transport jet vertical stabilizer and a 1.8 kg (4.0 lb) fixed-wing UAS at location 1 at 128.6 m/s (250 knots)

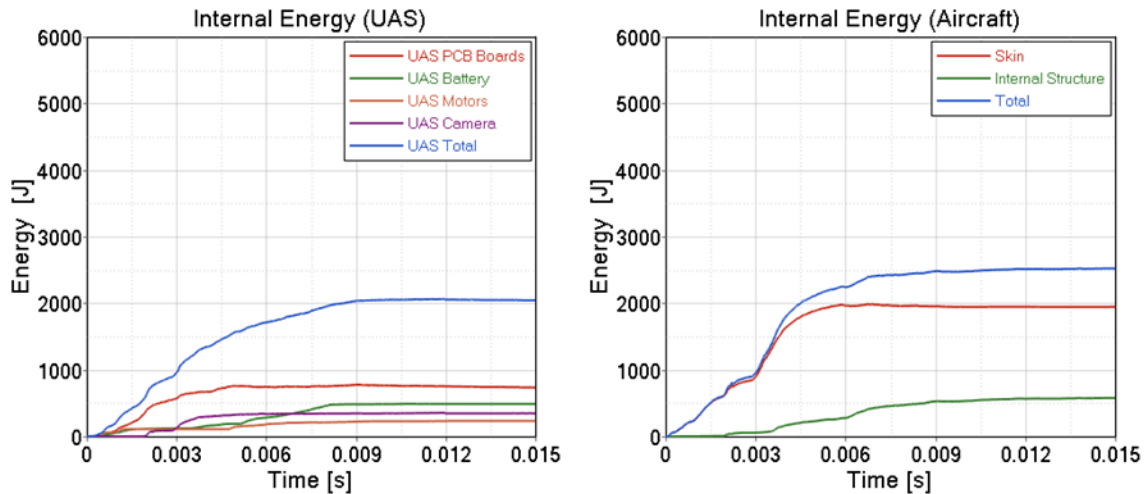


Figure 128. Internal energy per component of the impact between a commercial transport jet vertical stabilizer and a 1.8 kg (4.0 lb) fixed-wing UAS at location 1 at 128.6 m/s (250 knots)

The energy balance plot includes the UAS and vertical stabilizer kinetic and internal energies as well as frictional energy and total energy for the event. The vertical stabilizer and the UAS absorbed 17% and 14% of the impact energy respectively. The energy dissipated by friction reached 19% of the total energy. In Figure 128, internal energies for the UAS parts and the vertical stabilizer show that the UAS PCBs (being all the structural components constructed with PCB) and skin of the vertical stabilizer absorb the highest amount of internal energies.

4.3.2 Horizontal Stabilizer

The commercial transport jet horizontal stabilizer was subjected to impact at five impact locations that were selected based on the criteria described in section 4.1.2. The diagram in Figure 129 illustrates the impact locations and the naming assigned to each of the cases. The initial velocity assigned to the UAS was 128.6 m/s (250 knots) along the local x -axis of the aircraft. Fixed boundary conditions were considered at the root of both front and rear spars of the horizontal stabilizer.

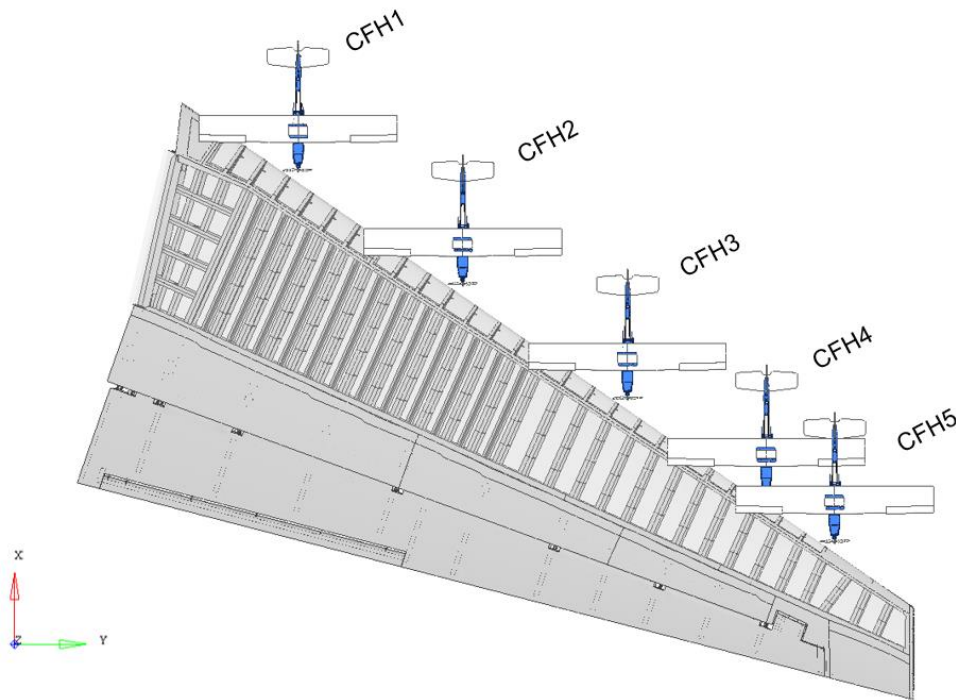


Figure 129. UAS impact locations – Commercial jet horizontal stabilizer

4.3.2.1 Summary of Results – Commercial Transport Jet Horizontal Stabilizer

A summary of the results of all five impact locations presented in Figure 129 is shown in Figure 130. Again, the left bar represents a summation of all the different energies involved in the impact event, measured at 15 ms after impact and normalized with the total energy at time zero. Each block indicates the percentage of total energy for each respective type of energy. The right bar specifies the severity level (1-4).

Consistent levels of damage for each impact target component were observed (Figure 130) indicating that the impact behavior of the UAS for a given target structure was generally not affected

by local features in the structure. The energy level of the impact was such that localized discrepancies did not significantly increase or decrease the overall damage level. It is worth noting that none of the cases showed situations where the battery penetrated the airframe, and therefore none of them showed potential risk for fire.

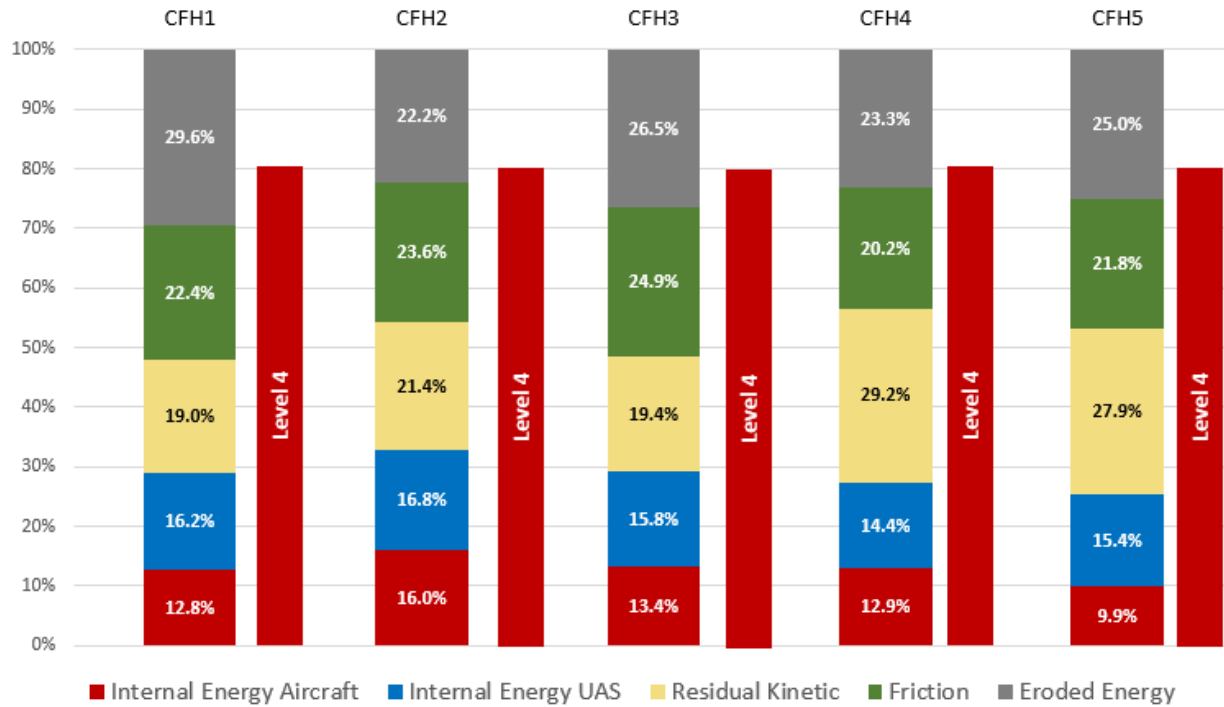


Figure 130. Energy distribution for commercial transport jet horizontal stabilizer cases

4.3.2.2 Critical Case – CFH2

As introduced in section 4.3.2.1 , CFH2 was considered the most critical damaging case for the horizontal stabilizer. The following section presents the results of this specific simulation. The results of the remaining cases may be found in APPENDIX C.

In this case, the UAS was impacted against the horizontal stabilizer at 128.6 m/s (250 knots) along the local x -axis direction of the aircraft. The impact location selected was at approximately 40% of the horizontal stabilizer semispan, with the CG of the UAS aligned with the leading edge, at the midpoint between ribs 12 and 13. Figure 131 presents the kinematics of the event. Figure 132 shows the damage caused to the skin and internal structure (ribs and spar) of the horizontal stabilizer.

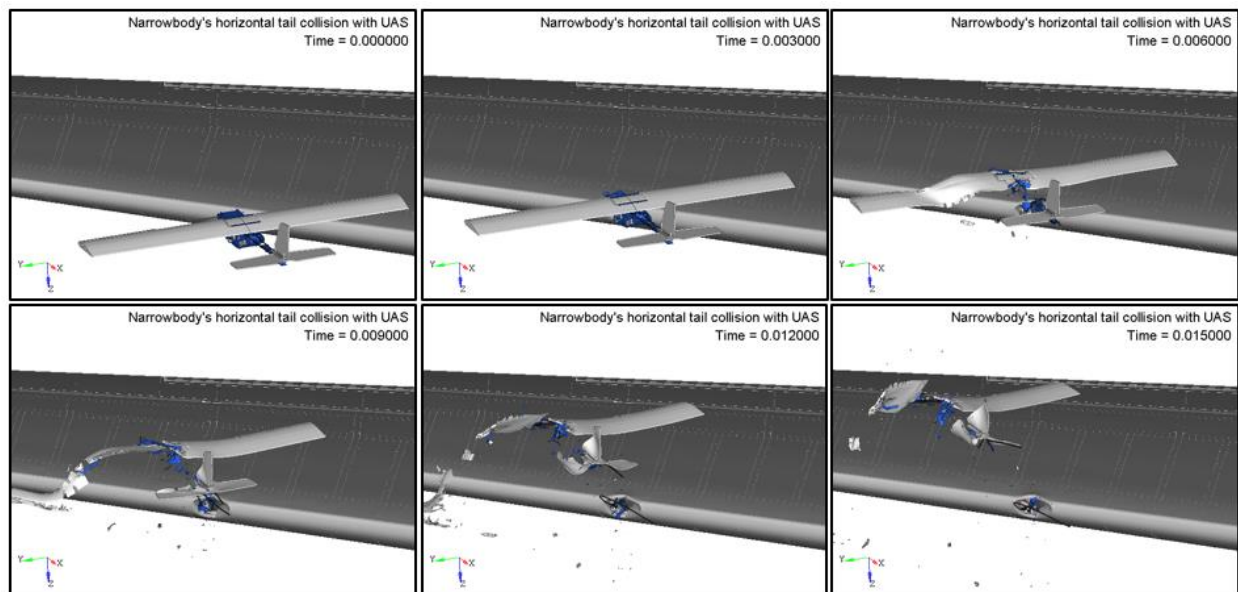


Figure 131. Kinematics of the impact between a commercial transport jet horizontal stabilizer and a 1.8 kg (4.0 lb) fixed-wing UAS at location 2 at 128.6 m/s (250 knots)

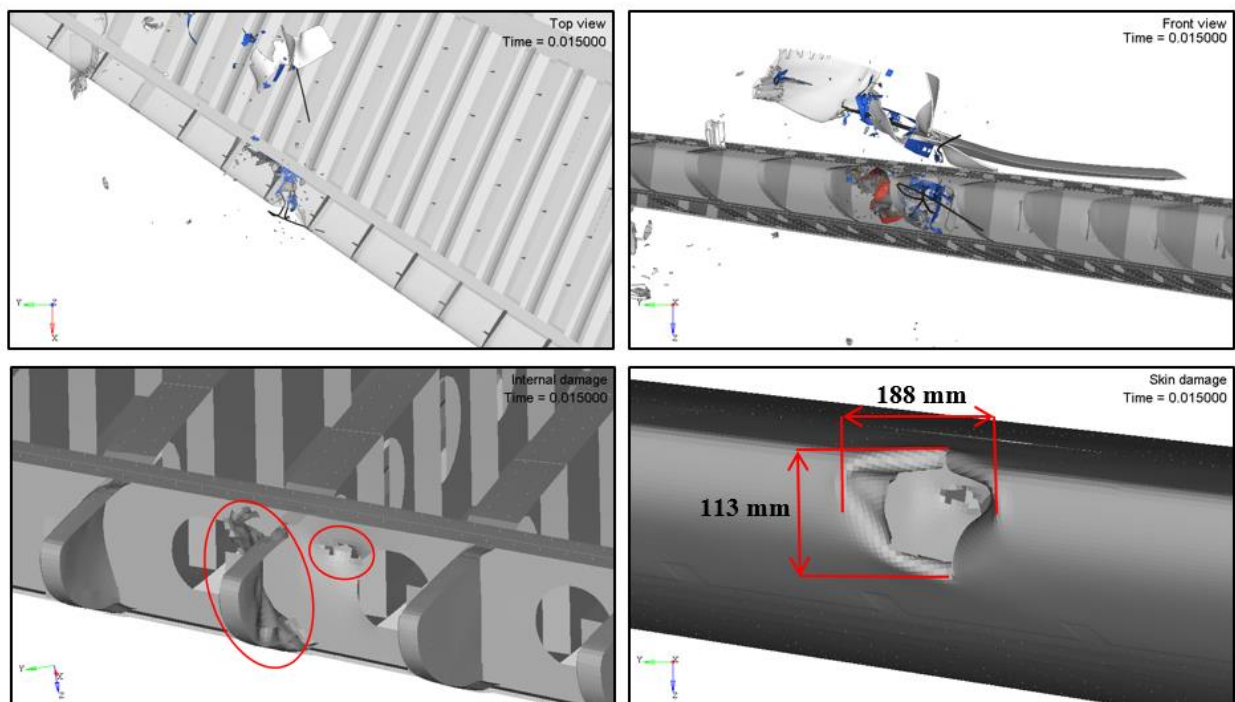


Figure 132. External/internal damage sustained by a commercial transport jet horizontal stabilizer impacted at location 2 with 1.8 kg (4.0 lb) fixed-wing UAS at 128.6 m/s (250 knots)

The UAS damaged the skin and the nose ribs, creating a 188 x 113 mm² damage zone on the skin surface and allowing considerable portions of UAS mass (including the battery) to penetrate the airframe. The UAS entering the airframe had enough kinetic energy to impact and damage the

front spar, causing a puncture next to the nose rib. The bottom left image at Figure 132 illustrates the damage and permanent deformation caused to the ribs and the front spar. In this case, the front spar sustained critical damage. Since the front spar is a critical load path of the horizontal stabilizer, it was considered to be a primary structure. Consequently, the damage introduced by the UAS in this case was classified as Level 4.

Figure 133 presents the impulse due to the contact force between the UAS and the horizontal stabilizer, as well as the energy balance for both of them. Figure 134 presents the internal energies of the UAS and horizontal stabilizer components directly involved in the impact.

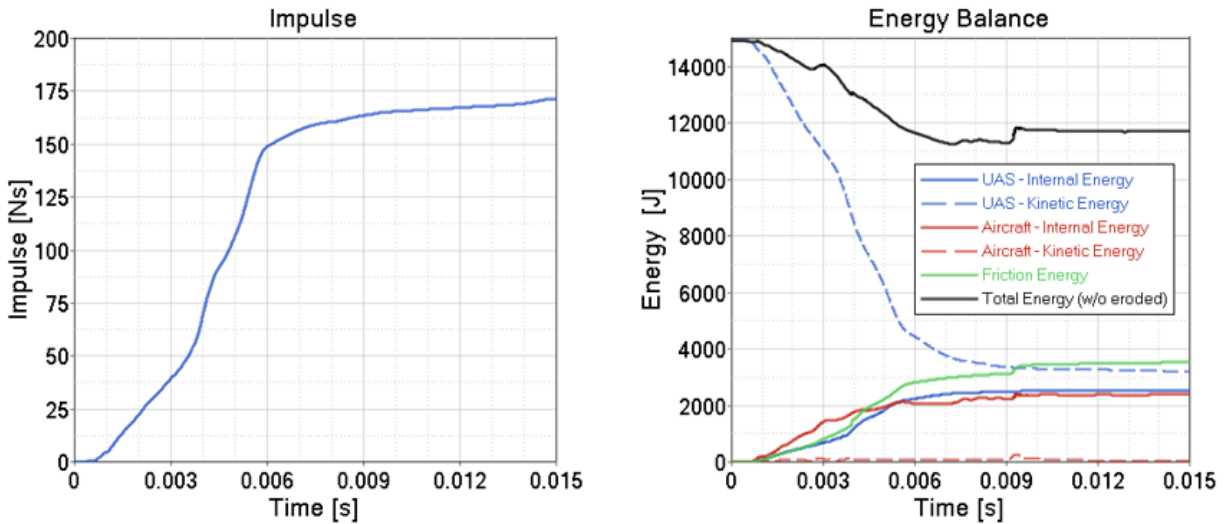


Figure 133. Impulse and energy balance of the impact between a commercial transport jet horizontal stabilizer and a 1.8 kg (4.0 lb) fixed-wing UAS at 128.6 m/s (250 knots)

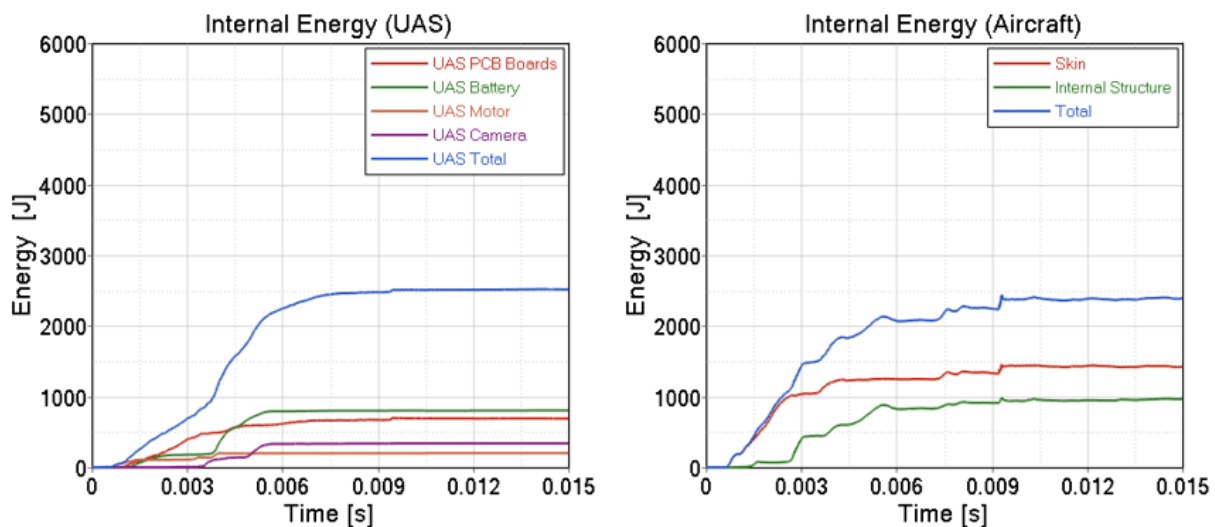


Figure 134. Internal energy per component of the impact between a commercial transport jet horizontal stabilizer at location 2 and a 1.8 kg (4.0 lb) fixed-wing UAS at 128.6 m/s (250 knots)

The energy balance plot includes the UAS and horizontal stabilizer kinetic and internal energies, as well as frictional energy and total energy for the event. The horizontal stabilizer and the UAS absorbed 16% and 17% of the impact energy, respectively. The energy dissipated by friction reached 24% of the total energy. In Figure 134, the internal energies for the UAS parts and the horizontal stabilizer show that the UAS battery, PCBs, and the skin of the horizontal stabilizer absorbed the most energy.

4.3.3 Wing Leading Edge

The commercial transport jet wing was subjected to impact at four impact locations that were selected based on the criteria described in section 4.1.2 . The diagram in Figure 135 illustrates the impact locations and the naming assigned to each of the cases. The initial velocity assigned to the UAS was 128.6 m/s (250 knots) along the local x -axis of the aircraft. The wing leading edge considered to be fixed at the inboard and outboard ends of the front spar and a symmetry constraint was applied at the free edge of the skin to represent the connection to the wing-box covers.

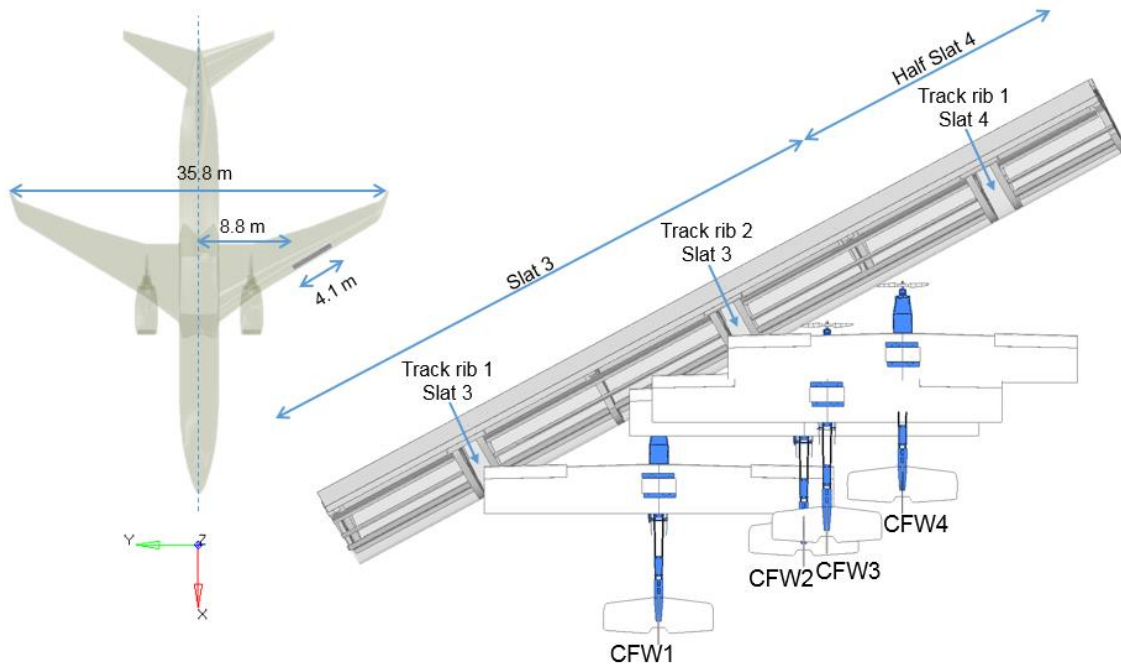


Figure 135. UAS impact locations – Commercial jet wing

4.3.3.1 Summary of Results – Commercial Transport Jet Wing

A summary of the results of all four cases presented in Figure 135 is shown in Figure 136. For each case, the left bar represents a summation of all the different energies involved in the impact event, measured at 15 ms after impact and normalized with the total energy at time zero. Each block indicates the percentage of total energy for each respective type of energy. The right bar specifies the severity level (1-4), as described in section 4.2.1 .

The impacted areas of the wing were concentrated only at one span-wise location, therefore span-wise effects may not be observed easily. However, a detailed model of the portion of the wing

leading edge allowed a better look into local effects, such as how impacting closer to a slat track rib pair or impacting aiming the center of the rib bay may affect damage.

Consistent levels of damage were observed for each impact target component (Figure 136) indicating that the impact behavior of the UAS for a given target structure was generally not affected by local features in the structure. The energy level of the impact was such that localized discrepancies did not significantly increase or decrease the overall damage level. It is worth noting that none of the cases showed situations where the battery penetrated the airframe, and therefore none of them can be considered with potential risk for fire.

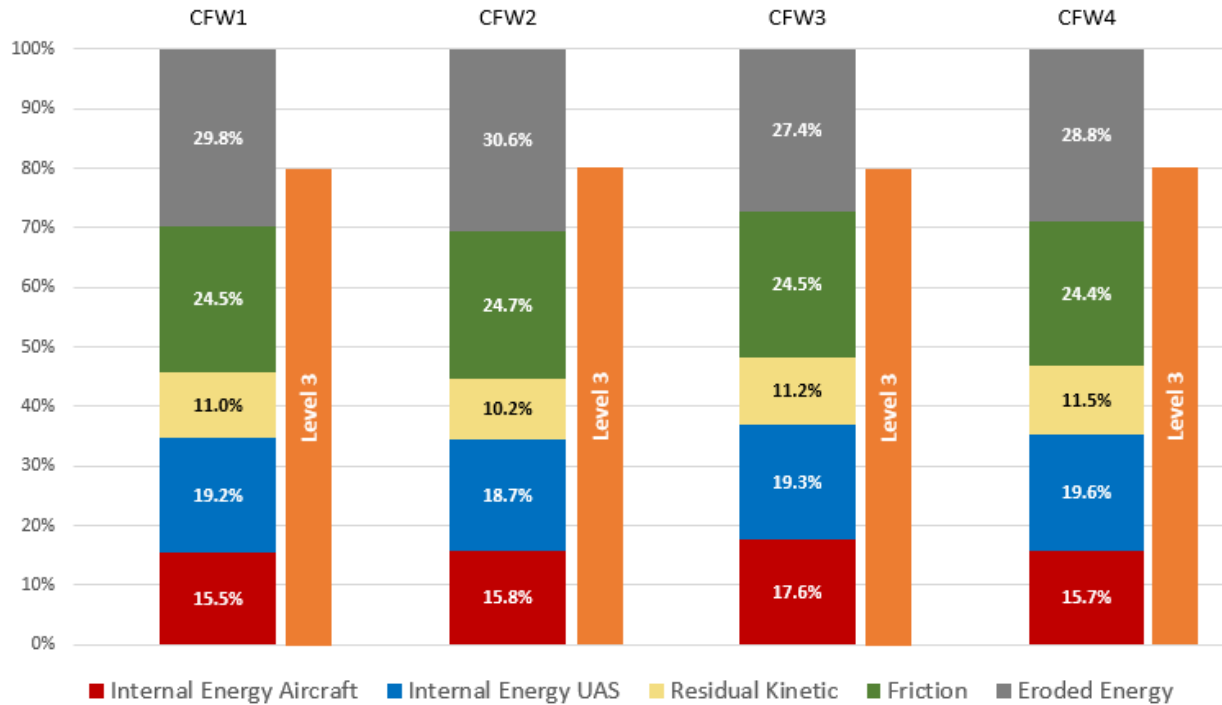


Figure 136. Energy distribution for commercial transport jet wing cases

4.3.3.2 Critical Case – CFW3

As introduced in section 4.3.3.1, CFW3 was considered the most critical damaging case for the wing leading edge. The following section contains the results of this specific simulation. The results of the remaining cases may be found in APPENDIX C.

In this case, the UAS was impacted against the leading edge of the wing at 128.6 m/s (250 knots) in the local x -axis direction of the aircraft. The impact location selected was at the outer portion of slat 3, with the UAS CG aligned with the leading edge at the midpoint between the intermediate rib and the slat track rib pair. Figure 137 depicts the kinematics of the event. Figure 138 shows the damage caused to the skin and internal structure (ribs and sub-spar) of the wing.

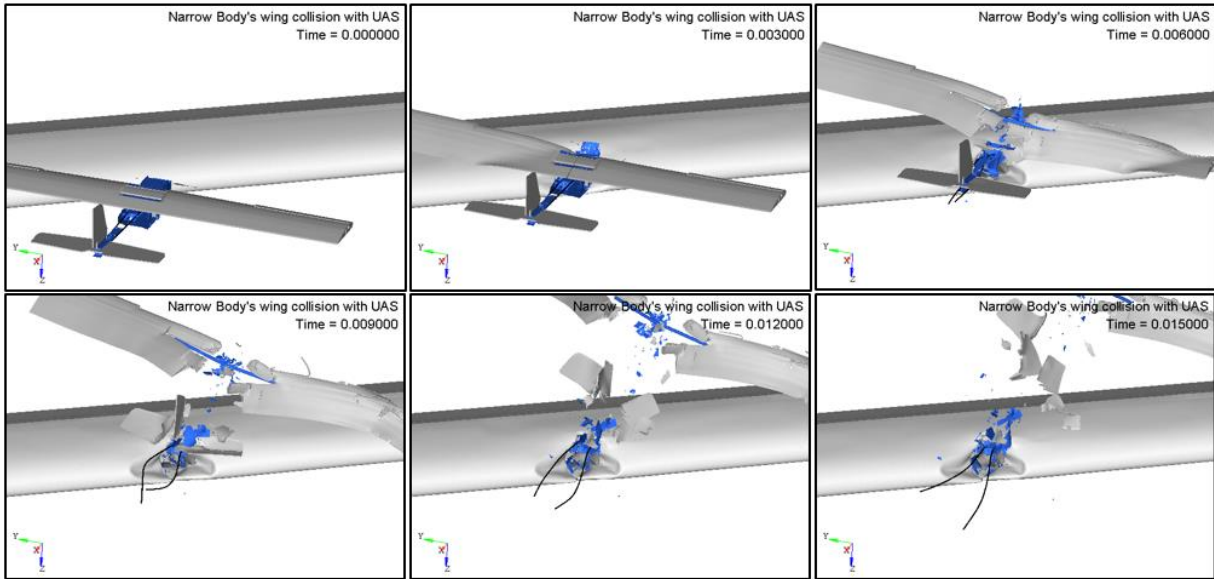


Figure 137. Kinematics of the impact between a commercial transport jet wing at location 3 and a 1.8 kg (4.0 lb) fixed-wing UAS at 128.6 m/s (250 knots)

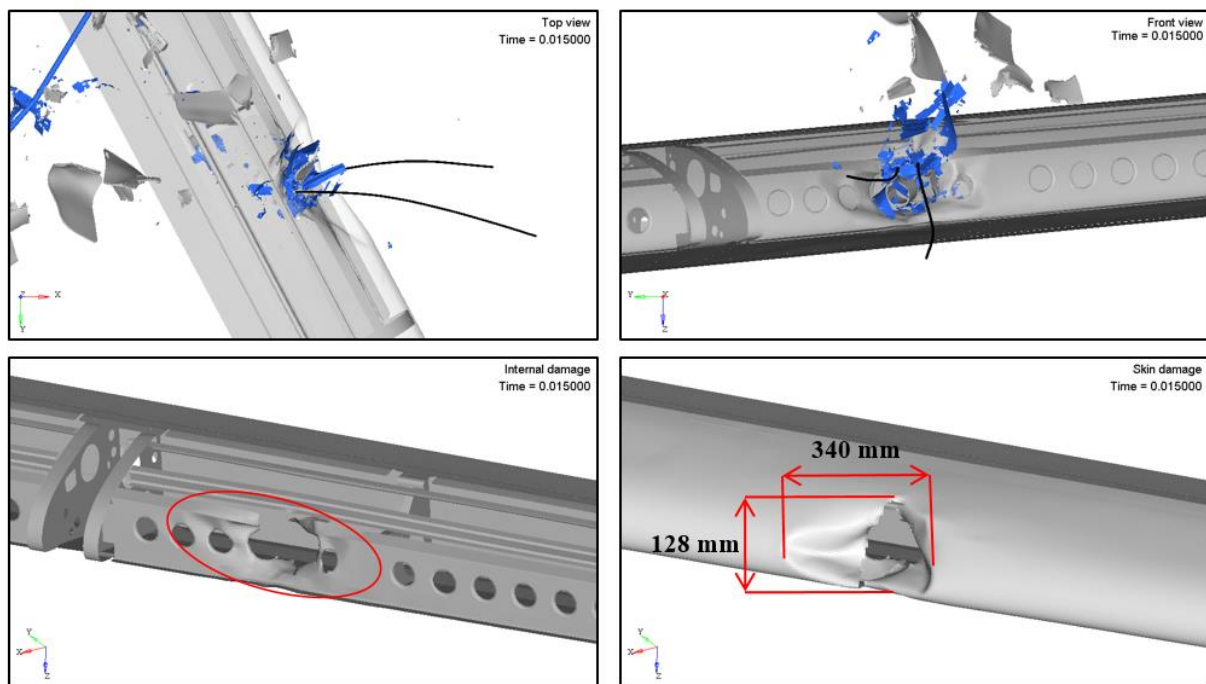


Figure 138. External/internal damage sustained by a commercial transport jet wing impacted at location 3 with a 1.8 kg (4.0 lb) fixed-wing UAS at 128.6 m/s (250 knots)

The UAS impacted the leading edge of the wing and created a vertical puncture on the D-nose skin surface and sub-spar, as shown in the bottom left and bottom right images of Figure 138, respectively. The UAS created an opening of 340 x 128 mm², penetrated the skin, and deposited debris within the airframe. Primary structural components, such as the front spar, received permanent

deformation but no critical damage. Fragments of the UAS penetrated the airframe. Consequently, the damaged introduced by the UAS in this case was classified as Level 3.

Figure 139 presents the impulse due to the contact force between UAS and wing as well as the energy balance for both of them. Figure 140 shows the internal energies of UAS and wing parts directly involved in the impact.

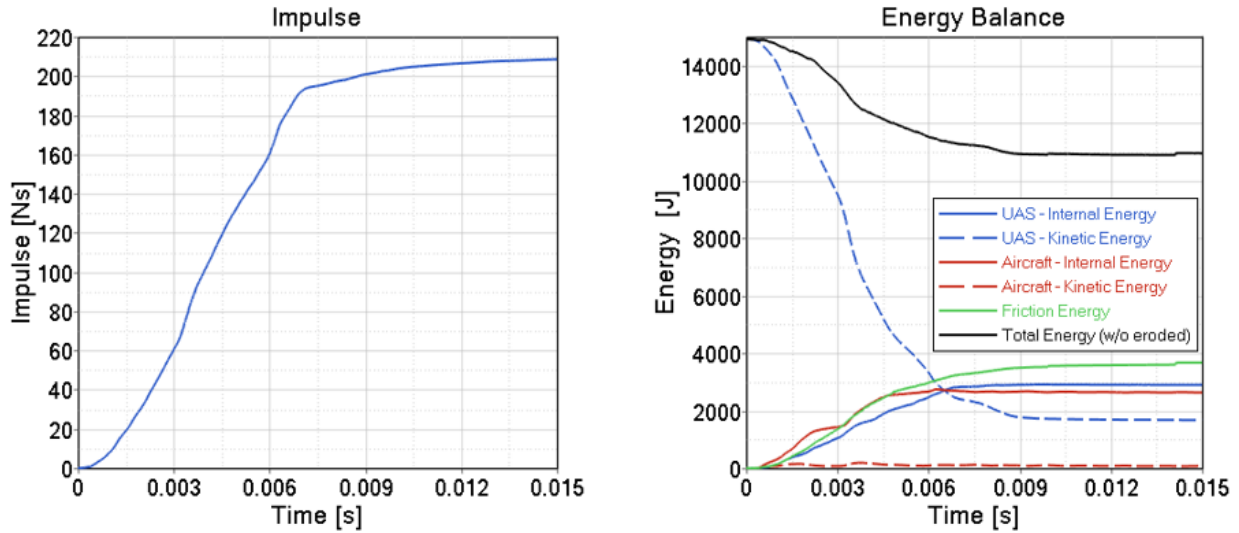


Figure 139. Impulse and energy balance of the impact between a commercial transport jet wing and a 1.8 kg (4.0 lb) fixed-wing UAS at 128.6 m/s (250 knots)

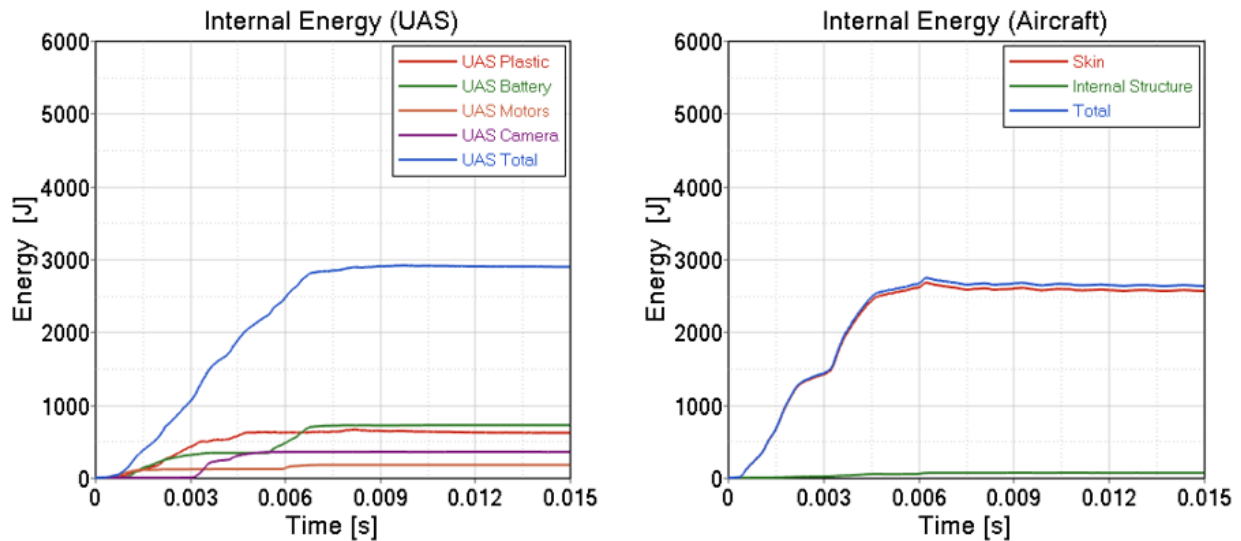


Figure 140. Internal energy per component of the impact between a commercial transport jet wing and a 1.8 kg (4.0 lb) fixed-wing UAS at 128.6 m/s (250 knots)

The energy balance plot includes the UAS and wing kinetic and internal energies as well as frictional energy and total energy for the event. The wing and the UAS absorb 18% and 19% of the impact energy, respectively. The energy dissipated by friction reaches 25% of the total energy. In Figure 140, internal energies for the UAS parts and the wing show that the UAS battery and the skin of the wing absorb the highest amount of internal energies.

4.3.4 Windshield

The windshield of the commercial transport jet was subjected to impact at three different locations that were selected based on the criteria described in section 4.1.2 . The diagram in Figure 141 illustrates the impact locations and the naming assigned to each of the cases. The UAS was assigned an initial speed of 128.6 m/s (250 knots) in the local x -axis of the aircraft. Symmetry boundary conditions were considered for the forward fuselage at the skin edge to connect it to the rest of the aircraft.

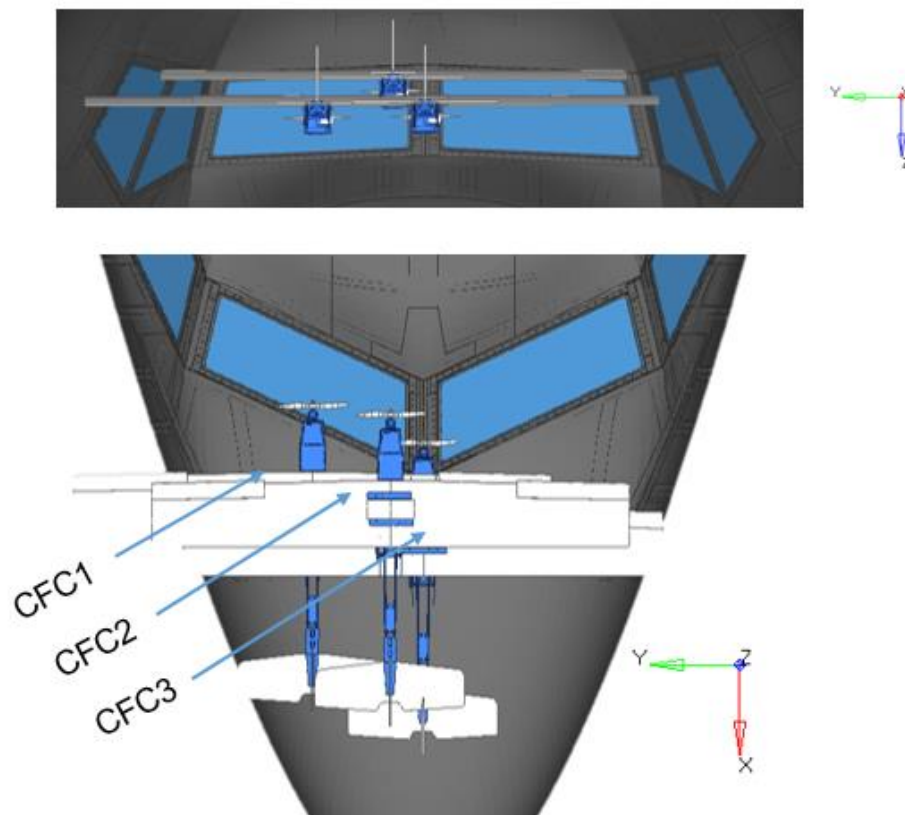


Figure 141. UAS impact locations – Commercial jet windshield

4.3.4.1 Summary of Results – Commercial Transport Jet Windshield

A summary of the results of all three cases presented in Figure 141 is shown in Figure 142. For each case, the left bar represents a summation of all the different energies involved in the impact event, measured at 15 ms and normalized with the total energy at time zero. Each block indicates

the percentage of total energy for each respective type of energy. The right bar specifies the severity level (1-4), as described in section 4.2.1 .

If compared with other impacted areas of the Commercial Transport Jet, the UAS impacts on the windshield resulted in a much higher residual kinetic energy. Due to the low angle impact to the transparency (approximately 45°), the UAS was deflected without any considerable damage to the windshield, as shown in Figure 143 and Figure 144. The windshield has a thick multilayered construction with a very high bulk stiffness. Consequently, a great amount of the energy of deformation is absorbed by the UAS. This can be seen from the energy distribution where the internal energy absorbed by the UAS is much greater than that of the aircraft.

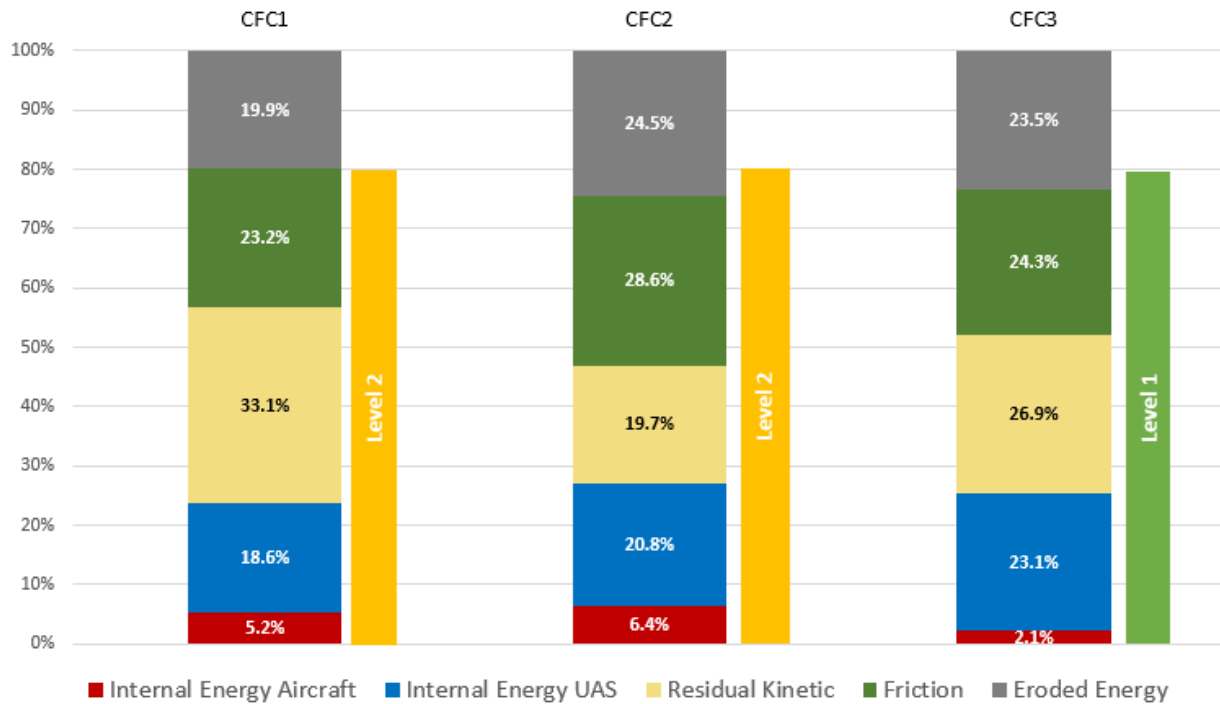


Figure 142. Energy distribution for commercial transport jet windshield cases

4.3.4.2 Critical Case – CFC1

As introduced in section 4.3.4.1 , CFC1 was considered the most critical damaging case. The following section presents the reader with the results of this specific simulation. The results of the remaining cases may be found in APPENDIX C.

In this case, the UAS was impacted against the center of the windshield at 128.6 m/s (250 knots) in the local x -axis direction of the aircraft. Figure 143 depicts the kinematics of the event. Figure 144 shows the damage caused to the windshield and surrounding structure. The bottom two images present the contour plot of the effective plastic strain after impact on the outer (bottom-left image) and middle (bottom-right image) layers of the transparency, which were the components that experienced greater damage. The legend was adjusted so that the maximum value corresponded to the failure strain of the material of each respective layer.

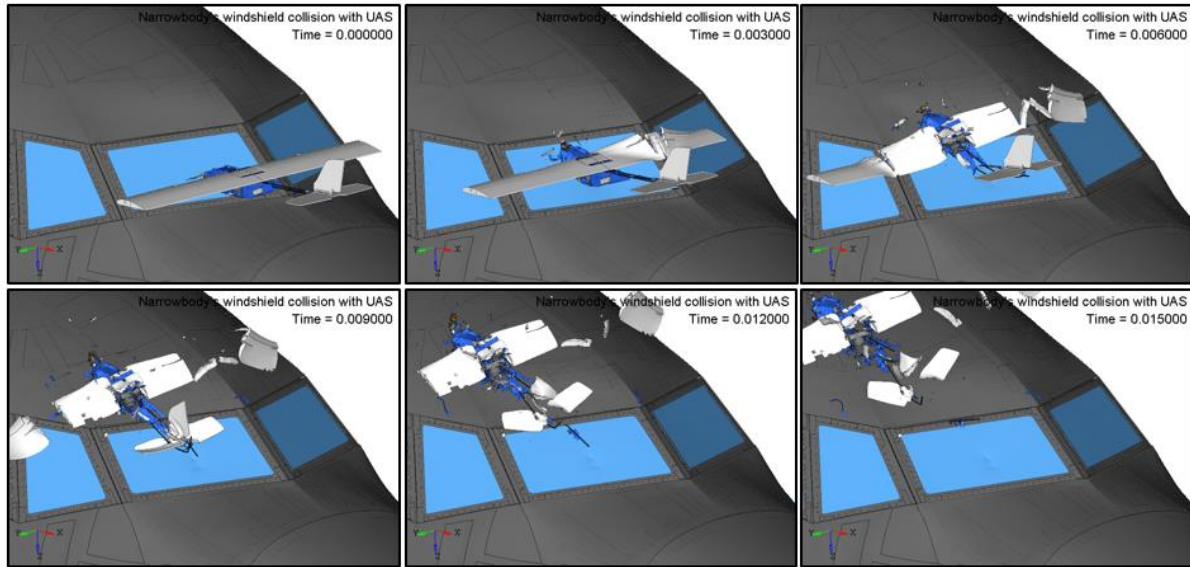


Figure 143. Kinematics of the impact between a commercial transport jet windshield at location 1 and a 1.8 kg (4.0 lb) fixed-wing UAS at 128.6 m/s (250 knots).

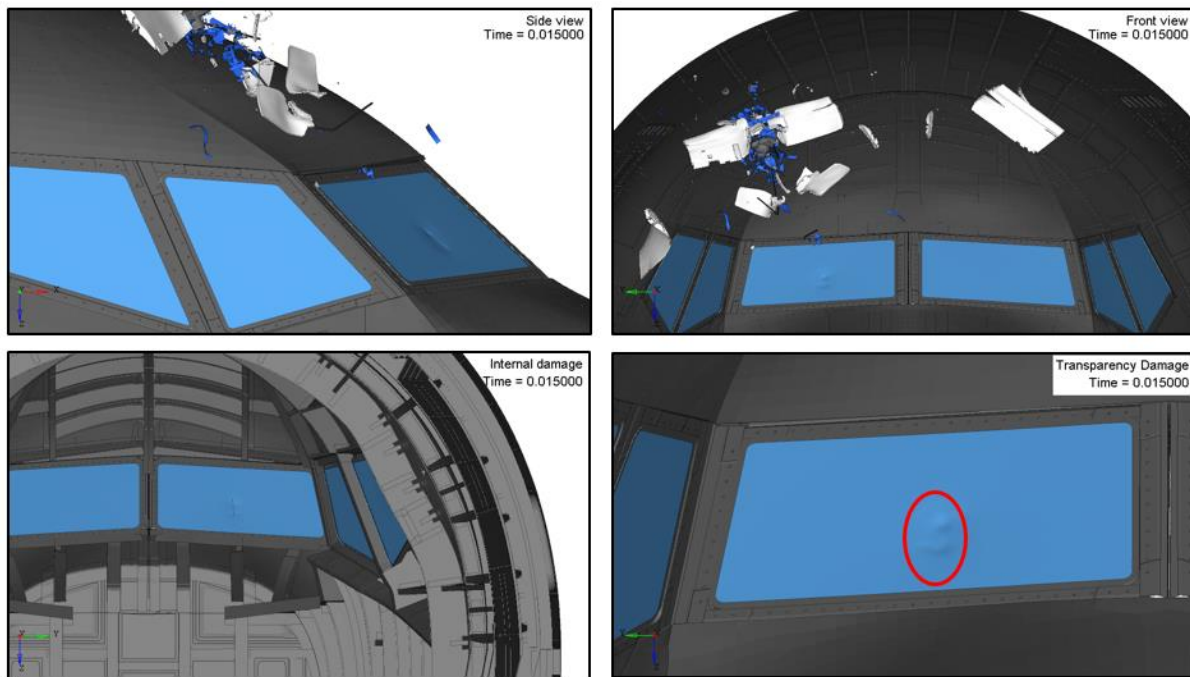


Figure 144. External/internal damage sustained by a commercial transport jet windshield impacted at location 1 with a 1.8 kg (4.0 lb) fixed-wing UAS at 128.6 m/s (250 knots)

The UAS impacted the windshield and slid over it due to the small windshield angle. The windshield did not sustain any failure or major damage. However, it did experience some permanent deformation in the outer layer of the transparency that can be observed in the bottom images in

Figure 144. Due to the small deformations experienced in the transparency and the lack of major damage or penetration, the severity of the event was categorized as Level 2.

Figure 145 presents the impulse due to the contact force between UAS and forward fuselage, as well as the energy balance for both of them. Figure 146 shows the internal energies of UAS and the forward fuselage components directly involved in the impact.

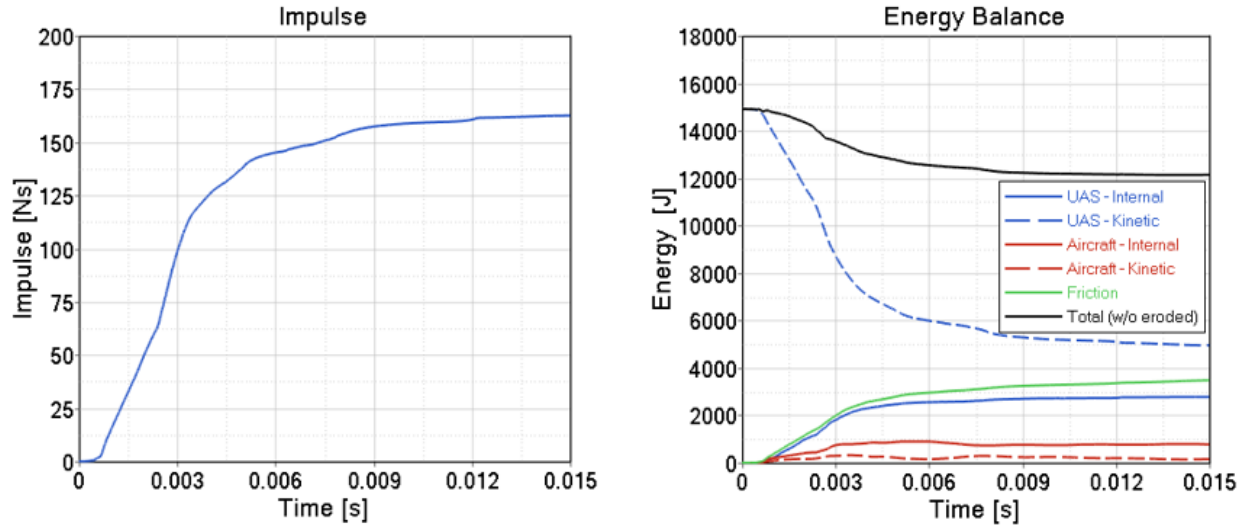


Figure 145. Impulse and energy balance of the impact between a commercial transport jet windshield and a 1.8 kg (4.0 lb) fixed-wing UAS at 128.6 m/s (250 knots)

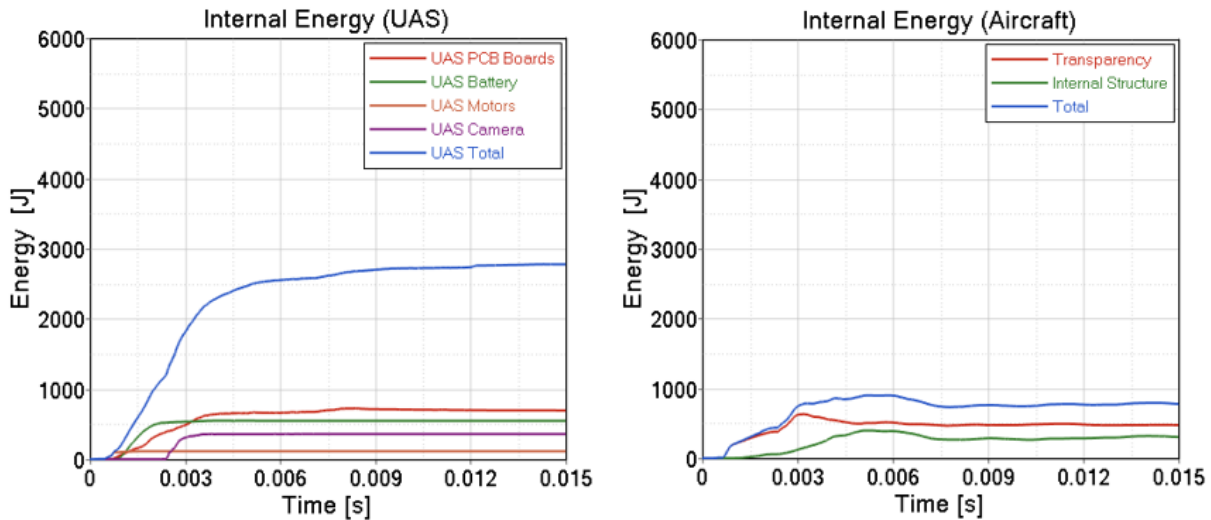


Figure 146. Internal energy per component of the impact between a commercial transport jet windshield and a 1.8 kg (4.0 lb) fixed-wing UAS at 128.6 m/s (250 knots)

The energy balance plot includes the UAS and forward fuselage kinetic and internal energies as well as frictional energy and total energy for the event. The forward fuselage and the UAS absorbed 5% and 19% of the impact energy, respectively. The energy dissipated by friction reached 23% of the total energy. In Figure 146, internal energies for the UAS parts and the forward fuselage show that the UAS PCBs and the transparency of the forward fuselage absorbed the highest amount of internal energies.

4.4 BUSINESS JET AIRBORNE COLLISION STUDIES

As introduced in section 3.1.3 , the targets areas for impact on the NIAR commercial transport jet are vertical stabilizer (section 4.4.1), horizontal stabilizer (section 4.4.2), wing leading edge (section 4.4.3), and windshield (section 4.4.4). This section presents the results of explicit dynamic simulations of impacts of the 1.8 kg (4.0 lb) fixed-wing UAS into the business jet.

Table 22 and Figure 147 summarize the results of the collision studies on the business transport jet. This section will describe in detail the results in each of the four subassemblies.

Table 22. Business jet airborne collision simulation – Severity levels and fire risk

	Business Jet											
	Vertical Stabilizer			Horizontal Stabilizer			Wing			Windshield		
Case	BFV1	BFV2	BFV3	BFH1	BFH2	BFH3	BFW1	BFW2	BFW3	BFC1	BFC2	BFC3
Severity	Level 4	Level 4	Level 4	Level 4	Level 4	Level 4	Level 2	Level 3	Level 3	Level 4	Level 1	Level 4
Fire Risk	No	No	No	No	No	No	No	No	No	No	No	No

As shown in Figure 147 for each one of the impact conditions we can quantify how the initial kinetic energy of the UAS prior to impact is transformed into aircraft and UAS internal energies through the structural deformations introduced during impact, a residual UAS kinetic energy that is a function of the UAS post-impact debris mass moving at a postimpact residual velocity; friction energy which is a function of the sliding contact energy between the UAS and the aircraft structure, and eroded energy from the mass of the UAS and aircraft eroded elements used to increase the stability of the calculation.

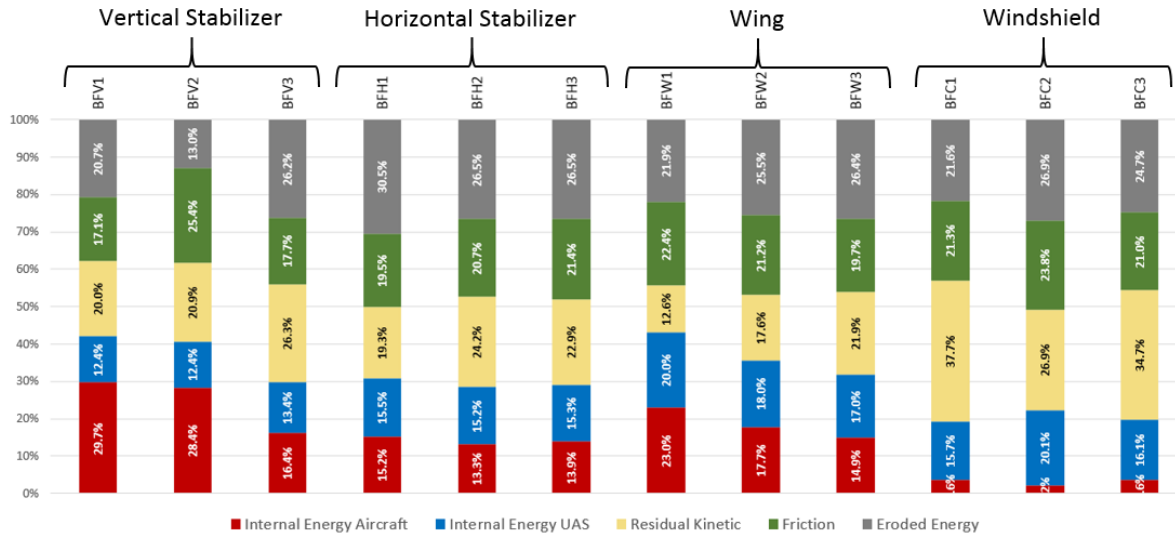


Figure 147. Business jet airborne collision simulation – Energy summary

4.4.1 Vertical Stabilizer

The vertical stabilizer of the business jet was subjected to impact at three different locations that were selected based on the criteria described in section 4.1.2 . The diagram in Figure 148 illustrates the positions being impacted and the naming assigned to each of the cases. The UAS was assigned an initial speed of 128.6 m/s (250 knots) in the local x -axis of the aircraft. The vertical stabilizer was constrained for displacement and rotation at the lower edge of the five spar members and the forward duct interface. The following subsections present the analysis results of the three different impact scenarios.

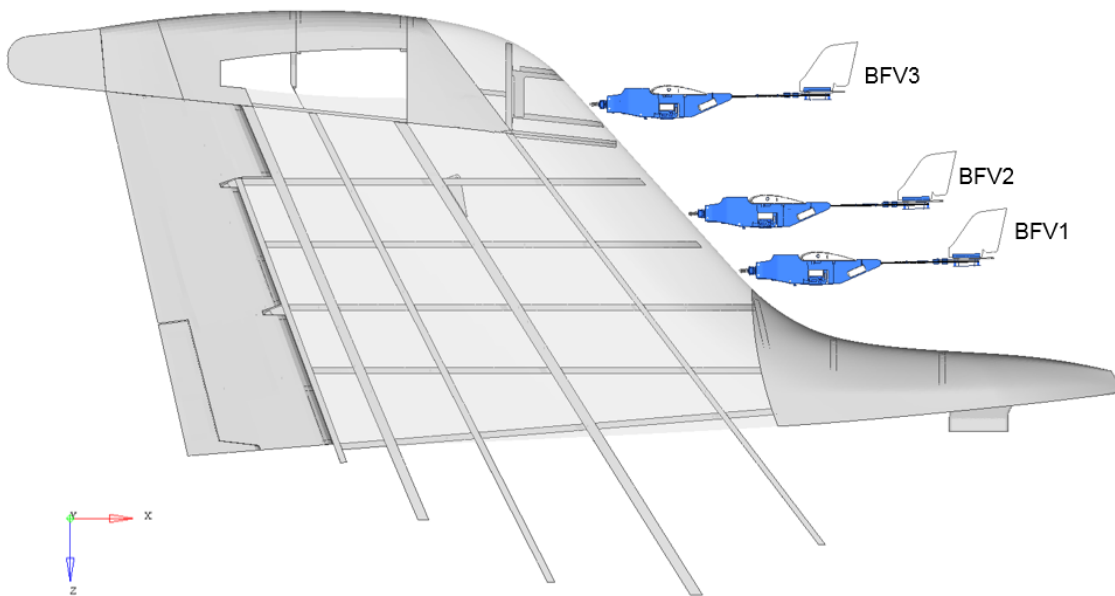


Figure 148. UAS impact locations – Business jet vertical stabilizer

4.4.1.1 Summary of Results – Business Jet Vertical Stabilizer

A summary of the results of all three cases presented in Figure 148 is shown in Figure 149. For each case, the left bar represents a summation of all the different energies involved in the impact event, measured at 15 ms and normalized with the total energy at time zero. Each block indicates the percentage total energy for the each type of energy. The right bar specifies the severity level (1-4), as described in section 4.2.1 .

Damage severity was determined based on a combination of the visual assessment of damage shown in the simulation and the impact energy distribution among the components involved. The majority of the UAS kinetic energy for these impact simulations was transferred to the internal energy of the vertical stabilizer. BFV1 was selected as the critical case because it sustained the most damage of the three.

Consistent levels of damage were observed at each impact target location (Figure 149) indicating that the UAS impact behavior for a given target structure was generally not affected by local features in the structure. The energy level of the impact was such that localized discrepancies did not significantly increase or decrease the overall damage level. It is worth noting that none of the cases showed situations where the battery penetrated the airframe, and therefore none of them can be considered with potential risk for fire.

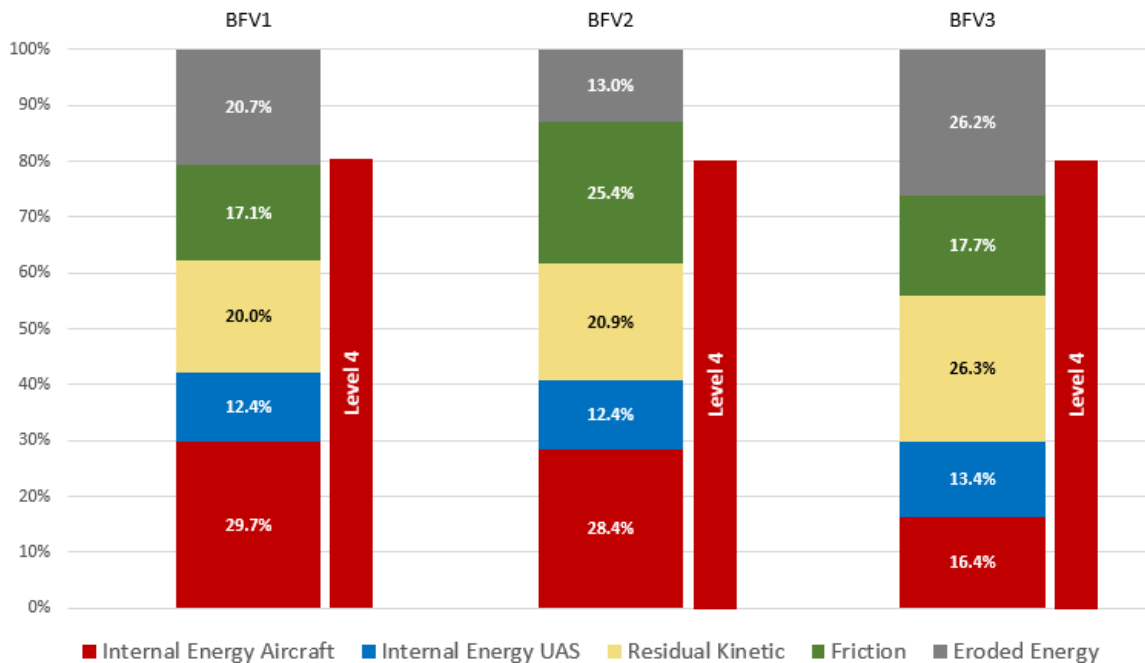


Figure 149. Energy distribution for business jet vertical stabilizer cases

4.4.1.2 Critical Case – BFV1

Of the three impact locations, BFV1 was considered the most critical damaging case. The results of the remaining cases are found in APPENDIX C.

The lower-middle portion of the vertical stabilizer between ribs 1 and 2 was chosen for impact in this case. The UAS was impacted against the vertical stabilizer at 128.6 m/s (250 knots) in the local x -axis direction of the aircraft. Figure 150 depicts the kinematics of the event. Figure 151 shows the damage caused to the skin and inner frames of the vertical stabilizer.

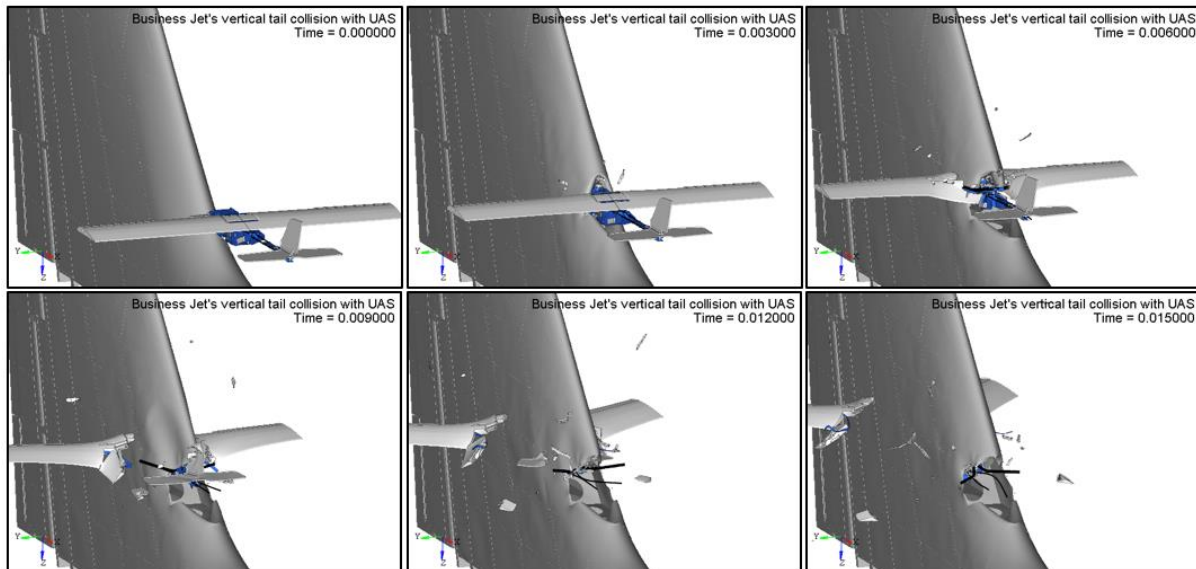


Figure 150. Kinematics of the impact between a business jet vertical stabilizer at location 1 and a 1.8 kg (4.0 lb) fixed-wing UAS at 128.6 m/s (250 knots)

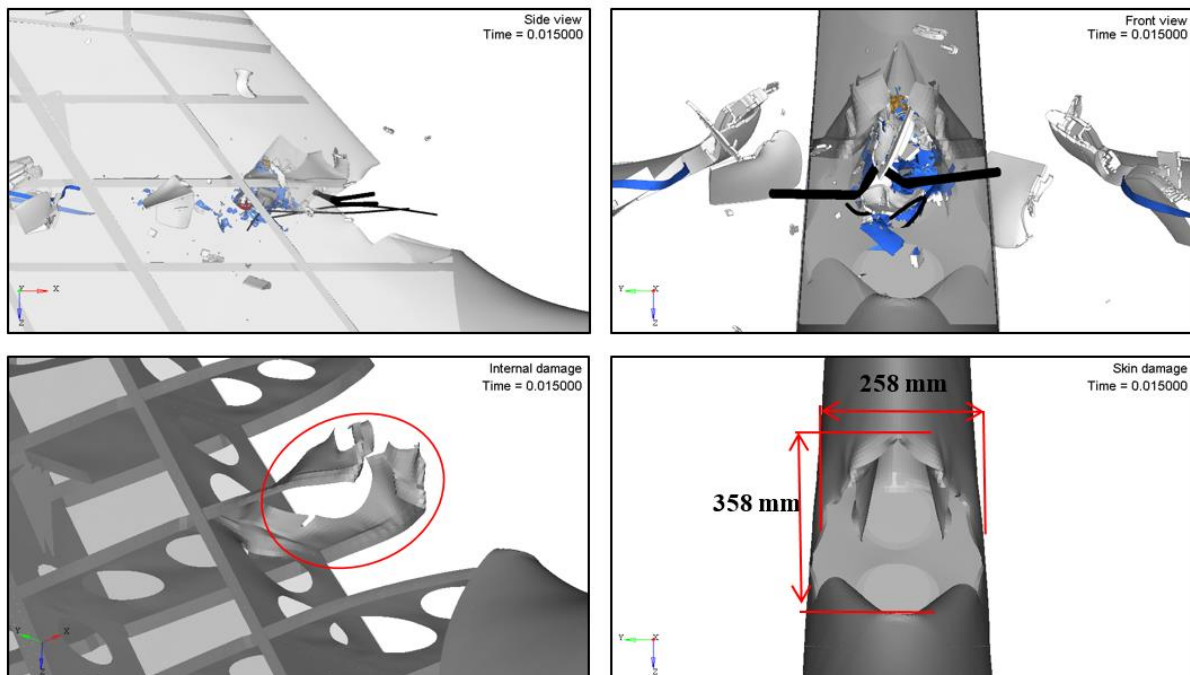


Figure 151. External/internal damage sustained by a business jet vertical stabilizer impacted at location 1 with a 1.8 kg (4.0 lb) fixed-wing UAS at 128.6 m/s (250 knots)

The UAS damaged the skin, the upper and lower ribs, and the lightninghole on the front spar, creating a 258 x 358 mm² damage zone on the skin surface. The permanent deformation of the ribs can be seen in the bottom left image in Figure 151. This impact considerably reduced the velocity of the UAS components such that the spar sustained only permanent deformation (no ruptures or punctures). The damage introduced by the UAS involved penetration of the skin and permanent deformation to the front spar and consequently the severity was classified as Level 4.

Figure 152 shows the impulse due to the contact force between UAS and vertical stabilizer, as well as the energy balance. Figure 153 shows the internal energies of UAS and vertical stabilizer parts directly involved in the impact.

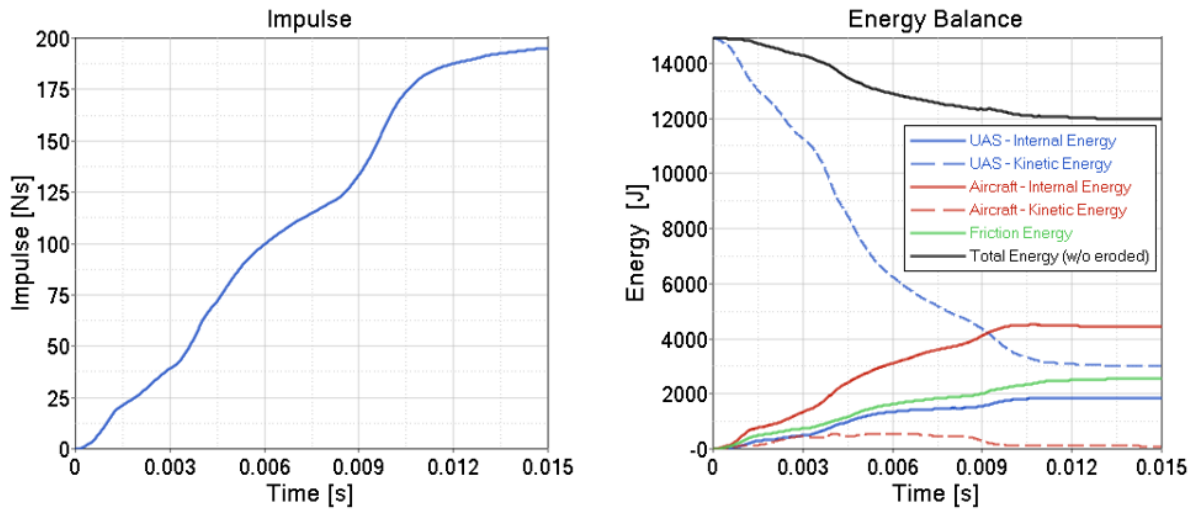


Figure 152. Impulse and energy balance of the impact between a business jet vertical stabilizer at location 1 and a 1.8 kg (4.0 lb) fixed-wing UAS at 128.6 m/s (250 knots)

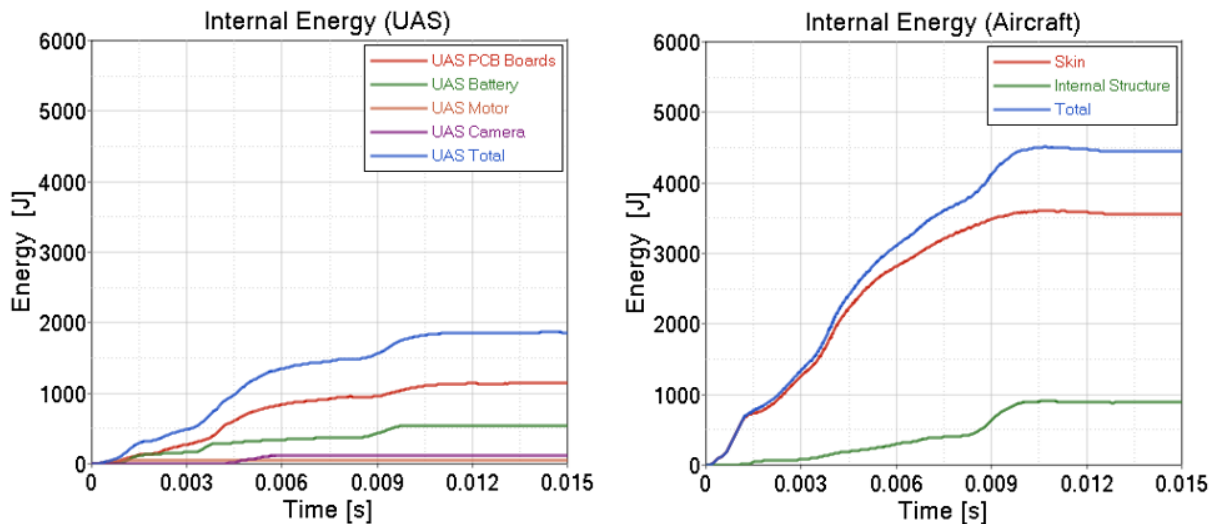


Figure 153. Internal energy per component of the impact between a business jet vertical stabilizer at location 1 and a 1.8 kg (4.0 lb) fixed-wing UAS at 128.6 m/s (250 knots)

The energy balance plot includes the UAS and vertical stabilizer kinetic and internal energies as well as frictional energy and total energy for the event. The vertical stabilizer and UAS absorbed 30% and 12% of the impact energy, respectively, while the energy dissipated by friction reached 17% of the total energy. In Figure 153, internal energies for the UAS parts and the vertical stabilizer show that the UAS PCBs and aircraft skin absorbed the highest amount of internal energies, respectively.

4.4.2 Horizontal Stabilizer

The business jet horizontal stabilizer was subjected to impact at three impact locations. Locations were selected such that the UAS could maximally penetrate into the structure of the aircraft. The initial velocity assigned to the UAS was 128.6 m/s (250 knots) along the local x -axis of the aircraft. In addition, the stabilizer was constrained for displacements and rotations at the forward and aft spars as well as the forward actuator attachment and aft pivot lug. The following subsections present the analysis results of the three different scenarios.

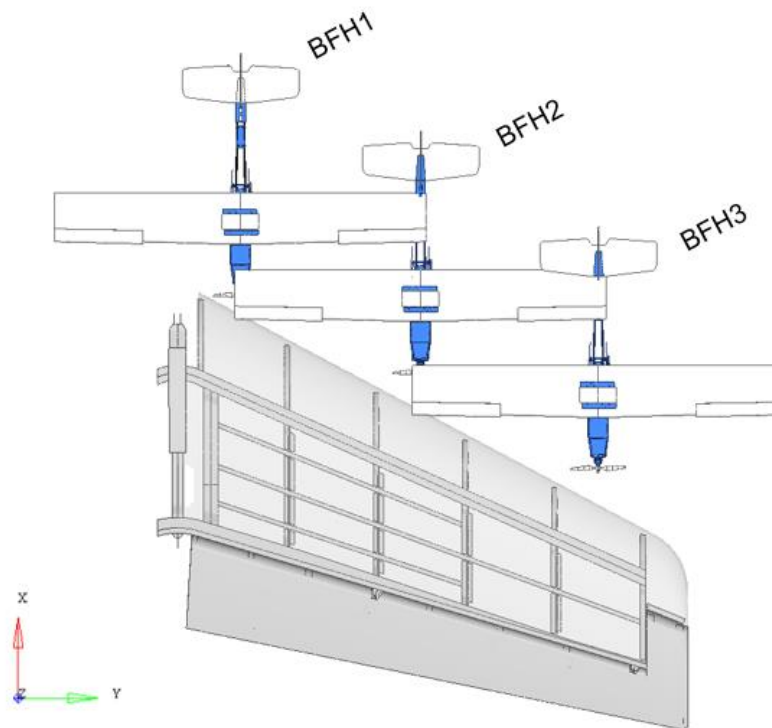


Figure 154. UAS impact locations – business jet horizontal stabilizer

4.4.2.1 Summary of Results – Business Jet Horizontal Stabilizer

A summary of the results of the three cases presented in Figure 154 is shown in Figure 155. For each case, the left bar represents a summation of all the different energies involved in the impact event, measured at 15 ms after impact and normalized with the total energy at time zero. Each block indicates the percentage of total energy for each respective type of energy. The right bar specifies the severity level (1-4), as described in section 4.2.1 .

Figure 154 shows consistent levels of damage for each impact target component, indicating that the impact behavior of the UAS for a given target structure is generally not affected by local features in the structure; the energy level of the impact is such that localized discrepancies do not significantly increase or decrease the overall damage level. None of the cases showed situations where the battery penetrated the airframe, and therefore none of them can be considered with potential risk for fire.

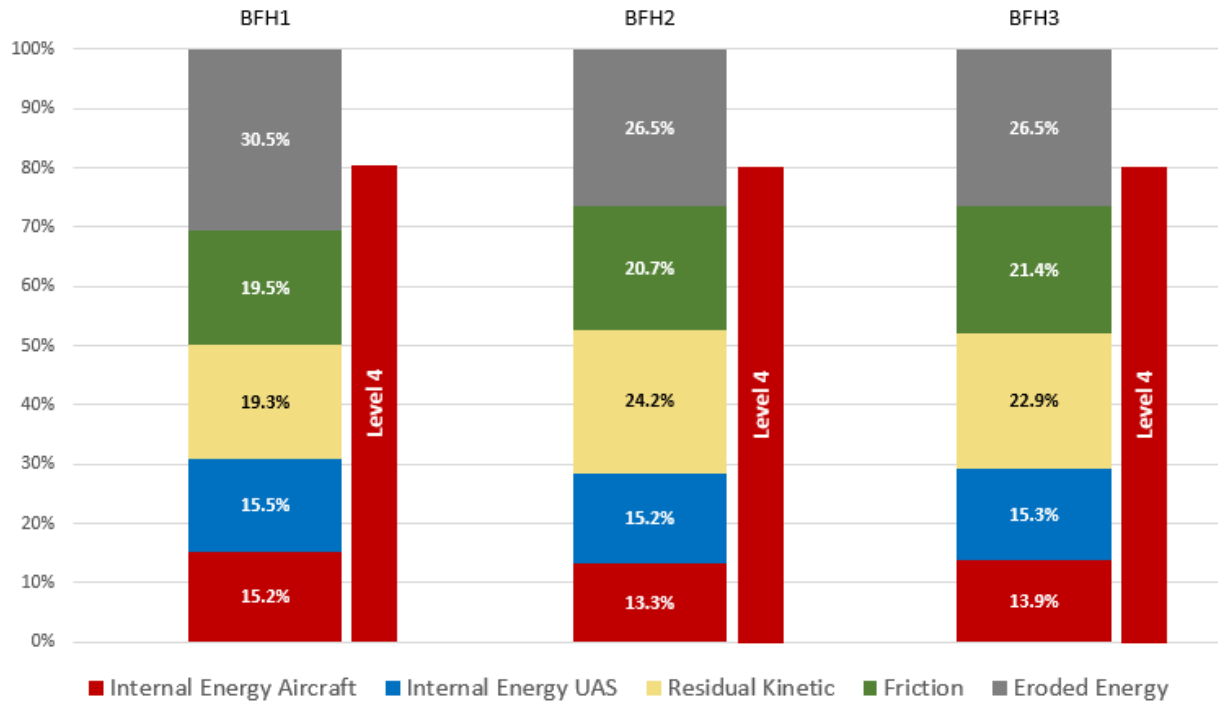


Figure 155. Energy distribution for business jet horizontal stabilizer cases

4.4.2.2 Critical Case – BFH1

Of the three impact locations, BFH1 was considered the most critical damaging case. The results of the remaining cases may be found in APPENDIX C.

Impact location 1 is located next to the horizontal stabilizer's root rib. The UAS was impacted against the stabilizer at 128.6 m/s (250 knots) along the local x -axis direction of the aircraft. Figure 156 presents the kinematics of the event. Figure 157 shows the damage caused to the inner frames and the skin.

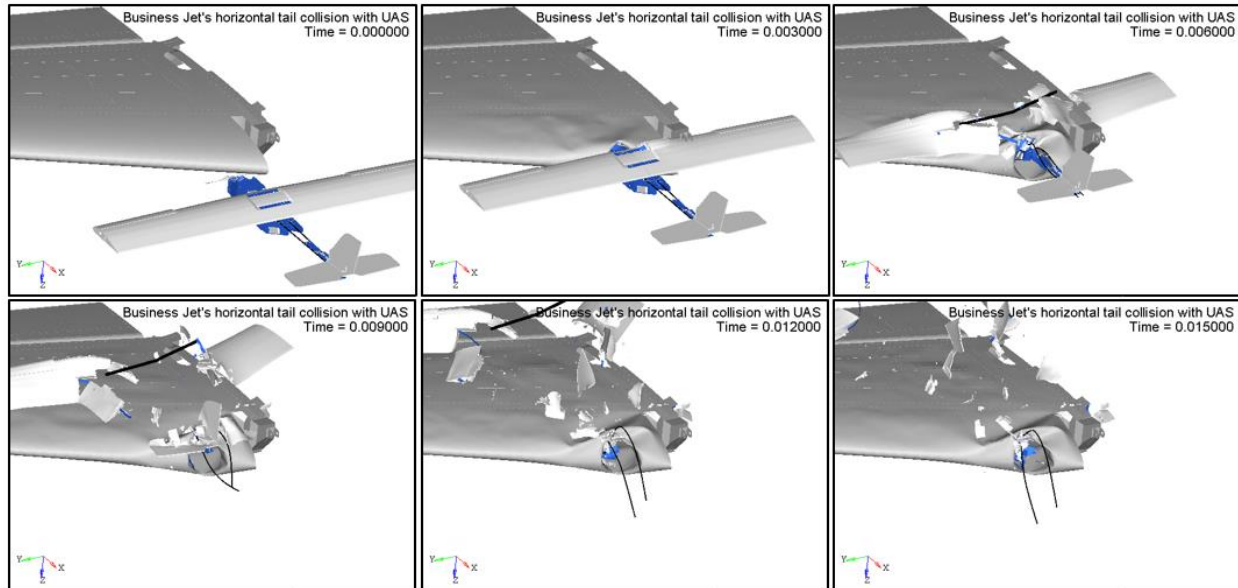


Figure 156. Kinematics of the impact between a business jet horizontal stabilizer at location 1 and a 1.8 kg (4.0 lb) fixed-wing UAS at 128.6 m/s (250 knots)

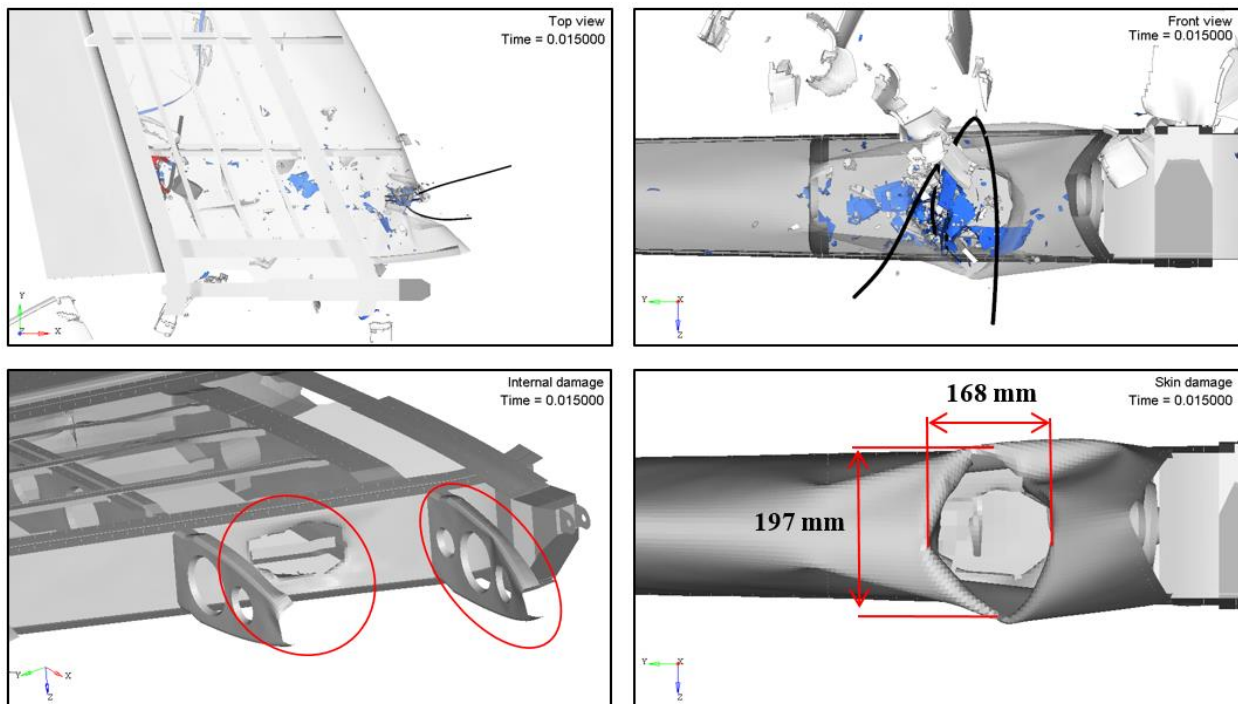


Figure 157. External/internal damage sustained by a business jet horizontal stabilizer impacted at location 1 with a 1.8 kg (4.0 lb) fixed-wing UAS at 128.6 m/s (250 knots)

The UAS damaged the skin and the nose ribs, creating a 197 x 168 mm² damage zone on the skin surface and allowing a significant fraction of the UAS mass to penetrate the front spar. On the bottom left image of Figure 157, penetration of the front spar, as well the deformation affecting the nose ribs was observed. The front spar sustained critical damage. Since the front spar is a critical load path for the horizontal stabilizer, it was considered a primary structure. Consequently, the damage introduced by the UAS in this case was classified as Level 4.

Figure 158 shows the impulse due to the contact force between the UAS and the horizontal stabilizer, as well as the energy balance for both of them. Figure 159 presents the internal energies of the UAS and horizontal stabilizer parts directly involved on the impact.

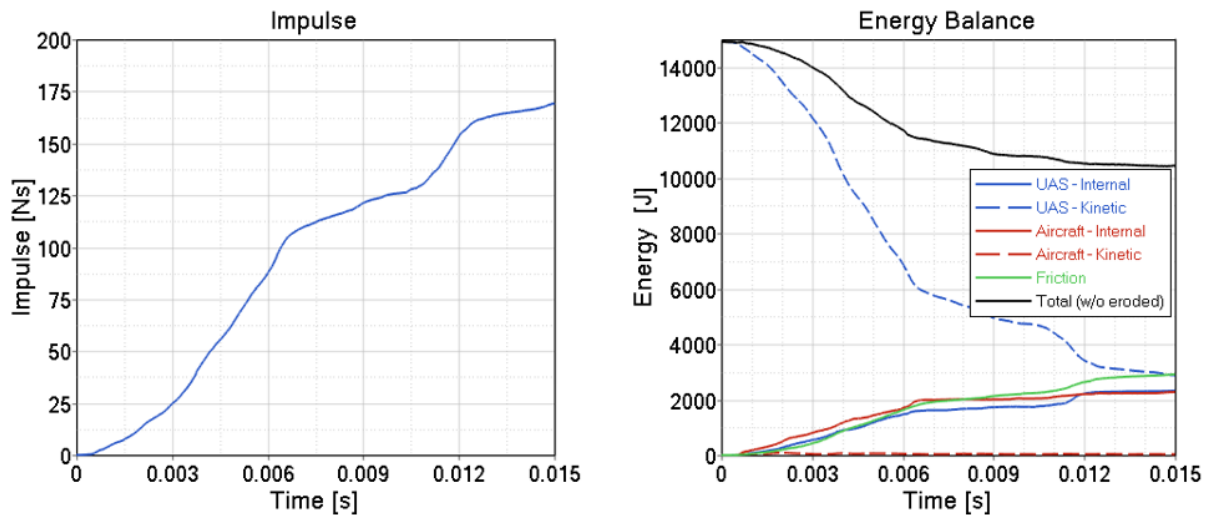


Figure 158. Impulse and energy balance of the impact between a business jet horizontal stabilizer and a 1.8 kg (4.0 lb) fixed-wing UAS at 128.6 m/s (250 knots)

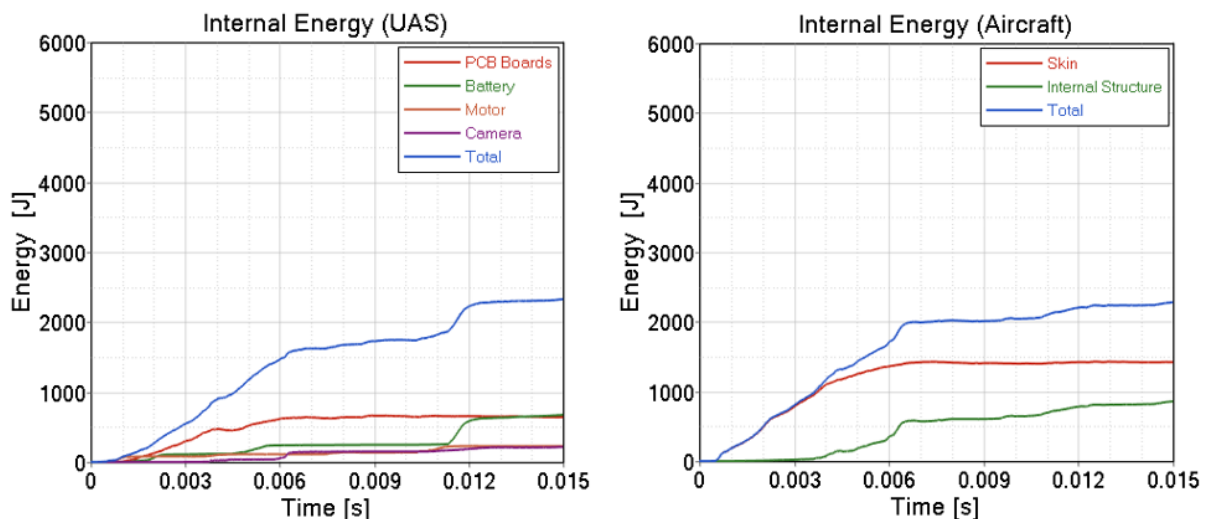


Figure 159. Internal energy per component of the impact between a business jet horizontal stabilizer and a 1.8 kg (4.0 lb) fixed-wing UAS at 128.6 m/s (250 knots)

The energy balance plot includes the UAS and horizontal stabilizer kinetic and internal energies, frictional energy and total energy for the event. The stabilizer and UAS absorbed 15% and 16% of

the impact energy, respectively, while the energy dissipated by friction reached 19% of the total energy. In Figure 159, internal energies for the UAS parts and the stabilizer structure show that the aircraft skin and UAS PCBs absorbed the highest internal energies of the event.

4.4.3 Wing Leading Edge

The simulated wing of the business jet was subjected to impact at three different locations. The locations were selected such that the UAS could maximally penetrate the leading edge upon impact. The UAS was assigned an initial speed of 128.6 m/s (250 knots) in the local x -axis of the aircraft. The nodal displacements and rotations were constrained at the centerline of the fuselage and at the wing-to-fuselage attachment fittings. The following subsections present the analysis results of the three different scenarios.

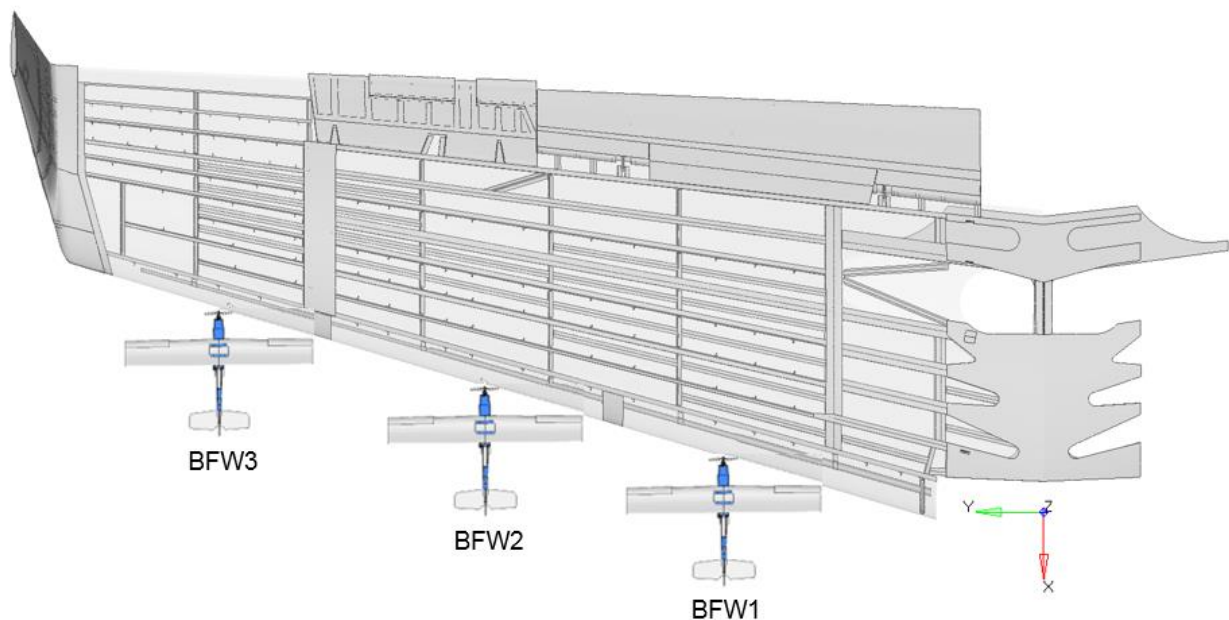


Figure 160. UAS impact locations – business jet wing leading edge

4.4.3.1 Summary of Results – Business Jet Wing

A summary of the results of the three cases presented in Figure 160 is shown in Figure 161. For each case, the left bar represents a summation of all the different energies involved in the impact event, measured at 15 ms and normalized with the total energy at time zero. Each block indicates percentage of total energy for each respective type of energy. The right bar specifies the severity level (1-4), as described in section 4.2.1 .

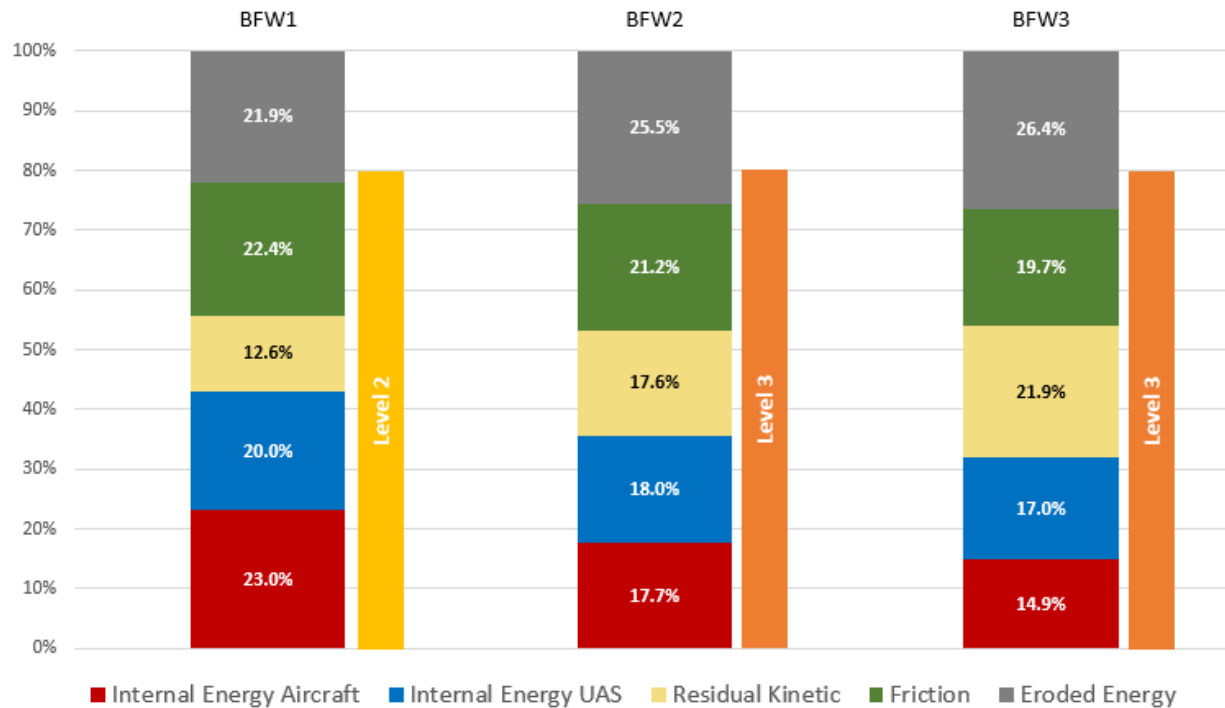


Figure 161. Energy distribution for business jet wing cases

As shown in Figure 161, there is a trend indicative of an increase in the internal energy absorbed by the aircraft structure when closer to the root of the wing. The inverse effect is observed for the residual kinetic energy.

Both phenomena may be explained with the cross-sectional height of the airfoil at the impacted location. The cross-section of the wing closer to the root was thicker than at the tip and had a greater nose radius. Consequently, the area of airframe that had a more perpendicular contact with the impacting projectile was greater, allowing a greater transfer of energy and therefore an increase in internal energy. Locations that offered less projected frontal area and had decreased nose radii tended to deflect the impact. This trend also explains the greater residual kinetic energy for out-board regions of the wing. For these, a greater portion of the UAS was deflected upwards and/or downwards.

4.4.3.2 Critical Case – BFW2

The middle portion of the wing between ribs 2 and 3 was chosen as the critical impact case for the wing leading edge. The UAS was impacted against the wing at 128.6 m/s (250 knots) in the local x -axis direction of the aircraft. Figure 162 depicts the kinematics of the event. Figure 163 shows the damage caused to the skin and inner frames of the wing.

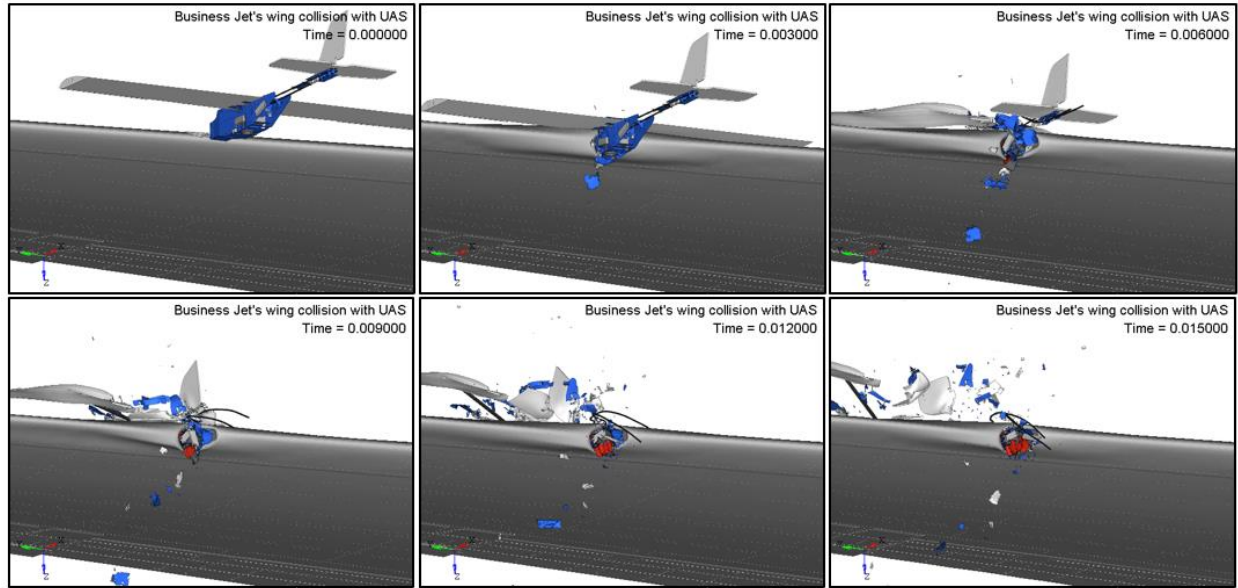


Figure 162. Kinematics of the impact between a business jet wing at location 2 and a 1.8 kg (4.0 lb) fixed-wing UAS at 128.6 m/s (250 knots)

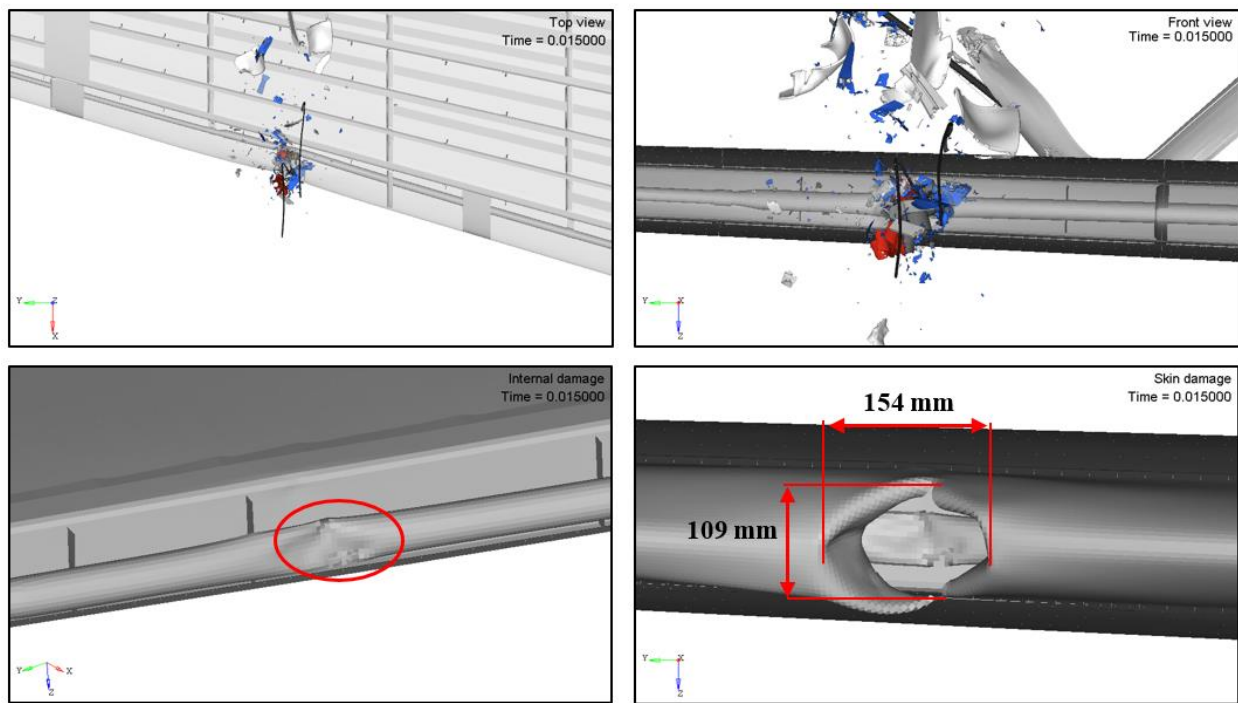


Figure 163. External/internal damage sustained by a business jet wing impacted at location 2 with a 1.8 kg (4.0 lb) fixed-wing UAS at 128.6 m/s (250 knots)

The UAS damaged the skin and the anti-ice tube, creating a 154 x 109 mm² damage zone on the skin surface. Permanent deformation of the tube can be seen in the bottom left image in Figure 163. This impact considerably reduced the velocity of the UAS components; the spar was not

impacted and sustained no damage. The damage introduced by the UAS involved penetration of the skin but no damage to the primary structure, and consequently, the severity was classified as Level 3.

Figure 164 shows the impulse due to the contact force between UAS and wing, as well as the energy balance for both of them. Figure 165 shows the internal energies of UAS and wing parts directly involved in the impact.

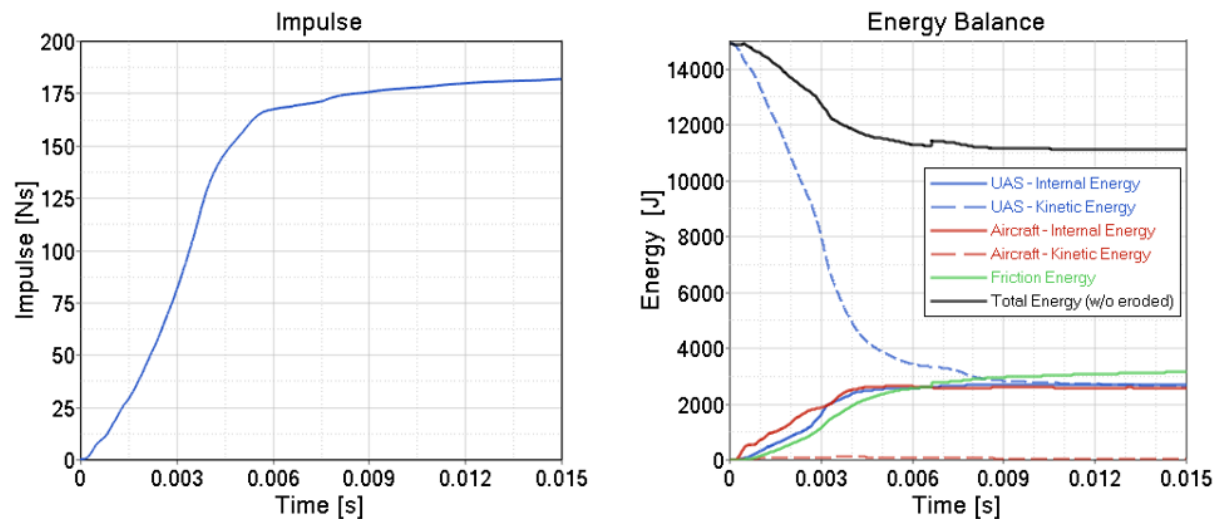


Figure 164. Impulse and energy balance of the impact between a business jet wing and a 1.8 kg (4.0 lb) fixed-wing UAS at 128.6 m/s (250 knots)

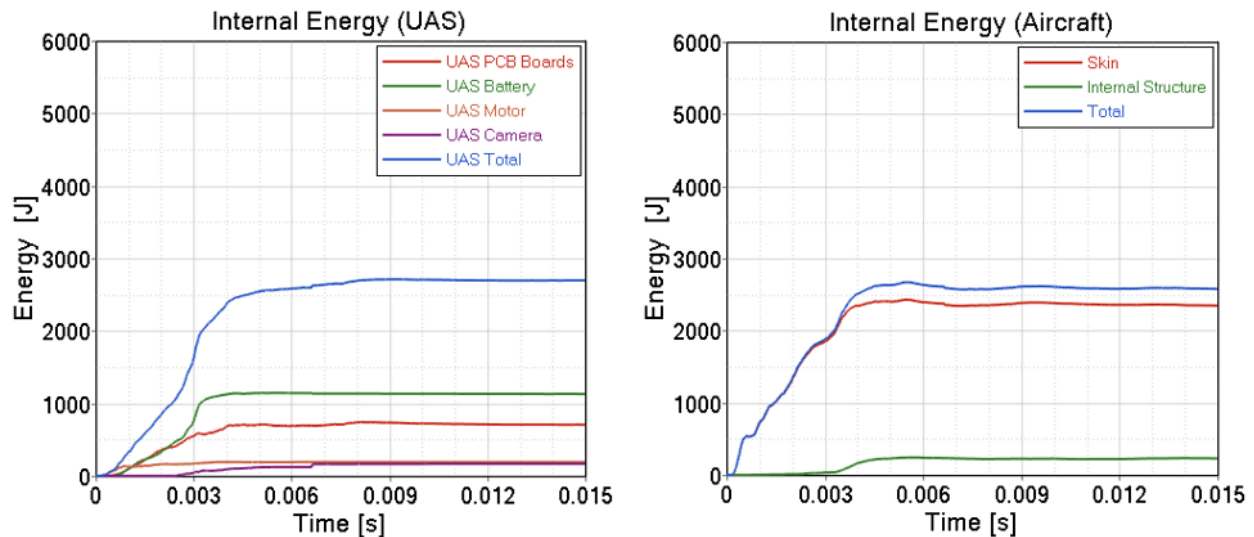


Figure 165. Internal energy per component of the impact between a business jet wing and a 1.8 kg (4.0 lb) fixed-wing UAS at 128.6 m/s (250 knots)

The energy balance plot includes the UAS and wing kinetic and internal energies as well as frictional energy and total energy for the event. The wing and UAS absorbed 17% and 18% of the impact energy, respectively while the energy dissipated by friction reaches 21% of the total energy. In Figure 165, the UAS battery and skin absorbed the highest amount of internal energies.

4.4.4 Windshield

The windshield of the business jet was subjected to impact at three different locations. The locations were selected based on the criteria described in section 4.1.2 .

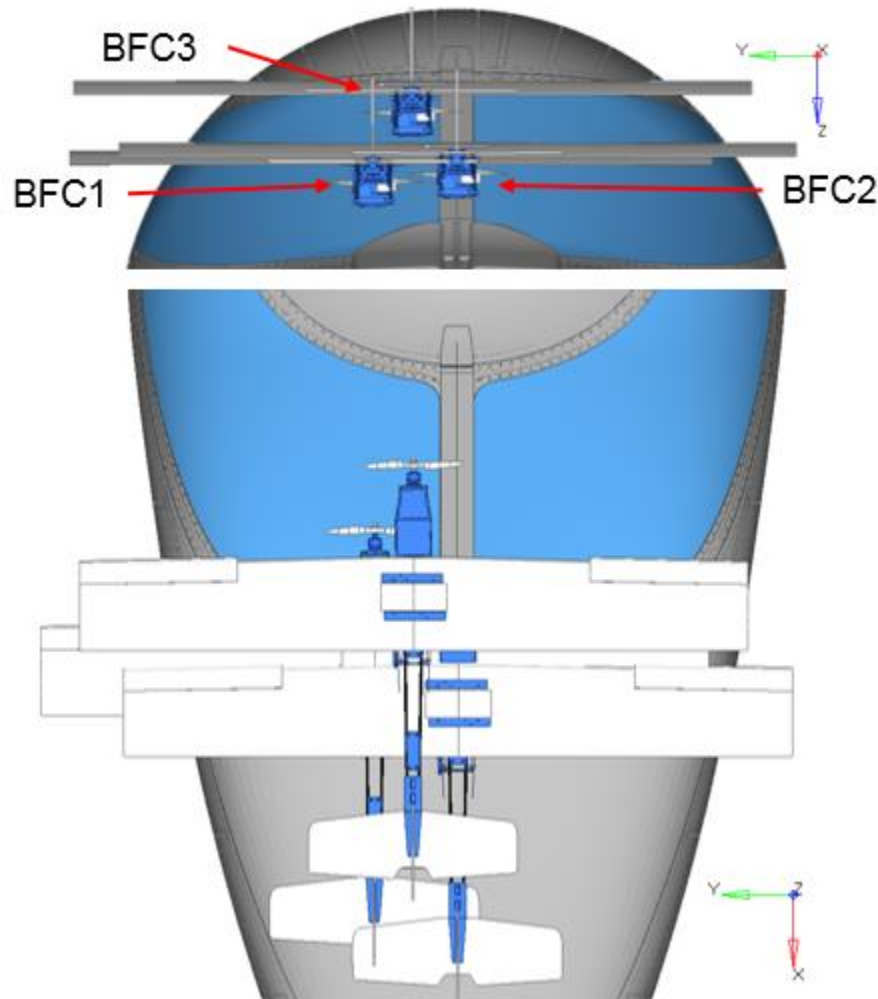


Figure 166. UAS impact locations – Business jet cockpit windshield

An initial velocity of 128.6 m/s (250 knots) along the local x -axis of the aircraft was applied to the simulated UAS. Axial displacements were constrained at all nodes around the perimeter of the fuselage at the aft-most boundary of the cockpit. The following subsections present the analysis results for the three different scenarios.

4.4.4.1 Summary of Results – Business Jet Cockpit Windshield

A summary of the results of the three cases presented in Figure 166 is shown in Figure 167. For each case, the left bar represents a summation of all the different energies involved in the impact event, measured at 10 ms and normalized with the total energy at time zero. Each block indicates the percentage of total energy for each respective type of energy. The right bar specifies the severity level (1-4), as described in section 4.2.1 .

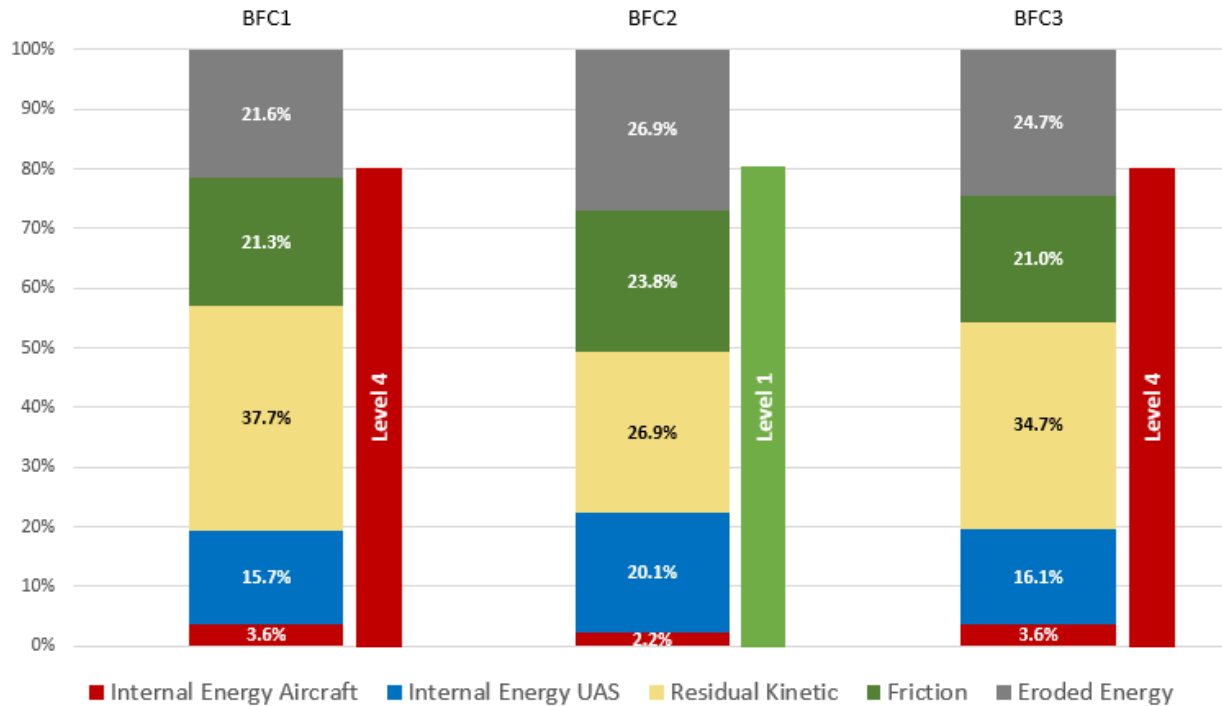


Figure 167. Energy distribution for of business jet horizontal stabilizer cases

Cases BFC1 and BFC3 experienced similar types of critical damage during the impact simulations (Figure 167). Both cases entailed a direct impact to the windshield transparency by the UAS while BFC2 had an impact to the metallic centerpost of the windshield retaining structure. Due to the low angle impact to the transparency (approximately 45°), the UAS was deflected for all three cases without any considerable damage.

4.4.4.2 Critical Case - BFC1

Impact location 1 was chosen based on two conditions: (1) the collision was as perpendicular as possible to the surface and (2) the influence of the centerpost was a relative minimum. Hence, the UAS was located at 1/3 of the distance outboard from the centerpost. The UAS was impacted against the windshield at 128.6 m/s (250 knots) along the local x -axis direction of the aircraft. Figure 168 presents the kinematics of the event. Figure 169 shows the damage caused to the windshield and the internal structure.

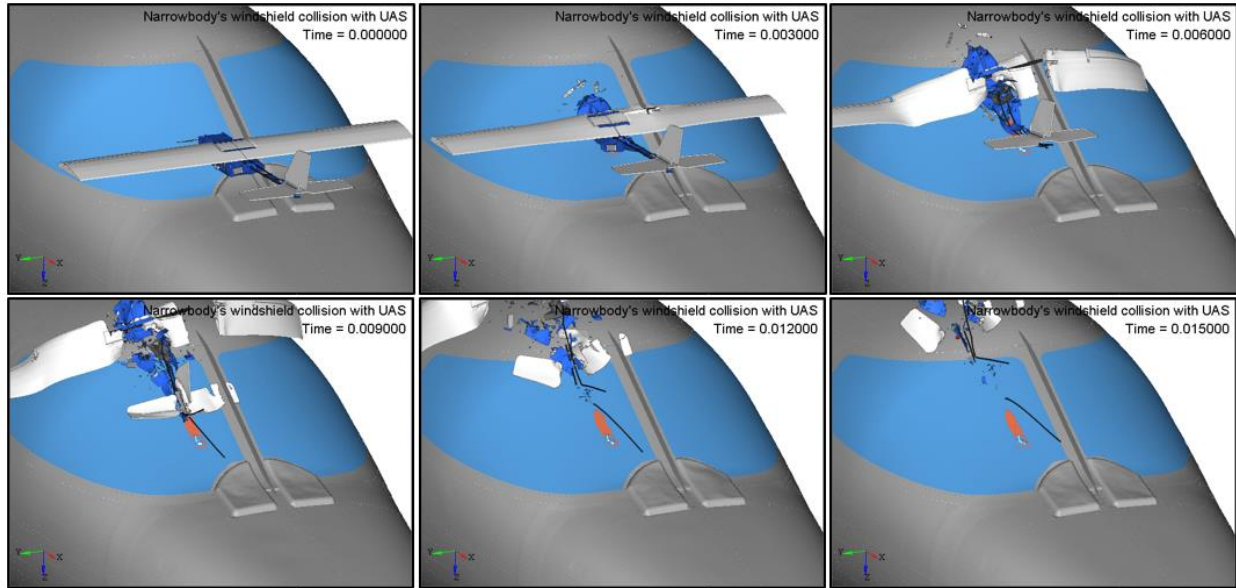


Figure 168. Kinematics of the impact between the business jet windshield and a 1.8 kg (4.0 lb) fixed-wing UAS at 128.6 m/s (250 knots)

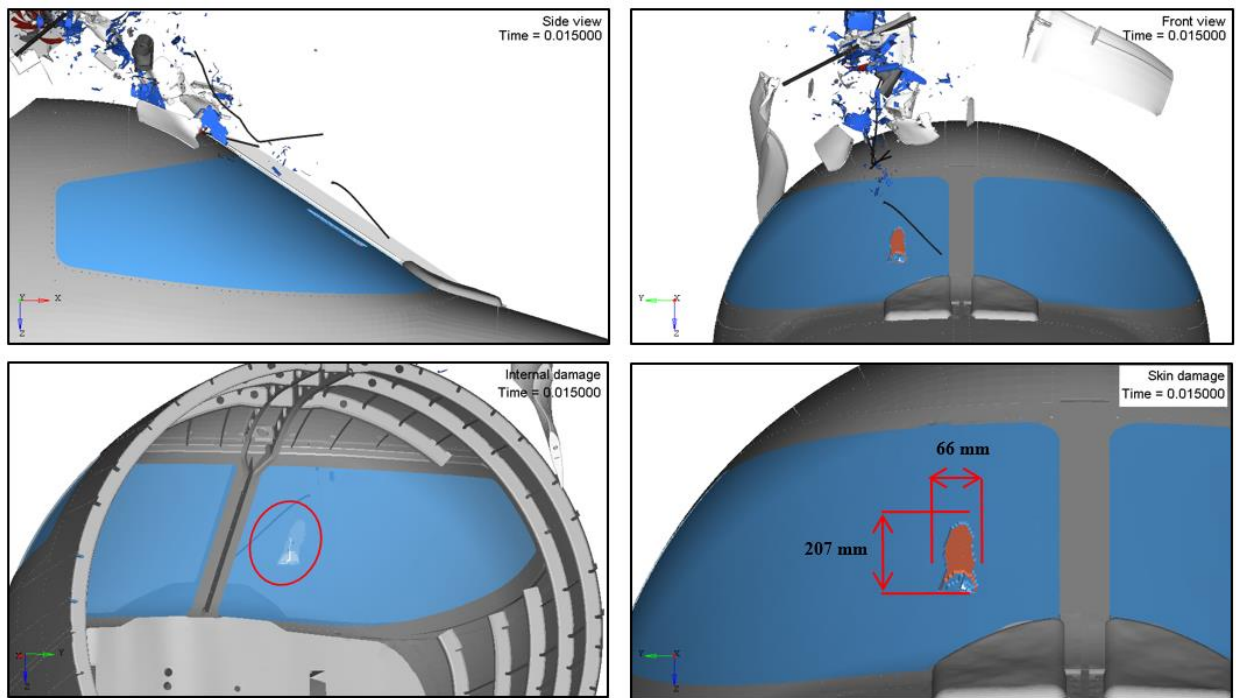


Figure 169. External/internal damage sustained by the business jet windshield impacted at location 1 with a 1.8 kg (4.0 lb) fixed-wing UAS at 128.6 m/s (250 knots)

The UAS impacted the windshield and slid over due to the windshield inclination angle. The outer layer of the transparency sustained a 66 x 207mm² damage zone and two other smaller failures in the middle and innermost layers. The permanent deformation on the windshield is presented on

the bottom right image in Figure 169. Since significant damage of the windshield surface occurred, the severity of the event was categorized as Level 4.

Figure 170 shows the impulse due to the contact force between the UAS and the forward fuselage, as well as the energy balance for both of them. Figure 171 shows the internal energies of the UAS and the forward fuselage parts directly involved in the impact.

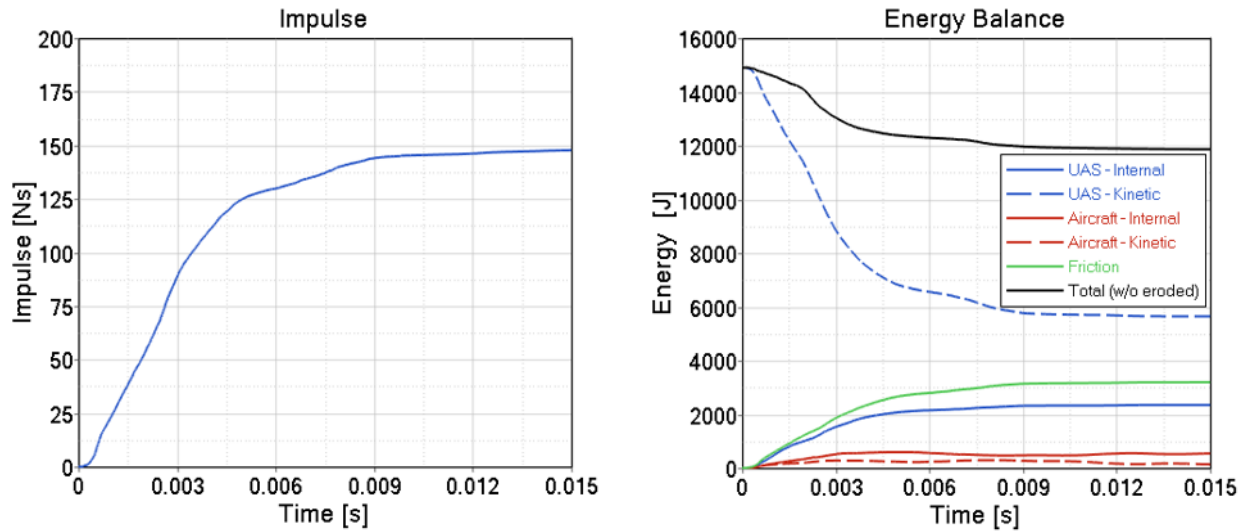


Figure 170. Impulse and energy balance of the impact between a business jet windshield and a 1.8 kg (4.0 lb) fixed-wing UAS at 128.6 m/s (250 knots)

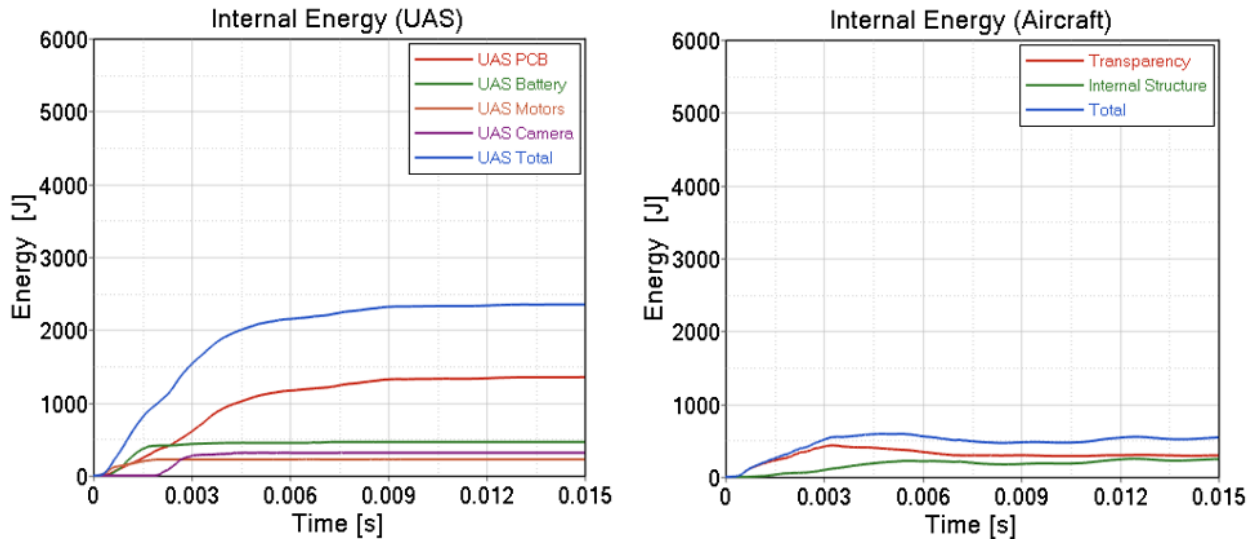


Figure 171. Internal energy per component of the impact between a business jet windshield and a 1.8 kg (4.0 lb) fixed-wing UAS at 128.6 m/s (250 knots)





The energy balance plot includes the UAS and forward fuselage kinetic and internal energies, frictional energy, and total energy for the event. The forward fuselage absorbed 4% of the impact energy, while the UAS absorbed 16%. The energy dissipated by friction reached 21% of the total energy. Due to the oblique angle of the windshield, a substantial fraction of the total energy after impact was residual kinetic energy. In Figure 171, internal energies for the UAS parts and forward fuselage show that the UAS PCBs and transparency absorb the highest amount of internal energies, respectively.

4.5 CONCLUSIONS

Chapter 4 presented the results of a total of 28 baseline simulations of collisions between a 1.8 kg (4.0 lb) fixed-wing UAS and critical areas of NIAR's commercial transport and business jets at 128.6 m/s (250 knots). Worst case scenarios were selected for further studies, presented in chapters 5. and 6. The diagrams in Figure 172 and Figure 173 present levels of severity at each location for both aircraft, respectively. Levels are based on the damage severity description in section 4.2.1 .

From the images, the tail was generally more vulnerable for both aircraft if impacted by the fixed-wing UAS. For the same type of impact, the commercial transport jet was more susceptible to receive critical damage than the business jet. Features such as a greater spacing between ribs or a smaller distance between the leading edge skin and the front spar may increase the chances of a severe collision. The specific design features of the business jet modeled for this project possibly resulted in less damage when compared to the commercial transport jet. Moreover, the windshields of both aircraft sustained relatively less damage after impact of the components investigated.

Based on the results of the simulations presented in this chapter, the impact severity of a midair collision between a 1.8 kg (4.0 lb) fixed-wing UAS with a commercial transport jet or a business jet aircraft is high. This statement is limited to a collision having the characteristics presented in this chapter. A different UAS configuration or mass, other impact velocities or orientations, and other factors may result in different severity levels, as investigated in chapter 5. Furthermore, the level of damage severity for a given impact increased for UAS components with more concentrated masses, parts that utilize dense, stiff materials, and the distribution and alignment of the masses within the UAS as a whole. A comparison between fixed-wing UAS impacts and bird strikes with similar kinetic energies is presented in chapter 6.

Level 1	
Level 2	
Level 3	
Level 4	

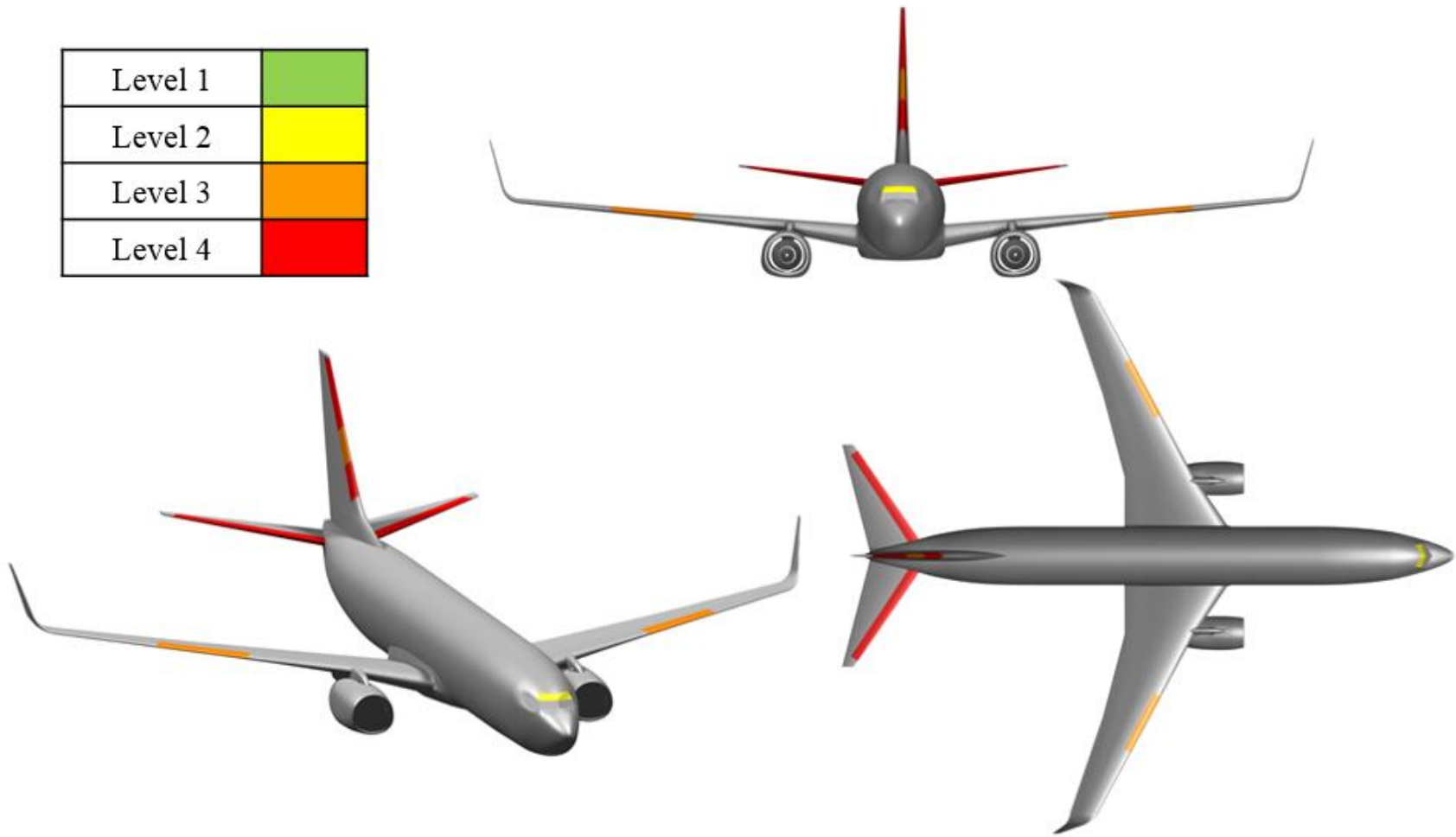


Figure 172. Summary of collision severity levels on commercial transport jet

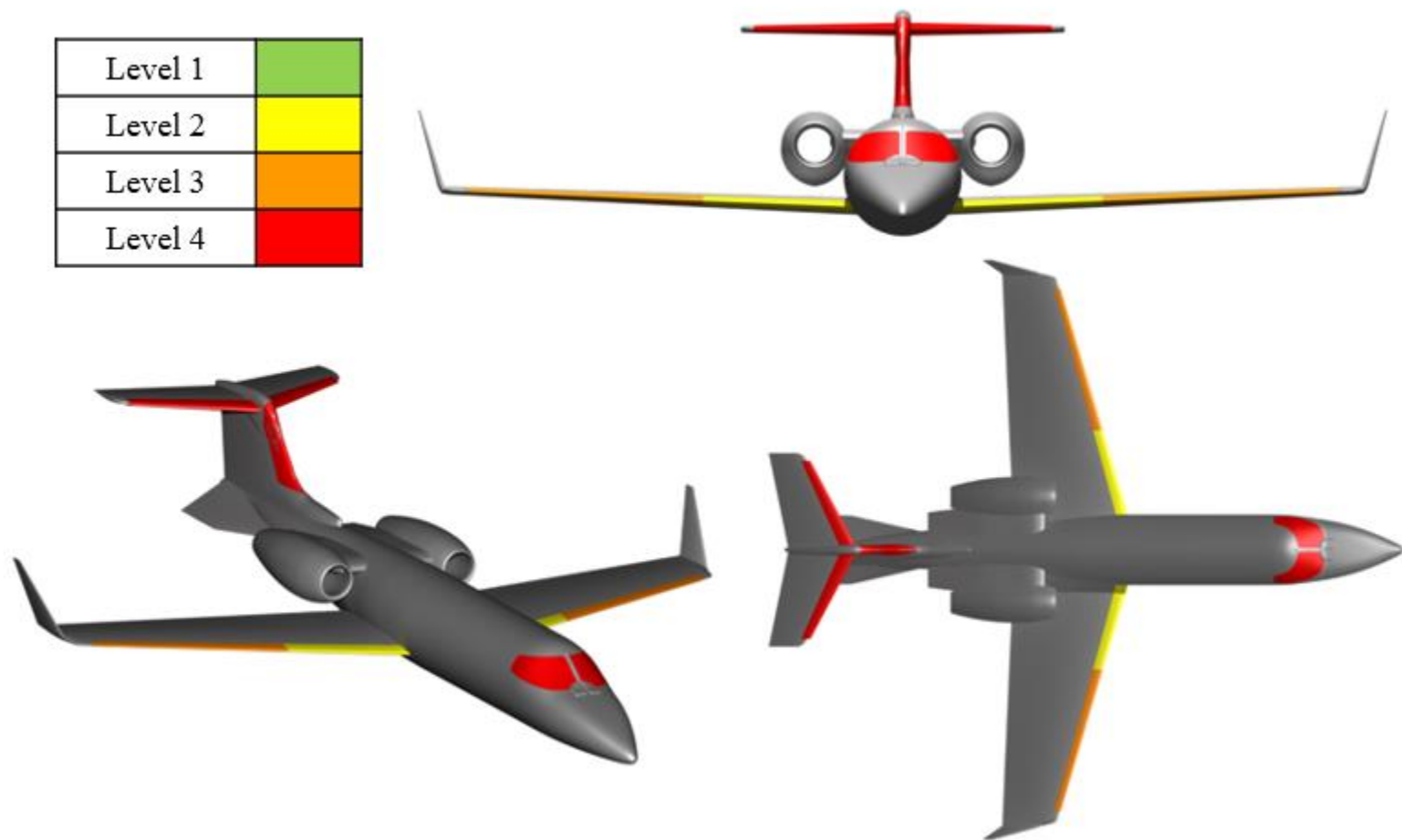


Figure 173. Summary of collision severity levels on business jet

5. KINETIC ENERGY PARAMETRIC STUDIES

5.1 INTRODUCTION

Following the baseline impact simulations discussed in chapter 4. , a parametric study was performed to determine the sensitivity of the FE models to variations in the parameters that define the impact energy: UAS mass and relative impact velocity. The mass of the UAS was scaled from 1.8 kg (4.0 lb) to 3.6 kg (8.0 lb), as described in section 5.2.1 . The velocities chosen for this study, detailed in section 5.3.1 , are representative of the cruise and landing speeds for each aircraft type; 187.8 m/s (365 knots) and 56.7 m/s (110 knots) for the commercial transport jet, 167.2 m/s (325 knots) and 44.8 m/s (87 knots) for the business jet, respectively. The results from these two velocities were compared to the baseline 128.6 m/s (250 knots) simulations discussed in chapter 4. .

5.1.1 Load Case Name Convention

In order to provide a brief label that accurately describes each combination of UAS, aircraft type, target component, and local impact position the following convention was used to name each load case:

The baseline impact conditions were coded using four characters (ABCD)

- A – Distinguishes between Commercial Transport(C) and Business (B) Jets
- B – Distinguishes between UAS type:
 - 1.2 kg (2.7 lb) Quadcopter (Q) or 1.8 kg (4.0 lb) Quadcopter (Qs)
 - 1.8 kg (4.0 lb) -Fixed-Wing (F) or 3.6 kg (8.0 lb) -wingFixed-Wing (Fs)
 - 1.2 kg (2.7 lb) Bird (B2) or 1.8 kg (4.0 lb) Bird (B4)
- C – Distinguishes between impact area:
 - Vertical Stabilizer (V)
 - Horizontal Stabilizer (H)
 - Wing (W)
 - Cockpit Windshield (C)
- D – Distinguishes between impact location (1 through 5)

Example CFV4

- Commercial
- Fixed-Wing
- Vertical Stabilizer
- Impact Location 4

The velocity studies utilized an additional character in the labeling code in order to differentiate between the baseline runs and the variations on the baselines, as follows:

- For baseline runs, use the original code
 - Example CFV4
 - Indicates holding velocity – 128.6 m/s (250 knots)
- For landing velocity cases, add letter “L” after the impact area designation
 - Example CFVL4
 - Commercial transport jet landing velocity – 56.7 m/s (110 knots)
 - Example BFVL2

- Business jet landing velocity – 44.8 m/s (87 knots)
- For cruise velocity cases, add letter “C” after the impact area designation
 - Example CFVC4
 - Commercial transport jet cruise velocity – 187.8 m/s (365 knots)
 - Example BFVC2
 - Business jet cruise velocity – 167.2 m/s (325 knots)

5.2 MASS SENSITIVITY STUDY

In this study, the influence of UAS mass on the severity of a mid-air collision was investigated. This study was limited to the baseline 1.8 kg (4.0 lb) UAS and one scaled-up 3.6 kg (8.0 lb) version of the UAS. These masses later allowed a comparison with a bird strike of standard mass as defined in the Airworthiness Requirements and presented in chapter 6. In future work, a more extensive selection of masses (see section 6.3.2) can be used to better understand the influence of UAS mass, which will allow establishing thresholds of severity.

Table 21 presents the simulation matrix with all the mass comparisons studied in this chapter. Eight different simulations of the scaled-up 3.6 kg (8.0 lb) UAS were performed with identical initial conditions as the critical load cases presented in chapter 4. These results for the scaled-up UAS were compared to the baseline UAS results discussed in chapter 4. .

Table 23. Load case definition

	Commercial Transport Jet				Business Jet			
	Vertical Stabilizer	Horizontal Stabilizer	Wing Leading Edge	Windshield	Vertical Stabilizer	Horizontal Stabilizer	Wing Leading Edge	Windshield
Baseline 1.8 kg (4.0 lb)	CFV2	CFH2	CFW3	CFC1	BFV1	BFH1	BFW2	BFC1
Scaled 3.6 kg (8.0 lb)	CFsV2	CFsH2	CFsW3	CFsC1	BFsV1	BFsH1	BFsW2	BFsC1

The following section presents the methodology followed to scale the UAS, the summary with all the results of the simulations completed, and some examples of observed differences in damage.

5.2.1 UAS Scaling Methodology

In order to perform simulations with a greater mass, a scaled version of the verified 1.8 kg (4.0 lb) fixed-wing UAS model was produced. The dimensions of solid FEs were increased by a factor of

roughly 1.3. The in-plane dimensions for all shell FEs were increased by the same factor; the thickness of PCBs, carbon/epoxy composites, etc. remained unchanged. In essence, the mass of the 1.3 scale UAS model (3.6 kg/8.0 lb) was double that of the original UAS model. The contact definitions in the scaled model were modified to maintain proper offset distances between master surfaces and slave nodes after scaling. In the scaling process, the aerodynamic properties of the scaled model were not considered.

The 1.3 scale UAS FE model was subjected to the same rigorous stability checks employed on the baseline component and full UAS models. An assessment of the total, kinetic, internal, hourglass, and contact energies, as well as the energy ratio was performed for a simulated 1.3 scale UAS impact to the NIAR test frame at 128.6 m/s. Similar assessments were performed for 128.6 m/s 1.3 scale UAS impacts to a rigid NIAR test frame and a rigid knife-edge fixed plate. Similar to the results obtained for the baseline model, the stability assessments suggested that the given 1.3 scale UAS/target models are relatively robust and stable.

Figure 174 contains images of the original UAS FE model as well as a 1.3 scale version. These models can be used to perform impact severity assessments for UASs with different masses akin to those used to establish 1.8 kg (4.0 lb) and 3.6 kg (8.0 lb) bird strike impact certification criteria. UAS model may be similarly scaled down in size to probe UAS impacts leading to damage below some desired threshold value.

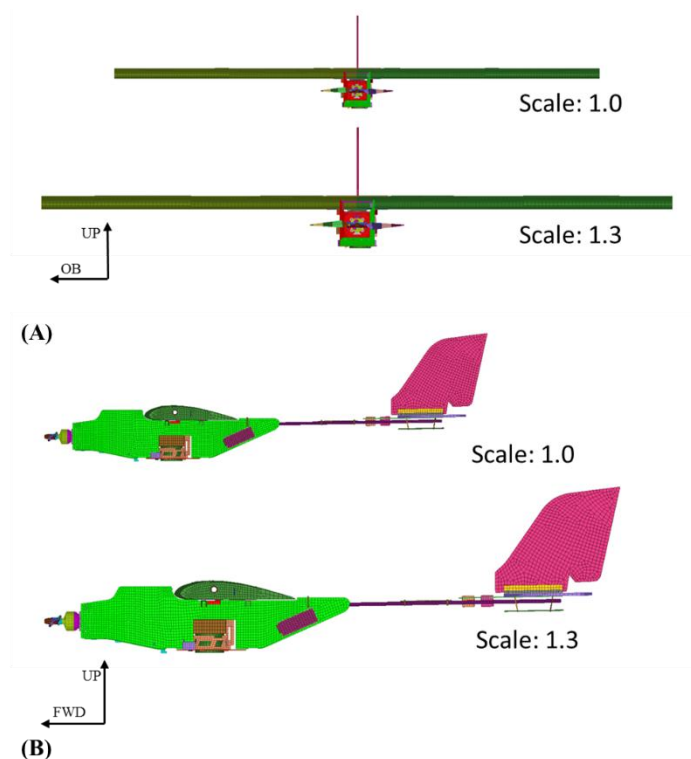


Figure 174. 1.0 scale and 1.3 scale fixed-wing UAS FE models: (a) front view and (b) side view

5.2.2 Simulation Results

Table 24 presents the levels of severity of the impacts with the scaled UAS and the respective baseline simulations. Results were compared to the critical cases outlined in chapter 4. and are presented in APPENDIX D.

Table 24. Mass scaled impact simulation results

	Commercial Transport Jet				Business Jet			
	Vertical Stabilizer	Horizontal Stabilizer	Wing	Windshield	Vertical Stabilizer	Horizontal Stabilizer	Wing	Windshield
Fixed-wing UAS Baseline 1.8 kg (4.0 lb)	Level 4	Level 4	Level 3	Level 2	Level 4	Level 4	Level 3	Level 4
Fixed-wing UAS Up-scaled 3.6 kg (8.0 lb)	Level 4	Level 4	Level 4	Level 3	Level 4	Level 4	Level 3	Level 4

For all cases, the damage severity level for the scaled-up UAS impacts was equal or greater than that of the baseline. For the cases in which the damage severity level was equal, the damage was more prevalent and was distributed among more components.

5.2.2.1 Commercial Jet

Figure 175 illustrates the damage sustained by the horizontal stabilizer after impact of a 1.8 kg (4.0 lb) and a 3.6 kg (8.0 lb) fixed-wing UAS. This case was selected to illustrate a situation in which the level of severity resulted to be the same for the baseline and scaled-up simulations. The top images show the contour plot of the effective plastic strain 10 ms after impact. Only effective plastic strains greater than 0.001 are shown on the plots; consequently, any translucent area would be deformed in the elastic region of the material with no permanent deformation. The lower set of images in Figure 175 was limited to the front spar. The skin sustained a similar amount of damage in both cases. However, the perforation size on the web of the front spar is greater for the case with the higher mass UAS. Even though both cases displayed level 4 damage, the extent of the permanent deformation and actual failure of the material was greater in the collision with the scaled-up UAS.

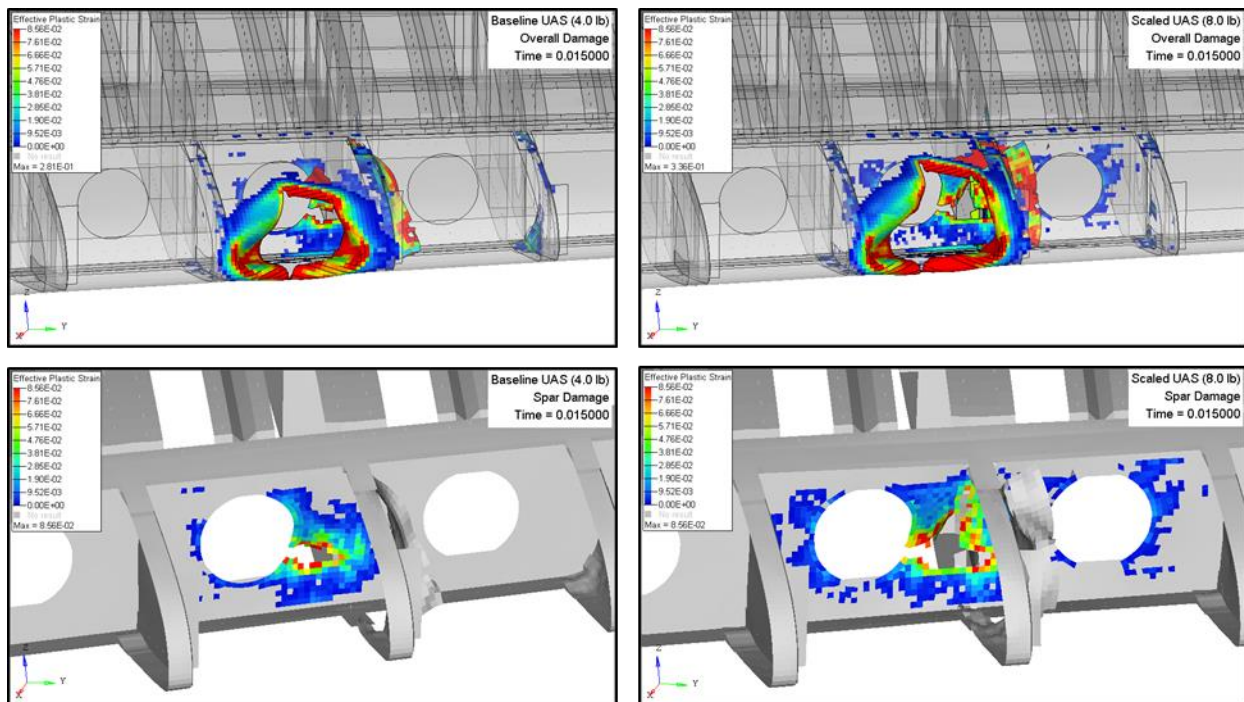


Figure 175. Comparison of skin and internal damage produced by a 1.8/3.6 kg (4.0/8.0 lb) UAS after impact with a commercial transport jet horizontal stabilizer

Similarly, Figure 176 presents the comparison of the damage sustained by the windshield. Both images display the contour plot of the effective plastic strain of the inner layer of the transparency after impact. The inner layer was selected for the plot because it sustained more deformation and the only one that fractured.

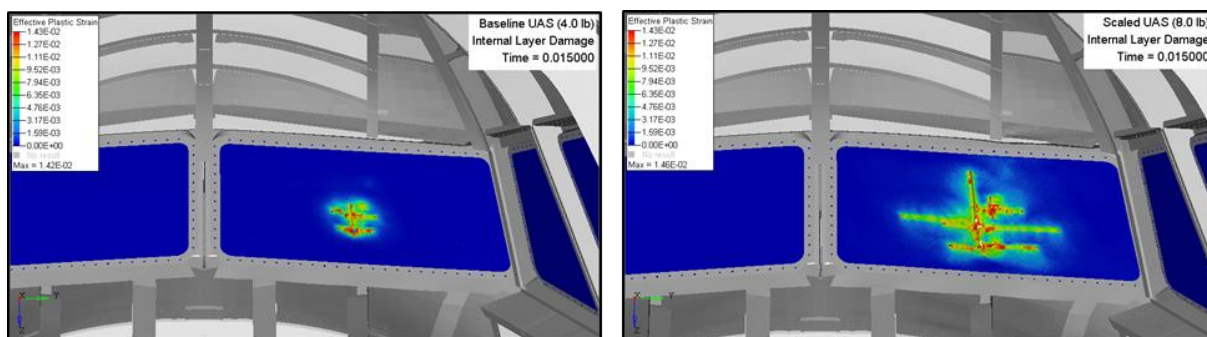


Figure 176. Comparison of the effective plastic deformation sustained by the inner layer of the commercial transport jet transparency after impact with a 1.8/3.6 kg (4.0/8.0 lb) UAS

From a comparison of both images in Figure 176, the impact of a 3.6 kg (8.0 lb) UAS created a greater damage area on the windshield when compared with a 1.8 kg (4.0 lb) UAS. The 1.8 kg (4.0 lb) UAS impact created a failure on the inner layer of the transparency. Hence, the severity level increased from 2 to 3.

5.2.2.2 Business Jet

Similarly, Figure 177 presents the resultant damage in the vertical stabilizer of the business jet aircraft due to impact of a 1.8 kg (4.0 lb) and a 3.6 kg (8.0 lb) UAS. The top images show the contour plot of the effective plastic strain 15 ms after impact. Only plastic strains greater than 0.001 are shown on the plots; consequently, any translucent area would be deformed in the elastic region of the material with no permanent deformation. The lower image portrays a similar plot without the skin so a comparison of the damage to the primary structure can be established.

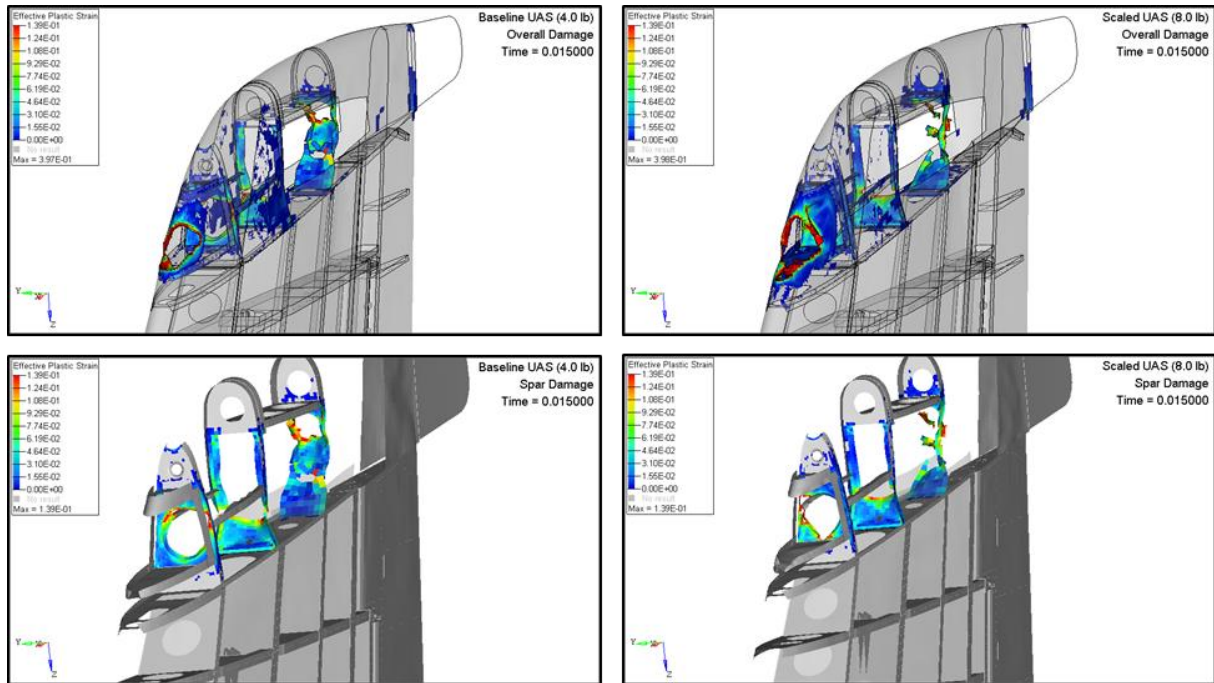


Figure 177. Damage comparison in business jet vertical stabilizer on impact with 1.8/3.6 kg UAS

It can be seen that the spar end members sustain critical damage and severe permanent deformation after impact of both the 1.8 kg (4.0 lb) UAS and 3.6 kg (8.0 lb) UAS. Consequently, the level of severity was considered to be level 4 for both cases even though the scaled-up UAS created relatively more damage.

5.3 VELOCITY PARAMETRIC STUDY

The impact velocity used for the baseline simulations is representative of the airspeed of an aircraft while in a holding pattern prior to landing. In order to characterize the potential damage severity of a collision occurring at alternate velocities, two additional velocities were selected from the literature [52][53][54] to represent a lower energy impact as well as a higher energy scenario. The selections represent a practical minimum energy level collision that might occur during landing and an effective maximum energy level indicative of an impact near cruise conditions. The mass of the UAS remained constant (1.8 kg (4.0 lb)) for this study.

Note that the maximum viable velocity is limited by the increasingly small timestep required to obtain a converged solution. In order to investigate higher energy interactions, the contact algorithms, failure criteria, and energy control definitions may need to be re-evaluated. Moreover, additional higher velocity component validation tests may become necessary. In all cases, the kinematics and energy distribution of the simulations were reviewed to determine if the results were feasible and the solution was stable. If so, damage severity levels were compared to their baseline counterparts.

5.3.1 Velocity Determination

The velocities used in this study were selected from a spectrum of minimum landing and cruise conditions that were available for a commercial transport jet and a business jet similar to the models being used. The simulated impact conditions and load case labels for the commercial transport and business jets are shown in Table 25 and Table 26, respectively.

Table 25. Commercial transport jet velocity variation load cases

	Commercial Transport Jet			
	Vertical Stabilizer	Horizontal Stabilizer	Wing Leading Edge	Cockpit Windshield
Holding – 128.6 m/s (250 knots)	CFV2	CFH2	CFW3	CFC1
Landing – 56.7 m/s (110 knots)	CFVL2	CFHL2	CFWL3	CFCL1
Cruise – 187.8 m/s (365 knots)	CFVC2	CFHC2	CFWC3	CFCC1

Table 26. Business jet velocity variation load cases

	Business Jet			
	Vertical Stabilizer	Horizontal Stabilizer	Wing Leading Edge	Cockpit Windshield
Holding – 128.6 m/s (250 knots)	BFV1	BFH1	BFW2	BFC1
Landing – 44.8 m/s (87 knots)	BFVL1	BFHL1	BFWL2	BFCL1
Cruise – 167.2 m/s (325 knots)	BFVC1	BFHC1	BFWC2	BFCC1

5.3.2 Simulation Results

The four aircraft critical impact locations for each aircraft studied in chapter 4. were used to perform sixteen additional simulations with varied impact velocities. Results are compared to the critical cases outlined in chapter 4. and presented in APPENDIX E. Table 27 presents the levels of severity of the impacts with the UAS with the corresponding levels for the respective baseline simulations. These results are discussed in the following sections.

Table 27. Velocity Impact Simulation Results

	Commercial Transport Jet				Business Jet			
	Vertical Stabilizer	Horizontal Stabilizer	Wing	Windshield	Vertical Stabilizer	Horizontal Stabilizer	Wing	Windshield
Landing Velocity (110/87 knots)	Level 2	Level 2	Level 2	Level 1	Level 2	Level 2	Level 2	Level 1
Holding Velocity (250/250 knots)	Level 4	Level 4	Level 3	Level 2	Level 4	Level 4	Level 3	Level 4
Cruise Velocity (365/325 knots)	Level 4	Level 4	Level 4	Level 3	Level 4	Level 4	Level 3	Level 4

5.3.2.1 Commercial Transport Jet

Typical results for a 1.8 kg (4.0 lb) UAS simulated impact to the commercial transport jet are presented in this section. The remaining results and comparisons can be found in Appendix E.1 . In general, the increased velocity cases imparted more visible damage to more components while the reduced velocity impacts created noticeably less damage than the baseline.

As shown in Figure 178, the effective plastic strain of the windshield transparency increased in relation to the increase in impact velocity. The effective plastic strain is plotted as a spectrum from blue to red indicating yield strains up to the material failure strains. The contour plots show that the low velocity case (left) and baseline case (middle) had localized regions of the windshield with plastic strain but that the increased velocity case (right) had a noticeably higher effective plastic strain as well as material failure.

The damage to the wing leading edge is shown in Figure 179 for 1.8 kg (4.0 lb) fixed-wing UAS impacts at three velocities. The three images in the upper half of Figure 179 show effective plastic strains (strains above the material yield limit) while the three lower images show effective plastic strains for only the forward spar. The leading edge of the commercial transport jet's wing showed an increase in damage severity due to the increased impact energy for the cruise velocity case, as seen in the right-hand side of Figure 179. The UAS penetrated through the skin and immediate substructure, allowing it to impact the forward spar. The spar web deformed and ruptured as shown

in the bottom right-hand plot. This damage is considered to be level 4 severity. The landing velocity case (left) showed minimal damage beyond the deformation of the leading edge skin.

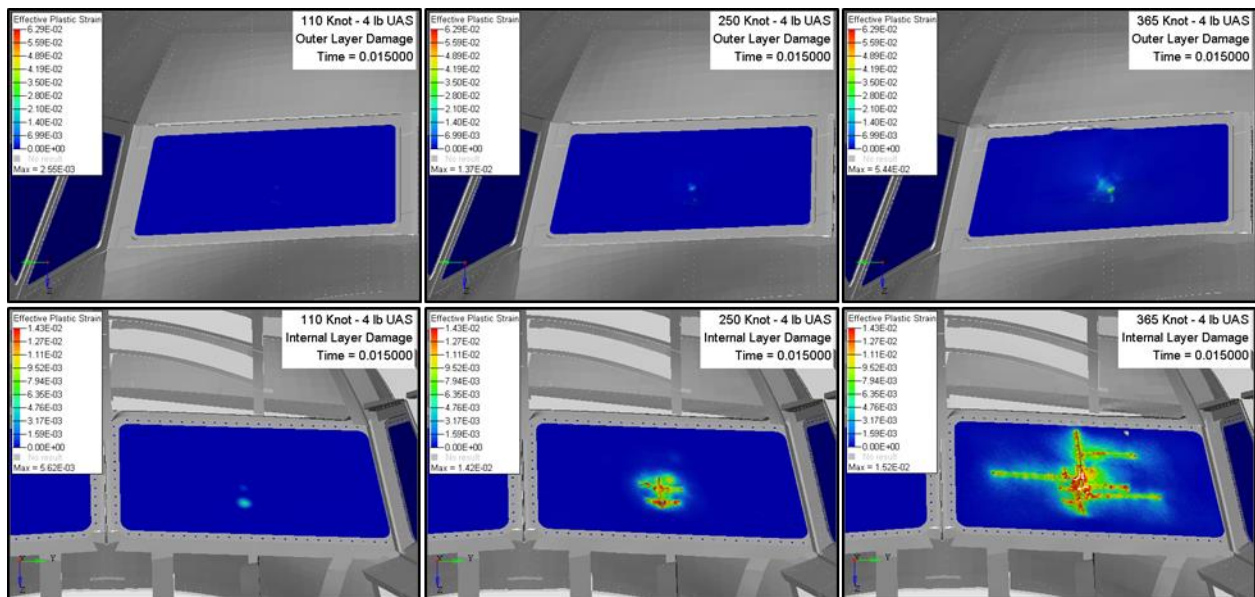


Figure 178. Comparison of windshield damage for CFCL1, CFC1, and CFCC1 – 56.7/128.6/187.8 m/s (110/250/365 knots)

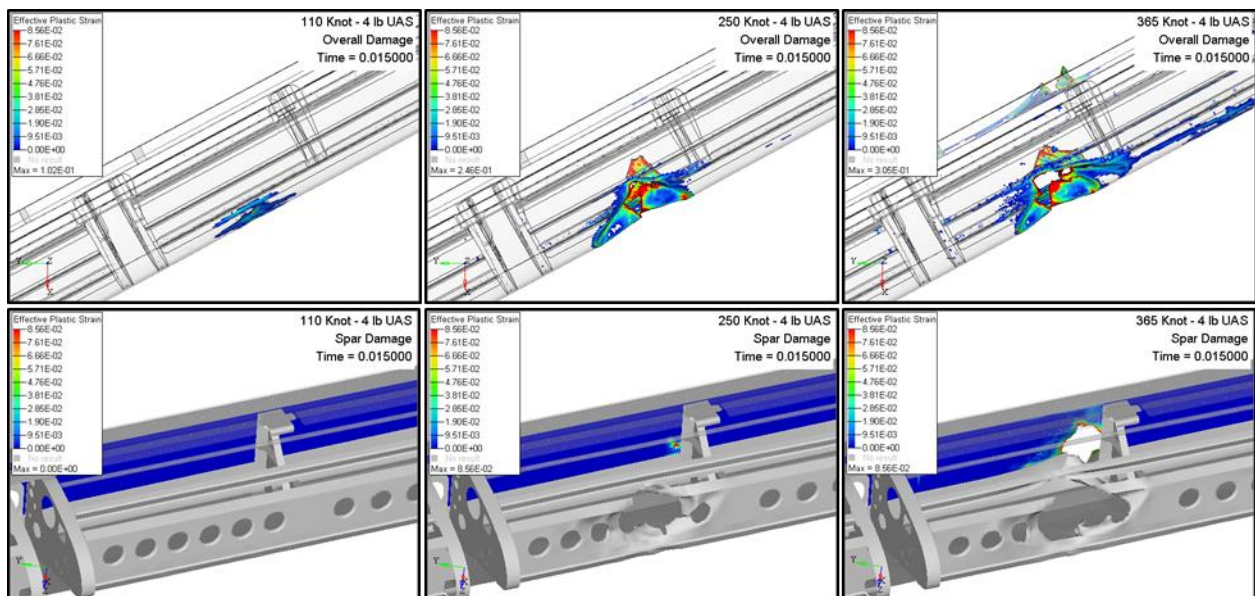


Figure 179. Comparison of wing leading edge damage for CFWL3, CFW3, and CFWC3 – 56.7/128.6/187.8 m/s (110/250/365 knots)

5.3.2.2 Business Jet

Typical results for a 1.8 kg (4.0 lb) UAS simulated impact to the business jet are presented in this section. The remaining results and comparisons can be found in Appendix E.2. In general, the increased velocity cases imparted more visible damage to more components while the reduced velocity impact created noticeably less damage than the baseline.

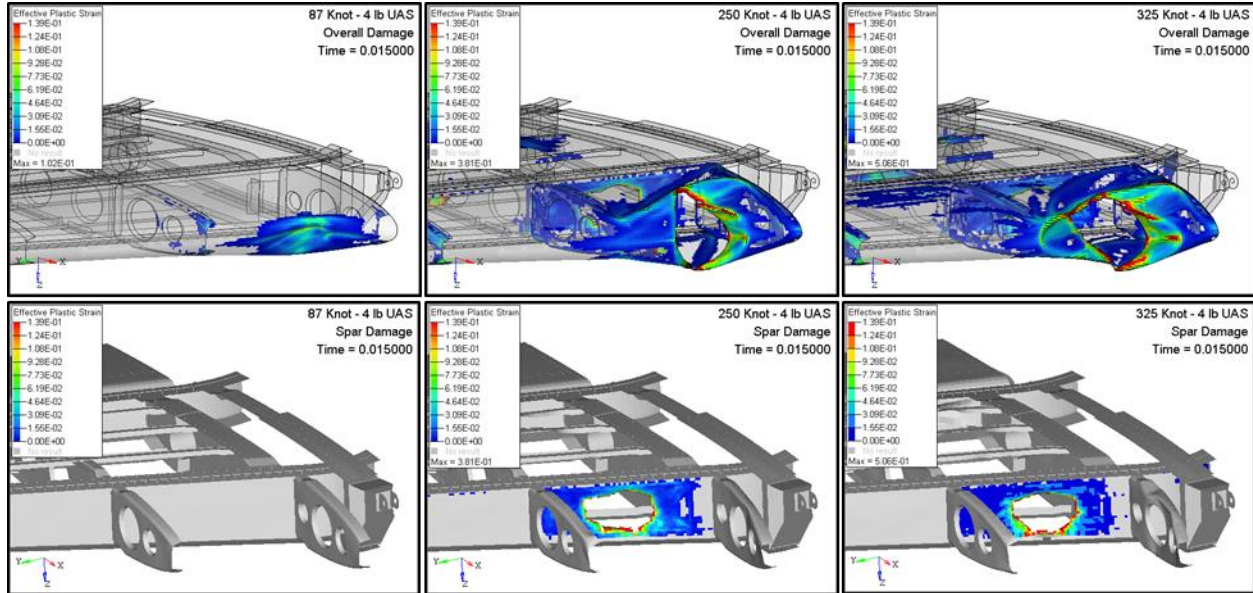


Figure 180. Comparison of horizontal stabilizer damage for BFHL1, BFH1, and BFHC1 – 44.8/128.6/167.2 m/s (87/250/325 knots)

The effective plastic strain after impact to the horizontal stabilizer is plotted in Figure 180 for three different velocities. Gray coloration corresponds to the elements that are below the yield strain limit for the material and a spectrum from blue to red indicates yield strains up to the material failure strains. The effective plastic strain plots in the upper half of Figure 180 show the predicted effective plastic strain for all of the components whereas the lower half shows only the effective plastic strain in the forward spar. The high energy cruise velocity case (right) was distinguished from the lower energy simulations (left and center) by the extensive internal damage caused by the UAS penetrating through the leading edge and forward spar. As shown in Figure 180, the effective plastic strain due to an impact to the horizontal stabilizer increased with increasing velocity. The aft spar of the horizontal stabilizer was also damaged but was not perforated.

5.4 CONCLUSIONS

In this study, the fixed-wing UAS mass and relative impact velocity were varied in order to explore differences in the impact energy of a collision. The kinetic energy of a midair collision between a fixed-wing UAS and two common manned aircraft: a commercial transport jet and a business jet. The simulation results were compared to their baseline impact counterparts and damage severity trends were presented.

5.4.1 Mass

The UAS was scaled from 1.8 kg (4.0 lb) to a final value of 3.6 kg (8.0 lb) in order to assess the potential increase in damage severity imparted by a larger UAS than was characterized in the baseline simulations of chapter 4. The mass of the UAS in this parametric study contributed to a linear increase in the kinetic energy of the collision. The increased kinetic energy resulted in increased damage severity levels in two of the eight simulations and more extensive damage for the remaining cases, in which the damage level classification remained the same.

5.4.2 Velocity

The velocity of the eight critical baseline simulations (four for each aircraft) was varied to determine impact reactions at typical aircraft landing speeds as well as in the range of cruise velocities in order to assess the minimum and maximum damage that can be expected for similar midair collisions. The landing velocity considered for the commercial and business jets was 56.7 m/s (110 knots) and 44.8 m/s (87 knots), respectively, and the cruise velocity was 187.8 m/s (365 knots) and 167.2 m/s (325 knots), respectively. An impact velocity increase (or decrease) in this study contributed to a quadratic increase (or decrease) in the total impact energy. The damage severity levels increased for two of the eight cruise velocity cases and the damage caused was more extensive in the remaining cases where the level remained the same. Similarly, the landing velocity cases showed decreased severity levels in all of the eight cases studied (all equal or below level 2).

Not surprisingly, the velocity component of the impact energy contributes to a greater amount of damage compared to the mass of the UAS. Moreover, increases in either parameter correlate to incrementally greater amounts of aircraft damage both in terms of severity and extent.

5.4.3 Future Work

These results indicate that a minimum damage threshold could be near the landing speed of a typical aircraft for an impact with a 1.8 kg (4.0 lb) fixed-wing UAS. The spectrum of damage has proven to be highly variable for greater velocities and masses. In order to determine acceptable thresholds or categories for each parameter, it is recommended to perform additional studies that account for a finer gradation of masses and velocities that may be possible for the UAS and aircraft discussed in this investigation.

6. UAS IMPACT COMPARISON TO EQUIVALENT BIRD STRIKES

A parametric study was performed to determine if a mid-air collision with a fixed-wing UAS is comparable to a bird strike with an equivalent impact energy. The four critical baseline simulations for each aircraft (chapter 4.) were used as a basis for comparing and contrasting the impact kinematics, energetics, and damage severity associated with soft-bodied projectiles such as birds.

6.1 BIRD STRIKE REQUIREMENTS

The current regulations regarding bird strike are summarized as follows [56] [57]:

- FAA’s *14 CFR Part 25.517* or EASA’s *CS-25.631*
 - The airplane must be capable of successfully completing a flight during which likely structural damage occurs as a result of an impact with a 4-pound bird when the velocity of the airplane relative to the bird along the airplane's flight path is equal to V_c at sea level or $0.85V_c$ at 8,000 feet, whichever is more critical.
 - The damaged structure must be able to withstand the static loads (considered as ultimate loads) which are reasonably expected to occur on the flight. Dynamic effects on these static loads need not be considered.
- FAA’s *14 CFR Part 25.631*
 - The empennage structure must be designed to assure capability of continued safe flight and landing of the airplane after impact with an 8-pound bird when the velocity of the airplane (relative to the bird along the airplane's flight path) is equal to V_C at sea level, selected under §25.335(a).
- FAA’s *14 CFR Part 25.775* and EASA’s *CS-25.775*
 - Windshield and supporting structure must withstand with no penetration the bird impact conditions specified in 25.631.
- FAA’s *14 CFR Part 23.775* and EASA’s *CS-23.775*
 - GA Aircraft are required to demonstrate single bird impact resistance of up to 0.91 kg at maximum approach flap speed and at least one pane with sufficient forward vision remaining to allow continued safe flight.

6.2 COMPARISON STUDY

In order to determine any possible discrepancies between bird strikes and fixed-wing UAS-aircraft midair collisions, a study was performed for each of the critical cases identified in chapter 4. . The fixed-wing UAS was replaced with a simulated gelatin bird of equivalent mass. The NIAR has previously conducted numerous simulations of bird strike events and compared the results with physical testing utilizing the gelatin bird substitutes [41]. Smooth Particle Hydrodynamics (SPH) [26] nodes were used to represent the gelatin bird models. The bird substitute is modeled as a cylinder having a rounded front end. The kinematics of the substitute bird correlates well with the impact behavior observed in bird strike testing and simulations. In each bird strike simulation, the boundary and initial conditions used in the fixed-wing UAS critical baseline cases were applied to the bird and aircraft target region to represent a direct replacement of the UAS projectile with the bird substitute.

Table 28 presents the simulation matrix with all the bird strike comparisons studied in this chapter. 1.8 kg (4.0 lb) and 3.6 kg (8.0 lb) bird FE models were used in eight and six different simulations, respectively, with identical initial and boundary conditions as the critical load cases presented in chapter 4. . These simulations were compared with the simulations presented in chapters 4. and 5. . The following section summarizes all the simulation results and some representative examples of observed differences in damage.

Table 28. Load case definition

	Commercial Transport Jet				Business Jet			
	Vertical Stabi- lizer	Horizontal Stabilizer	Wing Leading Edge	Windshield	Vertical Stabi- lizer	Horizontal Stabilizer	Wing Leading Edge	Windshield
Baseline UAS 1.8 kg (4.0 lb)	CFV1	CFH2	CFW3	CFC1	BFV3	BFH1	BFW2	BFC1
1.8 kg (4.0 lb) Bird	CB4V1	CB4H2	CB4W3	CB4C1	BB4V3	BB4H1	BB4W2	BB4C1
Scaled UAS 3.6 kg (8.0 lb)	CFsV1	CFsH2	CFsW3	CFsC1	BFsV3	BFsH1	BFsW2	BFsC1
3.6 kg (8.0 lb) Bird	CB8V1	CB8H2	N/A	N/A	BB8V3	BB8H1	N/A	N/A

6.2.1 1.8 kg (4.0 lb) Bird – Simulation Results

The four aircraft regions for each aircraft studied in chapter 4. were selected to perform a total eight simulations with a 1.8 kg (4.0 lb) bird FE model. Results were compared to those for the

critical cases outlined in chapter 4. and are presented in Appendix E. Table 29 presents the impact severity levels for the scaled UAS with respect to the corresponding baseline simulations.

Table 29. UAS and bird impact simulation results

	Commercial Transport Jet				Business Jet			
	Vertical Stabilizer	Horizontal Stabilizer	Wing	Windshield	Vertical Stabilizer	Horizontal Stabilizer	Wing	Windshield
Fixed-Wing UAS Baseline 1.8 kg (4.0 lb)	Level 4	Level 4	Level 3	Level 2	Level 4	Level 4	Level 3	Level 4
Bird 1.8 kg (4.0 lb)	Level 3	Level 2	Level 2	Level 2	Level 2	Level 2	Level 2	Level 1

For all cases the fixed-wing UAS created equal or more damage than the corresponding bird. The cases involving the horizontal stabilizer, wing, and windshield of the commercial transport jet and the vertical stabilizer, wing and windshield of the business jet demonstrated a reduction in the level of severity when impacted by the simulated bird as opposed to the UAS model.

6.2.1.1 Commercial Transport Jet

Typical results for simulated 1.8 kg (4.0 lb) UAS and bird strike impacts to the commercial transport jet are presented in this section. The remaining impact simulation results can be found in Appendix E. The following sections detail the impact characteristics of each projectile with images showing the resultant damage and discussion of the associated damage mechanisms.

Figure 181 depicts the kinematics of the simulated airborne collisions involving the horizontal stabilizer of a commercial transport jet, a 1.8 kg (4.0 lb) UAS in the upper half of the figure and a 1.8 kg (4.0 lb) bird in the lower half. The idealized bird impacted the leading edge of the horizontal stabilizer; the mass of the bird was distributed throughout the impact region. This tendency is similar to a fluid flow in that the mass is able to follow the path of least resistance and to deflect away from the solid boundary of the aircraft. In contrast, the UAS impact resulted in highly localized deformation/failure in the impact region and generally did not conform to the contour of the leading edge. The kinematics for the remaining cases are similar to that of Figure 181 and can be found in Appendix E.

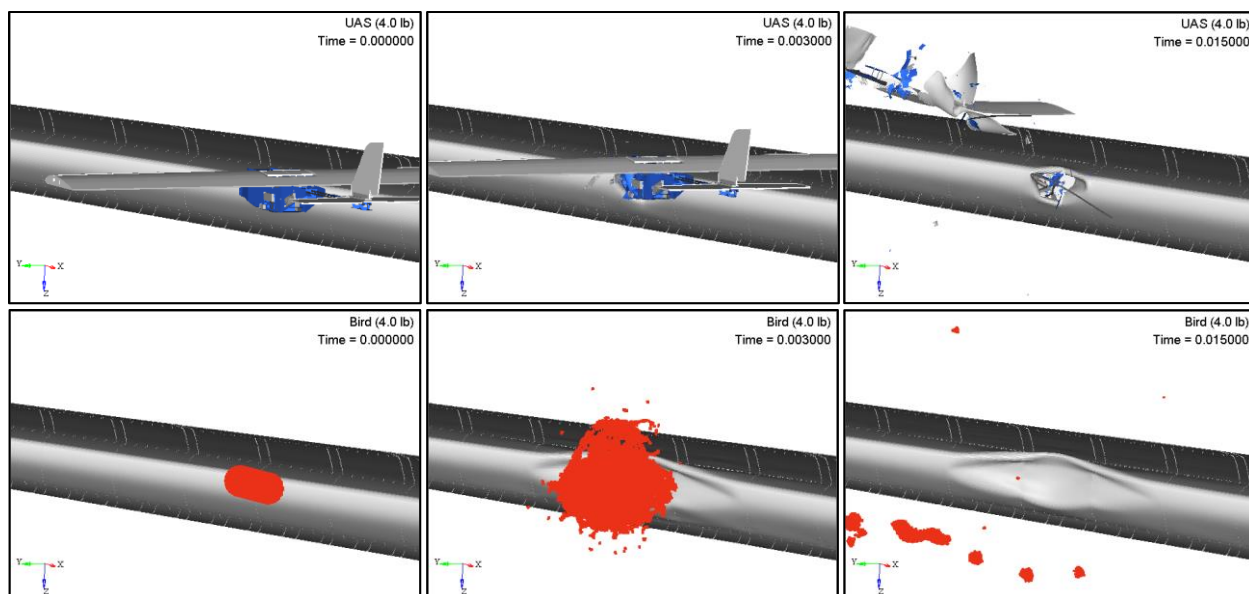


Figure 181. Kinematics of a commercial transport jet horizontal stabilizer impacted by an UAS (top) and a bird (bottom), of 1.8 kg (4.0 lb) – CFH2 vs. CB4H2

Figure 182 illustrates the damage sustained by the horizontal stabilizer of a commercial transport jet after impact with a 1.8 kg (4.0 lb) UAS, on the left-hand side of the figure, and a 1.8 kg (4.0 lb) bird on the right.

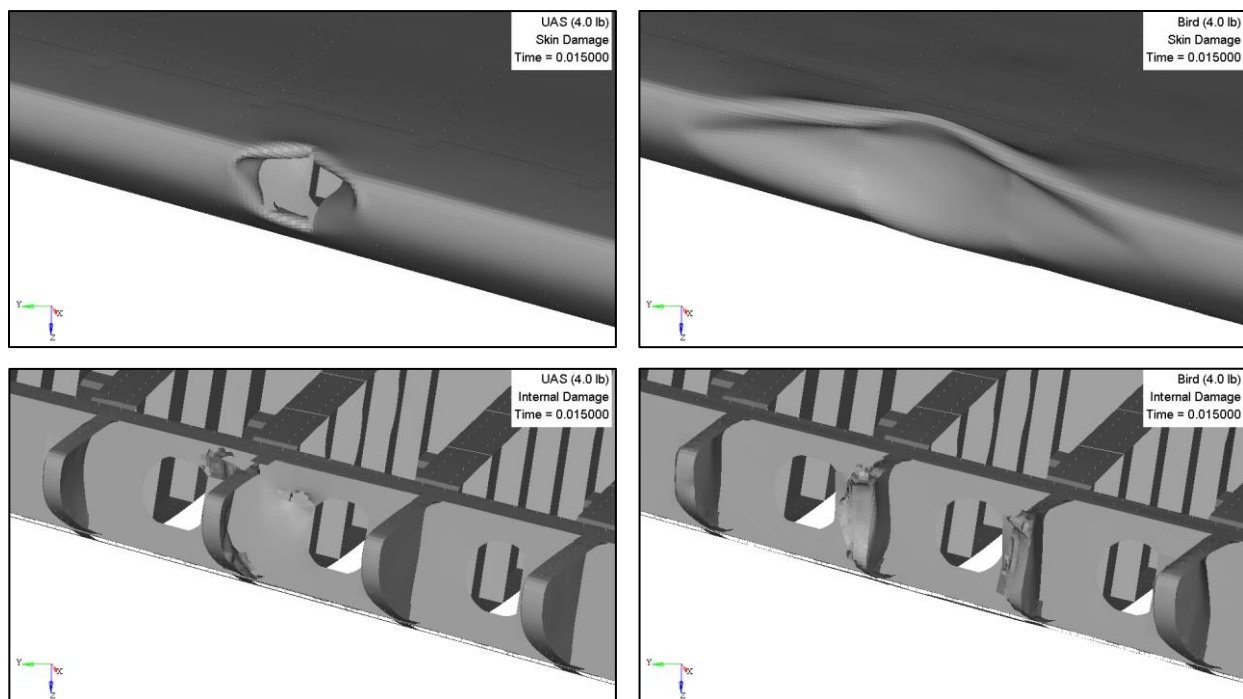


Figure 182. Comparison of damage on a commercial transport jet horizontal stabilizer, produced by a 1.8 kg (4.0 lb) UAS (left) and bird (right) impact at 128.6 m/s (250 knots)

The simulated bird strike in Figure 182 created a larger region of skin deformation of the leading edge of the horizontal stabilizer indicative of a soft-bodied impact. The UAS, on the other hand, created a more compact region of intense damage with skin penetration and more extensive damage to internal components. Such damage is an indication that the impact involved concentrated masses composed of rigid or dense materials. The simulated bird strike damaged the leading edge ribs to a greater degree than the UAS, but this damage is considered less critical than the skin and forward spar perforations caused by the UAS.

Similarly, Figure 183 presents the damage sustained by the commercial transport jet wing leading edge. As with the horizontal stabilizer, the wing leading edge was dented by the bird strike impact with some substructural deformation. This damage is considered less critical than that of the UAS impact which resulted in the failure of the leading edge skin and substructure. This penetration increases the potential for a significant fraction of the UAS to become lodged in the airframe.

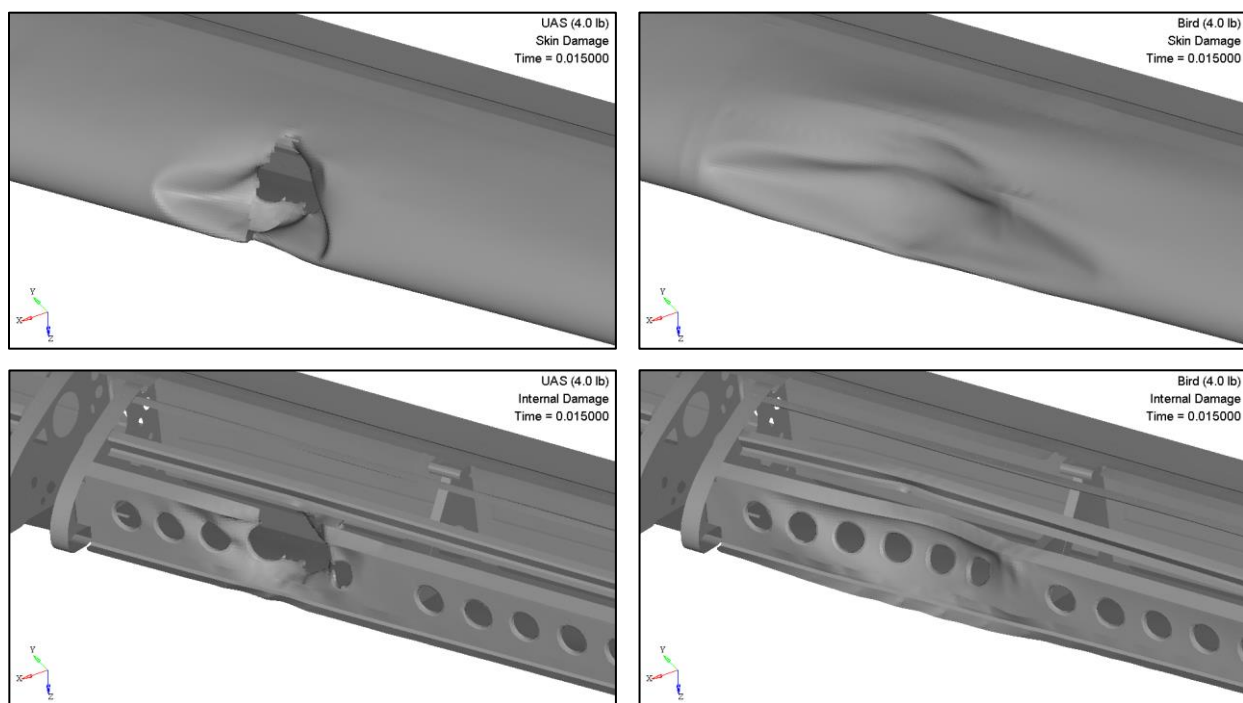


Figure 183. Comparison of skin and internal damage produced by a 1.8 kg (4.0 lb) UAS and Bird after impact with a commercial transport jet wing leading edge

6.2.1.2 Business Jet

As with the commercial transport jet, typical results for simulated 1.8 kg (4.0 lb) UAS and bird strike impacts to the business jet are presented in this section. . The remaining impact simulations can be found in Appendix E.

Figure 184 and Figure 185 present the resultant damage in the vertical stabilizer and the wing of the business jet due to impact with 1.8 kg (4.0 lb) UAS and bird projectiles.

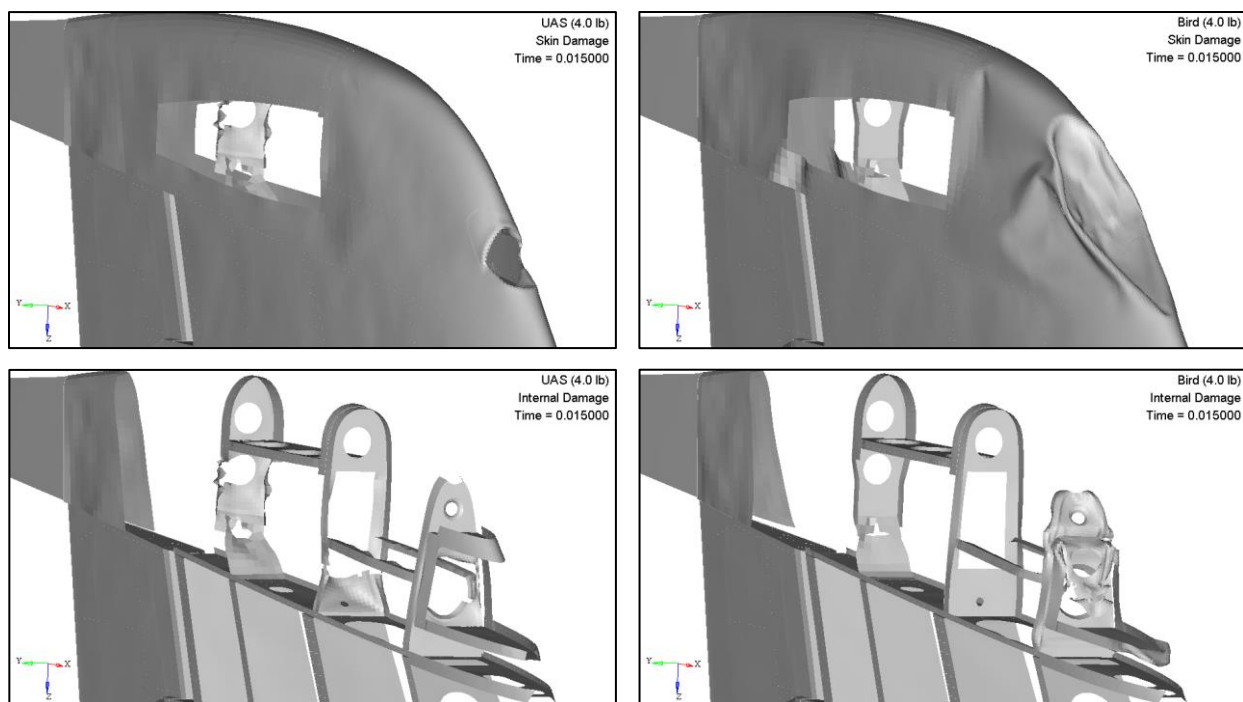


Figure 184. Comparison of skin and internal damage produced by a 1.8 kg (4.0 lb) UAS and Bird - business jet vertical stabilizer

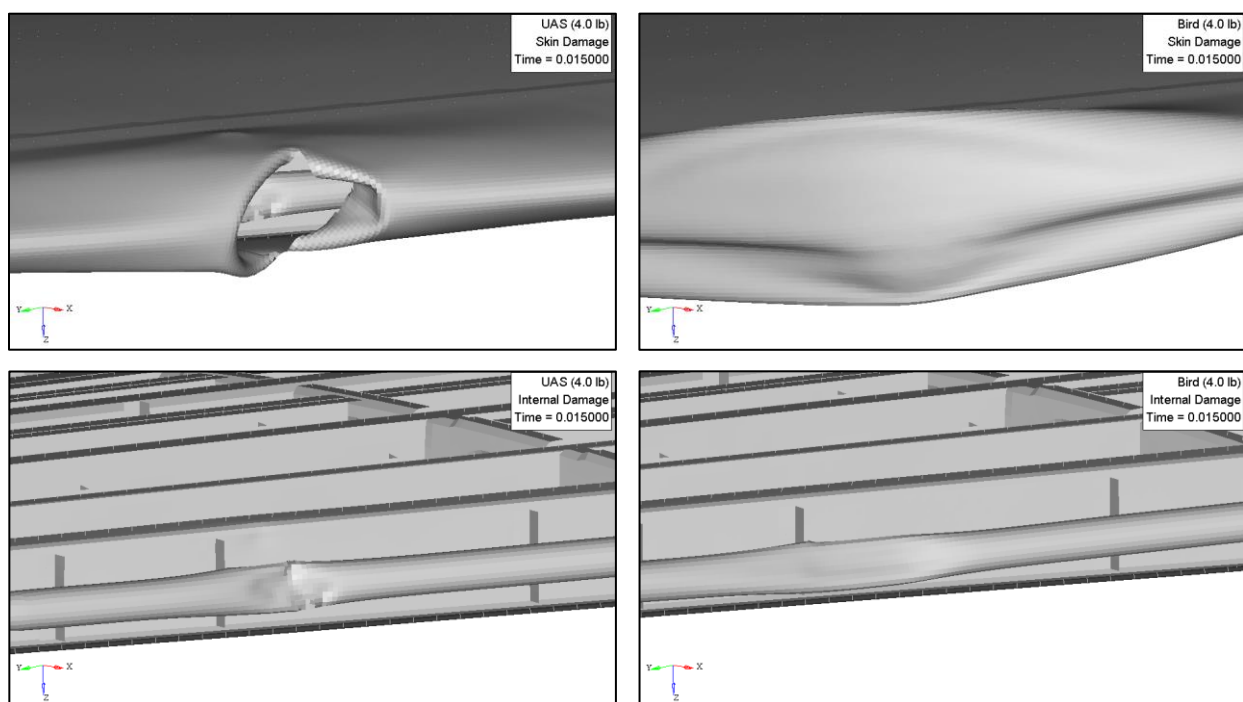


Figure 185. Comparison of skin and internal damage produced by a 1.8 kg (4.0 lb) UAS and Bird after impact with a business jet wing leading edge

The damage sustained by both the wing leading edge and the vertical stabilizer present similarities to the commercial transport jet scenarios. Both structures sustained an extensive permanent deformation of the skin by the bird strike impact, showing also some deformed substructure. On the contrary, the UAS impact resulted in the failure of the leading edge skin with partial penetration of the UAS skin. Additionally, in the case of the vertical stabilizer, the UAS impact produced damage to components of the substructure. Consequently, the damage produced by the bird strike was considered less critical than that of the UAS impact in both cases.

6.2.2 3.6 kg (8.0 lb) Bird – Simulation Results

The four impact locations for each aircraft studied in chapter 4. were selected to perform eight additional FE analyses with a simulated 3.6 kg (8.0 lb) bird. Results were compared to those for the critical cases outlined in chapter 5. and are presented in Appendix E. Table 30 presents the impact severity levels of the scaled UAS with respect to the corresponding baseline simulation.

Table 30. Scaled-up UAS and bird impact simulation results

	Commercial Transport Jet				Business Jet			
	Vertical Stabilizer	Horizontal Stabilizer	Wing	Windshield	Vertical Stabilizer	Horizontal Stabilizer	Wing	Windshield
Fixed-wing UAS Scaled 3.6 kg (8.0 lb)	Level 4	Level 4	Level 4	Level 3	Level 4	Level 4	Level 3	Level 4
Bird 3.6 kg (8.0 lb)	Level 3	Level 2	N/A*	N/A*	Level 2	Level 2	N/A	N/A

* N/A: Not applicable for windshield and wing as per *14 CFR Part 25* requirements.

For each case, the UAS created equal or more damage than the bird. This corresponded to a reduction in the level of severity when impacted by the simulated bird as opposed to the UAS model.

6.2.2.1 Commercial Transport Jet

Typical results for simulated 3.6 kg (8.0 lb) UAS and bird strike impacts to the commercial transport jet are presented in this section. The remaining impact simulations can be found in Appendix D. The following sections detail the impact characteristics of each projectile with images showing the resultant damage and discussion of the associated damage mechanisms.

Figure 186 shows the typical damage associated with a fixed-wing UAS impact on the left-hand side of the figure compared to the damage that is typical for a bird strike on the right-hand side. In the case of the horizontal stabilizer, the skin, forward spar and adjoining rib structure were all penetrated by the UAS, indicating that the relatively high mass components (motor, battery, and camera) remained intact and energetic enough to cause successive instances of severe damage. This is in contrast to the bird impact where the mass of the projectile was deflected by the deformed leading edge skin.

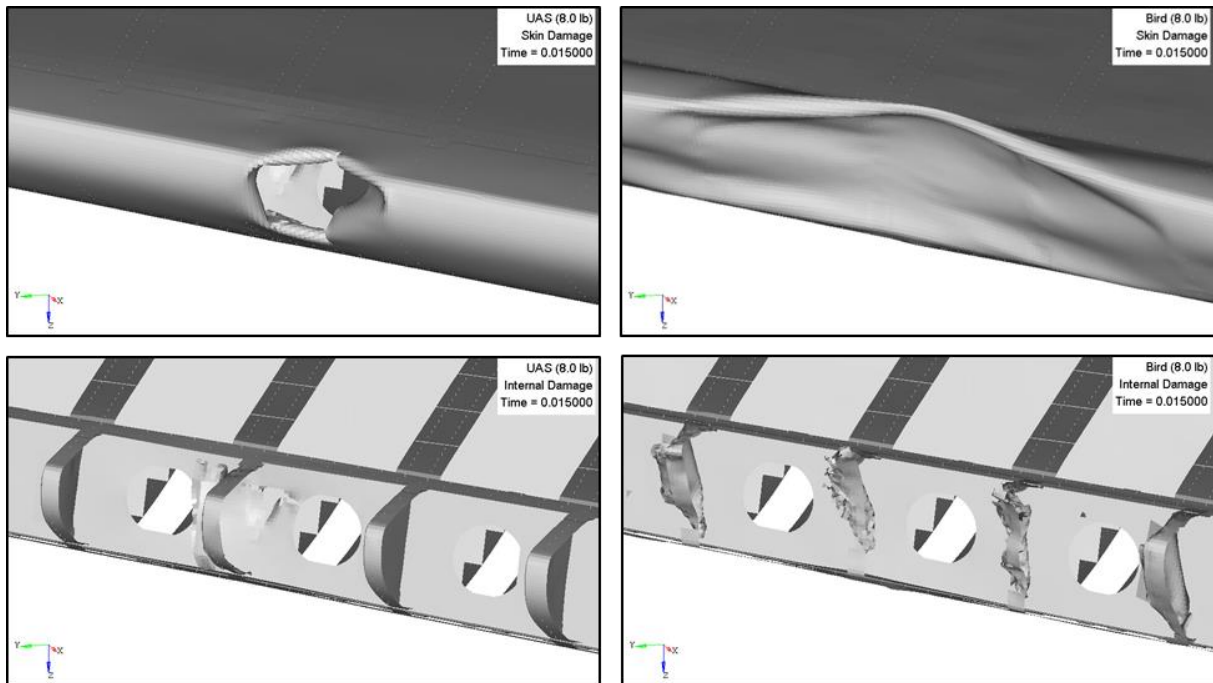


Figure 186. Comparison of skin and internal damage produced by a 3.6 kg (8.0 lb) UAS and Bird after impact with a commercial transport jet horizontal stabilizer

6.2.2.2 Business Jet

Typical results for simulated 3.6 kg (8.0 lb) UAS and bird strike impacts to the business jet are presented in this section. The remaining impact simulations can be found in Appendix E.

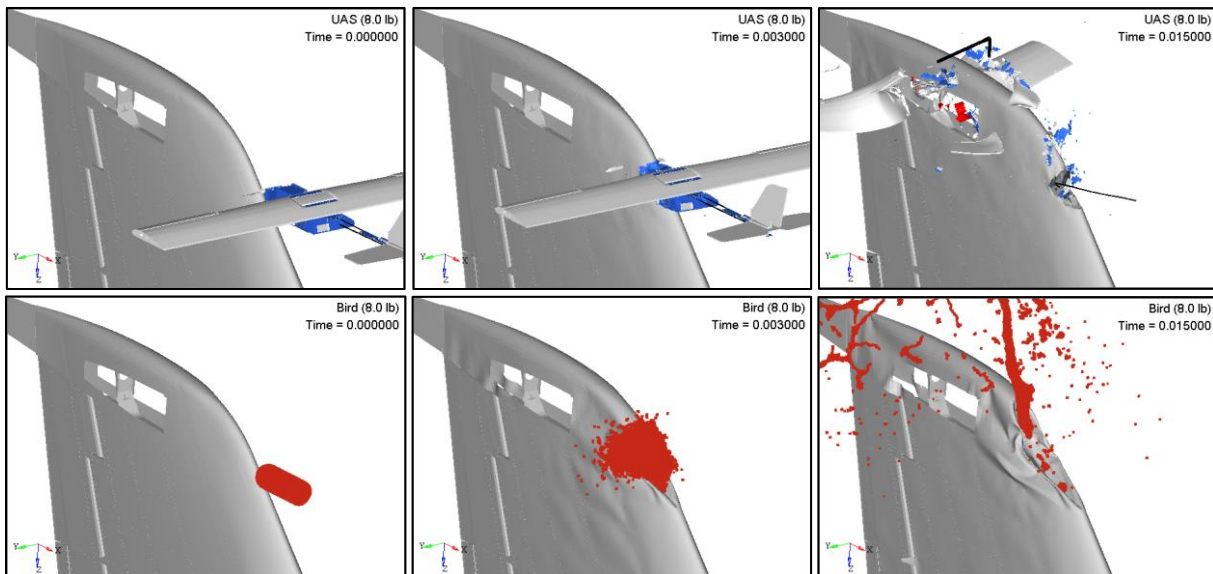


Figure 187. Comparison of skin and internal damage produced by a 3.6 kg (8.0 lb) UAS and Bird after impact with a business jet vertical stabilizer

Figure 187 presents the resultant damage in the vertical stabilizer due to impact with 3.6 kg (8.0 lb) UAS and bird projectiles. Leading edge skin and discrete impact damage was observed for the UAS collision. The UAS penetrated into the airframe and damaged the forward spar. The bird strike resulted in distributed skin deformation and damage to the underlying substructure.

6.3 CONCLUSIONS

This study assessed whether a fixed-wing UAS impact can be considered equivalent to a bird strike. The simulations utilized identical boundary conditions and impact energies in order to demonstrate the behavior of the two impact types.

Airborne collisions involving hard-bodied projectiles have characteristic features that distinguish them from bird strikes. Primarily, the damage zones for the fixed-wing UAS showed notable dents and penetrations due to the discrete masses and rigid, dense materials. The metallic motor promoted UAS penetration of the aircraft skin and associated damage to internal components (including the forward spar) in a majority of the simulations. It was shown in Figure 186 that the UAS created a smaller region of impact damage but that the penetration through the skin caused further penetration of the forward spar and damage to internal components of the aircraft. This is considered level 4 damage while the bird impact was classified as level 3.

6.3.1 Summary

Fixed-wing UAS impacts are likely to cause more damage than bird strikes of equivalent energy. The UAS impacts were generally associated with greater damage levels due to the hard-bodied mechanical construction of the UAS, its components made of dense, rigid, materials and its discrete distribution of masses. The initial impact penetrations (caused by contact with a dense, rigid, motor) were exacerbated as subsequent UAS components, such as the battery pack, impacted the aircraft structure causing progressively more and more damage including UAS ingress into the airframe.

6.3.2 Future Work

The results of this study indicate that the two projectile types have different characteristics and that the impact energy is only one of the factors that predict damage severity. Simulations using other UAS configurations may provide additional insights into the impact dynamics of midair collision.

7. COMPARISON BETWEEN BIRD, QUADCOPTER/FIXED-WING UAS IMPACTS

An additional comparison study was performed to determine if a mid-air collision between a fixed-wing UAS and a given aircraft is comparable to similar collisions involving a quadcopter UAS or a bird with an equivalent impact energy. One critical baseline simulation was used as a basis for comparing the impact kinematics, energetics, and damage severity associated with each projectile.

7.1 UAS CONFIGURATION COMPARISON

The range of UAS configurations currently available for consumer applications is extensive, encompassing many configurations of multicopter layouts as well as fixed-wing type puller/pusher UAS designs. This study utilized the fixed-wing UAS FE model used in the preceding chapters as well as the quadcopter UAS FE model presented in [2]. Figure 188 presents an isometric CAD representation of the quadcopter UAS.



Figure 188. Quadcopter UAS CAD model isometric view

One primary feature of the fixed-wing design, as opposed to the quadcopter, is that the leading critical masses (motor, battery, and camera) are generally aligned with the flight direction (*cf.*, Figure 9). For this reason, the most damaging impact orientation is assumed to be a head-on collision.

7.2 COMPARISON STUDY

Table 31 presents the simulation matrix for the comparisons studied in this chapter. 1.8 kg (4.0 lb) bird and fixed-wing and quadcopter UAS FE models were used in three different simulations. Identical initial and boundary conditions were applied consistent with the critical business jet load case presented in Chapter 4.

Table 31. Load case definitions for bird/UAS impact comparisons

	Business Jet			
	Vertical Stabilizer	Horizontal Stabilizer	Wing	Windshield
1.8 kg (4.0 lb) Bird	BB4V2	N/A	N/A	N/A
Scaled-up Quadcopter UAS 1.8 kg (4.0 lb)	BQsV2	N/A	N/A	N/A
Fixed-Wing UAS 1.8 kg (4.0 lb)	BFV2	N/A	N/A	N/A

The simulation setup is depicted in Figure 189 for the scaled-up quadcopter UAS. The remaining fixed-wing and bird impacts utilize the same target location as the quadcopter.

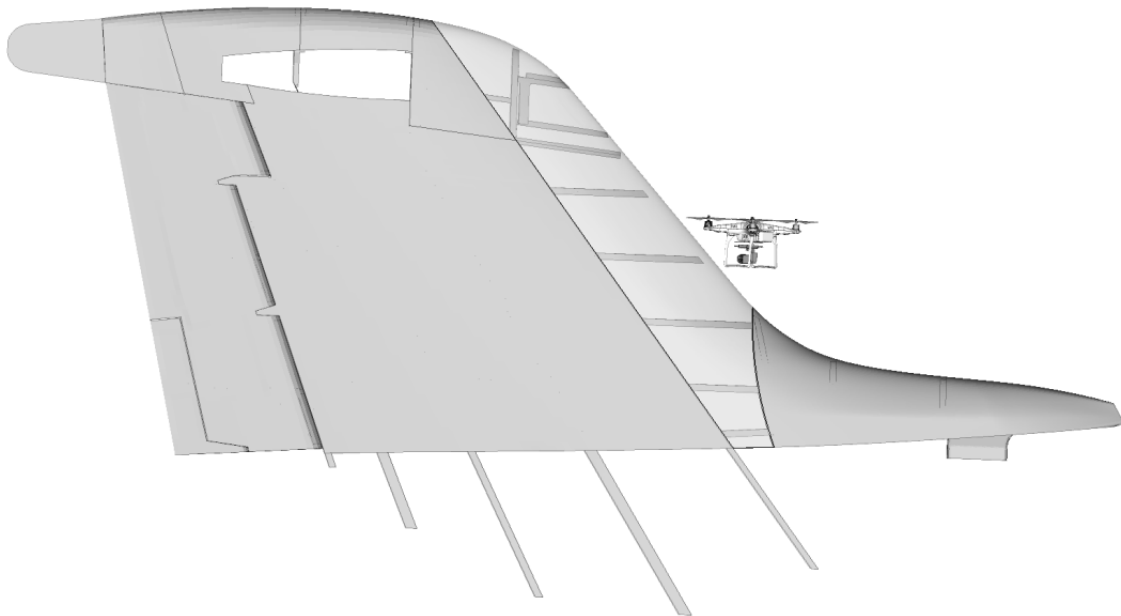


Figure 189. UAS impact location – business jet vertical stabilizer

7.2.1 Simulation Results –Bird and Quadcopter/Fixed-Wing UASs

The vertical stabilizer of the business jet studied in chapter 4 was selected to perform a total of three simulations with 1.8 kg (4.0 lb) projectile FE models. Table 32 presents the impact severity level for the bird, scaled-up quadcopter UAS, and baseline fixed-wing UAS simulations.

Table 32. Bird and UAS impact simulation results

	Business Jet			
	Vertical Stabilizer	Horizontal Stabilizer	Wing	Windshield
1.8 kg (4.0 lb) Bird	Level 2	N/A	N/A	N/A
Scaled-up Quadcopter UAS 1.8 kg (4.0 lb)	Level 4	N/A	N/A	N/A
Fixed-wing UAS 1.8 kg (4.0 lb)	Level 4	N/A	N/A	N/A

The impact kinematics of the three simulations are illustrated in Figure 190. The distributed damage associated with a bird impact (top) is characteristic of the bird strike results discussed in Chapter 6. As shown in Figure 191, the idealized bird projectile created a dent in the leading edge skin, which extended over a longer region of the vertical stabilizer than the two UAS impacts but did not penetrate the skin. The scaled-up quadcopter impact (Figure 191 middle column) resulted in critical damage and permanent deformation to the front spar along with intrusion of the UAS into the airframe. Similarly, the fixed-wing UAS collision resulted in penetration of the leading edge skin, significant permanent deformation of the adjoining structure, but with less damage to the front spar (Figure 191 right column) than the scaled-up quadcopter.

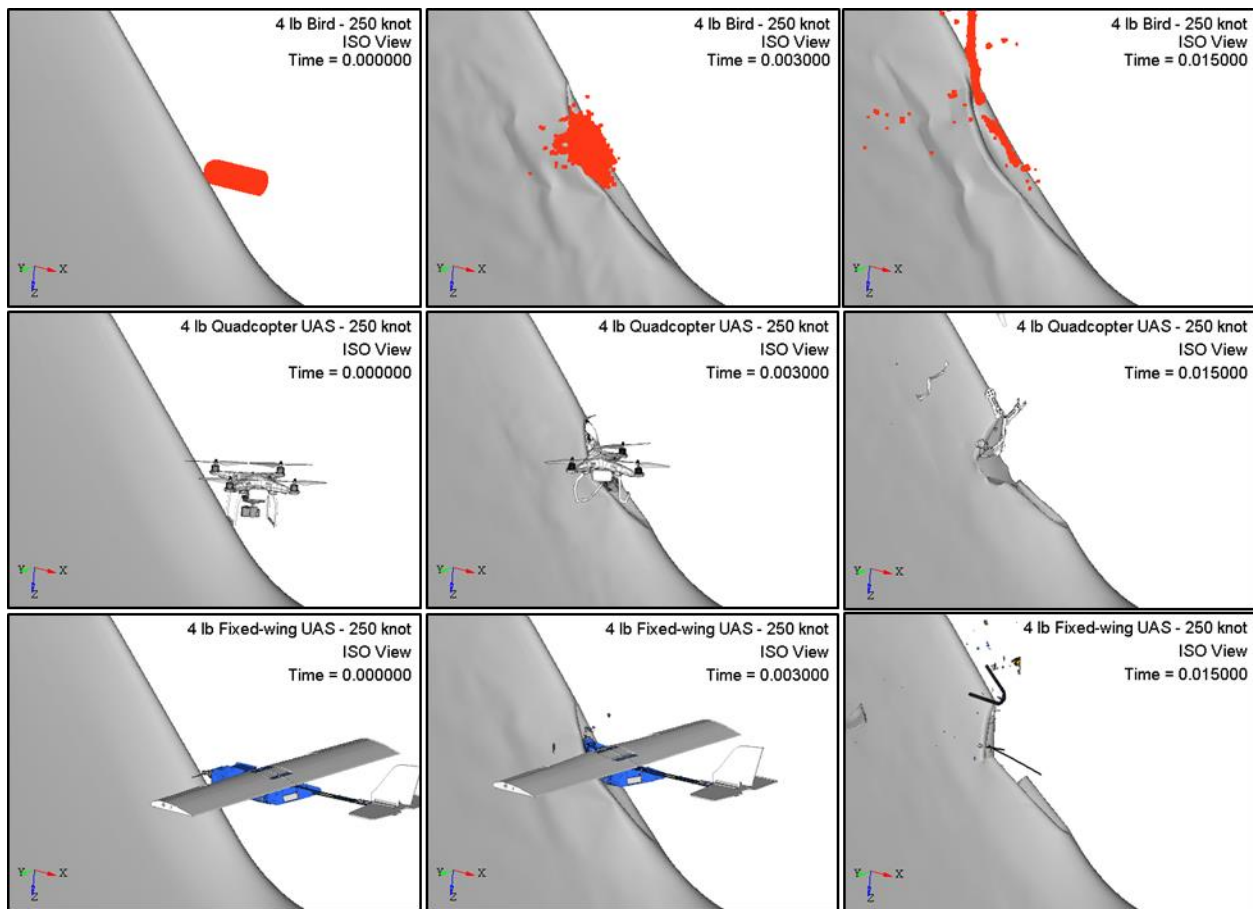


Figure 190. Comparison of impact kinematics for 1.8 kg (4.0 lb) projectiles: bird (top), quadcopter UAS (middle), and fixed-wing UAS (bottom)

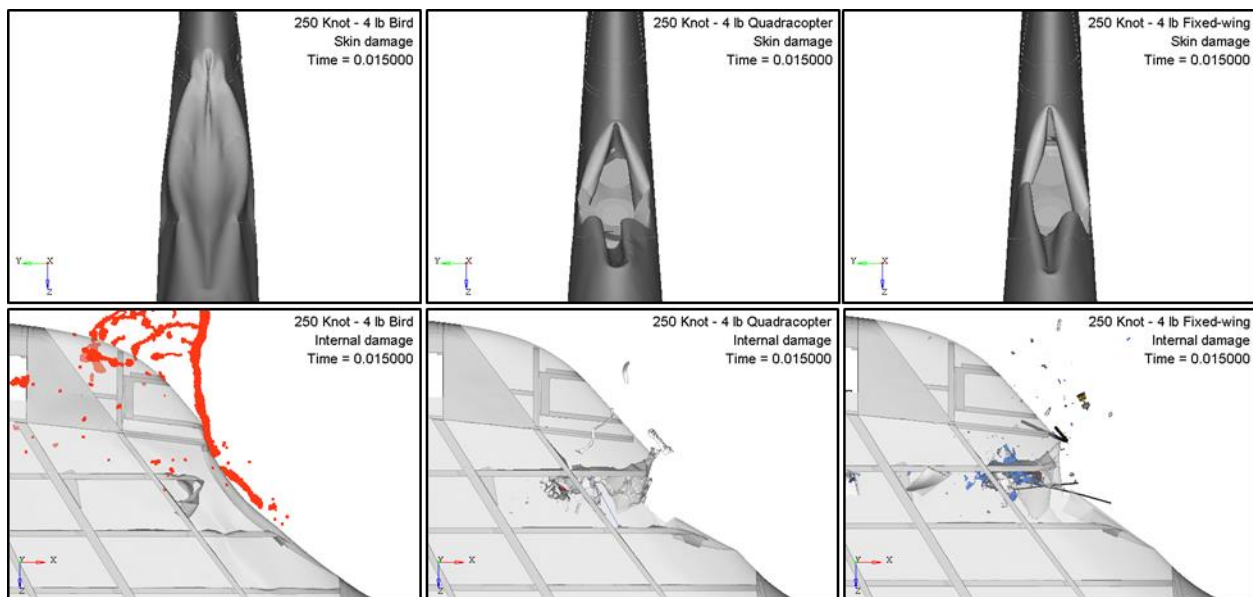


Figure 191. Comparison of skin and internal damage produced by 1.8 kg (4.0 lb) projectiles: bird (left), quadcopter UAS (middle), and fixed-wing UAS (right)

Figure 192 shows close-up views of the impacted region for each projectile (top) and effective plastic strain plots for the front spar (bottom). The contact force and impulse for each impact are shown in Figure 193. Note that the bird strike simulation creates the largest contact force magnitude but that this is not associated with corresponding damage levels. The energy balance plots shown in Figure 194 indicate that each of the three projectiles have differing ratios for each energy, attributed to their differing configurations and constructions.

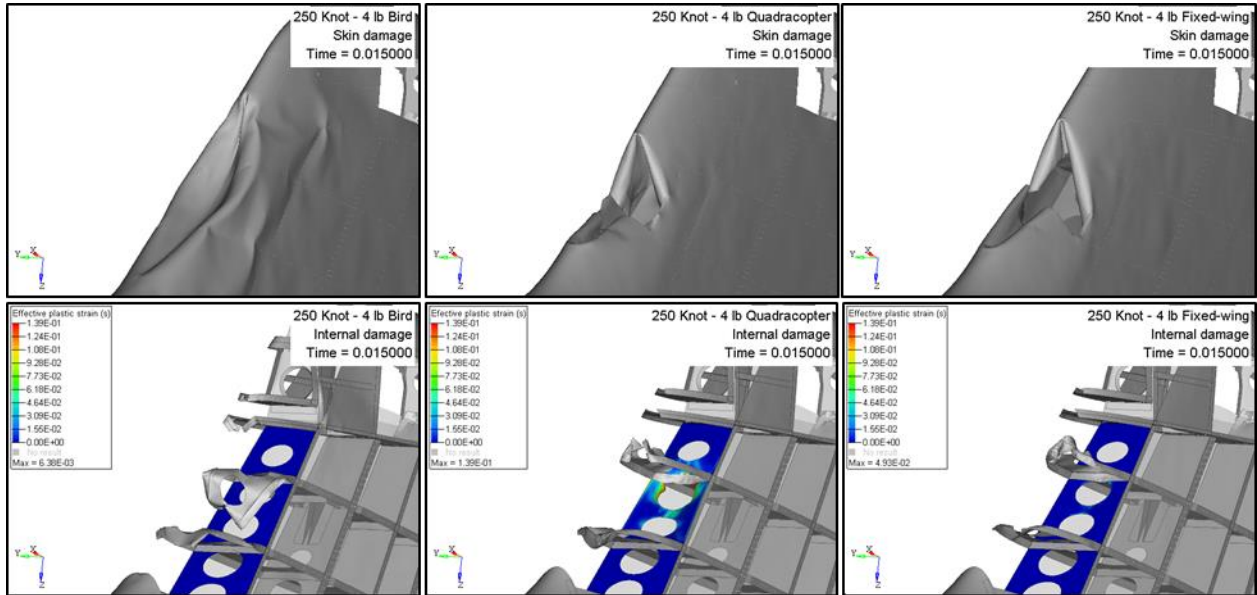


Figure 192. Comparison of skin and internal damage produced by 1.8 kg (4.0 lb) projectiles: bird (left), quadcopter UAS (middle), fixed-wing UAS (right)

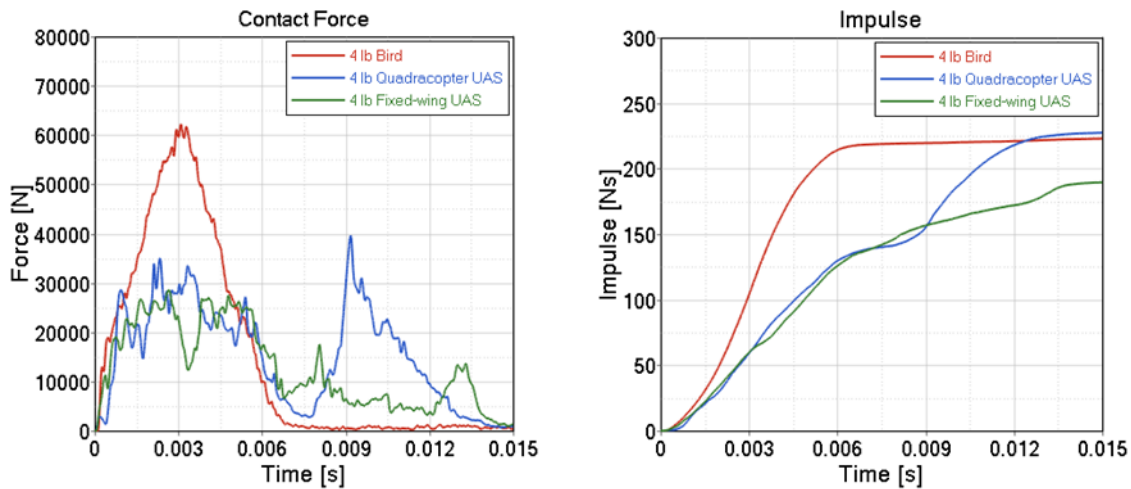


Figure 193. Contact force and impulse plots produced by 1.8 kg (4.0 lb) projectiles: bird, quadcopter, UAS, and fixed-wing UAS

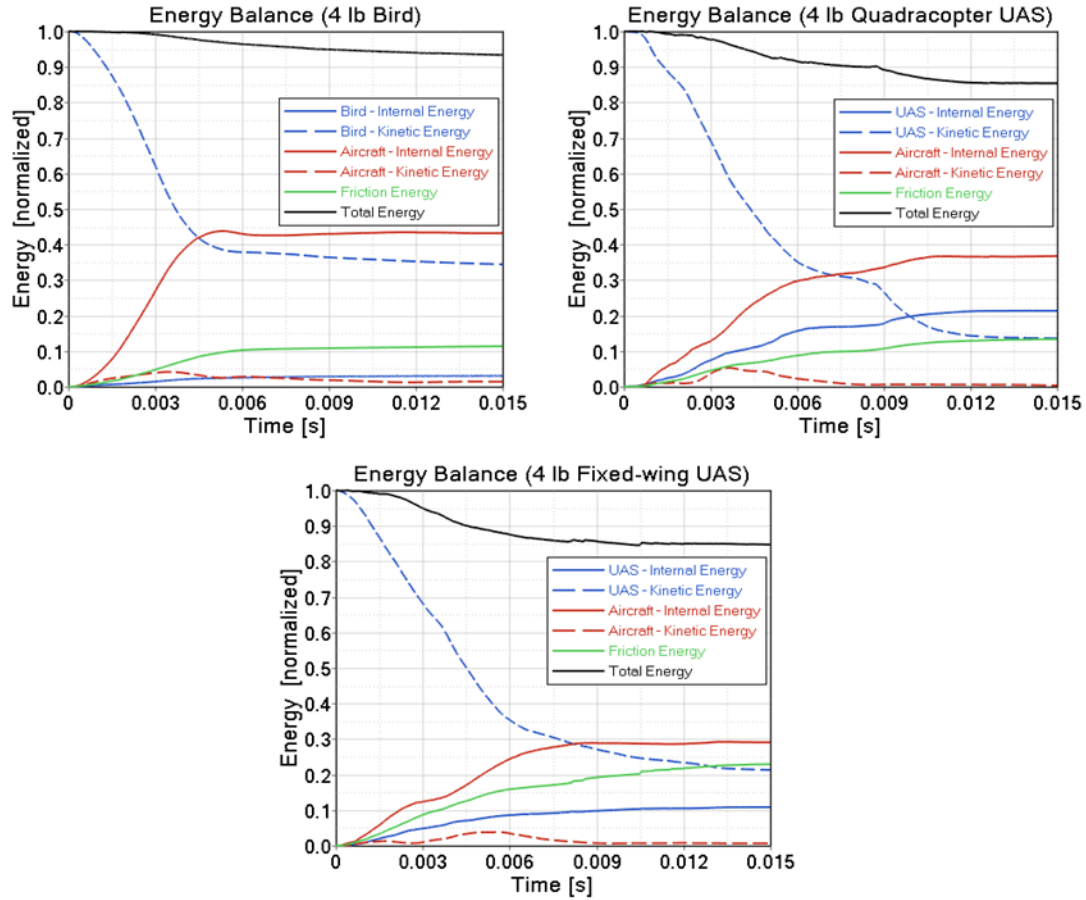


Figure 194. Normalized energy balance plots produced by 1.8 kg (4.0 lb) projectiles: bird, quadcopter UAS, and fixed-wing UAS

7.2.2 Comparison of UAS Architectures – Quadcopter and Fixed-Wing

The scaled-up quadcopter UAS was utilized in impact simulations at the same locations and velocity (128.6 m/s (250 knots)) as the baseline fixed-wing simulations presented in chapter 4. The spatial distribution of damage at a given impact location on the aircraft was distinct for the two UAS architectures. Moreover, the locations on the aircraft with critical damage were also different in many instances for quadcopter and fixed-wing UAS impacts [2]. However, damage initiation and propagation due to aligned localized UAS masses tended to be similar for both UAS configurations. In terms of damage initiation due to localized masses composed of dense and rigid materials followed by damage propagation due to successive impacts from items of mass within the UAS. The damage levels sustained at identical impact locations for the scaled-up quadcopter and fixed-wing UASs are shown in Table 33. Note that these locations are determined by the critical impact locations for the baseline quadcopter UAS presented in [2].

Table 33. Scaled-up quadcopter and fixed-wing UAS simulation results – comparison at identical impact locations

	Commercial Transport Jet				Business Jet			
	Vertical Stabilizer – CQsV3 & CFV3	Horizontal Stabilizer – CQsH3 & CFH3	Wing – CQsW1 & CFW1	Windshield – CQsC1 & CFC1	Vertical Stabilizer – BQsV2 & BFV2	Horizontal Stabilizer – BQsH2 & BFH2	Wing – BQsW1 & BFW1	Windshield – BQsC1 & BFC1
Scaled-up Quadcopter UAS 1.8 kg (4.0 lb)	Level 3	Level 4	Level 3	Level 3	Level 4	Level 4	Level 3	Level 2
Baseline Fixed-Wing UAS 1.8 kg (4.0 lb)	Level 3	Level 4	Level 3	Level 2	Level 4	Level 4	Level 3	Level 3

7.3 CONCLUSIONS

This study assessed whether airborne collisions involving 1.8 kg (4.0 lb) bird, quadcopter UAS, and fixed-wing UAS can be considered equivalent to one another. The simulations utilized identical initial and boundary conditions at an impact velocity of 128.6 m/s (250 knots)

Airborne collisions involving hard-bodied projectiles have characteristic features that distinguish them from bird strikes. The dense, rigid components of both UASs penetrated the aircraft skin and damaged the internal aircraft structural components. The data shown in Table 33 indicate that the two distinct UAS architectures impart similar levels of damage which generally exceed that for energetically similar bird impacts.

7.3.1 Future Work

In order to determine the similarities and differences between other UAS types, it is recommended to perform additional simulations that account for more UAS configurations and masses.

For example, there are a number of aspects of the fixed-wing UAS design that can be modified to reduce the severity of direct *frontal* impacts to manned aircraft. The fixed-wing UAS employs a tractor (“puller”) configuration. The motor basically acts as a dense sharp penetrator that exacerbates the degree of impact damage. In contrast, pusher motor configurations would allow the forward fuselage to serve as a crumple zone and likely reduce the initial local damage to the target, provided no additional high-density components remained in the forward fuselage. In addition, the

original fixed-wing UAS battery and payload subassembly locations and support structures promote significant momentum transfer along the line of impact. Alternatively, the subassembly support structures can be designed to facilitate sequential failures and controlled detachment trajectories consistent with engine mount designs for automobile crashworthiness. Lastly, the dense battery and payload can be redesigned to fragment/disintegrate at prescribed g-loadings. Some preliminary FE simulations employing several of these concepts suggest that such design features can dramatically reduce the impact severity. As part of future investigations, the role of UAS design features on enhanced frangibility should be explored.

8. CONCLUSIONS AND FUTURE WORK

According to the latest industry forecast studies, the Unmanned Aircraft System (UAS) market volume is expected to reach 4.7 million units by 2020 [1]. Nonetheless, safety, regulatory, social and technical challenges need to be addressed before the sight of an unmanned aircraft in the sky becomes as common and accepted by the public as its manned counterparts. The effect of an airborne collision between an UAS and a manned aircraft is a concern to the public and government officials at all levels. The primary goal of regulating UAS operations into the NAS system is to ensure an appropriate level of safety. Research is needed to define airborne hazard severity thresholds for collisions between unmanned and manned aircraft.

The results presented in this report focus the initial effort on analyzing a small fixed-wing UAS impacting on a typical commercial transport jet and a typical business jet aircraft, certified under *14 CFR Part 25* [56] or *Part 23* [57] requirements.

This research will help determine airworthiness requirements for unmanned aircraft based on their potential hazard severity to other airspace users in the NAS. The resulting severity thresholds will be based on UAS characteristics (kinetic energy, structure, shape, materials, etc.) under credible encounter scenarios and will provide for test criteria used to evaluate applicable operational and airworthiness standards. An UAS that meet test criteria based on thresholds for these characteristics may be certified as airworthy under different criteria than other UAS [19].

The main research questions being answered through this research are [19]:

- What are the hazard severity criteria for an UAS collision (weight, kinetic energy, etc.)?
- What is the severity of an UAS collision with an aircraft in the air?
- Can an UAS impact be classified similar to a bird strike?
- Will an UAS impacting an engine be similar to a bird engine ingestion?
- What are the characteristics of an UAS where it will not pose a risk to an aircraft if a collision in the air was to happen?
- Can the severity of an UAS mid-air collision with an aircraft be characterized into categories based on the UAS? What would those categories look like?

It is important to emphasize that the intent of this research was not to do an assessment of already certified products (*e.g. 14 CFR Part 23/25/27/29/33*) but to analyze the characteristics of small UAS that contribute to the damage of the airframe of manned aircraft as a result of an airborne collision.

8.1 TECHNICAL APPROACH

Due to the complexity of the problem, full-scale test article availability, time and budget constraints, it was decided to conduct the R&D effort by using the NIAR Physics Based FE modeling techniques based on the Building Block Approach methodology. Conducting these types of impact studies by analysis provides critical insight into the crashworthiness response of the target and the projectile. With physical testing, it is not possible to quantify internal energy distributions during the transient dynamic impact. It is also very difficult to conduct large-scale tests involving target air vehicles and UAS projectiles, due to availability of expensive test articles and long setup times, and to control the exact impact locations and attitude of the UAS projectile.

8.1.1 Building Block Approach FE Model Development and Validation

In order to build the fixed-wing UAS and target aircraft FE models, the NIAR and MSU followed a Physics Based Modeling approach. This methodology adopted by the NIAR takes advantage of advances in computational power, the latest computational tools, years of research in understanding the fundamental physics of the crashworthiness event, generated test-to-test variability data, and verification & validation (V&V) modeling methods. The method follows the Building Block Approach.

The building block approach is the incremental development of analysis and supporting tests where typically there is an increase in size and complexity of the test article and a decrease in number of supporting tests. In order to develop this method, it is necessary to have a good understanding of the physics and testing variability from the coupon to the system level. Full-scale level test results do not drive the definition of the numerical model; it is driven by a predefined, V&V building block modeling methodology.

Using this approach, simulations should be able to predict the system level test results within the scatter of the physical system test results. An objective validation criterion is used to evaluate the numerical models, where the correlation level between simulation and testing is defined by an understanding of the test-to-test variability of the physical system under evaluation.

8.1.2 Verification and Validation FEA Models: Coupon to Sub-Assembly Level Testing

FE models of a typical fixed-wing UAS was developed for the airborne collision studies. Different component level tests were conducted to validate the UAS FE models. The following paragraphs will summarize the testing conducted as well as identify further areas of work.

Coupon Level Testing:

- Basic coupon level test results were obtained from the literature for verification of the various material systems of the UAS.

Component Level Testing:

- The UAS battery and motor were tested in a compressed air gun facility under impact velocities similar to those of the mid-air collision being studied in this project, between 64.3 and 128.6 m/s (125 and 250 knots). The kinematics were captured with high-speed cameras, the reaction loads and the strains in the impacted panel were measured with four load cells and thirteen strain gages respectively, and a Digital Image Correlation (DIC) system captured the displacements of the impacted area.

All fixed-wing UAS component tests were replicated with the FE simulations. The simulation models correlated within the scatter of the data of the aforementioned test conditions. Therefore, it can be concluded that the FE models were verified for the conditions set by the physical tests.

The models are intended to be used for assessing impact dynamics with aircraft structures and to simulate mid-air collisions. These FE models should be limited to relative impact velocities between 64.3 and 128.6 m/s (125 and 250 knots), for which component level tests verified the behavior of the main components of the UAS. Further coupon to component level tests should be conducted in the future in order to use these UAS FE models for ground collisions impact scenarios or lower velocity airborne collisions with General Aviation (GA) aircraft and rotorcraft.

8.1.3 Selected Impact Conditions

As presented in Chapter 4, following the airworthiness requirements listed in the FAA General Operating and Flight Rules (*14 CFR Part 91*) [72], it was assumed that the most probable high velocity impact scenario was at holding flight phases. For this case and considering the categories of aircraft being studied in this report, the maximum flight speed is limited to 200 KIAS (*14 CFR Part 91.117(b)*). Considering a frontal impact between the UAS and the aircraft to be a worst-case scenario, an impact velocity can be established by adding the relative speeds of both bodies. Therefore, and considering the specifications of the UAS discussed in section 2.1, an impact velocity of 128.6 m/s (250 knots) was defined for all the airborne collision studies.

Moreover, a parametric study was completed with the objective of identifying the most critical local impact conditions and narrowing down the number of simulations to be run in each of the impacted aircraft subassemblies. To achieve this, the quadcopter UAS FE model was impacted into a wing leading edge FE model, developed and verified through simulation and testing by NIAR in a previous project for bird strike [41]. The influence of the local position of its CG with respect to the impacted aircraft was studied.

Based on the results obtained in these quadcopter parametric studies, a head-on UAS impact with the CG aligned with the leading edge of the target between the two closest ribs was identified as the most severe impact condition. This impact condition was consequently selected as a baseline for the collision study involving commercial and business jet targets.

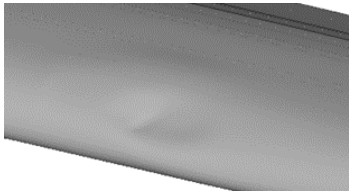
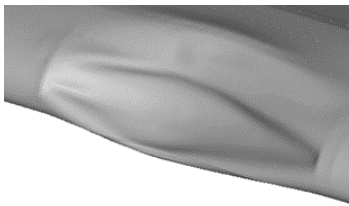
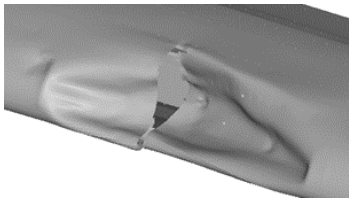
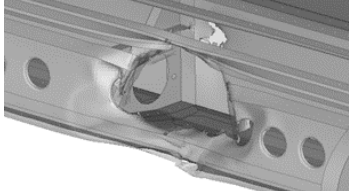
This study also highlighted the importance of having ideal initial conditions to produce the worst-case levels of damage. Small deviations in the impact location might underestimate the severity of the event.

8.1.4 Proposed Evaluation Criteria for Airborne Collisions

The results from over 70 impact scenarios involving the fixed-wing UAS were analyzed and categorized relative to one another, and a set of impact severity criteria was defined as shown in Table 34.

The lowest damage category, Level 1, generally corresponds to a minimal amount of localized damage. The next category, Level 2, represents significant visible damage to the external surface of the aircraft with some internal component damage but with no appreciable skin rupture. The third category, Level 3, describes impact events where the outer surface of the aircraft is compromised in a way that could allow ingress of foreign objects into the airframe, with some damage to substructure. Finally, Level 4 indicates damage that includes all of the preceding aspects as well as extensive damage to internal components and possibly compromising the primary structure.

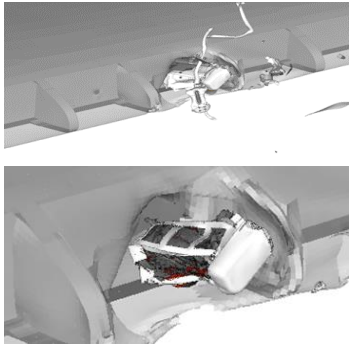
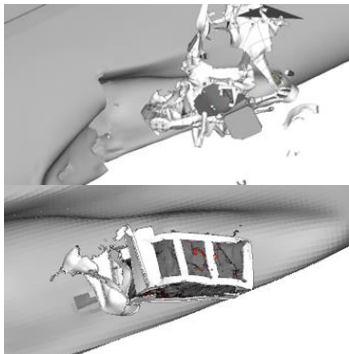
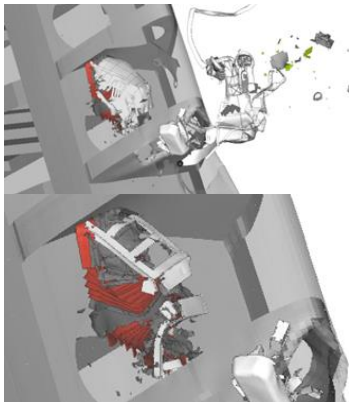
Table 34. Damage level categories

Severity	Description	Example
Level 1	<ul style="list-style-type: none"> • Airframe undamaged. • Small deformations. 	
Level 2	<ul style="list-style-type: none"> • Extensive permanent deformation on external surfaces. • Some deformation in internal structure. • No failure of skin. 	
Level 3	<ul style="list-style-type: none"> • Skin fracture. • Penetration of at least one component into the airframe. 	
Level 4	<ul style="list-style-type: none"> • Penetration of UAS into airframe. • In addition, failure of primary structure. 	

The risk of fire associated with damaged LiPo type batteries was addressed for each simulation based on the trends observed during component level ballistic testing [2] and the particular kinematics of a given impact scenario.

Table 35 presents the battery fire risk criteria used in this study. Note that the label of “Fire Risk” indicates a potential outcome rather than an impending event due to the qualitative nature of the assessment. Further studies and physical testing into this phenomenon would be required in order to determine any additional severity. During component level testing, the fire risk corresponded inversely to the velocity of the impact; higher velocities caused the battery to disintegrate reducing the heat generated after impact, while lower velocities allowed the battery pack to remain consolidated, increasing the post-impact heat generation.

Table 35. Risk of battery fire

Fire Risk	Description	Example
Yes	<ul style="list-style-type: none"> UAS (including the battery) penetrates the airframe. Battery deforms but stays undamaged. Verification tests showed that partly damaged batteries created heat and sparks. 	
No	<ul style="list-style-type: none"> The UAS does not penetrate the airframe. 	
No	<ul style="list-style-type: none"> UAS (including the battery) penetrates the airframe. The battery sustains great damage, destroying its cells. Verification tests showed that completely damaged batteries did not create heat or sparks. 	

8.2 AIRBORNE COLLISION SEVERITY EVALUATION

8.2.1 Unmanned Aircraft Systems Impact Severity Classification

Conventional 14 CFR system safety analyses include hazards to flight crew and occupants that may not be applicable to unmanned aircraft. However, UAS operations may pose unique hazards to other aircraft and people on the ground. It is necessary to determine hazard severity thresholds for UAS using safety characteristic factors that affect the potential severity of UAS in collisions with other aircraft on the ground or in airborne encounters. The factors that determine the outcome of an airborne collision are numerous and complex and are highly dependent on the structural

design and materials used for the construction of the UAS. The criteria summarized in Table 34 and Table 35 were used to evaluate the UAS Impact Severity Classification.

8.2.2 Commercial Transport Jet Airborne Collisions

As introduced in chapter 3, the target areas selected for impact on the NIAR commercial transport jet were the vertical stabilizer (4.3.1), horizontal stabilizer (4.3.2), wing leading edge (4.3.3), and windshield (4.3.4). Sixteen explicit dynamic simulations of impacts of the 1.8 kg (4.0 lb) fixed-wing UAS into the commercial transport jet were conducted. As defined in section 4.1.1 , an impact velocity of 128.6 m/s (250 knots) was defined for these airborne collision studies. Figure 195 illustrates the locations selected for impact with the commercial transport jet. Table 36 summarizes the results of the collision studies, in terms of severity level and risk of fire.

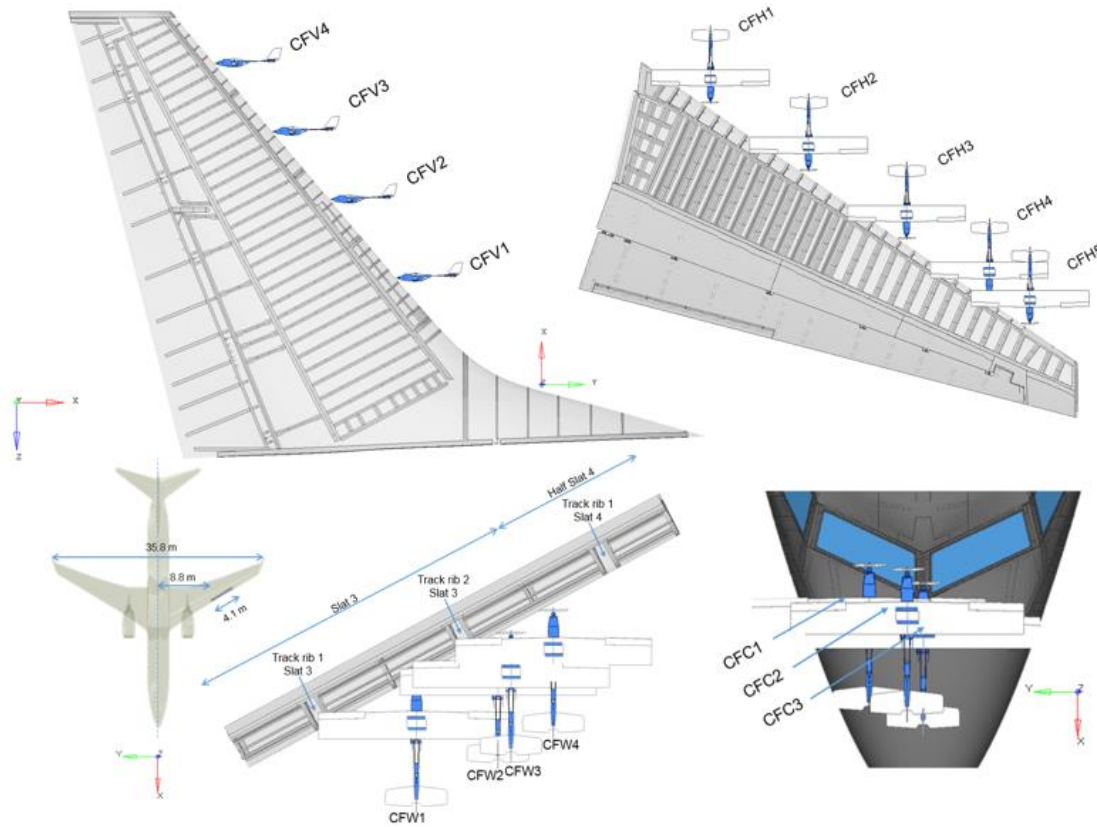


Figure 195. Commercial transport jet airborne collision impact locations

Table 36 shows consistent levels of damage at all locations for each impact target component, indicating that the impact behavior of the UAS for a given target structure is generally not affected by local features in the structure. The impact energy level was such that localized structural variations do not significantly increase or decrease the overall damage level. The impact to the vertical stabilizer at location 2 (CFV2) showed a reduced damage severity level due to a subjective assessment that the damage was the least critical of the vertical stabilizer impacts. The nomenclature convention was defined in section 4.1.3 .

A damage severity level 4 was achieved in nearly all the areas of the horizontal and vertical stabilizers as shown in Table 36. In these scenarios, the front spar, considered to be a primary structure, was damaged and even perforated. These were the most severe cases found in the fixed-wing UAS collision with the commercial transport jet.

Table 36. Commercial transport jet airborne collision simulation results – Severity levels and risk of battery fire

	Commercial Transport Jet																																																	
	Vertical Stabilizer				Horizontal Stabilizer					Wing				Windshield																																				
Fire Risk	Severity	Case	No	Level 4	CFV1	No	Level 3	CFV2	No	Level 4	CFV3	No	Level 4	CFV4	No	Level 4	CFH1	No	Level 4	CFH2	No	Level 4	CFH3	No	Level 4	CFH4	No	Level 4	CFH5	No	Level 3	CFW1	No	Level 3	CFW2	No	Level 3	CFW3	No	Level 3	CFW4	No	Level 2	CFC1	No	Level 2	CFC2	No	Level 2	CFC3

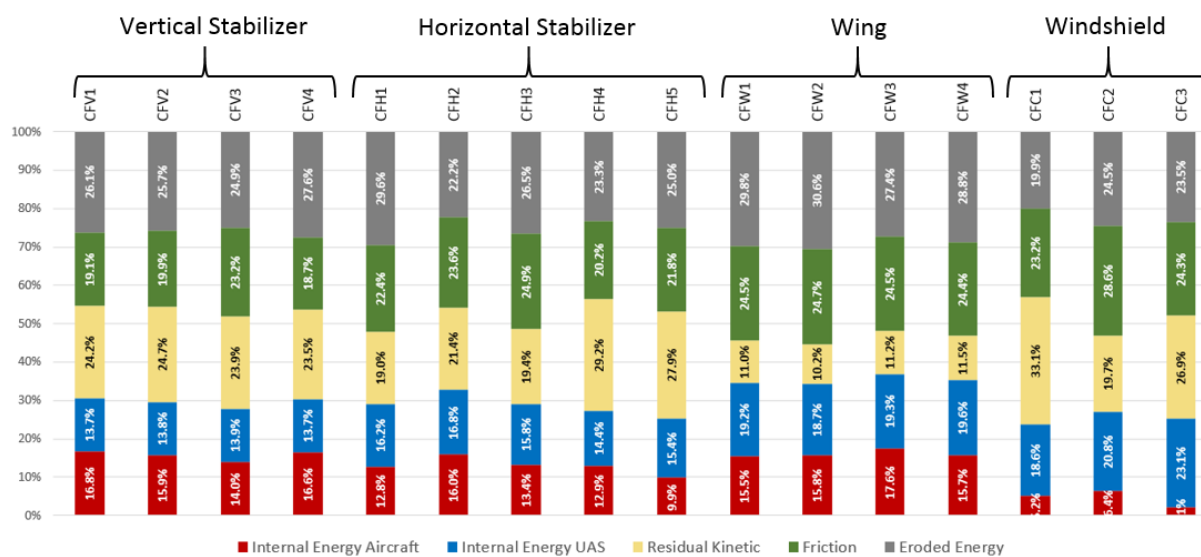


Figure 196. Commercial transport jet airborne collision – Energy summary

A summary of the results, in terms of energy balance of all the cases is shown in Figure 196. For each case, the bar represents a summation of all the different energies involved in the impact event,

measured at 15 ms after impact and normalized with the total energy at time zero. Each block indicates the ratio (in percentage) of energy versus total energy. For each impact condition we can quantify how the initial kinetic energy of the UAS prior to impact is transformed into aircraft and UAS internal energies through the structural deformations induced during impact; a residual UAS kinetic energy that is a function of the UAS post-impact debris mass moving at a post-impact residual velocity; friction energy which is a function of the sliding contact energy between the UAS and the aircraft structure, and eroded energy from the mass of the UAS and aircraft eroded elements to increase the stability of the calculation. Conclusions on how the energy is distributed can be established by analyzing these plots in detail.

In general, the internal energy absorbed by the aircraft structure increased when the fixed-wing UAS impacted closer to the root for any lifting surface (Figure 196). Note that the location for each impact case was numbered from root to tip, so smaller numbers would be inboard. This phenomenon may be explained with the cross-sectional height of the airfoil at the impacted location. Closer to the root, the airfoil cross-section is thicker and has a greater leading edge radius. Consequently, the area of airframe that will have a more perpendicular contact with the impacting projectile is greater, allowing a greater transfer of energy and therefore an increase in internal energy.

The impacted areas of the wing were concentrated at one span-wise location. Therefore span-wise effects cannot be assessed. However, a detailed model of the portion of the wing leading edge allowed a better look into local effects, such as how impacting closer to a slat track rib pair or impacting aiming the center of the rib bay may affect damage. It was observed that an impact further from rigid areas (*e.g.*, ribs) were more vulnerable (*i.e.*, cases CFW1 and CFW3). In these two cases, the D-nose sub-spar sustained greater damage. None of the cases involved battery penetration of the airframe. Hence, the risk of fire was negligible.

If compared with other areas of the commercial transport jet, the UAS impacts on the windshield resulted in much higher residual kinetic energies. Due to the low angle impact in the transparency ($\sim 45^\circ$), the UAS impacts were deflected without inducing considerable damage to the windshield. The windshield is constructed with a thick multilayered transparency with very high stiffness. Consequently, a significant fraction of the deformation due to the impact was absorbed by the UAS since the internal energy of the UAS was much greater than that of the aircraft.

8.2.3 Business Jet Airborne Collision

As introduced in chapter 3, the targets areas selected for impact on the NIAR business jet were the vertical stabilizer (4.4.1), horizontal stabilizer (4.4.2), wing leading edge (4.4.3), and windshield (4.4.4). Sixteen explicit dynamic simulations of impacts of the 1.8 kg (4.0 lb) fixed-wing UAS into the business jet were conducted. As defined in section 4.1.1 an impact velocity of 128.6 m/s (250 knots) was defined for these air-borne collision studies. Figure 197 illustrates the locations selected for impact with the business jet. Table 37 summarizes the results of the collision studies, in terms of severity level and risk of fire, on the business jet.

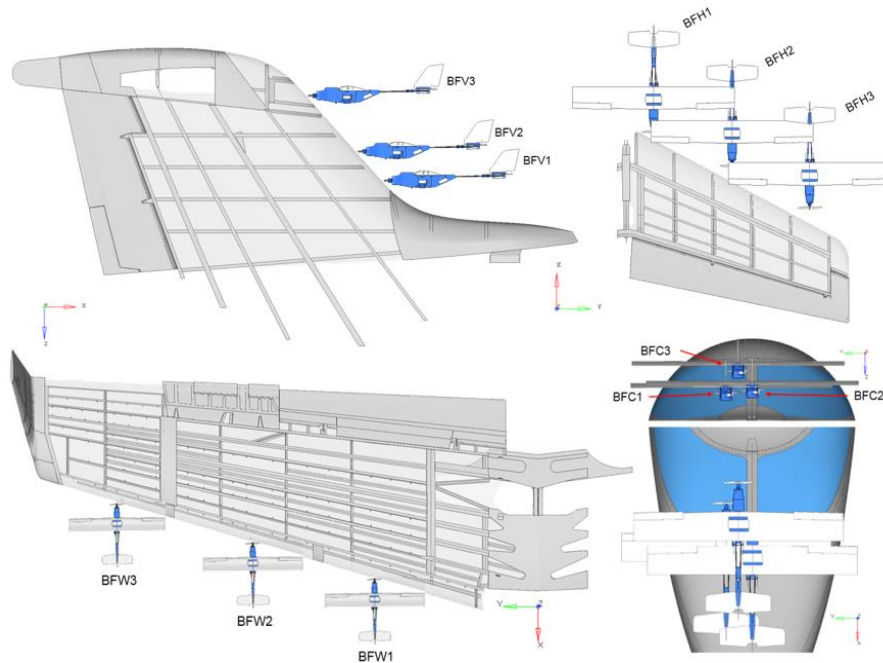


Figure 197. Business jet airborne collision impact locations

Table 37. Business jet airborne collision simulation results – Severity levels

Business Jet												
Case	Vertical Stabilizer			Horizontal Stabilizer			Wing			Windshield		
	BFV1	BFV2	BFV3	BFH1	BFH2	BFH3	BFW1	BFW2	BFW3	BFC1	BFC2	BFC3
Severity	Level 4	Level 4	Level 4	Level 4	Level 4	Level 4	Level 2	Level 3	Level 3	Level 4	Level 1	Level 4
Fire Risk	No	No	No	No	No	No	No	No	No	No	No	No

All cases involving the stabilizers plus two out of three cases on the windshield resulted in Level 4 damage. Impacts to the wing displayed lower levels of damage. A skin that was slightly thicker than the stabilizer and the pipe of the anti-icing system absorbed most of the damage, protecting

the front spar (primary structure) from a direct impact of the UAS. Furthermore, none of the cases induced a risk of battery fire.

A summary of the results of all impact cases is shown in Figure 198. For each case, the bar represents a summation of all the different energies involved in the impact event, measured at 15 ms and normalized with the total energy at time zero. Each block indicates the ratio (in percentage) of energy versus total energy. Similar to the commercial transport jet, in general, the internal energy absorbed by the aircraft structure increased when impacts occurred closer to the root of any lifting surface. In addition, the UAS impacts on the windshield resulted in a much higher residual kinetic energy due to the deflection of the projectile. Furthermore, the PCB fuselage construction of the fixed-wing UAS behaved in a more quasi-brittle fashion than the polycarbonate-bodied quadcopter UAS [2], breaking into many smaller pieces upon impact. This appeared in the energy balance as a greater amount of eroded energy for each case.

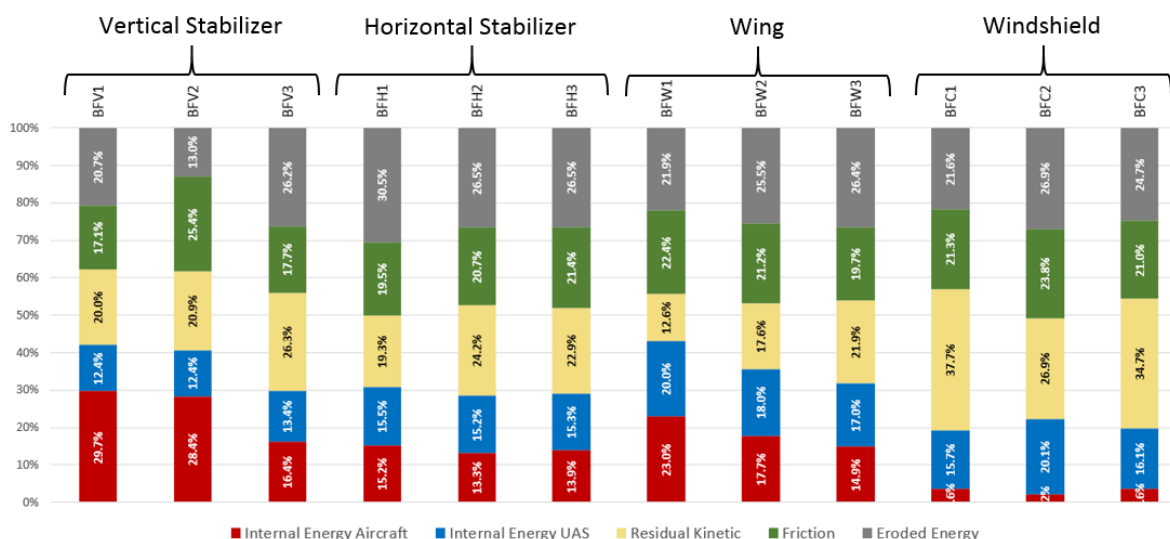


Figure 198. Business jet airborne collision – Energy summary

8.2.4 Airborne Collision Impact Severity Study Conclusions

According to the simulations presented in Chapter 4, an airborne collision between a commercial transport jet and a 1.8 kg (4.0 lb) fixed-wing UAS at 250 knots may result in a damage severity level of medium-high (3-4) in the horizontal and vertical stabilizer, medium (3) in the leading edge of the wing and medium-low (2) in the windshield. Figure 199 illustrates the severity levels in each area of the aircraft analyzed.

Similarly, an airborne collision between a business jet and a 1.8 kg (4.0 lb) fixed-wing UAS may result in a damage severity level of high (4) in the horizontal and vertical stabilizer, medium (2-3) in the leading edge of the wing. A high (4) damage severity level may occur for impacts to the windshield. Figure 200 shows the impact severity levels at different locations on the business jet airframe. Most of the damage to both aircraft was produced by the stiffer structural components (motors, battery, camera, etc.) of the UAS. This is consistent with observations from component level physical testing and simulations (Chapter 2).

Level 1	Green
Level 2	Yellow
Level 3	Orange
Level 4	Red

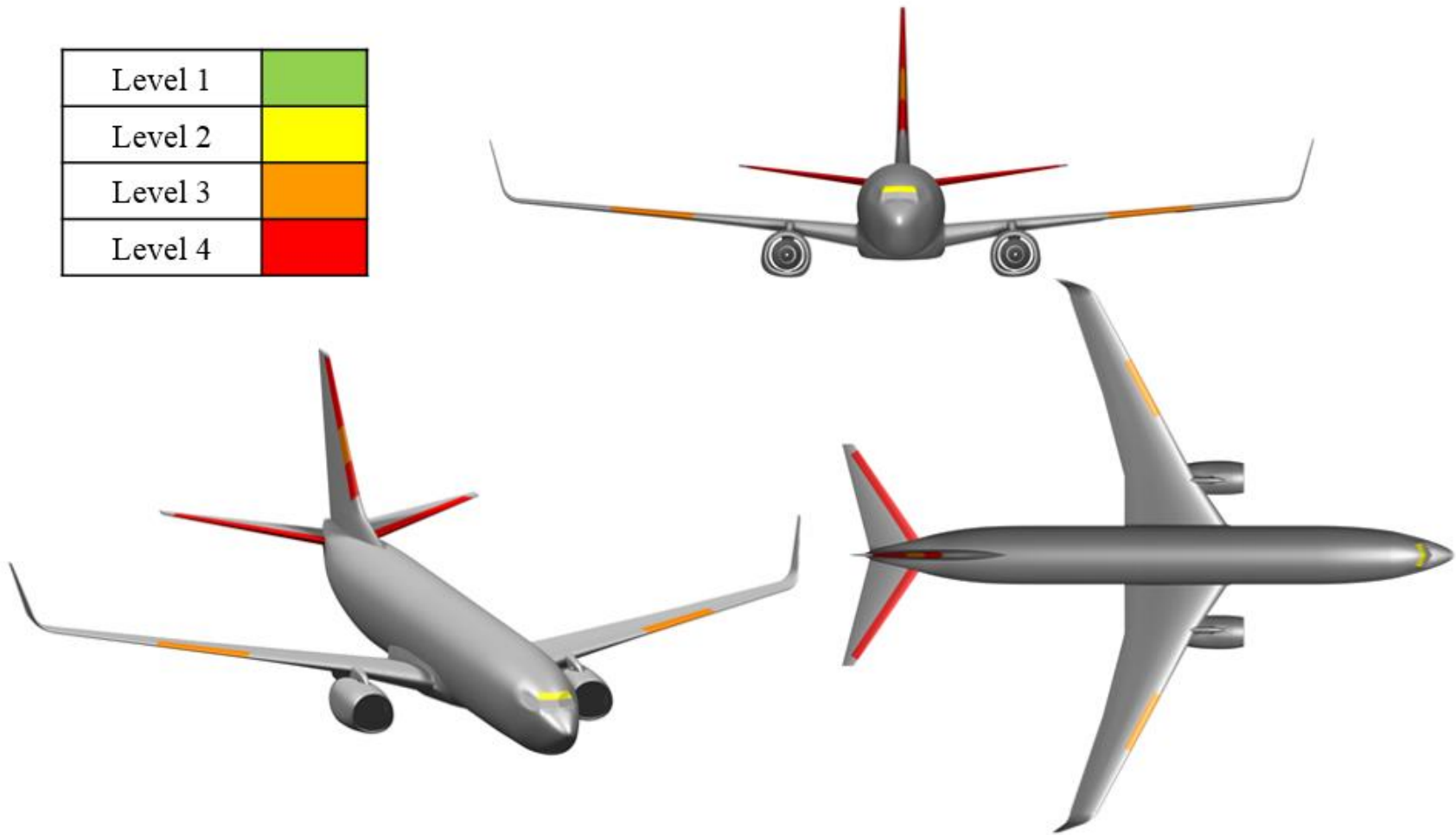


Figure 199. Summary of collision severity levels on commercial transport jet

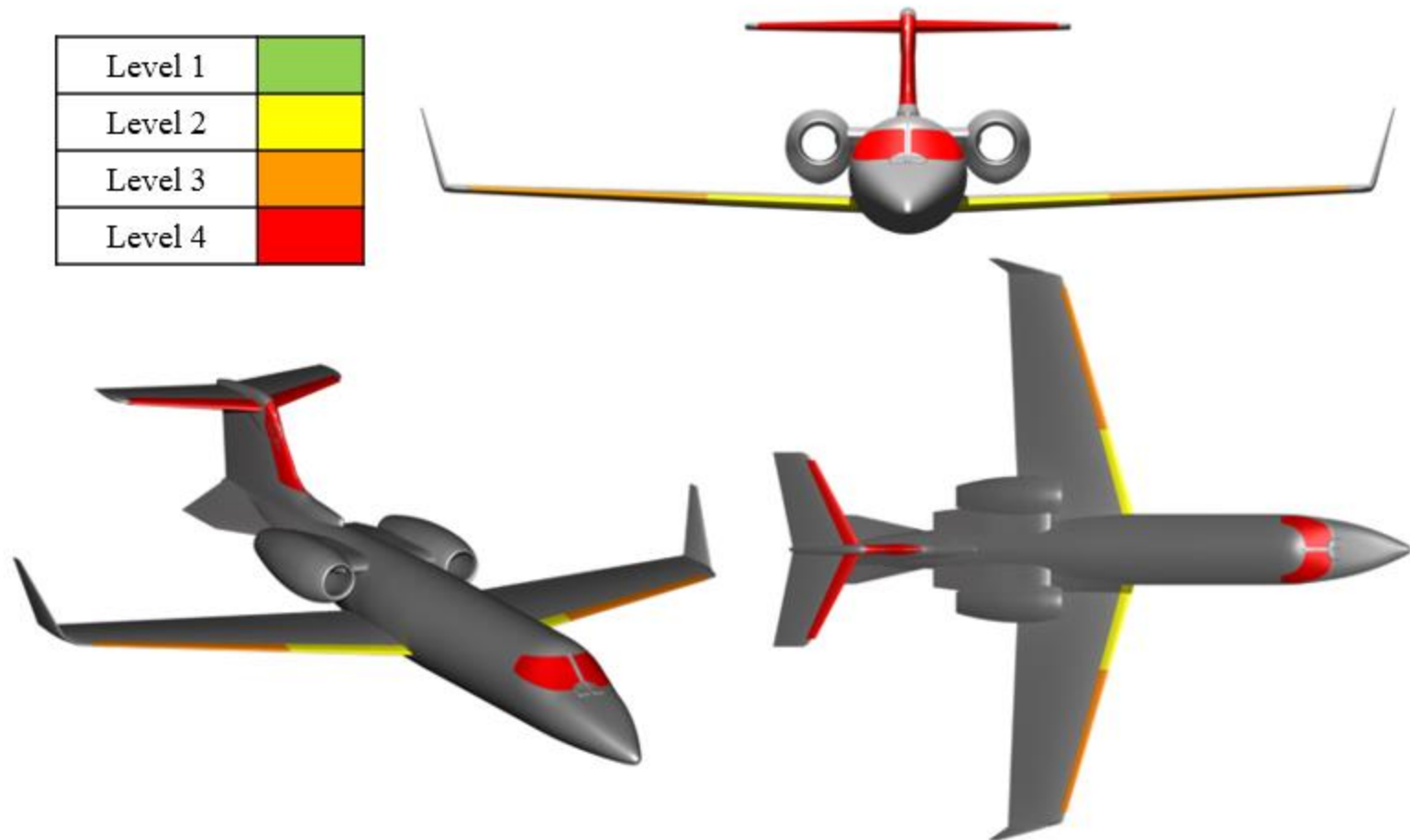


Figure 200. Summary of collision severity levels on business jet

8.3 IMPACT KINETIC ENERGY AND UAS ARCHITECTURE PARAMETRIC ANALYSES

The kinetic energy of a mid-air collision between an UAS and the two manned aircraft being studied in this project was characterized in terms of the UAS mass and relative impact velocity. The parametric study results and calculated damage severity levels were compared to those from corresponding baseline simulations. The results of this study are summarized in the following subsections. The worst-case impact conditions for each location identified in the airborne collision studies were used as a baseline for the parametric analyses. Additional work was conducted to compare the effect of the UAS configuration on the damage experienced by the target aircraft during airborne collisions.

8.3.1 Mass

The fixed-wing UAS was scaled-up from the 1.8 kg (4.0 lb) baseline mass to a final value of 3.6 kg (8.0 lb) in order to assess the potential increase in damage severity imparted by a heavier UAS. A 128.6 m/s (250 knots) impact velocity was defined for these airborne collision studies.

Table 38 presents the levels of severity of the impacts with the scaled-up UAS compared to their respective baseline simulations. The mass of the UAS in this parametric study contributed to a linear increase in the kinetic energy of the collision. The increased kinetic energy resulted in increased damage severity levels in two of the eight simulations and more extensive damage for those cases where the damage level classification remained the same.

Table 38. Mass scaled fixed-wing UAS impact simulation results

	Commercial Transport Jet				Business Jet			
	Vertical Stabilizer	Horizontal Stabilizer	Wing	Windshield	Vertical Stabilizer	Horizontal Stabilizer	Wing	Windshield
Baseline Fixed-Wing UAS 1.8 kg (4.0 lb)	Level 4	Level 4	Level 3	Level 2	Level 4	Level 4	Level 3	Level 4
Scaled-up Fixed-Wing UAS 3.6 kg (8.0 lb)	Level 4	Level 4	Level 4	Level 3	Level 4	Level 4	Level 3	Level 4

8.3.2 Impact Velocity

The impact velocity of the sixteen critical baseline simulations was varied to determine impact reactions at typical aircraft landing, holding, and cruise velocities for the commercial transport and business jets in order to assess the minimum and maximum damage that can be expected for similar mid-air collisions. The minimum landing velocity considered for the commercial and business jets was 56.7 m/s (110 knots) and 44.8 m/s (87 knots), respectively, and the cruise velocity was 187.8 m/s (365 knots) and 167.2 m/s (325 knots), respectively. The holding velocity was 128.6 m/s (250 knots) for both aircraft. In all cases, the UAS mass was 1.8 kg (4.0 lb). An increase

(or decrease) in the impact velocity resulted in a quadratic increase (or decrease) in the total impact energy

As shown in Table 39, the fixed-wing UAS impacts resulted in increased damage severity levels for two of the eight cruise velocity cases. The landing velocity cases showed decreased severity levels in all eight cases over the baseline. The damage was more extensive at higher velocities even for cases where the severity level remained the same.

Table 39. Velocity impact simulation results

	Commercial Transport Jet				Business Jet			
	Vertical Stabilizer	Horizontal Stabilizer	Wing	Windshield	Vertical Stabilizer	Horizontal Stabilizer	Wing	Windshield
Landing Velocity (110/87 knots)	Level 2	Level 2	Level 2	Level 1	Level 2	Level 2	Level 2	Level 1
Holding Velocity (250/250 knots)	Level 4	Level 4	Level 3	Level 2	Level 4	Level 4	Level 3	Level 4
Cruise Velocity (365/325 knots)	Level 4	Level 4	Level 4	Level 3	Level 4	Level 4	Level 3	Level 4

8.3.3 Conclusions Velocity and Mass Influence on Impact Damage

The impact velocity contributed to a greater amount of damage than the mass of the UAS. However, incremental increases in either parameter correlate to increased severity and extent of aircraft damage. Consequently, both velocity and mass have been identified as key factors on the severity of an airborne collision between an UAS and an aircraft. Aircraft velocities above minimum landing speeds are considered critical for a 1.8 kg (4.0 lb) fixed-wing UAS.

Note that the minimum landing velocity was selected to establish an absolute lower limit for impact velocity in the collision studies. However, a higher velocity is typical at normal operation of aircraft at take-off and landing, and therefore greater damage levels are expected. A more detailed velocity parametric analysis would be required to obtain conclusions of the actual risk posed by an airborne collision happening at those flight phases.

Finally, in this study the UAS masses investigated were between 1.8 and 3.6 kg (4.0 and 8.0 lb). Lower mass UASs will need to be studied in the future in order to determine a threshold in mass that will introduce level 1 or no damage into the airframe.

8.4 UAS IMPACT COMPARISONS TO EQUIVALENT BIRD IMPACTS

This study was conducted with the goal of determining whether an UAS impact can be considered equivalent to a bird strike with an identical mass and initial kinetic energy. Idealized birds of two different masses, 1.8 kg (4.0 lb) and 3.6 kg (8.0 lb), were selected for the comparison with fixed-wing UASs (see Chapter 6). No 8.0 lb bird strike analyses for the wing and windshield were conducted since *14 CFR Part 25.631* only requires 8.0 lb bird strike testing for the empennage.

The NIAR has conducted numerous studies of bird strike events and compared the results with physical testing [41]. SPH modeling techniques [26] were used to define the gelatin substitute bird models. These SPH bird models have been validated with experimental data [41].

Table 40 presents structural damage severity levels for each impact simulation. For all the cases the UAS created equal or more damage than the analogous bird. Hence, the bird strike cannot be considered equivalent to an UAS collision with the same mass and impact energy.

Table 40. UAS and bird impact simulation results

	Commercial Transport Jet				Business Jet			
	Vertical Stabilizer	Horizontal Stabilizer	Wing	Windshield	Vertical Stabilizer	Horizontal Stabilizer	Wing	Windshield
Fixed-wing UAS Baseline 1.8 kg (4.0 lb)	Level 4	Level 4	Level 3	Level 2	Level 4	Level 4	Level 3	Level 4
Bird 1.8 kg (4.0 lb)	Level 3	Level 2	Level 2	Level 2	Level 2	Level 2	Level 2	Level 1
Fixed-wing UAS Scaled 3.6 kg (8.0 lb)	Level 4	Level 4	Level 4	Level 3	Level 4	Level 4	Level 3	Level 4
Bird 3.6 kg (8.0 lb)	Level 3	Level 2	N/A	N/A	Level 2	Level 2	N/A	N/A

The simulations presented in chapter 6 identified that airborne collisions involving hard-bodied projectiles have characteristic features that distinguish them from bird strikes. Primarily, the damage zones for the fixed-wing UAS showed notable dents and penetrations due to the discrete masses and rigid, dense materials. The metallic motor promoted UAS penetration of the aircraft skin and associated damage to internal components (including the forward spar) in a majority of the simulations.

Figure 200 presents an example of the comparison UAS/Bird Strike, in this case against the horizontal stabilizer of the business jet. It can be seen that the UAS created a smaller region of impact

damage but that the penetration through the skin caused further penetration of the forward spar and damage to internal components of the aircraft. In contrast, the bird deformed considerably the external surface of the stabilizer, but with no penetration into the airframe. Consequently, the UAS impact is considered Level 4 damage while the bird impact was classified as Level 2.

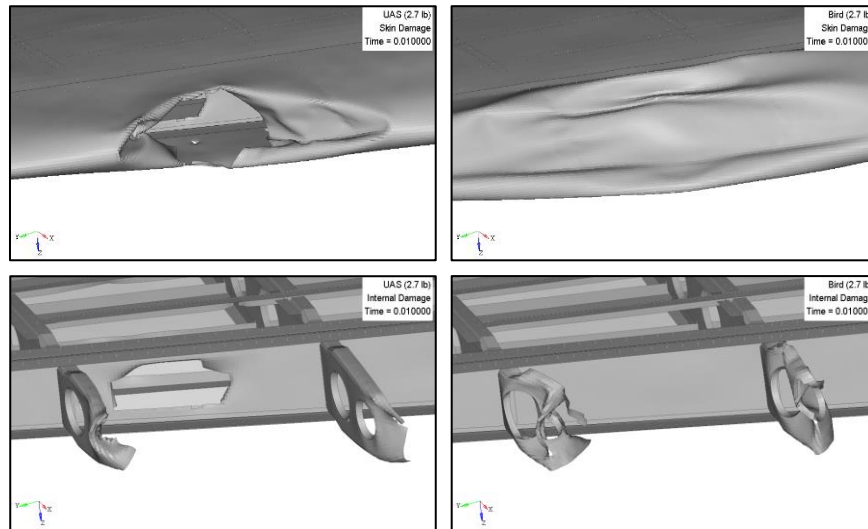


Figure 201. Comparison of damage after impact of a 1.8 kg (4.0 lb) fixed-wing UAS/Bird into a business jet horizontal stabilizer

8.4.1 Bird Strike – UAS Strike Comparison Conclusions

Fixed-wing UAS impacts are likely to cause more damage than bird strikes with an equivalent mass and initial kinetic energy. Since birds behave like a fluid during high velocity impacts, density is the main parameter that drives the magnitude of the damage in the target structure. In contrast, UASs do not exhibit this behavior. Structural rigidity (a combination of the structural geometry and material selection) drives the magnitude of the damage in the target structure.

The UAS impacts shown in this study were associated with greater damage levels than equivalent bird strikes due to the hard-bodied mechanical construction of the UAS, its components made of dense, rigid, materials and its discrete distribution of masses. Initial impact penetrations (caused by contact with a dense, rigid motor) were exacerbated as other high-density UAS components (*i.e.*, battery, camera) impacted subsequently the underlying aircraft structure causing progressively more structural damage. Therefore, a 4 lb/8 lb bird and a 4 lb/8 lb fixed-wing UAS will introduce profoundly different levels of damage to the aircraft structure.

While *14 CFR Part 25* aircraft were designed to withstand bird impact under the conditions described in *14 CFR 25.631: Bird Strike. Amdt. 25-23*, *14 CFR 25.775: Windshields and windows. Amdt. 25-38*, and *14 CFR 25.571: Damage-tolerance and fatigue evaluation of structure. Amdt. 25-96*, aircraft are not compliant to the same level as bird strikes when impacted by an analogous UAS [56] [57].

8.5 UAS SYSTEM ARCHITECTURE

This study was conducted with the goal of determining whether airborne collisions involving 1.8 kg (4.0 lb) quadcopter or fixed-wing UAS architectures can be considered equivalent to one-another. The simulations utilized identical initial and boundary conditions and impact energies.

As shown in the impact comparison presented in Chapters 6 and 7, airborne collisions involving hard-bodied projectiles have characteristic features that distinguish them from bird strikes. The primary similarity between the UAS simulations shown in Chapter 7 is that the dense, rigid components (motors and batteries) of both UAS models created penetrations in the aircraft skin which allowed the remaining mass of the UAS to enter the airframe and damage the internal components.

Table 41. Quadcopter and fixed-wing UAS impact simulation results - comparison at identical impact locations

	Commercial Transport Jet				Business Jet			
	Vertical Stabilizer	Horizontal Stabilizer	Wing	Windshield	Vertical Stabilizer	Horizontal Stabilizer	Wing	Windshield
Scaled-up Quadcopter 1.8 kg (4.0 lb)	Level 3	Level 4	Level 3	Level 3	Level 4	Level 4	Level 3	Level 2
Baseline Fixed-Wing 1.8 kg (4.0 lb)	Level 3	Level 4	Level 3	Level 2	Level 4	Level 4	Level 3	Level 3

The differences observed in the damage severity levels between quadcopter and fixed-wing UASs of the same mass indicate that the layout of the main UAS components is critical to the energy transfer during an airborne collision. The predicted critical damage occurred when the majority of the masses were aligned with the impact direction. The quadcopter UAS was oriented at the most critical yaw angle configuration, 45° [2]. At this orientation, the quadcopter UAS motor and battery align with the impact axis similar to the fixed-wing configuration as shown in Figure 202. Therefore, the damage levels to the aircraft airframe are similar for both UAS architectures.

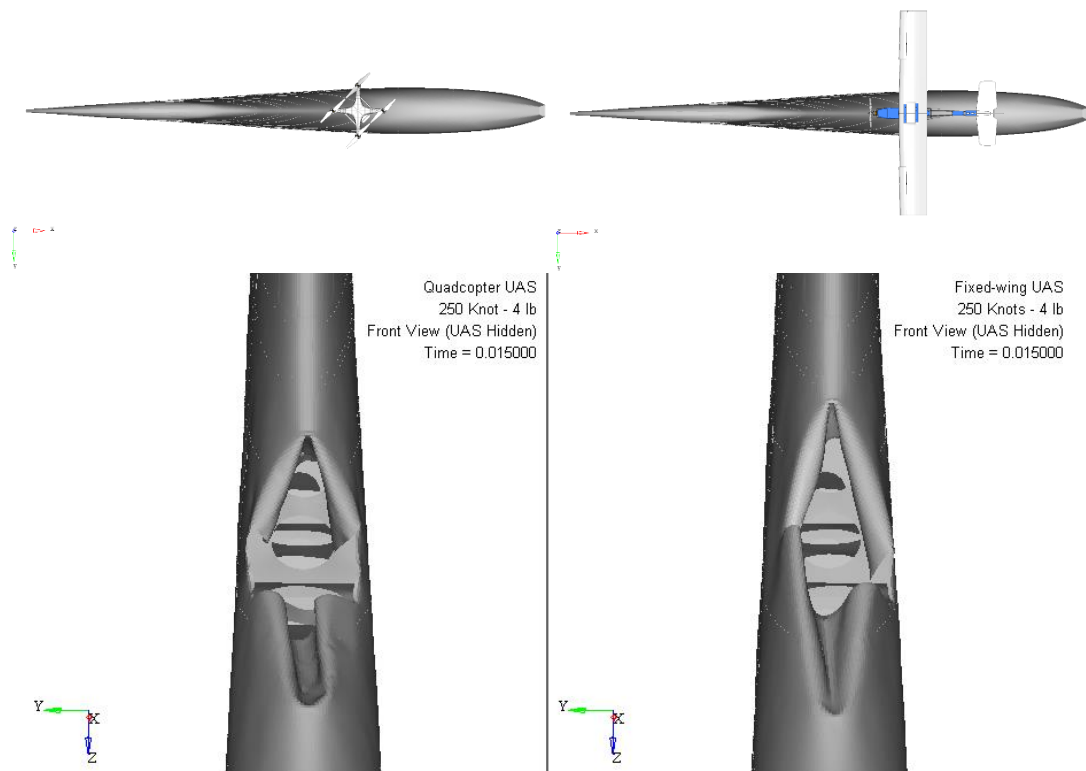


Figure 202. Comparison of damage after impact of 1.8 kg (4.0 lb) quadcopter (left) and fixed-wing (right) UASs into a business jet vertical stabilizer

8.6 FUTURE WORK

The research presented in this report shows that there is a risk of primary aircraft structure failures for several of the impact scenarios analyzed (commercial transport and business jets) with the 1.8 kg (4.0 lb) fixed-wing UAS configuration. Further research is needed to support the UAS airborne collision work:

8.6.1 UAS Airborne Collision R&D Roadmap

Define a Research and Development Roadmap to coordinate and prioritize airborne collision research activities required to support the FAA rulemaking objectives and timelines.

8.6.2 Airborne Collision Studies Phase II: General Aviation and Rotorcraft

Conduct a similar study as the one presented in this report to analyze mid-air collisions with GA aircraft and rotorcraft. The data generated in Phase I and Phase II can be used to aid in the development of an UAS Mid-Air Collisions Equivalent Level of Safety in order to regulate UAS operations in the NAS. This research should include additional component level testing at lower impact velocities from 50 to 100 knots to cover the GA impact collision scenarios and higher velocities as required by the tip speeds of rotorcraft blades and GA propellers.

8.6.3 Airborne Collision Standard: Development of an Unmanned Aircraft Systems Mid-Air-Collisions Equivalent Level of Safety

The primary goal of regulating UAS operations in the NAS is to assure an appropriate level of safety. This goal is quantified by national aviation agencies as ELOS with that of manned aviation. There are major key differences between manned and unmanned aviation that span the requisite level of automation, as well as the distinct variety of architectures and materials used for the construction of UASs. These differences could introduce new failure modes and, as a result, an increased perceived risk that needs to be evaluated [8].

In order to have an ELOS, the Range Commanders Council UAS guidelines stated that any UAS operation or test must show a level of risk to human life no greater than that for an operation or test of a piloted aircraft [9]. The aforementioned metrics can be used to provide statistical probabilities of UAS mid-air collisions according to specific parameters defined for the evaluation.

The risk assessment to develop an Airborne Collision UAS Impact Severity Classification can be divided into three elements:

- **Estimation of the probability of mid-air collision** between UASs and manned aircraft. This will be a function of the operating airspace, aircraft operated within the airspace, and the UAS configurations operating within the shared airspace. Methods to estimate the probability of impact are presented in references [10] [11].
- **Evaluation of severity of damage after collision for typical UASs.** Assess damage severity for mid-air collisions scenarios between unmanned aircraft (Classes based on weight, architecture, operational characteristics (altitude, velocity)) and manned aircrafts (commercial, GA, rotorcraft, etc.)). Several groups advocate use of simplified ballistic penetration models [15] and similar principles for establishing existing bird strike requirements or kinetic energy thresholds [16][17]. The objective of this project will be to evaluate the severity of a typical quadcopter and fixed-wing UAS airborne collision. These results will be compared with current proposed penetration mechanics and energy based criteria.
- Once the probability of an airborne collision is determined, **the damage models can be combined with the probabilistic collision models to define appropriate ELOS criteria.**

Using the data presented in this report and the data that will be developed in Phase II for GA aircraft and rotorcraft, a project should be performed in the near future to define the acceptable ELOS criteria to regulate UAS operations in the NAS.

8.6.4 UAS Certification by Analysis Protocol Development

In order to address the airborne collision severity levels for future UAS designs, it is necessary to develop a methodology that will enable industry to study the ELOS of new UAS designs.

It would be very difficult for UAS manufacturers to conduct future full scale physical testing to evaluate the structural impact behavior of UASs into various airframe locations. The limitations with physical testing are the following:

- Cost of representative airframe structures for testing is prohibitive.

- No standard representative airframe structure is available to conduct testing for all the possible UAS and aircraft collision scenarios.
- It is very difficult to conduct high velocity impact testing for complete UAS assemblies since their structures are not designed to withstand the aerodynamic loads generated by the required relative impact velocities (200+ knots).
- The UAS airframes likely will not withstand the acceleration levels required to achieve impact velocities (200+ knots) in the range of typical impact scenarios.
- It is difficult to quantify the damage, energy distributions, and overall crashworthiness behavior with full-scale experimental data only.

Based on the results of Phase I for the airborne collision studies, we recommend to develop a Certification by Analysis protocol supported by the Building Block Approach to be able to conduct future UAS impact evaluations and crashworthiness certification (similar research efforts are ongoing for certification of aircraft interiors and airframe crashworthiness per *AC20-146*).

8.6.5 Mass, Impact Velocity and Architecture Risk Classification

Develop a reference damage level matrix based on mass, velocity, and UAS configurations to cover the range of UAS configurations under the 55 lb limit defined by the Small Unmanned Aircraft Rule (*Part 107*).

9. REFERENCES

- [1] “Raise of the Drones. Managing the Unique Risks Associated with Unmanned Aircraft Systems”, Alliance Global Corporate & Specialty, 2016.
- [2] Olivares G., Gomez, L., Espinosa de los Monteros, J., Baldrige, R., Zinzuwadia, C., and Aldag, T., “Volume II – UAS Airborne Collision Severity Evaluation – Quadcopter”, Federal Aviation Administration, Report DOT/FAA/AR-XX/XX, (to be published).
- [3] D’Souza, K., Gregory, J.W., “Volume IV – UAS Airborne Collision Severity Evaluation – Engine Ingestion”, Federal Aviation Administration, Draft Report DOT/FAA/AR-XX/XX (to be published).
- [4] Public Law 112-95, Section 331-333(8).
- [5] FAA Advisory Circular AC 107-2, “Small Unmanned Aircraft System (sUAS)”, Washington, DC, 2016.
- [6] Micro Unmanned Aircraft Systems Aviation Rulemaking Committee, “ARC Recommendations Final Report”, 2016.
- [7] Unmanned Aircraft Systems: accessed at https://www.faa.gov/data_research/aviation/aerospace_forecasts/media/Unmanned_Aircraft_Systems.pdf
- [8] Dalamagkidis, K., Valavanis, K., and Piegler, L. A., *On Integrating Unmanned Aircraft Systems into the National Airspace System*, 2nd ed., Springer Netherlands, 2012.
- [9] Range Safety Group, Range Commanders Council, “Range Safety Criteria for Unmanned Air Vehicles”, Document 323-99, 2001.
- [10] Lum, C. W., and Waggoner, B., “A Risk Based Paradigm and Model for Unmanned Aerial Systems in the National Airspace”, *Infotech@Aerospace Conferences*, 2011-1424, AIAA, St. Louis, MO, 2011.
- [11] Weibel, R., Hansman, R. J., “Safety Considerations for Operation of Different UAVs in the NAS”, *AIAA 3rd Unmanned Unlimited Technical Conference, Workshop and Exhibit*, Paper No. 2004-6421, AIAA, Chicago, IL, 2004.
- [12] McQuarrie, D. A., and Simon, J. D., *Physical Chemistry: A Molecular Approach*, University Science Books, 1997.
- [13] McGeer, T., Newcome, L., and Vagners, J., “Quantitative Risk Management as a Regulatory Approach to Civil UAVs”, *International Workshop on UAV Certification*, 1999.
- [14] McGeer, T., “Aerosonde Hazard Estimation,” The Insitu Group, 1994.
- [15] Civil Aviation Safety Authority, “Potential Damage Assessment of a Mid-Air Collision with a Small UAV”, Technical Report, 2013.
- [16] Fraser, C. S. R., and Donnithorne-Tait, D., “An Approach to the Classification of Unmanned Aircraft”, *26th International Conference on Unmanned Air Vehicle Systems 2011*, Bristol, UK, 2011, pp. 157-211.
- [17] Marshall, M. M., Anderson, E. E., and Tighe, D. E., “A Literature Review in Support of TCRG 14-05: UAS Systems Safety Criteria”, Draft Report, FAA Award 14-G-007, 2015.

- [18] Jimenez, H., Mavris, D., Hoffman, D., Mines, J., and O'Sullivan, S., "A Survey of Evaluation Methods for Unmanned Aircraft Risk and Safety to Third Parties", Report, Federal Aviation Administration, 2015.
- [19] FAA COE Task: A11LUAS.COE.7 .2 UAS Airborne Collision Severity Evaluation.
- [20] "ASSURE," [Online]. Available: <http://assureuas.org>. [Accessed 2 11 2016]
- [21] Cairns, D. S., Johnson, G., Edens, M., and Arnold, F., "Volume I – UAS Airborne Collision Severity Evaluation – Projectile and Target Definition", Federal Aviation Administration, Report DOT/FAA/AR-XX/XX, (to be published).
- [22] FAA Modernization and Reform Act of 2012, Title III, Sec. 333, "Special Rules for Certain Unmanned Aircraft Systems", Washington, DC, U.S. Government Printing Office, 2012.
- [23] Dassault Systems, "CATIA PLM Software Solution," [Online]. Available: <http://www.3ds.com/products-services/catia/>. [Accessed 2 11 2016].
- [24] E. L. Fasanella and K. E. Jackson, "Best Practices for Crash Modeling and Simulation," NASA/TM-2002-211944, ARL-TR-2849, 2002.
- [25] "LS-DYNA Aerospace Working Group Modeling Guidelines Document," 2015.
- [26] "LS-DYNA Keyword User's Manual Volume I," Livermore Software Technology Corporation, 2015.
- [27] "LS-DYNA Keyword User's Manual Volume II: Material Models," Livermore Software Technology Corporation, 2015.
- [28] X. Quan, R. A. Clegg, M. S. Cowler, N. K. Birnbaum and C. J. Hayhurst, "Numerical Simulation of Long Rods Impacting Silicon Carbide Targets Using JH-1 Model," *International Journal of Impact Engineering*, vol. 33, pp. 634-644, 2006.
- [29] R. Shivpuri, X. Cheng and Y. Mao, "Elasto-plastic Pseudo-dynamic Numerical Model for the Design of Shot Peening Process Parameters," *Materials and Design*, vol. 30, pp. 3112-3120, 2009.
- [30] M. Buyuk, "Development of a Tabulated Thermo-viscoplastic Material Model with Regularized Failure for Dynamic Ductile Failure Prediction of Structures Under Impact Loading," 2012.
- [31] Aerospace Specification Metals Inc., "Aluminum 6061-T6; 6061-T651," [Online]. Available: <http://asm.matweb.com/search/SpecificMaterial.asp?bassnum=MA6061t6>. [Accessed 2 11 2016].
- [32] E. Sahraei, R. Hill and T. Wierzbicki, "Calibration and Finite Element Simulation of Pouch Lithium-ion Batteries for Mechanical Integrity," *Journal of Power Sources*, vol. 201, pp. 307-321, 2012.
- [33] Autum Imp & Exp Co., Ltd, "FR-4 Tg170 (AT-6167)," [Online]. Available: <http://www.autumintl.com/upload/pdf/AT6167.pdf>. [Accessed 2 11 2016].

- [34] P. D. Soden, M. J. Hinton and A. S. Kaddour, "Lamina Properties, Lay-up Configurations and Loading Conditions for a Range of Fibre-Reinforced Composite Laminates," *Composites Science and Technology*, vol. 58, pp. 1011-1022, 1998.
- [35] Plastics International, "ABS," [Online]. Available: <http://www.plasticsintl.com/abs.htm>. [Accessed 2 11 2016].
- [36] MatWeb, "BASF Capron® 8202 NL Nylon 6 (Dry)," 2 11 2016. [Online]. Available: <http://www.matweb.com/search/DataSheet.aspx?Mat-GUID=d233c57fac534034b79c9dd6ef622aa8>.
- [37] APC Propellers, "Research: Manufacturing Process Used To Develop APC Propellers," [Online]. Available: <https://www.apcprop.com/Articles.aspx?ID=263#mat>. [Accessed 11 2 2016].
- [38] MatWeb, "BASF Ultramid® B35EG3 BK 00564 15% Glass Filled PA6 (Dry)," [Online]. Available: <http://www.matweb.com/search/DataSheet.aspx?Mat-GUID=74bb39d035484dfe9e8eca6cbbd509f3>. [Accessed 11 2 2016].
- [39] C. C. Poe, Jr., "Stress Intensity Factor for a Cracked Sheet with Riveted and Uniformly spaced Stringers", Langley Center, NASA TR-T-356, May 1971.
- [40] T. Swift, FAA National Resource Specialist, "Damage tolerance Technology: A course in Stress Analysis Oriented Fracture Mechanics".
- [41] Olivares, G., "Simulation and Modeling of Bird Strike Testing", NIAR Report No. 09-039, National Institute for Aviation Research, 2009.
- [42] Society of Automotive Engineers, "Recommended Practice: Instrumentation for Impact Test – Part 1, Electronic Instrumentation," 1995.
- [43] Olivares G., Raju, S. K., and Acosta, J. F., "Certification by Analysis – Composite Materials Modeling", Draft Report DOT/FAA/AR-XX/XX, (not published).
- [44] Olivares, G., Zinzuwadia, C., and Dhole N., "Crashworthiness Analysis of a Generic Narrow Body Aircraft", Draft Report DOT/FAA/AR-XX/XX, (not published).
- [45] Olivares, G., and Zinzuwadia, C., "Joint modeling for large scale crashworthiness FE models – Single-point bolted joint", Draft Report DOT/FAA/AR-XX/XX, (not published).
- [46] Jackson, K.E., and Fasanella, E.L., "Crash Simulation of Vertical Drop Tests of Two Boeing 737 Fuselage Sections", Report DOT/FAA/AR-02/62, Federal Aviation Administration, 2002.
- [47] Olivares, G., Zinzuwadia, C., and Gomez, L., "Crashworthiness Certification by Analysis – Accident Reconstruction", Draft Report, DOT/FAA/AR-XX/XX, (not published).
- [48] "Current Market Outlook 2014-2034", The Boeing Company, URL: <http://www.boeing.com/commercial/market/long-term-market/>
- [49] "Delivering the Future – Global Market Forecast 2014-2034", Airbus SAS, URL: <http://www.airbus.com/company/market/forecast/>
- [50] "Orders and Deliveries", The Boeing Company, URL: <http://www.boeing.com/commercial/#/orders-deliveries/>

- [51] “Orders and Deliveries”, Airbus SAS, URL: <http://www.airbus.com/company/market/orders-deliveries/>
- [52] Jackson, P., *Jane’s All the World’s Aircraft 2007-2008*, Jane’s Information Group, 2007.
- [53] Jackson, P., *Jane’s All the World’s Aircraft 1999-2000*, Jane’s Information Group, 1999.
- [54] *Learjet 31A Airplane Flight Manual*, Bombardier Learjet Inc., 1991.
- [55] Dolbeer, R.A., Wright, S.E., Weller, J.R., Anderson, A.L., and Begier, M.J., “Wildlife strikes to civil aircrafts in the United States 1990-2014”, National Wildlife Strike Database, Serial Report No. 21, Federal Aviation Administration, 2015.
- [56] U.S. Code of Federal Regulations, Title 14, Part 25, “Airworthiness standards: transport category airplanes”, Washington, DC, U.S. Government Publishing Office, 2016.
- [57] U.S. Code of Federal Regulations, Title 14, Part 23, “Airworthiness standards: normal, utility, acrobatic, and commuter category airplanes”, Washington, DC, U.S. Government Publishing Office, 2016.
- [58] *737-800 Structural Repair Manual*, The Boeing Company, 2013.
- [59] *Learjet 20/30 Structural Repair Manual*, Bombardier Learjet, 2015.
- [60] Niu, M.C., *Airframe Structural Design*, Conmilit Press Ltd., 1993.
- [61] “PPG Aerospace Transparencies, Technical Data, Cockpit Windows, Next-Generation 737, Classic 737, 727, 707 Airplanes”, PPG Industries, Huntsville, Alabama.
- [62] Du Bois, P. A., “Crashworthiness engineering with LS-DYNA”, Daimler-Chrysler AG, 2000.
- [63] Day, J., and Bala, S., “General Guidelines for Crash Analysis in LS-DYNA”, Livermore Software Technology Corporation, 2012.
- [64] FAA Advisory Circulatory AC 43.13-1B, “Acceptable Methods, Techniques, and Practices - Aircraft Inspection and Repair”, Federal Aviation Administration, 1998.
- [65] Kay, G., “Failure Modeling of Titanium 6Al-4V and Aluminum 2024-T3 With the Johnson-Cook Material Model”, Report DOT/FAA/AR-03/57, Federal Aviation Administration, 2003.
- [66] Buyuk, M., “Development of a New Metal Material Model in LS-DYNA. Part 2: Development of A Tabulated Thermo-Viscoplastic Material Model With Regularized Failure for Dynamic Ductile Failure Prediction of Structures Under Impact Loading”, Technical Report DOT/FAA/TC-13/25, P2, Federal Aviation Administration, 2014.
- [67] MMPDS-09, Metallic Material Properties Development and Standardization (MMPDS), Chapter 9, Ed. 7, Battelle Memorial Institute, 2014.
- [68] Bala, S., “Material modeling in LS-DYNA”, LSTC Training Notes, Livermore Software Technology Corporation, 2005.
- [69] Wang, J., Xu, Y., and Zhang, W., “Finite Element Simulation of PMMA Aircraft Windshield against Bird Strike by Using a Rate and Temperature Dependent Nonlinear Viscoelastic Constitutive Model”, *Composite Structures*, Vol. 108, 2014, pp. 21-30.

- [70] Hidallana-Gamage, H.D., “Response of Laminated Glass Panels to Near Field Blast Events”, PhD Thesis, Queensland University of Technology, Australia, 2015.
- [71] Hassard, R.S., “Plastic for Aerospace Vehicles. Part II Transparent Glazing Materials”, MIL-HDBK-17A Part II, Air Force Materials Lab., 1973.
- [72] U.S. Code of Federal Regulations, Title 14, Part 91, “General Operation and Flight Rules”, Washington, DC, U.S. Government Publishing Office, 2016.
- [73] “Airspace Made Easy”, Federal Aviation Administration, URL:
https://www.faa.gov/files/events/ea/ea03/2012/ea0345029/airspace_made_easy.pdf
- [74] LS-DYNA Support, "Total Energy," [Online]. Available: <http://www.dynasupport.com/howtos/general/total-energy>. [Accessed 2 11 2016].

APPENDIX A – FIXED-WING UAS MODEL DETAILS

A.1 FE MODEL DETAILS

Table 42. Measured Precision Hawk subassemblies/components masses

SUBASSEMBLY	COMPONENT	MATERIAL	MASS (G)
FUSELAGE	Fuselage PCB (L)	FR4	487.0
	Fuselage PCB (R)	FR4	
	Top PCB	FR4	
	Sullins Connector	ABS	
	Mounting Brackets	Steel 4340	
	Top CPU Board	FR4	
	Wing Bolts	Steel 4340	
	Bottom Structural PCB	FR4	
	Front Green PCB	FR4	
	Front White PCB	FR4	
	LCD Screen	ABS	
	LCD Shell	ABS	
WING	Wing PCBs	FR4	28.6
	Connecting Rod	Carbon/epoxy	14.0
	Lug Nut And Screw for Wings	Steel 4340	370.0
	Sullins Connectors	ABS	
	Wing	Polystyrene	
	Spar	Carbon/epoxy	
TAIL	Top Digi Extend Board	FR4	143.4
	Side Internal Boards	FR4	
	Rear Center Vertical Board Front	FR4	
	Rear Center Vertical Board Back	FR4	
	Tail Connecting Hollow Tubes	Carbon/epoxy	
	Tail Green Board	FR4	
	Tail Servo Board	FR4	
	Tail Vertical Board	FR4	
	Tail White Board	FR4	
	Servomechanisms	ABS	
	Digi International	FR4	16.6
	Horizontal Stabilizer	Polystyrene	49.5
	Vertical Stabilizer	Polystyrene	41.1
	Tail Mount	ABS	

Table 42 (cont'd). Measured Precision Hawk subassemblies/components masses

SUBASSEMBLY	COMPONENT	MATERIAL	MASS (G)
MOTOR	Core	Steel 4340	90.6
	Grip Collar	AL 2024-T351	
	Gripper	AL 2024-T351	
	Motor Rotor	Steel 4340	
	Motor Stator	Steel 4340	
	Motor Firewall	FR4	20.0
	Motor Back Plate	Steel 4340	4.5
	Propeller Blade Mount	Nylon 6 GRP	2.7
	Propeller Blade	Nylon 6 GRP	17.4
BATTERY	Battery Bottom Wall	ABS	335.4
	Battery Back	FR4	
	Battery Wall (L)	FR4	
	Battery Wall (R)	FR4	
	Battery Support	FR4	
	Battery	LiPo	
PAYLOAD	Payload Part	FR4	394.3
	Payload Part2	FR4	
	Payload Part3	FR4	
	Payload Part4	FR4	
	Camera	AL 6061-T6	
	Black Sullins Connector	ABS	
TOTAL WEIGHT			2015.1

Table 43. Fixed-wing FE model material models and FE types

Part Name	Part Id	Material Name	Material Id	Material Type	Shell Fe Thickness (mm)	Section Name	Section Id	Section Type
Right Fuselage Board	20001	FR4_XZ	26513	MATL54_55	1.1	N/A	N/A	N/A
Left Fuselage Board	20002	FR4_XZ	26513	MATL54_55	1.1	N/A	N/A	N/A
Structural Boards	20003	FR4_XY	26515	MATL54_55	1.1	N/A	N/A	N/A
CPU Board	20004	FR4_XY	26515	MATL54_55	1.1	N/A	N/A	N/A
Power Board	20005	FR4_XY	26515	MATL54_55	1.1	N/A	N/A	N/A
GPS Board	20006	FR4_XY	26515	MATL54_55	1.1	N/A	N/A	N/A
Autopilot Board	20007	FR4_XY	26515	MATL54_55	1.1	N/A	N/A	N/A
Wing Mount_1	20008	MATL15_Mounts	26501	MATL15	0.7	SectShll_Mounts_0.7mm	27004	SectShll
Wing Mount_2	20009	MATL15_Mounts	26501	MATL15	0.7	SectShll_Mounts_0.7mm	27004	SectShll
Wing Mount_3	20010	MATL15_Mounts	26501	MATL15	0.7	SectShll_Mounts_0.7mm	27004	SectShll
Wing Mount_4	20011	MATL15_Mounts	26501	MATL15	0.7	SectShll_Mounts_0.7mm	27004	SectShll
Cam Mount_1	20012	MATL15_Mounts	26501	MATL15	0.7	SectShll_Mounts_0.7mm	27004	SectShll
Cam Mount_2	20013	MATL15_Mounts	26501	MATL15	0.7	SectShll_Mounts_0.7mm	27004	SectShll
Cam Mount_3	20014	MATL15_Mounts	26501	MATL15	0.7	SectShll_Mounts_0.7mm	27004	SectShll
Cam Mount_4	20015	MATL15_Mounts	26501	MATL15	0.7	SectShll_Mounts_0.7mm	27004	SectShll
GPS Mount_1	20016	MATL15_Mounts	26501	MATL15	0.7	SectShll_Mounts_0.7mm	27004	SectShll
GPS Mount_2	20017	MATL15_Mounts	26501	MATL15	0.7	SectShll_Mounts_0.7mm	27004	SectShll
GPS Mount_3	20018	MATL15_Mounts	26501	MATL15	0.7	SectShll_Mounts_0.7mm	27004	SectShll
GPS Mount_4	20019	MATL15_Mounts	26501	MATL15	0.7	SectShll_Mounts_0.7mm	27004	SectShll
Autopilot	20020	MATL24_ABS	26502	MATL24	1.35	SectShll_1.35mm	27010	SectShll
LCD Shell	20021	MATL24_ABS	26502	MATL24	1.35	SectShll_1.35mm	27010	SectShll
LCD Screen	20022	MATL24_ABS	26502	MATL24	N/A	SectSld	27041	SectSld
Right Sullins Connector	20023	MATL24_ABS	26502	MATL24	N/A	SectSld	27041	SectSld
Left Sullins Connector	20024	MATL24_ABS	26502	MATL24	N/A	SectSld	27041	SectSld
GPS Board Screws	20025	MATL24_SteelScrews	26503	MATL24	N/A	SectBeam_3.7mm	27026	SectBeam

Table 43 (cont'd). Fixed-wing FE model material models and FE types

Part Name	Part Id	Material Name	Material Id	Material Type	Shell FE Thickness (mm)	Section Name	Section Id	Section Type
Right Wing	21001	MATL63_Wings	26508	MATL63	N/A	SectSld	27041	SectSld
Left Wing	21002	MATL63_Wings	26508	MATL63	N/A	SectSld	27041	SectSld
Right Carbon/Epoxy Spar	21003	Carbon/Epoxy Spar	26510	MATL54_55	0.9	N/A	N/A	N/A
Left Carbon/Epoxy Spar	21004	Carbon/Epoxy Spar	26510	MATL54_55	0.9	N/A	N/A	N/A
Right PCB Spar	21005	FR4_XZ	26513	MATL54_55	0.7	N/A	N/A	N/A
Left PCB Spar	21006	FR4_XZ	26513	MATL54_55	0.7	N/A	N/A	N/A
Spar Connecting Rod	21007	Carbon/Epoxy Spar	26510	MATL54_55	0.7	N/A	N/A	N/A
Fore Top Connector	21008	FR4_XY	26515	MATL54_55	1.2	N/A	N/A	N/A
Aft Top connector	21009	FR4_XY	26515	MATL54_55	1.2	N/A	N/A	N/A
Fore Bottom Connector	21010	FR4_XY	26515	MATL54_55	1.2	N/A	N/A	N/A
Aft Bottom Connector	21011	FR4_XY	26515	MATL54_55	1.2	N/A	N/A	N/A
Wing Connector Screws	21012	MATL24_SteelScrews	26503	MATL24	N/A	SectBeam_3.7mm	27026	SectBeam
V_Tail	22001	MATL63_Wings	26508	MATL63	N/A	SectSld	27041	SectSld
H_Tail	22002	MATL63_Wings	26508	MATL63	N/A	SectSld	27041	SectSld
Right Sullins Female	22003	MATL24_ABS	26502	MATL24	N/A	SectSld	27041	SectSld
Left Sullins Female	22004	MATL24_ABS	26502	MATL24	N/A	SectSld	27041	SectSld
Plastic Flange V_Tail	22005	MATL24_ABS	26502	MATL24	N/A	SectSld	27041	SectSld
Plastic Flange V_tail	22006	MATL24_ABS	26502	MATL24	1	SectShll_1mm_NLOC-1	27017	SectShll
Fore Tail_Fuselage PCB	22007	FR4_YZ	26514	MATL54_55	1.4	N/A	N/A	N/A
Aft Tail_Fuselage PCB	22008	FR4_YZ	26514	MATL54_55	1.4	N/A	N/A	N/A
Right Tail_Fuselage PCB	22009	FR4_XZ	26513	MATL54_55	1.4	N/A	N/A	N/A
Left Tail_Fuselage PCB	22010	FR4_XZ	26513	MATL54_55	1.4	N/A	N/A	N/A
Right Tail Boom	22011	Carbon/Epoxy Tail-boom Right	26511	MATL54_55	1	N/A	N/A	N/A
Left Tail Boom	22012	Carbon/Epoxy Tail-boom Left	26512	MATL54_55	1	N/A	N/A	N/A
Fore Tail PCB	22013	FR4_YZ	26514	MATL54_55	1.4	N/A	N/A	N/A

Table 43 (cont'd). Fixed-wing FE model material models and FE types

Part Name	Part Id	Material Name	Material Id	Material Type	Shell FE Thickness (mm)	Section Name	Section Id	Section Type
Aft Tail PCB	22014	FR4_YZ	26514	MATL54_55	1.4	N/A	N/A	N/A
Top Tail PCB	22015	FR4_XY	26515	MATL54_55	1.4	N/A	N/A	N/A
Bottom Tail PCB	22016	FR4_XY	26515	MATL54_55	1.4	N/A	N/A	N/A
Fore Servo	22017	MATL24_ABS	26502	MATL24	1.4	SectShll_1.4mm	27011	SectShll
Aft Servo	22018	MATL24_ABS	26502	MATL24	1.4	SectShll_1.4mm	27011	SectShll
Antena	22019	FR4_XY	26515	MATL54_55	1.4	N/A	N/A	N/A
Antena_Board	22020	FR4_XY	26515	MATL54_55	1.4	N/A	N/A	N/A
Transmitter	22021	FR4_XY	26515	MATL54_55	1.4	N/A	N/A	N/A
Transmitter_Board	22022	FR4_XY	26515	MATL54_55	1.4	N/A	N/A	N/A
Tail Straps	22023	MATL24_Nylon6	26505	MATL24	0.8	SectShll_Tiestraps_0.8mm	27005	SectShll
V_Tail Screws	22024	MATL24_ABS	26502	MATL24	N/A	SectBeam_1.75mm	27021	SectBeam
Empennage Screws	22025	MATL24_ABS	26502	MATL24	N/A	SectBeam_5mm	27027	SectBeam
Firewall_Mounts	23001	MATL15_Mounts	26501	MATL15	0.7	SectShll_Mounts_0.7mm	27004	SectShll
Firewall	23002	FR4_YZ	26514	MATL54_55	1.7	N/A	N/A	N/A
Motor Backplate	23003	MATL15_Mounts	26501	MATL15	N/A	SectSld	27041	SectSld
Retainer	23004	MATL15_Mounts	26501	MATL15	N/A	SectSld	27041	SectSld
Stator Core	23005	MATL15_Mounts	26501	MATL15	N/A	SectSld	27041	SectSld
Rotor	23006	MATL15_Mounts	26501	MATL15	N/A	SectSld	27041	SectSld
Gripper	23007	MATL224	26516	MATL224	N/A	SectSld	27041	SectSld
Grip collar	23008	MATL224	26516	MATL224	N/A	SectSld	27041	SectSld
Top Center Hinge	23009	MATL24_Nylon6	26505	MATL24	N/A	SectSld	27041	SectSld
Bottom Center Hinge	23010	MATL24_Nylon6	26505	MATL24	N/A	SectSld	27041	SectSld
Right Propeller Hub	23011	MATL24_NylonGRP	26504	MATL24	N/A	SectSld	27041	SectSld
Right Propellor_1	23012	MATL24_NylonGRP	26504	MATL24	4	SectShll_Prop1_2_4mm	27016	SectShll
Right Propellor_2	23013	MATL24_NylonGRP	26504	MATL24	4	SectShll_Prop1_2_4mm	27016	SectShll
Right Propellor_3	23014	MATL24_NylonGRP	26504	MATL24	2.75	SectShll_Prop3_2.75mm	27015	SectShll


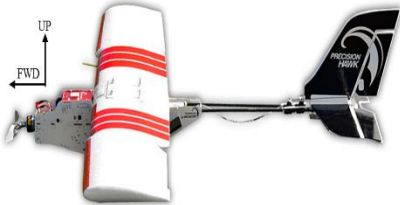
Table 43 (cont'd). Fixed-wing FE model material models and FE types

Part Name	Part Id	Material Name	Material Id	Material Type	Shell FE Thickness (mm)	Section Name	Section Id	Section Type
Right Propellor_4	23015	MATL24_NylonGRP	26504	MATL24	2	SectShll_Prop4_2mm	27014	SectShll
Right Propellor_5	23016	MATL24_NylonGRP	26504	MATL24	1.1	SectShll_1.1mm	27008	SectShll
Left propeller Hub	23017	MATL24_NylonGRP	26504	MATL24	N/A	SectSld	27041	SectSld
Left Propeller_1	23018	MATL24_NylonGRP	26504	MATL24	4	SectShll_Prop1_2_4mm	27016	SectShll
Left Propeller_2	23019	MATL24_NylonGRP	26504	MATL24	4	SectShll_Prop1_2_4mm	27016	SectShll
Left Propeller_3	23020	MATL24_NylonGRP	26504	MATL24	2.75	SectShll_Prop3_2.75mm	27015	SectShll
Left Propeller_4	23021	MATL24_NylonGRP	26504	MATL24	2	SectShll_Prop4_2mm	27014	SectShll
Left Propeller_5	23022	MATL24_NylonGRP	26504	MATL24	1.1	SectShll_1.1mm	27008	SectShll
Nozzle	23023	MATL224	26516	MATL224	N/A	SectSld	27041	SectSld
Firewall_Backplate Screws	23024	MATL24_SteelScrews	26503	MATL24	N/A	SectBeam_3.1mm	27024	SectBeam
Backplate_Stator Screws	23025	MATL24_SteelScrews	26503	MATL24	N/A	SectBeam_2.54mm	27022	SectBeam
Propeller Hinge Screws	23026	MATL24_SteelScrews	26503	MATL24	N/A	SectBeam_3.05mm	27023	SectBeam
Bottom Battery PCB	24001	FR4_XY	26515	MATL54_55	1.5	N/A	N/A	N/A
Aft Battery PCB	24002	FR4_YZ	26514	MATL54_55	1.5	N/A	N/A	N/A
Right Battery PCB	24003	FR4_XZ	26513	MATL54_55	1.5	N/A	N/A	N/A
Left Battery PCB	24004	FR4_XZ	26513	MATL54_55	1.5	N/A	N/A	N/A
Right Support PCB	24005	FR4_XZ	26513	MATL54_55	1	N/A	N/A	N/A
Left Support PCB	24006	FR4_XZ	26513	MATL54_55	1	N/A	N/A	N/A
Bottom Cell	24007	MATL63_Battery	26509	MATL63	N/A	SectSld_Battery	27042	SectSld
Middle Cell	24008	MATL63_Battery	26509	MATL63	N/A	SectSld_Battery	27042	SectSld
Top Cell	24009	MATL63_Battery	26509	MATL63	N/A	SectSld_Battery	27042	SectSld
Al Foil Wrap	24010	MATL24_Camera	26507	MATL24	0.11	SectShll_AlFoil_0.11mm	27001	SectShll
Battery Shell	24011	MATL24_BaShell	26506	MATL24	0.38	SectShll_BatteryShell_0.38mm	27003	SectShll
Foam blocks	24012	MATL63_Wings	26508	MATL63	N/A	SectSld	27041	SectSld
Tie straps	24013	MATL24_Nylon6	26505	MATL24	0.32	SectShll_BottBattery_0.32mm	27002	SectShll

Table 43 (cont'd). Fixed-wing FE model material models and FE types

Part Name	Part Id	Material Name	Material Id	Material Type	Shell FE Thickness (mm)	Section Name	Section Id	Section Type
Top Payload PCB	25001	FR4_XY	26515	MATL54_55	1	N/A	N/A	N/A
Bottom Payload PCB	25002	FR4_XY	26515	MATL54_55	1.3	N/A	N/A	N/A
Fore Payload PCB	25003	FR4_YZ	26514	MATL54_55	1	N/A	N/A	N/A
Aft Payload PCB	25004	FR4_YZ	26514	MATL54_55	1	N/A	N/A	N/A
Right Payload PCB	25005	FR4_XZ	26513	MATL54_55	1	N/A	N/A	N/A
Left Payload PCB	25006	FR4_XZ	26513	MATL54_55	1	N/A	N/A	N/A
Fore Payload Mount	25007	MATL15_Mounts	26501	MATL15	0.7	SectShll_Mounts_0.7mm	27004	SectShll
Aft Payload Mount	25008	MATL15_Mounts	26501	MATL15	0.7	SectShll_Mounts_0.7mm	27004	SectShll
Camera	25009	MATL24_Camera	26507	MATL24	1	SectShll_1mm	27007	SectShll
Camera Battery	25010	MATL63_Battery	26509	MATL63	N/A	SectSld_Battery	27042	SectSld
Camera Lense	25011	MATL24_Camera	26507	MATL24	N/A	SectSld	27041	SectSld
Right Sullins Connect	25012	MATL24_ABS	26502	MATL24	N/A	SectSld	27041	SectSld
Left Sullins Connect	25013	MATL24_ABS	26502	MATL24	N/A	SectSld	27041	SectSld
Cammount Screws	25014	MATL24_SteelScrews	26503	MATL24	N/A	SectBeam_3.3mm	27025	SectBeam
Fuselage_Engine_screws	26001	MATL24_SteelScrews	26503	MATL24	N/A	SectBeam_3.3mm	27025	SectBeam
Fuselage_Wings_Screws	26002	MATL24_SteelScrews	26503	MATL24	N/A	SectBeam_3.3mm	27025	SectBeam
Fuselage_Camera_Screws	26003	MATL24_SteelScrews	26503	MATL24	N/A	SectBeam_3.3mm	27025	SectBeam
Fuselage_Battery_Screws	26004	MATL24_SteelScrews	26503	MATL24	N/A	SectBeam_3.3mm	27025	SectBeam
ConNodRB	26005	Rigids	N/A	N/A	N/A	N/A	N/A	N/A

Table 44 Summary of the key differences between the quadcopter [2] and fixed-wing UAS finite element models

	Quadrotor	Fixed-wing
Selected UAS [21]	DJI Phantom 3	Precision Hawk - Lancaster Hawkeye Mark III
		
Mass	1216 g (2.68 lb)	1810 g (4 lb)
Dimensions	290x289x186 mm ³ (0.951x0.948x0.61 ft ³)	Length: 800 mm (2.62 ft) Wingspan: 1500 mm (4.91 ft)
Max. Speed	16 m/s (31 knots)	19.5 m/s (38 knots)
Max. Service Ceiling	6000 m (19685 ft)	4000 m (13120 ft)
Battery - LiPo	363 g (4 cell)	335 g (3 cell)
Motor(s) – Brushless DC	50 g x 4	76 g x 1
Motor Speed	1240 rad/s (11840 rpm)	1280 rad/s (12240 rpm)
Camera	52 g	372 g
CAD model	Achieved from 3D scan	Reverse engineered - manually measured each component
Total # of elements in FE model	137325	99089
Total # of nodes in FE model	191455	132924
Materials	<ul style="list-style-type: none"> - Polycarbonate - Nylon - Cast Aluminum 520-F - Steel 4030 - G-10 Fiberglass (PCB) - Li-Po Battery Cell - Aluminum Film 1145-O 	<ul style="list-style-type: none"> - Steel 4340 - Aluminum 2024 T-351 - Aluminum Foil - Aluminum 2024 T-6 - Carbon/Epoxy Composite - FR4 Glass/Epoxy Composite - Glass-Reinforced Nylon 6 - Expanded Polystyrene - Nylon 6 - ABS

Material Models	<ul style="list-style-type: none"> - Johnson Cook (*MAT_015) - Piecewise Linear Plasticity (*MAT_024) - Enhanced Composite with Damage (*MAT_054) - Crushable Foam (*MAT_063) 	<ul style="list-style-type: none"> - Johnson Cook (*MAT_015) - Piecewise Linear Plasticity (*MAT_024) - Enhanced Composite with Damage (*MAT_054) - Crushable Foam (*MAT_063) - Tabulated Johnson Cook (*MAT_224)
Testing	<ul style="list-style-type: none"> - Lateral compression test (Battery) - Punch indentation (Battery) - Drop tower test (UAS upper body) - Free-fall drop test - Component level ballistic tests (Motor, Battery, and Camera) 	<ul style="list-style-type: none"> - Component level ballistic tests (Motor and Battery)

A.2 COMPONENT LEVEL TEST DETAILS

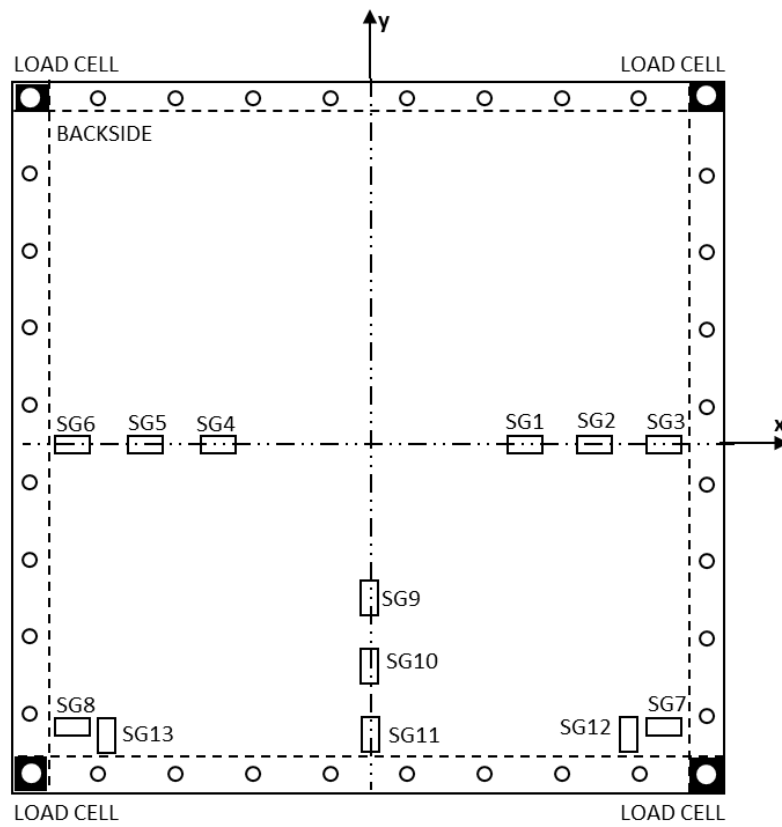


Figure 203. Target panel strain gage and load cell locations

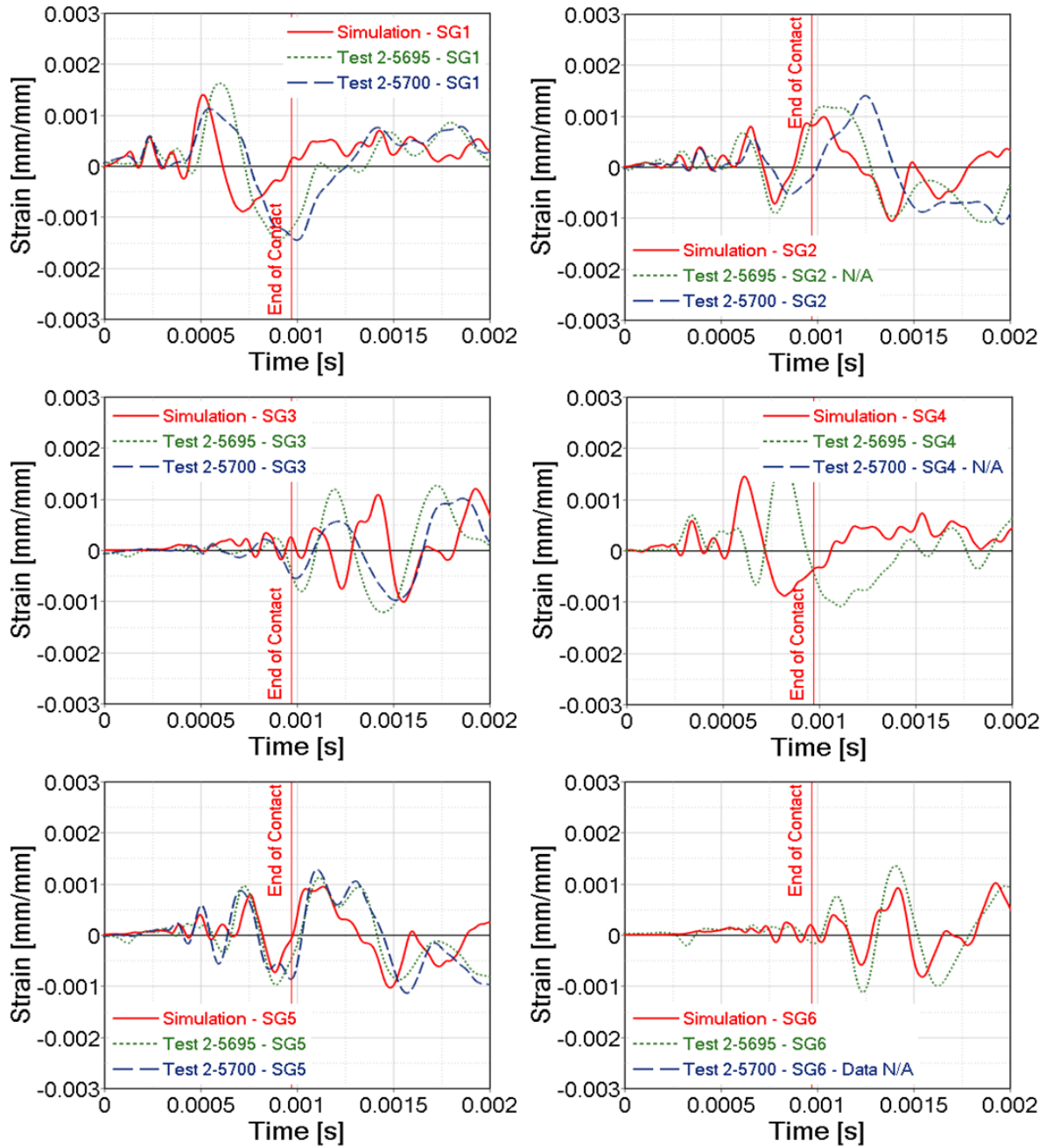


Figure 204. Measured and predicted target panel extensional strain in the x-direction at strain gages SG1-SG6 for a motor impact at 128.6 m/s nominal velocity

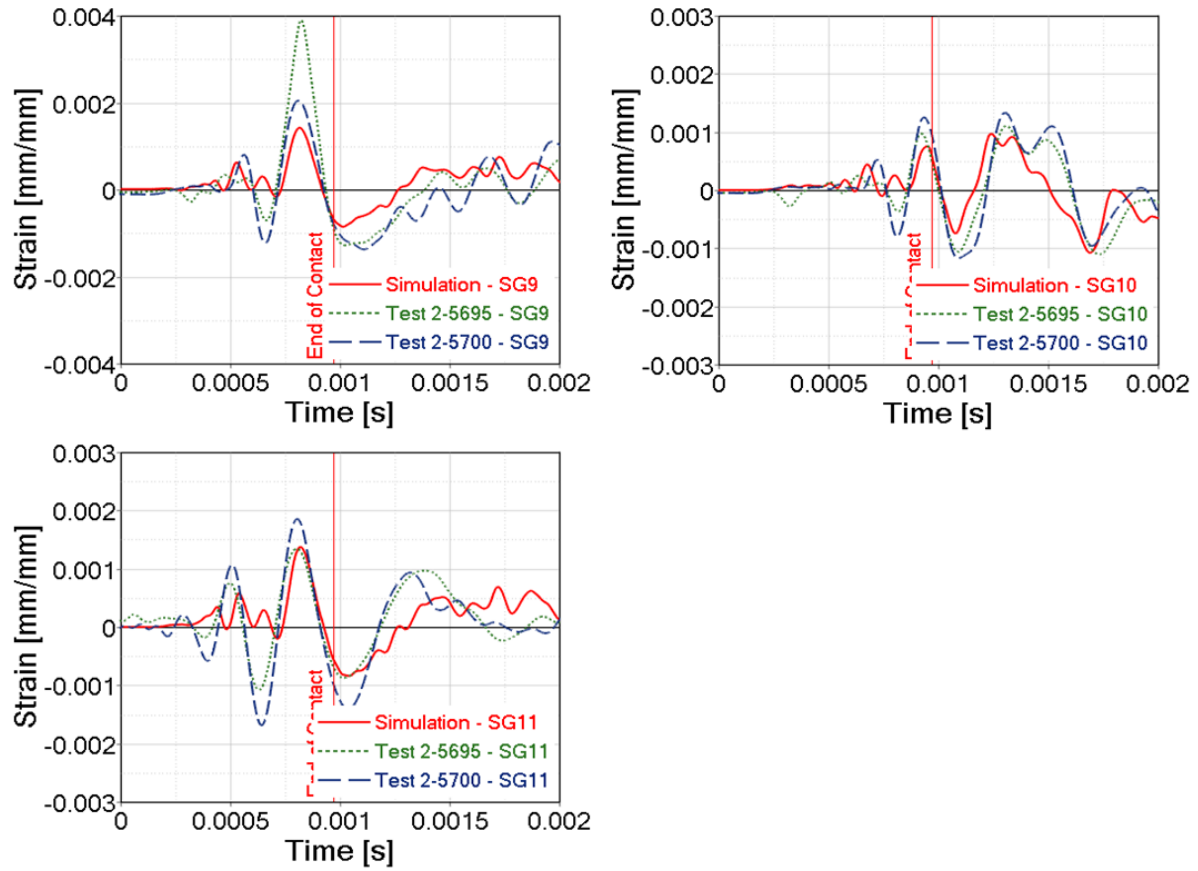


Figure 205. Measured and predicted target panel extensional strain in the y-direction at strain gages SG9-SG11 for a motor impact at 128.6 m/s nominal velocity

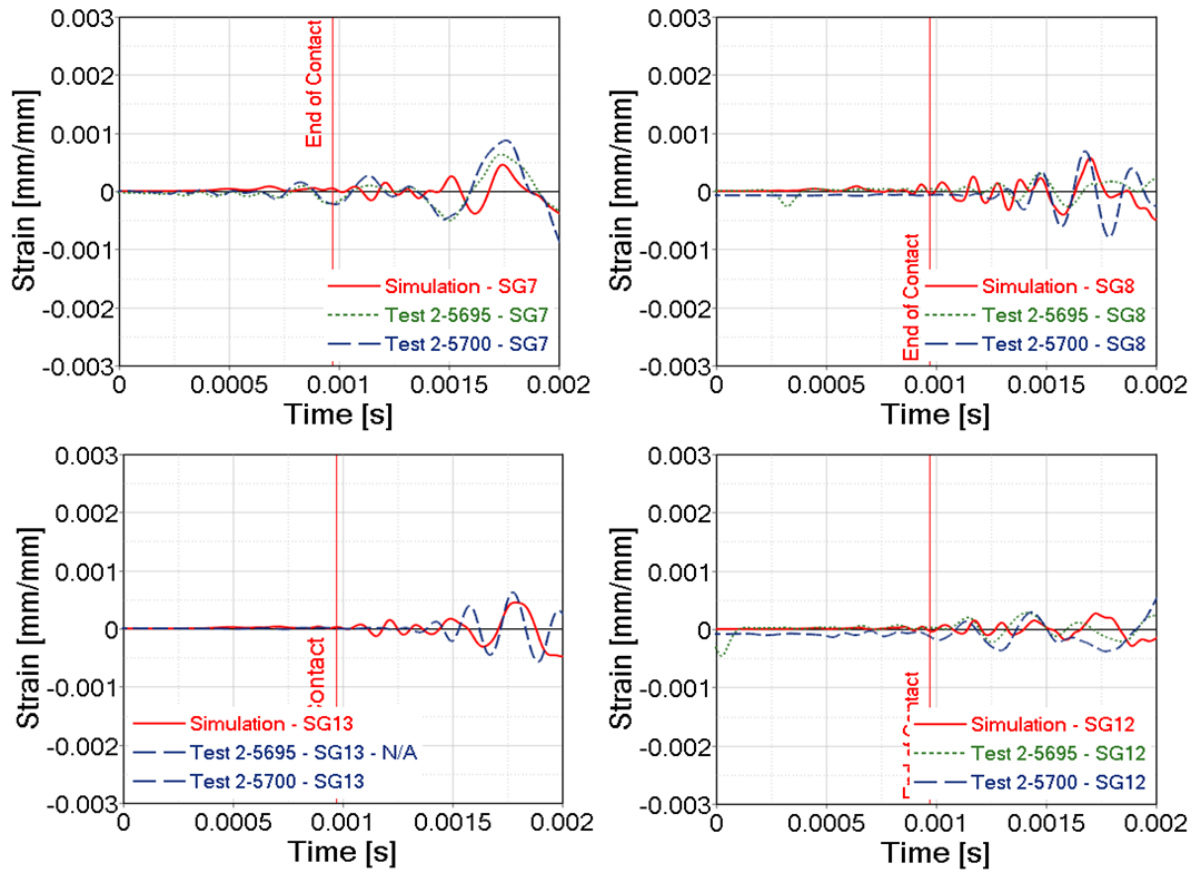


Figure 206. Measured and predicted target panel extensional strain at strain gages SG7, SG8, SG12 and SG13 for a motor impact at 128.6 m/s nominal velocity

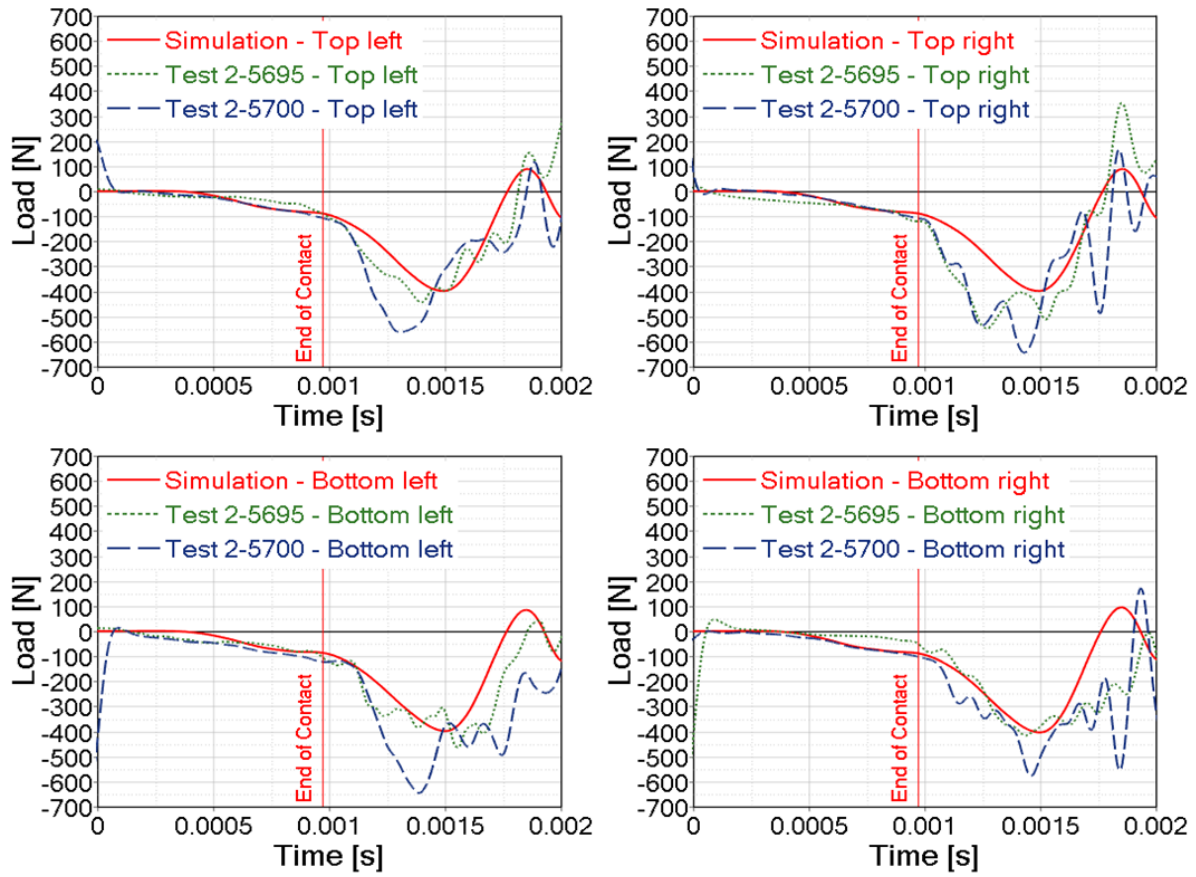


Figure 207. Measured and predicted force in all four load cells for a motor impact at a nominal velocity of 128.6 m/s

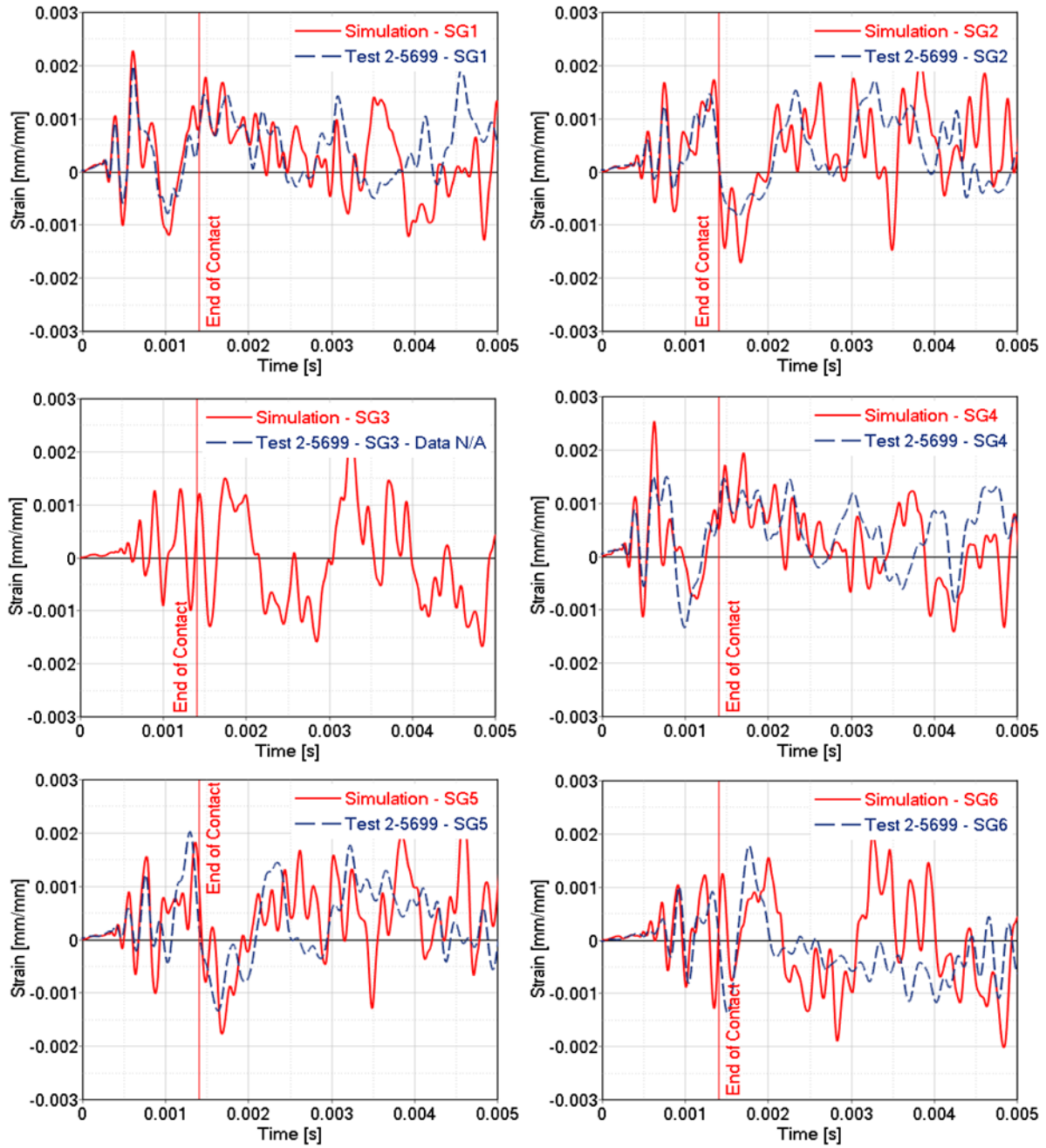


Figure 208. Measured and predicted target panel extensional strain in the x -direction at strain gauges SG1-SG6 for a motor impact at a 65.2 m/s velocity

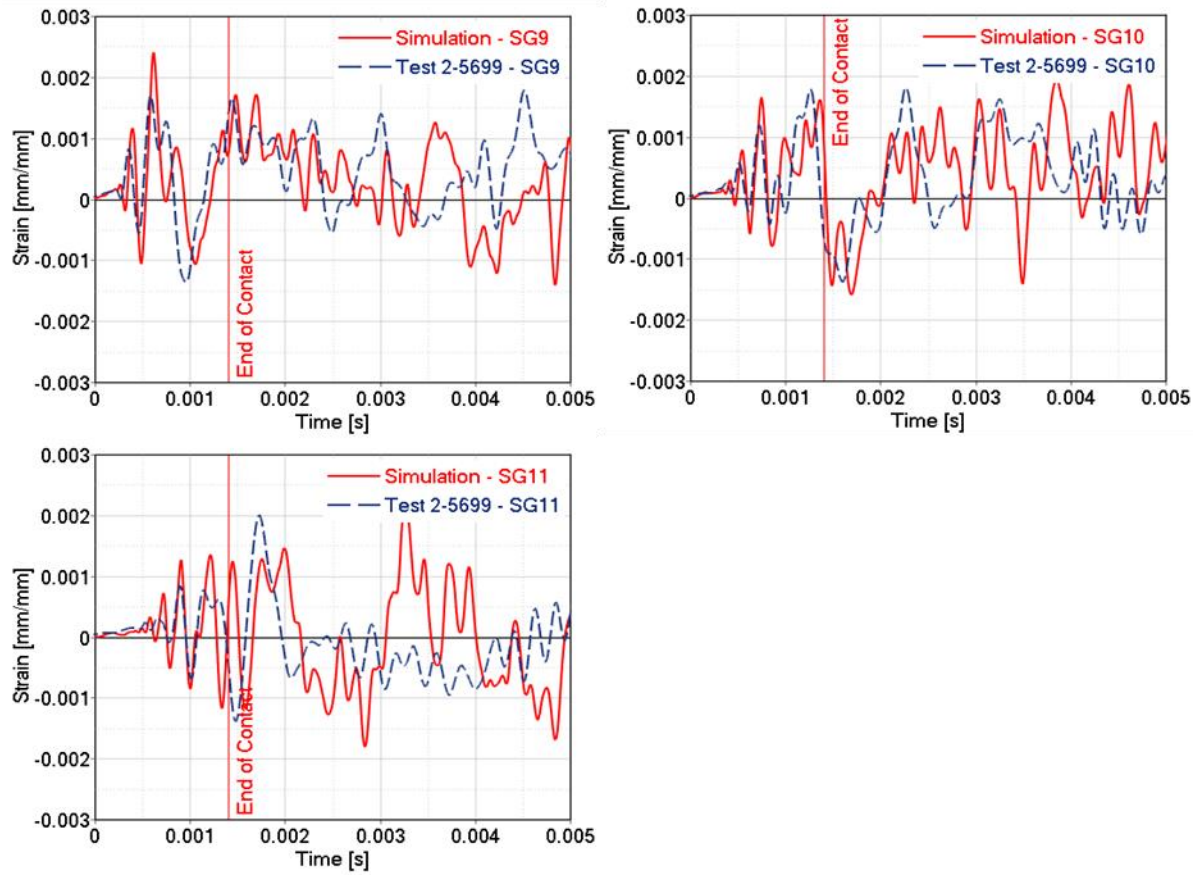


Figure 209. Measured and predicted target panel extensional strain in the y-direction at strain gages SG9-SG11 for a motor impact at a 65.2 m/s velocity

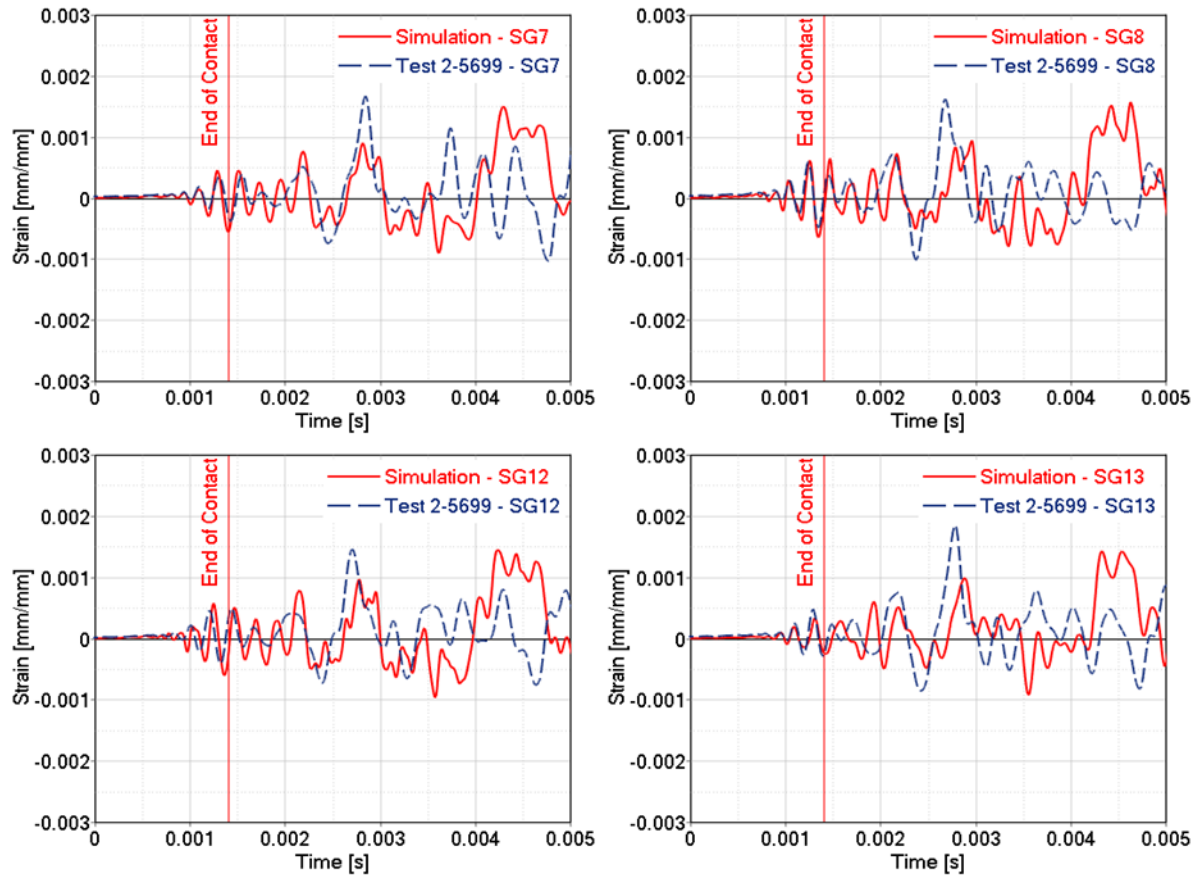


Figure 210. Measured and predicted target panel extensional strain at strain gages SG7, SG8, SG12, and SG13 for a motor impact at a 65.2 m/s velocity

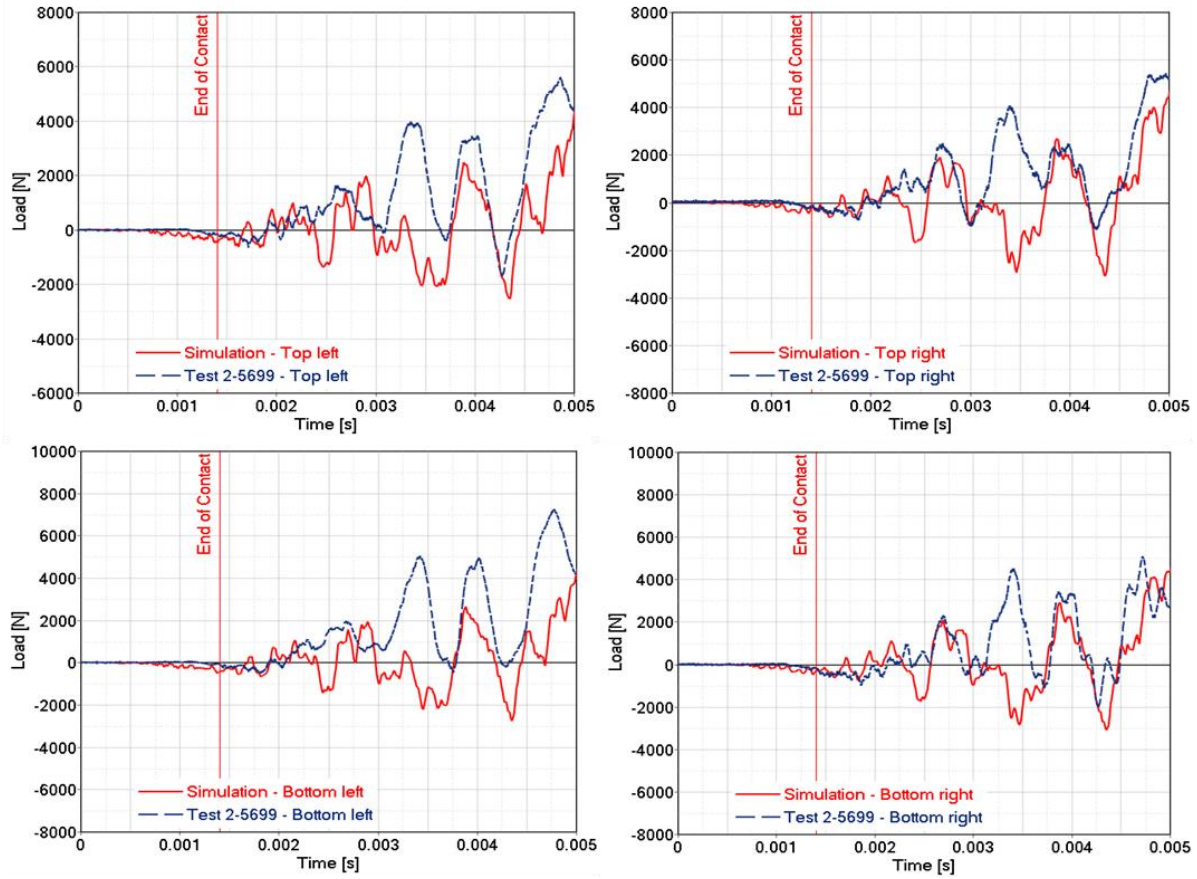


Figure 211. Measured and predicted force in all four load cells for a motor impact at a velocity of 65.2 m/s

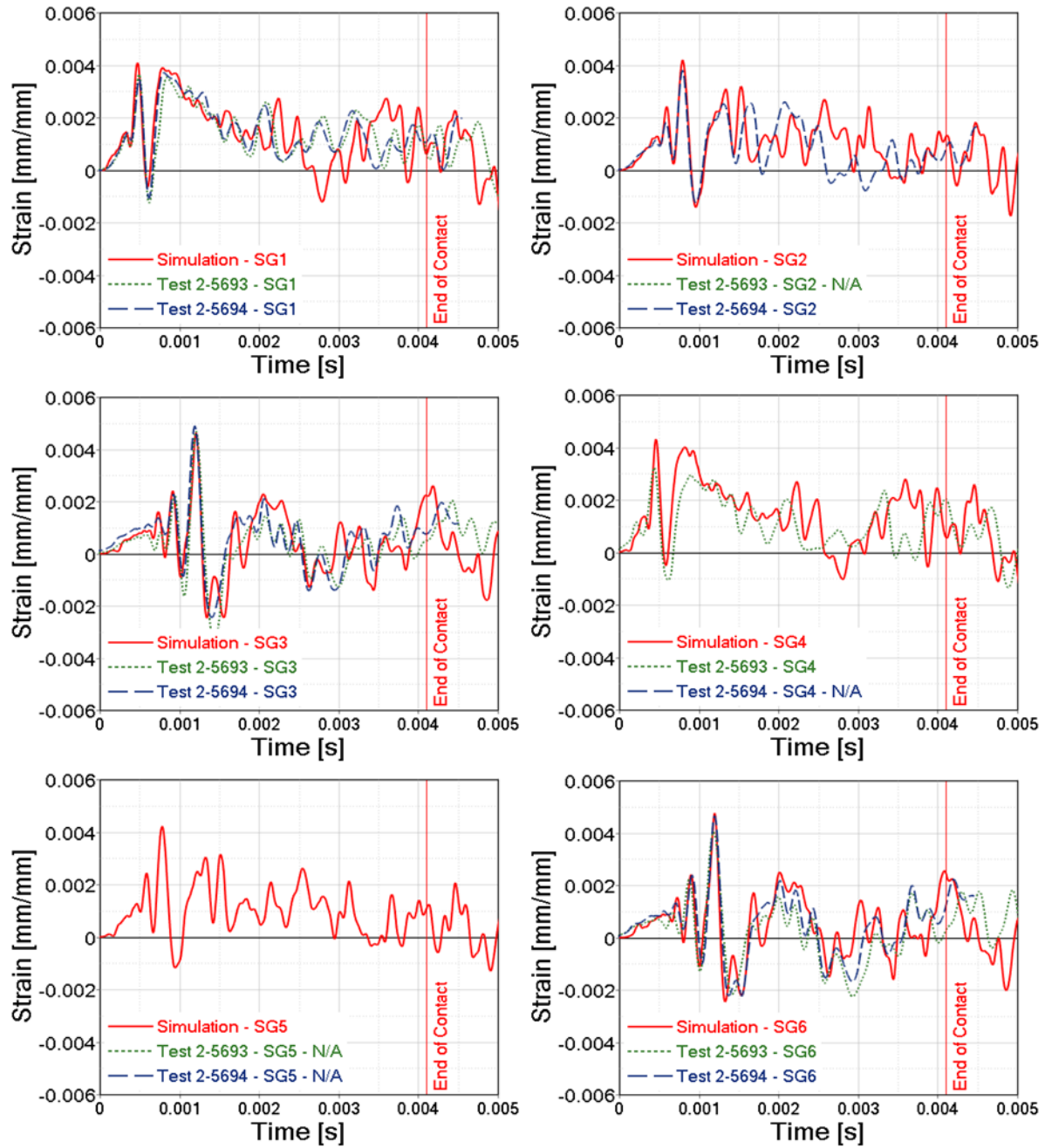


Figure 212. Measured and predicted target panel extensional strain in the x -direction at strain gauges SG1-SG6 for a battery subassembly impact at a 128.6 m/s nominal velocity

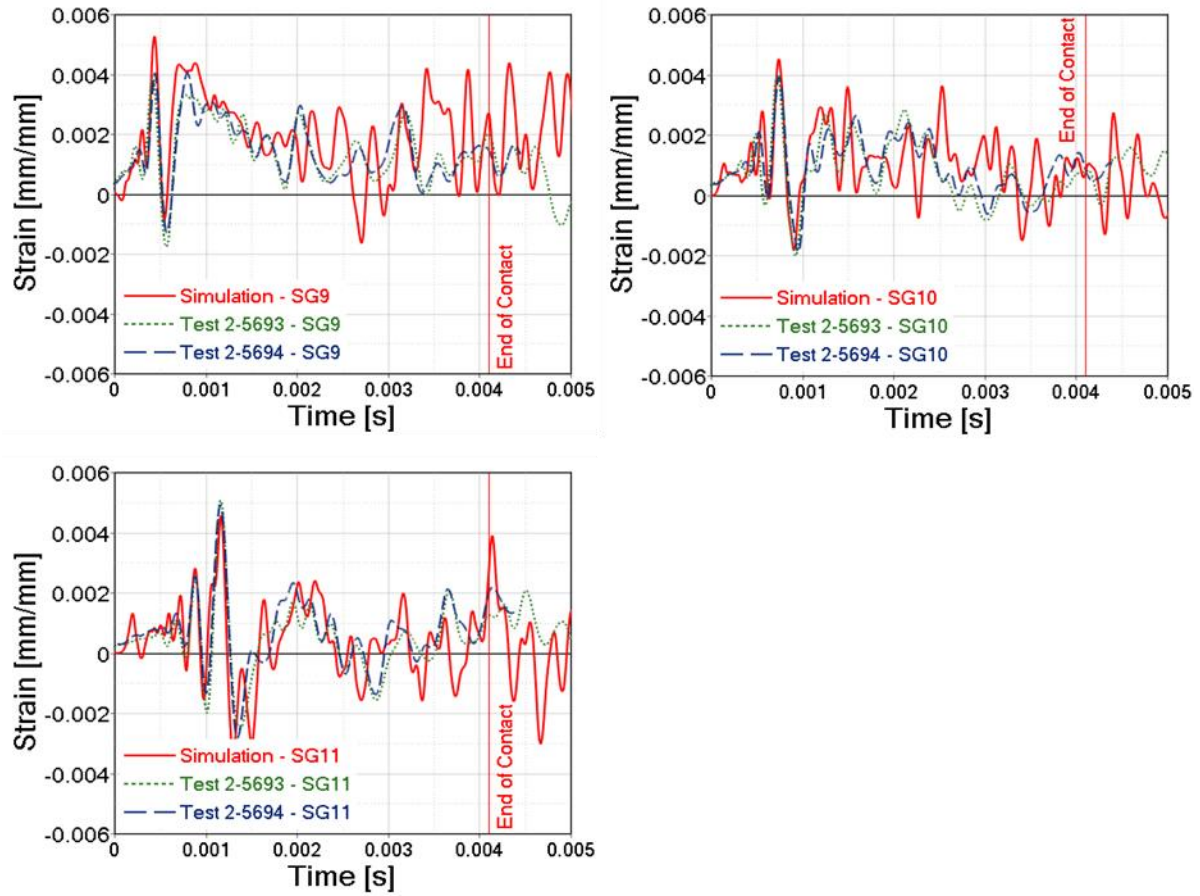


Figure 213. Measured and predicted target panel extensional strain in the y-direction at strain gages SG9-SG11 for a battery subassembly impact at a 128.6 m/s nominal velocity

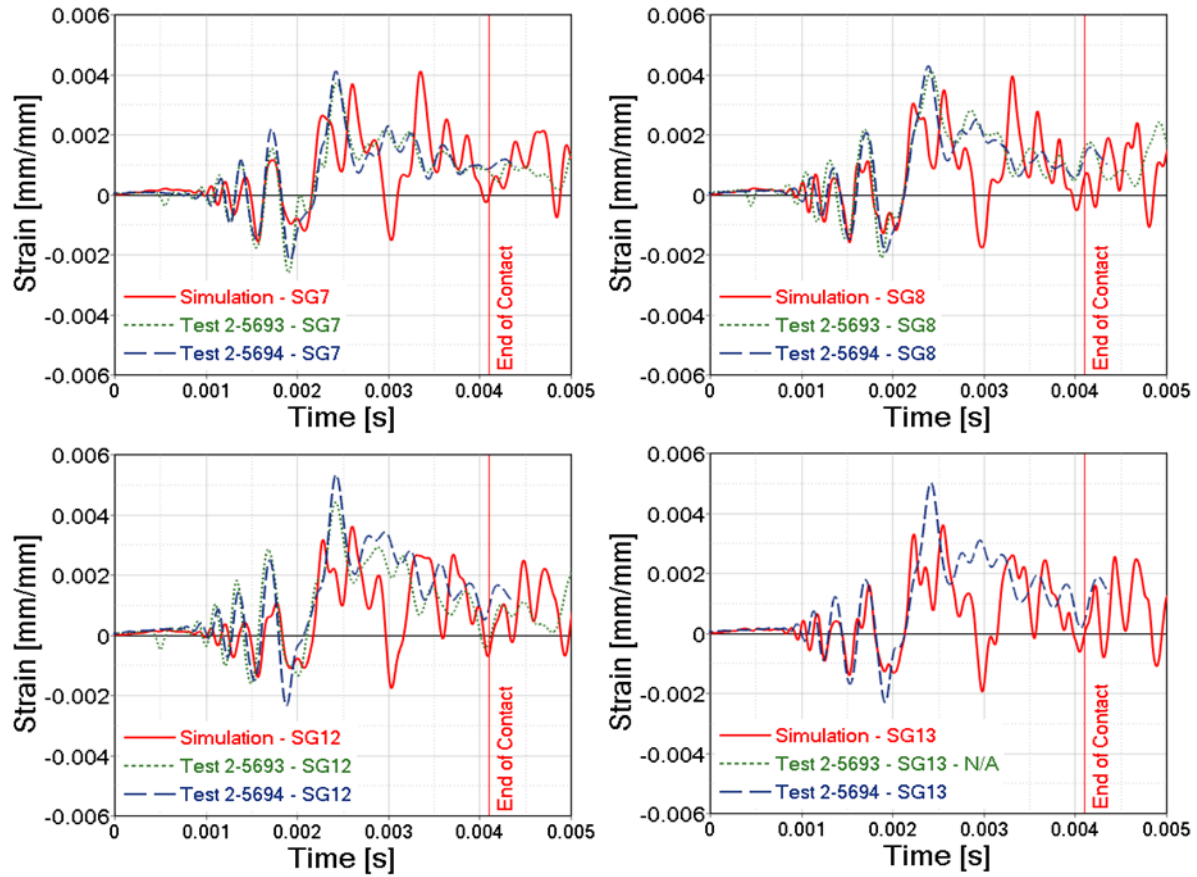


Figure 214. Measured and predicted target panel extensional strain at strain gages SG7, SG8, SG12, and SG13 for a battery subassembly impact at a 128.6 m/s nominal velocity

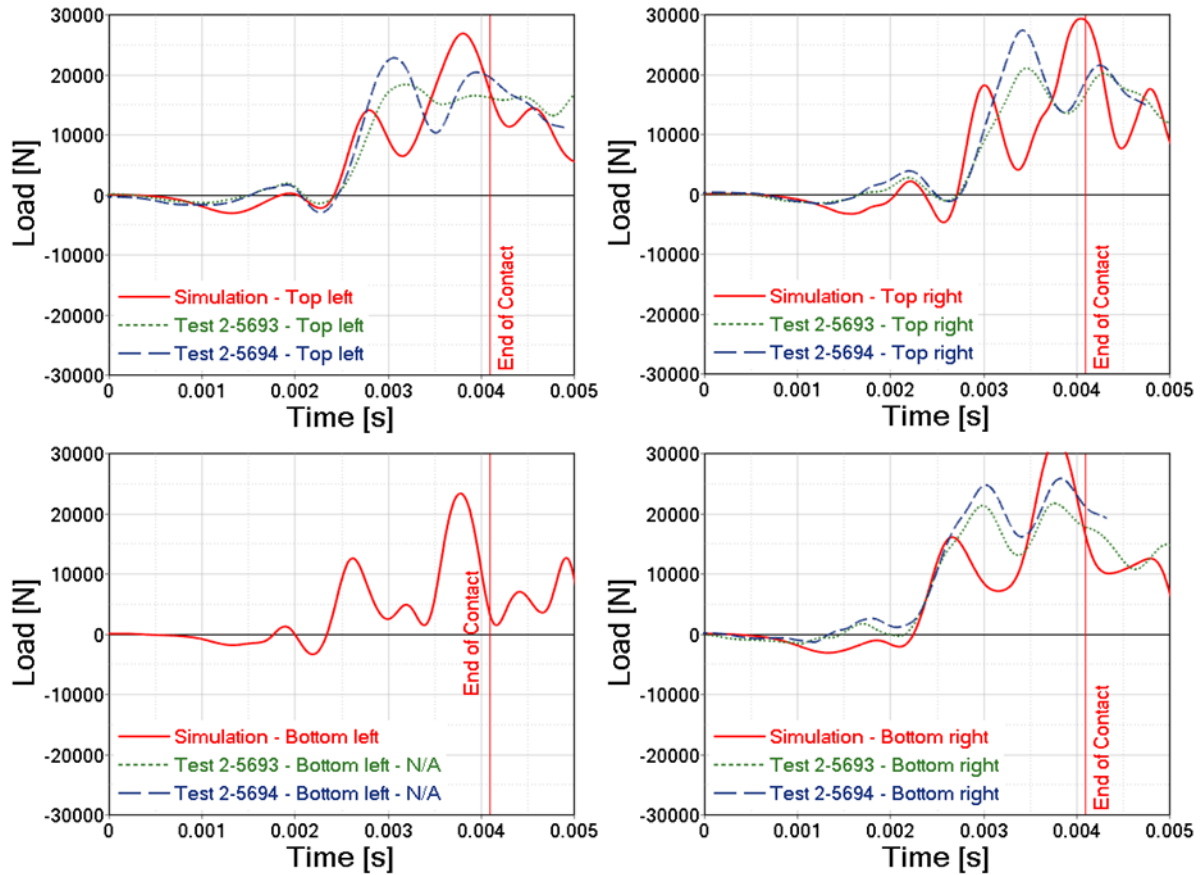


Figure 215. Measured and predicted force in all four load cells for a battery subassembly impact at a nominal velocity of 128.6 m/s

A.3 FIXED-WING UAS FLAT-PLATE IMPACT SIMULATIONS

For illustration purposes, a structurally complete FE model of the fixed-wing UAS was used to simulate fixed-wing UAS normal impacts to the center of the NIAR test frame [41]. Since the wingspan of the fixed-wing UAS is 1.5 m and the width of the NIAR test frame is approximately 1.04 m, a portion of each simulated wing extended beyond the edges of simulated test frame. A series of FE analyses were performed over a range of impact velocities in order to verify the stability of the fixed-wing model. Fixed-wing UAS impacts to the NIAR test frame as well as a rigid test frame were modeled. In addition, fixed-wing UAS impacts to targets with sharp “knife-edge” geometries were performed. Representative analyses conducted at an impact velocity of 128.6 m/s (250 knots) are summarized in this report.

A.3.1 Contact Definitions

As previously mentioned, LS-DYNA offers a variety of contact algorithms [27]. Contact among the individual parts of the fixed-wing model was described in Section 2.3.5. For these impact analyses, the *ERODING_SURFACE_TO_SURFACE* contact algorithm was used to define the contact behavior between the fixed-wing model and NIAR test frame. The target panel model was selected as the master segment for the contact definition while the fixed-wing model was selected as the slave segment. Similar to the component-level impact simulations, nominal static and dynamic

friction coefficients (0.2) were assumed between the contact surfaces. The segment-based contact (*SOFT* = 2) parameter and warped segment checking (*SBOPT* = 3) option were enabled consistent with the previous component-level simulations.

A.3.2 FE Stability Assessment

FE model stability is a major concern when explicit dynamic solution procedures are employed. In addition, the largest stable time increment is limited by the characteristic length of the smallest FE [24]. One technique to increase the stable time increment is to artificially add mass to the system by increasing the FE mass densities. Generally, the “added mass” due to this density increase should not exceed 5% of the individual component and system masses [25]. For these simulations, the added mass was negligible. A series of stability checks were also performed in order to ensure the stability of the explicit dynamic solution procedure. For each simulation, the total, kinetic, internal, hourglass, and contact energies were calculated and used to determine if any model instabilities were present. The total energy of the system should not vary more than 1% throughout the simulation [25]. Since reduced-integration FEs were used in the fixed-wing FE model, the energy associated with minimizing possible hourglass modes was determined. The hourglass energy should be less than 10% of the peak internal energy for the entire system [25]. Since friction was included in all contact definitions, the contact energy should be positive [74]. A negative contact energy, however, could indicate the existence of inappropriate node/FE interpenetrations in the model. The energy ratio (defined as the ratio between the total energy and the sum of the initial total energy and external work) was also used to evaluate model stability. This ratio describes the energy balance for the system and should be in the range 0.99-1.01 [25].

A.3.3 Simulated Fixed-Wing UAS Impacts on the NIAR Test Frame

A simulated 128.6 m/s (250 knots) impact between the fixed-wing model and the NIAR test frame was performed. The 1.59 mm (0.0625 in) thick Aluminum 2024-T3 flat target panel is representative of typical aircraft skins. Similar to the 128.6 m/s motor impact simulations (Section 2.4.8.7), the fixed-wing UAS penetrated the target panel. A detailed analysis of the predicted collision between the fixed-wing UAS projectile and target was performed after assessing model stability. The total, kinetic, internal, hourglass, and contact energies from this simulation are shown in Figure 216. The total energy remained relatively constant throughout the simulation. The total kinetic energy of the system decreased as the projectile penetrated the target. Analogously, the internal energy of the system increased with time as both the target and fixed-wing UAS projectile deformed. The hourglass energy remained a negligible fraction of the peak internal energy throughout the entire simulation; this suggests spurious zero-energy modes associated with reduced-integration FEs were minimized. The contact energy remained positive during the simulation indicating no serious node/FE interpenetrations. The calculated energy ratio was relatively constant and well within the desired 0.99-1.01 range (Figure 217). The results suggest that the combined fixed-wing UAS/NIAR test frame model is relatively robust and numerically stable. Similar assessments will be required when integrating the fixed-wing UAS FE model with other target models.

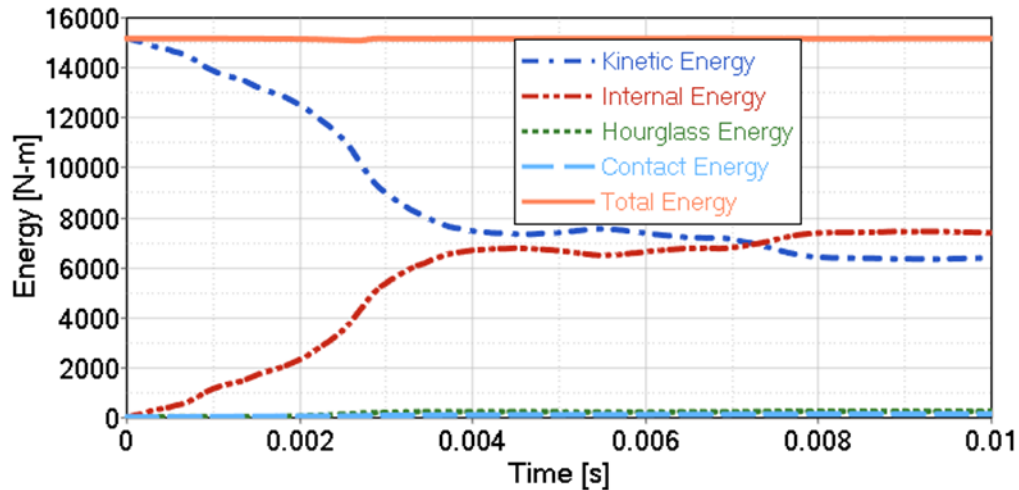


Figure 216. Predicted total, kinetic, internal, hourglass, and contact energies for a 128.6 m/s fixed-wing UAS impact into the NIAR test frame

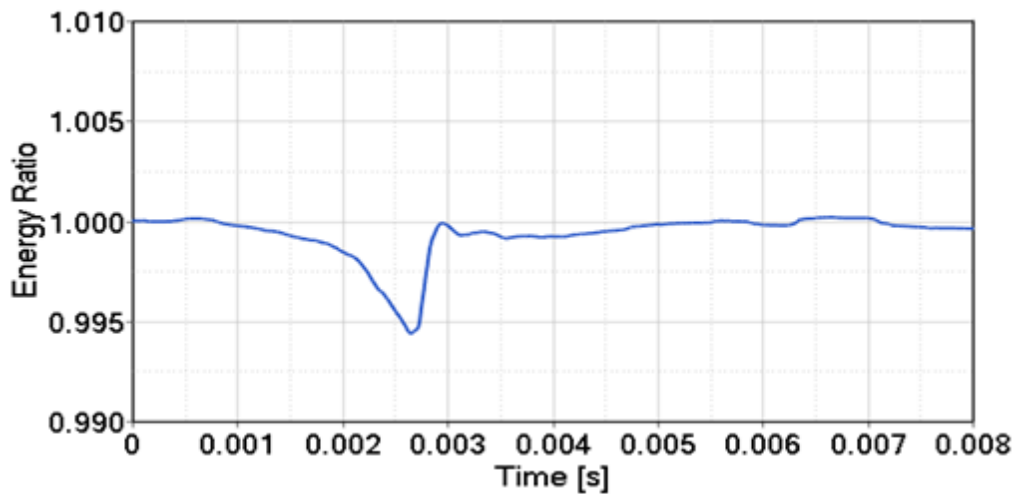


Figure 217. Predicted energy ratio for a 128.6 m/s fixed-wing UAS impact into the NIAR test frame

Isometric views of a 128.6 m/s (250 knots) fixed-wing UAS impact to the NIAR test frame are shown in Figure 218 at three instants in time. The fixed-wing UAS is shown in Figure 218 (A) at the center of the test frame immediately prior to impact (time, 0.0 ms). As the fixed-wing UAS began to impact the test frame (time, 2.5 ms), the motor penetrated the target panel, and the PCBs crumpled as shown in Figure 218 (B). The motor essentially acted as a sharp penetrator and was mostly intact after penetration. In addition, since the expanded polystyrene foam portions of the wings extended beyond the test frame, the wingtips began to shear off after impacting the sides of the test frame. The size of the hole created from the motor penetration increased as the remainder of the fixed-wing UAS impacted the target panel (time, 5.0 ms). As a result, the battery and camera were mostly intact after passing through the target panel (Figure 218 (C)).

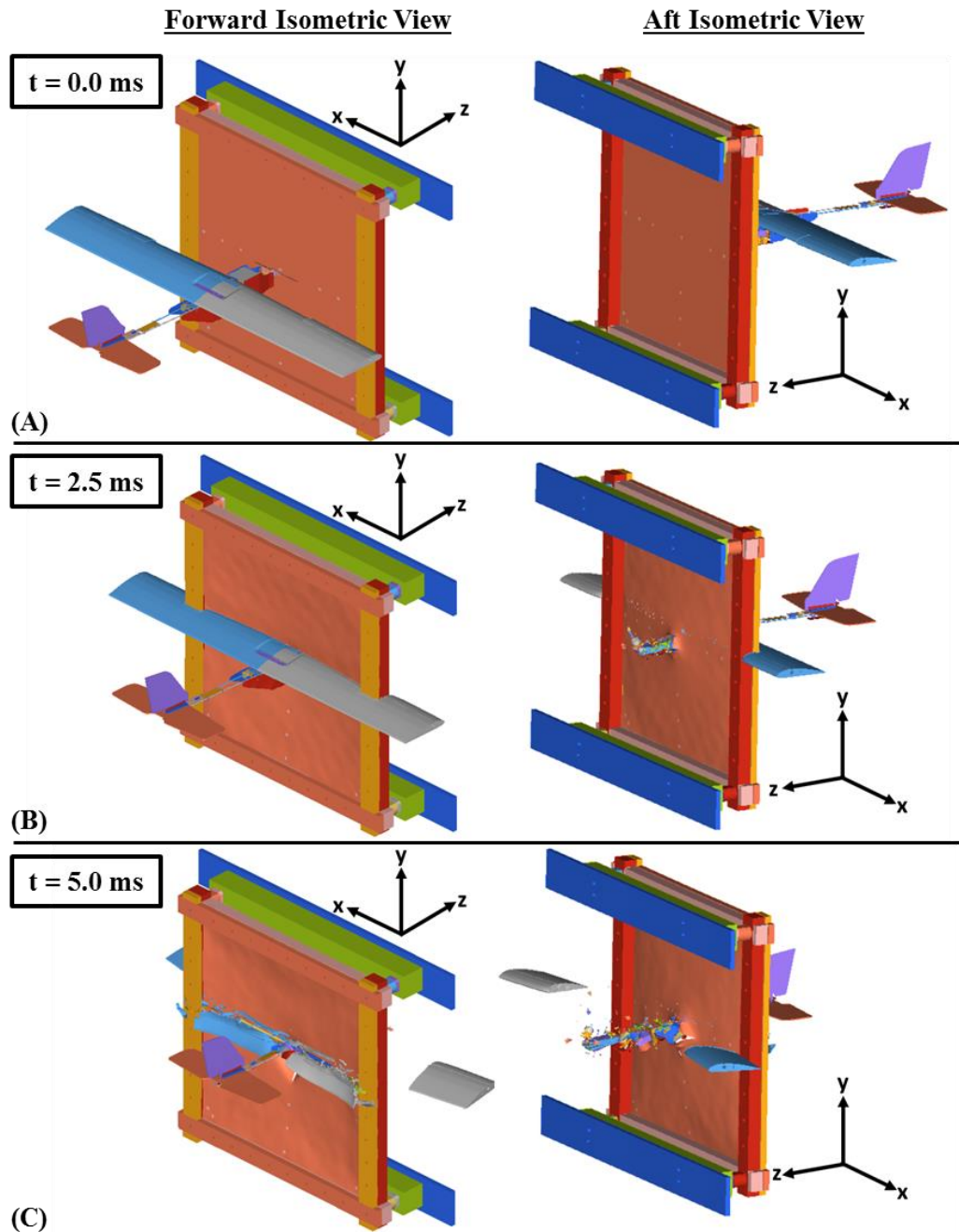


Figure 218. Isometric views of the predicted fixed-wing UAS impact at 128.6 m/s to the NIAR test frame at three times: (A) $t = 0 \text{ ms}$, (B) $t = 2.5 \text{ ms}$, and (C) $t = 5 \text{ ms}$

Side view images of the fixed-wing UAS for this impact are shown in Figure 219 at six instants in time.

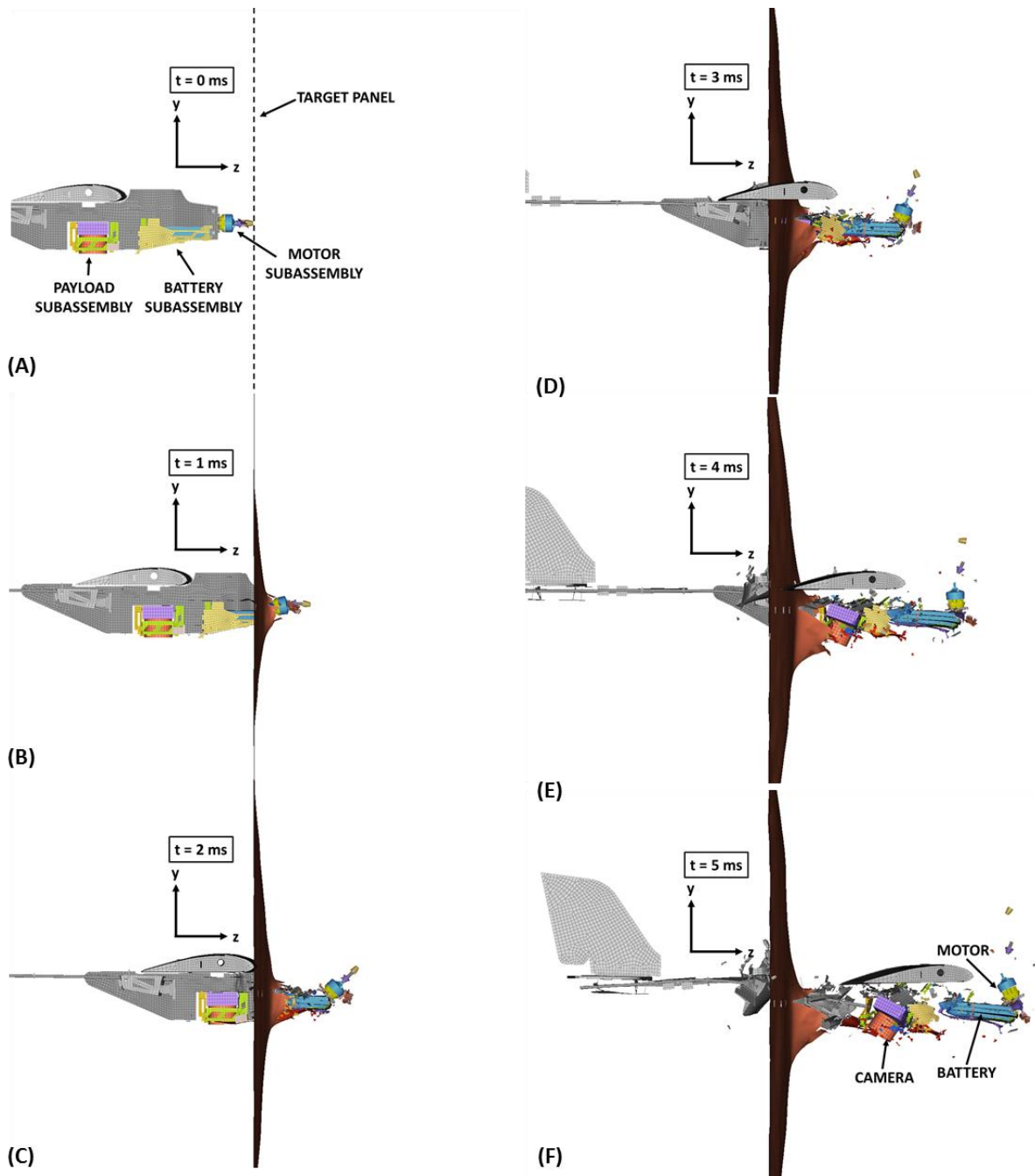


Figure 219. Predicted fixed-wing UAS impact at 128.6 m/s to NIAR test frame at six times: (A) $t = 0$ ms, (B) $t = 1$ ms, (C) $t = 2$ ms, (D) $t = 3$ ms, (E) $t = 4$ ms, and (F) $t = 5$ ms

A close-up view of the fixed-wing UAS fuselage is shown in Figure 219 (A) just prior to impact (time, 0.0 ms). The FEs for the motor, battery, and payload subassemblies are highlighted in color while all other fixed-wing FEs are gray. The motor and battery each remained essentially intact as they penetrated the target panel as shown in Figure 219 (B) and Figure 219 (C), respectively. In addition, the PCB fuselage and battery subassembly support structure began to crumple (Figure 219 (C)). The PCB battery enclosure became detached from the battery shortly thereafter as shown

in Figure 219 (D). No significant damage to the camera was observed as it penetrated the target panel (Figure 219 (E)). The relatively high density motor, battery, and camera remained mostly intact as shown in Figure 219 (F) and continued roughly on the initial projectile trajectory. These results suggest that a 1.59 mm thick target panel would not significantly prevent the fixed-wing UAS penetration at 128.6 m/s. As a consequence, the high mass motor, battery, and camera pose a significant threat to any underlying structure or payload (*e.g.*, ribs, frames, fuel tanks).

A.3.4 Simulated Fixed-wing UAS Impacts to a Rigid Test Frame

Simulated compliant projectile impacts to rigid targets arguably represent a significant challenge in the development of a numerically stable projectile model. Additional fixed-wing UAS model verification and stability assessments were performed at a 128.6 m/s (250 knots) impact velocity using the fixed-wing model and a *rigid* NIAR test frame model. In essence, all FEs in the target model were converted to rigid FEs by employing the *DEFORMABLE_TO_RIGID* card in the LS-DYNA keyword file. Similar to the calculated results for the combined fixed-wing UAS/NIAR test frame model, an assessment of the total, kinetic, internal, hourglass, and contact energies (Figure 220) as well as the energy ratio (Figure 221) suggested that the combined compliant projectile/rigid target model was numerically stable. Extreme FE distortions resulting in negative FE volumes were avoided in the analysis suggesting that the fixed-wing model can be used successfully to predict normal impacts to hard/stiff flat targets.

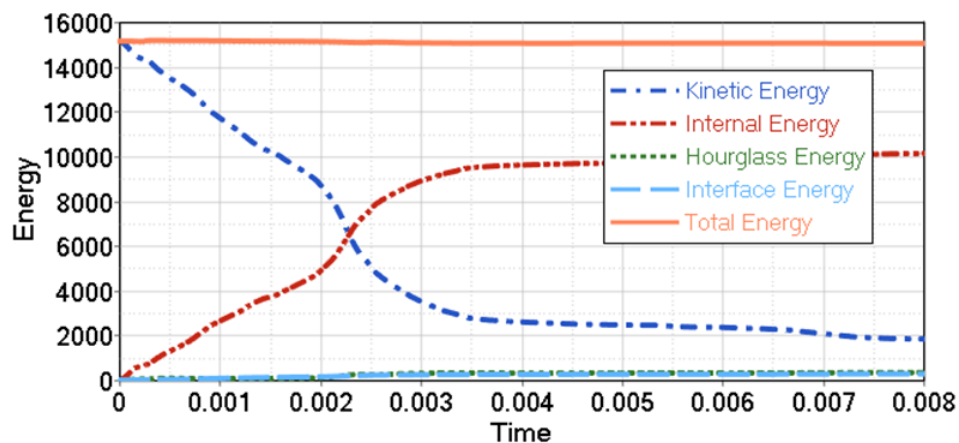


Figure 220. Predicted total, kinetic, internal, hourglass, and contact energies for a 128.6 m/s fixed-wing UAS impact into a rigid NIAR test frame

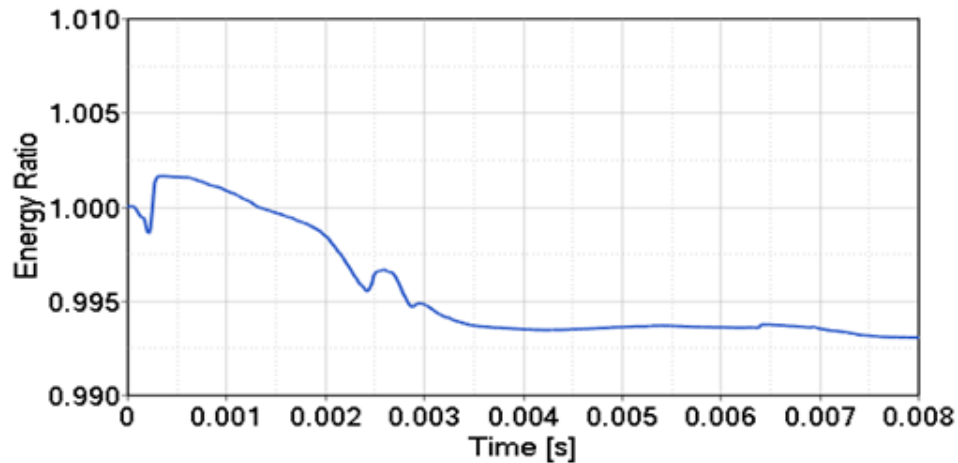


Figure 221. Predicted energy ratio for the fixed-wing UAS impact to a rigid NIAR test frame at 128.6 m/s

A.4 SIMULATED FIXED-WING UAS KNIFE-EDGE IMPACTS TO A RIGID PLATE

As mentioned previously, the stability of a given impact model strongly depends on the structural geometry, morphology, and material properties of both the projectile and target. One key challenge involves knife-edge impacts between a compliant projectile and relatively stiff plates. Knife-edge impacts are a concern in air-to-air collisions when a projectile penetrates a leading edge skin and subsequently strikes the web of an underlying rib and/or frame. Simulating such impacts can result in numerical instabilities due to the intense local deformation in the contact region between the projectile and target. LS-DYNA simulations of fixed-wing UAS knife-edge impacts with a flat rigid plate (thickness, 1.59 mm) were performed at a 128.6 m/s (250 knots) impact velocity (Figure 222). An evaluation of the total, kinetic, internal, hourglass, and contact energies (Figure 223) as well as the energy ratio (Figure 224) suggested that the combined fixed-wing/rigid knife-edge target model was numerically stable. Hence, the fixed-wing model appears to be numerically stable over a range of candidate target models.

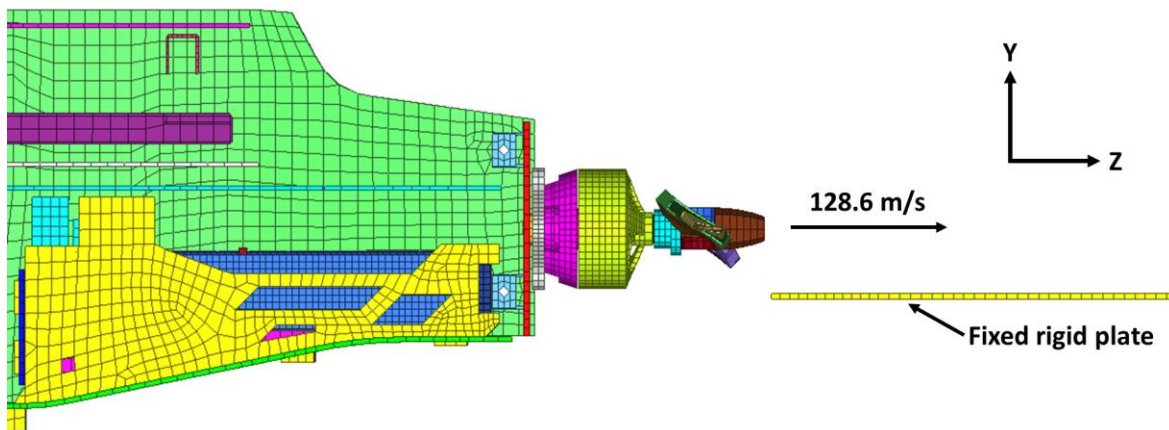


Figure 222. Schematic of the fixed-wing UAS rigid knife-edge impact (vertical sidewall not shown) at 128.6 m/s

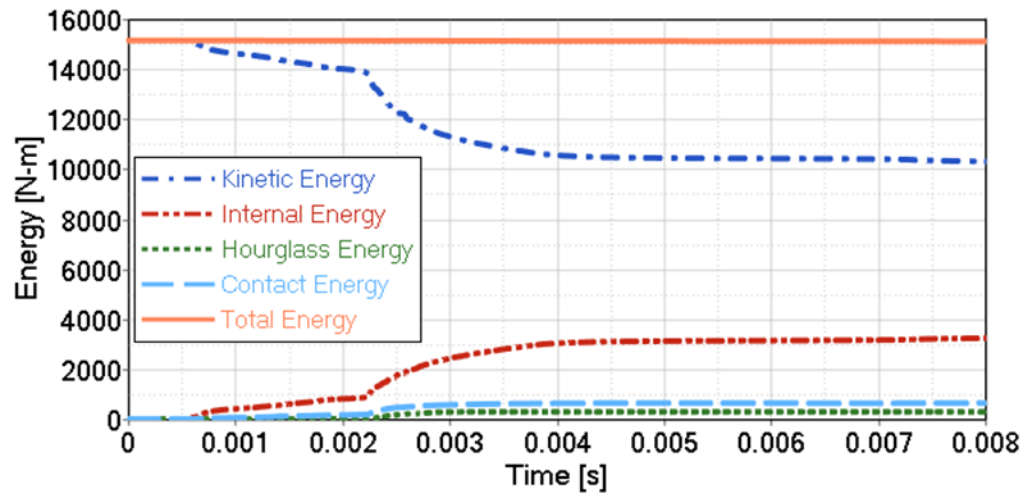


Figure 223. Predicted total, kinetic, internal, hourglass, and contact energies for the rigid knife-edge impact of the fixed-wing UAS at 128.6 m/s

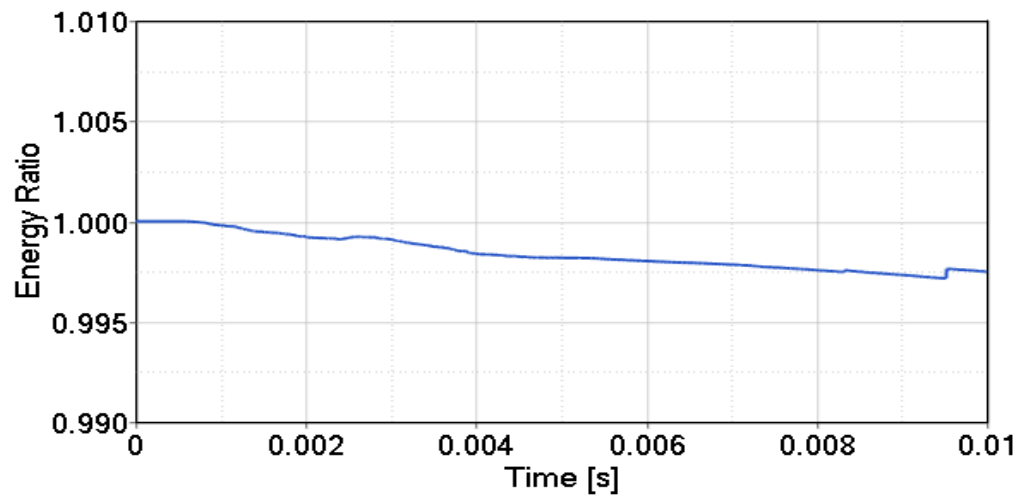


Figure 224. Predicted energy ratio for the rigid knife-edge impact of the fixed-wing UAS at 128.6 m/s

APPENDIX B – IDENTIFICATION OF UAS CRITICAL COMPONENTS

B.1 MATERIAL STUDY

The objective of this study was to understand the behavior of materials typical of an UAS construction under impact conditions similar to a bird strike. To achieve this, several simulations compared the material behavior and load transfer to the target of 1.81 kg (4 lb) projectiles of different materials (steel, ABS plastic, an equivalent battery material) with a 1.81 kg (4 lb) bird projectile under a 169.8 m/s (330 knots) impact.

B.1.1 Setup

Figure 225 shows the setup for the study in which a 1.81 kg (4 lb) projectile was impacted against a 3.175 mm thick aluminum panel at 169.8 m/s (330 knots).

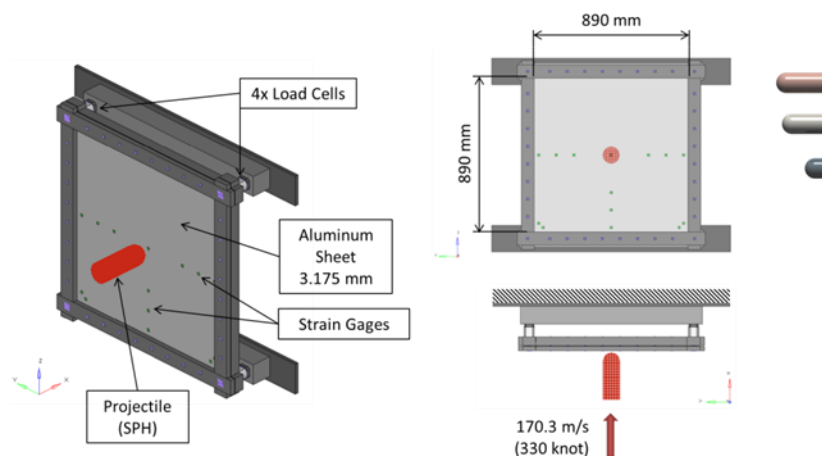


Figure 225. Material study setup

The panel was based on the design for a previous project of NIAR that involved bird strike testing, and from which a validated FE model was available to use in this project. A similar configuration was used for the ballistic component level tests in Section [2.4.1].

All the projectiles had the same mass and diameter but variable lengths to account for the material density variations. The material properties used were the same as described in Section [2.3.2]. Each projectile was modelled using the Smoothed-Particle Hydrodynamics method, available in LS-Dyna software.

B.1.2 Results and Conclusions

Figure 226 and Figure 227 illustrate the effective plastic strain and the energy transfer due to the impact of four different projectiles.

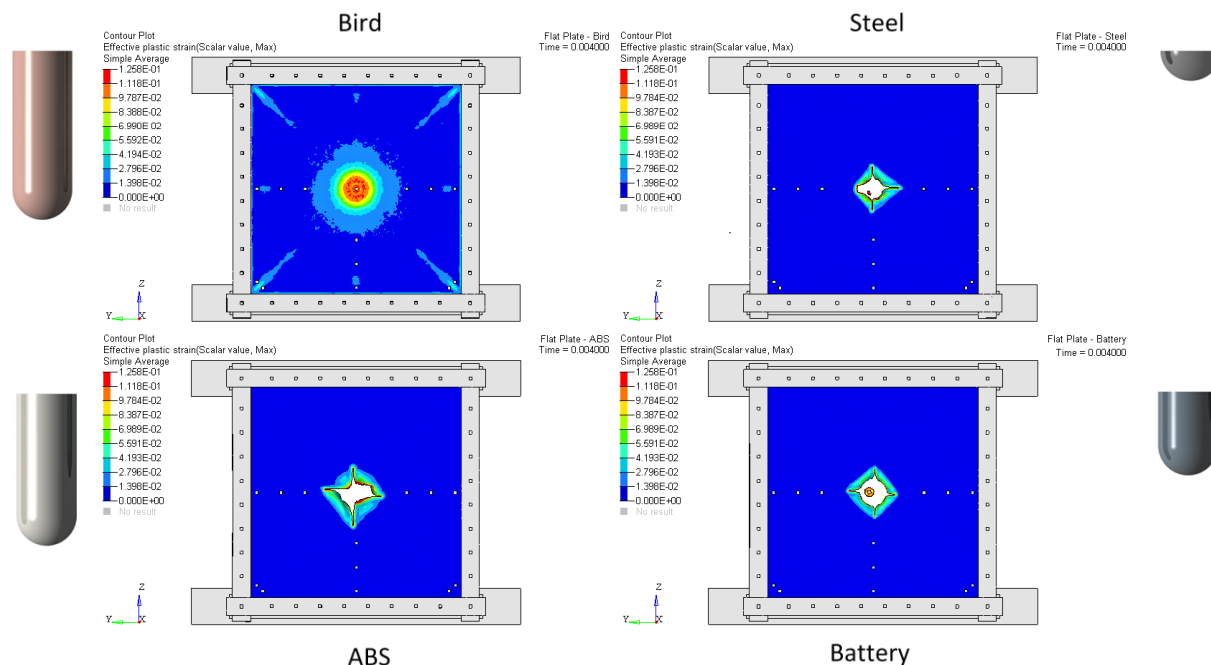


Figure 226. Material study results – effective plastic strain

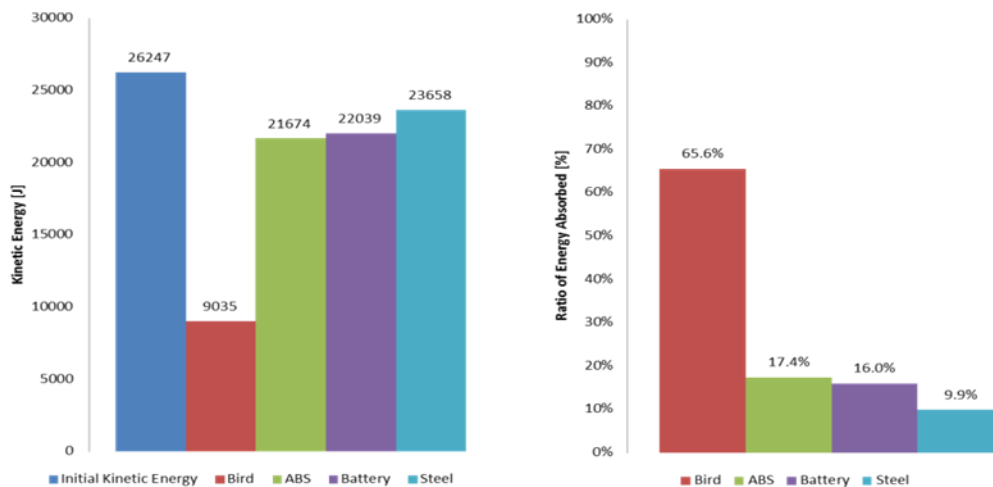


Figure 227. Material study results – energy transfer

From the results, it can be inferred that the materials with higher strength and stiffness induced greater damage and higher loads into the aluminum panel. UAS components such as the motors or the camera are constructed with this materials, so they will be identified as potential sources of damage into the aircraft structure.

B.2 MASS DISTRIBUTION STUDY

The objective of this study was to understand the influence of concentrating or spreading the mass of the projectile. The steel projectile of the study presented in B.1 was used as a baseline. The 1.81 kg (4 lb) spherical steel projectile was spread into several (2, 4, 6 and 8) spherical masses.

B.2.1 Setup

Figure 228 shows the setup for the study in which the 1.81 kg (4 lb) steel projectile was impacted against a 3.175 mm thick aluminum panel at 169.8 m/s (330 knots).

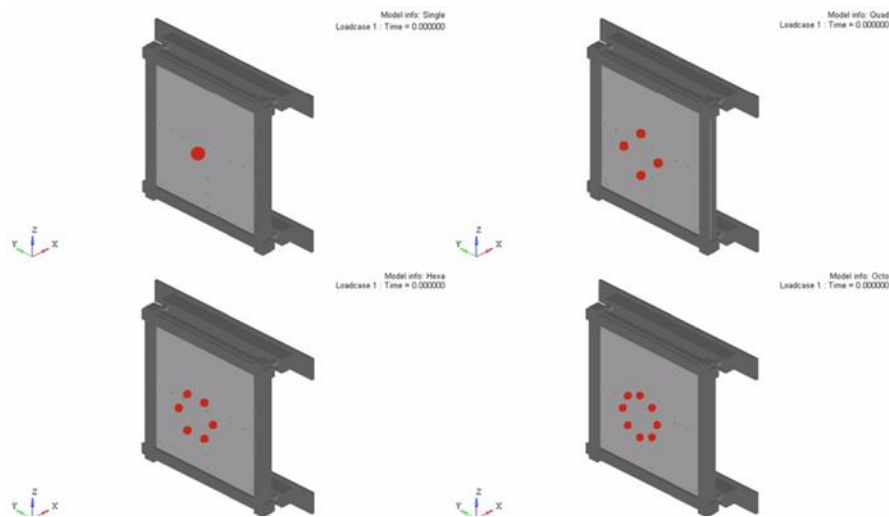


Figure 228. Mass distribution study setup

The masses were independent bodies and had no physical connection between them. The radius of mass distribution was set to 330 mm. The mass spreading represents motor distribution on the UAS. The same panel model and impact conditions was setup for this study as in B.1 .

B.2.2 Results and Conclusions

Figure 229 and Figure 230 show the effective plastic strain and the energy transfer due to the impact of projectile spread into different spherical masses.

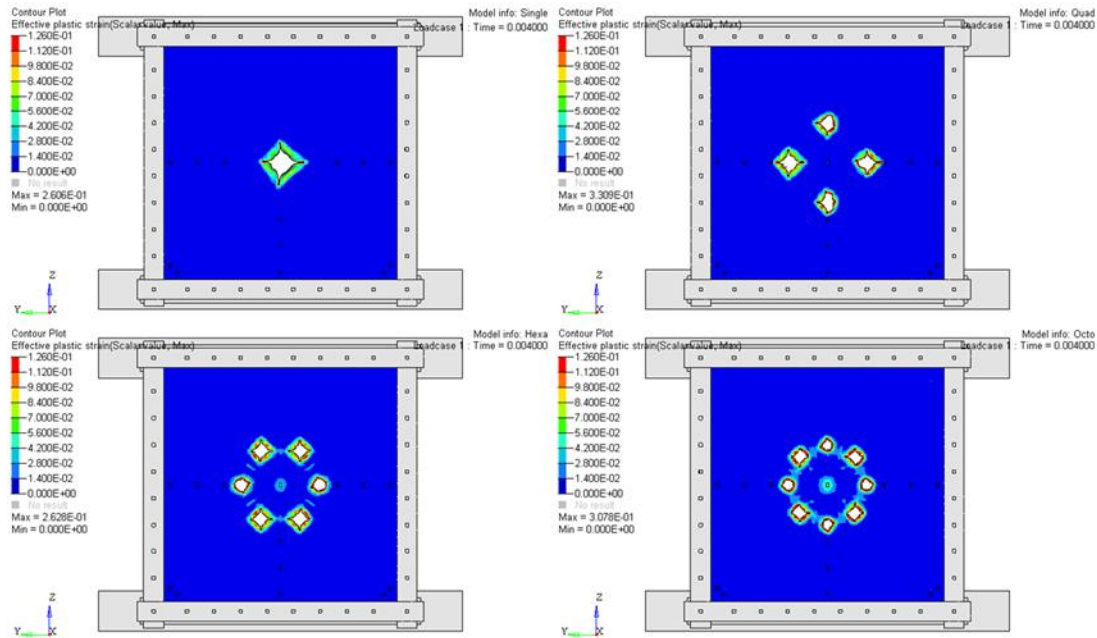


Figure 229. Mass distribution study results – effective plastic strain

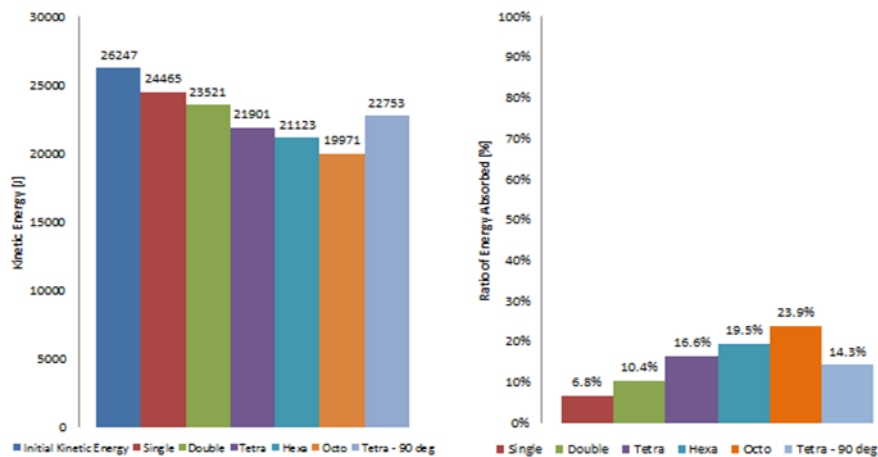


Figure 230. Mass distribution study results – energy transfer

From the results, it can be inferred that the spreading of the projectile into separate spherical masses progressively increases the internal energy absorbed by the aluminum panel. For higher the number of spherical masses the velocity of the projectiles is reduced more. Eventually, a more spread mass will not produce failure in the panel. UAS components with greater concentrated mass (such as the battery or the motors) will pose a greater threat to the impacted airframe.

B.3 COMPARISON WITH HAIL IMPACT

The objective of these study was to investigate how materials of an UAS will behave under impact loads if compared with a well-known event in aircraft, hail impact. Impact of 34 g (0.07 lb) projectiles of different materials of UAS were compared with a hail impact of same mass and observed the material behavior and load transfer into the structure.

B.3.1 Setup

Figure 231 shows the setup for the study in which the 34 g projectiles were impacted against aluminum panel for velocities ranging from 56.6 to 180 m/s (110 to 350 knots). The projectiles had a spherical shape with varying diameters to account for the variation in material density.

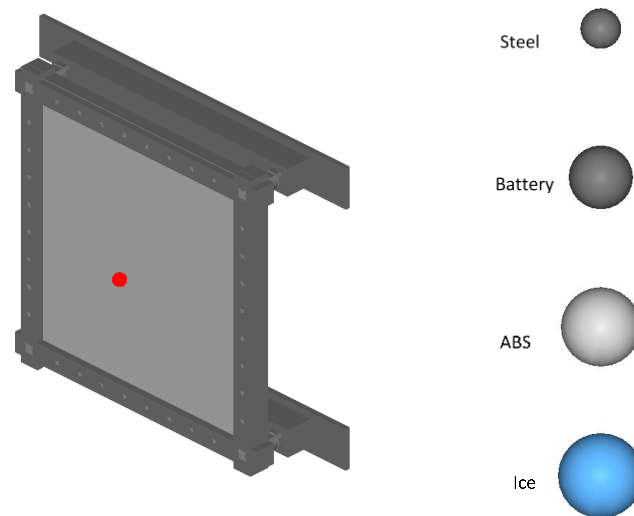


Figure 231. Comparison with hail impact setup

B.3.2 Results and Conclusions

Figure 232 depicts the effective plastic strain and Figure 233 shows the contact loads and permanent deformation in the aluminum panel due to the impact of projectiles at 180 m/s (350 knots).

It was observed that the steel projectile was the only producing perforation of the plate. Hail behaved as a fluid, spreading the load on the surface of the panel, while ABS and Battery material behaved in a stiffer manner, but not enough to produce failure in the panel.

It can be concluded that the stronger material, steel produced maximum deformation on the panel at speeds over 200 knots compared to other materials. This indicates the criticality of the motor, which has the mass comparable to a hail stone and that may introduce much more damage into the airframe.

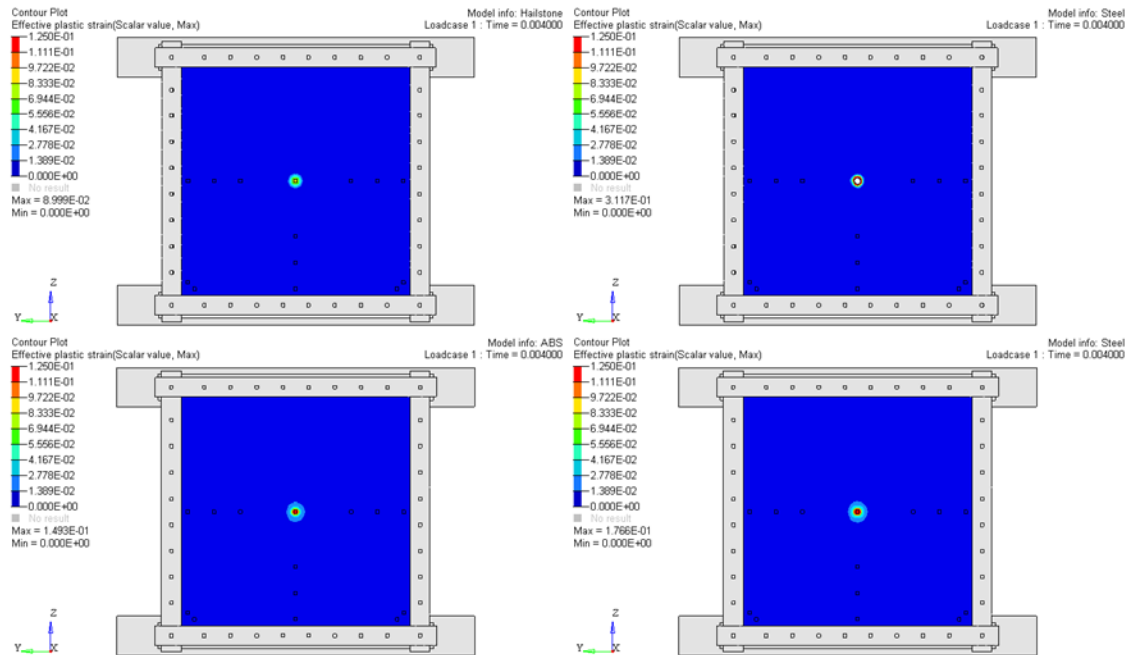


Figure 232. Comparison with hail impact results – effective plastic strain at 180 m/s (350 knots)

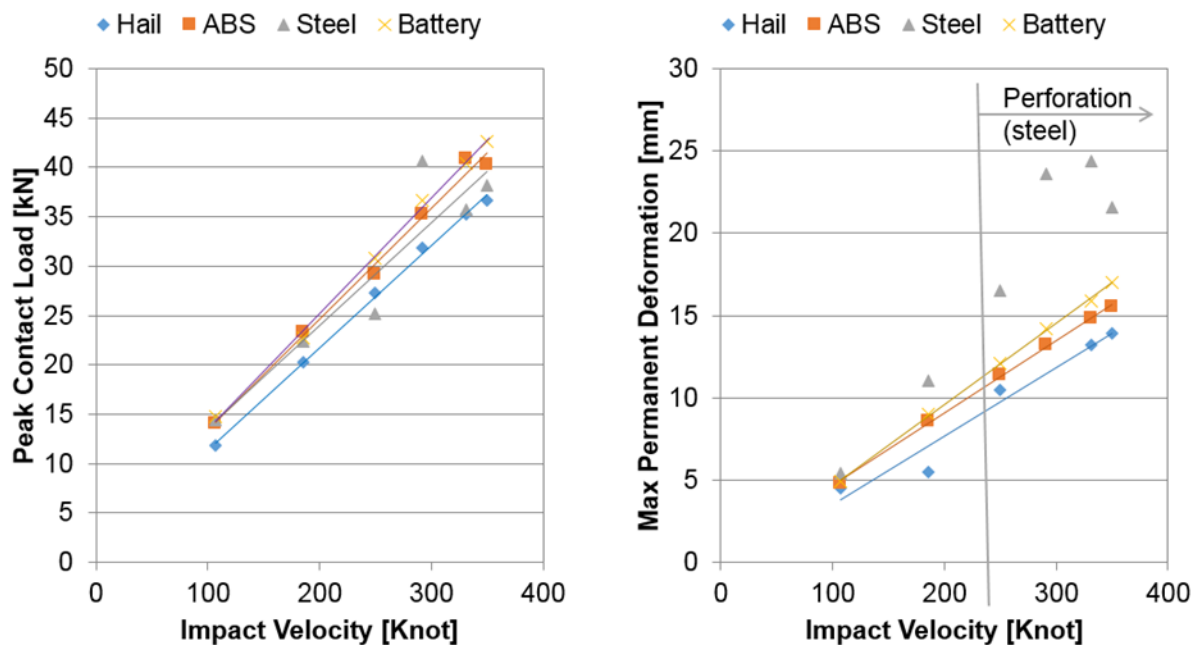


Figure 233. Comparison with hail impact results – contact loads and permanent deformation at 180 m/s (350 knots)

APPENDIX C – AIRBORNE COLLISION ANALYSIS REPORT

C.1 COMMERCIAL TRANSPORT JET

C.1.1 Vertical Stabilizer

C.1.1.1 CFV1

This impact location was identified as the critical baseline simulation for the commercial transport jet vertical stabilizer and is discussed in section 4.3.1.2 of the main report body.

C.1.1.2 CFV2

The UAS was impacted against the vertical stabilizer at 128.6 m/s (250 knots) along the local x -axis direction of the aircraft. The impact location selected was at approximately 55% of the vertical stabilizer span, with the center of gravity of the UAS aligned with the leading edge, at the midpoint between ribs 13 and 14. Figure 234 depicts the kinematics of the event. Figure 235 shows the damage caused to the skin and inner structure of the vertical stabilizer.

The UAS damaged the skin and the upper and lower ribs, creating a 128 x 249 mm² damage zone on the skin surface and allowing some fragments of UAS components to penetrate into airframe. The permanent deformation in the ribs can be perceived in the bottom left image of Figure 235. The front spar did not sustain any visible damage.

The damage introduced by the UAS involved penetration of the skin but no damage to the front spar, and consequently the severity was classified as Level 3.

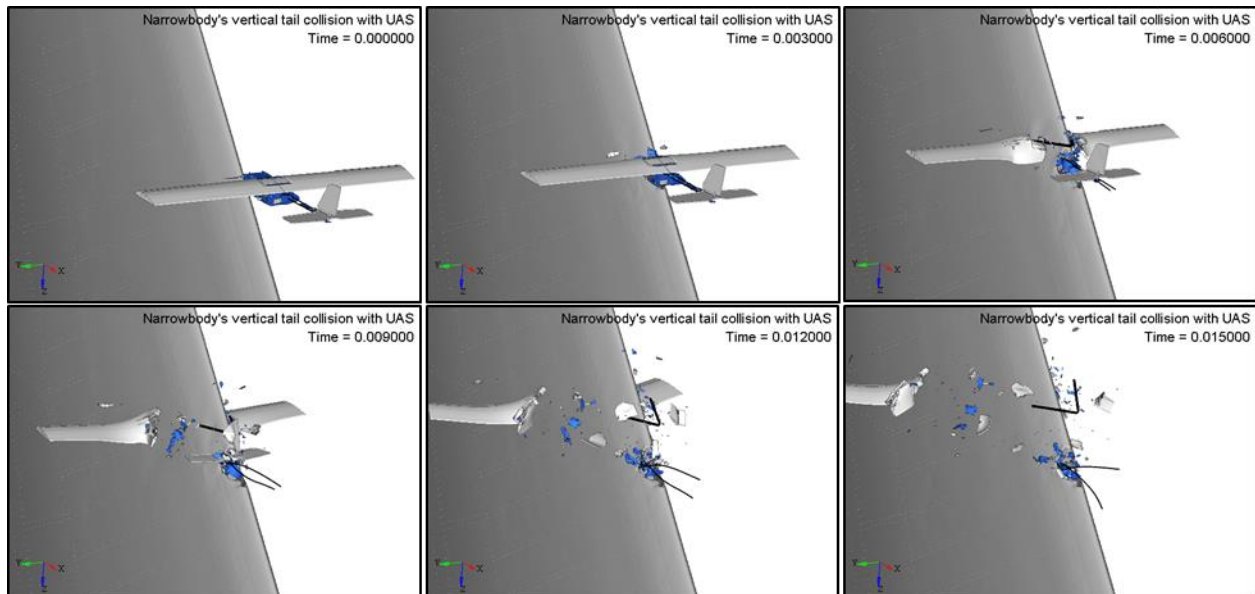


Figure 234. Kinematics of the impact between a commercial transport jet vertical stabilizer and a 1.8 kg (4.0 lb) UAS at location 2 at 128.6 m/s (250 knots)

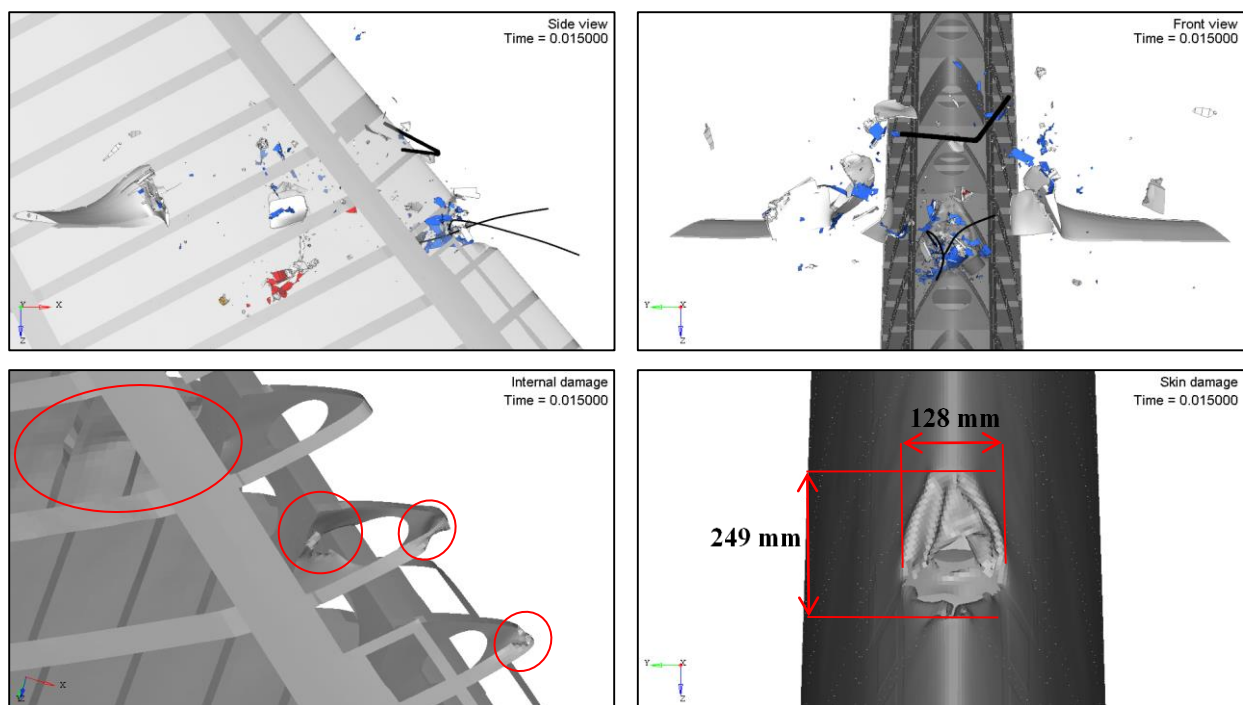


Figure 235. External/internal damage sustained by a commercial transport jet vertical stabilizer impacted at location 2 with a 1.8 kg (4.0 lb) UAS at 128.6 m/s (250 knots)

Figure 236 shows the impulse due to the contact force between UAS and vertical stabilizer, as well as the energy balance for both of them. Figure 237 shows the internal energies of UAS and vertical stabilizer parts directly involved in the impact.

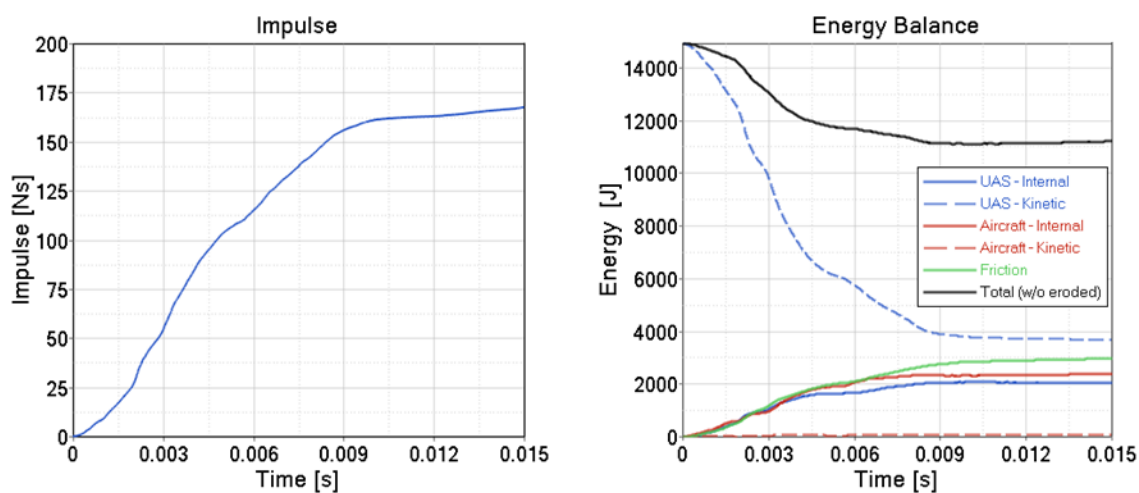


Figure 236. Impulse and energy balance of the impact between a commercial transport jet vertical stabilizer and a 1.8 kg (4.0 lb) UAS at location 2 at 128.6 m/s (250 knots)

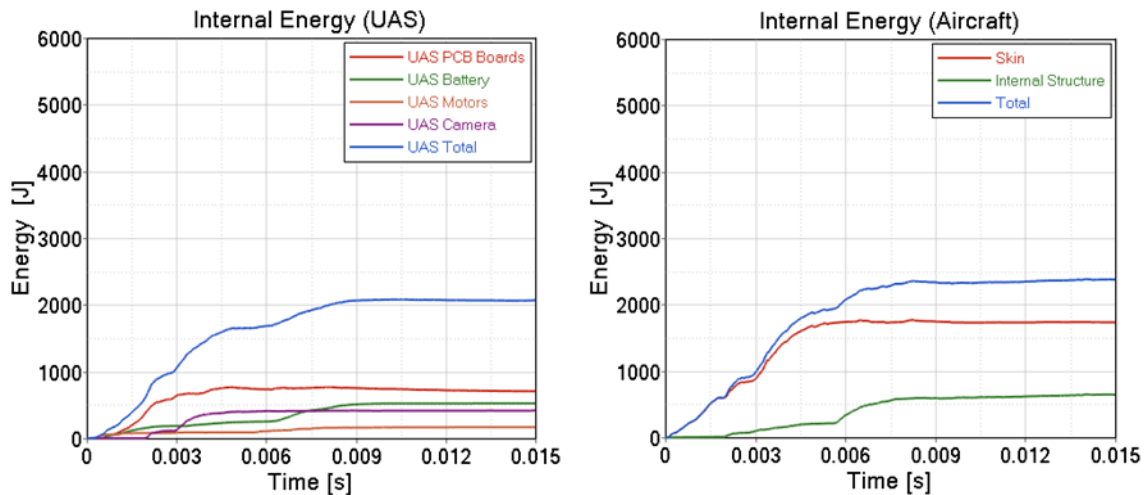


Figure 237. Internal energy per component of the impact between a commercial transport jet vertical stabilizer and a 1.8 kg (4.0 lb) UAS at location 2 at 128.6 m/s (250 knots)

The energy balance plot includes the UAS and vertical stabilizer kinetic and internal energies as well as frictional energy and total energy for the event. The vertical stabilizer and the UAS absorbed 16% and 14% of the impact energy respectively. The energy dissipated by friction reached 20% of the total energy. In Figure 237, internal energies for the UAS parts and the vertical stabilizer show that the polycarbonate carcass of the UAS and skin of the vertical stabilizer absorb the highest amount of internal energies.

C.1.1.3 CFV3

The UAS was impacted against the vertical stabilizer at 128.6 m/s (250 knots) along the local x-axis direction of the aircraft. The impact location selected was at approximately 70% of the vertical stabilizer span, with the center of gravity of the UAS aligned with the leading edge, at the midpoint between ribs 19 and 20. Figure 238 depicts the kinematics of the event. Figure 239 shows the damage caused to the skin and inner structure of the vertical stabilizer.

The UAS damaged the skin, the leading edge ribs and front spar, creating a 120x233 mm² damage zone on the skin surface and allowing some fragments of UAS components to penetrate into airframe. The damage and permanent deformation in the ribs and the front spar can be perceived in the bottom left image of Figure 239. The front spar sustained critical damage with a 44mm fracture.

The damage introduced by the UAS involved penetration of the skin and the front spar, and consequently the severity was classified as Level 4.

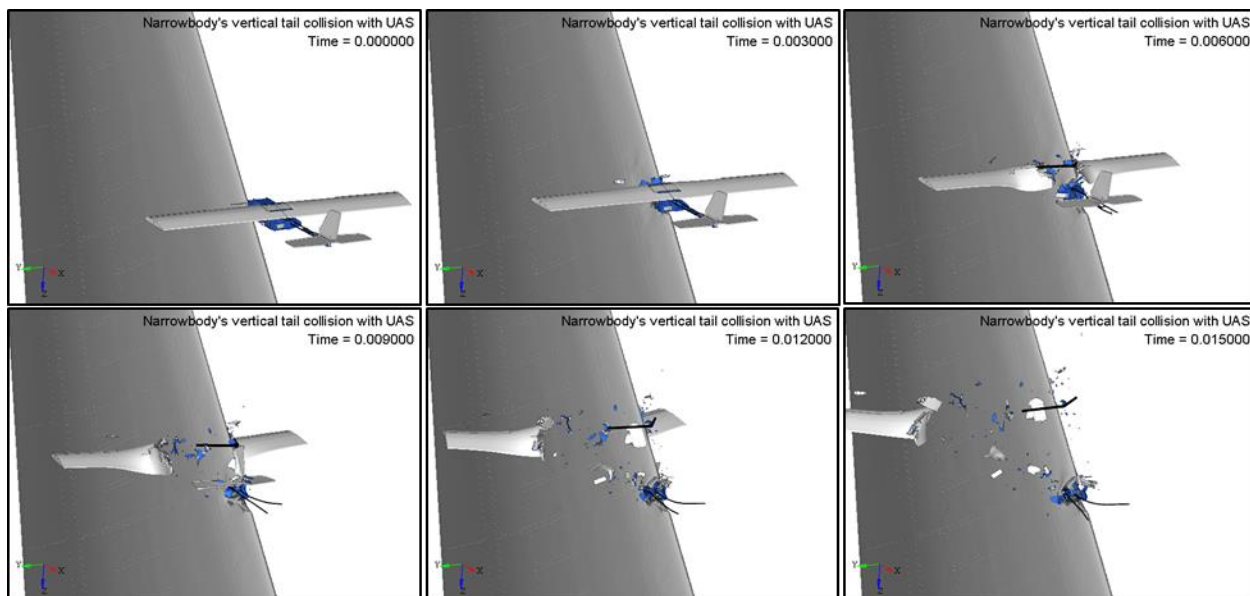


Figure 238. Kinematics of the impact between a commercial transport jet vertical stabilizer and a 1.8 kg (4.0 lb) UAS at location 3 at 128.6 m/s (250 knots)

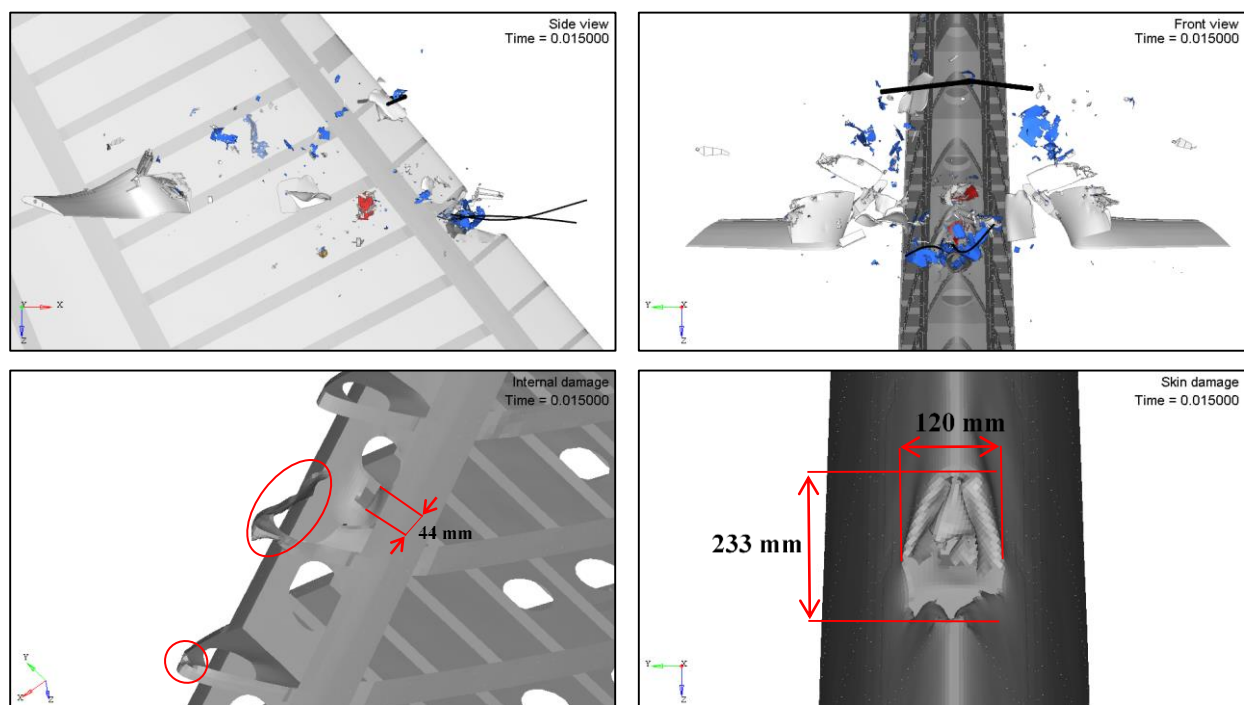


Figure 239. External/internal damage sustained by a commercial transport jet vertical stabilizer impacted at location 3 with a 1.8 kg (4.0 lb) UAS at 128.6 m/s (250 knots)

Figure 240 presents the impulse due to the contact force between UAS and vertical stabilizer, as well as the energy balance for both of them. Figure 241 shows the internal energies of UAS and vertical stabilizer parts directly involved in the impact.

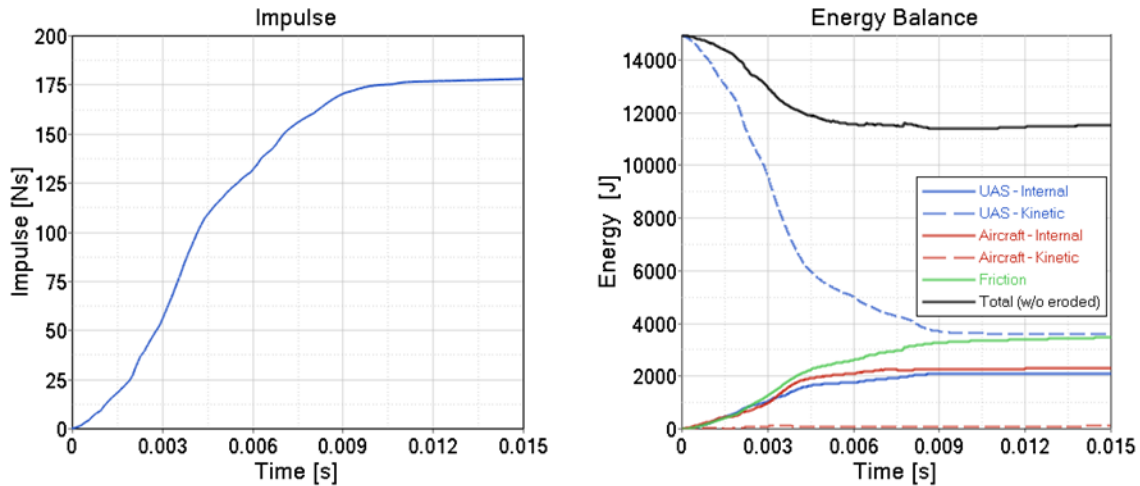


Figure 240. Impulse and energy balance of the impact between a commercial transport jet vertical stabilizer and a 1.8 kg (4.0 lb) UAS at location 3 at 128.6 m/s (250 knots)

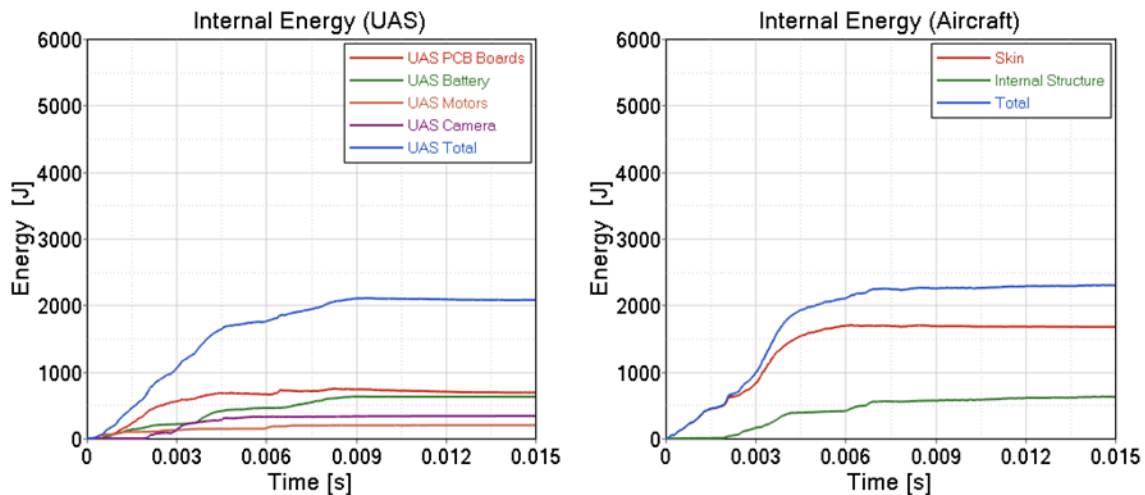


Figure 241. Internal energy per component of the impact between a commercial transport jet vertical stabilizer and a 1.8 kg (4.0 lb) UAS at location 3 at 128.6 m/s (250 knots)

The energy balance plot includes the UAS and vertical stabilizer kinetic and internal energies as well as frictional energy and total energy for the event. The vertical stabilizer and the UAS absorbed 14% and 14% of the impact energy respectively. The energy dissipated by friction reached 23% of the total energy. In Figure 241, internal energies for the UAS parts and the vertical stabilizer show that the polycarbonate carcass of the UAS and the skin of the vertical stabilizer absorb the highest amount of internal energies.

C.1.1.4 CFV4

The UAS was impacted against the vertical stabilizer at 128.6 m/s (250 knots) along the local x-axis direction of the aircraft. The impact location selected was at approximately 85% of the vertical stabilizer span, with the center of gravity of the UAS aligned with the leading edge, at the midpoint

between ribs 25 and 26. Figure 242 depicts the kinematics of the event. Figure 243 shows the damage caused to the skin and inner structure of the vertical stabilizer.

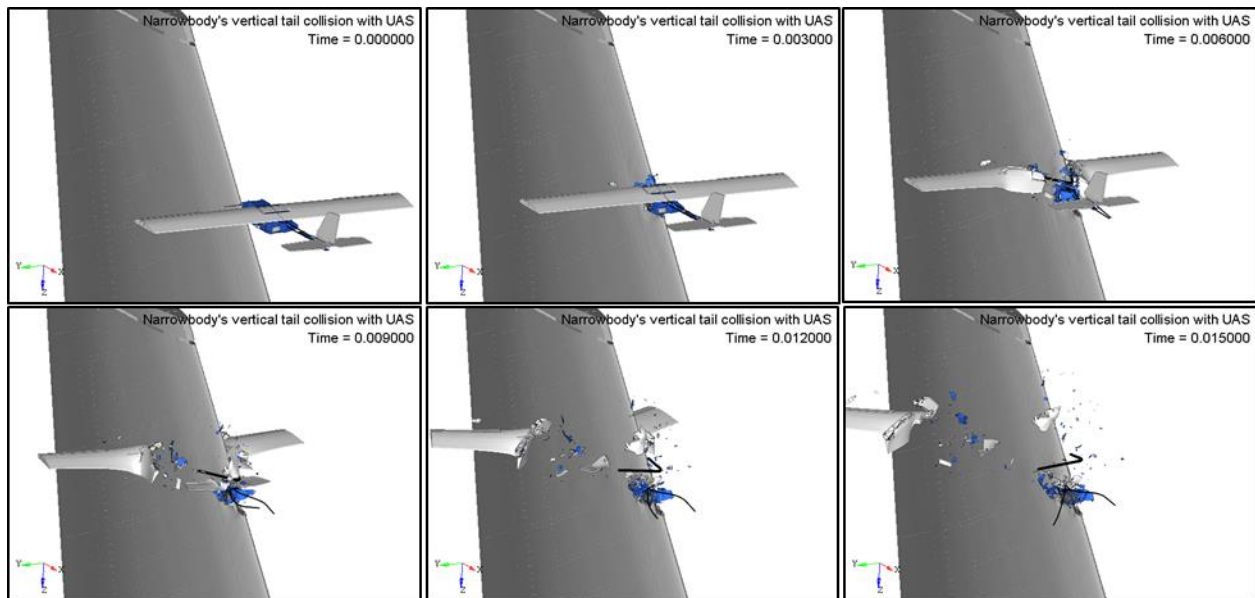


Figure 242. Kinematics of the impact between a commercial transport jet vertical stabilizer and a 1.8 kg (4.0 lb) UAS at location 4 at 128.6 m/s (250 knots)

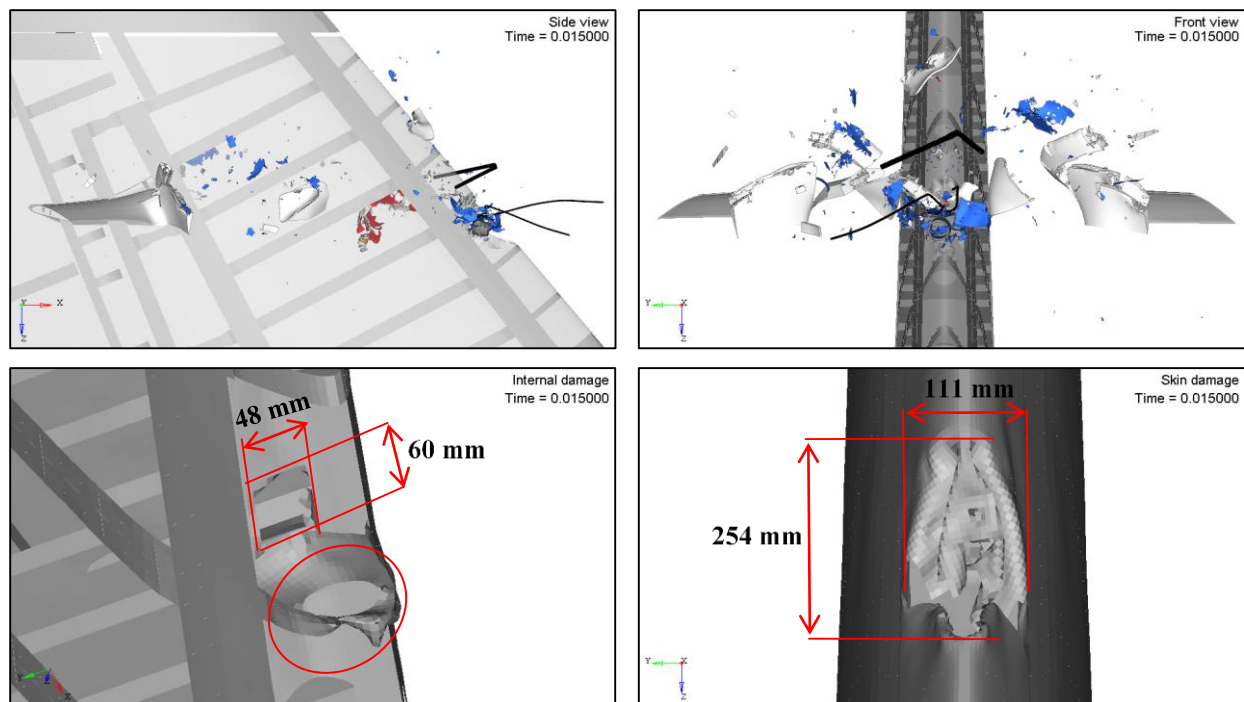


Figure 243. External/internal damage sustained by a commercial transport jet vertical stabilizer impacted at location 4 with a 1.8 kg (4.0 lb) UAS at 128.6 m/s (250 knots)

The UAS damaged the skin, the upper and lower ribs and the front spar, creating a 111x254 mm² damage zone on the skin surface and allowing some fragments of the UAS components to enter the airframe and penetrate the front spar. The permanent deformation and damage in the ribs and front spar can be seen in the bottom left image of Figure 243. The front spar sustained critical damage with a 48x60mm damaged zone.

The damage introduced by the UAS involved penetration of the skin and the front spar, and consequently the severity was classified as Level 4.

Figure 244 shows the impulse due to the contact force between UAS and vertical stabilizer, as well as the energy balance for both of them. Figure 245 shows the internal energies of UAS and vertical stabilizer parts directly involved in the impact.

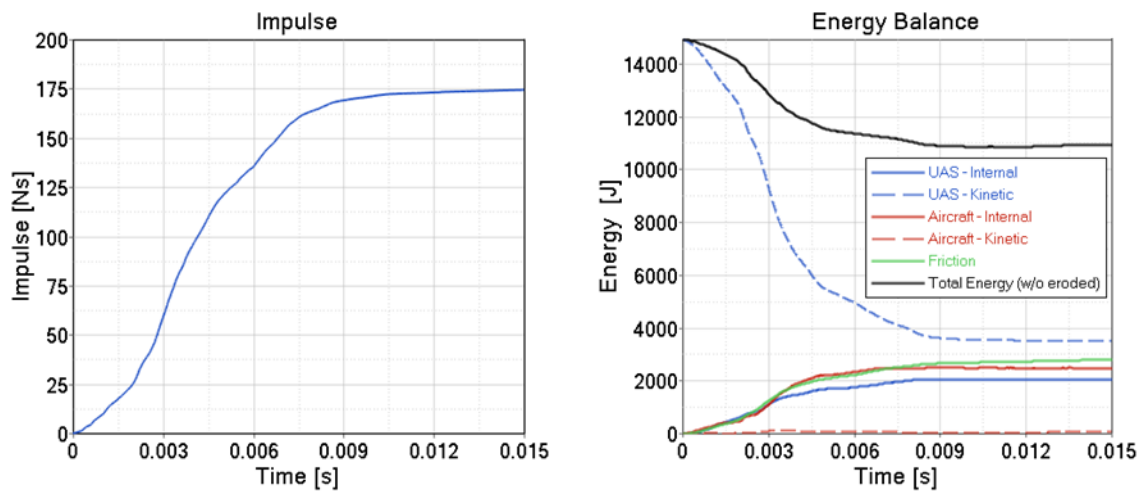


Figure 244. Impulse and energy balance of the impact between a commercial transport jet vertical stabilizer and a 1.8 kg (4.0 lb) UAS at location 4 at 128.6 m/s (250 knots)

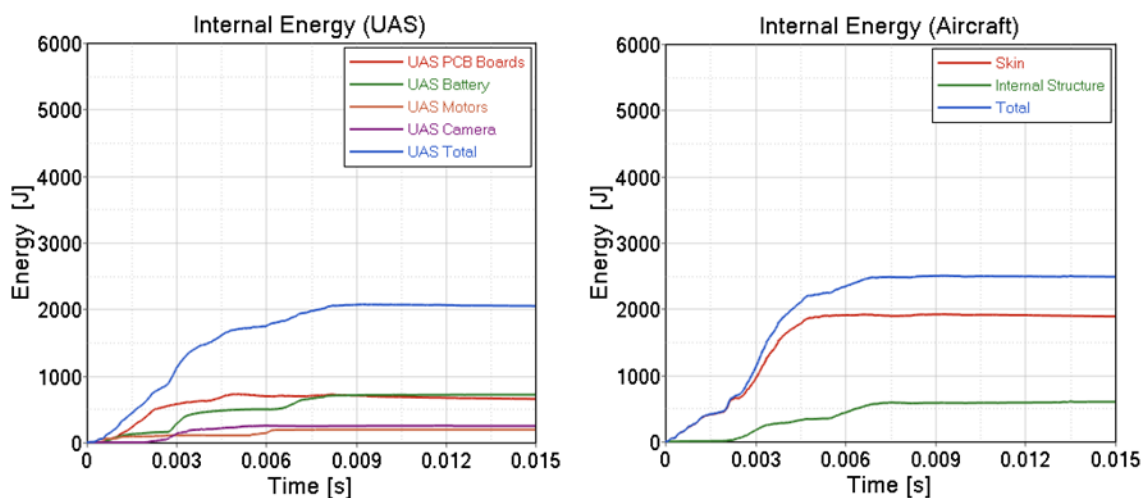


Figure 245. Internal energy per component of the impact between a commercial transport jet vertical stabilizer and a 1.8 kg (4.0 lb) UAS at location 4 at 128.6 m/s (250 knots)

The energy balance plot includes the UAS and vertical stabilizer kinetic and internal energies as well as frictional energy and total energy for the event. The vertical stabilizer and the UAS absorbed 17% and 14% of the impact energy respectively. The energy dissipated by friction reached 19% of the total energy. In Figure 245, internal energies for the UAS parts and the vertical stabilizer show that the UAS battery and skin of the vertical stabilizer absorb the highest amount of internal energies.

C.1.2 Horizontal Stabilizer

C.1.2.1 CFH1

The UAS was impacted against the horizontal stabilizer at 128.6 m/s (250 knots) along the local x-axis direction of the aircraft. The impact location selected was at approximately 15% of the horizontal stabilizer semispan, with the center of gravity of the UAS aligned with the leading edge, at the midpoint between ribs 5 and 6. Figure 246 depicts the kinematics of the event. Figure 247 shows the damage caused to the skin and the inner structure of horizontal stabilizer.

The UAS damaged the skin, the leading edge ribs and front spar, creating a 205x114 mm² damage zone on the skin surface and allowing some fragments of the UAS components to penetrate into airframe. The permanent deformation and damage in the ribs and front spar can be seen in the bottom left image of Figure 247. The front spar did not sustain critical damage.

The damage introduced by the UAS involved penetration of the skin and slight damage to the front spar, and consequently the severity was classified as Level 4.

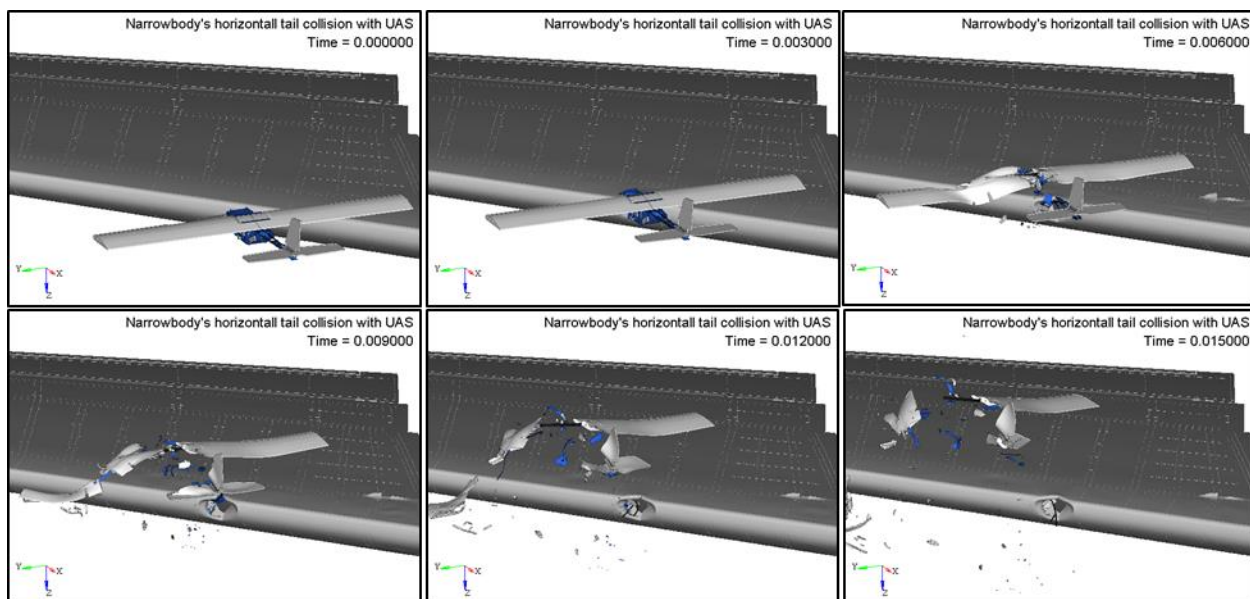


Figure 246. Kinematics of the impact between a commercial transport jet horizontal stabilizer and a 1.8 kg (4.0 lb) UAS at location 1 at 128.6 m/s (250 knots)

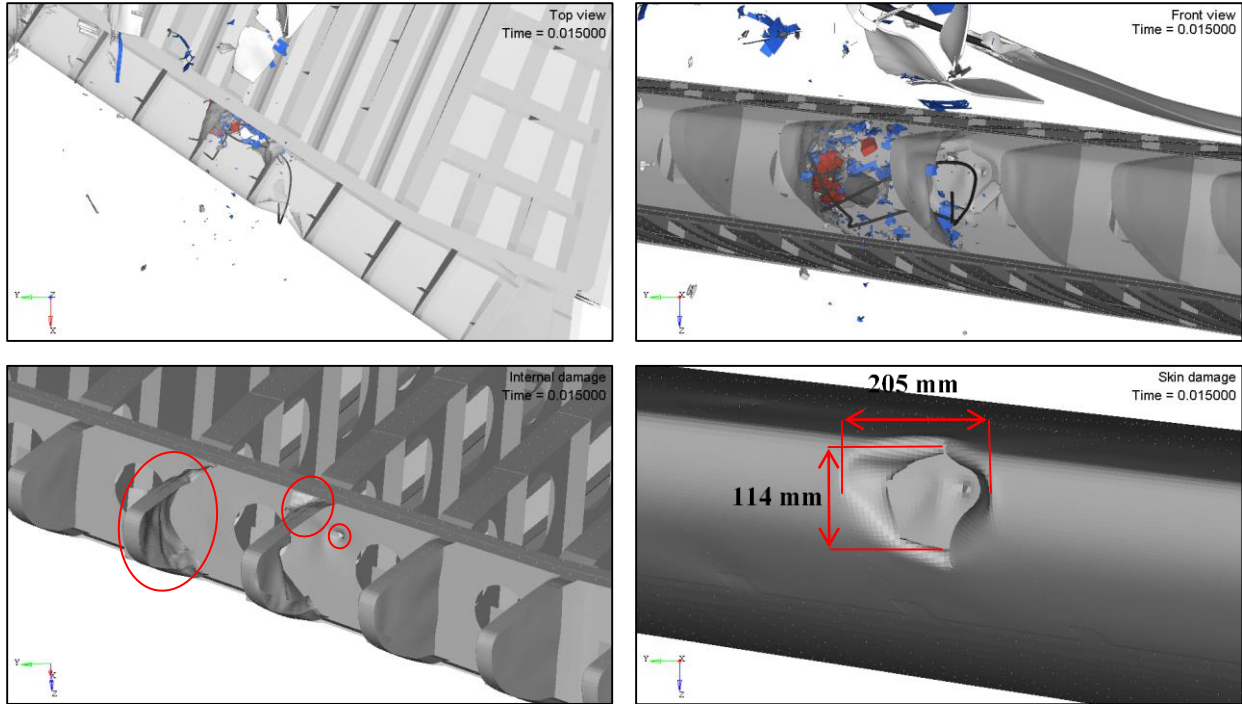


Figure 247. External/internal damage sustained by a commercial transport jet horizontal stabilizer impacted at location 1 with a 1.8 kg (4.0 lb) UAS at 128.6 m/s (250 knots)

Figure 248 shows the impulse due to the contact force between the UAS and the horizontal stabilizer, as well as the energy balance for both of them. Figure 249 presents the internal energies of the UAS and horizontal stabilizer parts directly involved on the impact.

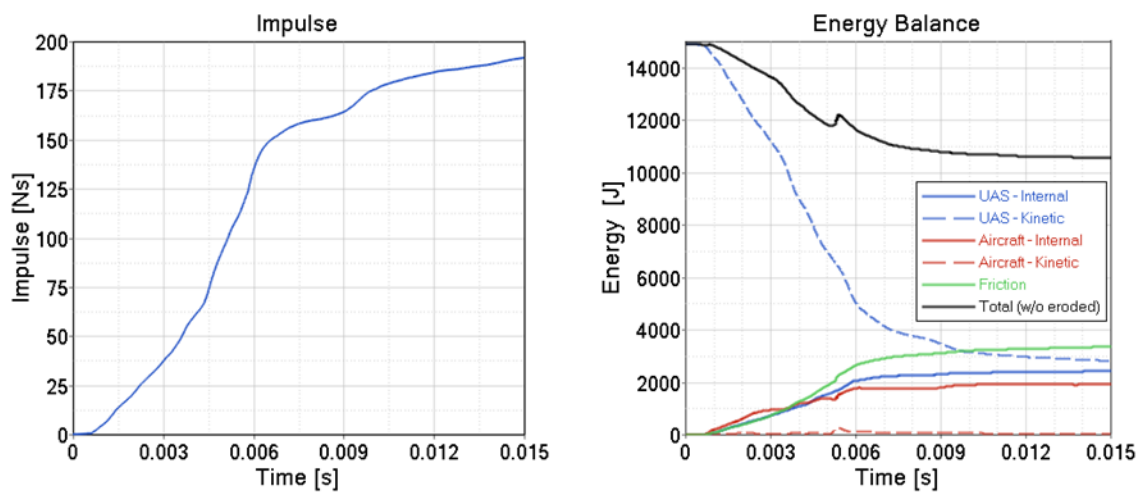


Figure 248. Impulse and energy balance of the impact between a commercial transport jet horizontal stabilizer and a 1.8 kg (4.0 lb) UAS at location 1 at 128.6 m/s (250 knots)

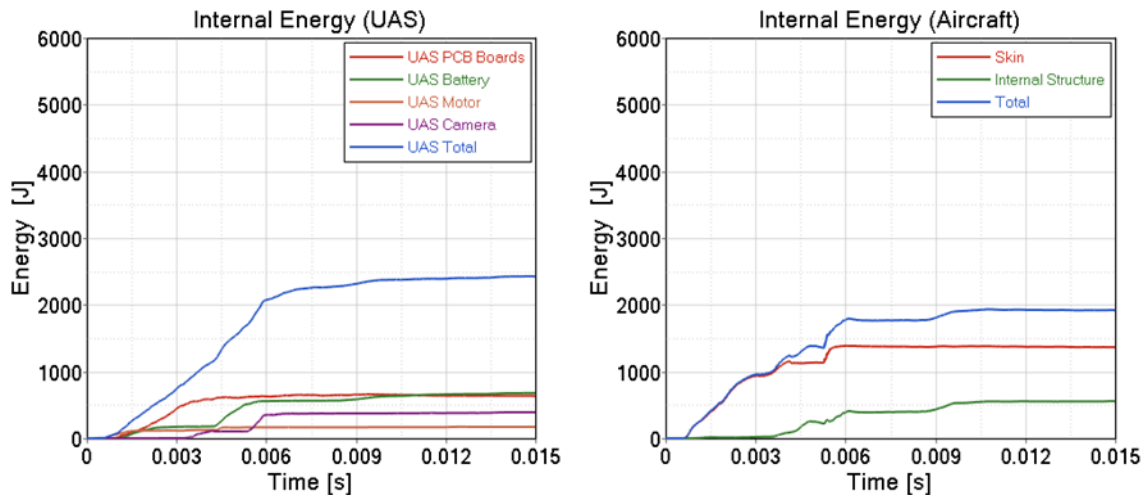


Figure 249. Internal energy per component of the impact between commercial transport jet horizontal stabilizer and 1.8 kg (4.0 lb) UAS at location 1 at 128.6 m/s (250 knots)

The energy balance plot includes the UAS and horizontal stabilizer kinetic and internal energies, as well as frictional energy and total energy for the event. The horizontal stabilizer and the UAS absorbed 13% and 16% of the impact energy respectively. The energy dissipated by friction reached 22% of the total energy. In Figure 249, internal energies for the UAS parts and the horizontal stabilizer show that the UAS battery and skin of the horizontal stabilizer absorb the highest internal energies.

C.1.2.2 CFH2

This impact location was identified as the critical baseline simulation for the commercial transport jet horizontal stabilizer and is discussed in section 4.3.2.2 of the main report body.

C.1.2.3 CFH3

The UAS was impacted against the horizontal stabilizer at 128.6 m/s (250 knots) along the local x-axis direction of the aircraft. The impact location selected was at approximately 60% of the horizontal stabilizer semispan, with the center of gravity of the UAS aligned with the leading edge, at the midpoint between ribs 19 and 20. Figure 250 depicts the kinematics of the event. Figure 251 shows the damage caused to the skin and inner structure of the horizontal stabilizer.

The UAS damaged the skin, the leading edge ribs, and front spar, creating a 218x114 mm² damage zone on the skin surface and allowing some fragments of the UAS components to enter the airframe and penetrate the front spar. The damage and permanent deformation in the ribs and the front spar can be perceived in the bottom left image of Figure 251. The front spar sustained critical damage with a damaged zone of 109x80 mm.

The damage introduced by the UAS involved penetration of the skin and considerable damage to the front spar. Consequently, the severity was classified as Level 4.

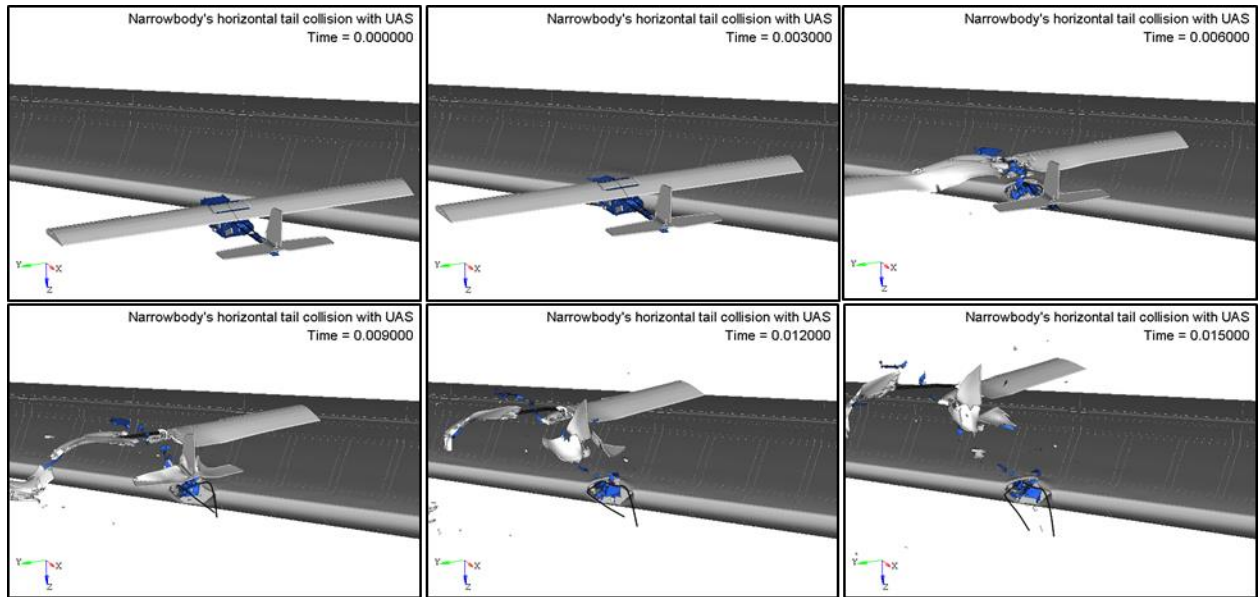


Figure 250. Kinematics of the impact between a commercial transport jet horizontal stabilizer and a 1.8 kg (4.0 lb) UAS at location 3 at 128.6 m/s (250 knots)

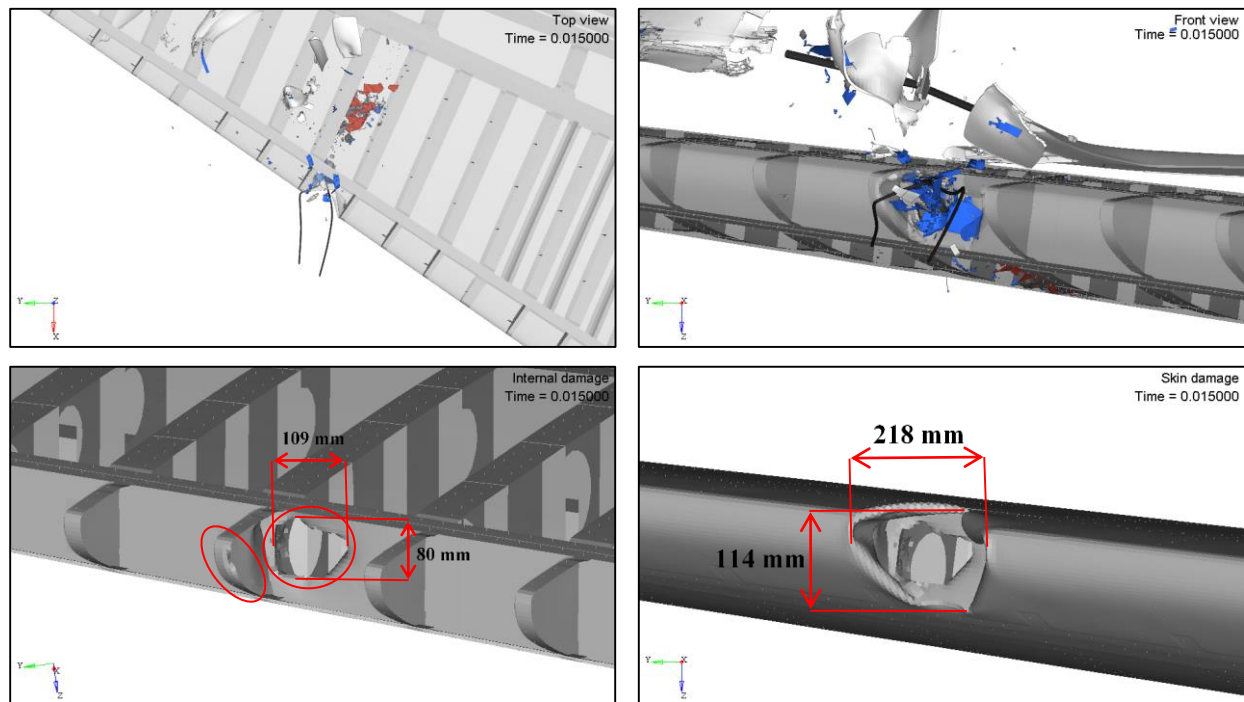


Figure 251. External/internal damage sustained by a commercial transport jet horizontal stabilizer impacted at location 3 with 1.8 kg (4.0 lb) UAS at 128.6 m/s (250 knots)

Figure 252 presents the impulse due to the contact force between the UAS and the horizontal stabilizer, as well as the energy balance for both of them. Figure 253 presents the internal energies of the UAS and horizontal stabilizer components directly involved in the impact.

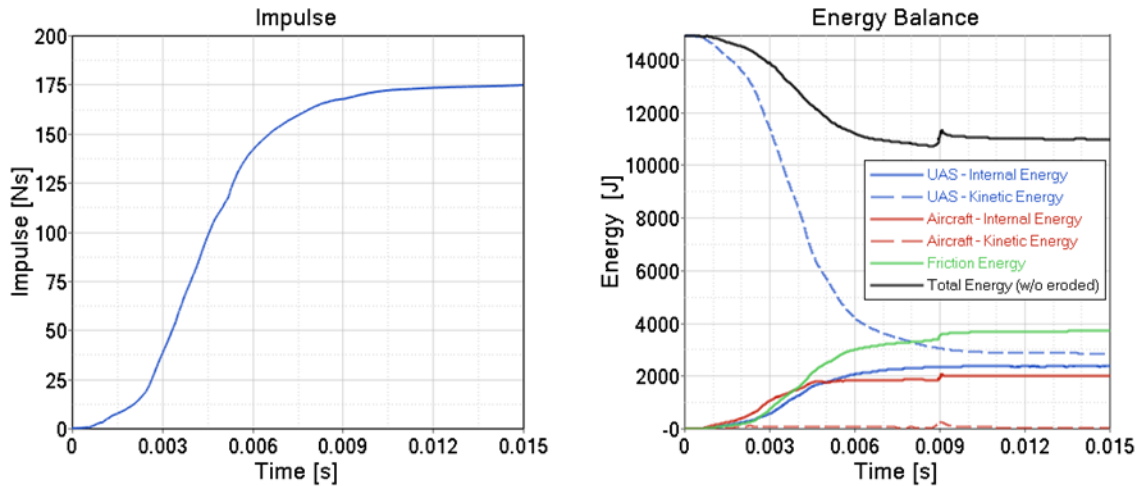


Figure 252. Impulse and energy balance of the impact between a commercial transport jet horizontal stabilizer and a 1.8 kg (4.0 lb) UAS at location 3 at 128.6 m/s (250 knots)

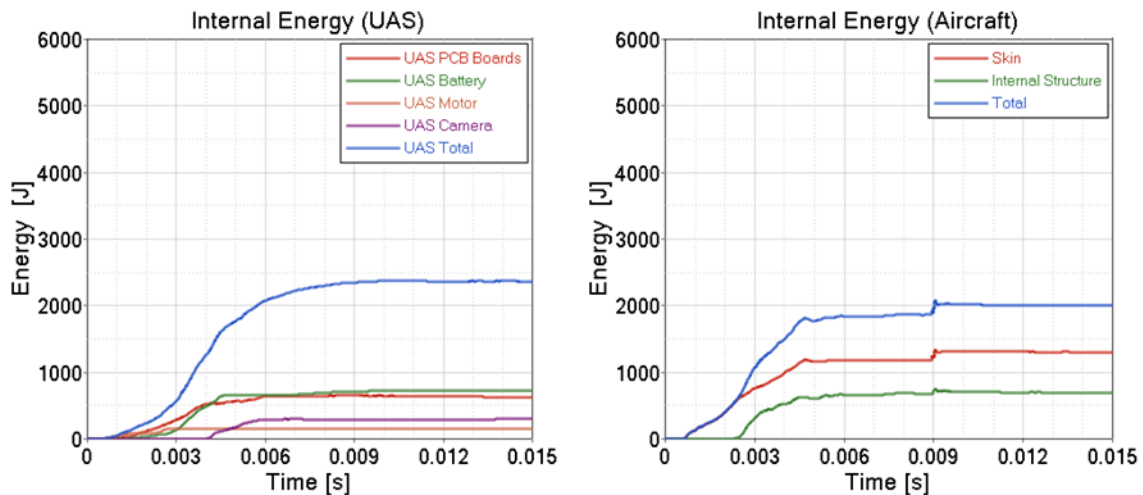


Figure 253. Internal energy per component of the impact between commercial transport jet horizontal stabilizer and 1.8 kg (4.0 lb) UAS at location 3 at 128.6 m/s (250 knots)

The energy balance plot includes the UAS and horizontal stabilizer kinetic and internal energies, as well as frictional energy and total energy for the event. The horizontal stabilizer and the UAS absorbed 13% and 16% of the impact energy respectively. The energy dissipated by friction reaches 25% of the total energy. In Figure 253, internal energies for the UAS parts and the horizontal stabilizer show that the UAS battery and the skin of the horizontal stabilizer absorb the highest internal energies.

C.1.2.4 CFH4

The UAS was impacted against the horizontal stabilizer at 128.6 m/s (250 knots) along the local x-axis direction of the aircraft. The impact location selected was at approximately 80% of the horizontal stabilizer semispan, with the center of gravity of the UAS aligned with the leading edge, at

the midpoint between ribs 25 and 26. Figure 254 depicts the kinematics of the event. Figure 255 shows the damage caused to the skin and inner structure of the horizontal stabilizer.

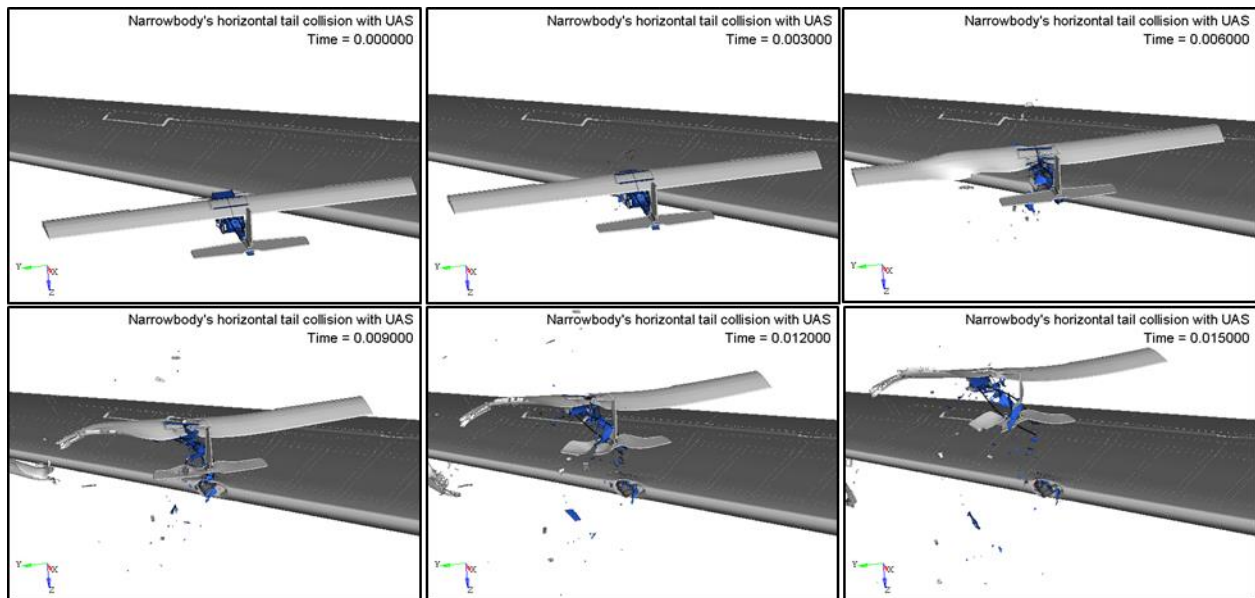


Figure 254. Kinematics of the impact between a commercial transport jet horizontal stabilizer and a 1.8 kg (4.0 lb) UAS at location 4 at 128.6 m/s (250 knots)

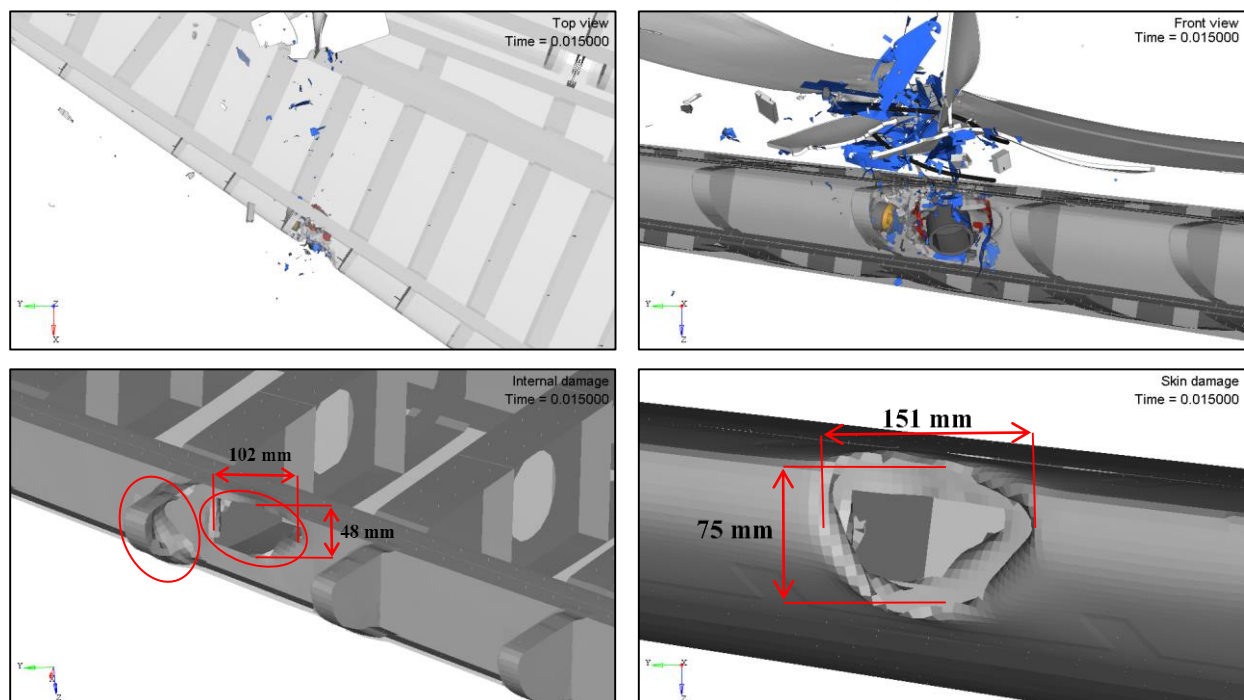


Figure 255. External/internal damage sustained by a commercial transport jet horizontal stabilizer impacted at location 4 with a 1.8 kg (4.0 lb) UAS at 128.6 m/s (250 knots)

The UAS damaged the skin, the leading edge ribs, and the front spar, creating a 151x75 mm² damage zone on the skin surface and allowing some fragments of the UAS components to enter the airframe and penetrate the front spar. The permanent deformation and damage in the ribs and front spar can be perceived in the bottom left image of Figure 255. The front spar sustained critical damage with a fracture of 102x48 mm.

The damage introduced by the UAS involved penetration of the skin and considerable damage to the front spar, and consequently the severity was classified as Level 4.

Figure 256 shows the impulse due to the contact force between the UAS and the horizontal stabilizer, as well as the energy balance for both of them. Figure 257 presents the internal energies of the UAS and horizontal stabilizer parts directly involved on the impact.

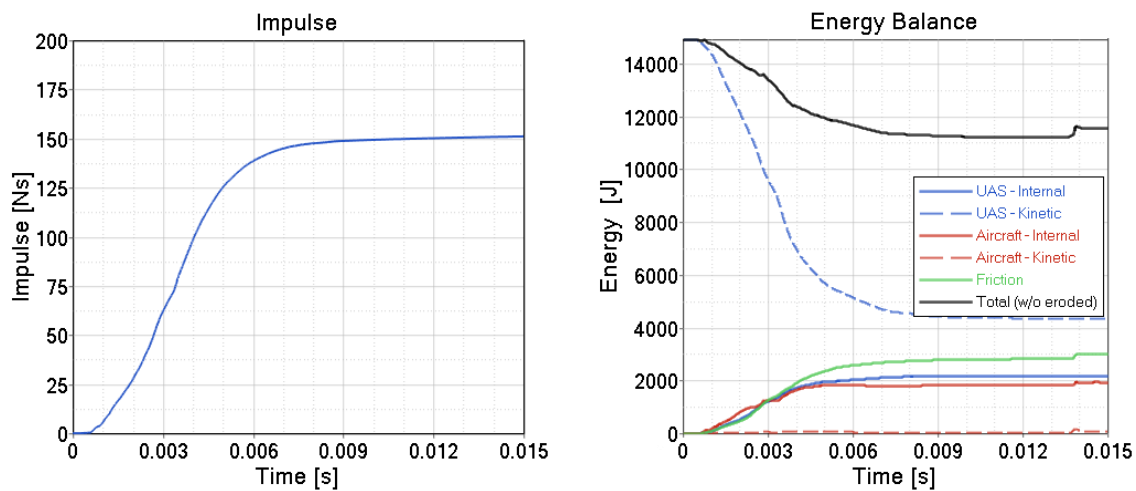


Figure 256. Impulse and energy balance of the impact between a commercial transport jet horizontal stabilizer and a 1.8 kg (4.0 lb) UAS at location 4 at 128.6 m/s (250 knots)

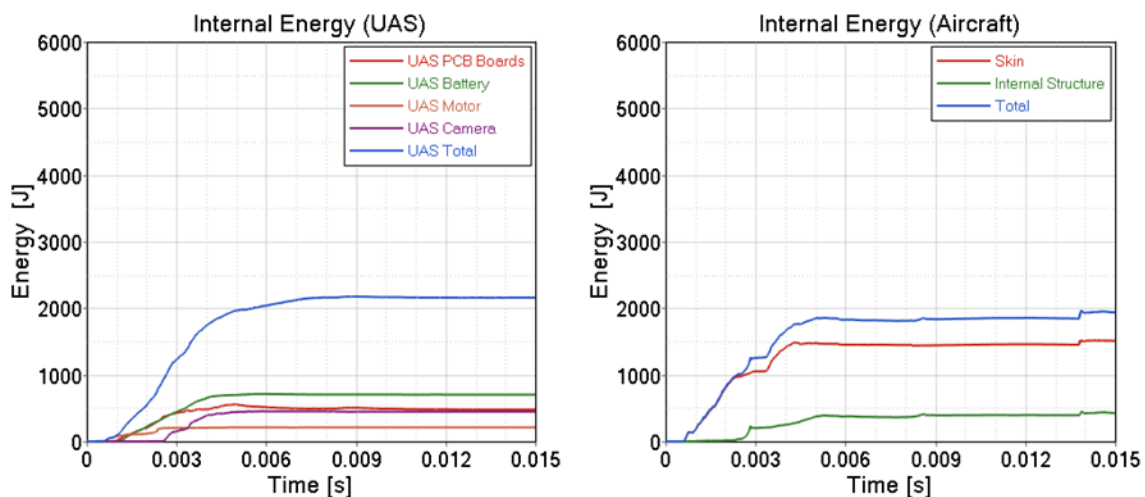


Figure 257. Internal energy per component of the impact between commercial transport jet horizontal stabilizer and 1.8 kg (4.0 lb) UAS at location 4 at 128.6 m/s (250 knots)

The energy balance plot includes the UAS and horizontal stabilizer kinetic and internal energies, as well as frictional energy and total energy for the event. The horizontal stabilizer and the UAS absorbed 13% and 14% of the impact energy respectively. The energy dissipated by friction reached 20% of the total energy. In Figure 257, internal energies for the UAS parts and the horizontal stabilizer show that the UAS battery and the skin of the horizontal stabilizer absorb the highest internal energies.

C.1.2.5 CFH5

The UAS was impacted against the horizontal stabilizer at 128.6 m/s (250 knots) along the local x-axis direction of the aircraft. The impact location selected was at approximately 90% of the horizontal stabilizer semispan, with the center of gravity of the UAS aligned with the leading edge, at the midpoint between ribs 28 and 29. Figure 258 depicts the kinematics of the event. Figure 259 shows the damage caused to the skin and inner structure of the horizontal stabilizer.

The UAS damaged the skin, the leading edge ribs, and the front spar, creating a 137x83 mm² damage zone on the skin surface and allowing some fragments of the UAS components to enter the airframe and penetrate the front spar. The permanent deformation and damage in the ribs and front spar can be perceived in the bottom left image of Figure 259. The front spar sustained critical damage with a fracture of 101x59 mm.

The damage introduced by the UAS involved penetration of the skin and consirable damage to the front spar, and consequently the severity was classified as Level 4.

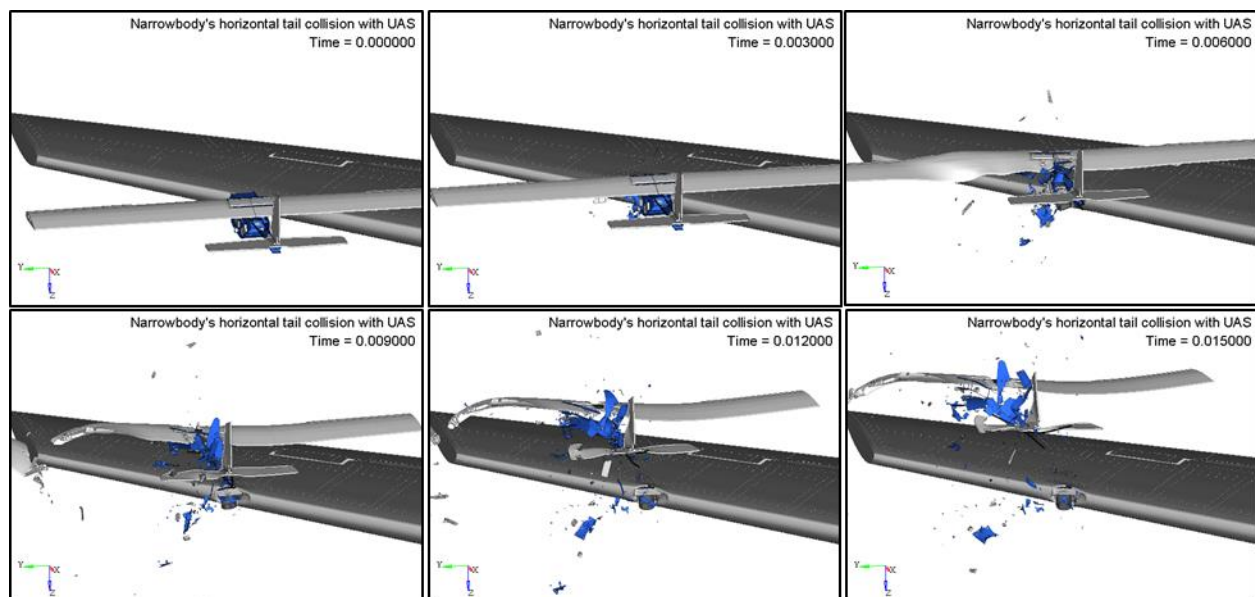


Figure 258. Kinematics of the impact between a commercial transport jet horizontal stabilizer and a 1.8 kg (4.0 lb) UAS at location 5 at 128.6 m/s (250 knots)

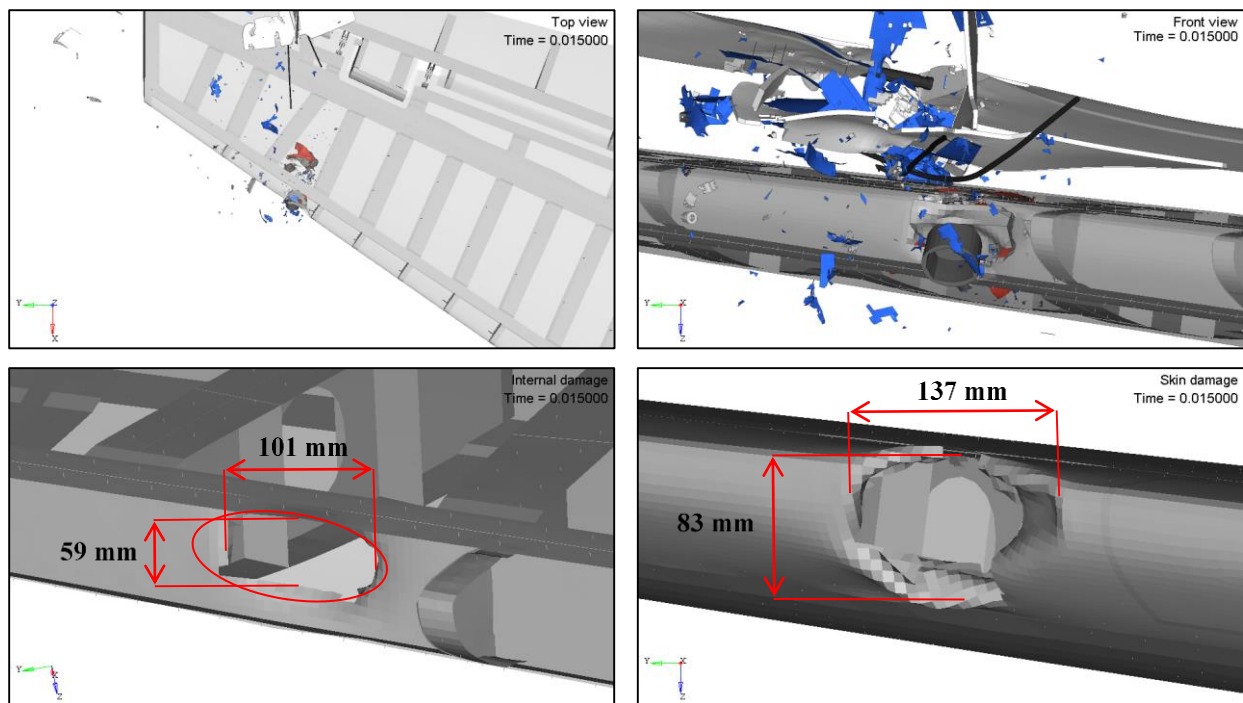


Figure 259. External/internal damage sustained by a commercial transport jet horizontal stabilizer impacted at location 5 with a 1.8 kg (4.0 lb) UAS at 128.6 m/s (250 knots)

Figure 260 shows the impulse due to the contact force between the UAS and the horizontal stabilizer, as well as the energy balance for both of them. Figure 261 presents the internal energies of the UAS and horizontal stabilizer parts directly involved on the impact.

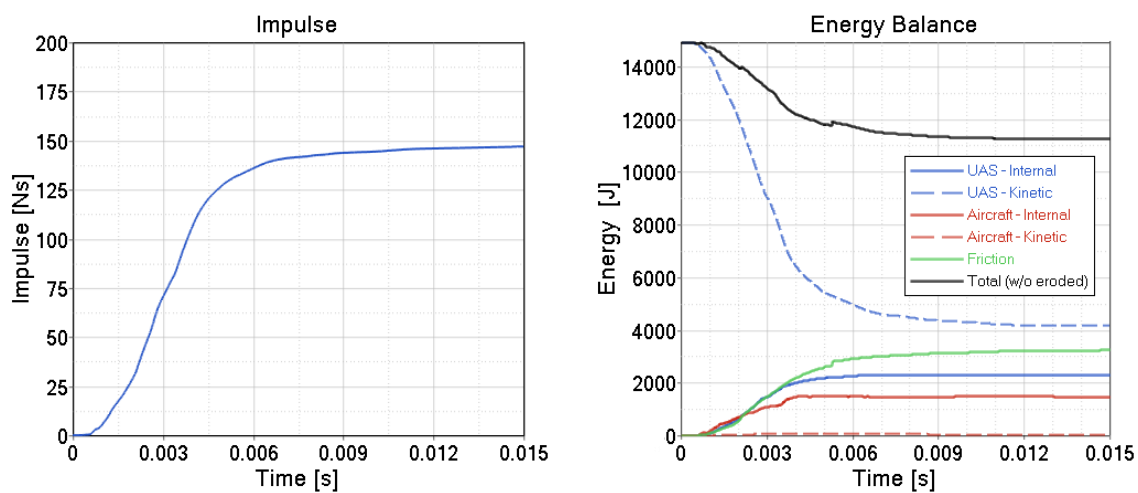


Figure 260. Impulse and energy balance of the impact between a commercial transport jet horizontal stabilizer and a 1.8 kg (4.0 lb) UAS at location 5 at 128.6 m/s (250 knots)

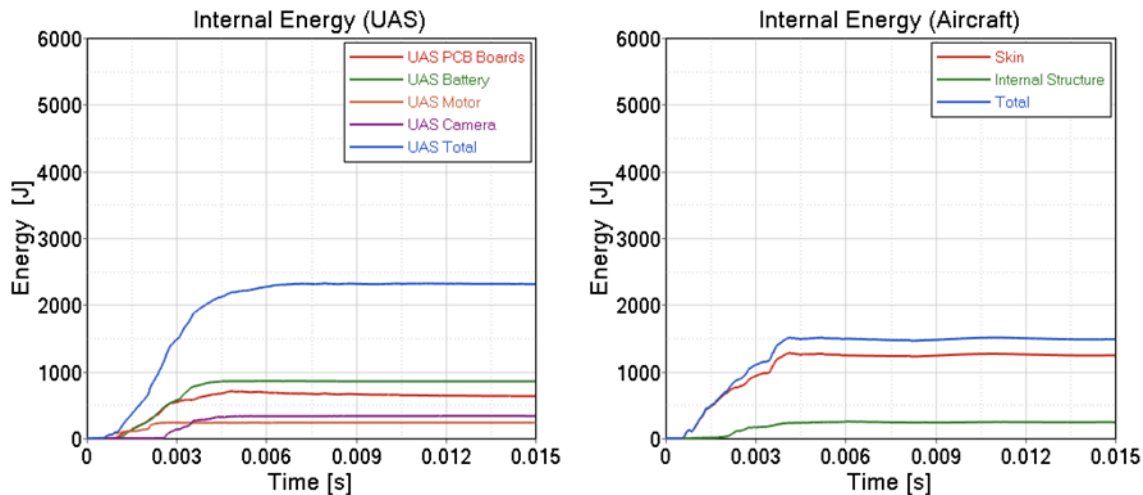


Figure 261. Internal energy per component of the impact between commercial transport jet horizontal stabilizer and 1.8 kg (4.0 lb) UAS at location 5 at 128.6 m/s (250 knots)

The energy balance plot includes the UAS and horizontal stabilizer kinetic and internal energies, as well as frictional energy and total energy for the event. The horizontal stabilizer and the UAS absorbed 10% and 15% of the impact energy respectively. The energy dissipated by friction reached 22% of the total energy. In Figure 261, internal energies for the UAS parts and the horizontal stabilizer show that the UAS battery and skin of horizontal stabilizer absorb the highest internal energies.

C.1.3 Wing

C.1.3.1 CFW1

The UAS was impacted against the leading edge of the wing at 128.6 m/s (250 knots) in the local x-axis direction of the aircraft. The impact location selected was at the central area of slat 3, with the center of gravity of the UAS aligned with the leading edge, at the midpoint between the intermediate rib and the slat track rib pair. Figure 262 depicts the kinematics of the event. Figure 263 shows the damage caused to the skin and inner structure of the wing.

The UAS damaged the leading edge skin, the sub and front spar, deforming an area of 320x133 mm on the skin surface and allowing some fragments of the UAS components to enter the airframe and penetrate the sub-spar. The damage in the sub and front spar can be perceived in the bottom left image of Figure 263. The front spar did not sustain critical damage.

The damage introduced by the UAS involved penetration of the skin and slight damage to the front spar, and consequently the severity was classified as Level 3.

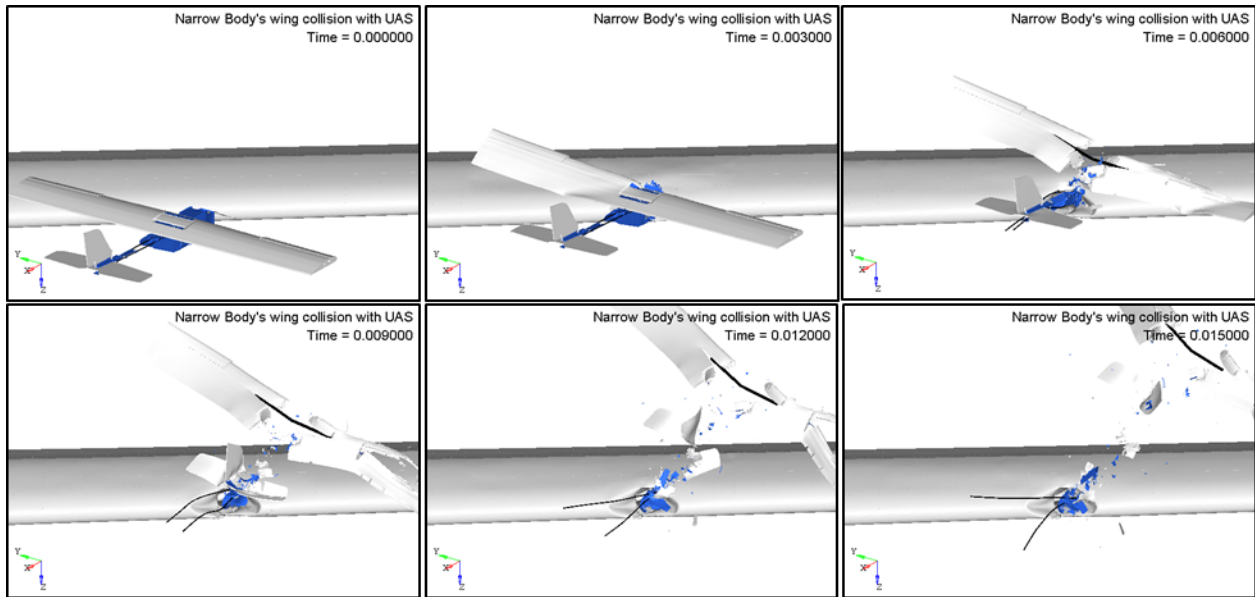


Figure 262. Kinematics of the impact between a commercial transport jet wing and a 1.8 kg (4.0 lb) UAS at location 1 at 128.6 m/s (250 knots)

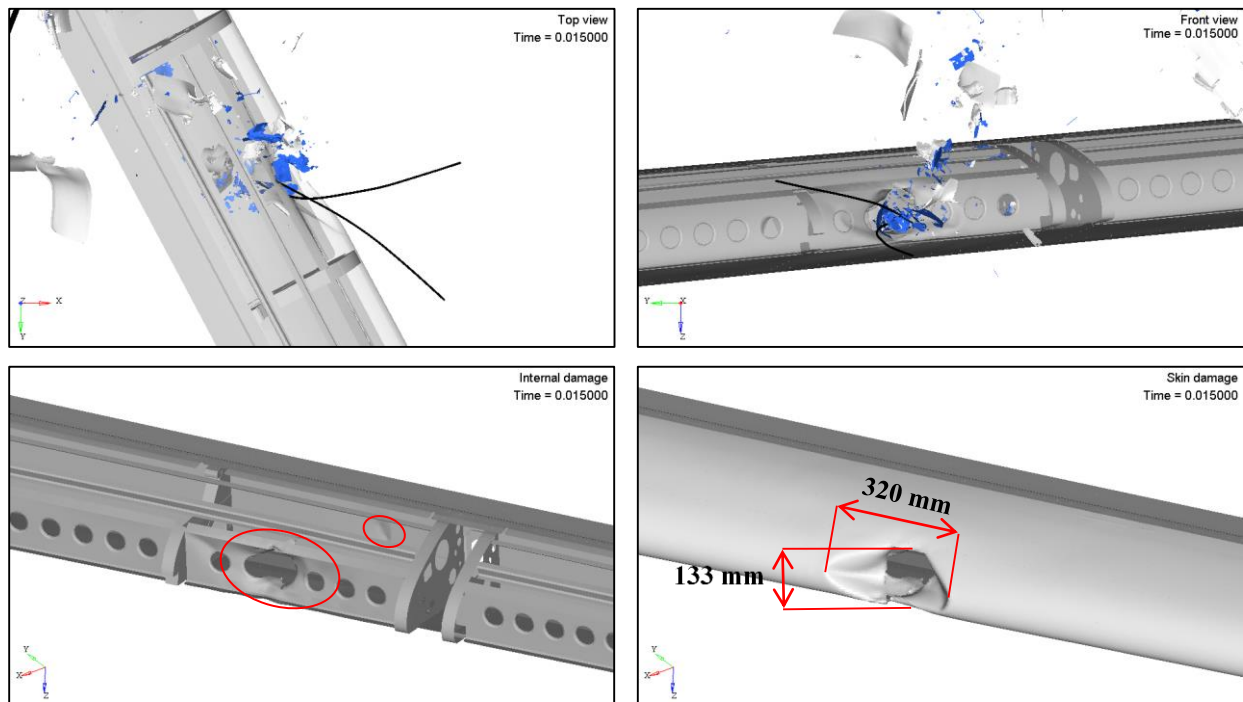


Figure 263. External/internal damage sustained by a commercial transport jet wing impacted at location 1 with a 1.8 kg (4.0 lb) UAS at 128.6 m/s (250 knots)

Figure 264 presents the impulse due to the contact force between UAS and wing, as well as the energy balance for both of them. Figure 265 shows the internal energies of UAS and wing parts directly involved in the impact.

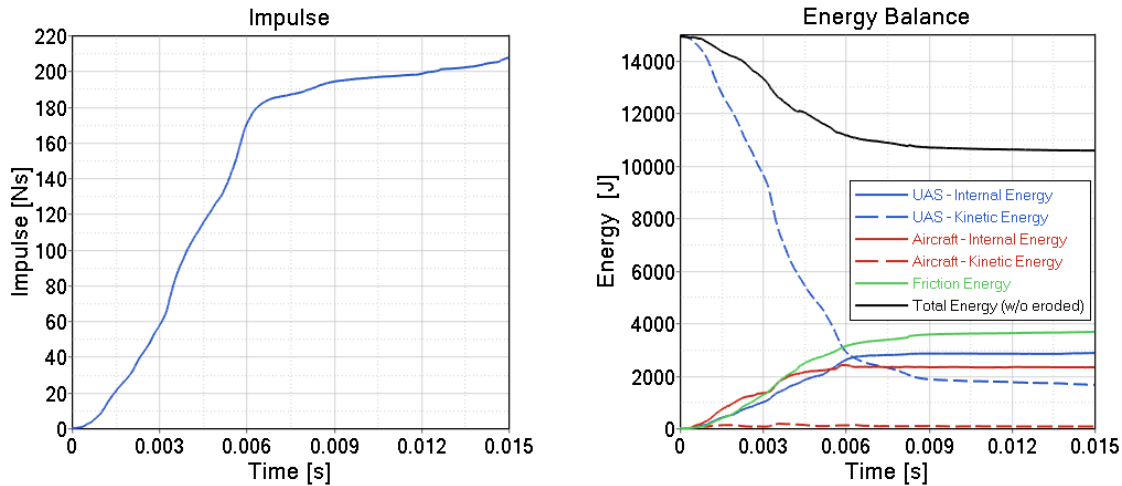


Figure 264. Impulse and energy balance of the impact between a commercial transport jet wing and a 1.8 kg (4.0 lb) UAS at location 1 at 128.6 m/s (250 knots)

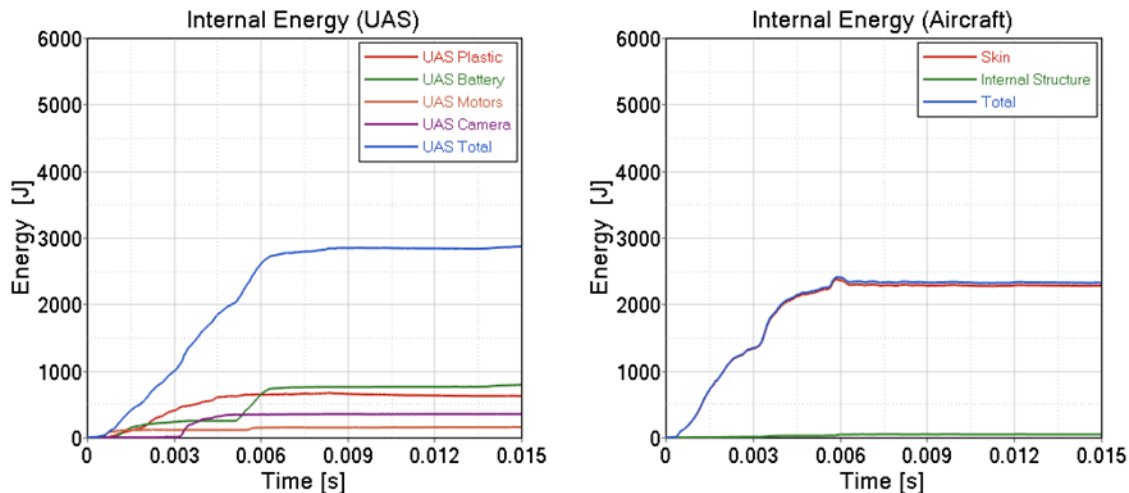


Figure 265. Internal energy per component of the impact between a commercial transport jet wing and a 1.8 kg (4.0 lb) UAS at location 1 at 128.6 m/s (250 knots)

The energy balance plot includes the UAS and wing kinetic and internal energies as well as frictional energy and total energy for the event. The wing and the UAS absorbed 16% and 19% of the impact energy respectively. The energy dissipated by friction reached 25% of the total energy. In Figure 265, internal energies for the UAS parts and the wing show that the UAS battery and the skin of the wing absorb the highest amount of internal energies.

C.1.3.2 CFW2

The UAS was impacted against the leading edge of the wing at 128.6 m/s (250 knots) in the local x-axis direction of the aircraft. The impact location selected was at the outer portion of slat 3, with the center of gravity of the UAS aligned with the leading edge, close to the slat track rib pair. Figure

266 depicts the kinematics of the event. Figure 267 shows the damage caused to the skin and inner structure of the wing.

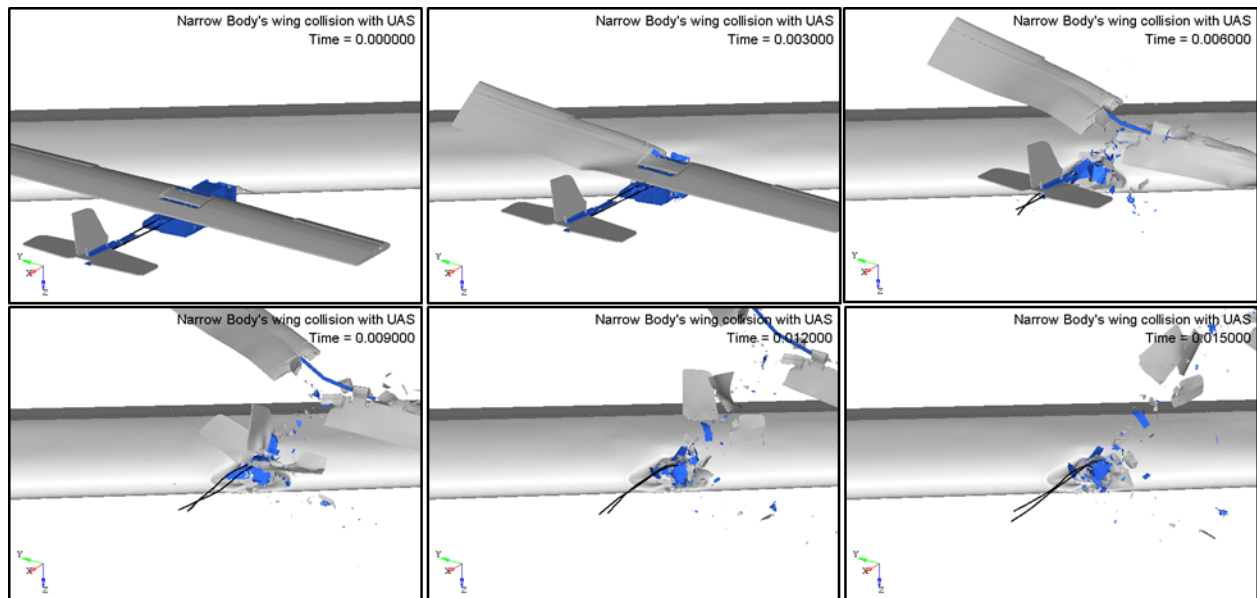


Figure 266. Kinematics of the impact between a commercial transport jet wing and a 1.8 kg (4.0 lb) UAS at location 2 at 128.6 m/s (250 knots)

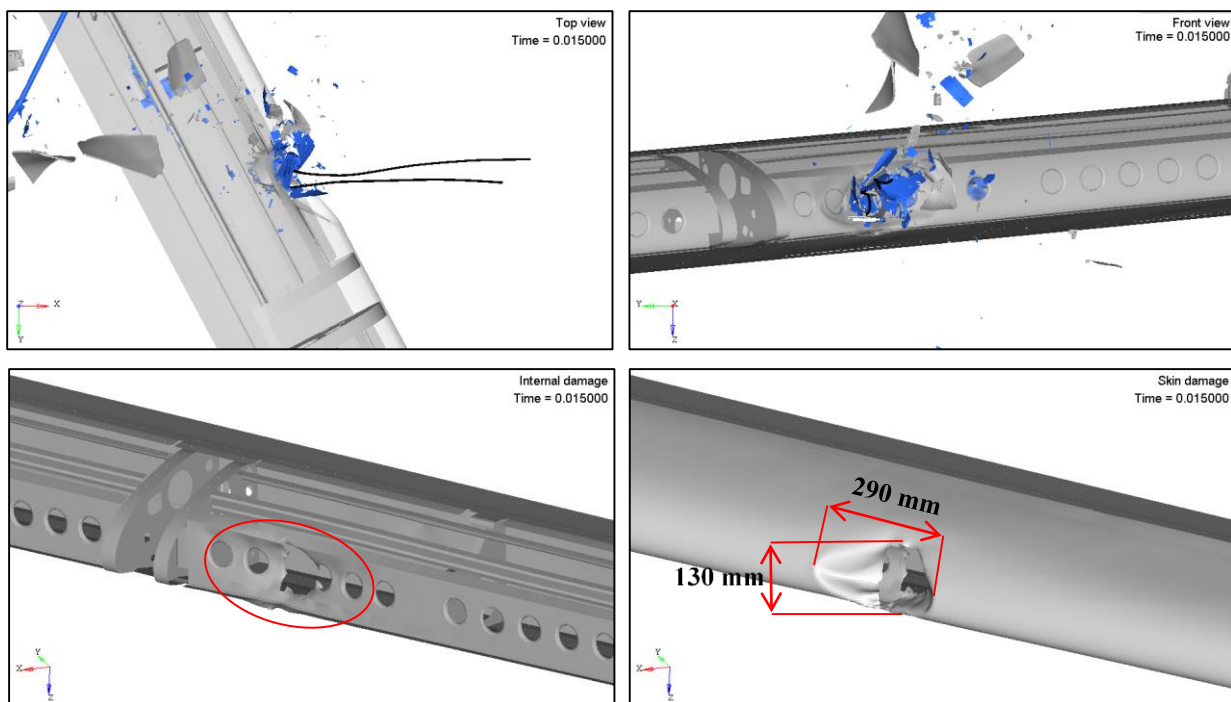


Figure 267. External/internal damage sustained by a commercial transport jet wing impacted at location 2 with a 1.8 kg (4.0 lb) UAS at 128.6 m/s (250 knots)

The UAS damaged the leading edge skin, and the sub-spar, deforming an area of 290x130 mm on the skin surface and allowing some fragments of the UAS components to enter the airframe and penetrate the sub-spar. The damage in the sub-spar can be perceived in the bottom left image of Figure 267. The front spar did not sustain critical damage.

The damage introduced by the UAS involved penetration of the skin but no visible damage to the front spar, and consequently the severity was classified as Level 3.

Figure 268 presents the impulse due to the contact force between UAS and wing, as well as the energy balance for both of them. Figure 269 shows the internal energies of UAS and wing parts directly involved in the impact.

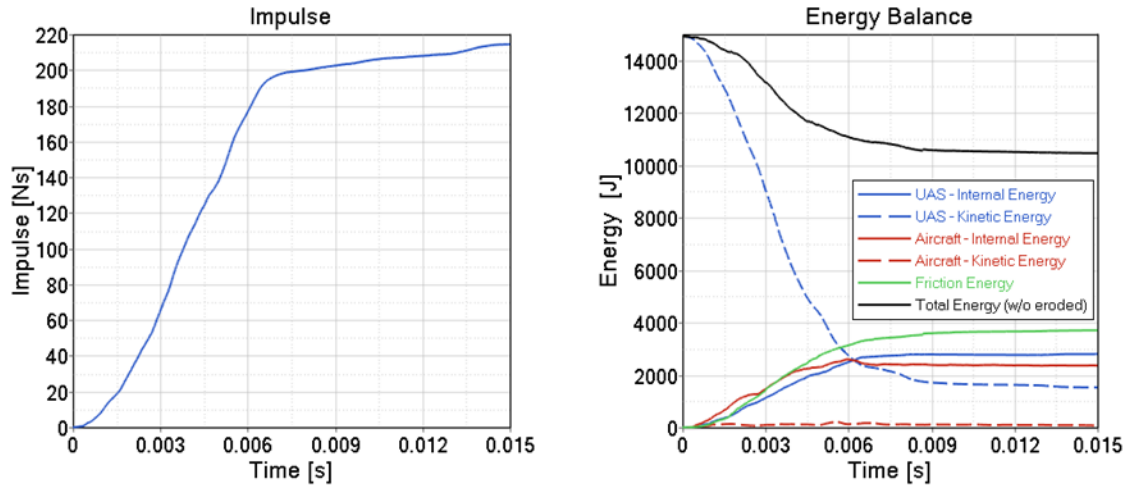


Figure 268. Impulse and energy balance of the impact between a commercial transport jet wing and a 1.8 kg (4.0 lb) UAS at location 2 at 128.6 m/s (250 knots)

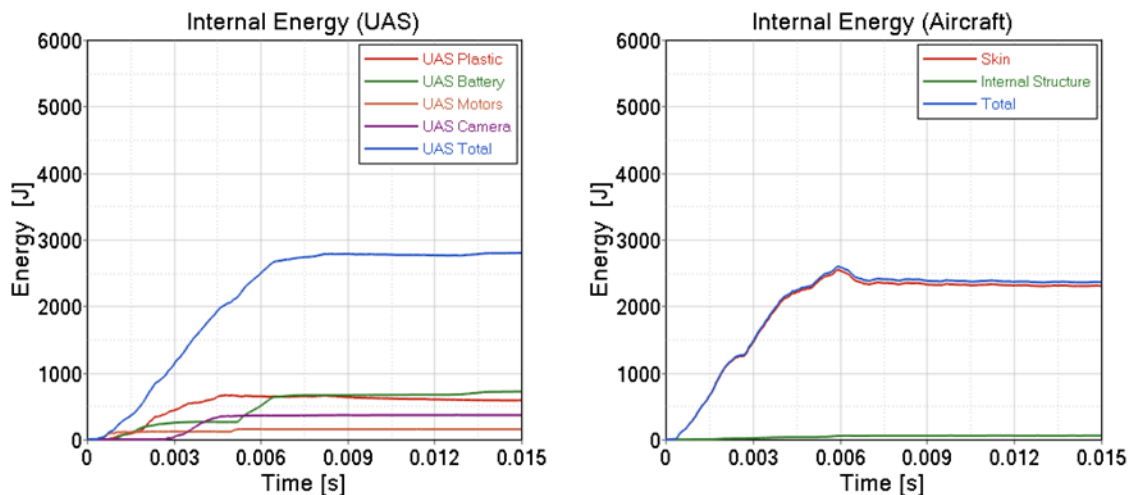


Figure 269. Internal energy per component of the impact between a commercial transport jet wing and a 1.8 kg (4.0 lb) UAS at location 2 at 128.6 m/s (250 knots)

The energy balance plot includes the UAS and wing kinetic and internal energies as well as frictional energy and total energy for the event. The wing and the UAS absorbed 16% and 19% of the

impact energy respectively. The energy dissipated by friction reached 25% of the total energy. In Figure 269, internal energies for the UAS parts and the wing show that the UAS battery and the skin of the wing absorb the highest amount of internal energies.

C.1.3.3 CFW3

This impact location was identified as the critical baseline simulation for the commercial transport jet wing and is discussed in section 4.3.3.2 of the main report body.

C.1.3.4 CFW4

The UAS was impacted against the leading edge of the wing at 128.6 m/s (250 knots) in the local x-axis direction of the aircraft. The impact location selected was at the inboard portion of slat 4, with the center of gravity of the UAS aligned with the leading edge, at the midpoint between the intermediate rib and the slat track rib pair. Figure 270 depicts the kinematics of the event. Figure 271 shows the damage caused to the skin and inner structure of the wing.

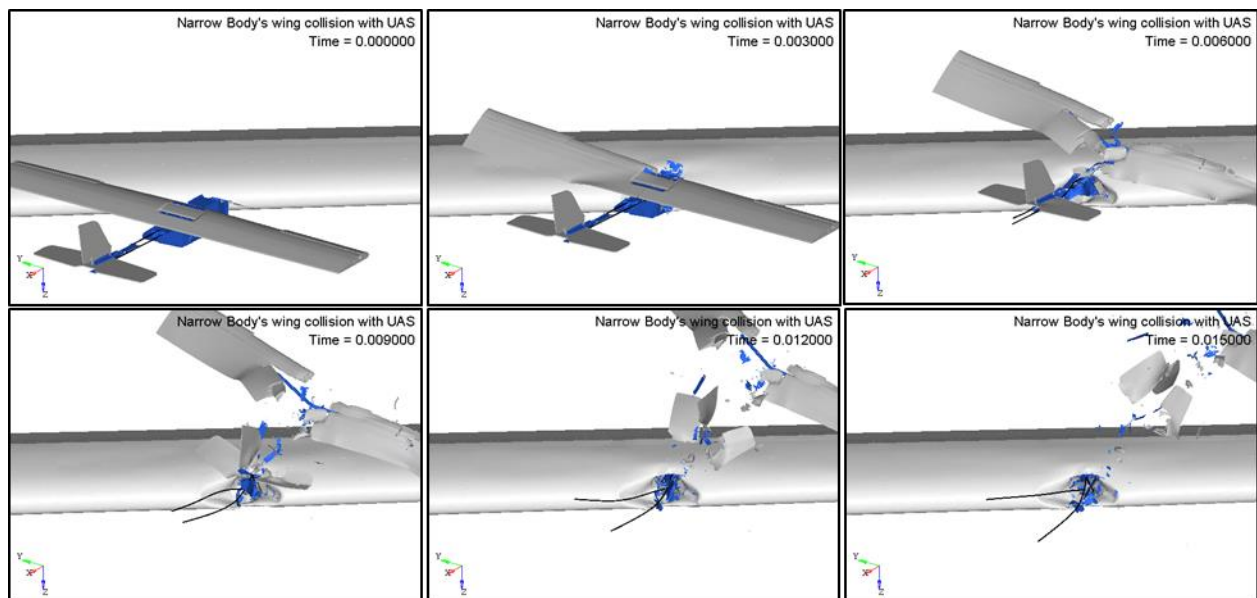


Figure 270. Kinematics of the impact between a commercial transport jet wing and a 1.8 kg (4.0 lb) UAS at location 4 at 128.6 m/s (250 knots)

The UAS damaged the leading edge skin, and the sub-spar, deforming an area of 308x121 mm on the skin surface and allowing some fragments of the UAS components to enter the airframe and penetrate the sub-spar. The damage in the sub-spar can be perceived in the bottom left image of Figure 271. The front spar did not sustain critical damage.

The damage introduced by the UAS involved penetration of the skin and slight damage to the front spar, and consequently the severity was classified as Level 3.

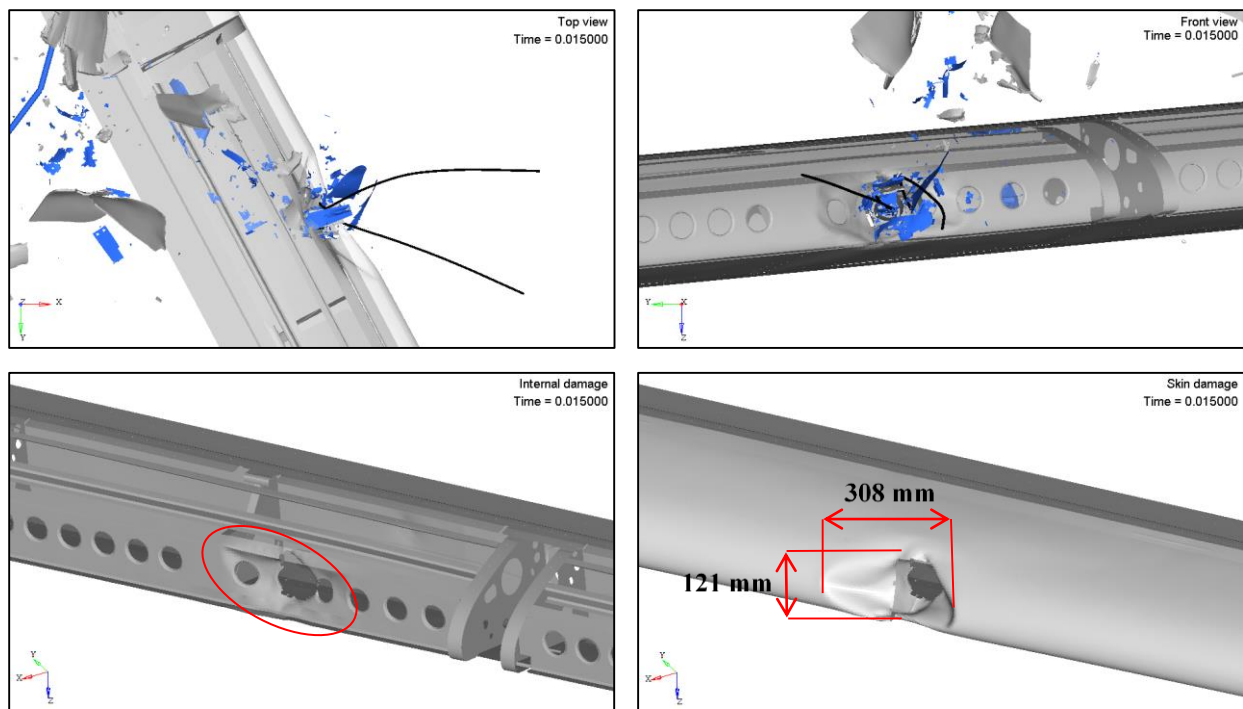


Figure 271. External/internal damage sustained by a commercial transport jet wing impacted at location 4 with a 1.8 kg (4.0 lb) UAS at 128.6 m/s (250 knots)

Figure 272 presents the impulse due to the contact force between UAS and wing, as well as the energy balance for both of them. Figure 273 shows the internal energies of UAS and wing parts directly involved in the impact.

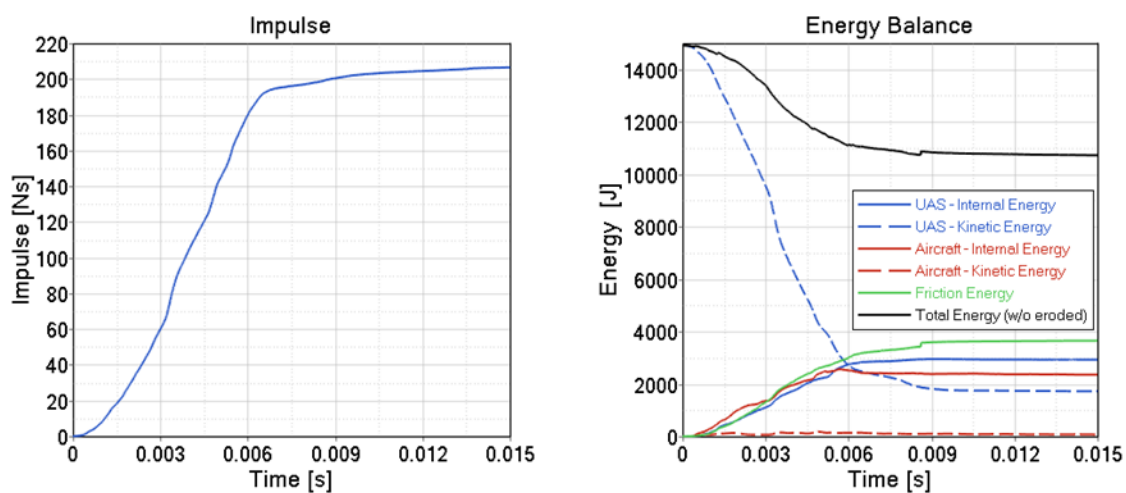


Figure 272. Impulse and energy balance of the impact between a commercial transport jet wing and a 1.8 kg (4.0 lb) UAS at location 4 at 128.6 m/s (250 knots)

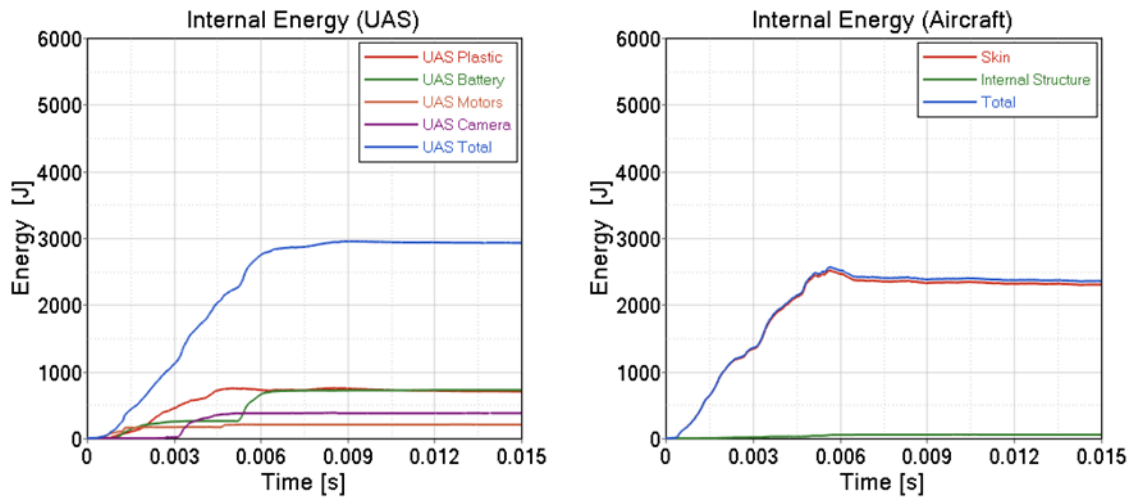


Figure 273. Internal energy per component of the impact between a commercial transport jet wing and a 1.8 kg (4.0 lb) UAS at location 4 at 128.6 m/s (250 knots)

The energy balance plot includes the UAS and wing kinetic and internal energies as well as frictional energy and total energy for the event. The wing and the UAS absorbed 16% and 20% of the impact energy respectively. The energy dissipated by friction reached 24% of the total energy. In Figure 273, internal energies for the UAS parts and the wing show that the polycarbonate carcass of the UAS and the skin of the wing absorb the highest amount of internal energies.

C.1.4 Windshield

C.1.4.1 CFC1

This impact location was identified as the critical baseline simulation for the commercial transport jet windshield and is discussed in section 4.3.4.2 of the main report body.

C.1.4.2 CFC2

The UAS was impacted against the top corner of the windshield at 128.6 m/s (250 knots) along the local x-axis direction of the aircraft. Figure 274 depicts the kinematics of the event. Figure 275 shows the damage caused to the windshield and its internal structure.

The UAS impacted, damaged the transparency and was deflected due to the windshield angle. The permanent deformation in the transparency can be perceived in the bottom right image of Figure 275. The internal structure did not sustain any visible damage.

The damage introduced by the UAS involved slight damage to the transparency but no damage to the internal structure, and consequently the severity was classified as Level 2.

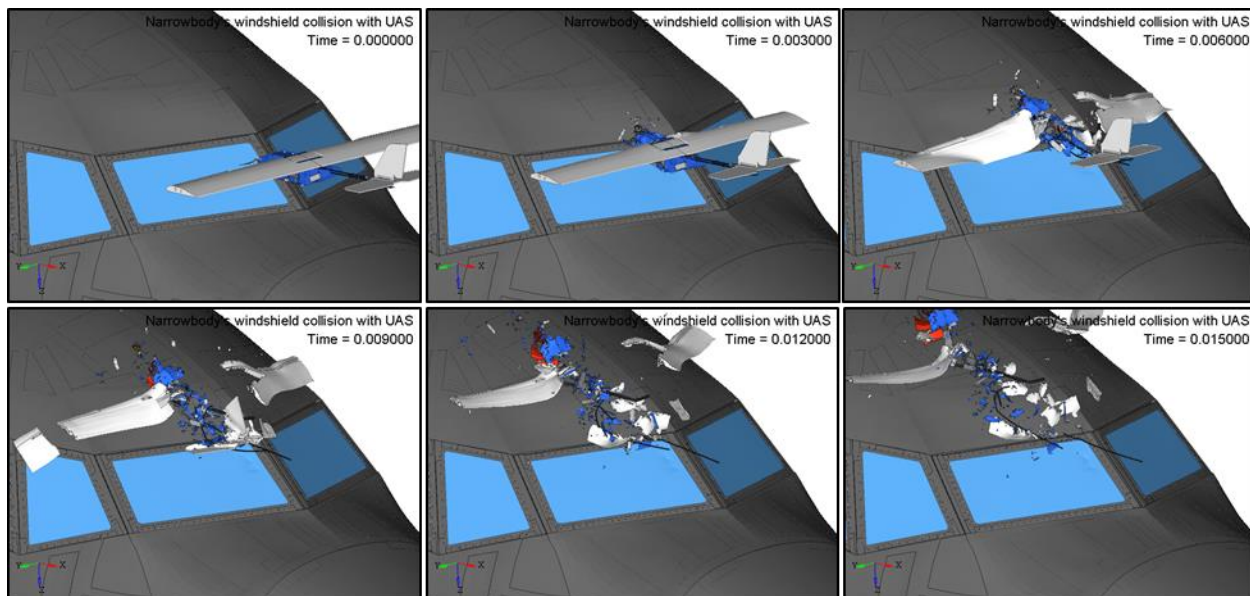


Figure 274. Kinematics of the impact between a commercial transport jet windshield and a 1.8 kg (4.0 lb) UAS at location 2 at 128.6 m/s (250 knots)

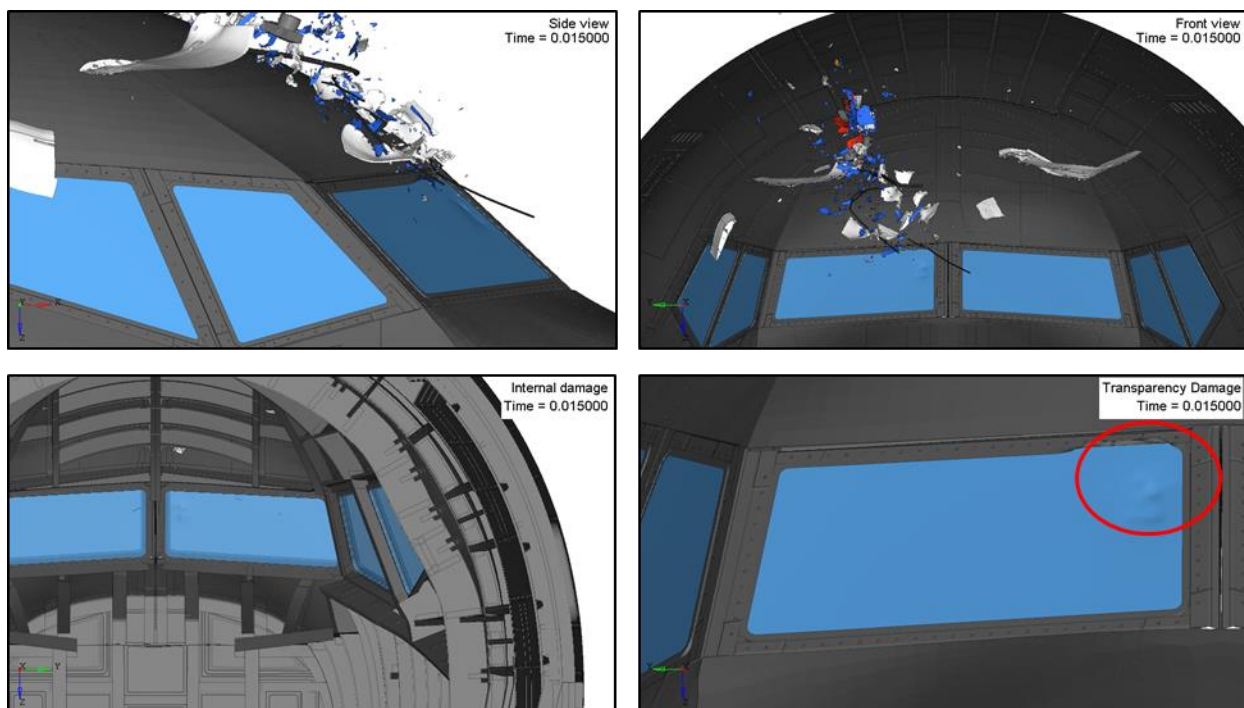


Figure 275. External/internal damage sustained by a commercial transport jet windshield impacted at location 2 with a 1.8 kg (4.0 lb) UAS at 128.6 m/s (250 knots)

Figure 276 shows the impulse due to the contact force between UAS and forward fuselage, as well as the energy balance for both of them. Figure 277 shows the internal energies of UAS and the forward fuselage parts directly involved in the impact.

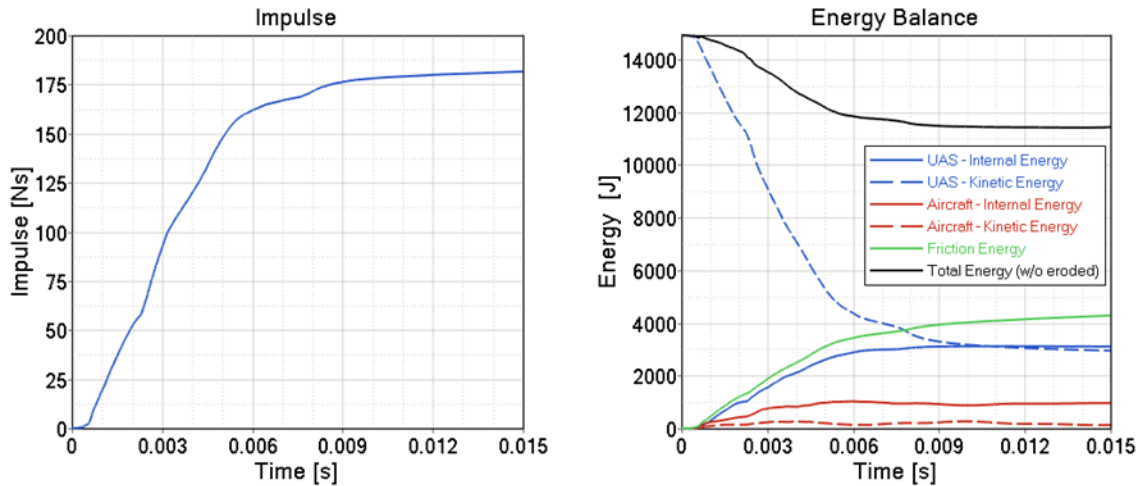


Figure 276. Impulse and energy balance of the impact between a commercial transport jet windshield and a 1.8 kg (4.0 lb) UAS at location 2 at 128.6 m/s (250 knots)

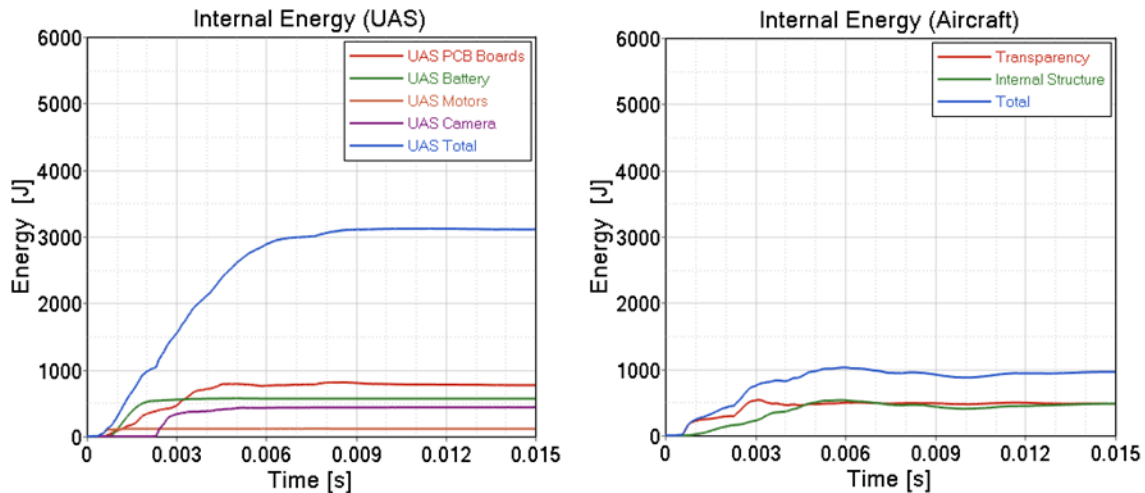


Figure 277. Internal energy per component of the impact between a commercial transport jet windshield and a 1.8 kg (4.0 lb) UAS at location 2 at 128.6 m/s (250 knots)

The energy balance plot includes the UAS and forward fuselage kinetic and internal energies as well as frictional energy and total energy for the event. The forward fuselage and the UAS absorbed 6% and 21% of the impact energy respectively. The energy dissipated by friction reached 29% of the total energy. In Figure 277, internal energies for the UAS parts and the forward fuselage show that the polycarbonate carcass of the UAS and transparency of the forward fuselage absorb the highest amount of internal energies respectively.

C.1.4.3 CFC3

The UAS was impacted against the windshield at 128.6 m/s (250 knots) along the local x-axis direction of the aircraft. The impact location selected was at middle of the center post. Figure 278 depicts the kinematics of the event. Figure 279 shows the damage caused to the windshield and its internal structure.

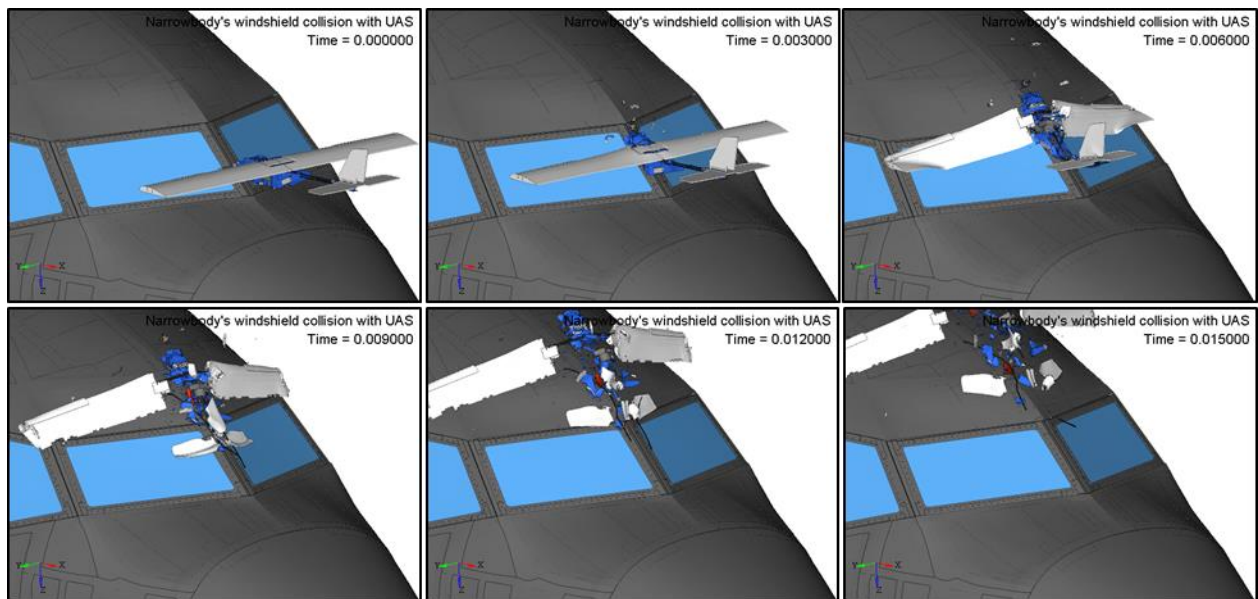


Figure 278. Kinematics of the impact between a commercial transport jet windshield and a 1.8 kg (4.0 lb) UAS at location 3 at 128.6 m/s (250 knots)

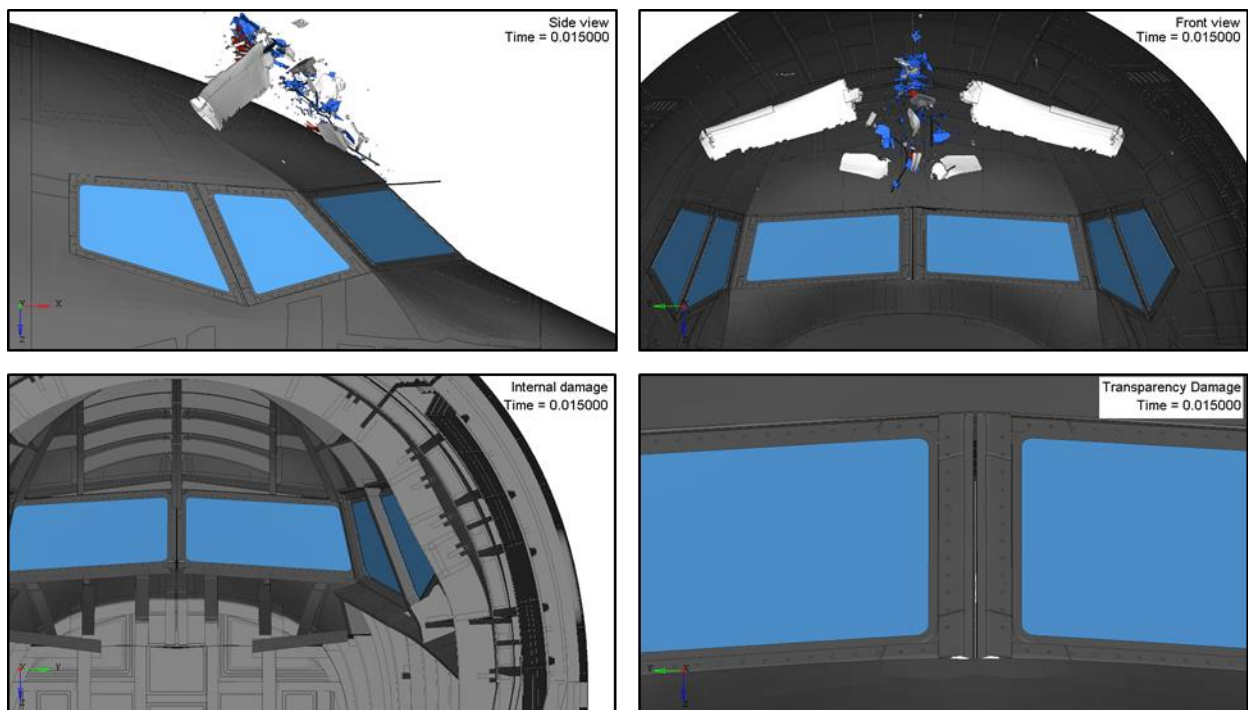


Figure 279. External/internal damage sustained by a commercial transport jet windshield impacted at location 3 with a 1.8 kg (4.0 lb) UAS at 128.6 m/s (250 knots)

The UAS impacted, damaged the center post and was deflected due to the windshield angle. The permanent deformation in the frame can be perceived in the bottom right image of Figure 279. The internal structure did not sustain any visible damage.

The damage introduced by the UAS involved deformation of the center post, and consequently the severity was classified as Level 1.

Figure 280 shows the impulse due to the contact force between UAS and forward fuselage, as well as the energy balance for both of them. Figure 281 shows the internal energies of UAS and the forward fuselage parts directly involved in the impact.

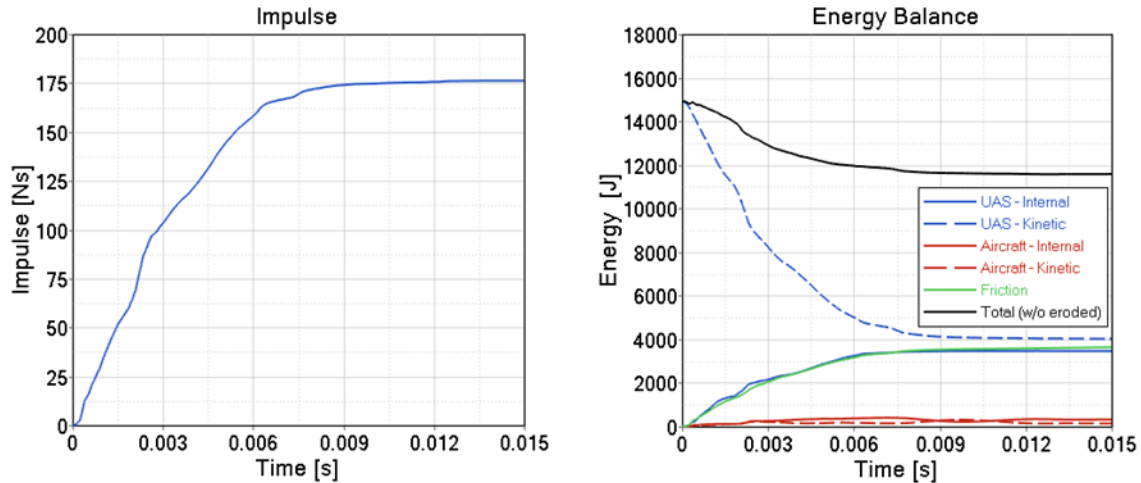


Figure 280. Impulse and energy balance of the impact between a commercial transport jet windshield and a 1.8 kg (4.0 lb) UAS at location 3 at 128.6 m/s (250 knots)

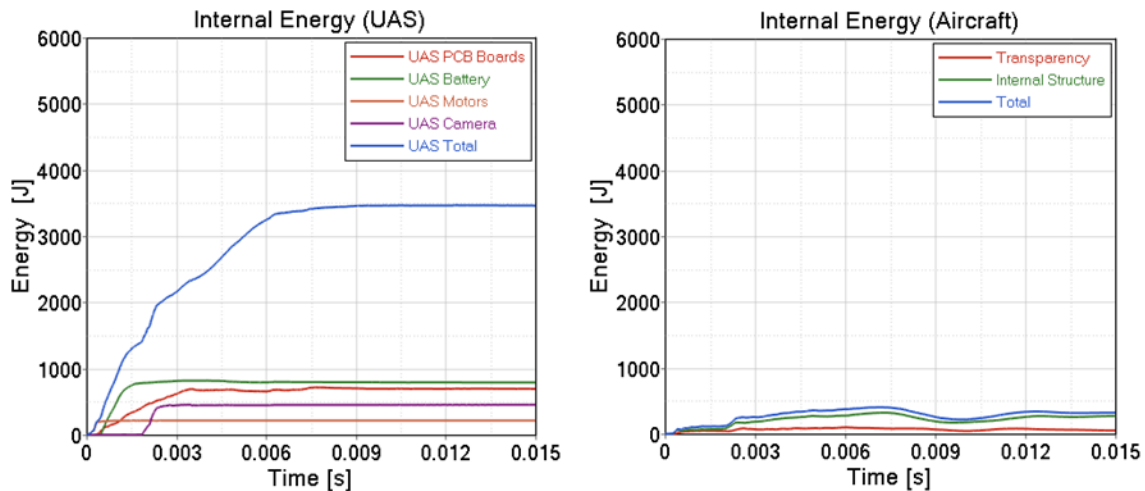


Figure 281. Internal energy per component of the impact between a commercial transport jet windshield and a 1.8 kg (4.0 lb) UAS at location 3 at 128.6 m/s (250 knots)

The energy balance plot includes the UAS and forward fuselage kinetic and internal energies as well as frictional energy and total energy for the event. The forward fuselage and the UAS absorbed 2% and 23% of the impact energy respectively. The energy dissipated by friction reached 24% of

the total energy. In Figure 281, internal energies for the UAS parts and the forward fuselage show that the polycarbonate and internal structure absorb the highest amount of internal energies.

C.1.5 Summary of Results of Collision with Commercial Transport Jet

Assembly	Case	Severity	Fire Risk	Internal Energy Aircraft [J]	Internal Energy UAS [J]	Residual Kinetic Energy [J]	Friction Energy [J]	Eroded Energy [J]
Vertical Stabilizer	CFV1	Level 4	No	2520	2045	3630	2865	3909
	CFV2	Level 3	No	2375	2070	3695	2980	3849
	CFV3	Level 4	No	2100	2080	3585	3475	3729
	CFV4	Level 4	No	2485	2050	3515	2795	4124
Horizontal Stabilizer	CFH1	Level 4	No	1920	2425	2840	3360	4424
	CFH2	Level 4	No	2389	2517	3205	3530	3328
	CFH3	Level 4	No	2000	2370	2900	3725	3974
	CFH4	Level 4	No	1938	2159	4365	3023	3484
	CFH5	Level 4	No	1483	2309	4180	3257	3740
Wing	CFW1	Level 3	No	2322	2868	1652	3670	4457
	CFW2	Level 3	No	2360	2799	1525	3702	4583
	CFW3	Level 3	No	2631	2895	1675	3674	4094
	CFW4	Level 3	No	2356	2928	1720	3653	4312
Windshield	CFC1	Level 2	No	777	2777	4953	3480	2982
	CFC2	Level 2	No	958	3108	2954	4283	3666
	CFC3	Level 1	No	321	3462	4026	3637	3523

C.2 BUSINESS JET

C.2.1 Vertical Stabilizer

C.2.1.1 BFV1

This impact location was identified as the critical baseline simulation for the business jet vertical stabilizer and is discussed in section 4.4.1.2 of the main report body.

C.2.1.2 BFV2

The UAS was impacted against the vertical stabilizer at 128.6 m/s (250 knots) along the local x-axis direction of the aircraft. The impact location selected was at the middle portion of the vertical stabilizer between ribs 2 and 3. Figure 281 depicts the kinematics of the event. Figure 282 shows the damage caused to the skin and inner structure of the vertical stabilizer.

The UAS damaged the skin, the upper and lower ribs, and front spar, creating a 210x385 mm² damage zone on the skin surface and allowing some fragments of the UAS components to penetrate into airframe. The permanent deformation in the ribs and front spar can be perceived in the bottom left image of Figure 151. The front spar did not sustain critical damage.

The damage introduced by the UAS involved penetration of the skin and slight damage to front spar, and consequently the severity was classified as Level 4.

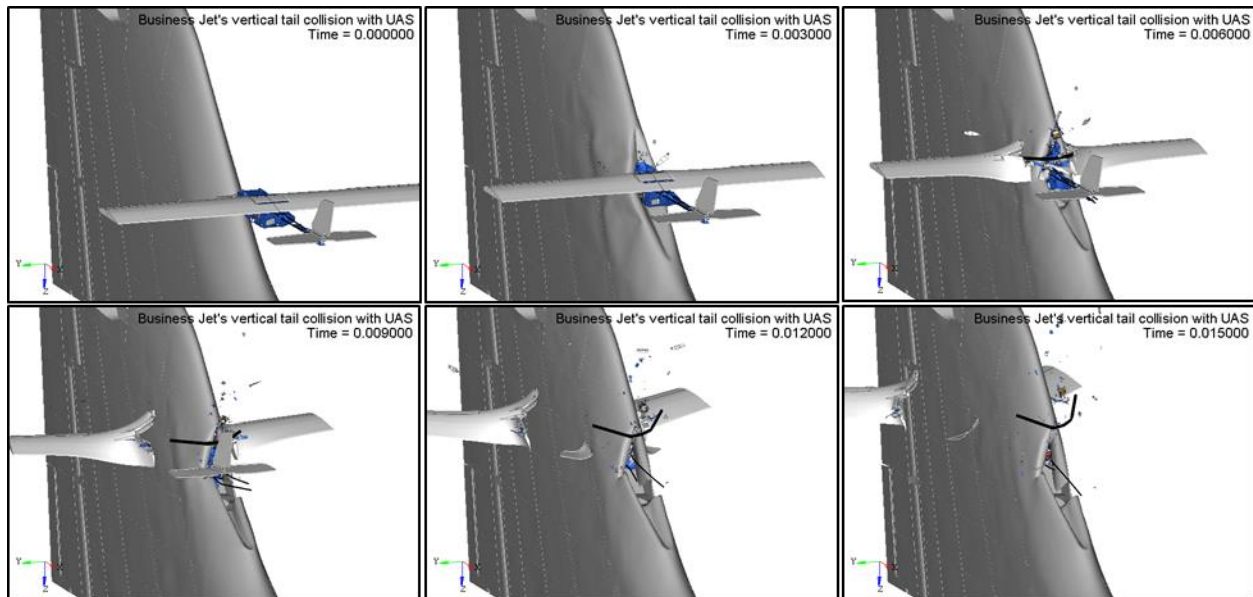


Figure 282. Kinematics of the impact between a business jet vertical stabilizer and a 1.8 kg (4.0 lb) UAS at location 2 at 128.6 m/s (250 knots)

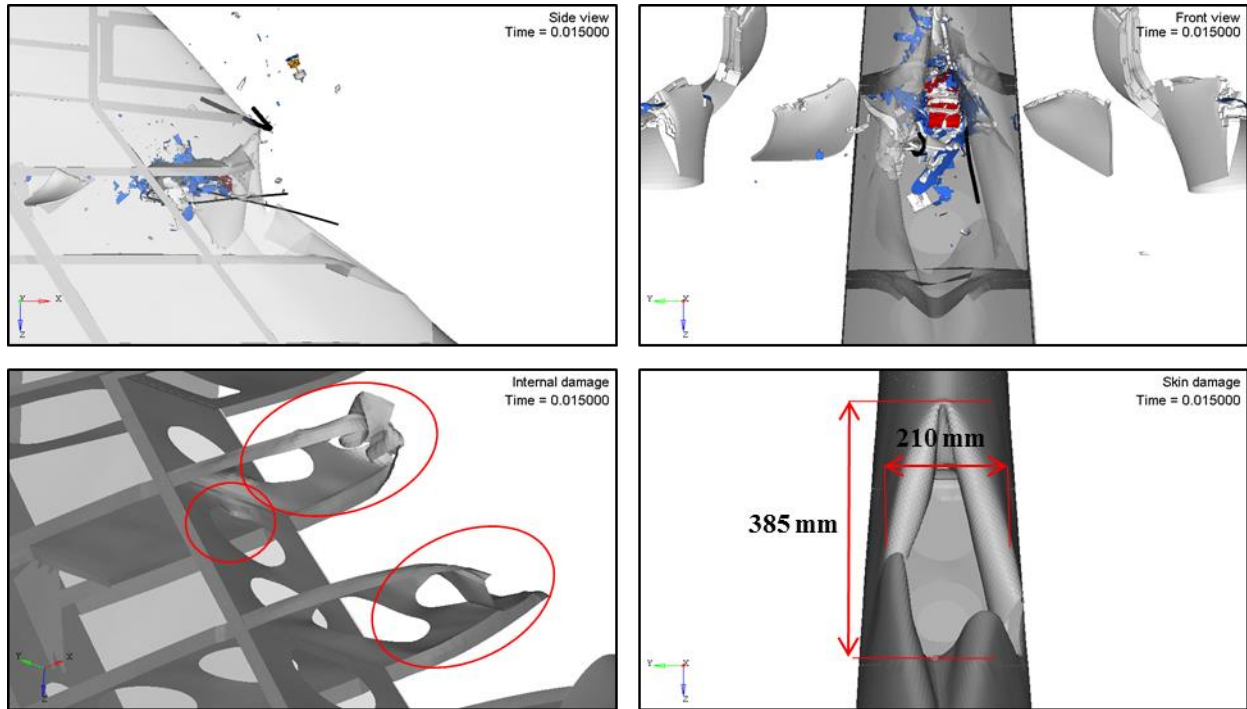


Figure 283. External/internal damage sustained by a business jet vertical stabilizer impacted at location 2 with a 1.8 kg (4.0 lb) UAS at 128.6 m/s (250 knots)

Figure 152 shows the impulse due to the contact force between UAS and vertical stabilizer, as well as the energy balance for both of them. Figure 153 shows the internal energies of UAS and vertical stabilizer parts directly involved in the impact.

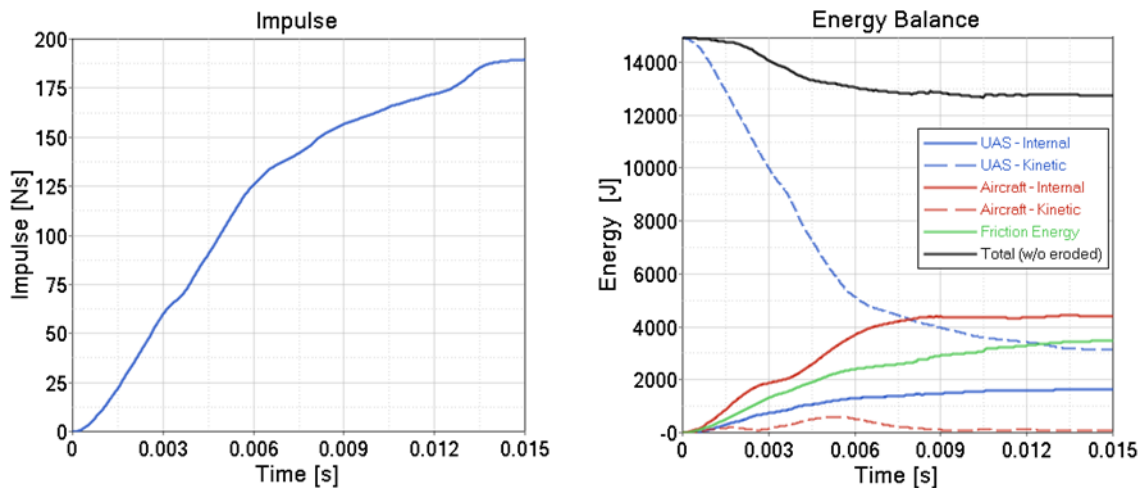


Figure 284. Impulse and energy balance of the impact between a business jet vertical stabilizer and a 1.8 kg (4.0 lb) UAS at location 2 at 128.6 m/s (250 knots)

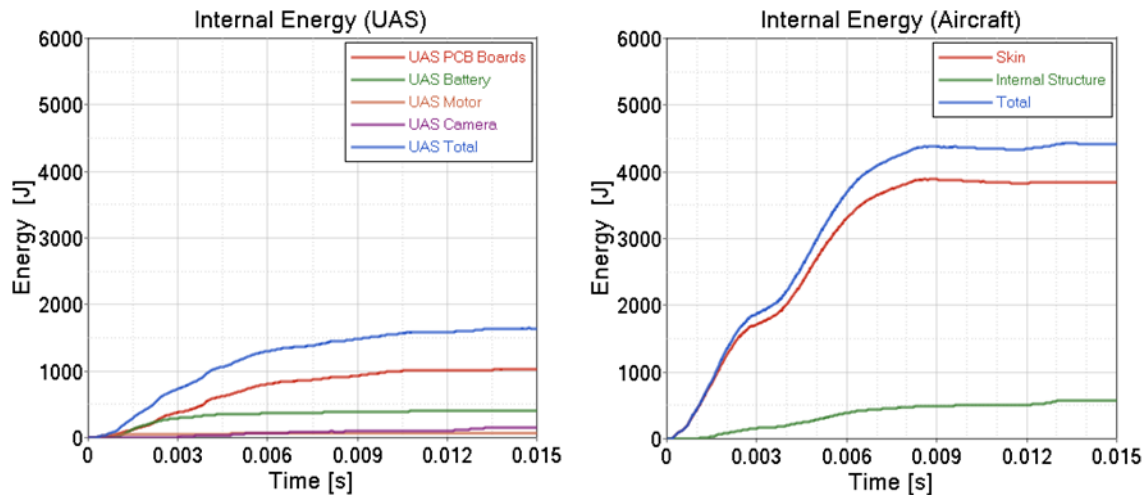


Figure 285. Internal energy per component of the impact between a business jet vertical stabilizer and a 1.8 kg (4.0 lb) UAS at location 2 at 128.6 m/s (250 knots)

The energy balance plot includes the UAS and vertical stabilizer kinetic and internal energies as well as frictional energy and total energy for the event. The vertical stabilizer and the UAS absorbed 28% and 12% of the impact energy respectively. The energy dissipated by friction reached 25% of the total energy. In Figure 153, internal energies for the UAS parts and the vertical stabilizer show that the polycarbonate carcass of the UAS and skin of the vertical stabilizer absorb the highest amount of internal energies.

C.2.1.3 BFV3

The UAS was impacted against the vertical stabilizer at 128.6 m/s (250 knots) along the local x-axis direction of the aircraft. The impact location selected was at the upper portion of the vertical stabilizer between fin tip ribs 1 and 2. This portion of the vertical stabilizer holds the horizontal stabilizer, which is not too far from the impact location. If the UAS does penetrate by a considerable amount, it might damage the connections or the mechanisms for operating the horizontal stabilizer. Figure 286 depicts the kinematics of the event. Figure 287 shows the damage caused to the skin and inner structure of the vertical stabilizer.

The UAS damaged the skin and the inner spars, creating a 87x161 mm² damage zone on the skin surface and allowing some fragments of the UAS components to penetrate into airframe. The permanent deformation in the spars can be perceived in the bottom left image of Figure 287. The third spar sustained critical damage, and any further penetration of the UAS may result in damage to the mechanisms that controls the horizontal stabilizer.

The damage introduced by the UAS involved penetration of the skin and considerable damage to the spars, and consequently the severity was classified as Level 4.

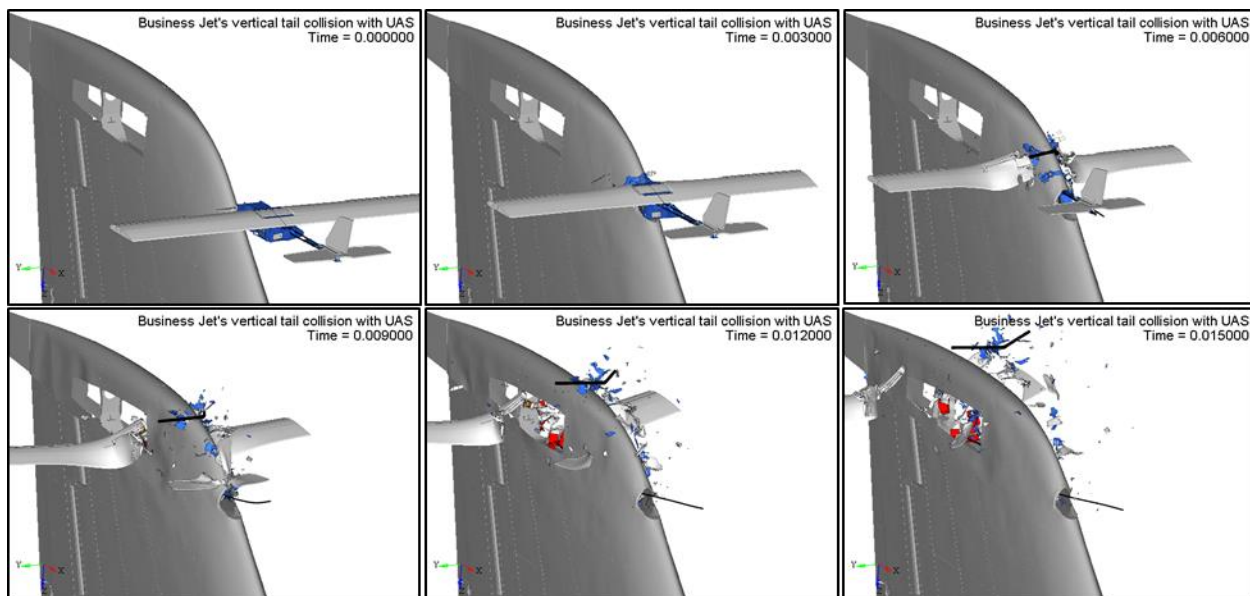


Figure 286. Kinematics of the impact between a business jet vertical stabilizer and a 1.8 kg (4.0 lb) UAS at location 3 at 128.6 m/s (250 knots)

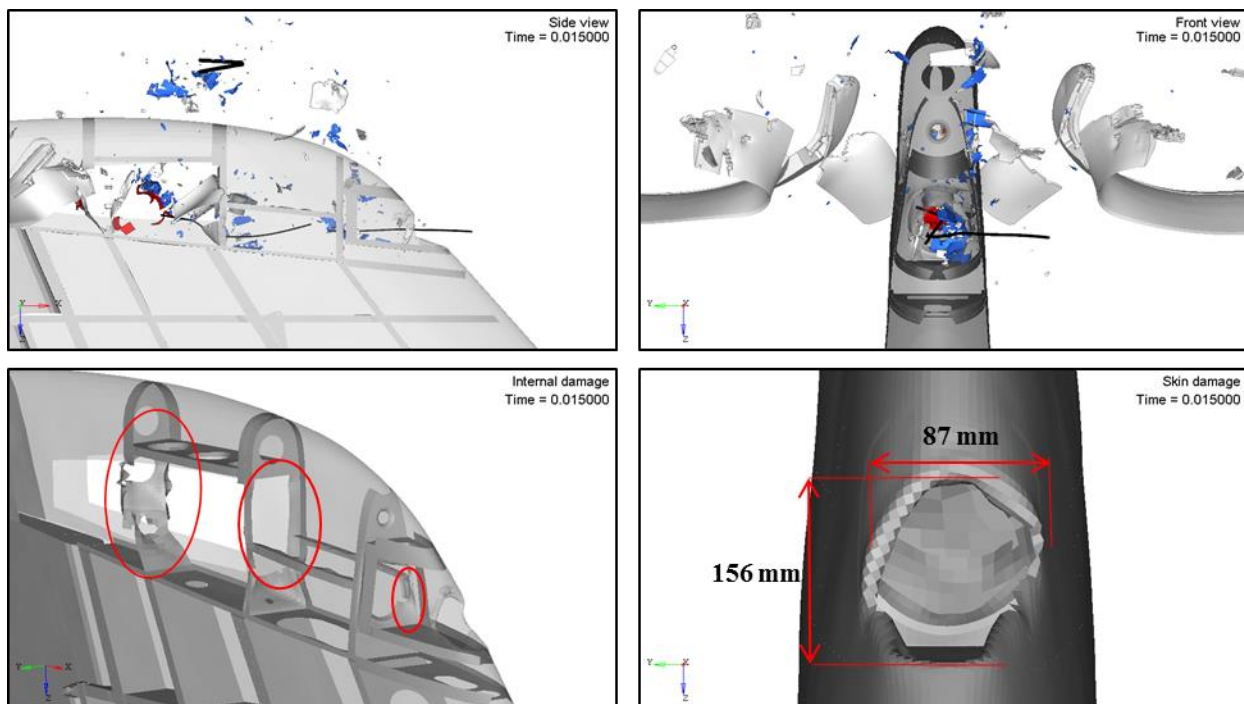


Figure 287. External/internal damage sustained by a business jet vertical stabilizer impacted at location 3 with a 1.8 kg (4.0 lb) UAS at 128.6 m/s (250 knots)

Figure 288 shows the impulse due to the contact force between UAS and vertical stabilizer, as well as the energy balance for both of them. Figure 289 shows the internal energies of UAS and vertical stabilizer parts directly involved in the impact.

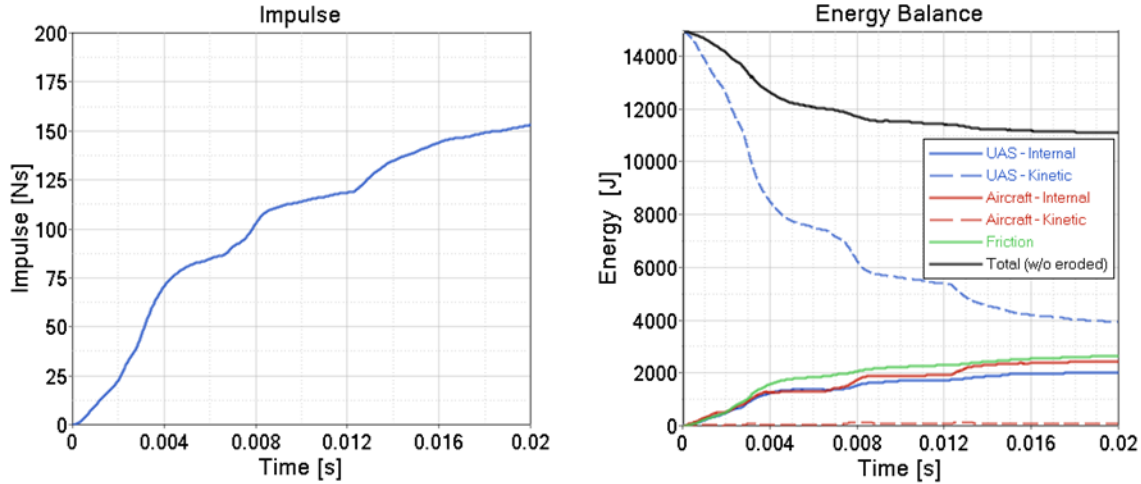


Figure 288. Impulse and energy balance of the impact between a business jet vertical stabilizer and a 1.8 kg (4.0 lb) UAS at location 3 at 128.6 m/s (250 knots)

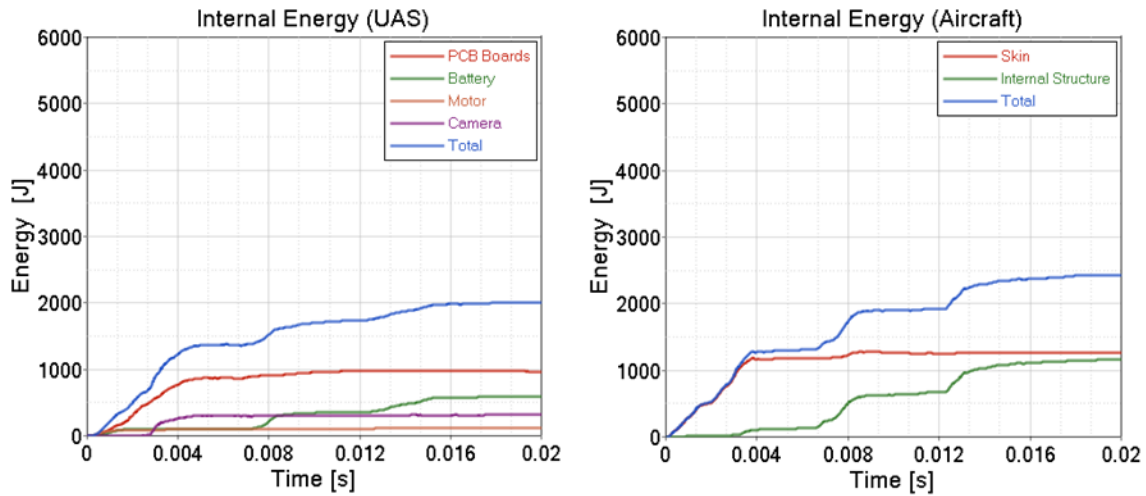


Figure 289. Internal energy per component of the impact between a business jet vertical stabilizer and a 1.8 kg (4.0 lb) UAS at location 3 at 128.6 m/s (250 knots)

The energy balance plot includes the UAS and vertical stabilizer kinetic and internal energies as well as frictional energy and total energy for the event. The vertical stabilizer and the UAS absorbed 16% and 13% of the impact energy respectively. The energy dissipated by friction reached 18% of the total energy. In Figure 289, internal energies for the UAS parts and the vertical stabilizer show that the polycarbonate carcass of the UAS and skin of the vertical stabilizer absorb the highest amount of internal energies.

C.2.2 Horizontal Stabilizer

C.2.2.1 BFH1

This impact location was identified as the critical baseline simulation for the business jet horizontal stabilizer and is discussed in section 4.4.2.2 of the main report body.

C.2.2.2 BFH2

The UAS was impacted against the stabilizer at 128.6 m/s (250 knots) along the local x-axis direction of the aircraft. The impact location selected was at the center of the horizontal stabilizer leading edge, between the two center leading edge ribs. Figure 289 depicts the kinematics of the event. Figure 290 shows the damage caused to the skin and inner structure of the horizontal stabilizer.

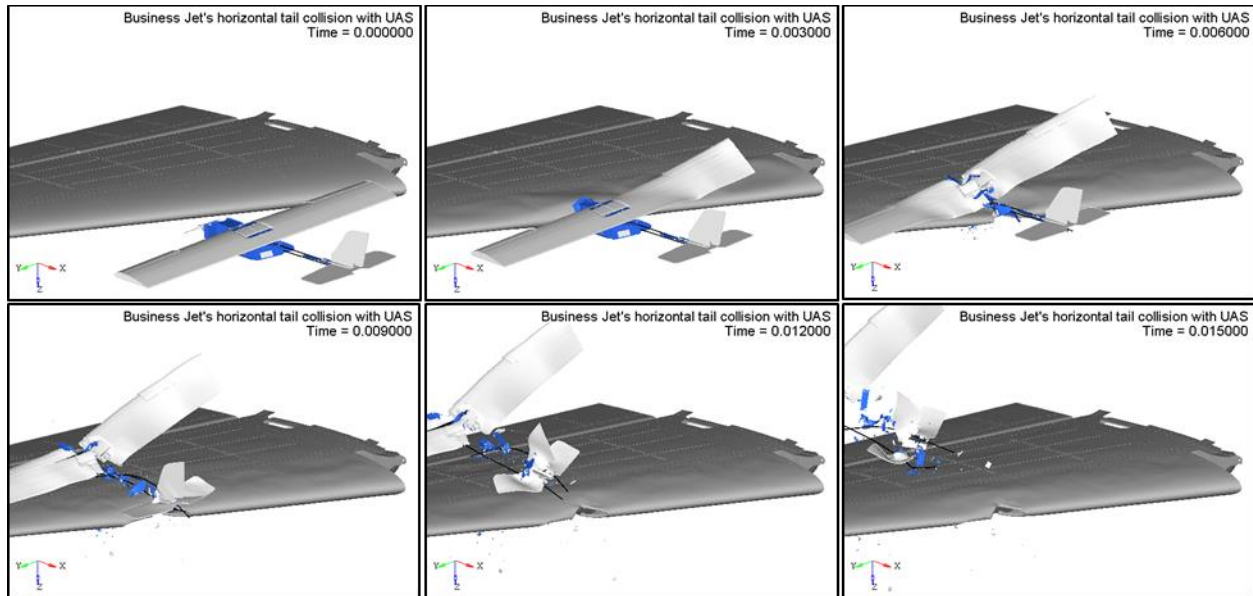


Figure 290. Kinematics of the impact between a business jet horizontal stabilizer and a 1.8 kg (4.0 lb) UAS at location 2 at 128.6 m/s (250 knots)

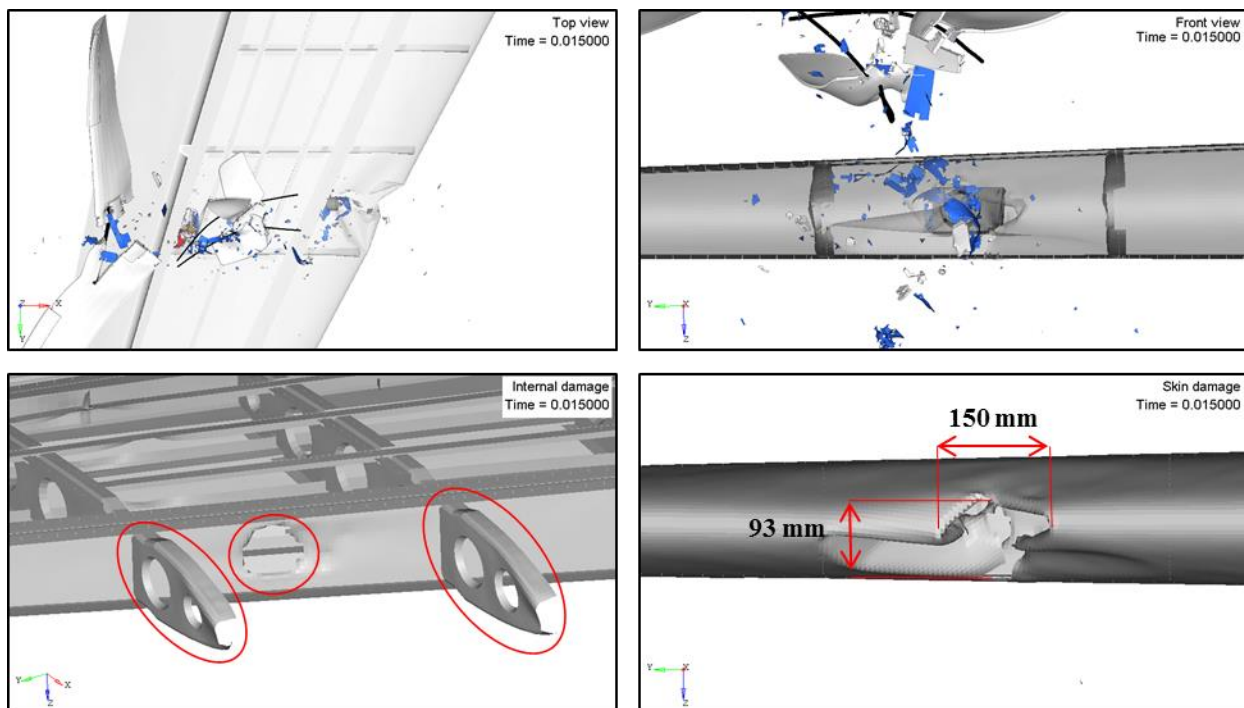


Figure 291. External/internal damage sustained by a business jet horizontal stabilizer impacted at location 2 with a 1.8 kg (4.0 lb) UAS at 128.6 m/s (250 knots)

The UAS damaged the skin, the leading edge ribs, and the front spar, creating a 150x93 mm² damage zone on the skin surface and allowing some fragments of the UAS components to enter airframe and penetrate the front spar. The permanent deformation and damage in the ribs and front spar can be perceived in the bottom left image of Figure 290,. The front spar sustained critical damage.

The damage introduced by the UAS involved penetration of the skin and front spar, and consequently the severity was classified as Level 4.

Figure 291 shows the impulse due to the contact force between the UAS and the horizontal stabilizer, as well as the energy balance for both of them. Figure 292 presents the internal energies of the UAS and horizontal stabilizer parts directly involved on the impact.

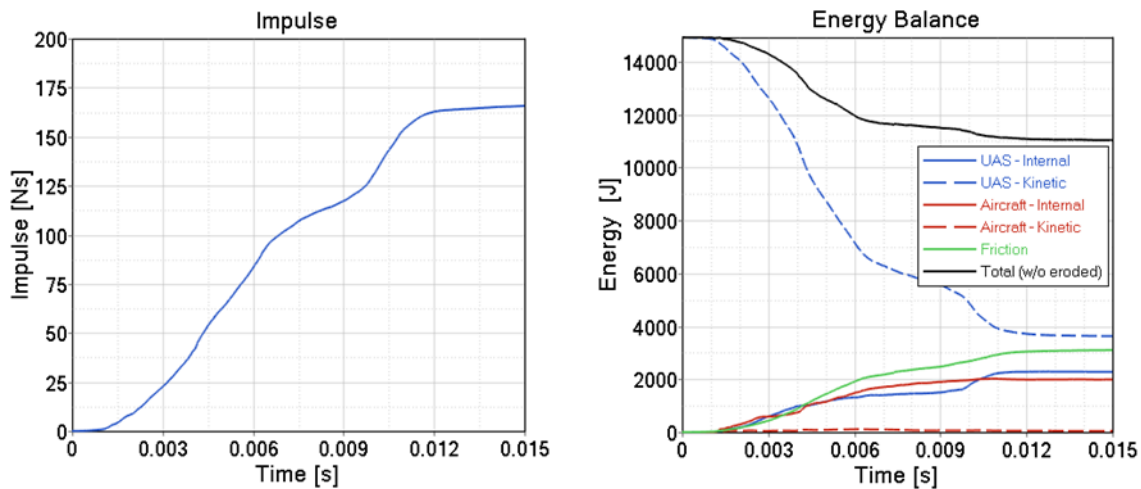


Figure 292. Impulse and energy balance of the impact between a business jet horizontal stabilizer and a 1.8 kg (4.0 lb) UAS at location 2 at 128.6 m/s (250 knots)

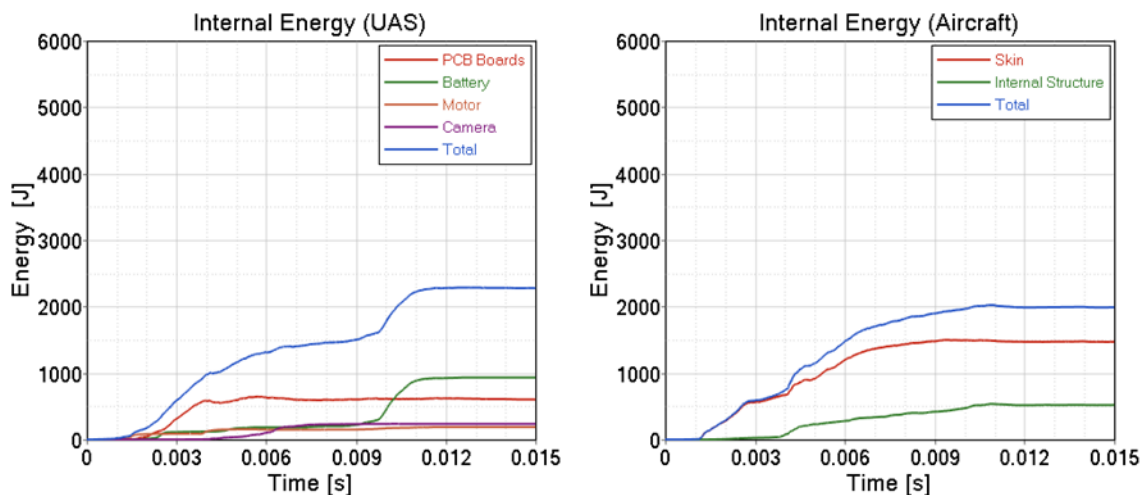


Figure 293. Internal energy per component of the impact between a business jet horizontal stabilizer and a 1.8 kg (4.0 lb) UAS at location 2 at 128.6 m/s (250 knots)

The energy balance plot includes the UAS and horizontal stabilizer kinetic and internal energies, as well as frictional energy and total energy for the event. The horizontal stabilizer and the UAS absorbed 13% and 15% of the impact energy respectively. The energy dissipated by friction reached 21% of the total energy. In Figure 292, internal energies for the UAS parts and the stabilizer structure show that the UAS battery and skin of the horizontal stabilizer absorb the highest internal energies.

C.2.2.3 BFH3

The UAS was impacted against the stabilizer at 128.6 m/s (250 knots) along the local x-axis direction of the aircraft. The impact location selected was near the tip of the horizontal stabilizer. Figure 294 depicts the kinematics of the event. Figure 294 shows the damage caused to the skin and inner structure of the horizontal stabilizer.

The UAS damaged the skin, the leading edge rib, and the front spar, creating a 157x116 mm² damage zone on the skin surface and allowing some fragments of the UAS components to enter the airframe and penetrate the front spar. The permanent deformation and damage in the leading edge rib and front spar can be perceived in the bottom left image of Figure 295. The front spar sustained critical damage.

The damage introduced by the UAS involved penetration of the skin and front spar, and consequently the severity was classified as Level 4.

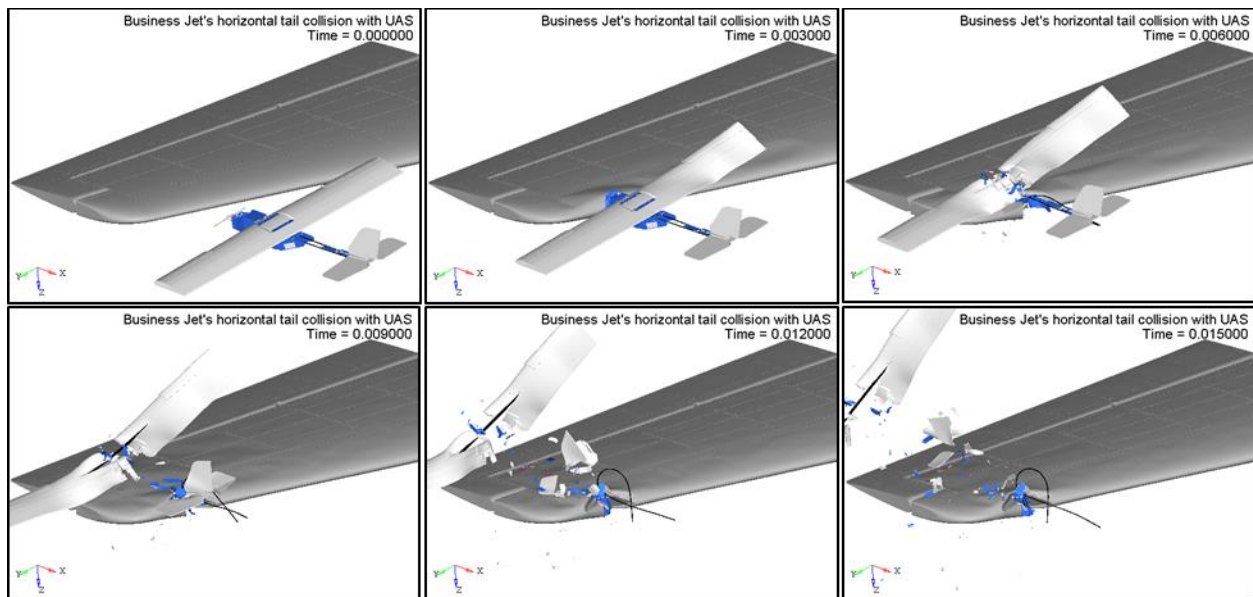


Figure 294. Kinematics of the impact between a business jet horizontal stabilizer and a 1.8 kg (4.0 lb) UAS at location 3 at 128.6 m/s (250 knots)

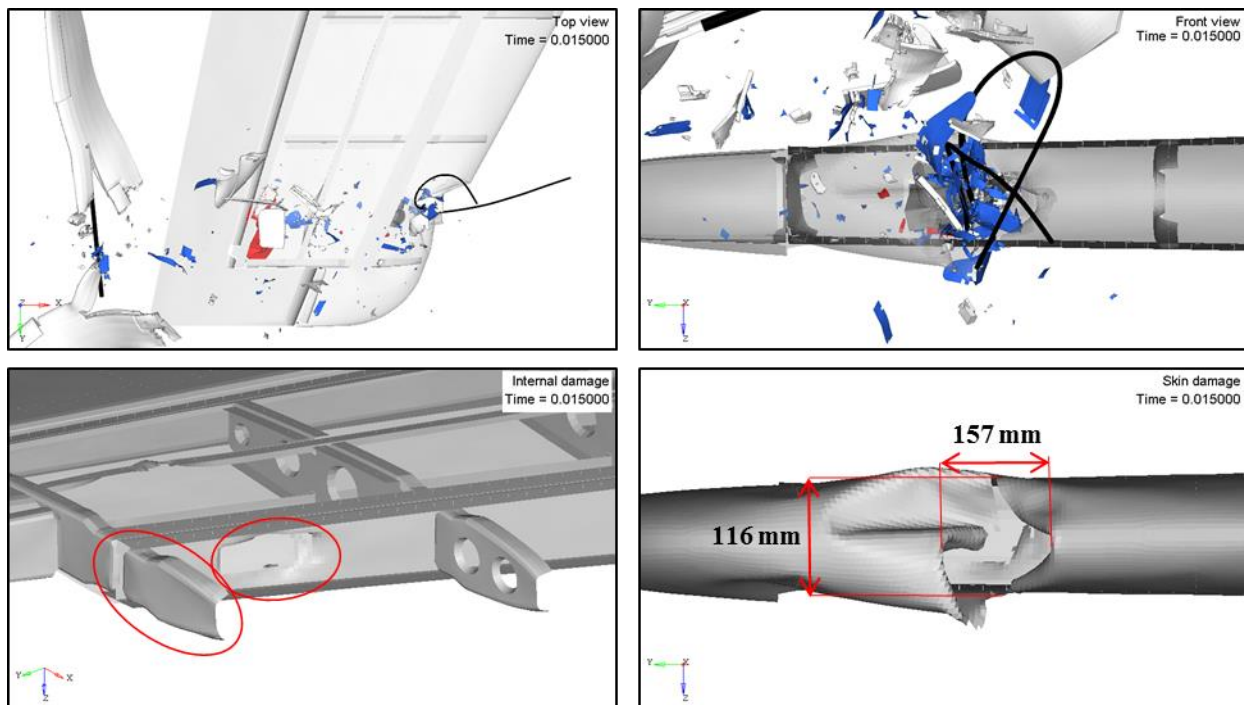


Figure 295. External/internal damage sustained by a business jet horizontal stabilizer impacted at location 3 with a 1.8 kg (4.0 lb) UAS at 128.6 m/s (250 knots)

Figure 296 shows the impulse due to the contact force between the UAS and the horizontal stabilizer, as well as the energy balance for both of them. Figure 297 presents the internal energies of the UAS and horizontal stabilizer parts directly involved on the impact.

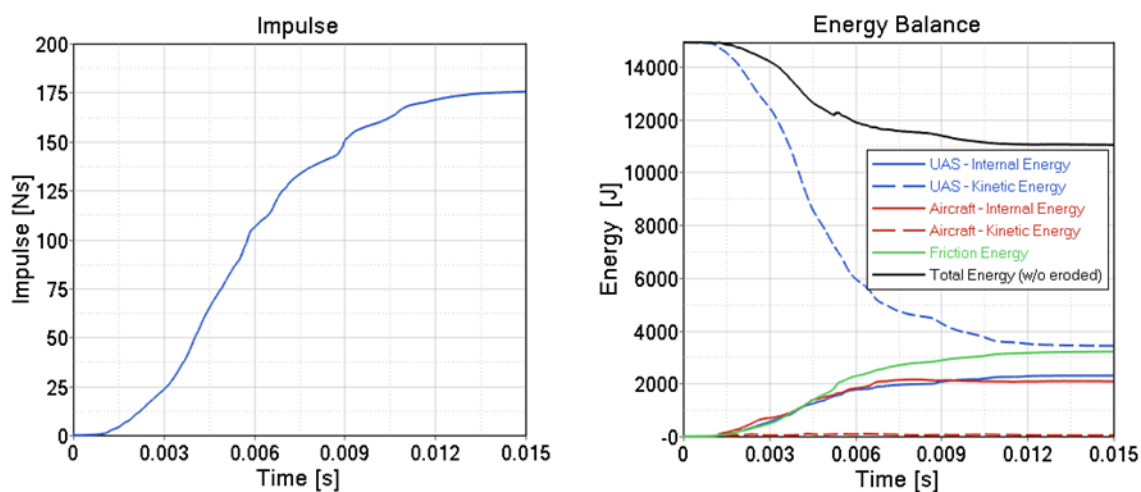


Figure 296. Impulse and energy balance of the impact between a business jet horizontal stabilizer and a 1.8 kg (4.0 lb) UAS at location 3 at 128.6 m/s (250 knots)

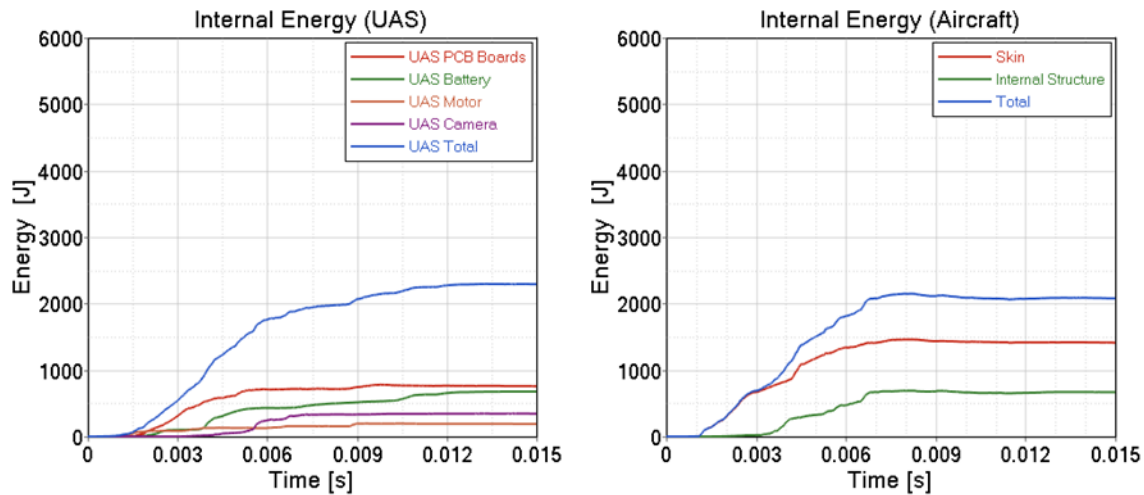


Figure 297. Internal energy per component of the impact between a business jet horizontal stabilizer and a 1.8 kg (4.0 lb) UAS at location 3 at 128.6 m/s (250 knots)

The energy balance plot includes the UAS and horizontal stabilizer kinetic and internal energies, as well as frictional energy and total energy for the event. The horizontal stabilizer and the UAS absorbed 14% and 15% of the impact energy respectively. The energy dissipated by friction reached 21% of the total energy. In Figure 297, internal energies for the UAS parts and the horizontal stabilizer show that the polycarbonate carcass of the UAS and the skin of the horizontal stabilizer absorb the highest internal energies.

C.2.3 Wing

C.2.3.1 BFW1

The UAS was impacted against the wing at 128.6 m/s (250 knots) along the local x-axis direction of the aircraft. The impact location selected was at the inboard portion of the wing between ribs 1 and 2. Figure 297 depicts the kinematics of the event. Figure 298 shows the damage caused to the skin and inner structure of the wing.

The UAS damaged the skin deforming the leading edge shape. The permanent deformation in the skin surface can be perceived in the bottom left image of Figure 298. The front spar did not sustain any visible damage

The damage introduced by the UAS involved considerable deformation of the skin but no damage to the front spar, and consequently the severity was classified as Level 2.

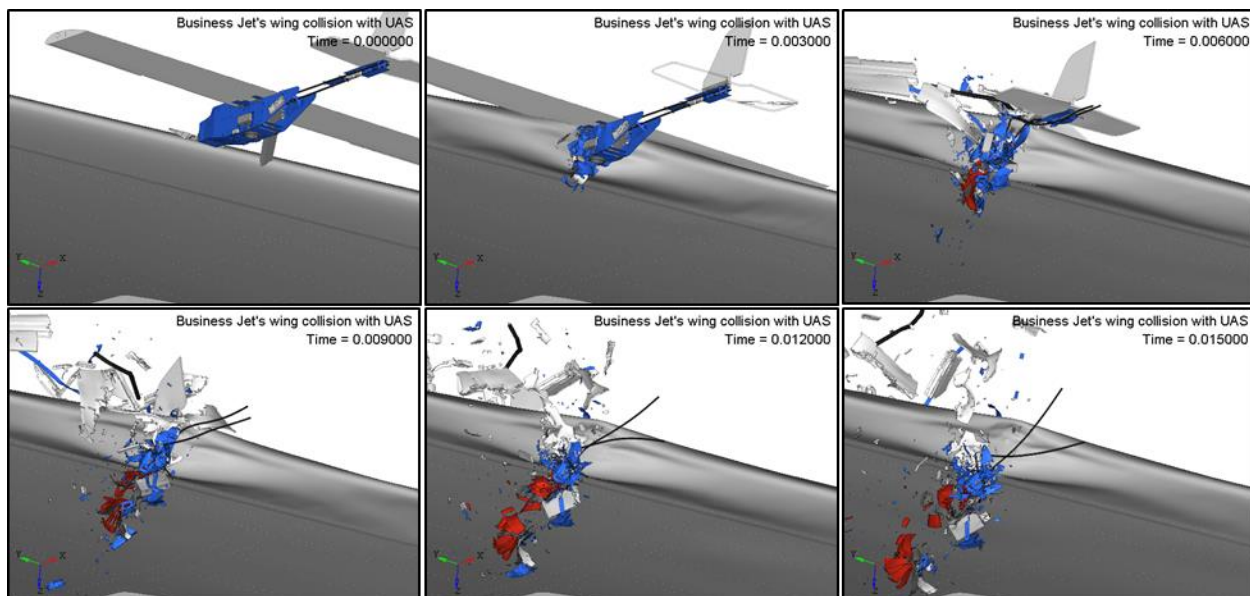


Figure 298. Kinematics of the impact between a business jet wing and a 1.8 kg (4.0 lb) UAS at location 1 at 128.6 m/s (250 knots)

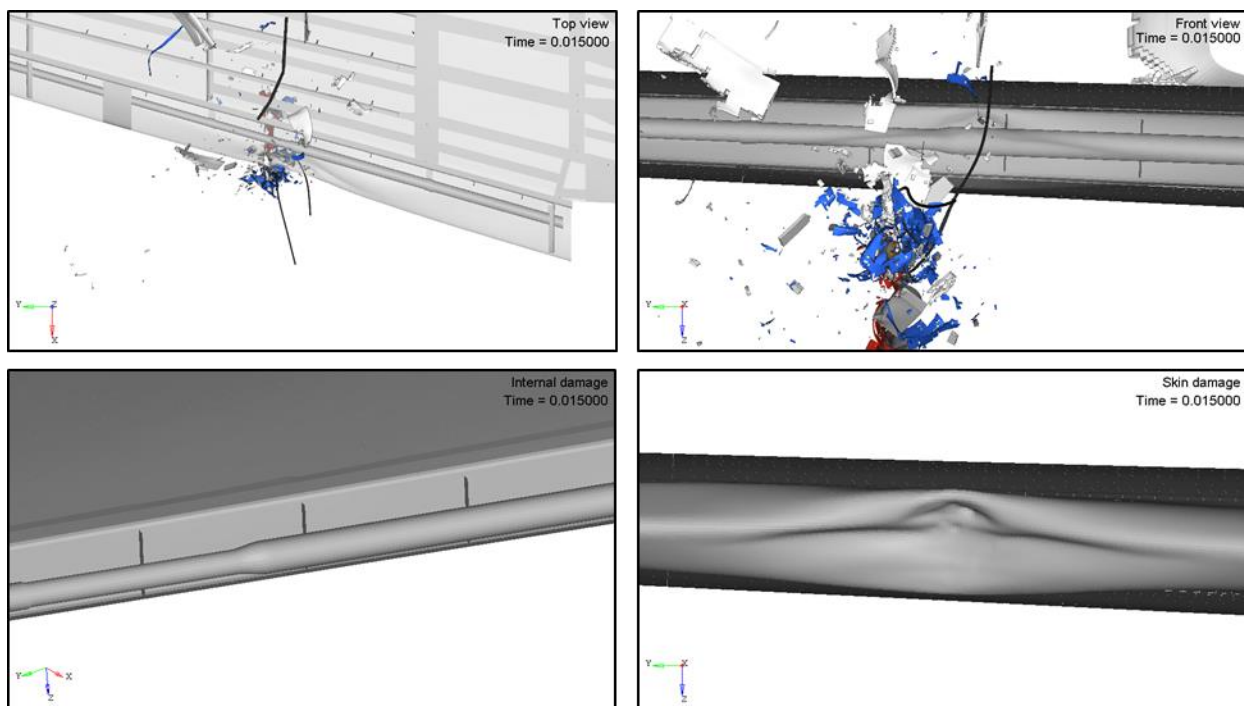


Figure 299. External/internal damage sustained by a business jet wing impacted at location 1 with a 1.8 kg (4.0 lb) UAS at 128.6 m/s (250 knots)

Figure 299 shows the impulse due to the contact force between UAS and wing, as well as the energy balance for both of them. Figure 300 shows the internal energies of UAS and wing parts directly involved in the impact.

The energy balance plot includes the UAS and wing kinetic and internal energies as well as frictional energy and total energy for the event. The wing and the UAS absorbed 23% and 20% of the impact energy respectively. The energy dissipated by friction reached 22% of the total energy. In Figure 300, internal energies for the UAS parts and the wing show that the polycarbonate carcass and battery of the UAS and skin of the wing leading edge absorb the highest amount of internal energies.

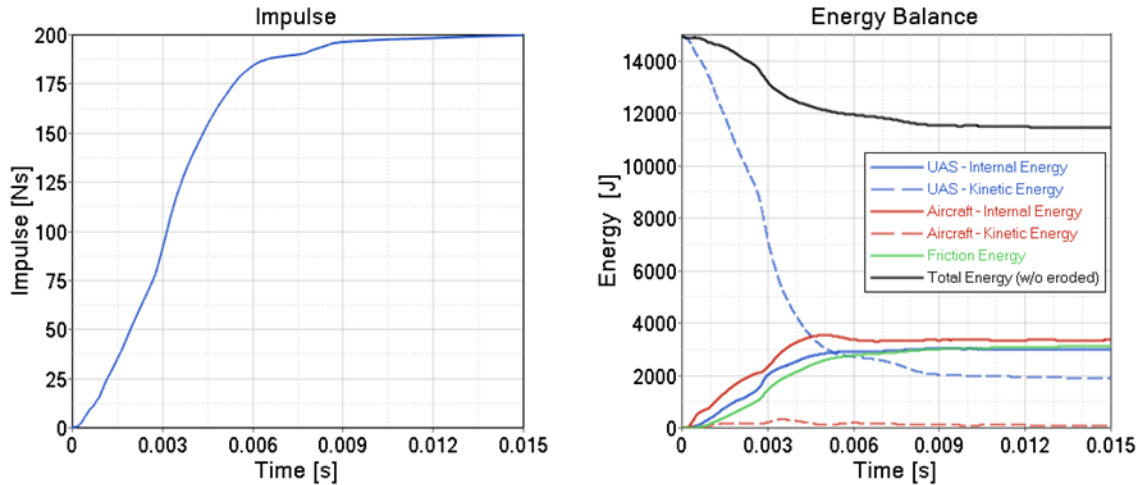


Figure 300. Impulse and energy balance of the impact between a business jet wing and a 1.8 kg (4.0 lb) UAS at location 1 at 128.6 m/s (250 knots)

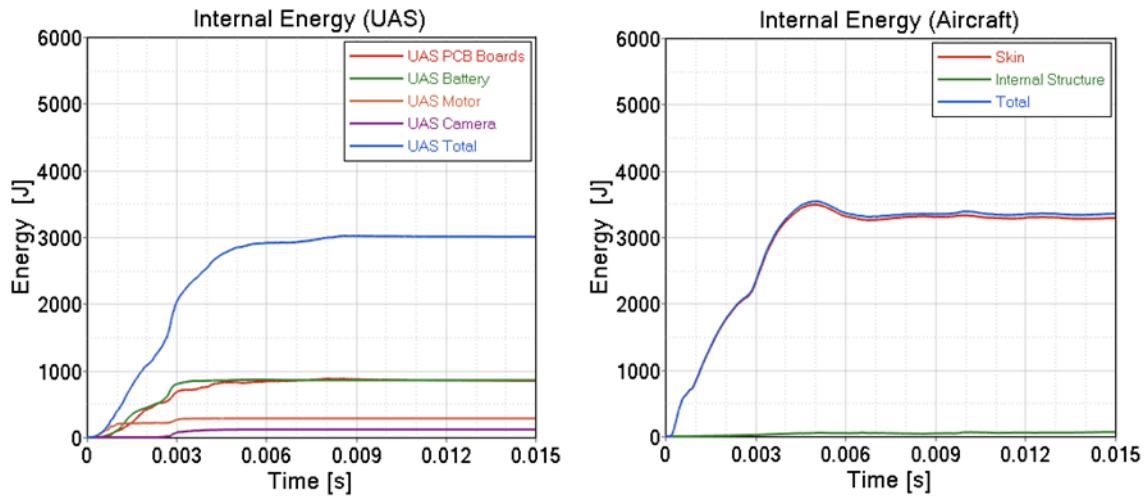


Figure 301. Internal energy per component of the impact between a business jet wing and a 1.8 kg (4.0 lb) UAS at location 1 at 128.6 m/s (250 knots)

C.2.3.2 BFW2

This impact location was identified as the critical baseline simulation for the business jet wing and is discussed in section 4.4.3.2 of the main report body.

C.2.3.3 BFW3

The UAS was impacted against the wing at 128.6 m/s (250 knots) along the local x-axis direction of the aircraft. The impact location selected was at the outboard portion of the wing between ribs 3 and 4. Figure 302 depicts the kinematics of the event. Figure 303 shows the damage caused to the skin and inner structure of the wing.

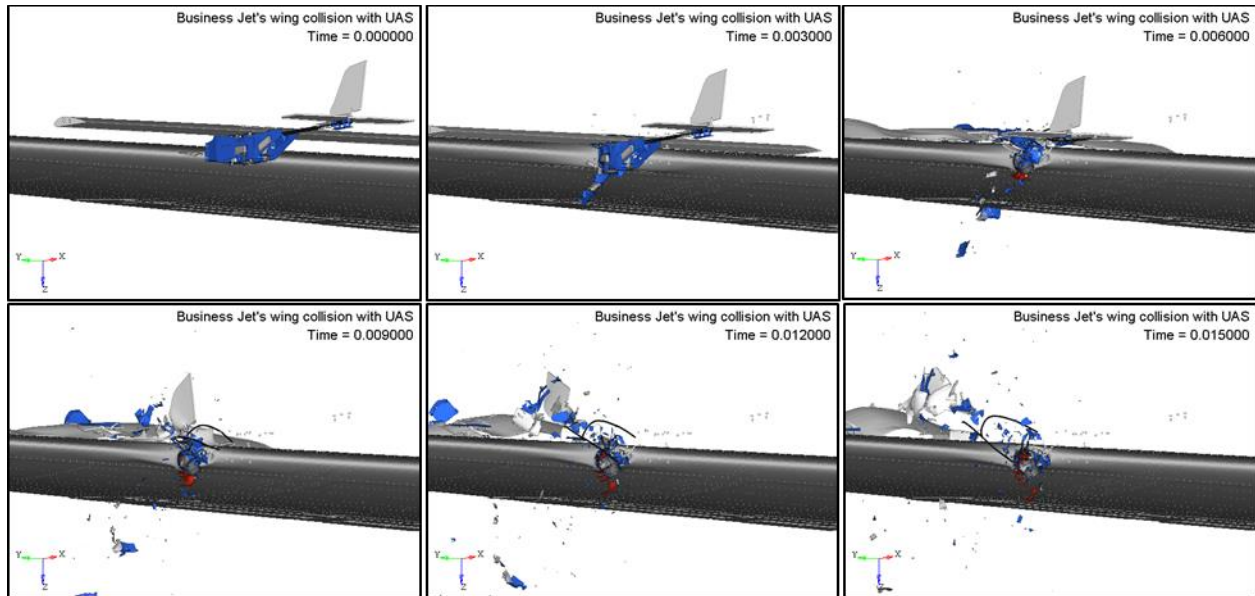


Figure 302. Kinematics of the impact between a business jet wing and a 1.8 kg (4.0 lb) UAS at location 3 at 128.6 m/s (250 knots)

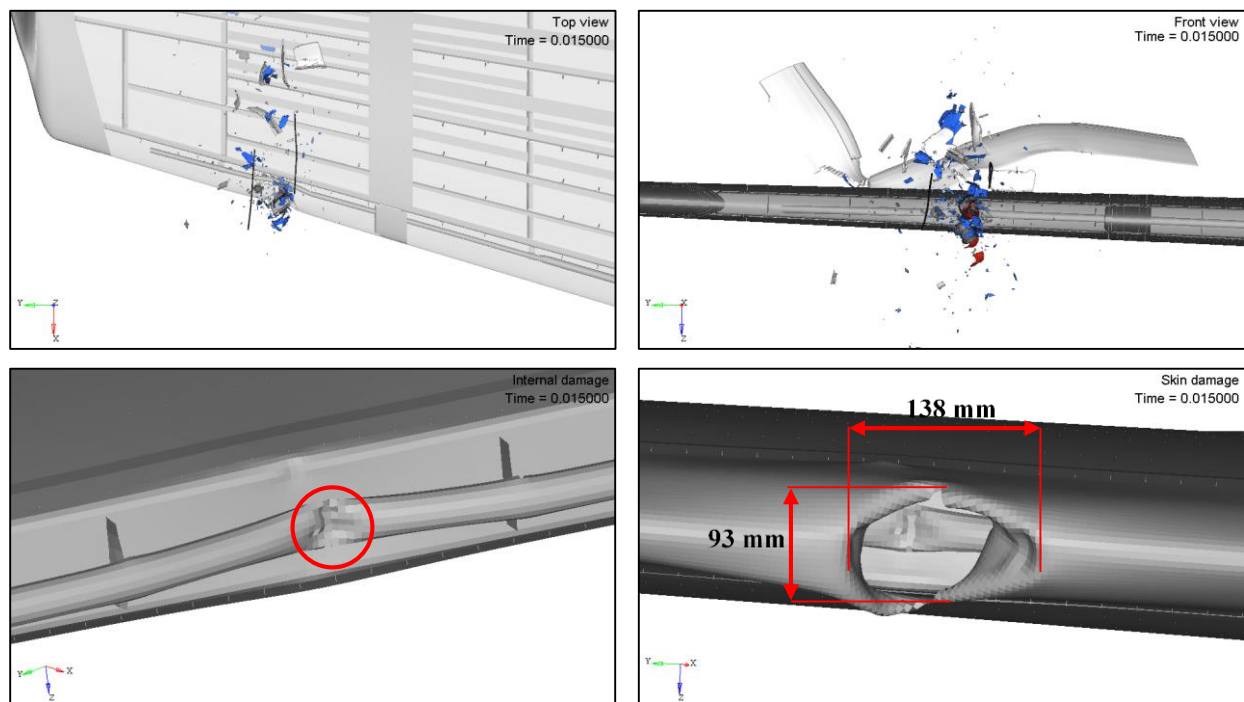


Figure 303. External/internal damage sustained by a business jet wing impacted at location 3 with a 1.8 kg (4.0 lb) UAS at 128.6 m/s (250 knots)

The UAS damaged the skin and anti-ice tube, creating a 138x93 mm² damage zone on the skin surface and allowing some fragments of the UAS components to penetrate into airframe. The damage in anti-ice tube can be perceived in the bottom left image of Figure 303. The front spar did not sustain any visible damage.

The damage introduced by the UAS involved penetration of the skin but no damage to the front spar, and consequently the severity was classified as Level 3.

Figure 304 shows the impulse due to the contact force between UAS and wing, as well as the energy balance for both of them. Figure 305 shows the internal energies of UAS and wing parts directly involved in the impact.

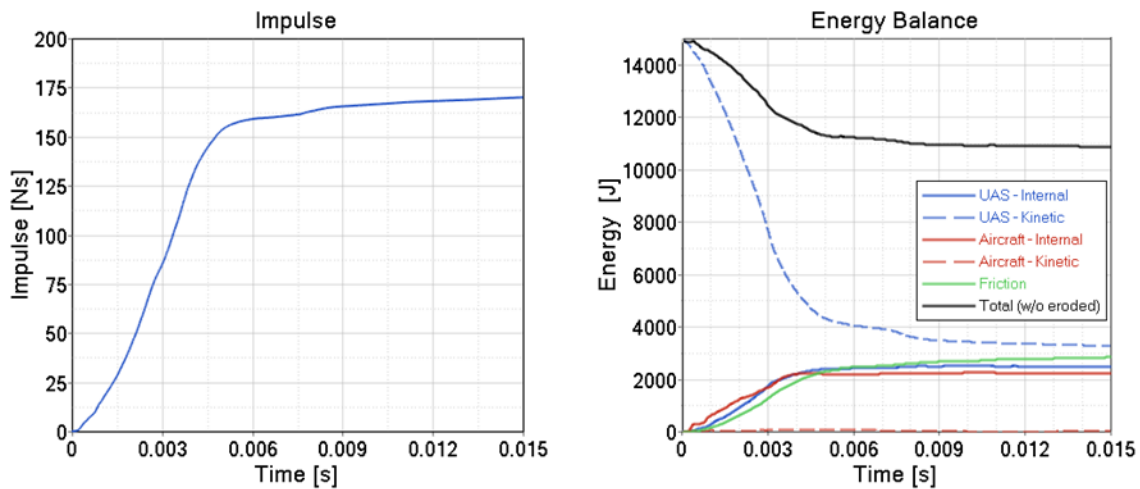


Figure 304. Impulse and energy balance of the impact between a business jet wing and a 1.8 kg (4.0 lb) UAS at location 3 at 128.6 m/s (250 knots)

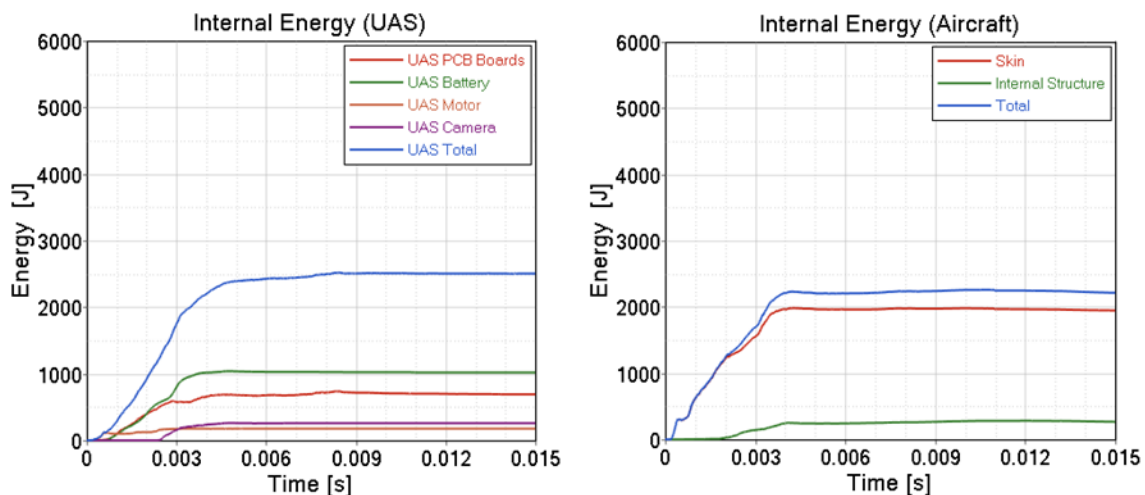


Figure 305. Internal energy per component of the impact between a business jet wing and a 1.8 kg (4.0 lb) UAS at location 3 at 128.6 m/s (250 knots)

The energy balance plot includes the UAS and wing kinetic and internal energies as well as frictional energy and total energy for the event. The wing and the UAS absorbed 15% and 17% of the

impact energy respectively. The energy dissipated by friction reached 20% of the total energy. In Figure 305, internal energies for the UAS parts and the wing show that the UAS battery and skin of the wing leading edge absorb the highest amount of internal energies.

C.2.4 Windshield

C.2.4.1 BFC1

This impact location was identified as the critical baseline simulation for the business jet windshield and is discussed in section 4.4.4.2 of the main report body.

C.2.4.2 BFC2

The UAS was impacted against the windshield at 128.6 m/s (250 knots) along the local x-axis direction of the aircraft. The impact location selected was at middle of the center post. Figure 306 depicts the kinematics of the event. Figure 307 shows the damage caused to the windshield and its internal structure.

The UAS impacted, damaged the center post, and was deflected due to the windshield angle. The permanent deformation in the center post can be perceived in the bottom right image of Figure 307. The internal structure did not sustain any visible damage.

The damage introduced by the UAS involved deformation of the center post, and consequently the severity was classified as Level 1.

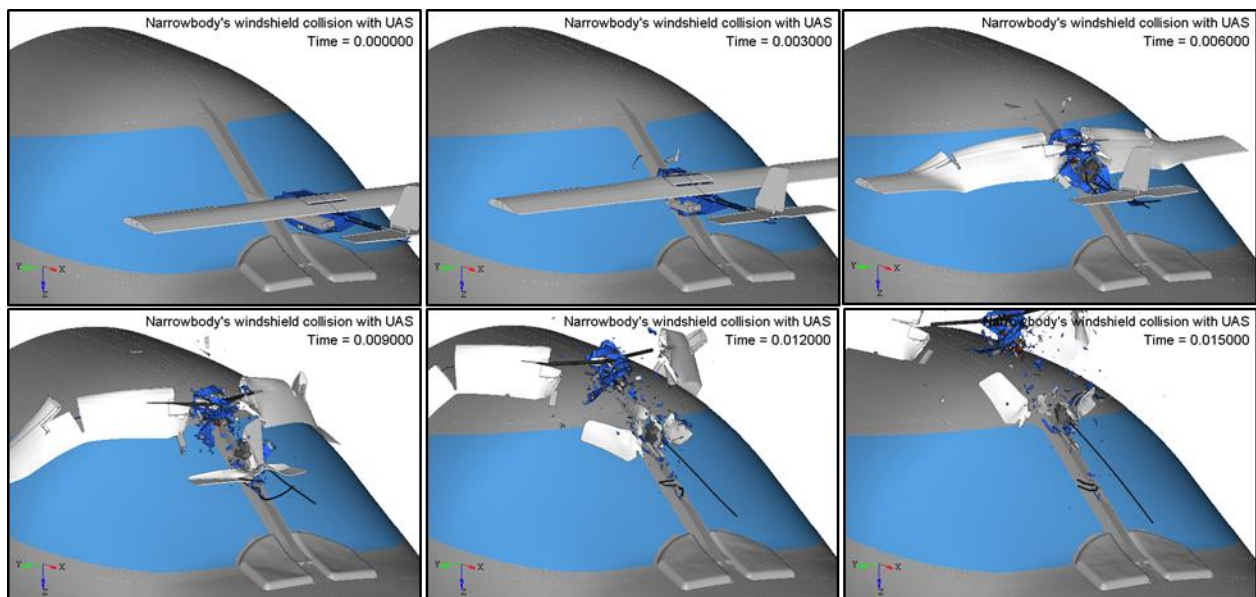


Figure 306. Kinematics of the impact between a business jet windshield and a 1.8 kg (4.0 lb) UAS at location 2 at 128.6 m/s (250 knots)

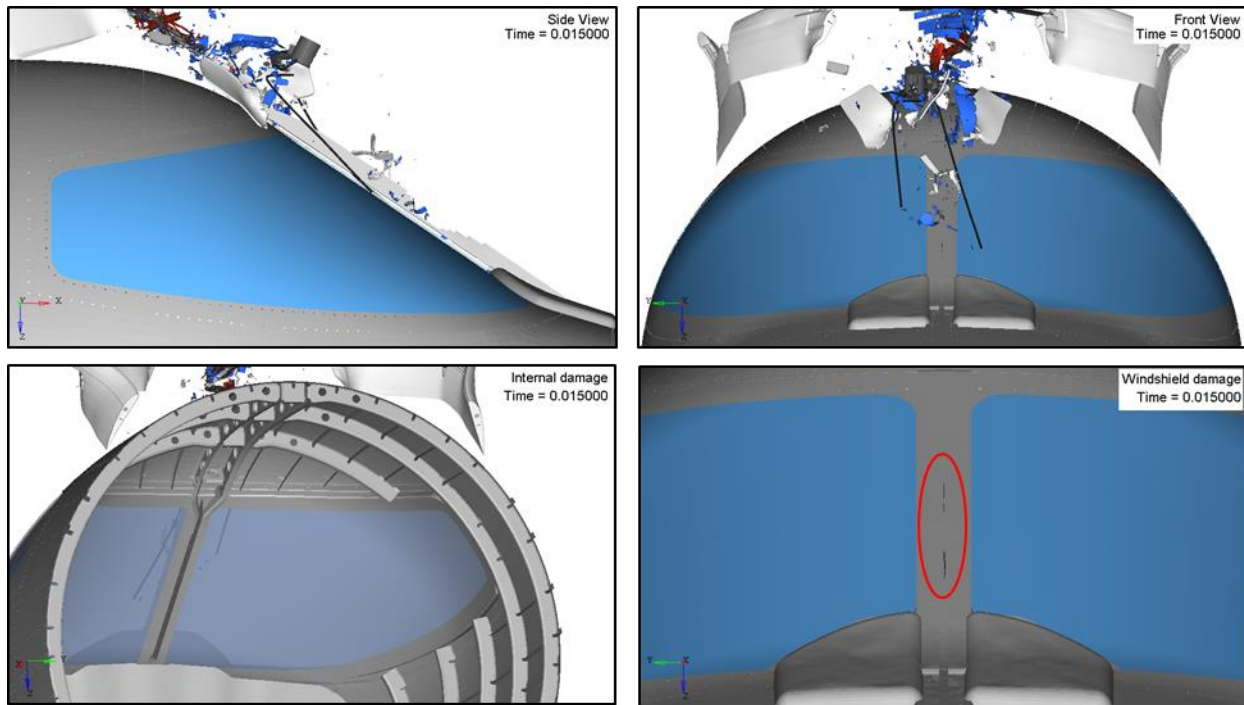


Figure 307. External/internal damage sustained by a business jet windshield impacted at location 2 with a 1.8 kg (4.0 lb) UAS at 128.6 m/s (250 knots)

Figure 308 shows the impulse due to the contact force between the UAS and the forward fuselage, as well as the energy balance for both of them. Figure 309 shows the internal energies of the UAS and the forward fuselage parts directly involved in the impact.

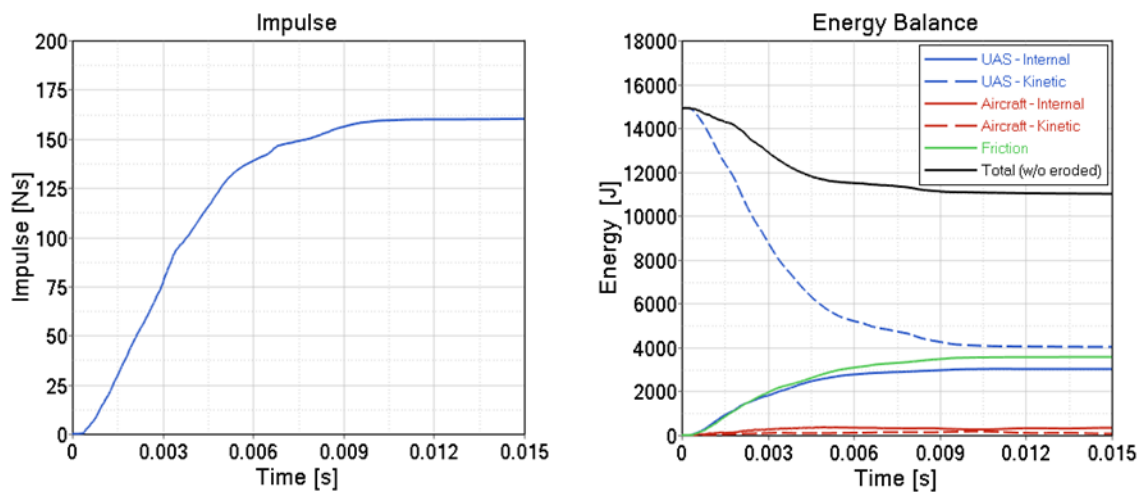


Figure 308. Impulse and energy balance of the impact between a business jet windshield and a 1.8 kg (4.0 lb) UAS at location 2 at 128.6 m/s (250 knots)

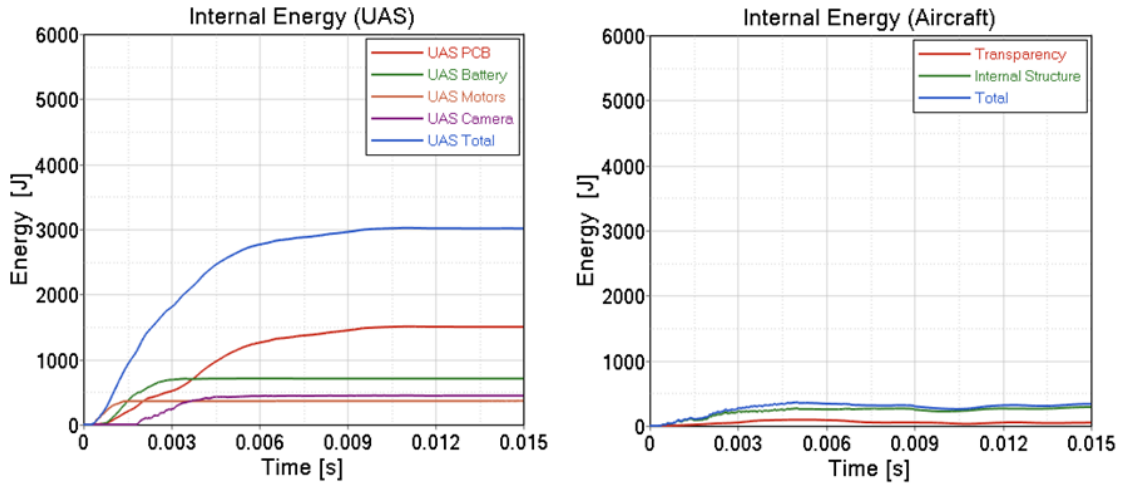


Figure 309. Internal energy per component of the impact between a business jet windshield and a 1.8 kg (4.0 lb) UAS at location 2 at 128.6 m/s (250 knots)

The energy balance plot includes the UAS and forward fuselage kinetic and internal energies as well as frictional energy and total energy for the event. The forward fuselage and the UAS absorbed 2% and 20% of the impact energy respectively. The energy dissipated by friction reached 24% of the total energy. In Figure 309, internal energies for the UAS parts and forward fuselage show that the polycarbonate carcass of the UAS and internal structure of the forward fuselage absorb the highest amount of internal energies.

C.2.4.3 BFC3

The UAS was impacted against the top corner of windshield at 128.6 m/s (250 knots) along the local x-axis direction of the aircraft. Figure 310 depicts the kinematics of the event. Figure 311 shows the damage caused to the windshield and the internal structure.

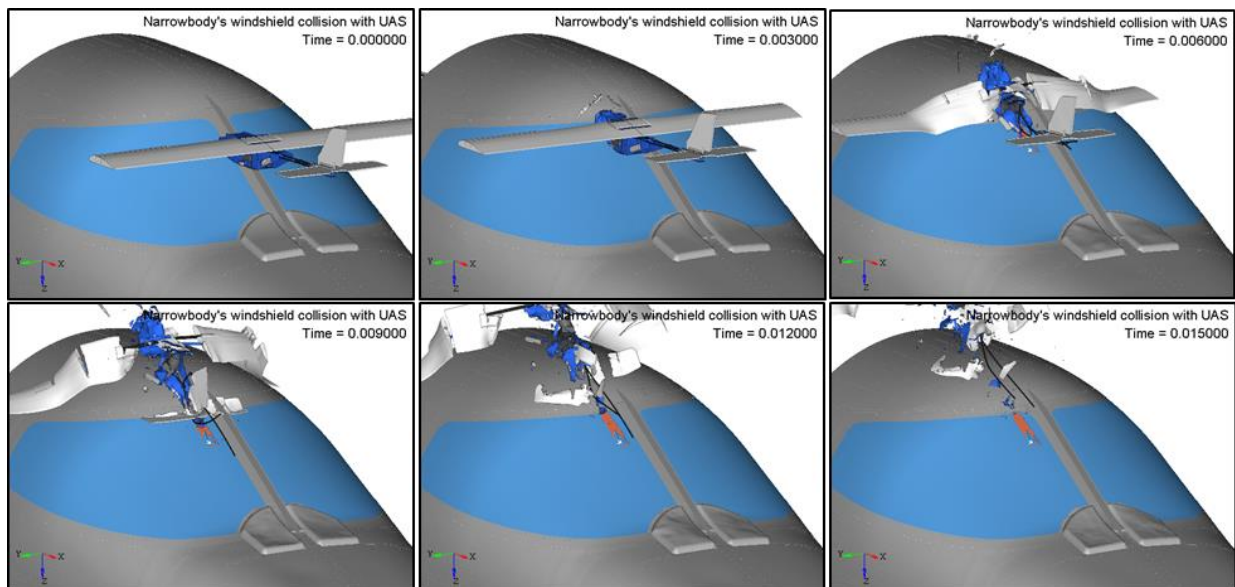


Figure 310. Kinematics of the impact between a business jet windshield and a 1.8 kg (4.0 lb) UAS at location 3 at 128.6 m/s (250 knots)

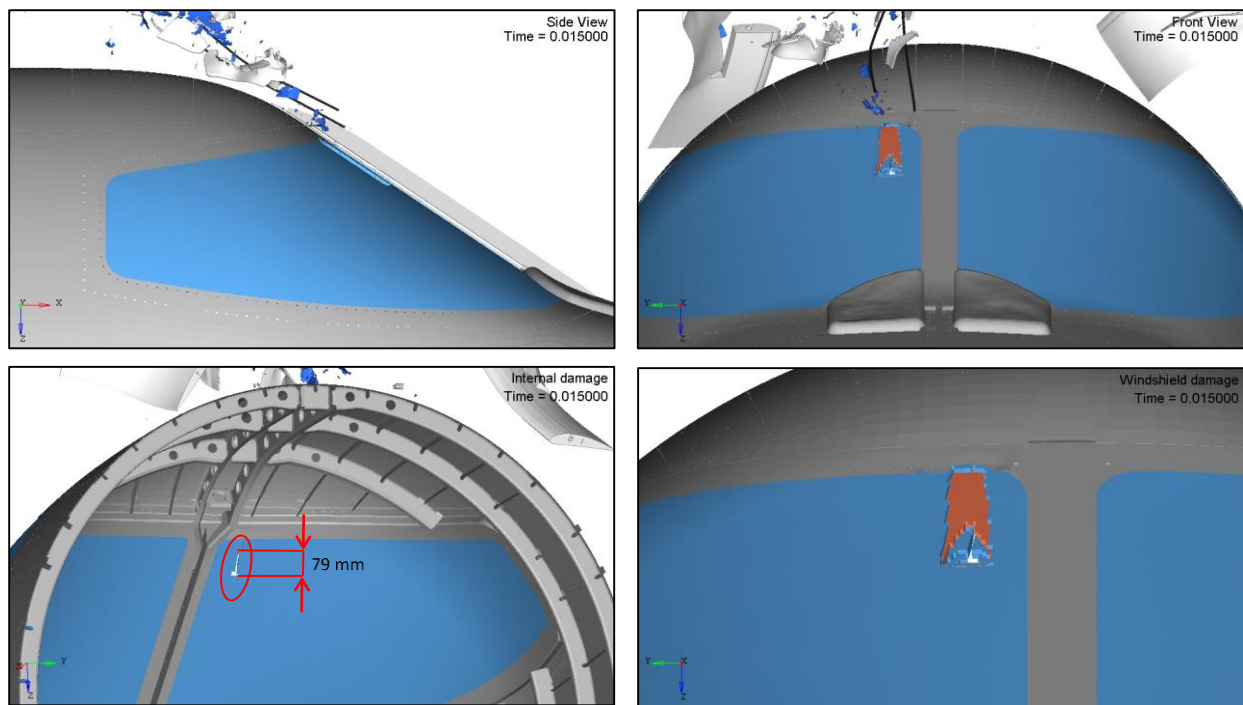


Figure 311. External/internal damage sustained by a business jet windshield impacted at location 3 with a 1.8 kg (4.0 lb) UAS at 128.6 m/s (250 knots)

The UAS impacted, damaged the transparency and was deflected due to the windshield angle, creating a fracture of 79 mm on inner layer of transparency. The damage in the transparency can be perceived in the bottom right image of Figure 311. The internal structure did not sustain any visible damage.

The damage introduced by the UAS involved damage to the transparency but no damage to the internal structure, and consequently the severity was classified as Level 4.

Figure 312 shows the impulse due to the contact force between the UAS and the forward fuselage, as well as the energy balance for both of them. Figure 313 shows the internal energies of the UAS and the forward fuselage parts directly involved in the impact.

The energy balance plot includes the UAS and forward fuselage kinetic and internal energies as well as frictional energy and total energy for the event. The forward fuselage and the UAS absorbed 4% and 16% of the impact energy respectively. The energy dissipated by friction reached 21% of the total energy. In Figure 313, internal energies for the UAS parts and forward fuselage show that polycarbonate carcass of the UAS and the transparency and internal structure of the forward fuselage absorb the highest amount of internal energies.

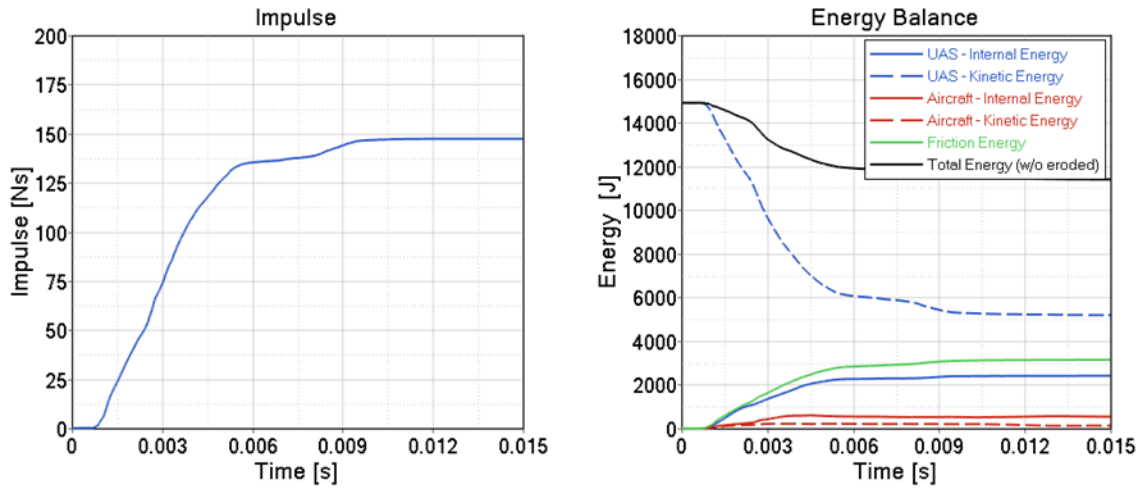


Figure 312. Impulse and energy balance of the impact between a business jet windshield and a 1.8 kg (4.0 lb) UAS at location 3 at 128.6 m/s (250 knots)

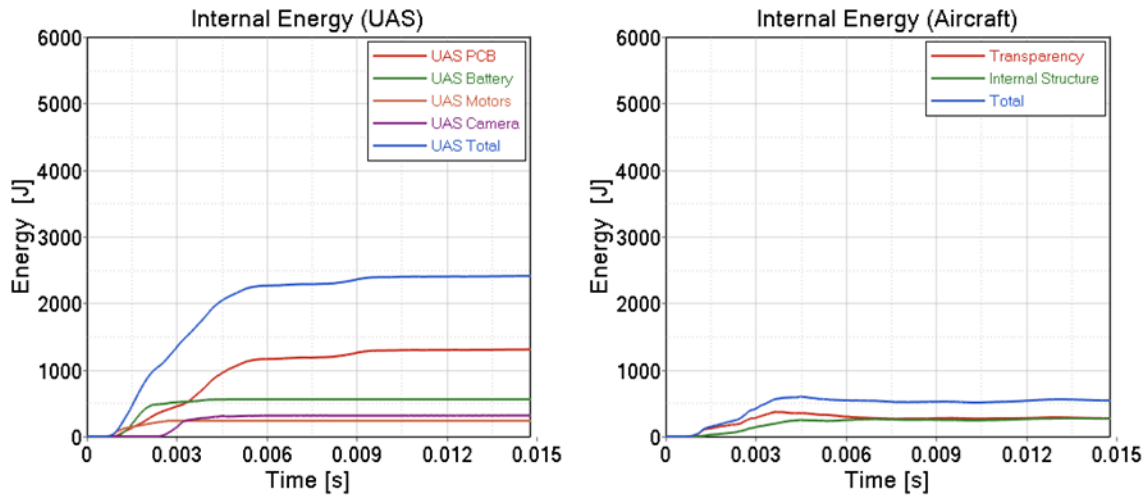


Figure 313. Internal energy per component of the impact between a business jet windshield and a 1.8 kg (4.0 lb) UAS at location 3 at 128.6 m/s (250 knots)

C.2.5 Summary of Results of Collision with Business Jet

Assembly	Case	Severity	Fire Risk	Internal Energy Aircraft [J]	Internal Energy UAS [J]	Residual Kinetic Energy [J]	Friction Energy [J]	Eroded Energy [J]
Vertical Stabilizer	BFV1	Level 4	No	4450	1860	3000	2560	3929
	BFV2	Level 4	No	4250	1850	3130	3800	1939
	BFV3	Level 4	No	2450	2000	3940	2650	3099
Horizontal Stabilizer	BFH1	Level 4	No	2279	2327	2885	2915	4563
	BFH2	Level 4	No	1989	2278	3629	3100	3973
	BFH3	Level 4	No	2080	2292	3423	3206	3968
Wing	BFW1	Level 2	No	3450	3000	1885	3350	3284
	BFW2	Level 3	No	2650	2690	2635	3170	3824
	BFW3	Level 3	No	2230	2550	3285	2950	3954
Windshield	BFC1	Level 4	No	541	2350	5643	3195	3240
	BFC2	Level 1	No	336	3013	4023	3566	4031
	BFC3	Level 4	No	540	2408	5187	3142	3692

APPENDIX D – MASS SENSITIVITY STUDY

D.1 TRANSPORT JET – BASELINE UAS (1.8 KG) VS SCALED UAS (3.6 KG)

D.1.1 Vertical Stabilizer

Impact simulations of a 1.8 kg (4 lb) UAS (case CFV1) and 3.6 kg (8.0 lb) UAS (case CFsV1) against a vertical stabilizer are compared in terms of damage severity and kinematics. The initial conditions for both cases were based on CFV1, which was identified as the most critical case in the baseline simulations (see Section 4.3.1.1). Figure 314 depicts the comparison of the kinematics of the event. Figure 315 shows the comparison of the damage caused to the skin and the inner structure of the vertical stabilizer.

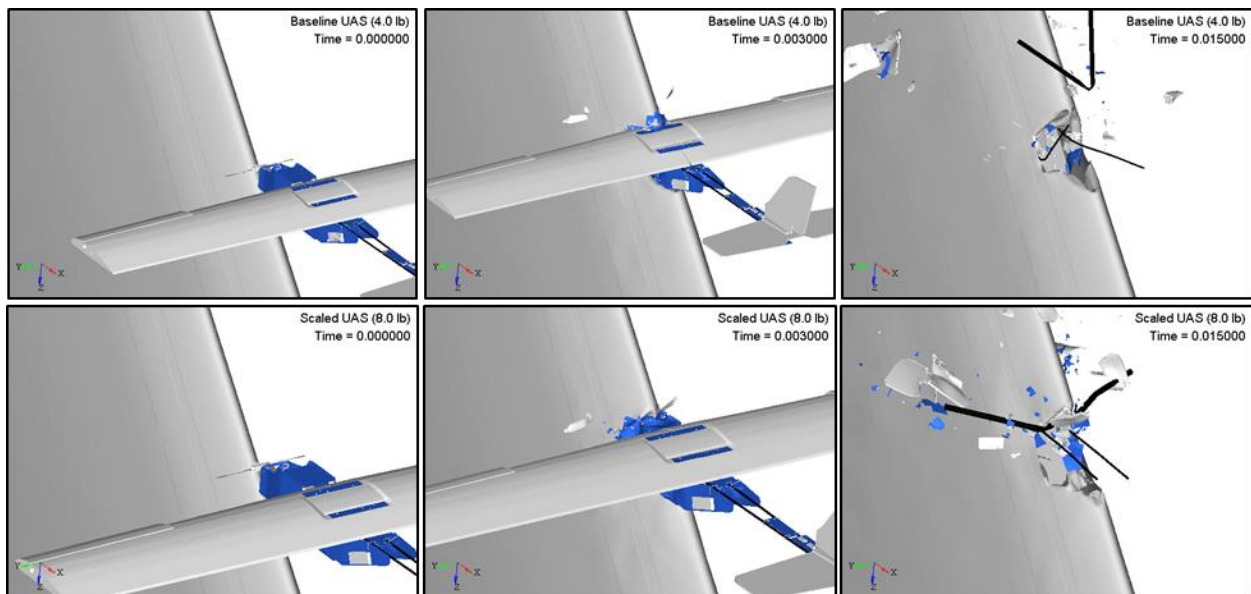


Figure 314. Comparison of the impact kinematics between a commercial transport jet vertical stabilizer and a 1.8/3.6 kg (4.0/8.0 lb) UAS at 128.6 m/s (250 knots)

The 3.6 kg (8.0 lb) UAS damaged the skin, upper and lower ribs, and the lightening hole above the impact location in the front spar while the 1.8 kg (4.0 lb) UAS damaged the skin, just the upper rib, and the front spar to a lesser degree. It can also be perceived in Figure 315 that the damage introduced into the skin, the ribs, and the front spar was considerably more spread out for the 3.6 kg (8.0 lb) UAS) UAS than for the 1.8 kg (4.0 lb) UAS.

The damage introduced by both the UAS is classified as Level 4. Even with the same level, in terms of damage, the 3.6 kg (8.0 lb) UAS can be considered slightly more severe than the 1.8 kg (4.0 lb) UAS.

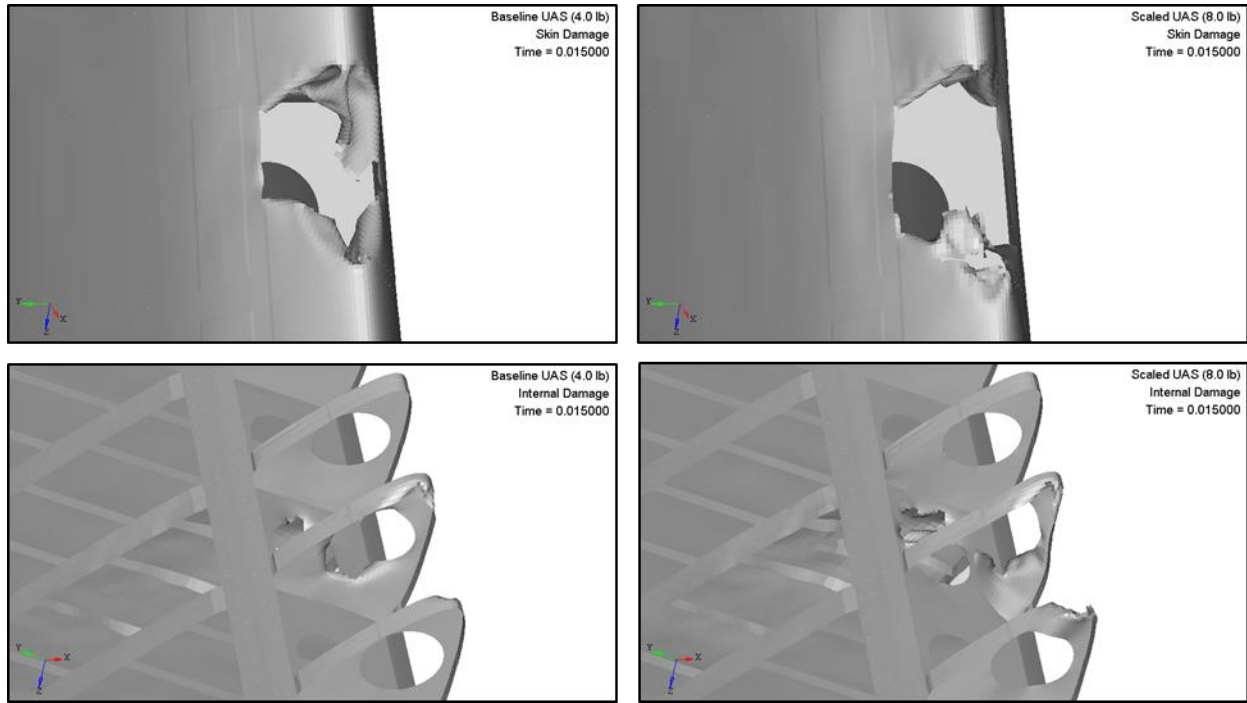


Figure 315. Comparison of external/internal damage sustained by a commercial transport jet vertical stabilizer impacted with a 1.8/3.6 kg (4.0/8.0 lb) UAS at 128.6 m/s (250 knots)

Figure 316 shows the comparison for the contact force and impulse between the 1.8/3.6 kg (4.0/8.0 lb) UAS and vertical stabilizer. Figure 317 shows the energy balance, normalized with the initial kinetic energy, for the impact comparison.

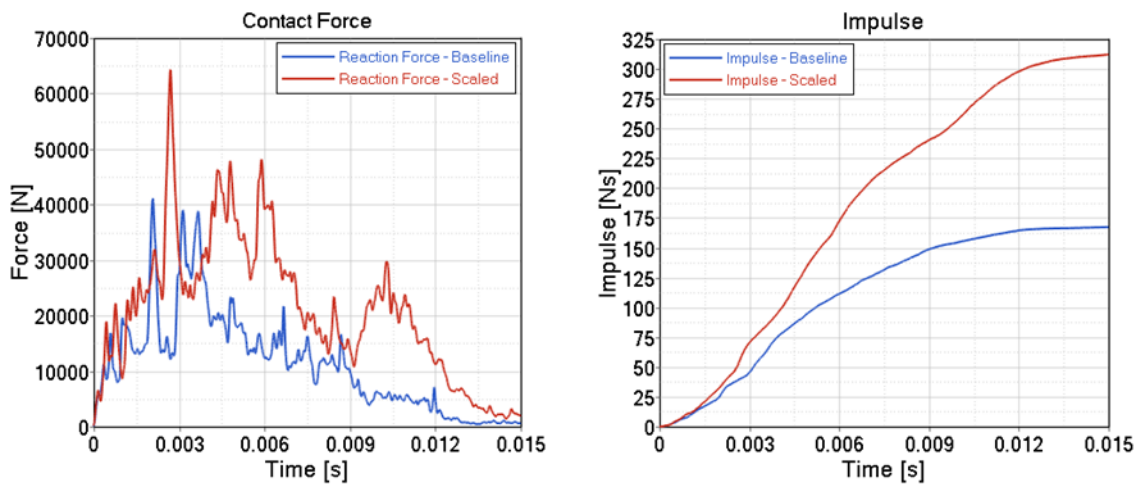


Figure 316. Comparison of the contact force and impulse of the impact between a commercial transport jet vertical stabilizer and a 1.8/3.6 kg (4.0/8.0 lb) UAS at 128.6 m/s (250 knots)

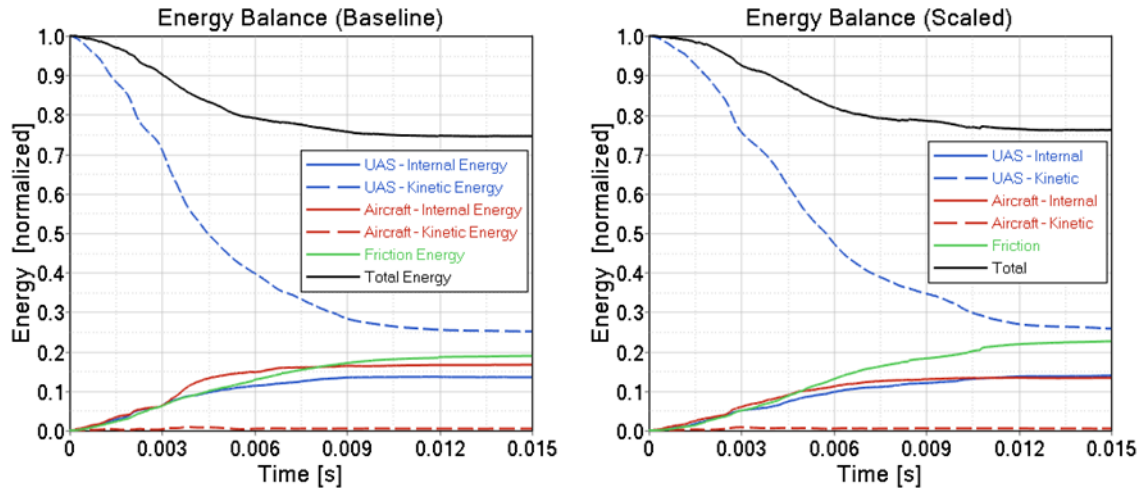


Figure 317. Comparison of the energy balance of the impact between a commercial transport jet vertical stabilizer and a 1.8/3.6 kg (4.0/8.0 lb) UAS at 128.6 m/s (250 knots)

The impulse for the 3.6 kg (8.0 lb) UAS was greater than for the 1.8 kg (4.0 lb) UAS. From the energy balance comparison, it can be observed that the 3.6 kg (8.0 lb) UAS absorbed a similar ratio of internal energy than the 1.8 kg (4.0 lb) UAS. In addition, it is apparent that the residual kinetic energy of the 3.6 kg (8.0 lb) UAS after impact was relatively smaller than the 1.8 kg (4.0 lb) UAS.

D.1.2 Horizontal Stabilizer

Impact simulations of a 1.8 kg (4.0 lb) UAS (case CFH2) and 3.6 kg (8.0 lb) UAS (case CFsH2) against a horizontal stabilizer are compared in terms of damage severity and kinematics. The initial conditions for both cases were based on CFH2, which was identified as the most critical case in the baseline simulations (see Section 4.3.2.1). Figure 318 depicts the comparison of the kinematics of the event. Figure 319 shows the comparison of the damage caused to the skin and the inner structure of the horizontal stabilizer.

The 3.6 kg (8.0 lb) UAS damaged the skin, the nose ribs, and the front spar while the 1.8 kg (4.0 lb) UAS damaged the skin, the nose ribs, and the front spar to a lesser degree. It can also be perceived in Figure 319 that the damage introduced into the skin, the ribs, and the front spar for the 3.6 kg (8.0 lb) UAS was considerably greater than for the 1.8 kg (4.0 lb) UAS.

The damage introduced by both the UAS is classified as Level 4 with risk of fire due to the battery. Even with the same level, in terms of damage, the 3.6 kg (8.0 lb) UAS can be considered more severe than the 1.8 kg (4.0 lb) UAS.

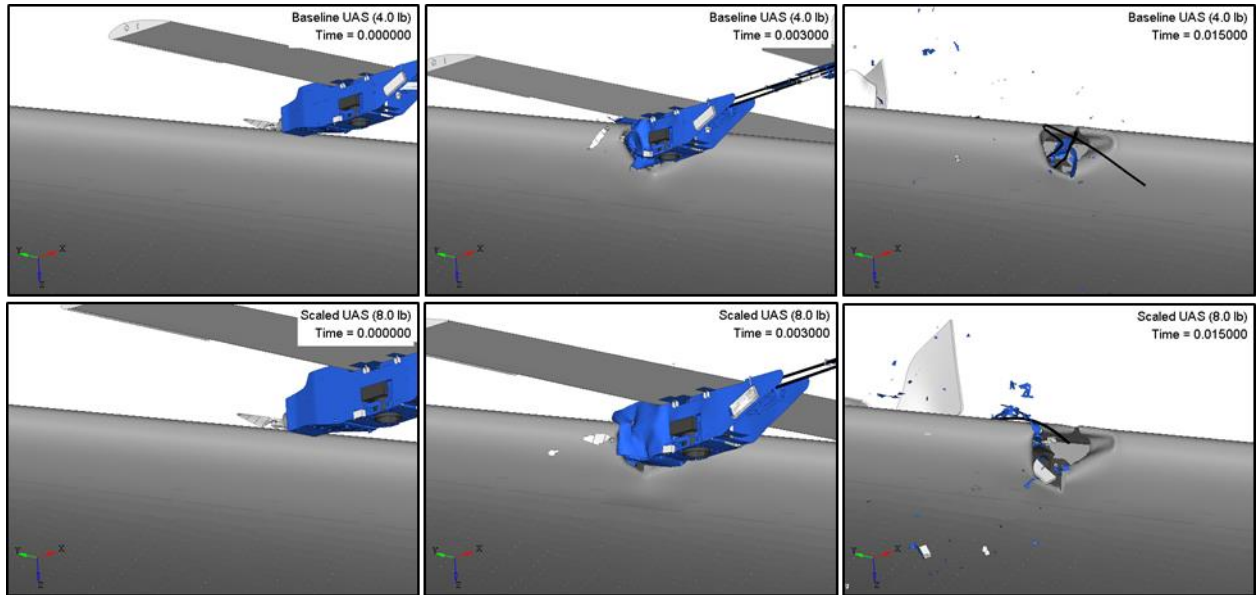


Figure 318. Comparison of the impact kinematics between a commercial transport jet horizontal stabilizer and a 1.8/3.6 kg (4.0/8.0 lb) UAS at 128.6 m/s (250 knots)

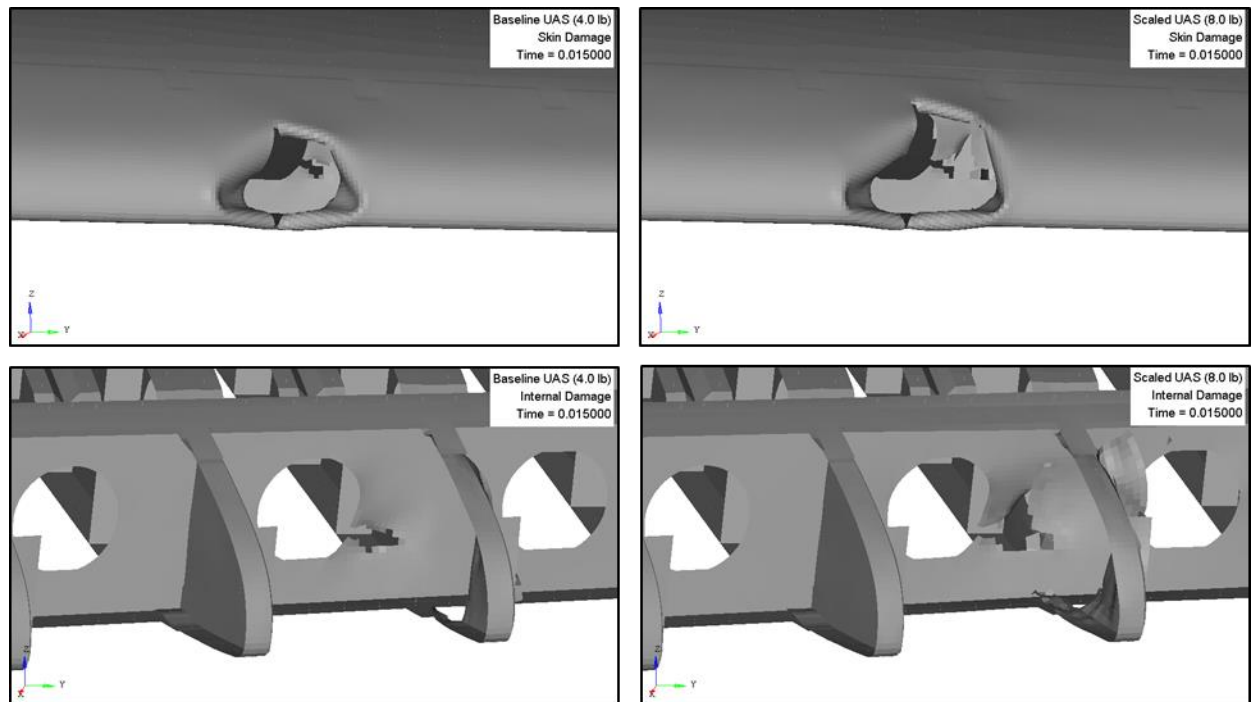


Figure 319. Comparison of external/internal damage sustained by a commercial transport jet horizontal stabilizer impacted with a 1.8/3.6 kg (4.0/8.0 lb) UAS at 128.6 m/s (250 knots)

Figure 320 shows the comparison for the contact force and impulse between the 1.8/3.6 kg (4.0/8.0 lb) UAS and horizontal stabilizer. Figure 321 shows the energy balance, normalized with the initial kinetic energy, for the impact comparison.

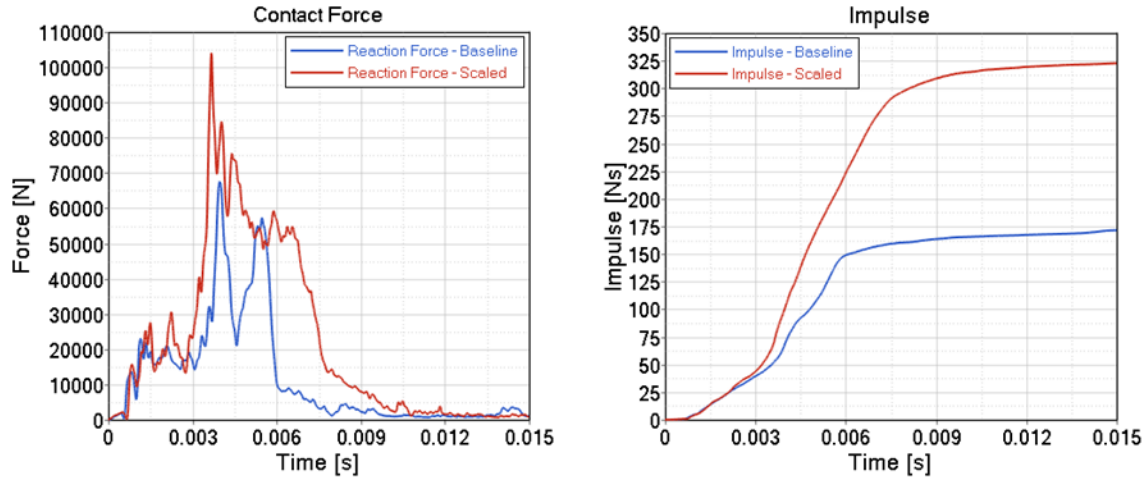


Figure 320. Comparison of the contact force and impulse of the impact between a commercial transport jet horizontal stabilizer and a 1.8/3.6 kg (4.0/8.0 lb) UAS at 128.6 m/s (250 knots)

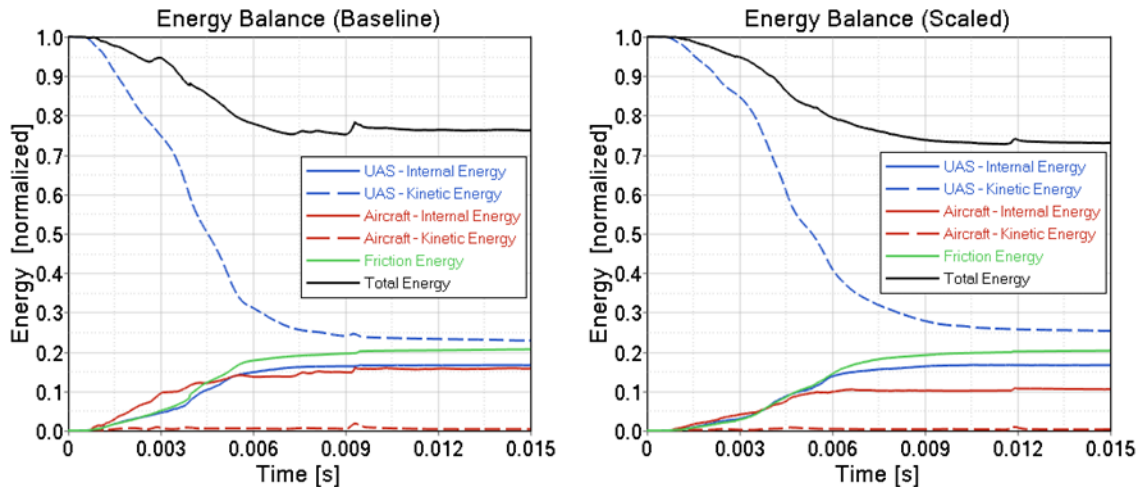


Figure 321. Comparison of the energy balance of the impact between a commercial transport jet horizontal stabilizer and a 1.8/3.6 kg (4.0/8.0 lb) UAS at 128.6 m/s (250 knots)

The impulse for the 3.6 kg (8.0 lb) UAS was greater than for the 1.8 kg (4.0 lb) UAS. From the energy balance comparison, it can be observed that the 3.6 kg (8.0 lb) UAS absorbed a ratio of internal energy similar to the 1.8 kg (4.0 lb) UAS. In addition, it is apparent that the residual kinetic energy of the 3.6 kg (8.0 lb) UAS after impact was smaller relatively than the 1.8 kg (4.0 lb) UAS.

D.1.3 Wing Leading Edge

Impact simulations of a 1.8 kg (4.0 lb) UAS (case CFW3) and 3.6 kg (8.0 lb) UAS (case CFsW3) against a wing leading edge are compared in terms of damage severity and kinematics. The initial conditions for both cases were based on CFW3, which was identified as the most critical case in the baseline simulations (see Section 4.3.3.1). Figure 322 depicts the comparison of the kinematics of the event. Figure 323 shows the comparison of the damage caused to the skin and the inner structure of the wing.

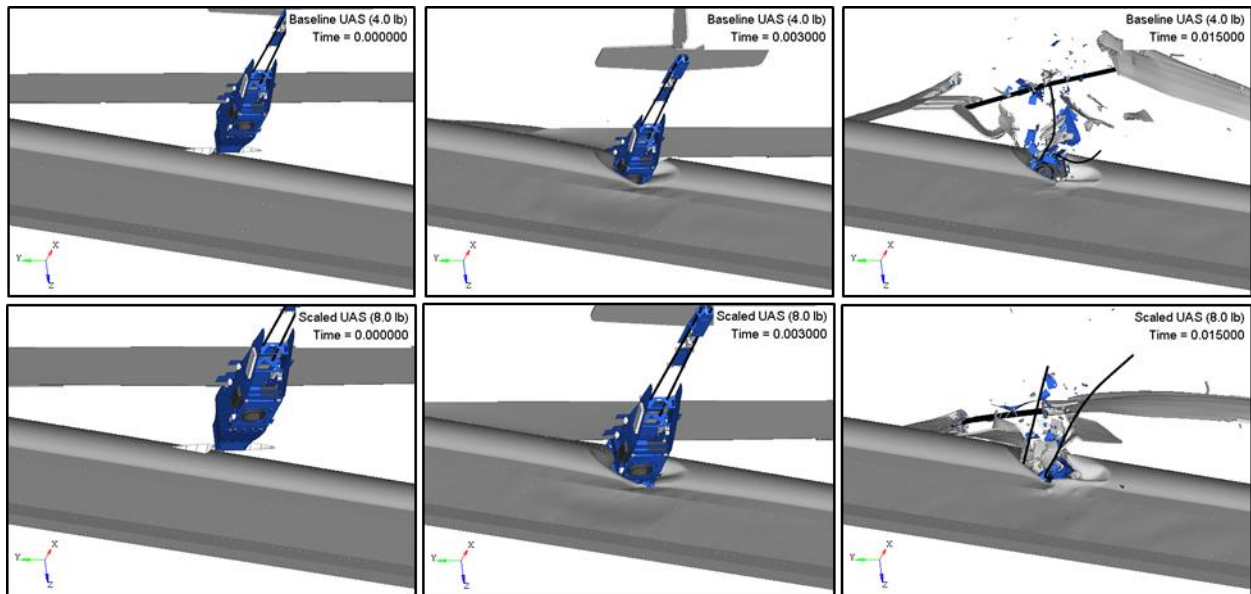


Figure 322. Comparison of the impact kinematics between a commercial transport jet wing and a 1.8/3.6 kg (4.0/8.0 lb) UAS at 128.6 m/s (250 knots)

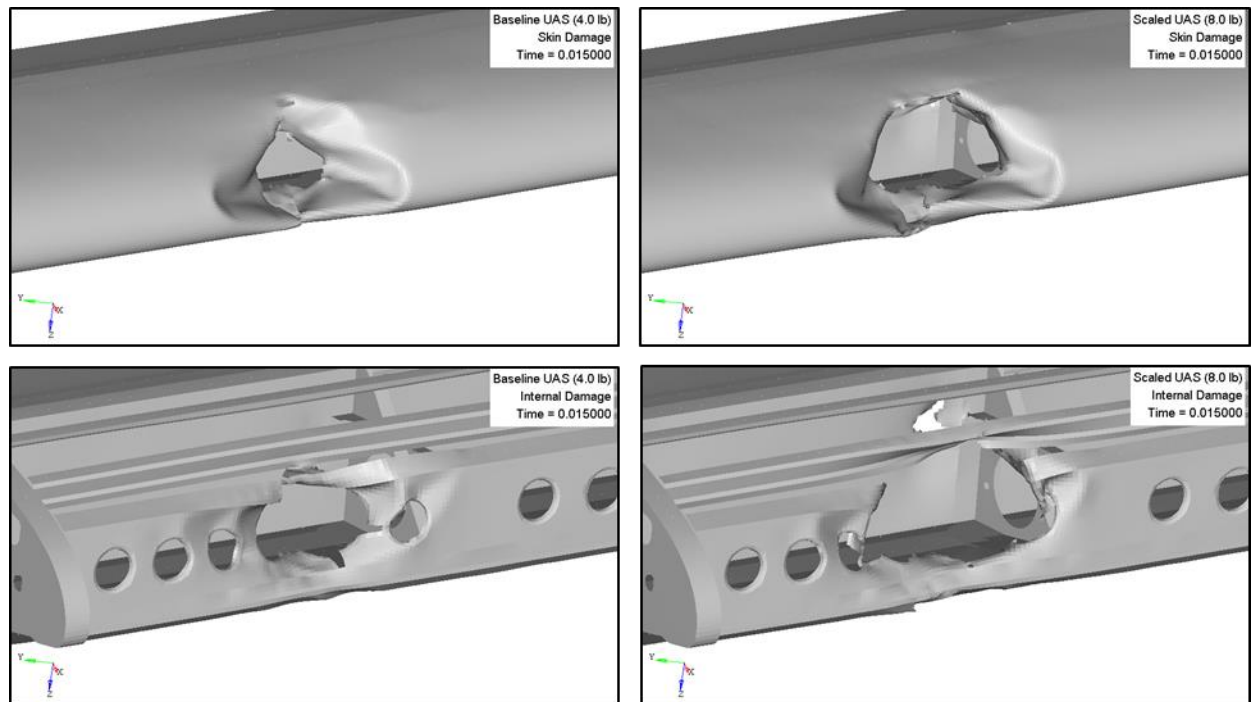


Figure 323. Comparison of external/internal damage sustained by a commercial transport jet wing impacted with a 1.8/3.6 kg (4.0/8.0 lb) UAS at 128.6 m/s (250 knots)

The 3.6 kg (8.0 lb) UAS damaged the leading edge skin, the hold down rib, the sub-spar, and the front spar while the 1.8 kg (4.0 lb) UAS damaged the skin and the sub-spar to a lesser degree. It can also be perceived in Figure 323 that the damage introduced into the skin and the sub-spar was greater for the case of 3.6 kg (8.0 lb) UAS than for the 1.8 kg (4.0 lb) UAS.

The damage introduced by the 1.8 kg (4.0 lb) UAS is classified as Level 3 whereas the damage introduced by the 3.6 kg (8.0 lb) UAS is classified as Level 4. In addition, the risk of fire due to the battery is present only for the impact of the 3.6 kg (8.0 lb) UAS. In terms of damage, the 3.6 kg (8.0 lb) UAS can be considered more severe than the 1.8 kg (4.0 lb) UAS.

Figure 324 shows the comparison for the contact force and impulse between the 1.8/3.6 kg (4.0/8.0 lb) UAS and wing. Figure 325 shows the energy balance, normalized with the initial kinetic energy, for the impact comparison.

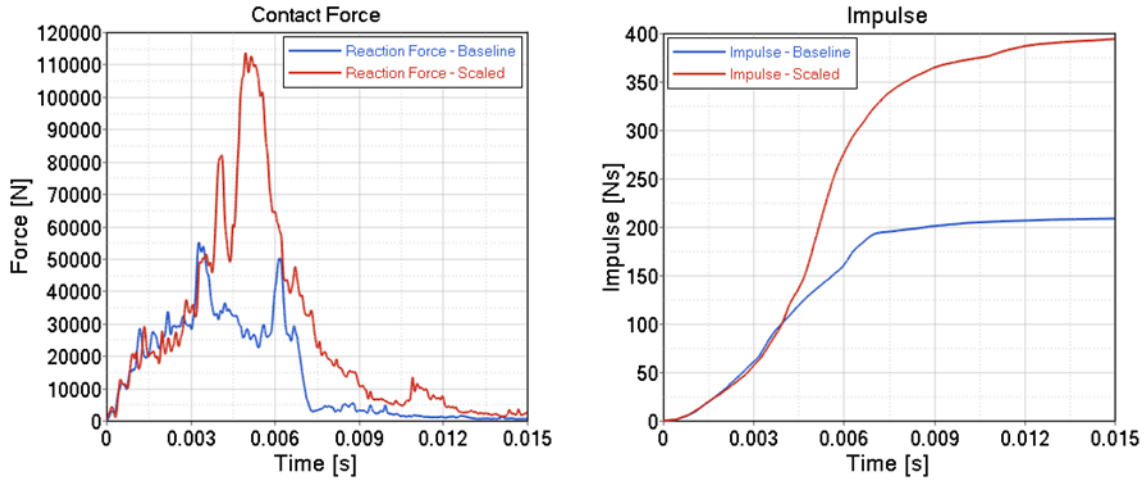


Figure 324. Comparison of the contact force and impulse of the impact between a commercial transport jet wing and a 1.8/3.6 kg (4.0/8.0 lb) UAS at 128.6 m/s (250 knots)

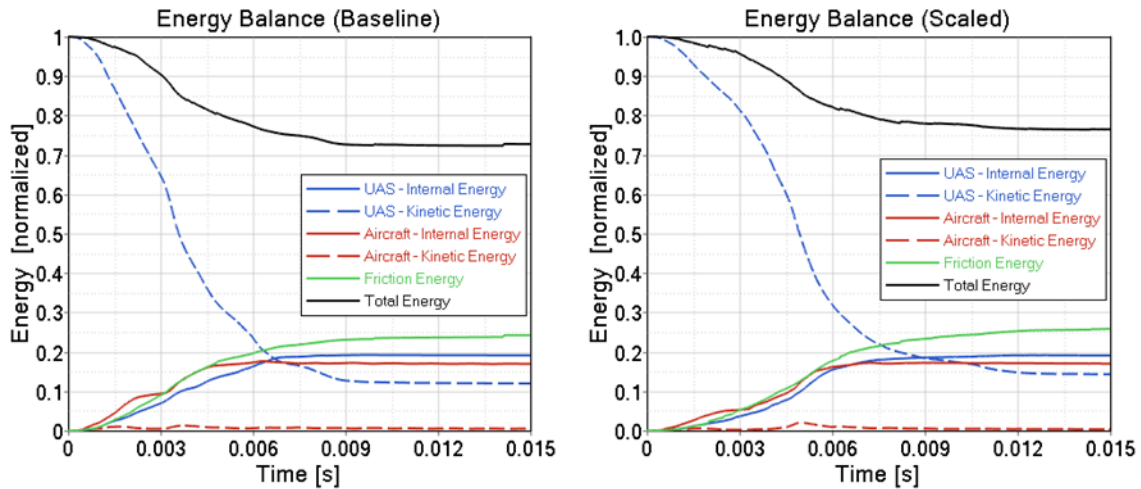


Figure 325. Comparison of the energy balance of the impact between a commercial transport jet wing and a 1.8/3.6 kg (4.0/8.0 lb) UAS at 128.6 m/s (250 knots)

The impulse for the 3.6 kg (8.0 lb) UAS was greater than for the 1.8 kg (4.0 lb) UAS. From the energy balance comparison, it can be observed that the 3.6 kg (8.0 lb) UAS absorbed a ratio of

internal energy similar to the 1.8 kg (4.0 lb) UAS. In addition, it is apparent that the residual kinetic energy of the 3.6 kg (8.0 lb) UAS after impact was slightly higher than the 1.8 kg (4.0 lb) UAS.

D.1.4 Windshield

Impact simulations of a 1.8 kg (4.0 lb) UAS (case CFC1) and 3.6 kg (8.0 lb) UAS (case CFsC1) against a windshield are compared in terms of damage severity and kinematics. The initial conditions for both cases were based on CFC1, which was identified as the most critical case in the baseline simulations (see Section 4.3.4.1). Figure 326 depicts the comparison of the kinematics of the event. Figure 327 shows the comparison of the damage caused to the windshield and surrounding structure.

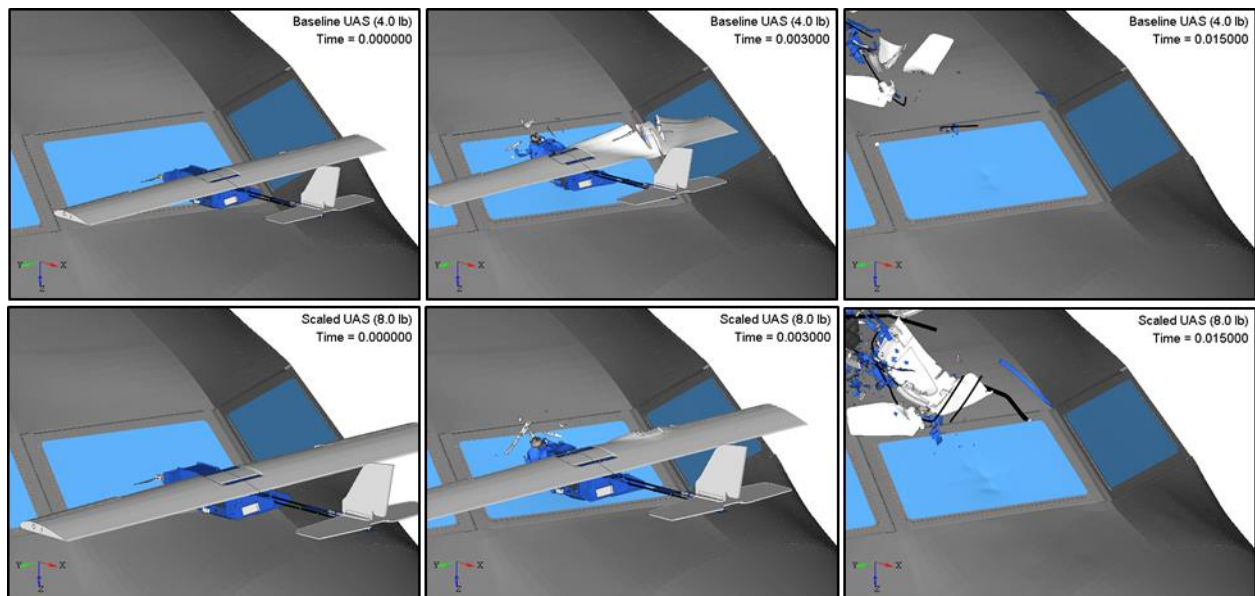


Figure 326. Comparison of the impact kinematics between a commercial transport jet windshield and a 1.8/3.6 kg (4.0/8.0 lb) UAS at 128.6 m/s (250 knots)

Both UASs impacted the windshield and slid over it due to the small windshield angle, leaving some permanent deformation. The internal structure did not sustain any visible damage. It can also be perceived in Figure 327 that the deformation introduced into windshield by the 3.6 kg (8.0 lb) UAS was greater than that of the 1.8 kg (4.0 lb) UAS. Note that the top three plastic strain plots show only the outer layer of the windshield transparency and that the lower three plots show the layer which sustained the maximum plastic strain.

The damage introduced by both the UAS is classified as Level 2. Even with the same severity level, in terms of damage, the 3.6 kg (8.0 lb) UAS can be considered slightly more severe than the 1.8 kg (4.0 lb) UAS.

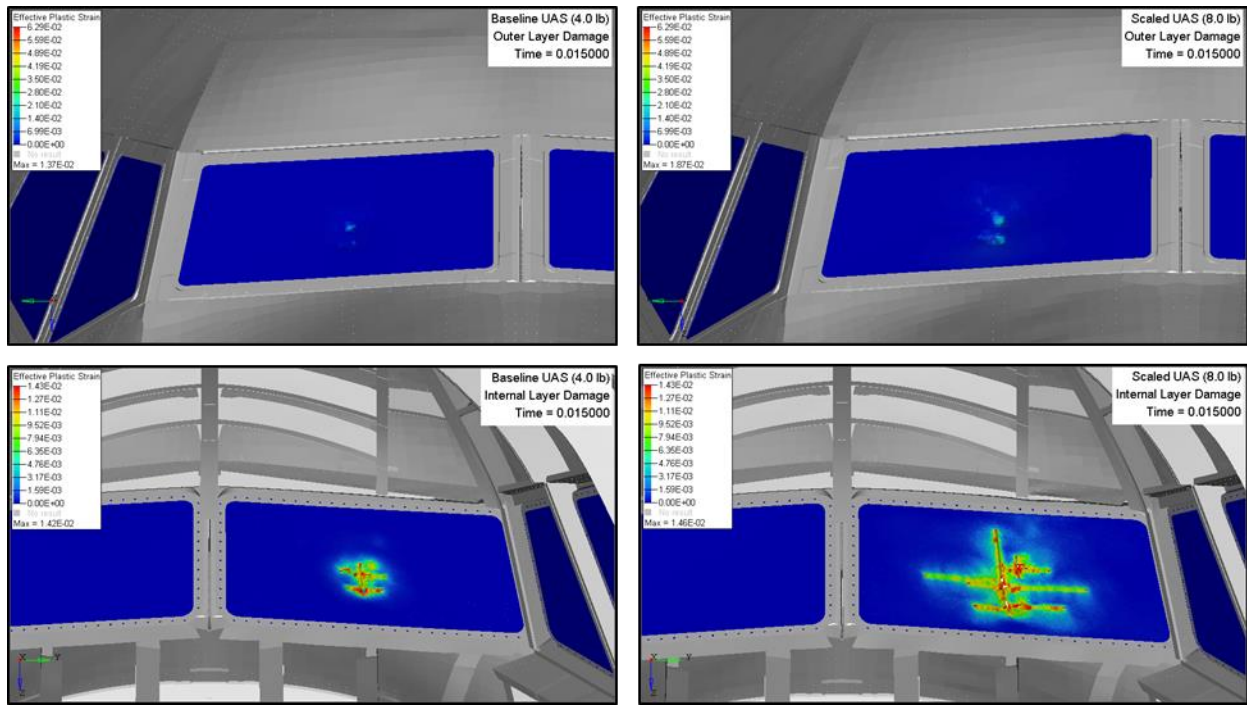


Figure 327. Comparison of external/internal damage sustained by a commercial transport jet windshield impacted with a 1.8/3.6 kg (4.0/8.0 lb) UAS at 128.6 m/s (250 knots)

Figure 328 shows the comparison for the contact force and impulse between the 1.8/3.6 kg (4.0/8.0 lb) UAS and windshield. Figure 329 shows the energy balance, normalized with the initial kinetic energy, for the impact comparison.

The impulse for the 3.6 kg (8.0 lb) UAS was greater than for the 1.8 kg (4.0 lb) UAS. From the energy balance comparison, it can be observed that the 3.6 kg (8.0 lb) UAS absorbed a ratio of internal energy similar to the 1.8 kg (4.0 lb) UAS. In addition, it is apparent that the residual kinetic energy of the 3.6 kg (8.0 lb) UAS after impact was relatively smaller than the 1.8 kg (4.0 lb) UAS.

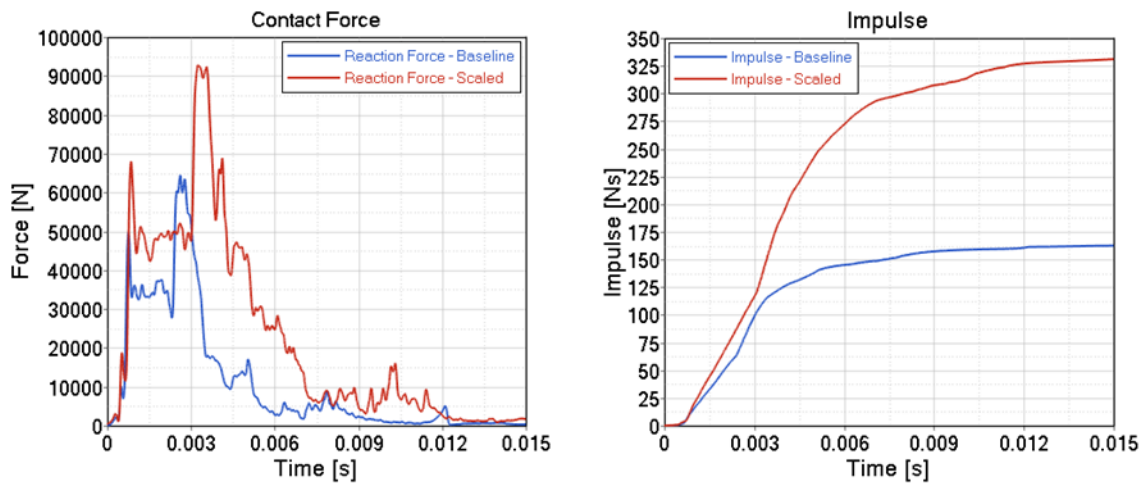


Figure 328. Comparison of the contact force and impulse of the impact between a commercial transport jet windshield and a 1.8/3.6 kg (4.0/8.0 lb) UAS at 128.6 m/s (250 knots)

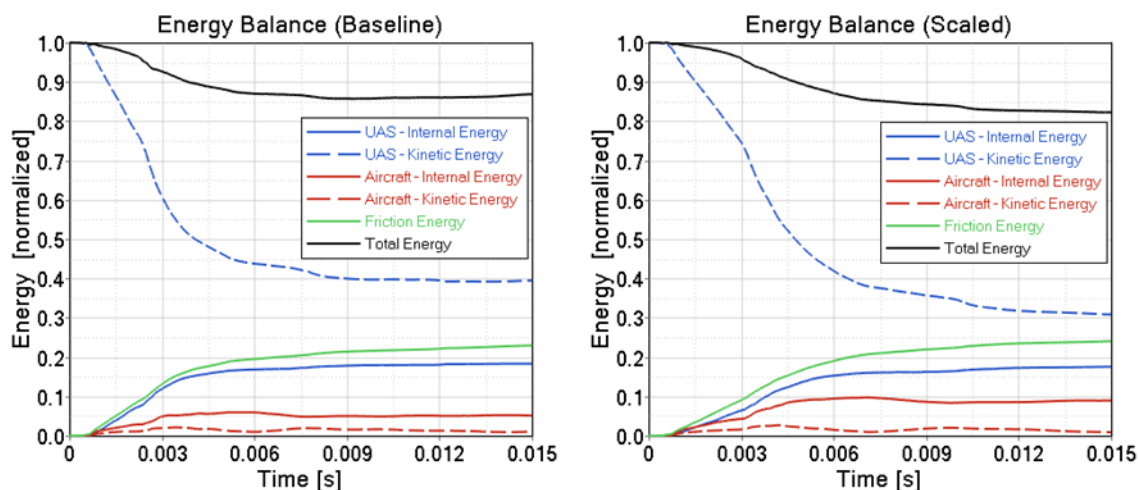


Figure 329. Comparison of the energy balance of the impact between a commercial transport jet windshield and a 1.8/3.6 kg (4.0/8.0 lb) UAS at 128.6 m/s (250 knots)

D.2 BUSINESS JET – BASELINE UAS (1.2 KG) VS SCALED UAS (1.8 KG)

D.2.1 Vertical Stabilizer

Impact simulations of a 1.8 kg (4.0 lb) UAS (case BFV1) and 3.6 kg (8.0 lb) UAS (case BF_sV1) against a vertical stabilizer are compared in terms of damage severity and kinematics. The initial conditions for both cases were based on BFV1, which was identified as the most critical case in the baseline simulations (see Section 4.4.1.1). Figure 330 depicts the comparison of the kinematics of the event. Figure 331 shows the comparison of the damage caused to the skin and the inner structure of the vertical stabilizer.

The 3.6 kg (8.0 lb) UAS damaged the skin, upper and lower ribs, and the front spar while the 1.8 kg (4.0 lb) UAS damaged the skin, upper, lower ribs and the front spar to a lesser degree. It can also be perceived in Figure 331 that the damage introduced into the skin and the ribs was greater for the case of 3.6 kg (8.0 lb) UAS than of the 1.8 kg (4.0 lb) UAS.

The damage introduced by both the UAS is classified as Level 4. Even with the same severity level, in terms of damage, the 3.6 kg (8.0 lb) UAS can be considered more severe than the 1.8 kg (4.0 lb) UAS.

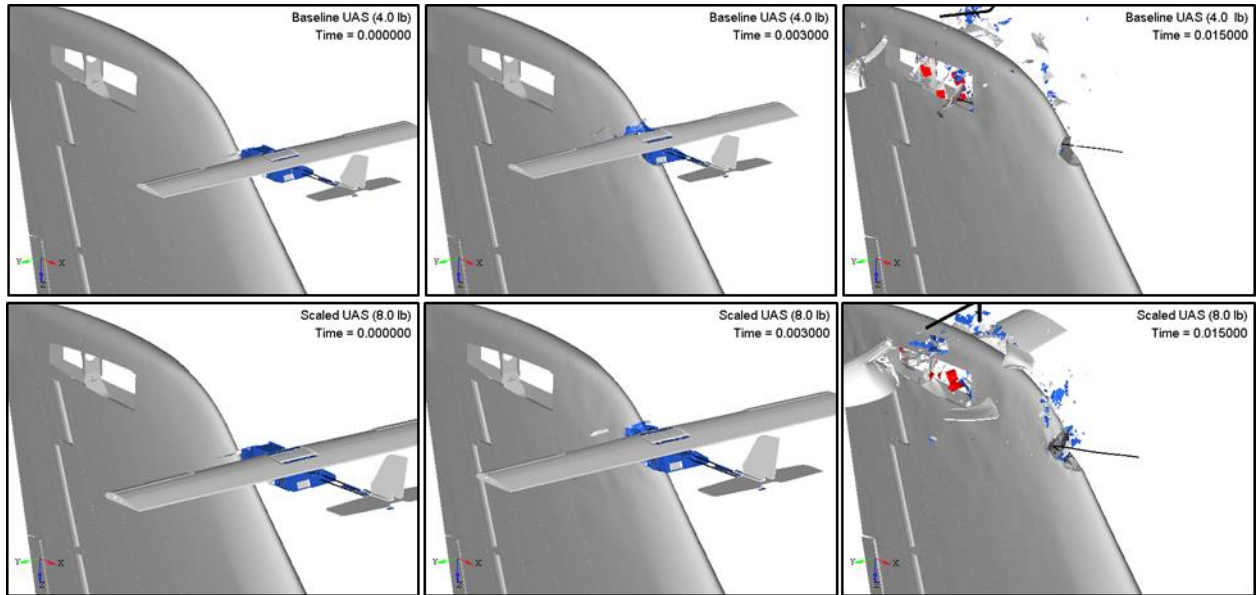


Figure 330. Comparison of the impact kinematics between a business jet vertical stabilizer and a 1.8/3.6 kg (4.0/8.0 lb) UAS at 128.6 m/s (250 knots)

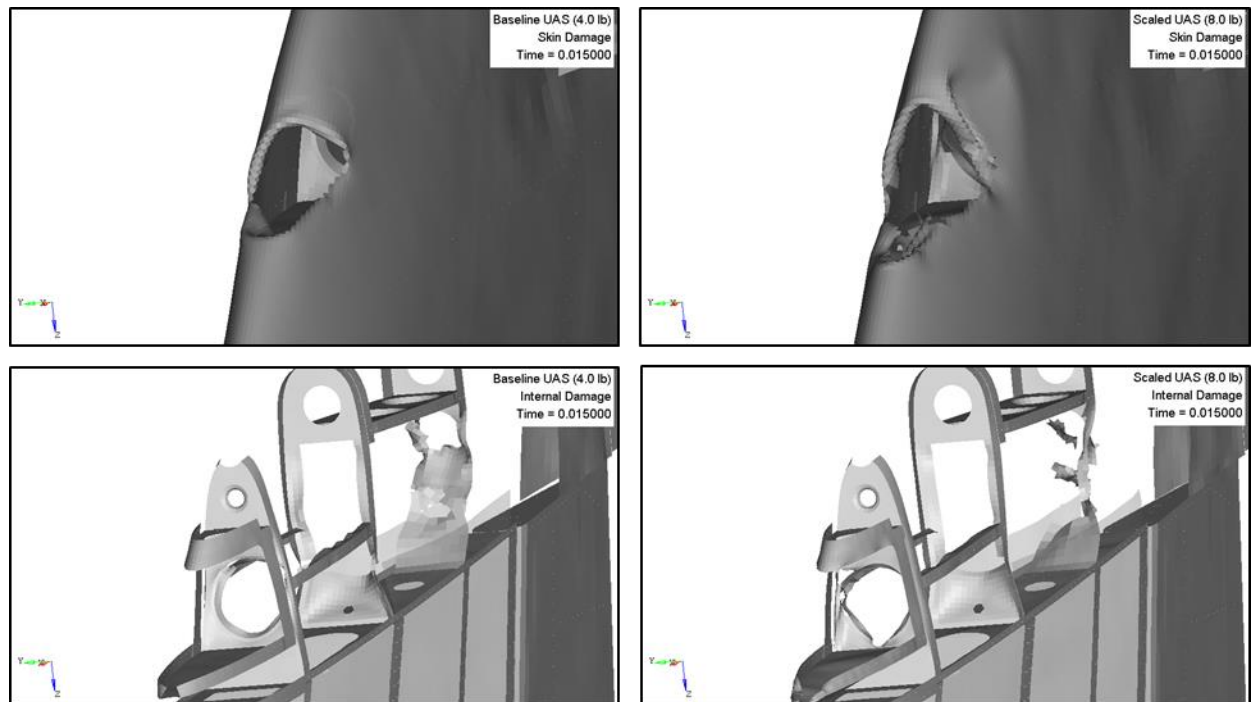


Figure 331. Comparison of external/internal damage sustained by a business jet vertical stabilizer impacted with a 1.8/3.6 kg (4.0/8.0 lb) UAS at 128.6 m/s (250 knots)

Figure 332 shows the comparison for the contact force and impulse between the 1.8/3.6 kg (4.0/8.0 lb) UAS and vertical stabilizer. Figure 333 shows the energy balance, normalized with the initial kinetic energy, for the impact comparison.

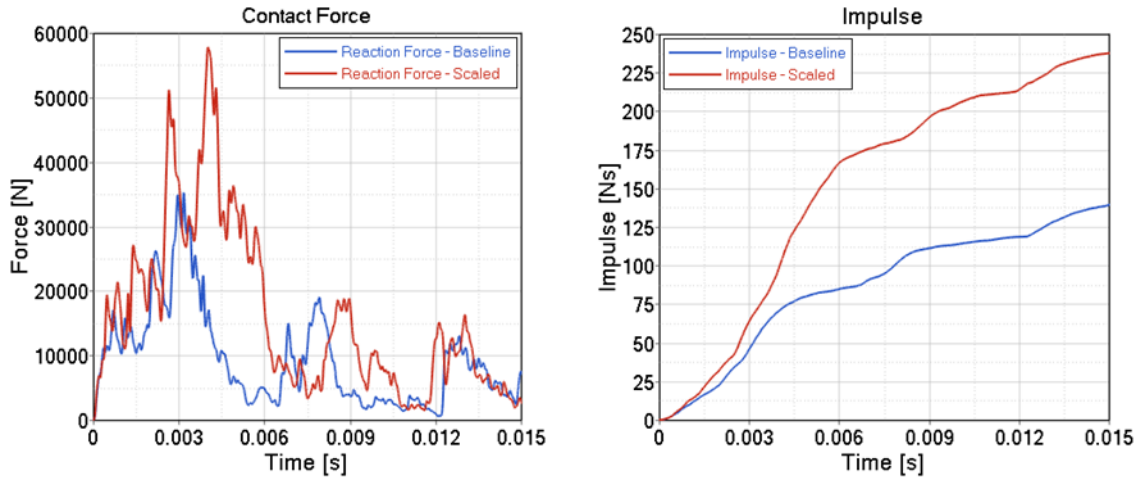


Figure 332. Comparison of the contact force and impulse of the impact between a business jet vertical stabilizer and a 1.8/3.6 kg (4.0/8.0 lb) UAS at 128.6 m/s (250 knots)

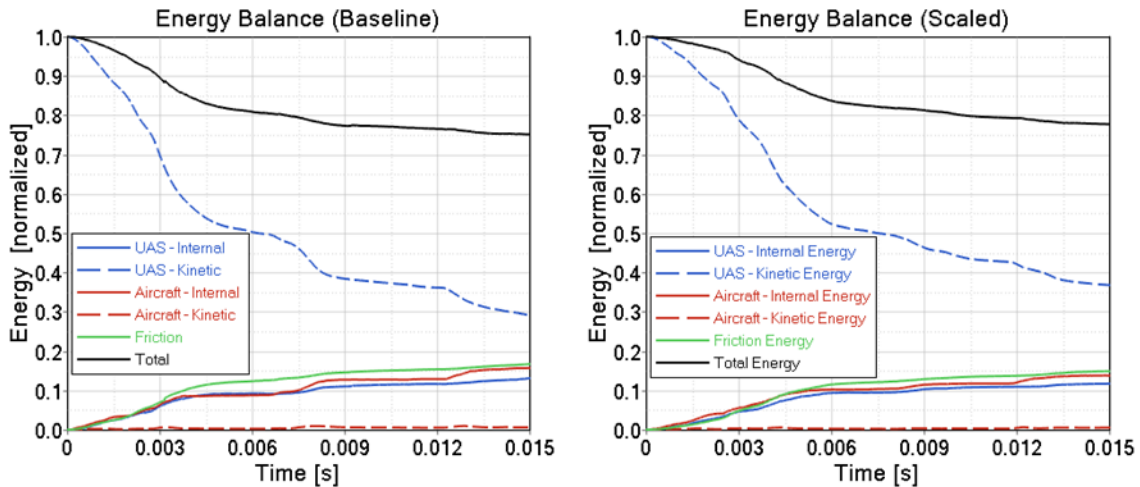


Figure 333. Comparison of the energy balance of the impact between a business jet vertical stabilizer and a 1.8/3.6 kg (4.0/8.0 lb) UAS at 128.6 m/s (250 knots)

The impulse for the 3.6 kg (8.0 lb) UAS was greater than for the 1.8 kg (4.0 lb) UAS. From the energy balance comparison, it can be observed that the 3.6 kg (8.0 lb) UAS absorbed a ratio of internal energy similar to the 1.8 kg (4.0 lb) UAS. In addition, it is apparent that the residual kinetic energy of the 3.6 kg (8.0 lb) UAS after impact was relatively higher than the 1.8 kg (4.0 lb) UAS.

D.2.2 Horizontal Stabilizer

Impact simulations of a 1.8 kg (4.0 lb) UAS (case BFH1) and 3.6 kg (8.0 lb) UAS (case BFH1) against a horizontal stabilizer are compared in terms of damage severity and kinematics. The initial conditions for both cases were based on BFH1, which was identified as the most critical case in the baseline simulations (see Section 4.4.2.1). Figure 334 depicts the comparison of the kinematics of the event. Figure 335 shows the comparison of the damage caused to the skin and the inner structure of the horizontal stabilizer.

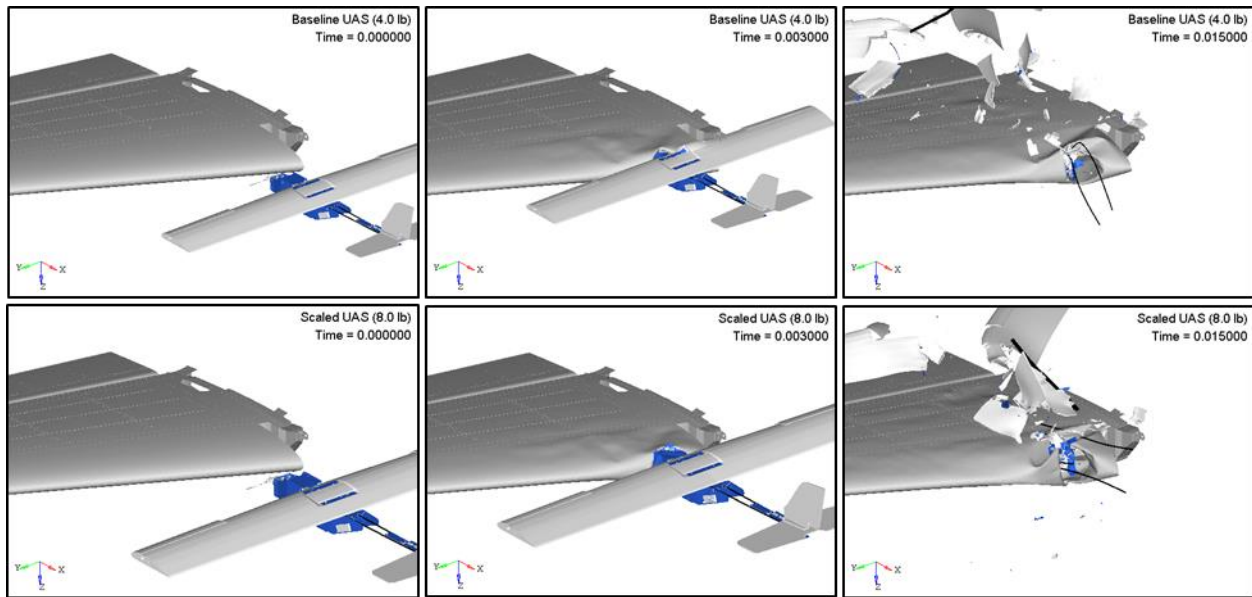


Figure 334. Comparison of the impact kinematics between a business jet horizontal stabilizer and a 1.8/3.6 kg (4.0/8.0 lb) UAS at 128.6 m/s (250 knots)

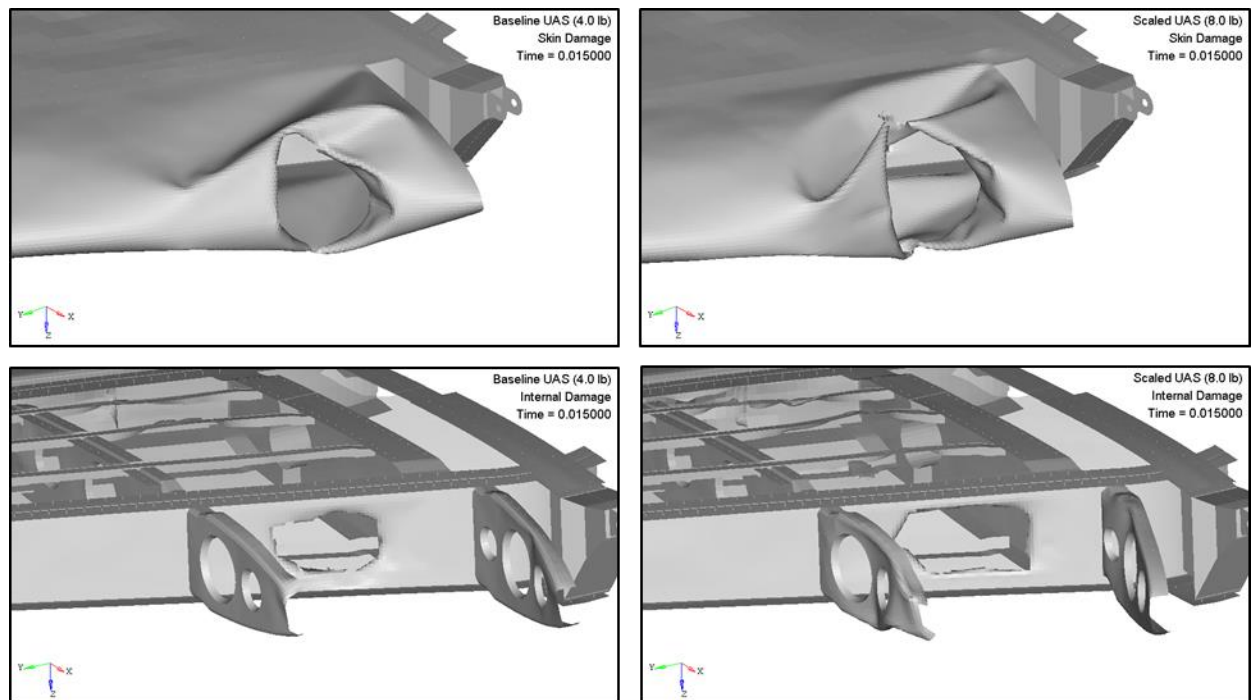


Figure 335. Comparison of external/internal damage sustained by a business jet horizontal stabilizer impacted with a 1.8/3.6 kg (4.0/8.0 lb) UAS at 128.6 m/s (250 knots)

Both 1.8 kg (4.0 lb) and 3.6 kg (8.0 lb) UAS damaged the skin, the nose ribs, and the front spar. From Figure 335, it can also be perceived that the damage introduced into the skin and front spar for the 3.6 kg (8.0 lb) UAS was considerably greater than the 1.8 kg (4.0 lb) UAS.

The damage introduced by the 1.8 kg (4.0 lb) UAS as well as by the 3.6 kg (8.0 lb) UAS are classified as Level 4. In terms of damage, the 3.6 kg (8.0 lb) UAS can be considered slightly more severe than the 1.8 kg (4.0 lb) UAS due to the increase in size of the damage.

Figure 336 shows the comparison for the contact force and impulse between the 1.8/3.6 kg (4.0/8.0 lb) UAS and horizontal stabilizer. Figure 337 shows the energy balance, normalized with the initial kinetic energy, for the impact comparison.

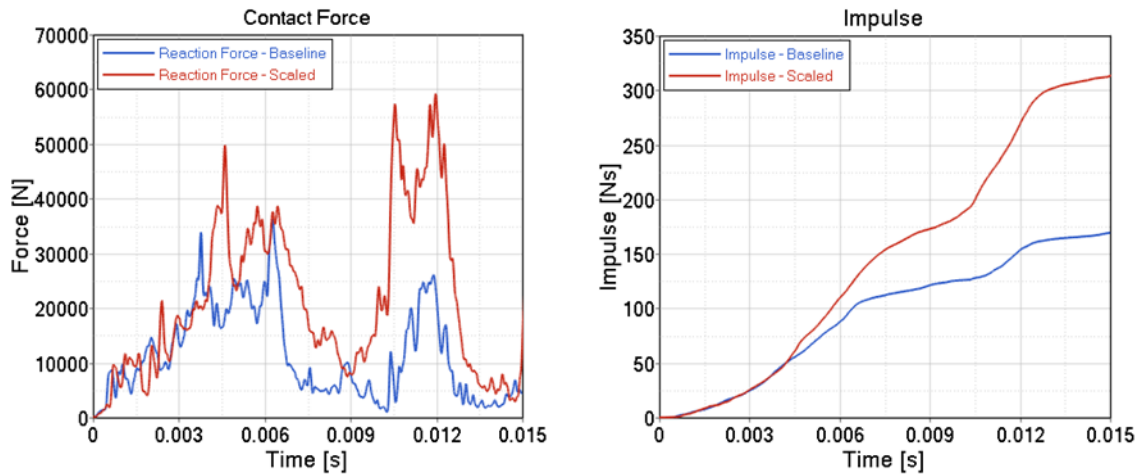


Figure 336. Comparison of the contact force and impulse of the impact between a business jet horizontal stabilizer and a 1.8/3.6 kg (4.0/8.0 lb) UAS at 128.6 m/s (250 knots)

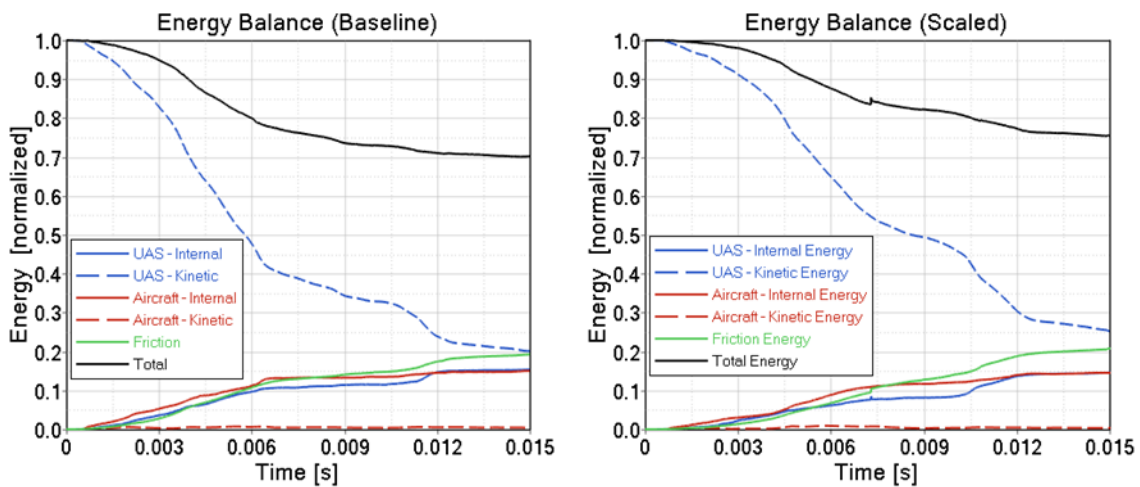


Figure 337. Comparison of the energy balance of the impact between a business jet horizontal stabilizer and a 1.8/3.6 kg (4.0/8.0 lb) UAS at 128.6 m/s (250 knots)

The impulse for the 3.6 kg (8.0 lb) UAS was greater than for the 1.8 kg (4.0 lb) UAS. From the energy balance comparison, it can be observed that the 3.6 kg (8.0 lb) UAS absorbed a similar ratio of internal energy as the 1.8 kg (4.0 lb) UAS. In addition, it is apparent that the residual kinetic energy of the 3.6 kg (8.0 lb) UAS after impact was relatively higher than the 1.8 kg (4.0 lb) UAS.

D.2.3 Wing Leading Edge

Impact simulations of a 1.8 kg (4.0 lb) UAS (case BFW2) and 3.6 kg (8.0 lb) UAS (case BFsW2) against a wing leading edge are compared in terms of damage severity and kinematics. The initial conditions for both cases were based on BFW2, which was identified as the most critical case in the baseline simulations (see Section 4.4.3.1). Figure 338 depicts the comparison of the kinematics of the event. Figure 339 shows the comparison of the damage caused to the skin and the inner structure of the wing.

Both cases displayed damaged to the skin and the anti-icing system with no visible deformation in the front spar. It can also be perceived in Figure 339 that the damage introduced into the skin and the anti-icing system for the case of 3.6 kg (8.0 lb) UAS was considerably greater than the 1.8 kg (4.0 lb) UAS.

The damage introduced by both UASs is classified as Level 3 with risk of fire due to battery. Even with the same damage level, the 3.6 kg (8.0 lb) UAS can be considered more severe than the 1.8 kg (4.0 lb) UAS.

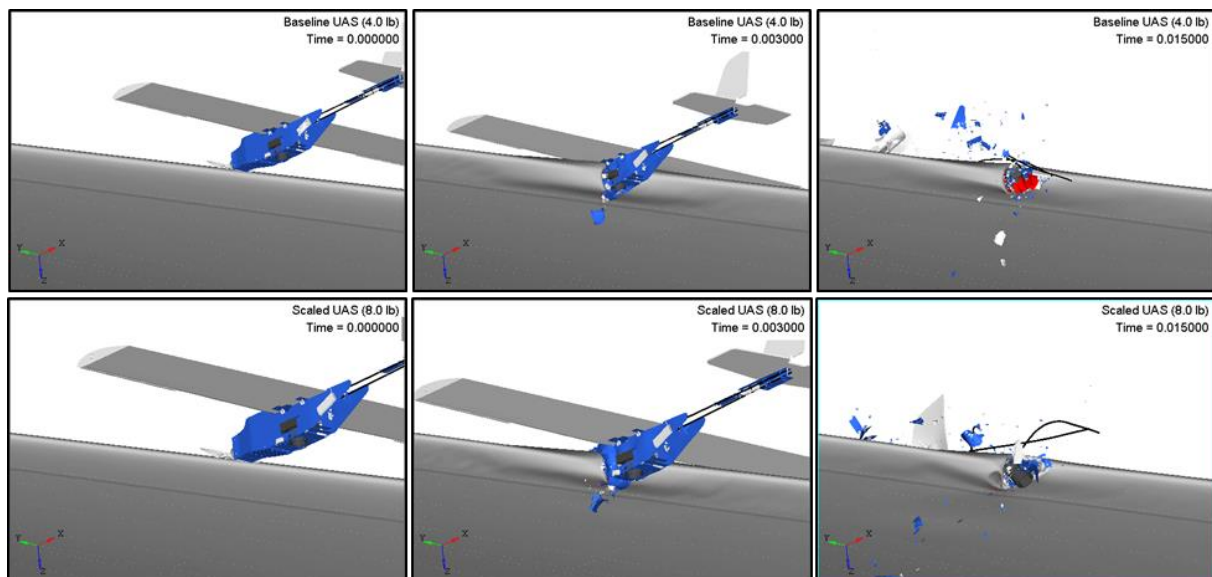


Figure 338. Comparison of the impact kinematics between a business jet wing and a 1.8/3.6 kg (4.0/8.0 lb) UAS at 128.6 m/s (250 knots)

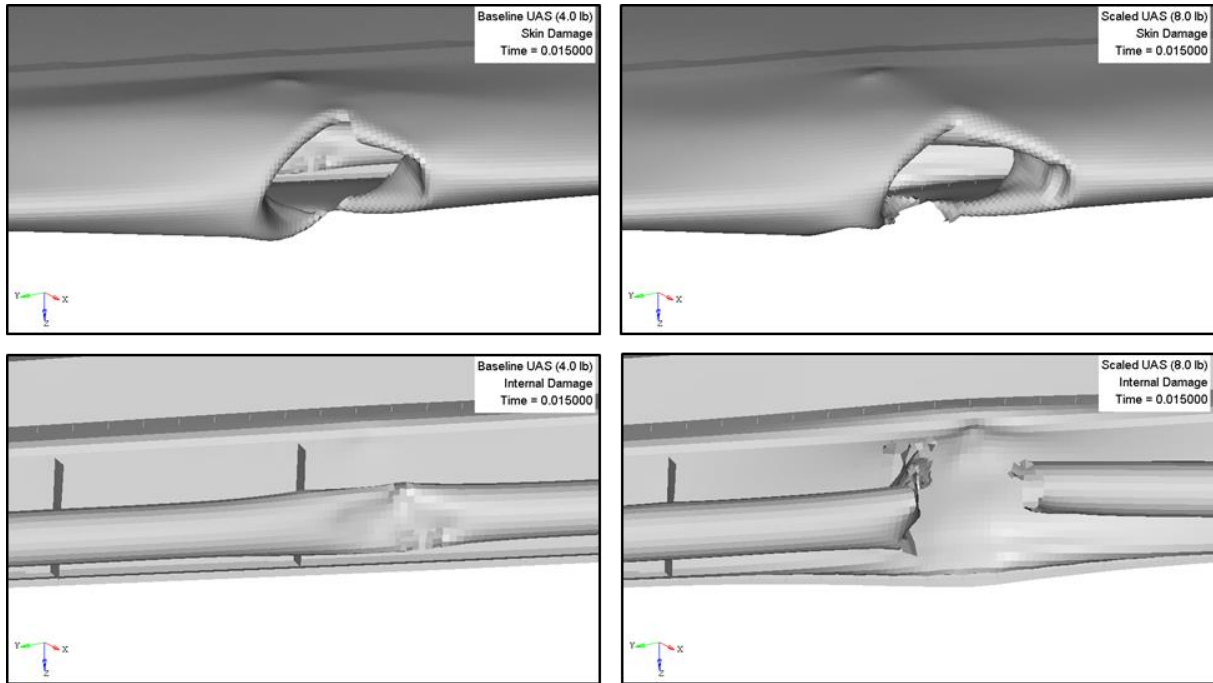


Figure 339. Comparison of external/internal damage sustained by a business jet wing impacted with a 1.8/3.6 kg (4.0/8.0 lb) UAS at 128.6 m/s (250 knots)

Figure 340 shows the comparison for the contact force and impulse between the 1.8/3.6 kg (4.0/8.0 lb) UAS and wing. Figure 341 shows the energy balance, normalized with the initial kinetic energy, for the impact comparison.

The impulse for the 3.6 kg (8.0 lb) UAS was greater than for the 1.8 kg (4.0 lb) UAS. From the energy balance comparison, it can be observed that the 3.6 kg (8.0 lb) UAS absorbed a ratio of internal energy similar to the 1.8 kg (4.0 lb) UAS. In addition, it is apparent that the residual kinetic energy of the 3.6 kg (8.0 lb) UAS after impact was higher relatively than the 1.8 kg (4.0 lb) UAS.

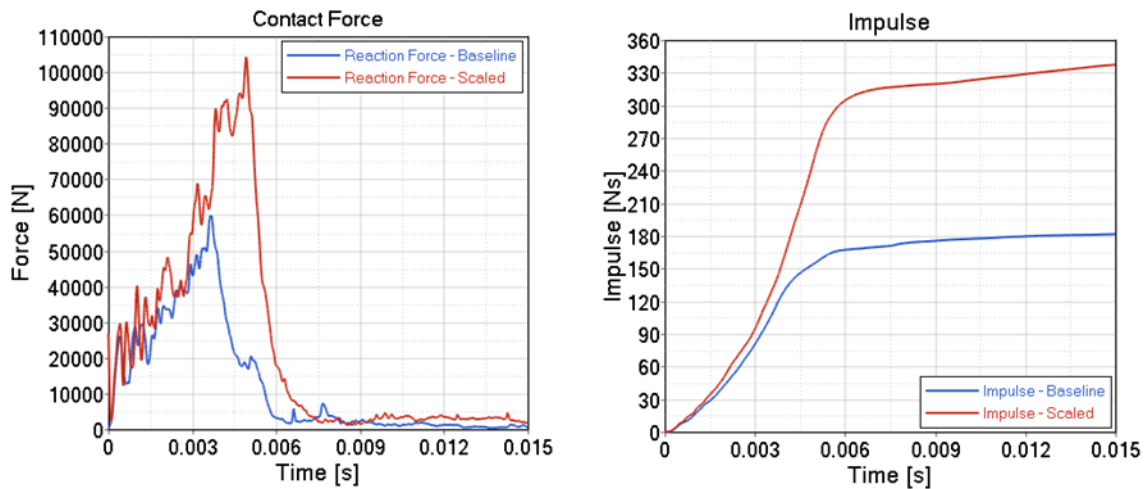


Figure 340. Comparison of the contact force and impulse of the impact between a business jet wing and a 1.8/3.6 kg (4.0/8.0 lb) UAS at 128.6 m/s (250 knots)

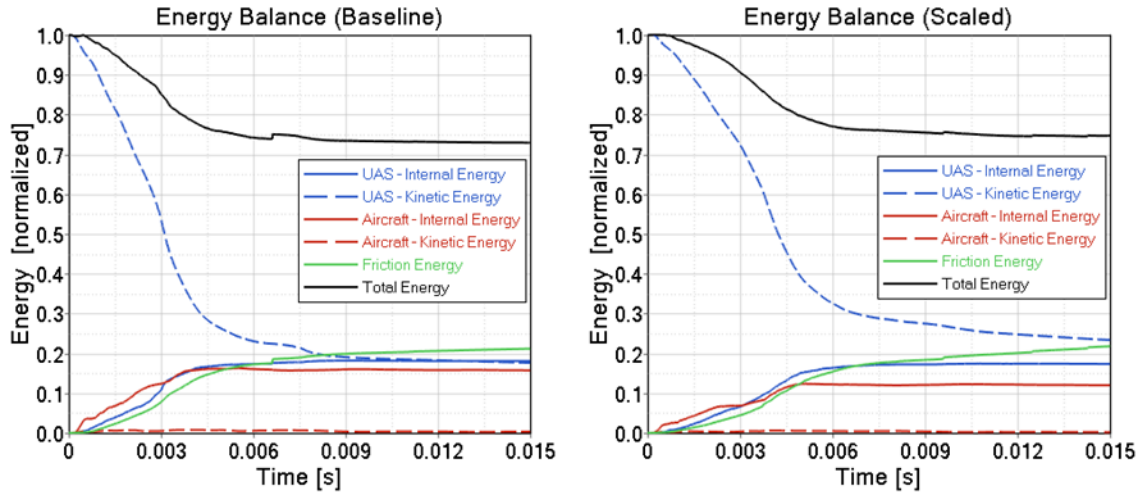


Figure 341. Comparison of the energy balance of the impact between a business jet wing and a 1.8/3.6 kg (4.0/8.0 lb) UAS at 128.6 m/s (250 knots)

D.2.4 Windshield

Impact simulations of a 1.8 kg (4.0 lb) UAS (case BFC1) and 3.6 kg (8.0 lb) UAS (case BFC1) against a windshield are compared in terms of damage severity and kinematics. The initial conditions for both cases were based on BFC1, which was identified as the most critical case in the baseline simulations (see Section 4.4.4.1). Figure 342 depicts the comparison of the kinematics of the event. Figure 343 shows the comparison of the damage caused to the windshield and surrounding structure.

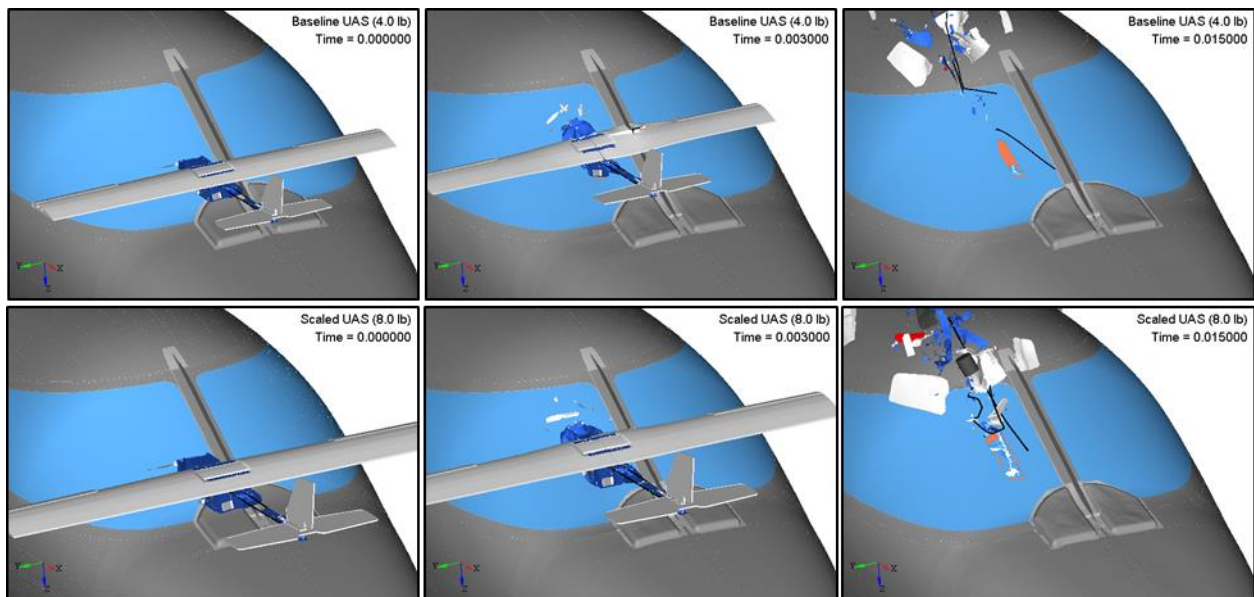


Figure 342. Comparison of the impact kinematics between a business jet windshield and a 1.8/3.6 kg (4.0/8.0 lb) UAS at 128.6 m/s (250 knots)

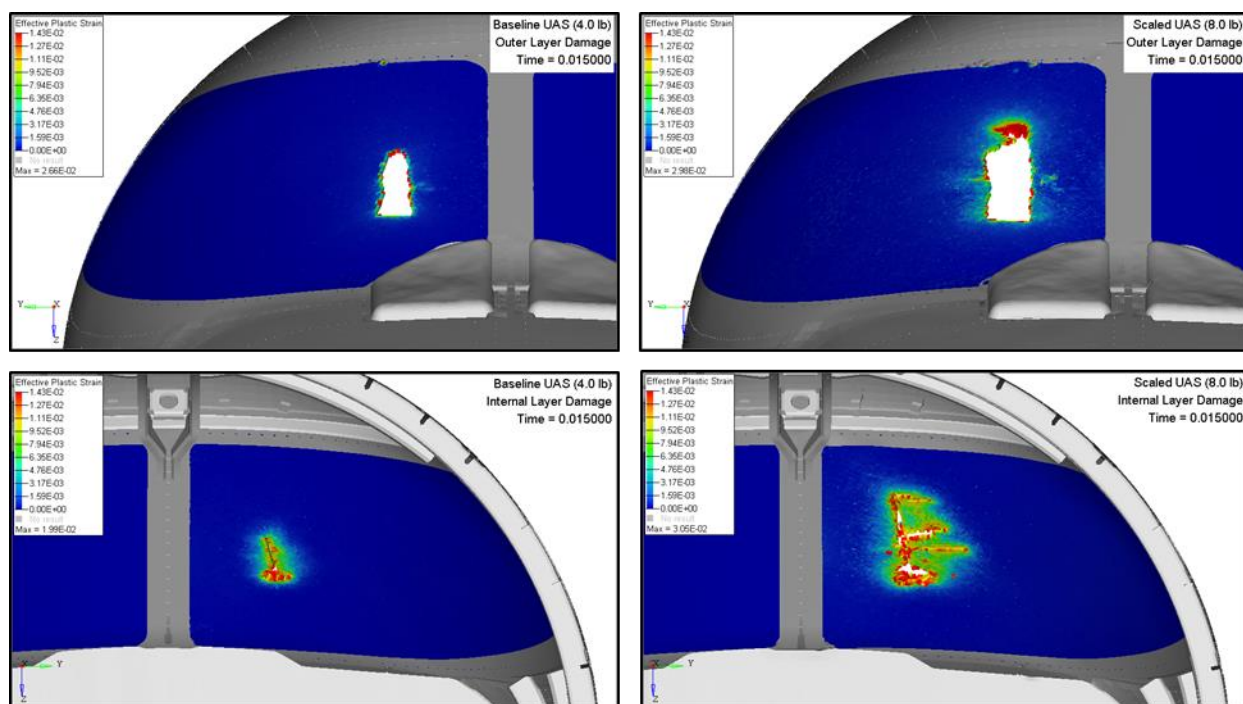


Figure 343. Comparison of external/internal damage sustained by a business jet windshield impacted with a 1.8/3.6 kg (4.0/8.0 lb) UAS at 128.6 m/s (250 knots)

Both UAS impacted the windshield and slid over because of the windshield deflection. The 1.8 kg (4.0 lb) UAS caused severe damage to the outer windshield layer and permanent deformation to the internal layer while the 3.6 kg (8.0 lb) UAS severely damaged the outer and internal windshield layer. Note that the top three plastic strain plots show only the outer layer of the windshield transparency and that the lower three plots show the layer which sustained the maximum plastic strain.

The damage introduced by the 1.8 kg (4.0 lb) UAS is classified as Level 3 whereas the damage introduced by the 3.6 kg (8.0 lb) UAS is classified as Level 4. With no sign of severe damage on the internal layer from the 1.8 kg (4.0 lb) UAS impact, it is evident that 3.6 kg (8.0 lb) UAS impact is considered more severe.

Figure 344 shows the comparison for the contact force and impulse between the 1.8/3.6 kg (4.0/8.0 lb) UAS and windshield. Figure 345 shows the energy balance, normalized with the initial kinetic energy, for the impact comparison.

The impulse for the 3.6 kg (8.0 lb) UAS was greater than for the 1.8 kg (4.0 lb) UAS. From the energy balance comparison, it can be observed that the 3.6 kg (8.0 lb) UAS absorbed a slightly smaller internal energy than the 1.8 kg (4.0 lb) UAS. In addition, it is apparent that the residual kinetic energy of the 3.6 kg (8.0 lb) UAS after impact was smaller relatively than the 1.8 kg (4.0 lb) UAS.

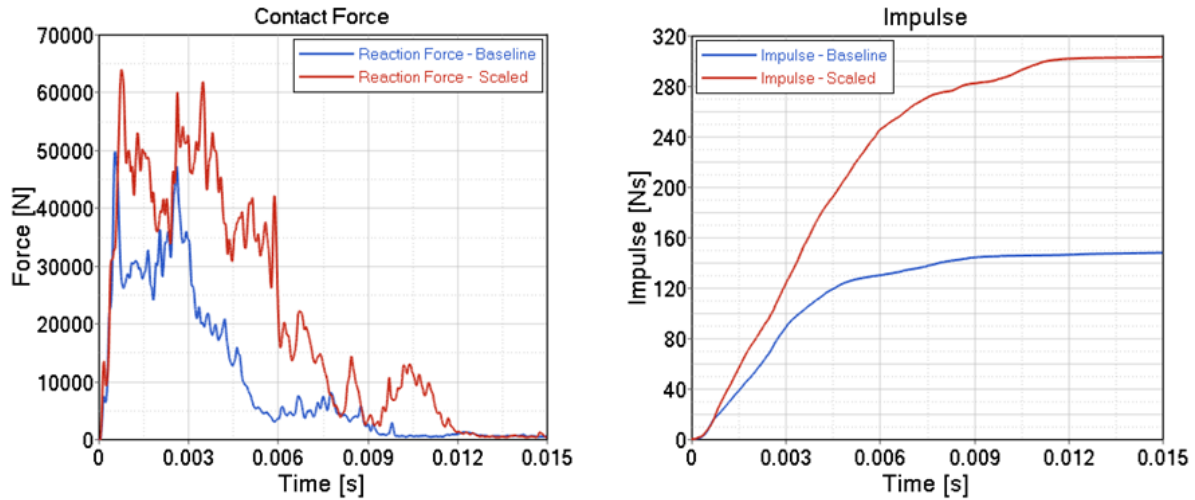


Figure 344. Comparison of the contact force and impulse of the impact between a business jet windshield and a 1.8/3.6 kg (4.0/8.0 lb) UAS at 128.6 m/s (250 knots)

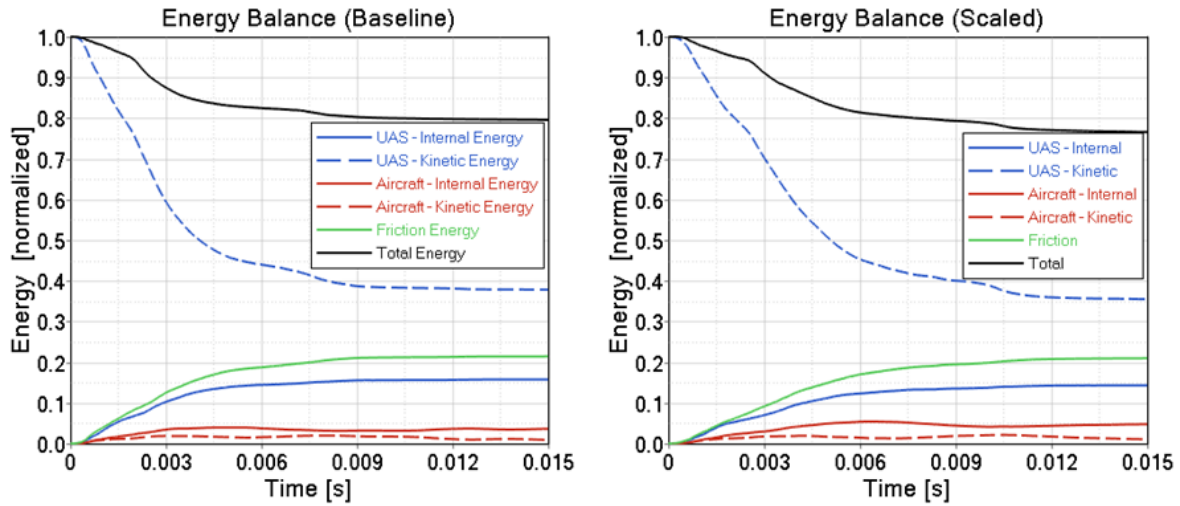


Figure 345. Comparison of the energy balance of the impact between a business jet windshield and a 1.8/3.6 kg (4.0/8.0 lb) UAS at 128.6 m/s (250 knots)

APPENDIX E – VELOCITY SENSITIVITY STUDY

E.1 COMMERCIAL TRANSPORT JET

E.1.1 Vertical Stabilizer

Impact simulations of a 1.8 kg (4.0 lb) UAS (case CFV1) with three different velocities (56.7, 128.6, 187.8 m/s; or 110, 250, 365 knots) against a vertical stabilizer are compared in terms of damage severity and kinematics. The initial conditions for all the above cases except for the velocity were based on CFV1, which was identified as the most critical case in the baseline simulations (see Section 4.3.1.1). Figure 345 depicts the comparison of the kinematics of the event. Figure 345 shows the comparison of the damage caused to the skin and the inner structure of the vertical stabilizer.

The UAS at 56.7 m/s (110 knots) slightly deformed the skin with no visible internal damage. On the other hand, the UAS at 128.6 m/s (250 knots) damaged the skin, the upper and lower ribs and front spar while the UAS at 187.8 m/s (365 knots) damaged the skin, upper and lower ribs, the front spar to a greater degree and the inspar ribs. It can also be perceived in Figure 345 that the damage severity increases with respect to the increase in velocity.

The damage introduced by UAS at 56.7 m/s (110 knots) is classified as level 2 whereas the damage introduced by both UAS at 128.6 m/s (250 knots) and 187.8 m/s (365 knots) is classified as level 4. It is evident that higher velocity results in greater damage.

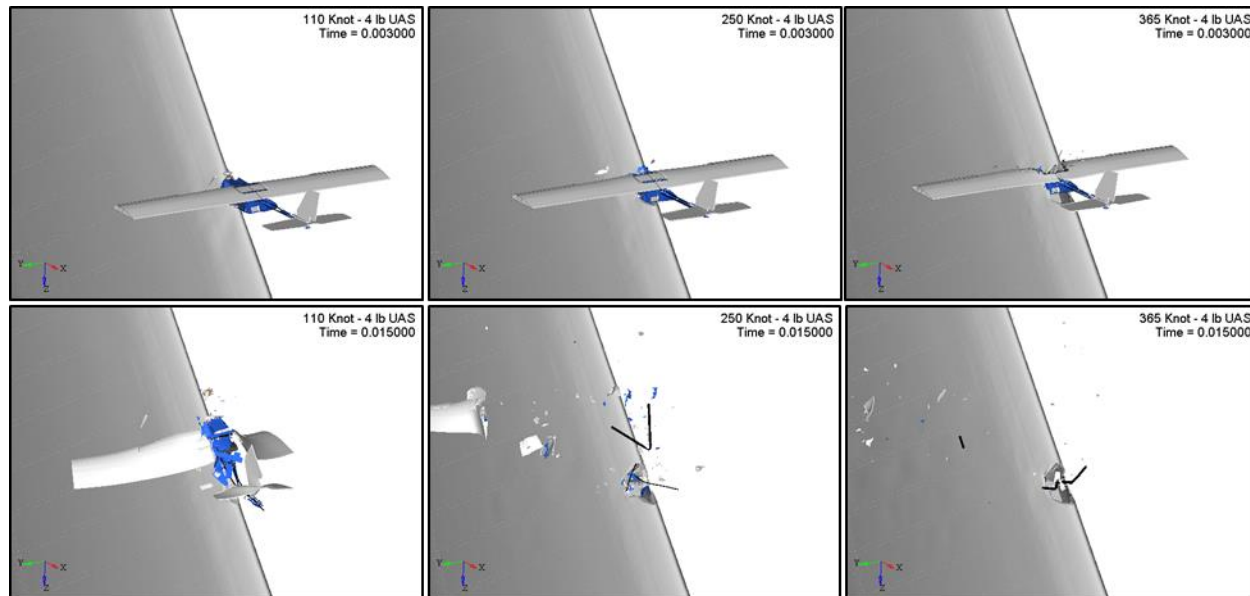


Figure 346. Comparison of the impact kinematics between a commercial transport jet vertical stabilizer and a 1.81 kg UAS at 56.7/128.6/187.8 m/s (110/250/365 knots)

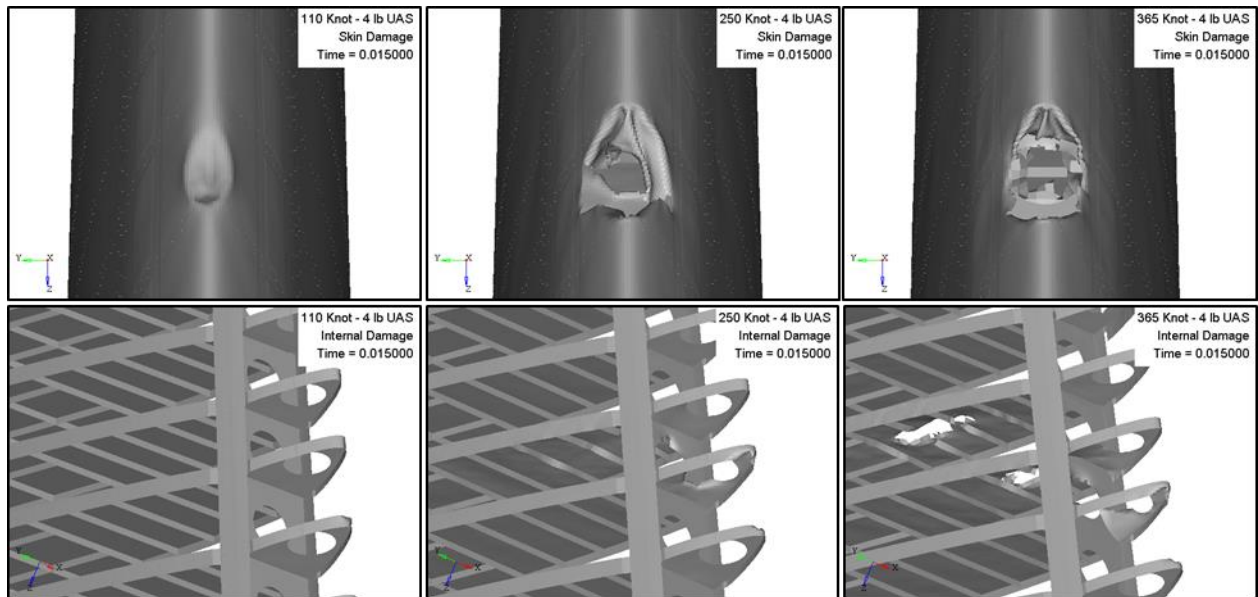


Figure 347. Comparison of external/internal damage sustained by a commercial transport jet vertical stabilizer impacted with a 1.81 kg UAS at 56.7/128.6/187.8 m/s (110/250/365 knots)

Figure 347 shows the comparison for the contact force and impulse between the UAS and vertical stabilizer for three different velocities. Figure 348 shows the normalized energy balance for the impact comparison.

The impulse increases with higher velocities. From the energy balance comparison, it can be observed that the UAS absorbed greater internal energy at lower velocity than the UAS at higher velocity. The kinetic energy ratios do not appear to have specific trends related to the impact velocity; therefore, the visible damage and kinematics are used to draw conclusions.

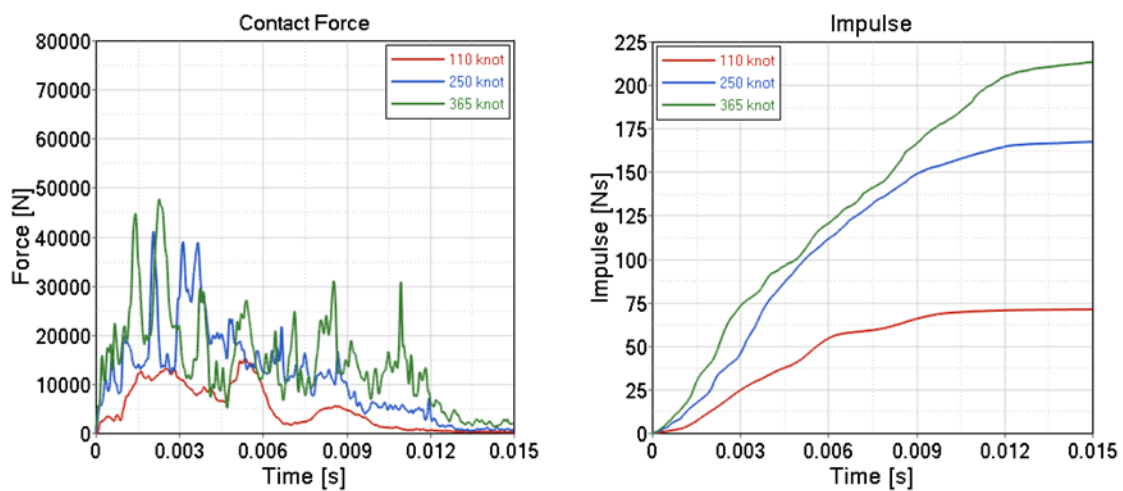


Figure 348. Comparison of the contact force and impulse of the impact between a commercial transport jet vertical stabilizer and a 1.81 kg UAS at 56.7/128.6/187.8 m/s (110/250/365 knots)

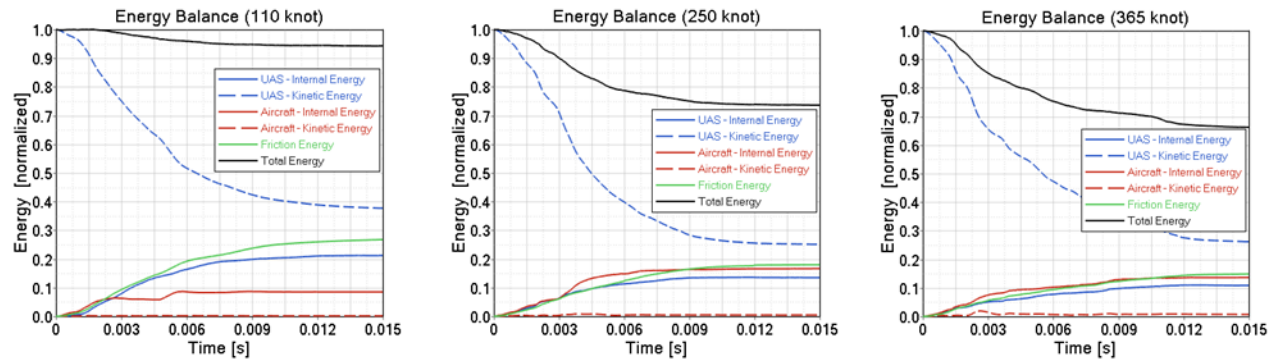


Figure 349. Comparison of the normalized energy balance of the impact between a commercial transport jet vertical stabilizer and a 1.81 kg UAS at 56.7/128.6/187.8 m/s (110/250/365 knots)

E.1.2 Horizontal Stabilizer

Impact simulations of a 1.8 kg (4.0 lb) UAS (case CFH2) with three different velocities (56.7, 128.6, 187.8 m/s; or 110, 250, 365 knots) against a horizontal stabilizer are compared in terms of damage severity and kinematics. The initial conditions for all the above cases except for the velocity were based on CFH2, which was identified as the most critical case in the baseline simulations (see Section 4.3.2.1). Figure 350 depicts the comparison of the kinematics of the event. Figure 351 shows the comparison of the damage caused to the skin and the inner structure of the horizontal stabilizer.

The UAS at 56.7 m/s (110 knots) slightly deformed the skin and the nose rib with no other visible internal damage. On the other hand, the UAS at 128.6 m/s (250 knots) damaged the skin, the nose ribs and front spar while the UAS at 187.8 m/s (365 knots) damaged the skin, the nose ribs and the front spar to a greater degree. It can also be perceived in Figure 351 that the damage severity increases with respect to the increase in velocity.

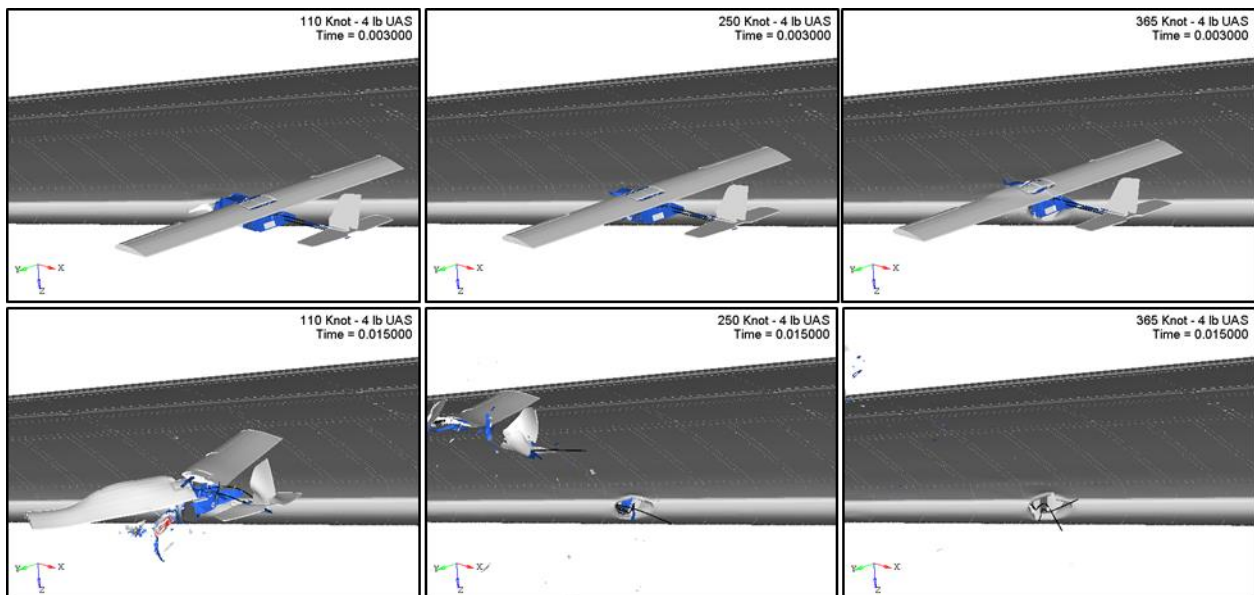


Figure 350. Comparison of the impact kinematics between a commercial transport jet horizontal stabilizer and a 1.81 kg UAS at 56.7/128.6/187.8 m/s (110/250/365 knots)

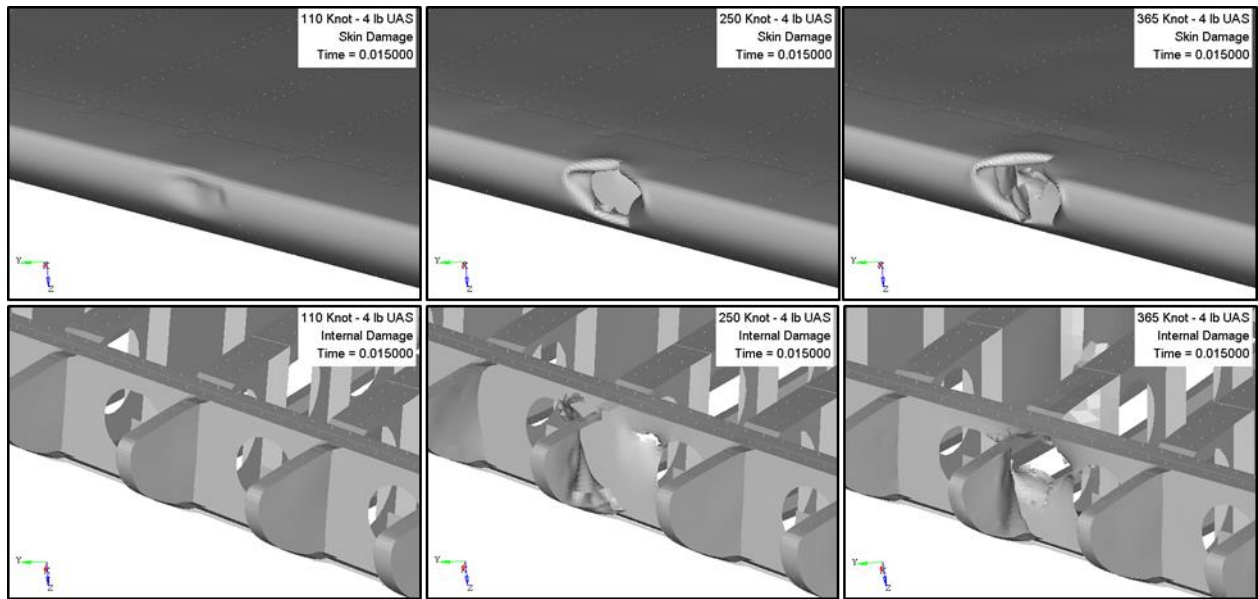


Figure 351. Comparison of external/internal damage sustained by a commercial transport jet horizontal stabilizer impacted with a 1.81 kg UAS at 56.7/128.6/187.8 m/s (110/250/365 knots)

The damage introduced by UAS at 56.7 m/s (110 knots) is classified as level 3 whereas the damage introduced by both UAS at 128.6 m/s (250 knots) and 187.8 m/s (365 knots) is classified as level 4. In addition, the risk of fire due to the battery is present only for the impacts of UAS at 56.7 and 128.6 m/s (110 and 250 knots). It is evident that higher velocity results in greater damage.

Figure 352 shows the comparison for the contact force and impulse between the UAS and horizontal stabilizer for three different velocities. Figure 353 shows the normalized energy balance for the impact comparison.

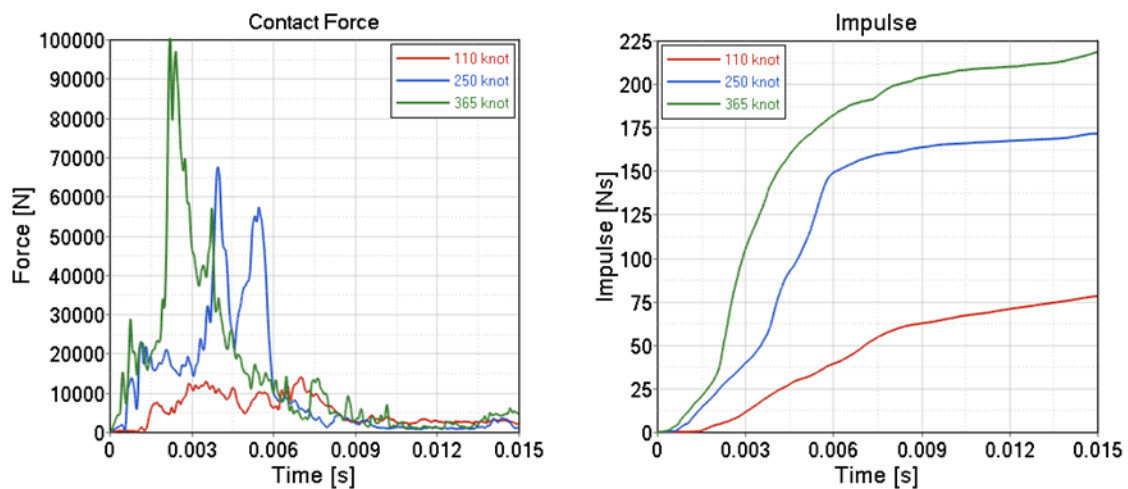


Figure 352. Comparison of the contact force and impulse of the impact between a commercial transport jet horizontal stabilizer and a 1.81 kg UAS at 56.7/128.6/187.8 m/s (110/250/365 knots)

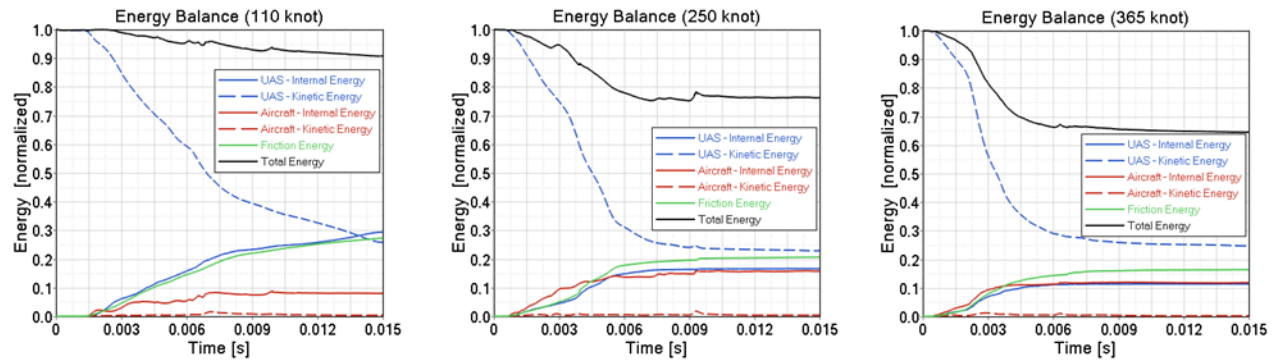


Figure 353. Comparison of the normalized energy balance of the impact between a commercial transport jet horizontal stabilizer and a 1.81 kg UAS at 56.7/128.6/187.8 m/s (110/250/365 knots)

The impulse increases with higher velocities. From the energy balance comparison, it can be observed that the UAS absorbed greater internal energy at lower velocity than the UAS at higher velocity. The kinetic energy ratios do not appear to have specific trends related to the impact velocity; therefore, the visible damage and kinematics are used to draw conclusions.

E.1.3 Wing Leading Edge

Impact simulations of a 1.8 kg (4.0 lb) UAS (case CFW3) with three different velocities (56.7, 128.6, 187.8 m/s; or 110, 250, 365 knots) against a wing leading edge are compared in terms of damage severity and kinematics. The initial conditions for all the above cases except for the velocity were based on CFW3, which was identified as the most critical case in the baseline simulations (see Section 4.3.3.1). Figure 354 depicts the comparison of the kinematics of the event. Figure 355 shows the comparison of the damage caused to the skin and the inner structure of the wing.

The UAS at 56.7 m/s (110 knots) damaged slightly the skin with no visible internal deformation. On the other hand, the UAS at 128.6 m/s (250 knots) damaged the skin and sub-spar while the UAS at 187.8 m/s (365 knots) damaged the skin, the sub-spar to a greater degree and also the front spar. It can also be perceived in Figure 355 that the damage severity increases with respect to the increase in velocity.

The damage introduced by UAS at 56.7 m/s (110 knots) is classified as level 2 whereas the damage introduced by UAS at 128.6 m/s (250 knots) is classified as level 3 and for the 187.8 m/s (365 knots) velocity is classified as level 4. In addition, the risk of fire due to the battery is only present for the impact of UAS at 187.8 m/s (365 knots). It is evident that higher velocity results in greater damage.

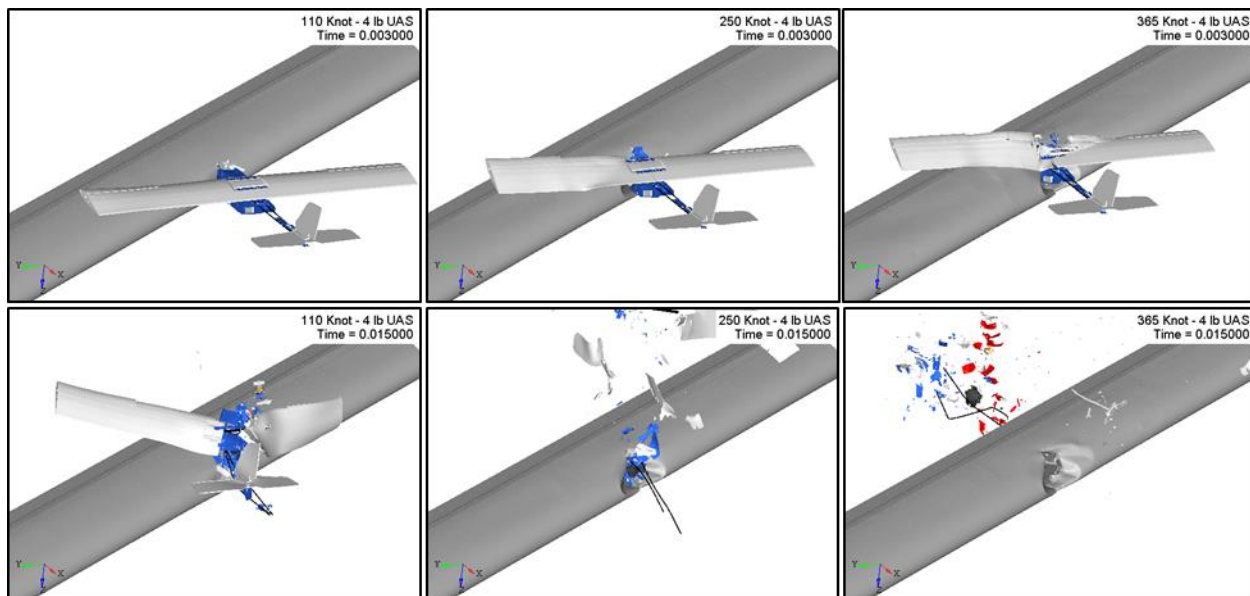


Figure 354. Comparison of the impact kinematics between a commercial transport jet wing and a 1.81 kg UAS at 56.7/128.6/187.8 m/s (110/250/365 knots)

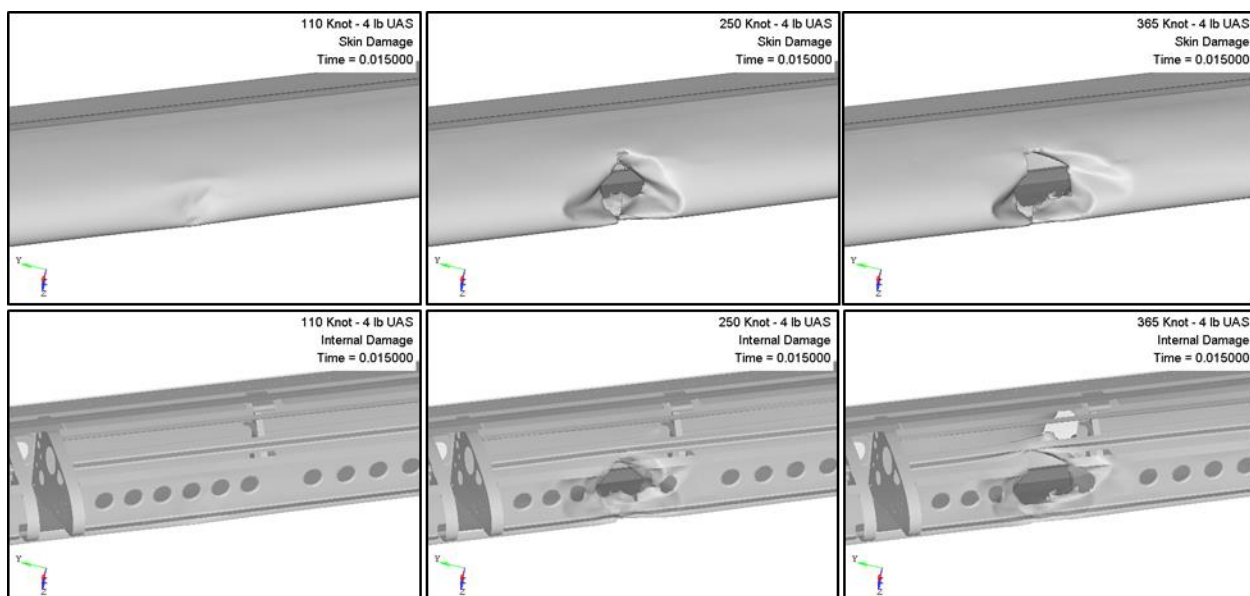


Figure 355. Comparison of external/internal damage sustained by a commercial transport jet wing impacted with a 1.81 kg UAS at 56.7/128.6/187.8 m/s (110/250/365 knots)

Figure 356 shows the comparison for the contact force and impulse between the UAS and wing for three different velocities. Figure 357 shows the normalized energy balance for the impact comparison.

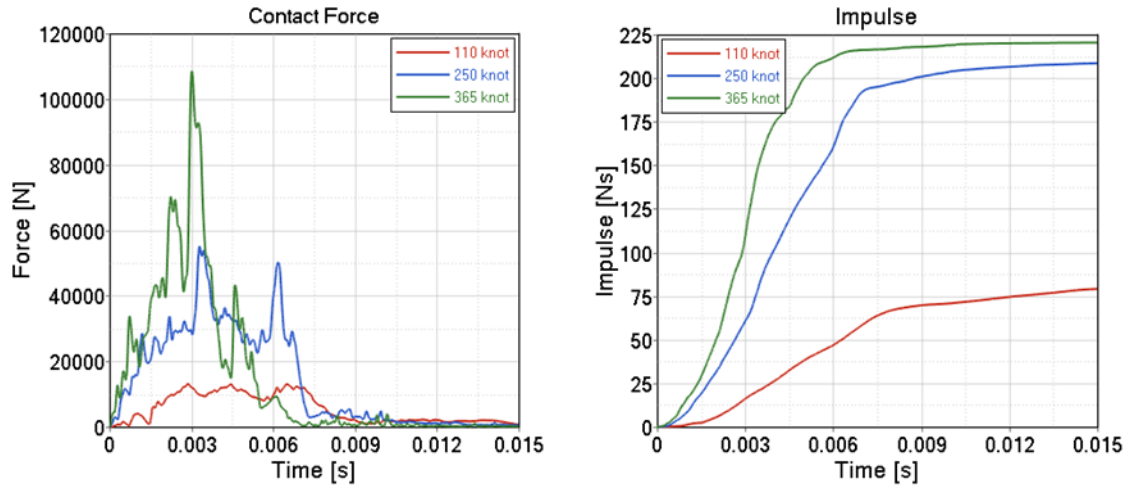


Figure 356. Comparison of the contact force and impulse of the impact between a commercial transport jet wing and a 1.81 kg UAS at 56.7/128.6/187.8 m/s (110/250/365 knots)

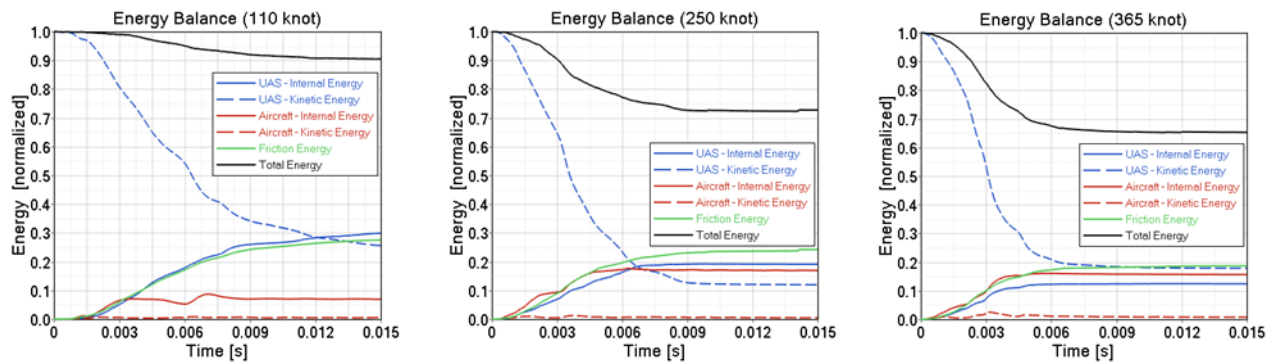


Figure 357. Comparison of the normalized energy balance of the impact between a commercial transport jet wing and a 1.81 kg UAS at 56.7/128.6/187.8 m/s (110/250/365 knots)

The impulse increases with higher velocities. From the energy balance comparison, it can be observed that the internal energy ratios do not appear to have specific trends related to the impact velocity. In addition, the residual kinetic energy after the impact was greater for UAS at lower velocities than for the UAS at higher velocities. This is an indication that the kinetic energy of the UAS at lower velocities was deflected more efficiently than that of the UAS at higher velocities, for which most of the energy was absorbed in the impact.

E.1.4 Windshield

Impact simulations of a 1.8 kg (4.0 lb) UAS (case CFC1) with three different velocities (56.7, 128.6, 187.8 m/s; or 110, 250, 365 knots) against a windshield are compared in terms of damage severity and kinematics. The initial conditions for all the above cases except for the velocity were based on CFC1, which was identified as the most critical case in the baseline simulations (see Section 4.3.4.1). Figure 358 depicts the comparison of the kinematics of the event. Figure 359 shows the comparison of the damage caused to the windshield and surrounding structure.

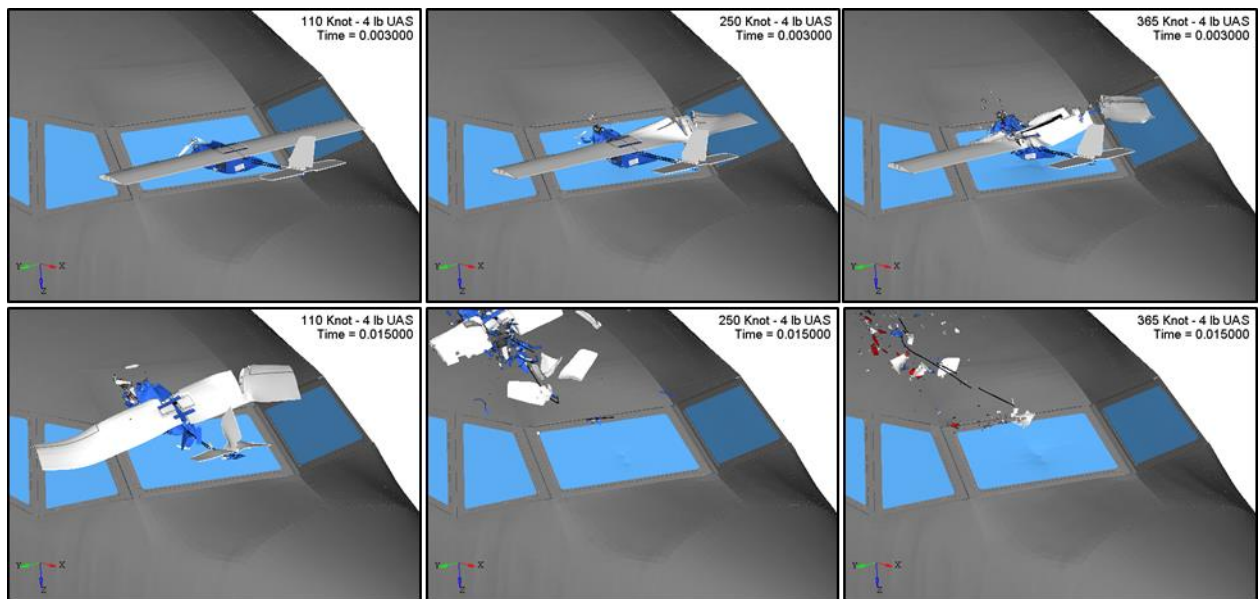


Figure 358. Comparison of the impact kinematics between a commercial transport jet windshield and a 1.81 kg UAS at 56.7/128.6/187.8 m/s (110/250/365 knots)

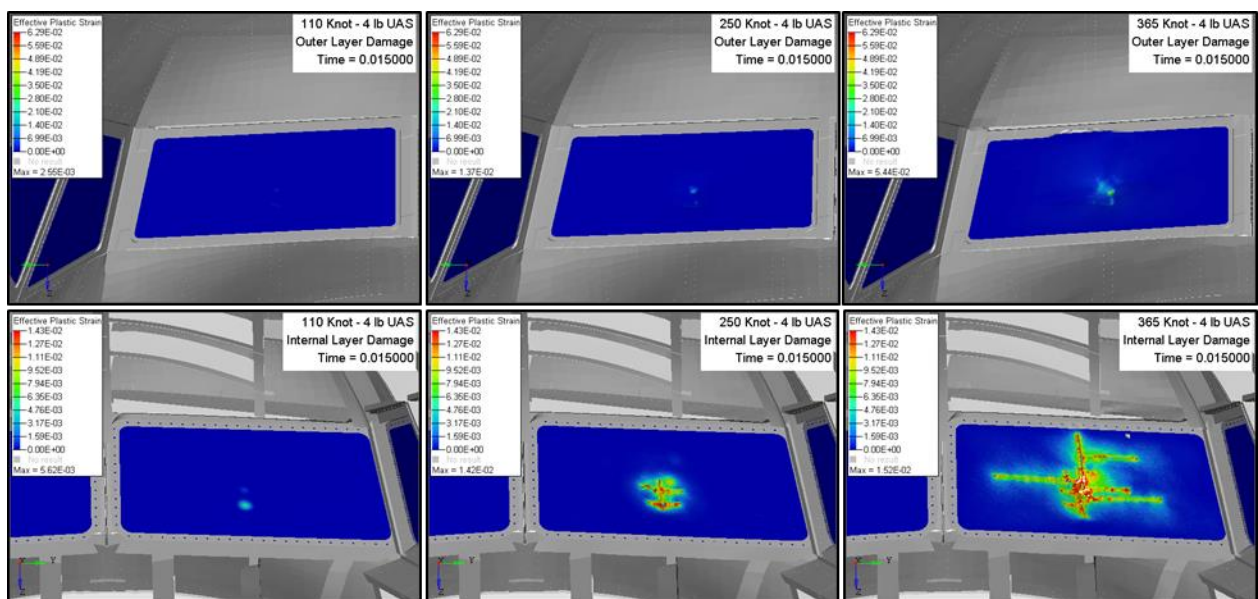


Figure 359. Comparison of external/internal damage sustained by a commercial transport jet windshield impacted with a 1.81 kg UAS at 56.7/128.6/187.8 m/s (110/250/365 knots)

All the UAS impacted the windshield and slid over it due to the small windshield angle. The UAS at 56.7 m/s (110 knots) did not damage the windshield. On the other hand, the UAS at 128.6 m/s (250 knots) slightly deformed the windshield while the UAS at 187.8 m/s (365 knots) damaged the windshield to a greater degree. It can also be perceived in Figure 359 that the damage severity increases with respect to the increase in velocity. Note that the top three plastic strain plots show

only the outer layer of the windshield transparency and that the lower three plots show the layer which sustained the maximum plastic strain.

The damage introduced by UAS at 56.7, 128.6, and 187.8 m/s (110, 250 and 365 knots) is classified as Level 1, 2, and 3 respectively. It is evident that higher velocity results in greater damage.

Figure 360 shows the comparison for the contact force and impulse between the UAS and windshield for three different velocities. Figure 361 shows the normalized energy balance for the impact comparison.

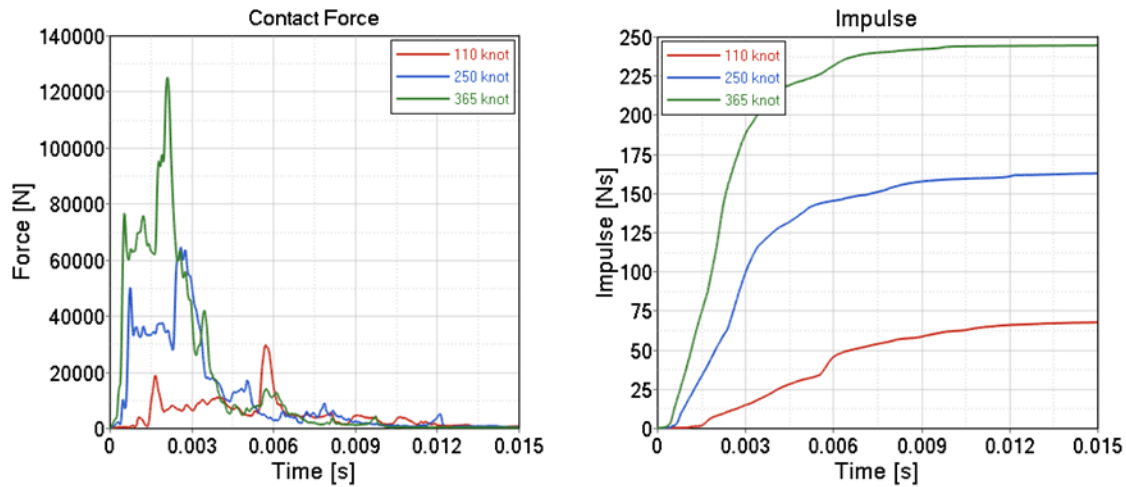


Figure 360. Comparison of the contact force and impulse of the impact between a commercial transport jet windshield and a 1.81 kg UAS at 56.7/128.6/187.8 m/s (110/250/365 knots)

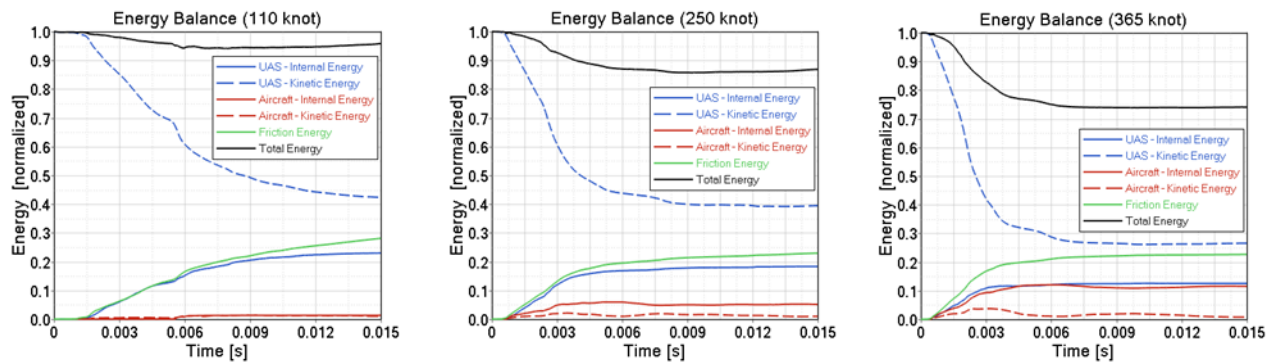


Figure 361. Comparison of the normalized energy balance of the impact between a commercial transport jet windshield and a 1.81 kg UAS at 56.7/128.6/187.8 m/s (110/250/365 knots)

The impulse increases with higher velocities. From the energy balance comparison, it can be observed that the UAS absorbed greater internal energy at lower velocity than the UAS at higher velocity. In addition, the residual kinetic energy after impact was greater for the UAS at lower velocities than for the UAS at higher velocities. This is an indication that the kinetic energy of the UAS at lower velocities was deflected more efficiently than that of the UAS at higher velocities, for which most of the energy was absorbed in the impact.

E.2 BUSINESS JET

E.2.1 Vertical Stabilizer

Impact simulations of a 1.8 kg (4.0 lb) UAS (case BFV1) with three different velocities (44.7, 128.6, 167.2 m/s; or 87, 250, 325 knots) against a vertical stabilizer are compared in terms of damage severity and kinematics. The initial conditions for all the above cases except for the velocity were based on BFV1, which was identified as the most critical case in the baseline simulations (see Section 4.4.1.1). Figure 362 depicts the comparison of the kinematics of the event. Figure 363 shows the comparison of the damage caused to the skin and the inner structure of the vertical stabilizer.

The UAS at 44.7 m/s (87 knots) slightly deformed the skin with no visible internal damage. On the other hand, the UAS at 128.6 m/s (250 knots) damaged the skin, the upper and lower ribs, and the front spar while the UAS at 167.2 m/s (325 knots) damaged the skin, upper and lower ribs to a greater degree, and the front spar. It can also be perceived in Figure 363 that the damage severity increases with respect to the increase in velocity.

The damage introduced by UAS at 44.7, 128.6 and 167.2 m/s (87, 250, and 325 knots) is classified as level 2, 4, and 4 respectively. It is evident that higher velocity results in greater damage.

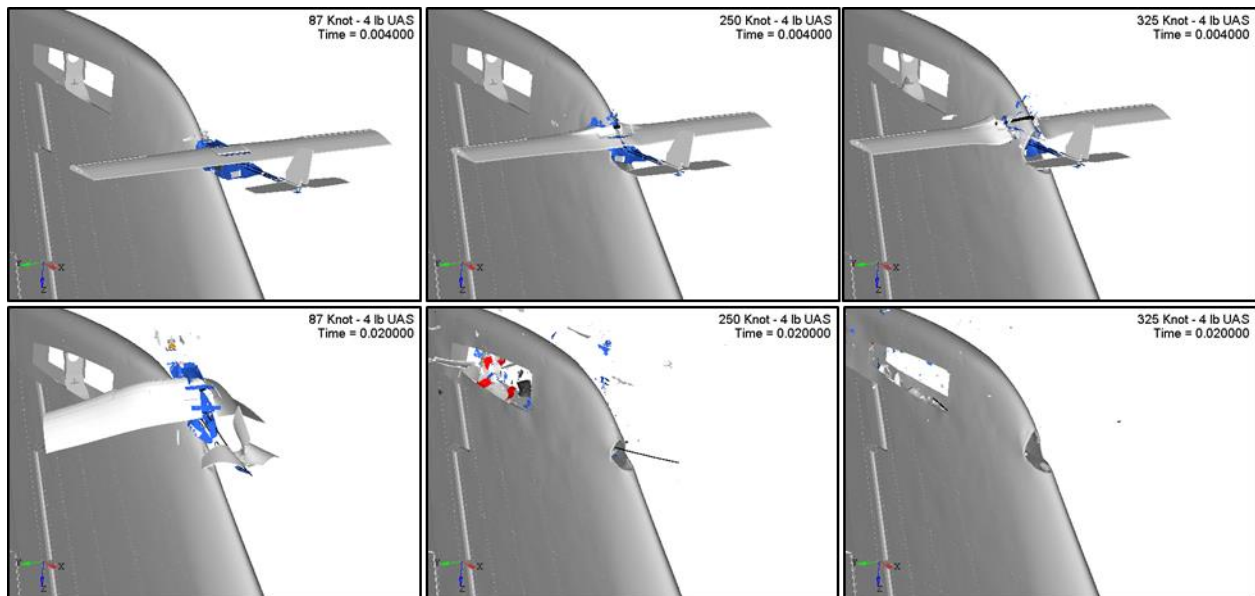


Figure 362. Comparison of the impact kinematics between a business jet vertical stabilizer and a 1.81 kg UAS at 44.7/128.6/167.2 m/s (87/250/325 knots)

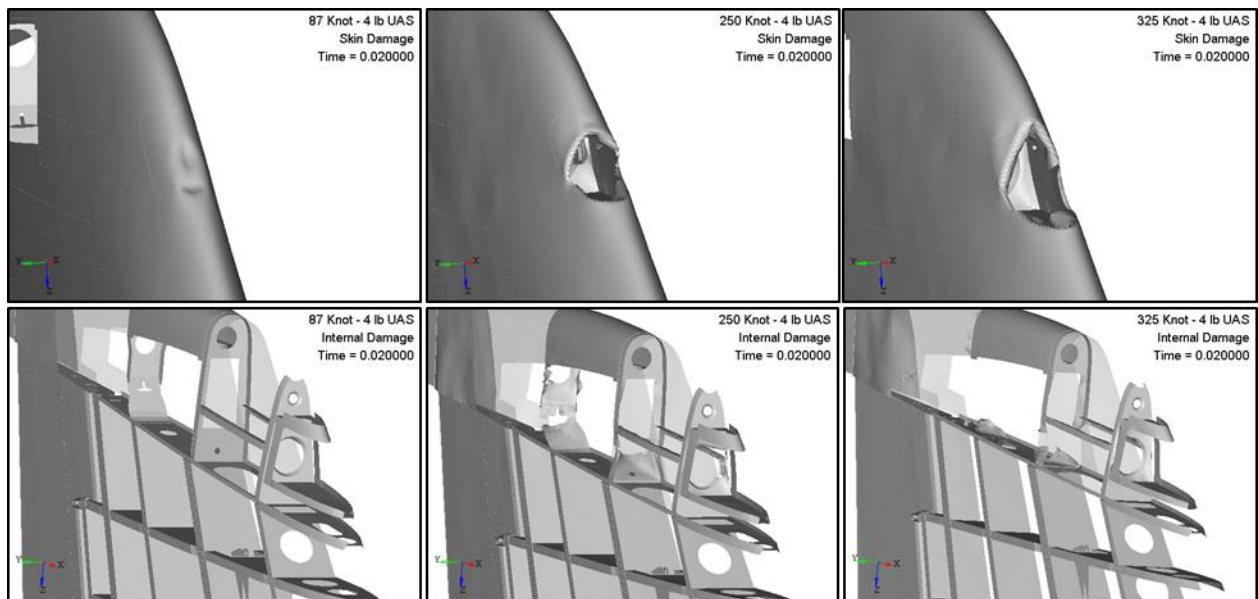


Figure 363. Comparison of external/internal damage sustained by a business jet vertical stabilizer impacted with a 1.81 kg UAS at 44.7/128.6/167.2 m/s (87/250/325 knots)

Figure 364 shows the comparison for the contact force and impulse between the UAS and vertical stabilizer for three different velocities. Figure 365 shows the normalized energy balance for the impact comparison.

The impulse increases with higher velocities. From the energy balance comparison, it can be observed that the UAS absorbed greater internal energy at lower velocity than the UAS at higher velocity. The kinetic energy ratios do not appear to have specific trends related to the impact velocity; therefore, the visible damage and kinematics are used to draw conclusions.

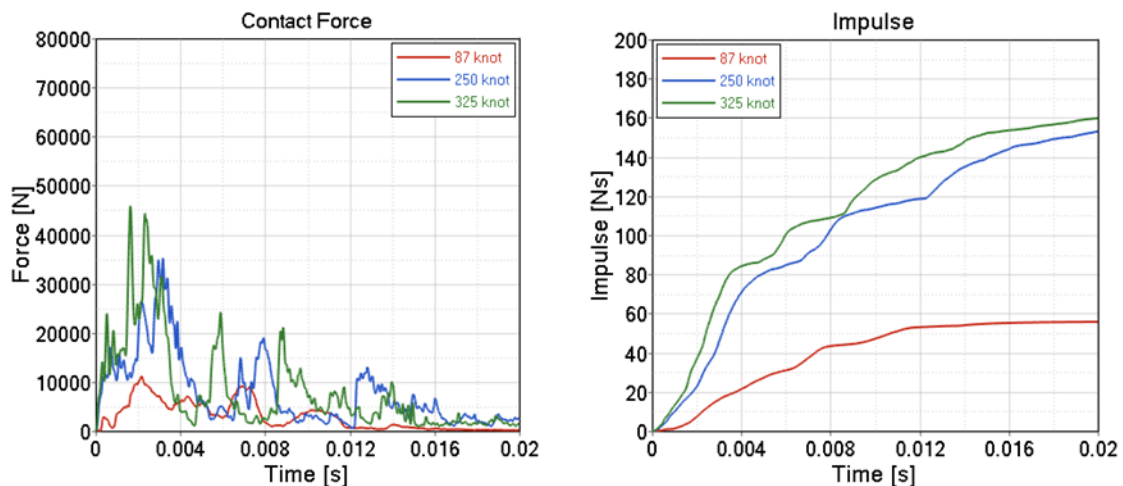


Figure 364. Comparison of the contact force and impulse of the impact between a business jet vertical stabilizer and a 1.81 kg UAS at 44.7/128.6/167.2 m/s (87/250/325 knots)

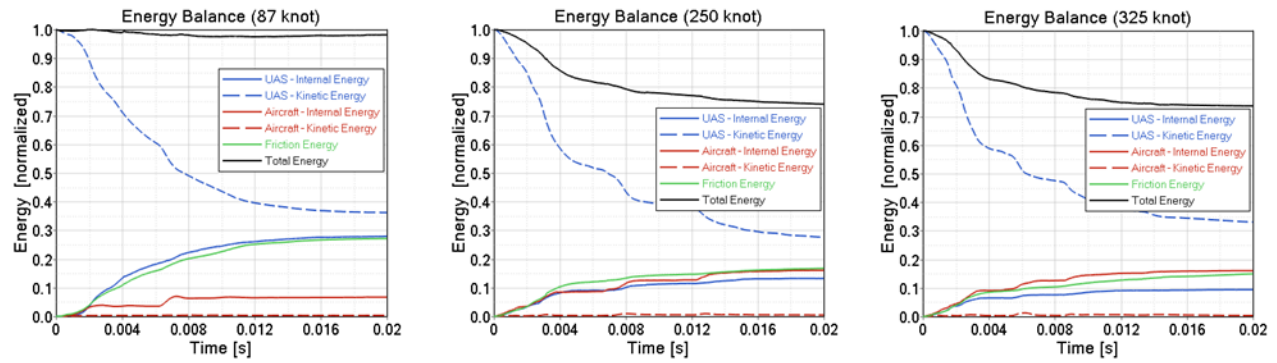


Figure 365. Comparison of the normalized energy balance of the impact between a business jet vertical stabilizer and a 1.81 kg UAS at 44.7/128.6/167.2 m/s (87/250/325 knots)

E.2.2 Horizontal Stabilizer

Impact simulations of a 1.8 kg (4.0 lb) UAS (case BFH1) with three different velocities (44.7, 128.6, 167.2 m/s; or 87, 250, 325 knots) against a horizontal stabilizer are compared in terms of damage severity and kinematics. The initial conditions for all the above cases except for the velocity were based on BFH1, which was identified as the most critical case in the baseline simulations (see Section 4.4.2.1). Figure 366 depicts the comparison of the kinematics of the event. Figure 367 shows the comparison of the damage caused to the skin and the inner structure of the horizontal stabilizer.

The UAS at 44.7 m/s (87 knots) slightly deformed the skin and the nose ribs with no other visible internal damage. On the other hand, the UAS at 128.6 m/s (250 knots) damaged the skin, the nose ribs, and the front spar while the UAS at 167.2 m/s (325 knots) damaged the skin, the nose ribs, and the front spar to a greater degree. It can also be perceived in Figure 367 that the damage severity increases with respect to the increase in velocity.

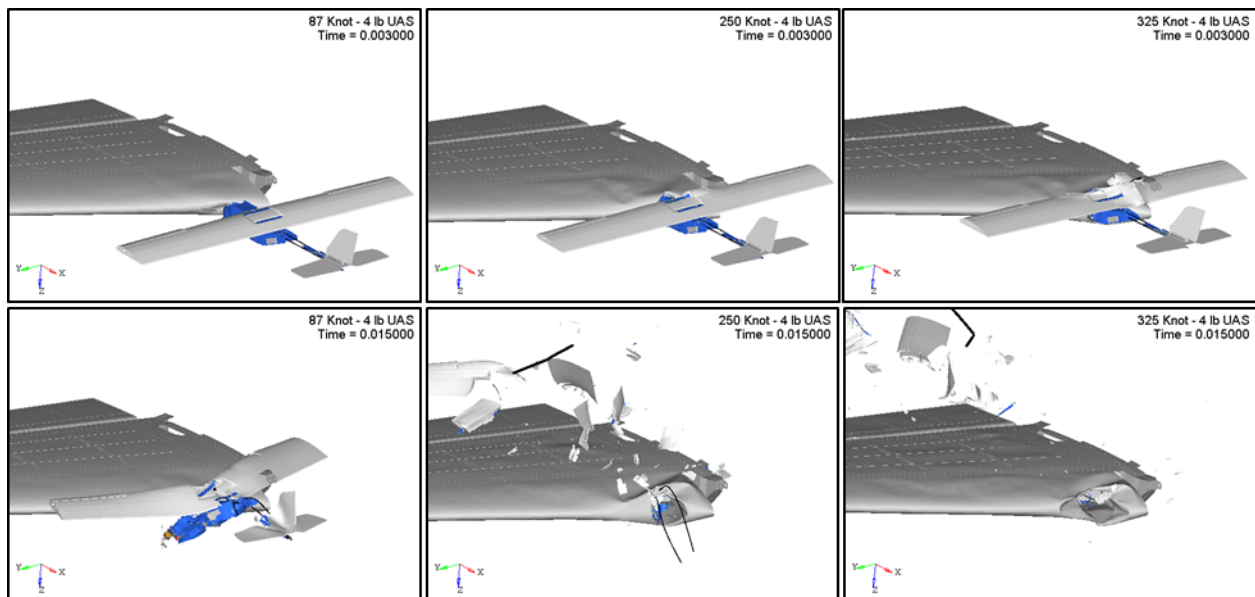


Figure 366. Comparison of the impact kinematics between a business jet horizontal stabilizer and a 1.81 kg UAS at 44.7/128.6/167.2 m/s (87/250/325 knots)

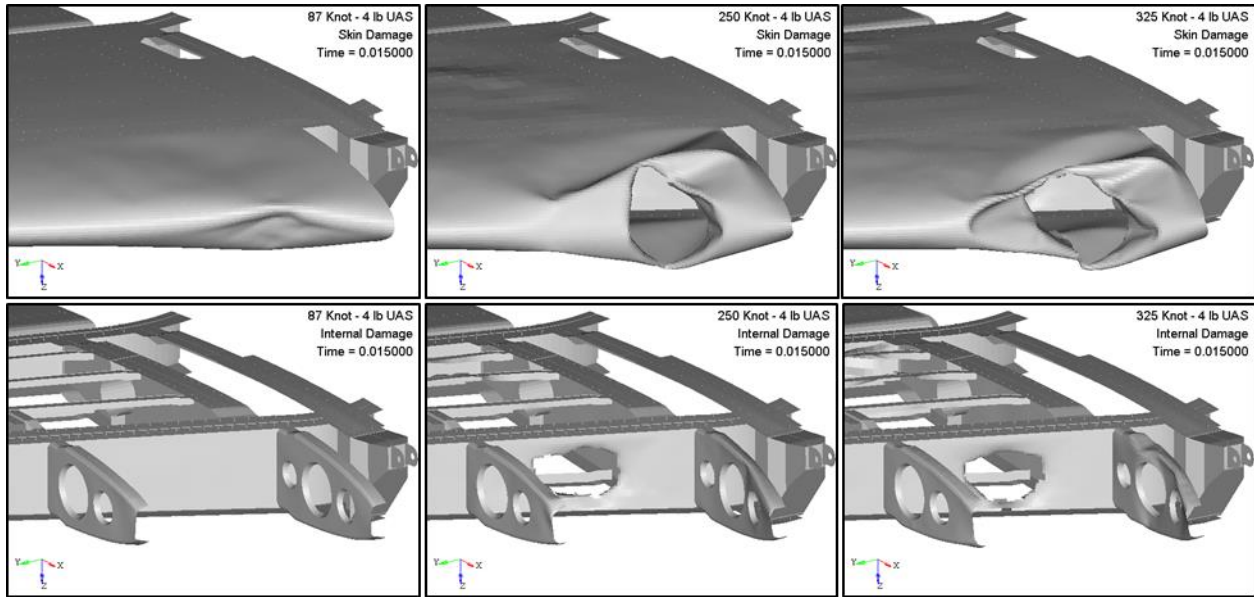


Figure 367. Comparison of external/internal damage sustained by a business jet horizontal stabilizer impacted with a 1.81 kg UAS at 44.7/128.6/167.2 m/s (87/250/325 knots)

The damage introduced by UAS at 44.7 m/s (87 knots) is classified as level 2 whereas the damage introduced by both UAS at 128.6 m/s (250 knots) and 167.2 m/s (325 knots) is classified as level 4 with risk of fire due to the battery. It is evident that higher velocity results in greater damage.

Figure 368 shows the comparison for the contact force and impulse between the UAS and horizontal stabilizer for three different velocities. Figure 369 shows the normalized energy balance for the impact comparison.

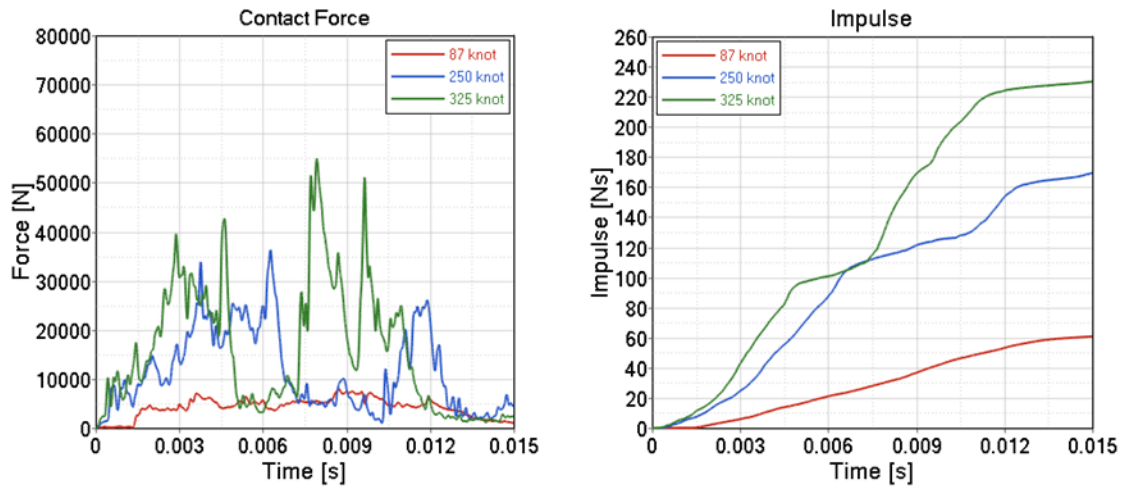


Figure 368. Comparison of the contact force and impulse of the impact between business jet horizontal stabilizer and 1.81 kg UAS at 44.7/128.6/167.2 m/s (87/250/325 knots)

The impulse increases with higher velocities. From the energy balance comparison, it can be observed that the internal energy ratios do not appear to have specific trends related to the impact velocity. In addition, the residual kinetic energy after the impact was greater for UAS at lower velocities than for the UAS at higher velocities. This is an indication that the kinetic energy of the

UAS at lower velocities was deflected more efficiently than that of the UAS at higher velocities, for which most of the energy was absorbed in the impact.

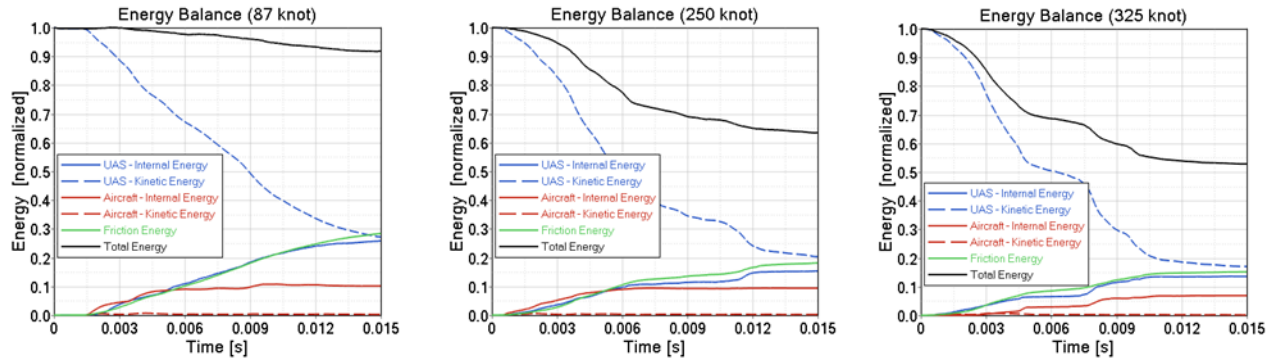


Figure 369. Comparison of the normalized energy balance of the impact between business jet horizontal stabilizer and 1.81 kg UAS at 44.7/128.6/167.2 m/s (87/250/325 knots)

E.2.3 Wing Leading Edge

Impact simulations of a 1.8 kg (4.0 lb) UAS (case BFW2) with three different velocities (44.7, 128.6, 167.2 m/s; or 87, 250, 325 knots) against a wing leading edge are compared in terms of damage severity and kinematics. The initial conditions for all the above cases except for the velocity were based on BFW2, which was identified as the most critical case in the baseline simulations (see Section 4.4.3.1). Figure 370 depicts the comparison of the kinematics of the event. Figure 371 shows the comparison of the damage caused to the skin and the inner structure of the wing.

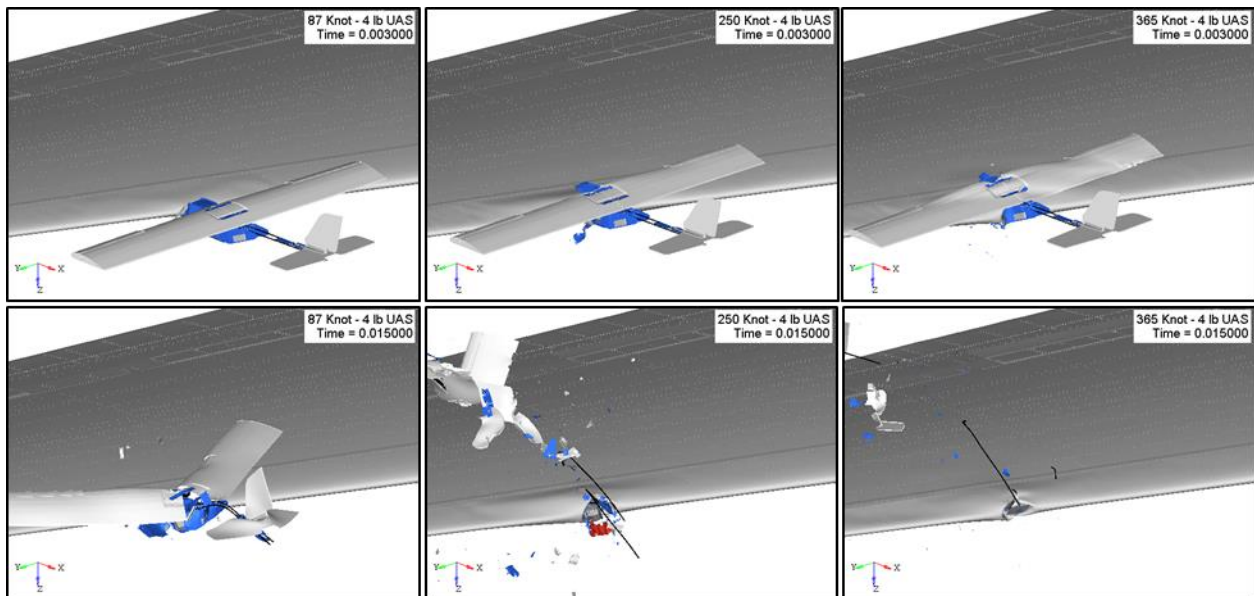


Figure 370. Comparison of the impact kinematics between a business jet wing and a 1.81 kg UAS at 44.7/128.6/167.2 m/s (87/250/325 knots)

The UAS at 44.7 m/s (87 knots) slightly deformed the skin with no visible internal damage. On the other hand, the UAS at 128.6 m/s (250 knots) damaged the skin and the anti-ice tube while the

UAS at 167.2 m/s (325 knots) damaged the skin and the anti-ice tube to a greater degree, and the front spar. It can also be perceived in Figure 371 that the damage severity increases with respect to the increase in velocity.

The damage introduced by UAS at 44.7 m/s (87 knots) is classified as level 2 whereas the damage introduced by UAS at 128.6 m/s (250 knots) and 167.2 m/s (325 knots) are classified as level 3. In addition, the risk of fire due to the battery is only present for the impacts of UAS at 128.6 and 167.2 m/s (250 and 325 knots). It is evident that higher velocity results in greater damage.

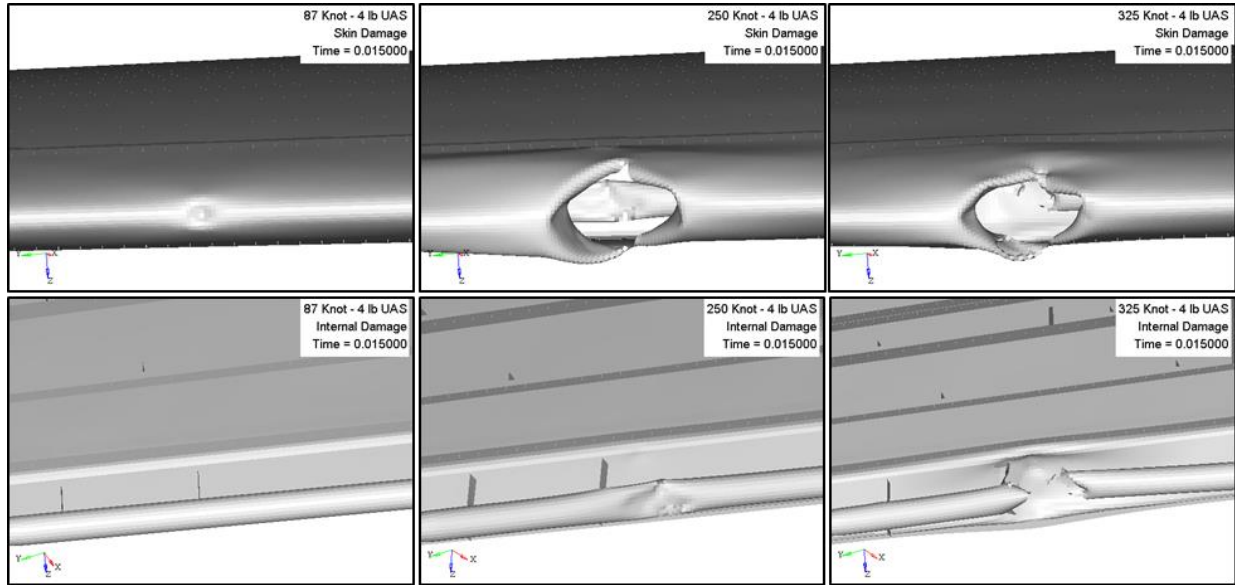


Figure 371. Comparison of external/internal damage sustained by a business jet wing impacted with a 1.81 kg UAS at 44.7/128.6/167.2 m/s (87/250/325 knots)

Figure 372 shows the comparison for the contact force and impulse between the UAS and wing for three different velocities. Figure 373 shows the normalized energy balance for the impact comparison.

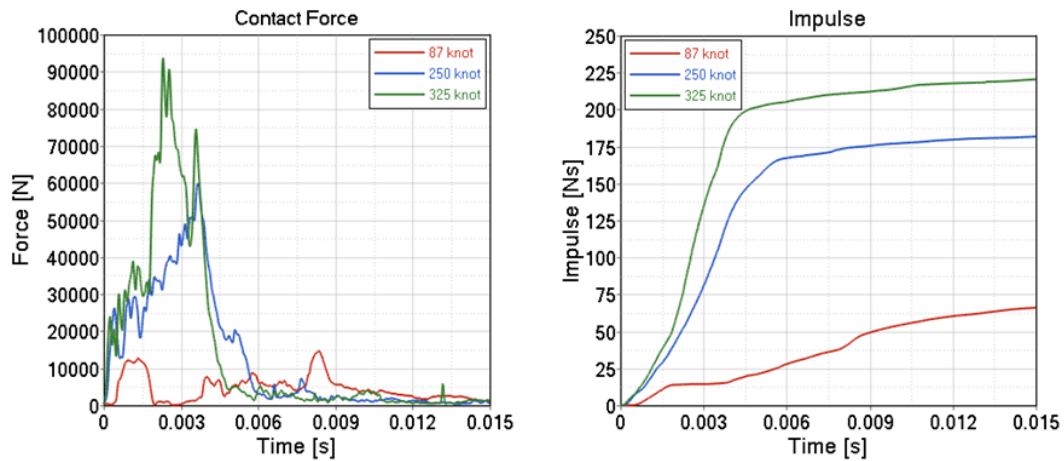


Figure 372. Comparison of the contact force and impulse of the impact between a business jet wing and a 1.81 kg UAS at 44.7/128.6/167.2 m/s (87/250/325 knots)

The impulse increases with higher velocities. From the energy balance comparison, it can be observed that the UAS absorbed greater internal energy at lower velocity than the UAS at higher velocity. The kinetic energy ratios do not appear to have specific trends related to the impact velocity; therefore, the visible damage and kinematics are used to draw conclusions.

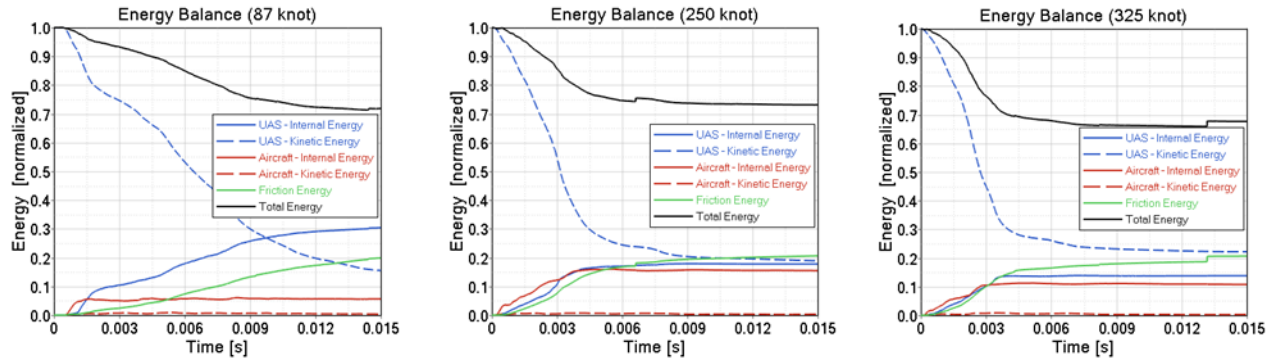


Figure 373. Comparison of the normalized energy balance of the impact between a business jet wing and a 1.81 kg UAS at 44.7/128.6/167.2 m/s (87/250/325 knots)

E.2.4 Windshield

Impact simulations of a 1.8 kg (4.0 lb) UAS (case BFC1) with three different velocities (44.7, 128.6, 167.2 m/s; or 87, 250, 325 knots) against a windshield are compared in terms of damage severity and kinematics. The initial conditions for all the above cases except for the velocity were based on BFC1, which was identified as the most critical case in the baseline simulations (see Section 4.4.4.1). Figure 374 depicts the comparison of the kinematics of the event. Figure 375 shows the comparison of the damage caused to the windshield and surrounding structure.

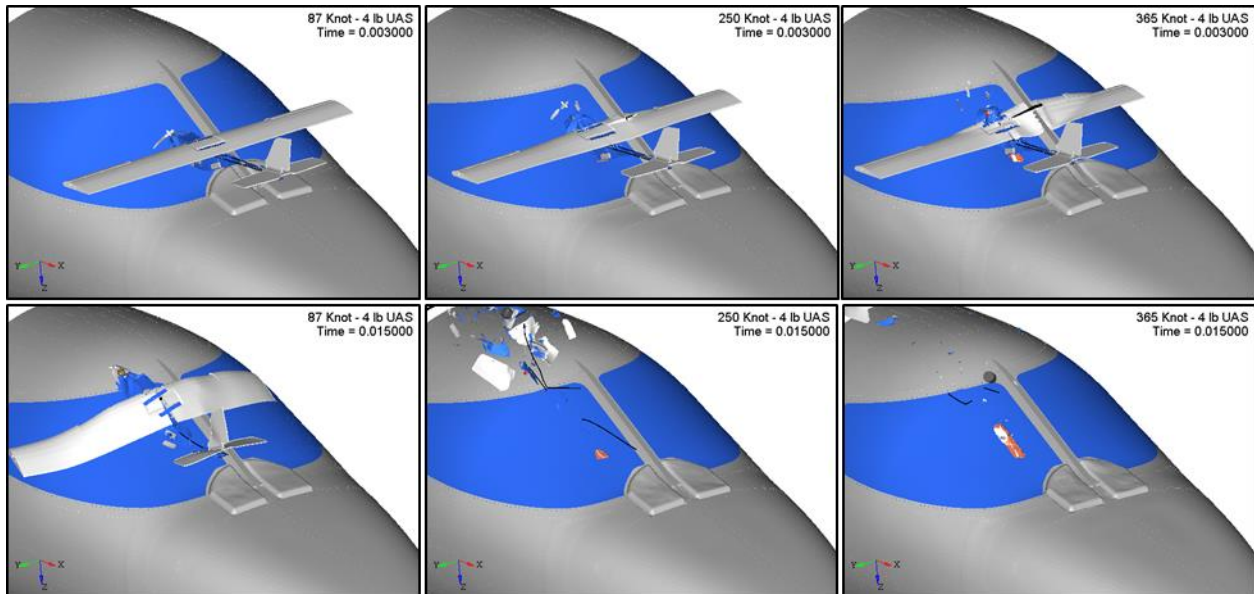


Figure 374. Comparison of the impact kinematics between a business jet windshield and a 1.81 kg UAS at 44.7/128.6/167.2 m/s (87/250/325 knots)

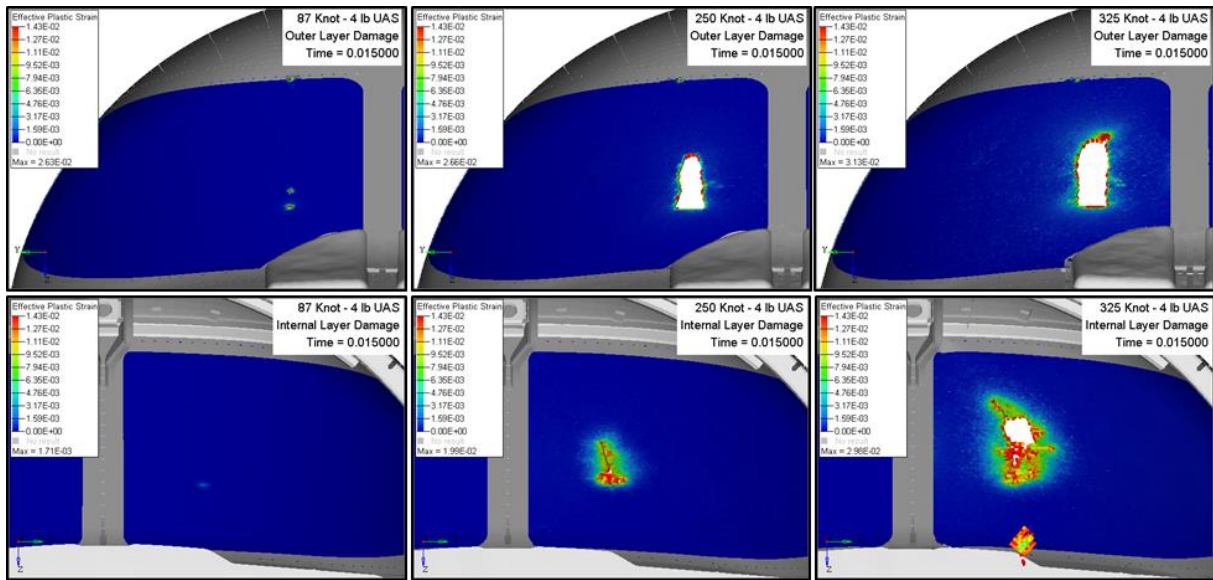


Figure 375. Comparison of external/internal damage sustained by a business jet windshield impacted with a 1.81 kg UAS at 44.7/128.6/167.2 m/s (87/250/325 knots)

All the UAS impacted the windshield and slid over it due to the small windshield angle. The UAS at 44.8 m/s (87 knots) did not damage the windshield. On the other hand, the UAS at 128.6 m/s (250 knots) damaged the windshield while the UAS at 187.8 m/s (365 knots) damaged the windshield to a greater degree. It can also be perceived in Figure 375 that the damage severity increases with respect to the increase in velocity. Note that the top three plastic strain plots show only the outer layer of the windshield transparency and that the lower three plots show the layer which sustained the maximum plastic strain.

The damage introduced by UAS at 44.8 m/s (87 knots) is classified as Level 1 whereas the damage introduced by UAS at 128.6 and 167.2 m/s (250 and 325 knots) are classified as Level 4. It is evident that higher velocity results in greater damage.

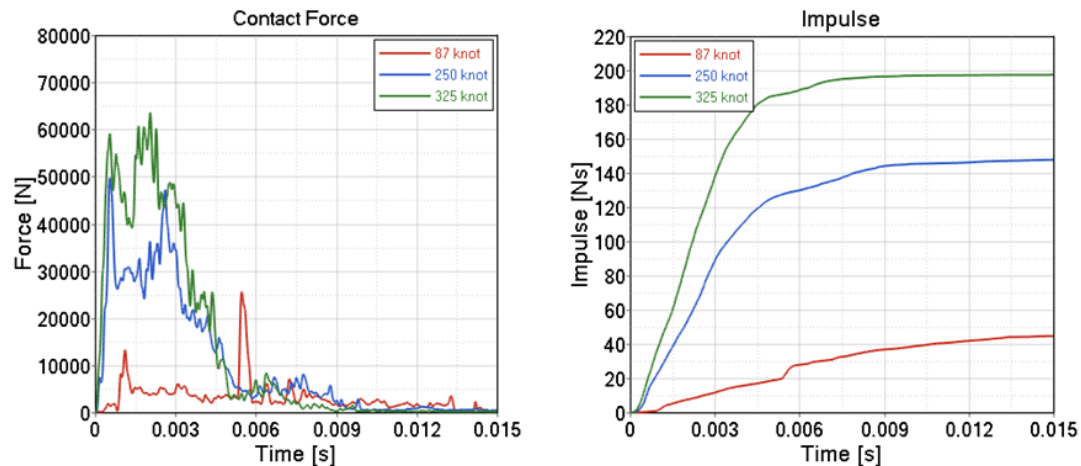


Figure 376. Comparison of the contact force and impulse of the impact between a business jet windshield and a 1.81 kg UAS at 44.7/128.6/167.2 m/s (87/250/325 knots)

Figure 376 shows the comparison for the contact force and impulse between the UAS and windshield for three different velocities. Figure 377 shows the normalized energy balance for the impact comparison.

The impulse increases with higher velocities. From the energy balance comparison, it can be observed that the internal energy ratios do not appear to have specific trends related to the impact velocity. In addition, the residual kinetic energy after impact was greater for the UAS at lower velocities than for the UAS at higher velocities. This is an indication that the kinetic energy of the UAS at lower velocities was deflected more efficiently than that of the UAS at higher velocities, for which most of the energy was absorbed in the impact.

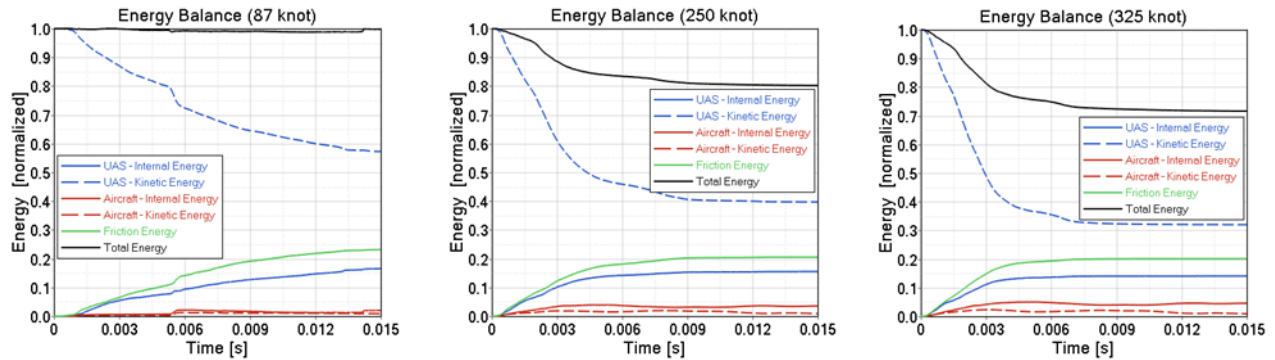


Figure 377. Comparison of the normalized energy balance of the impact between a business jet windshield and a 1.81 kg UAS at 44.7/128.6/167.2 m/s (87/250/325 knots)

APPENDIX F – BIRD STRIKE COMPARISON

F.1 TRANSPORT JET – UAS VS. BIRD (4.0 LB)

F.1.1 Vertical Stabilizer

Impact simulations of a 1.8 kg (4.0 lb) UAS (case CFV1) and a 1.8 kg (4.0 lb) bird (case CB4V1) against a vertical stabilizer are compared in terms of damage severity and kinematics. The initial conditions were based on the above UAS case which was identified as the most critical in the baseline simulations (see Section 4.3.1.1). Figure 378 depicts the comparison of the kinematics of the event. Figure 379 shows the comparison of the damage caused to the skin and the inner structure of the vertical stabilizer.

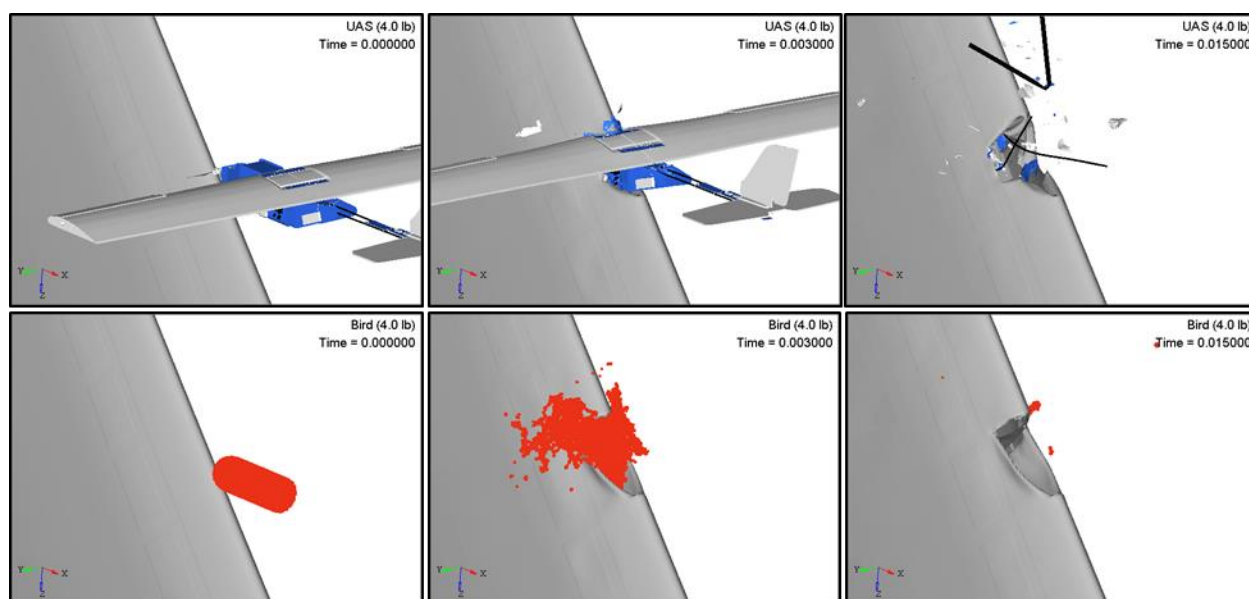


Figure 378. Comparison of the kinematics of impact between a commercial transport jet vertical stabilizer and a 1.8 kg (4.0 lb) UAS/Bird at 128.6 m/s (250 knots)

The UAS damaged the skin, the upper and lower ribs while the bird damaged the skin to a lesser degree and the upper and lower ribs. It can also be seen in Figure 379 that amount of damage introduced into the skin was considerably smaller for the case of bird than the UAS.

The damage introduced by both the UAS and the bird is classified as Level 3. For this case, the UAS impact can be considered more severe than the equivalent bird strike in terms of damage.

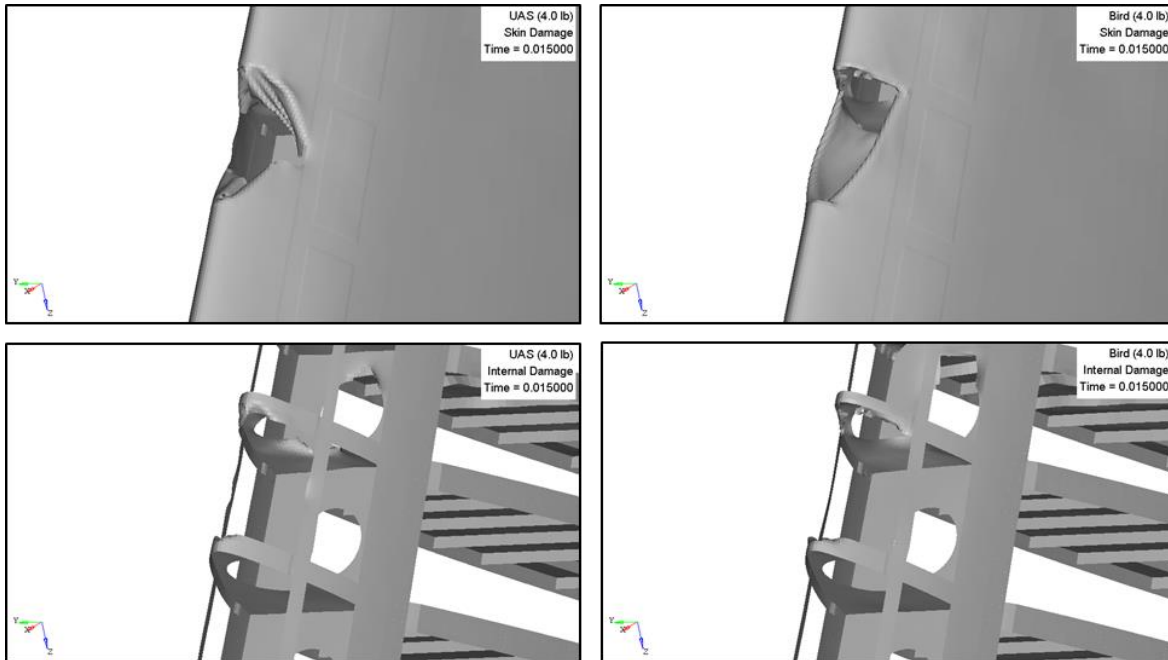


Figure 379. Comparison of external/internal damage sustained by a commercial transport jet vertical stabilizer impacted with a 1.8 kg (4.0 lb) UAS/Bird at 128.6 m/s (250 knots)

Figure 382 shows the comparison for the contact force and impulse between the UAS/bird and vertical stabilizer. Figure 380 shows the energy balance for the impact comparison.

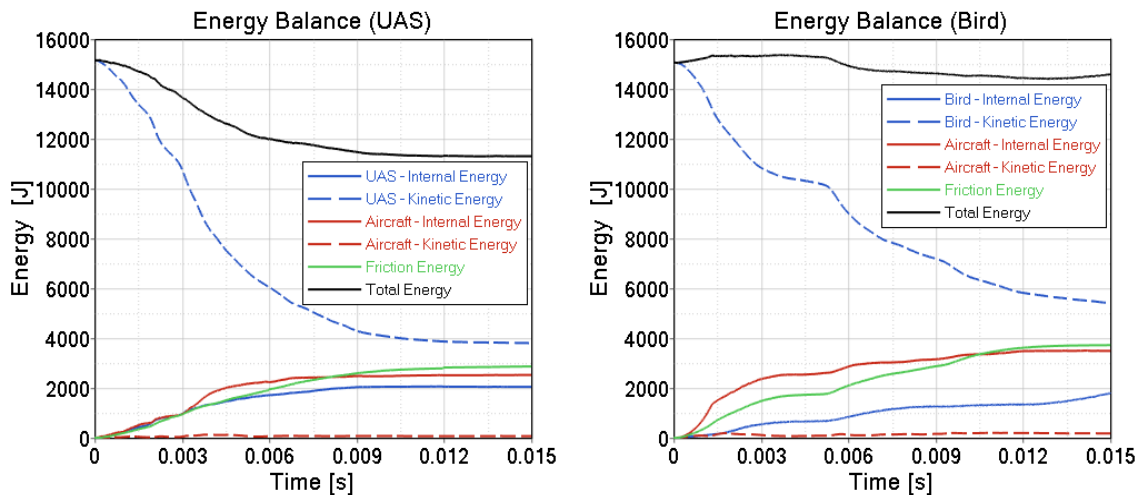


Figure 380. Comparison of the energy balance of the impact between a commercial transport jet vertical stabilizer and a 1.8 kg (4.0 lb) UAS/bird at 128.6 m/s (250 knots)

The impulse for the bird was higher than that of the UAS. From the energy balance comparison, it can be observed that both the UAS and the bird absorbed the same magnitude of internal energy. Also, it is apparent that the residual kinetic energy of the bird after impact was greater than

that of the UAS. This is an indication that the kinetic energy of the bird was deflected more efficiently than that of the UAS, for which most of the energy was absorbed in the impact.

F.1.2 Horizontal Stabilizer

Impact simulations of a 1.8 kg (4.0 lb) UAS (case CFH2) and a 1.8 kg (4.0 lb) bird (case CB4H2) against a horizontal stabilizer are compared in terms of damage severity and kinematics. The initial conditions were based on the above UAS case which was identified as the most critical in the baseline simulations (see Section 4.3.2.1). Figure 381 depicts the comparison of the kinematics of the event. Figure 382 shows the comparison of the damage caused to the skin and the inner structure of the horizontal stabilizer.

The UAS damaged the skin, the left nose rib and the sub-spar while the bird damaged the skin to a lesser degree and both the nose ribs. It can also be seen in Figure 382 that amount of damage introduced into the skin was considerably smaller for the case of bird than the UAS.

The damage introduced by the UAS is classified as Level 4 whereas the damage introduced by the bird is classified as Level 2. For this case, the UAS impact can be considered as more severe than the equivalent bird strike in terms of damage.

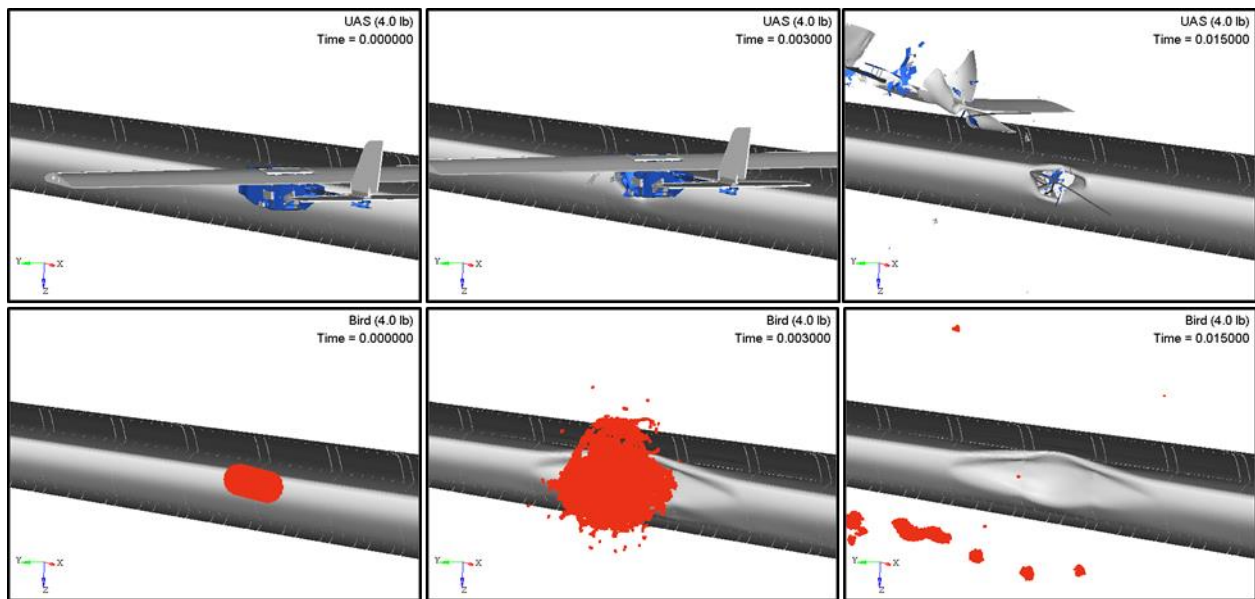


Figure 381. Comparison of the kinematics of impact between a commercial transport jet horizontal stabilizer and a 1.8 kg (4.0 lb) UAS/Bird at 128.6 m/s (250 knots)

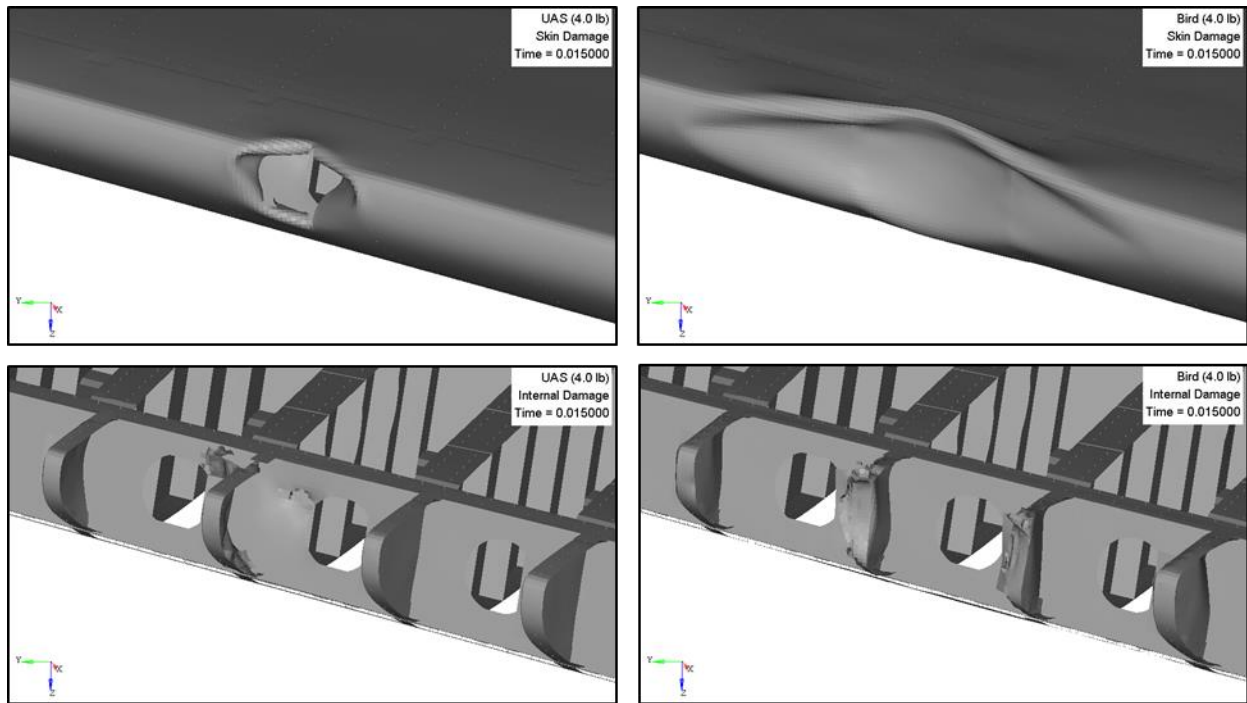


Figure 382. Comparison of external/internal damage sustained by a commercial transport jet horizontal stabilizer impacted with a 1.8 kg (4.0 lb) UAS/Bird at 128.6 m/s (250 knots)

Figure 383 shows the comparison for the contact force and impulse between the UAS/bird and horizontal stabilizer. Figure 384 shows the energy balance for the impact comparison.

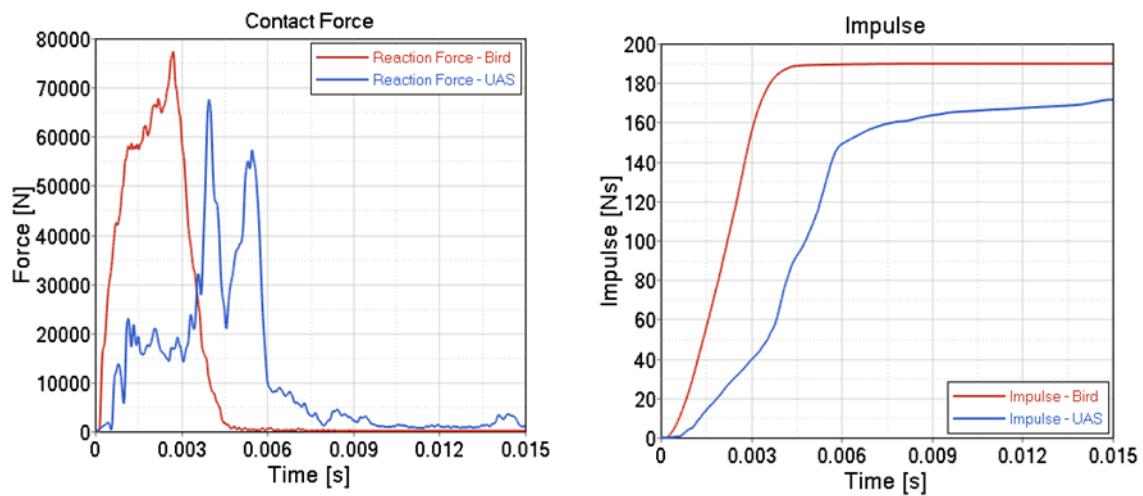


Figure 383. Comparison of the contact force and impulse of the impact between a commercial transport jet horizontal stabilizer and a 1.8 kg (4.0 lb) UAS/bird at 128.6 m/s (250 knots)

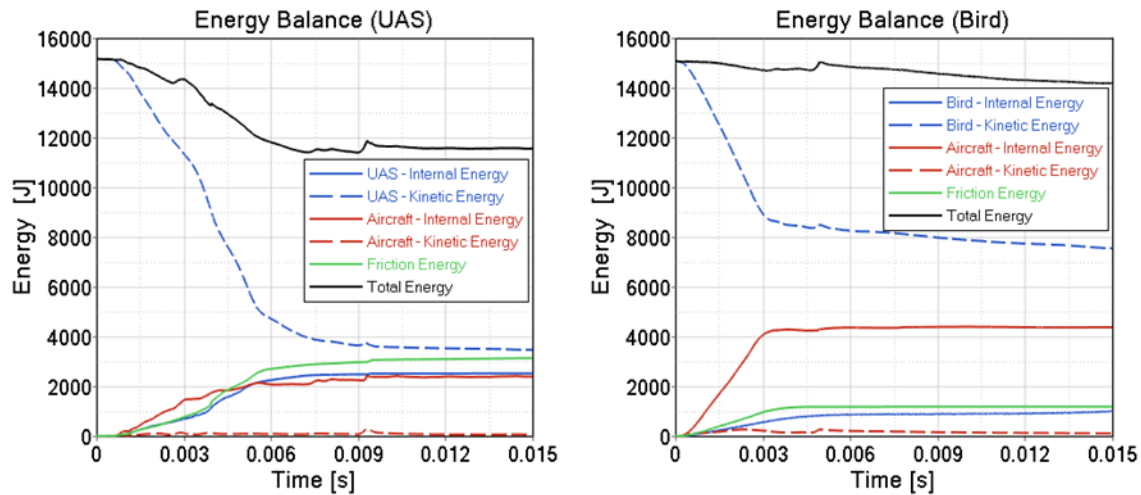


Figure 384. Comparison of the energy balance of the impact between a commercial transport jet horizontal stabilizer and a 1.8 kg (4.0 lb) UAS/bird at 128.6 m/s (250 knots)

The impulse for the bird was higher than that of the UAS. From the energy balance comparison, it can be observed that the UAS absorbed considerably greater internal energy than the bird. Also, it is apparent that the residual kinetic energy of the bird after impact was greater than that of the UAS. This is an indication that the kinetic energy of the bird was deflected more efficiently than that of the UAS, for which most of the energy was absorbed in the impact.

F.1.3 Wing Leading Edge

Impact simulations of a 1.8 kg (4.0 lb) UAS (case CFW3) and a 1.8 kg (4.0 lb) bird (case CB4W3) against the leading edge of a wing are compared in terms of damage severity and kinematics. The initial conditions were based on the above UAS case which was identified as the most critical in the baseline simulations (see Section 4.3.3.1). Figure 385 depicts the comparison of the kinematics of the event. Figure 386 shows the comparison of the damage caused to the skin and the inner structure of the wing.

The UAS damaged the skin and the front spar while the bird damaged the skin and the front spar to a lesser degree. It can also be seen in Figure 386 that amount of damage introduced into the skin was considerably smaller for the case of bird than the UAS.

The damage introduced by the UAS is classified as Level 3, whereas the damage introduced by the bird is classified as Level 2. For this case, the UAS impact can be considered more severe than the equivalent bird strike in terms of damage.

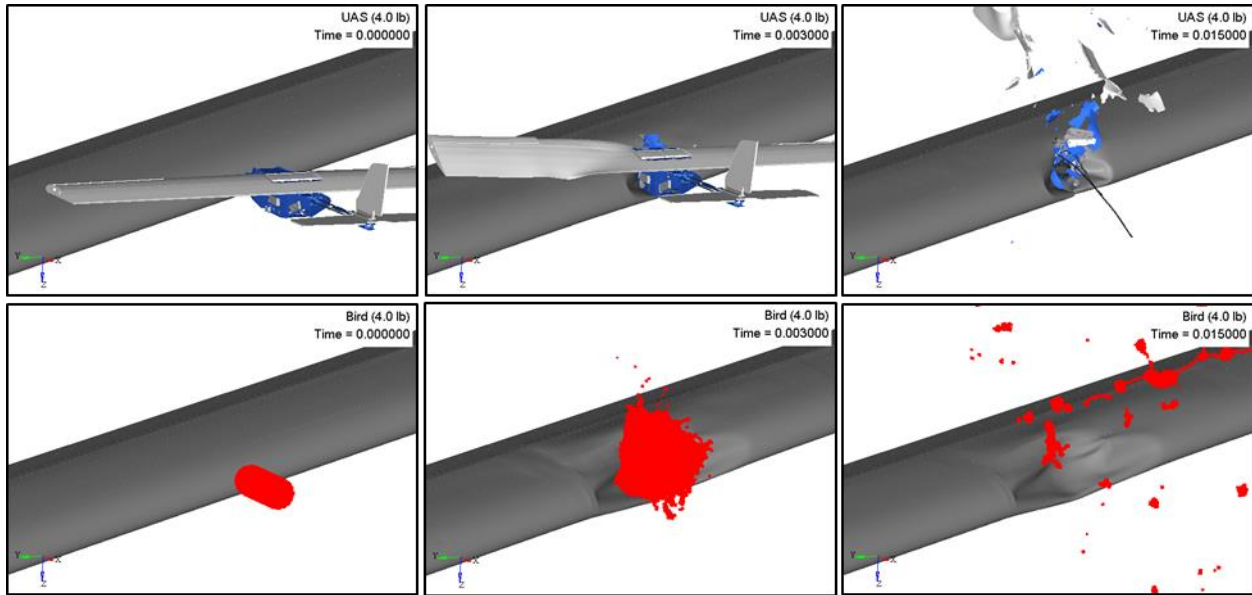


Figure 385. Comparison of the kinematics of impact between a commercial transport jet wing and a 1.8 kg (4.0 lb) UAS/Bird at 128.6 m/s (250 knots)

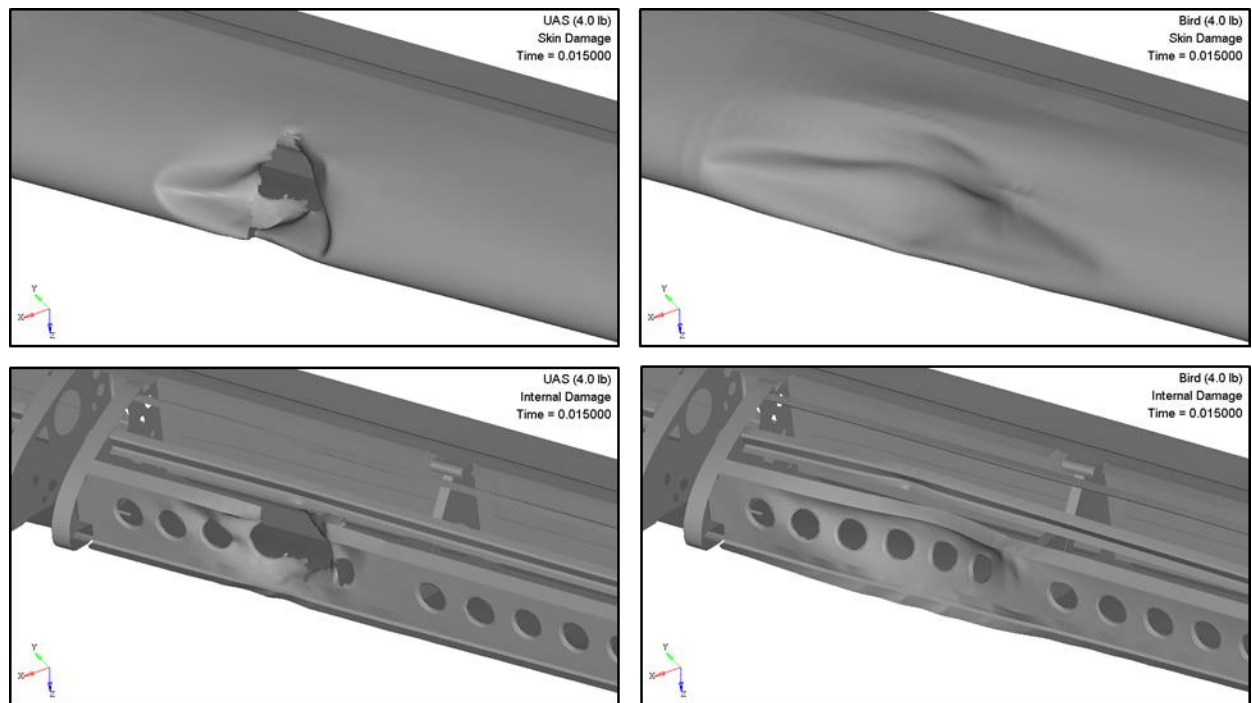


Figure 386. Comparison of external/internal damage sustained by a commercial transport jet wing impacted with a 1.8 kg (4.0 lb) UAS/Bird at 128.6 m/s (250 knots)

Figure 387 shows the comparison for the contact force and impulse between the UAS/bird and wing. Figure 388 shows the energy balance for the impact comparison.

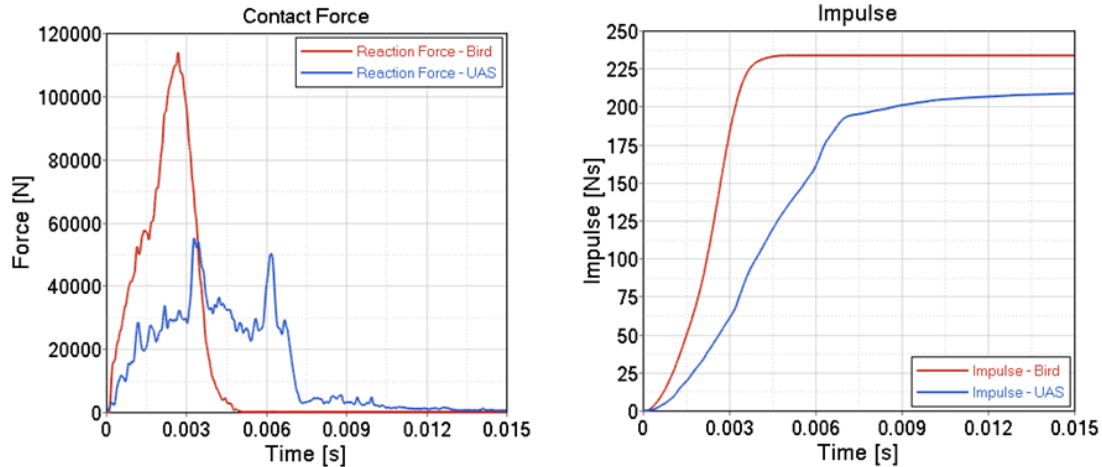


Figure 387. Comparison of the contact force and impulse of the impact between a commercial transport jet wing and a 1.8 kg (4.0 lb) UAS/bird at 128.6 m/s (250 knots)

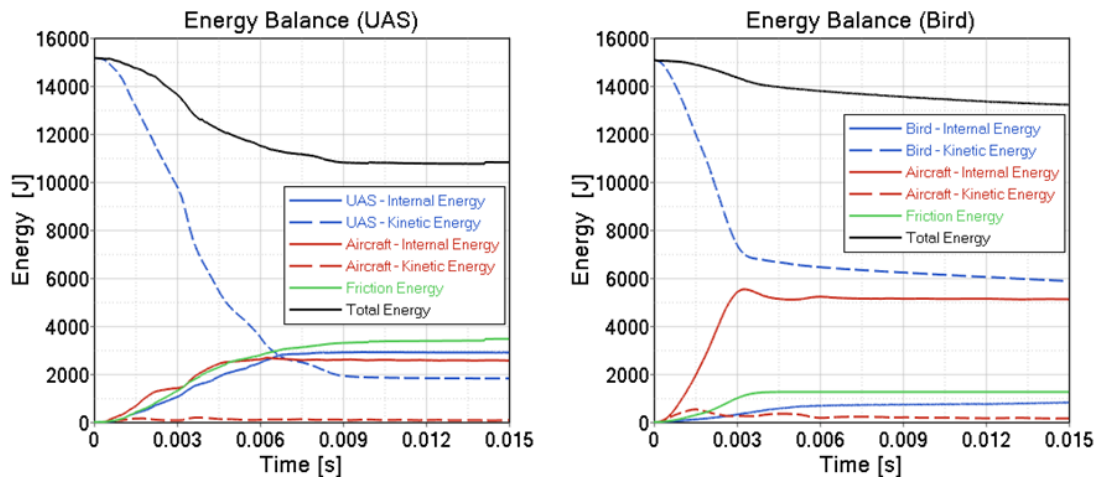


Figure 388. Comparison of the energy balance of the impact between a commercial transport jet wing and a 1.8 kg (4.0 lb) UAS/bird at 128.6 m/s (250 knots)

The impulse for the bird was higher than that of the UAS. From the energy balance comparison, it can be observed that the UAS absorbed considerably greater internal energy than the bird. Also, it is apparent that the residual kinetic energy of the bird after impact was greater than that of the UAS. This is an indication that the kinetic energy of the bird was deflected more efficiently than that of the UAS, for which most of the energy was absorbed in the impact.

F.1.4 Windshield

Impact simulations of a 1.8 kg (4.0 lb) UAS (case CFC1) and a 1.8 kg (4.0 lb) bird (case CB4C1) against a windshield are compared in terms of damage severity and kinematics. The initial conditions were based on the above UAS case which was identified as the most critical in the baseline simulations (see Section 4.3.4.1). Figure 389 depicts the comparison of the kinematics of the event. Figure 390 shows the comparison of the damage caused to the windshield and surrounding structure.

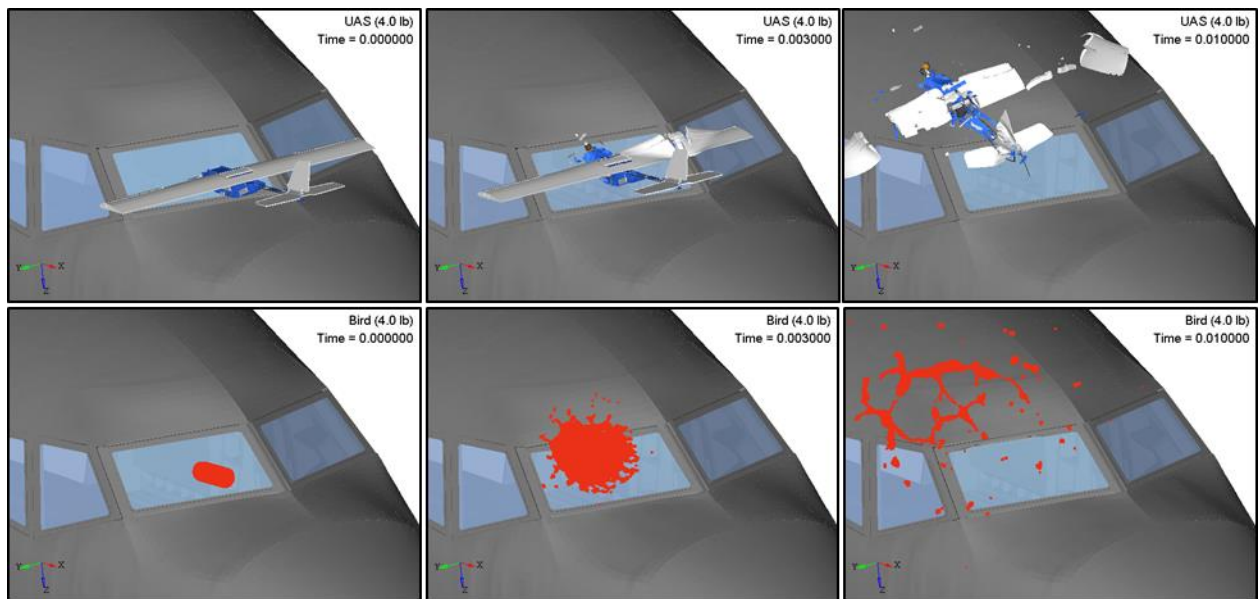


Figure 389. Comparison of the kinematics of impact between a commercial transport jet windshield and a 1.8 kg (4.0 lb) UAS/Bird at 128.6 m/s (250 knots)

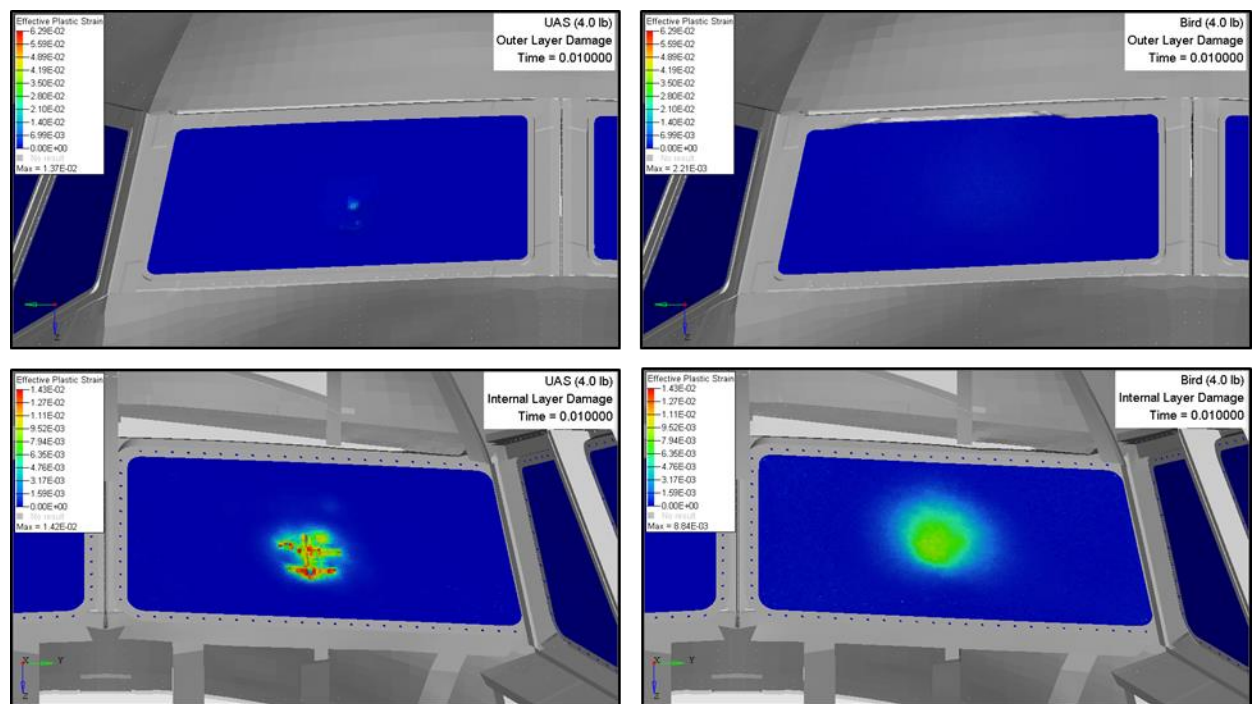


Figure 390. Comparison of external/internal damage sustained by a commercial transport jet windshield impacted with a 1.8 kg (4.0 lb) UAS/Bird at 128.6 m/s (250 knots)

The UAS impacted the windshield, causing noticeable permanent deformations on the transparency and slid over it due to the small windshield angle, whereas the bird also slid over the windshield but without causing any noticeable damage to the transparency. It can also be seen in Figure 390 that amount of damage introduced into the windshield was considerably smaller for the case

of bird than the UAS. Note that the top three plastic strain plots show only the outer layer of the windshield transparency and that the lower three plots show the layer which sustained the maximum plastic strain.

The damage introduced by the UAS is classified as Level 2, whereas the damage introduced by the bird is classified as Level 1. For this case, the UAS impact can be considered more severe than the equivalent bird strike in terms of damage.

Figure 391 shows the comparison for the contact force and impulse between the UAS/bird and windshield. Figure 392 shows the energy balance for the impact comparison.

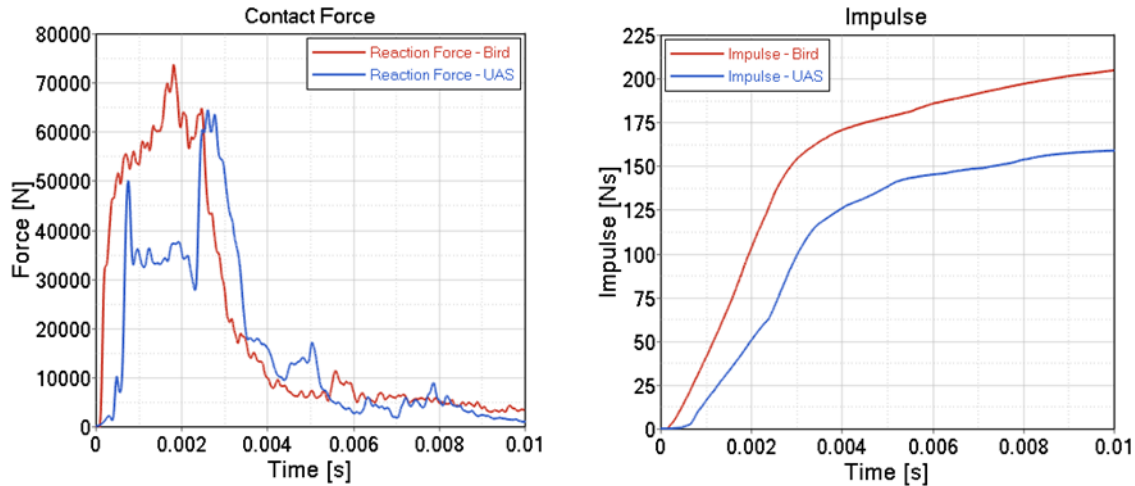


Figure 391. Comparison of the contact force and impulse of the impact between a commercial transport jet windshield and a 1.8 kg (4.0 lb) UAS/bird at 128.6 m/s (250 knots)

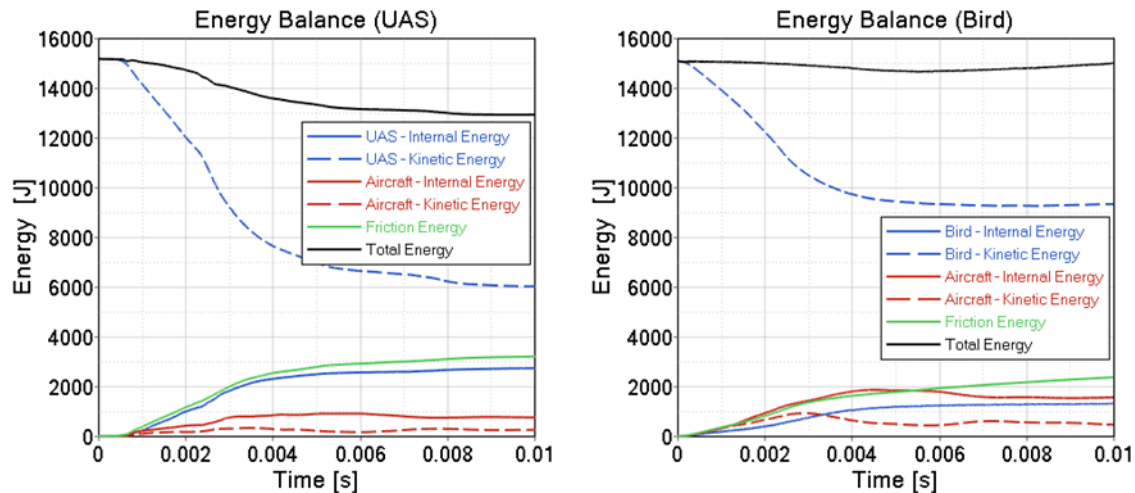


Figure 392. Comparison of the energy balance of the impact between a commercial transport jet windshield and a 1.8 kg (4.0 lb) UAS/bird at 128.6 m/s (250 knots)

The impulse for the bird was higher than that of the UAS. From the energy balance comparison, it can be observed that the UAS absorbed considerably greater internal energy than the bird. Also, it is apparent that the residual kinetic energy of the bird after impact was greater than that

of the UAS. This is an indication that the kinetic energy of the bird was deflected more efficiently than that of the UAS, for which most of the energy was absorbed in the impact.

F.2 BUSINESS JET – UAS VS. BIRD (4.0 LB)

F.2.1 Vertical Stabilizer

Impact simulations of a 1.8 kg (4.0 lb) UAS (case BFV3) and a 1.8 kg (4.0 lb) bird (case BB4V3) against a vertical stabilizer are compared in terms of damage severity and kinematics. The initial conditions were based on the above UAS case which was identified as the most critical in the baseline simulations (see Section 4.4.1.1). Figure 393 depicts the comparison of the kinematics of the event. Figure 394 shows the comparison of the damage caused to the skin and the inner structure of the vertical stabilizer.

The UAS damaged the skin, the lightening hole in the front spar and the two fin tip ribs behind the spar, while the bird damaged the skin to a lesser degree and the front ribs. It can also be seen in Figure 394 that amount of damage introduced into the skin was considerably smaller for the case of bird than the UAS.

The damage introduced by the UAS is classified as Level 4, whereas the damage introduced by the bird is classified as Level 2. For this case, the UAS impact can be considered more severe than the equivalent bird strike in terms of damage.

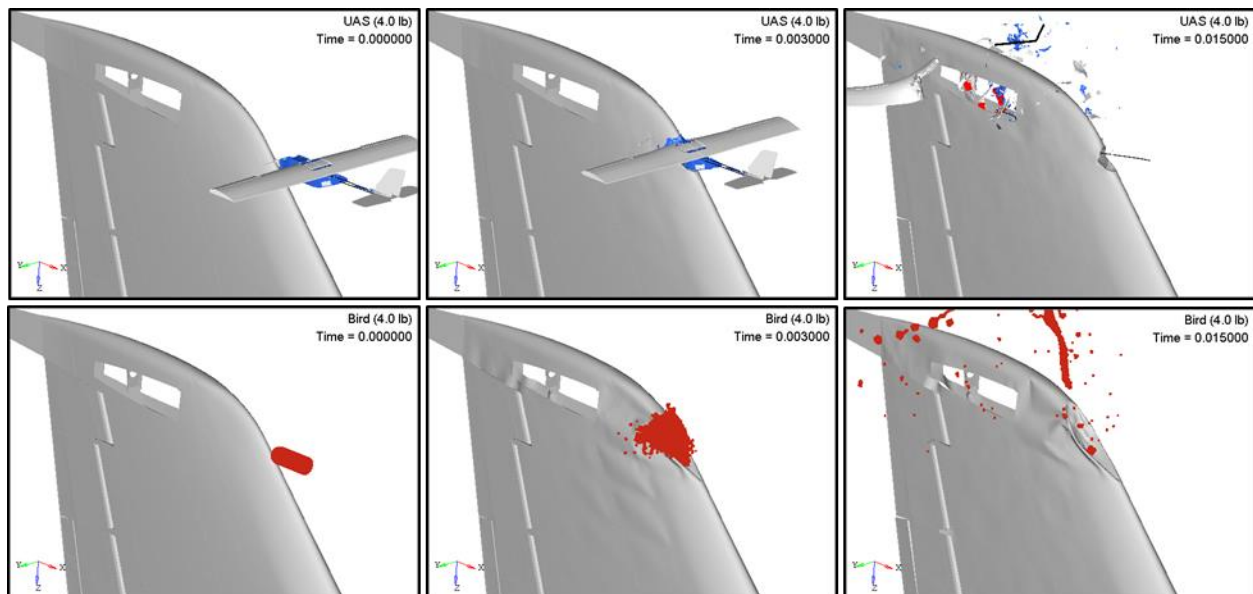


Figure 393. Comparison of the kinematics of impact between a business jet vertical stabilizer and a 1.8 kg (4.0 lb) UAS/Bird at 128.6 m/s (250 knots)

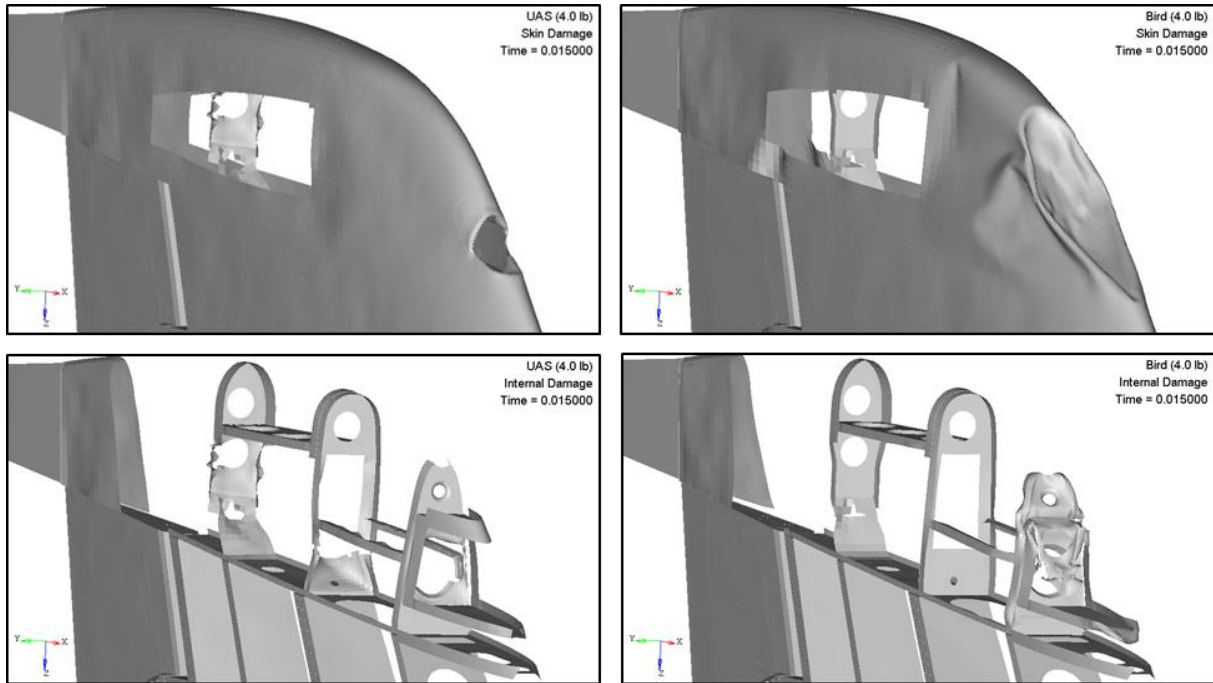


Figure 394. Comparison of external/internal damage sustained by a business jet vertical stabilizer impacted with a 1.8 kg (4.0 lb) UAS/Bird at 128.6 m/s (250 knots)

Figure 395 shows the comparison for the contact force and impulse between the UAS/bird and vertical stabilizer. Figure 396 shows the energy balance for the impact comparison.

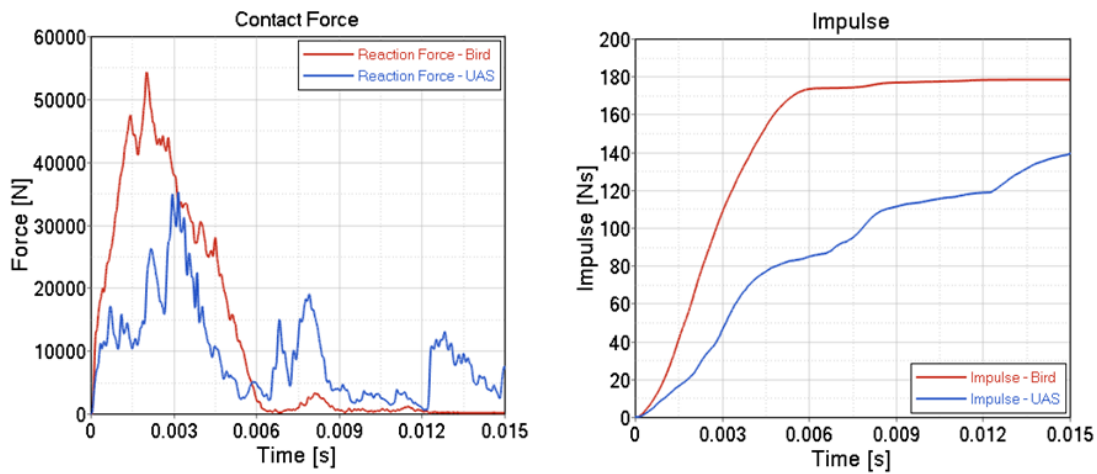


Figure 395. Comparison of the contact force and impulse of the impact between a business jet vertical stabilizer and a 1.8 kg (4.0 lb) UAS/bird at 128.6 m/s (250 knots)

The impulse for the bird was higher than that of the UAS. From the energy balance comparison, it can be observed that the UAS absorbed considerably greater internal energy than the bird. Also, it is apparent that the residual kinetic energy of the bird after impact was greater than that of the UAS. This is an indication that the kinetic energy of the bird was deflected more efficiently than that of the UAS, for which most of the energy was absorbed in the impact.

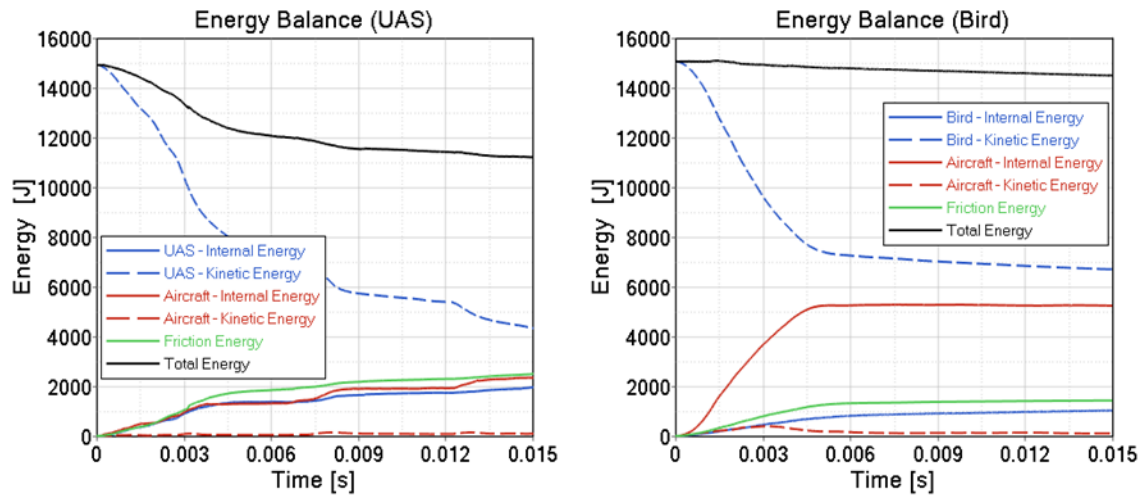


Figure 396. Comparison of the energy balance of the impact between a business jet vertical stabilizer and a 1.8 kg (4.0 lb) UAS/bird at 128.6 m/s (250 knots)

F.2.2 Horizontal Stabilizer

Impact simulations of a 1.8 kg (4.0 lb) UAS (case BFH1) and a 1.8 kg (4.0 lb) bird (case BB4H1) against a horizontal stabilizer are compared in terms of damage severity and kinematics. The initial conditions were based on the above UAS case which was identified as the most critical in the baseline simulations (see Section 4.4.2.1). Figure 397 depicts the comparison of the kinematics of the event. Figure 398 shows the comparison of the damage caused to the skin and the inner structure of the horizontal stabilizer.

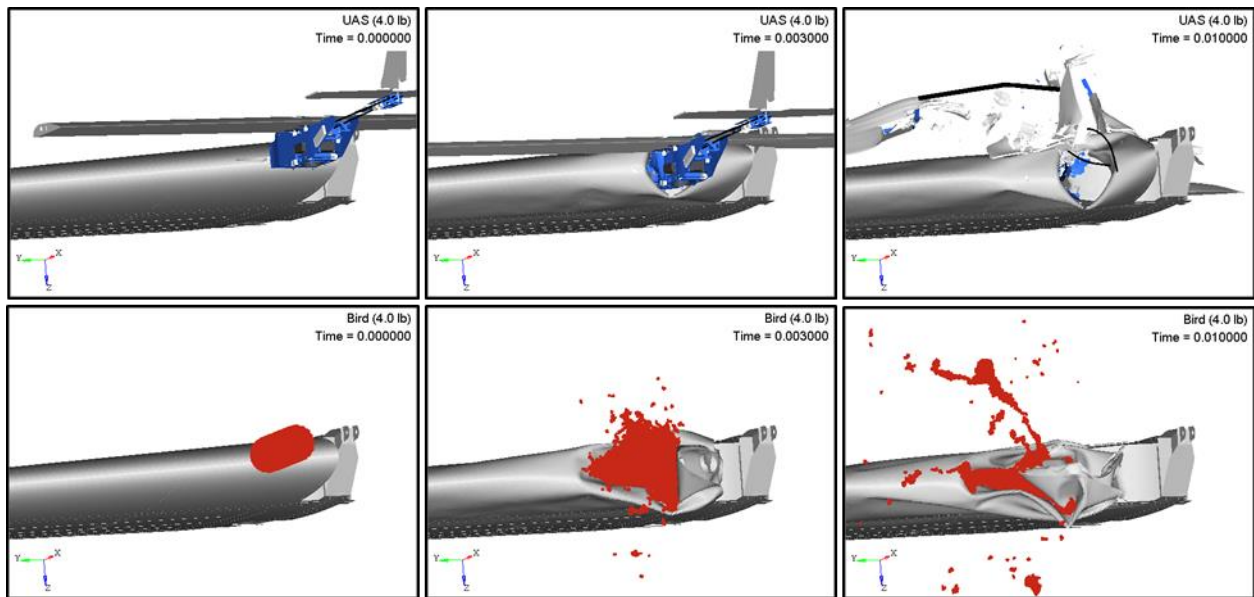


Figure 397. Comparison of the kinematics of impact between a business jet horizontal stabilizer and a 1.8 kg (4.0 lb) UAS/Bird at 128.6 m/s (250 knots)

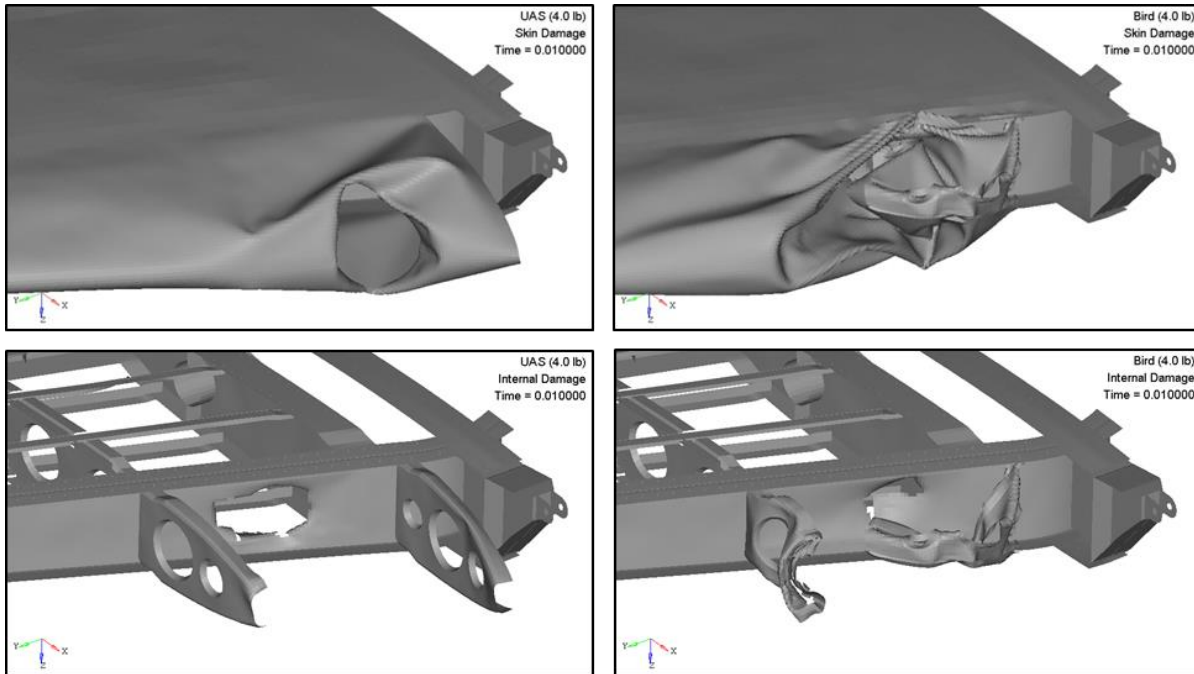


Figure 398. Comparison of external/internal damage sustained by a business jet horizontal stabilizer impacted with a 1.8 kg (4.0 lb) UAS/Bird at 128.6 m/s (250 knots)

Both the UAS and the bird damaged the skin. However, the UAS damages and penetrates the front spar's web to a higher degree. It can also be seen in Figure 398 that amount of damage introduced into the skin by the bird is more extensive in terms of deformed surface.

The damage introduced by the UAS is classified as Level 4, whereas the damage introduced by the bird is classified as Level 2. For this case, the UAS impact can be considered much more severe than the equivalent bird strike in terms of damage.

Figure 399 shows the comparison for the contact force and impulse between the UAS/bird and horizontal stabilizer. Figure 400 shows the energy balance for the impact comparison.

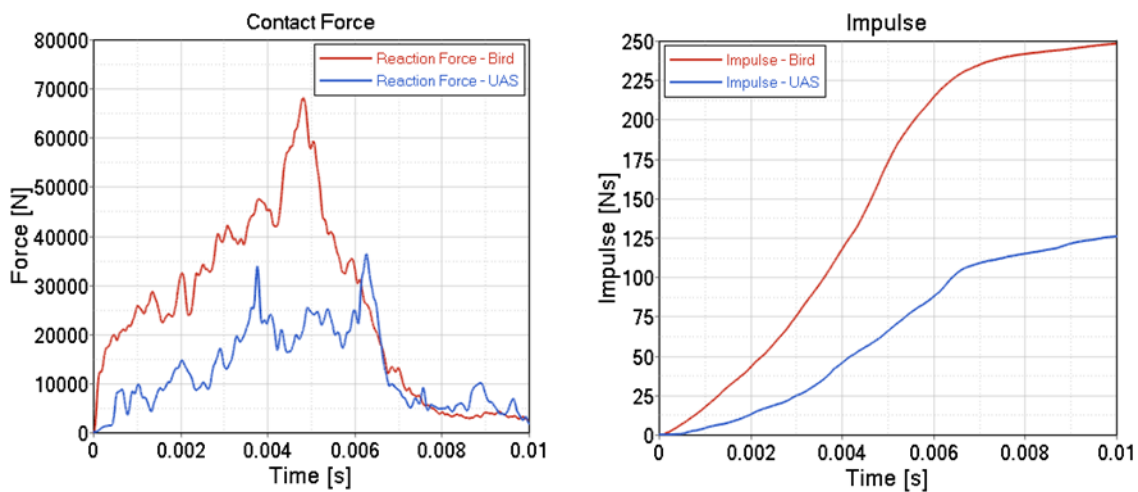


Figure 399. Comparison of the contact force and impulse of the impact between a business jet horizontal stabilizer and a 1.8 kg (4.0 lb) UAS/bird at 128.6 m/s (250 knots)

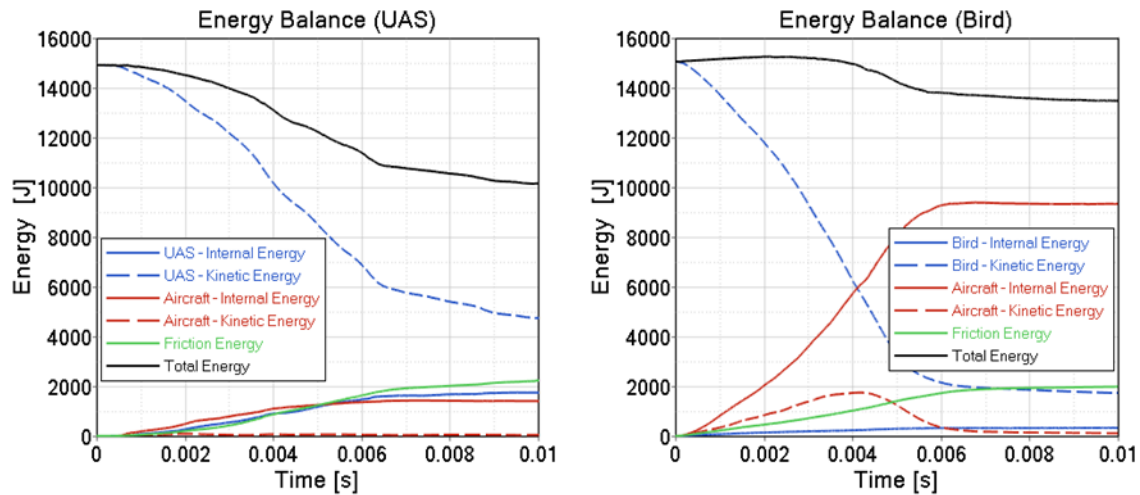


Figure 400. Comparison of the energy balance of the impact between a business jet horizontal stabilizer and a 1.8 kg (4.0 lb) UAS/bird at 128.6 m/s (250 knots)

The impulse for the bird was higher than that of the UAS. From the energy balance comparison, it can be observed that the UAS absorbed considerably greater internal energy than the bird. Also, it is apparent that the residual kinetic energy of the UAS after impact was greater than that of the bird. This is an indication that the kinetic energy of the UAS was deflected more efficiently than that of the bird, for which most of the energy was absorbed in the impact.

F.2.3 Wing Leading Edge

Impact simulations of a 1.8 kg (4.0 lb) UAS (case BFW2) and a 1.8 kg (4.0 lb) bird (case BB4W2) against the leading edge of a wing are compared in terms of damage severity and kinematics. The initial conditions were based on the above UAS case which was identified as the most critical in the baseline simulations (see Section 4.4.3.1). Figure 401 depicts the comparison of the kinematics of the event. Figure 402 shows the comparison of the damage caused to the skin and the inner structure of the wing.

The UAS damaged the skin and the anti-ice tube while the bird also damaged the skin and the anti-ice tube but to a lesser degree. It can also be seen in Figure 402 that amount of damage introduced into the skin was considerably smaller for the case of bird than the UAS.

The damage introduced by the UAS is classified as Level 3 whereas the damage introduced by the bird is classified as Level 2. For this case, the UAS impact can be considered more severe than the equivalent bird strike in terms of damage.

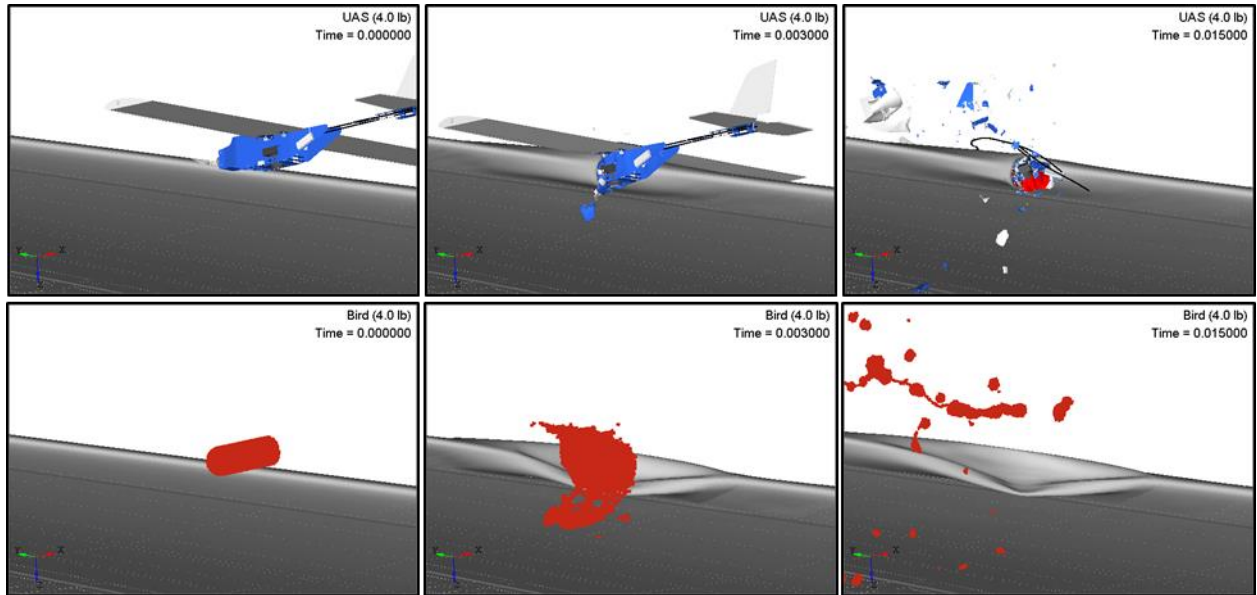


Figure 401. Comparison of the kinematics of impact between a business jet wing and a 1.8 kg (4.0 lb) UAS/bird at 128.6 m/s (250 knots)

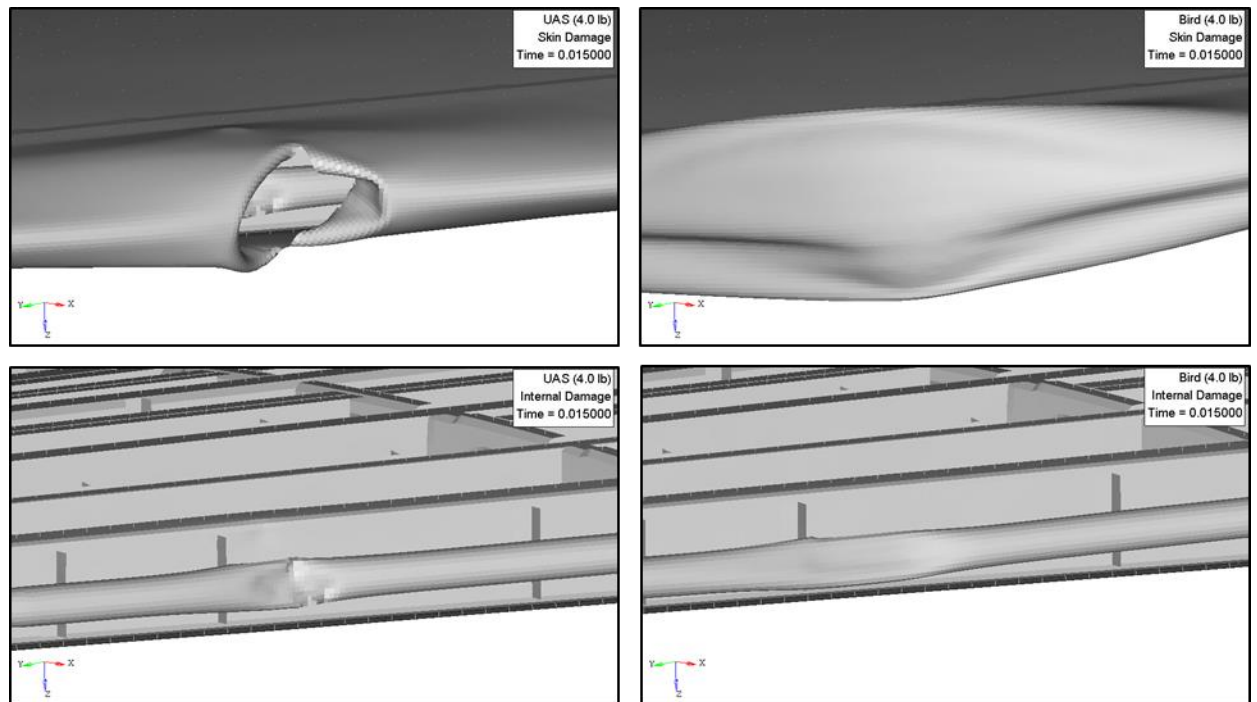


Figure 402. Comparison of external/internal damage sustained by a business jet wing impacted with a 1.8 kg (4.0 lb) UAS/bird at 128.6 m/s (250 knots)

Figure 403 shows the comparison for the contact force and impulse between the UAS/bird and wing. Figure 404 shows the energy balance for the impact comparison.

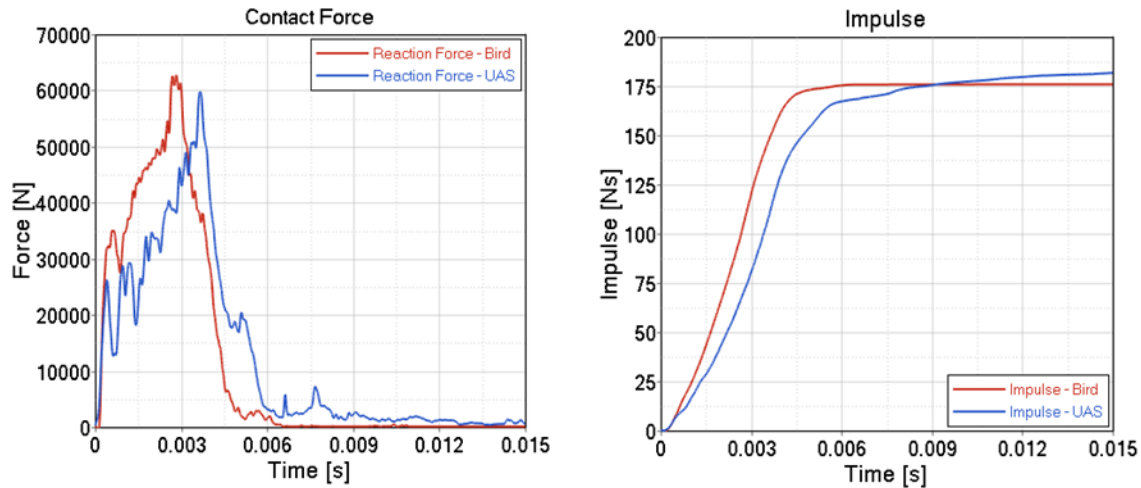


Figure 403. Comparison of the contact force and impulse of the impact between a business jet wing and a 1.8 kg (4.0 lb) UAS/bird at 128.6 m/s (250 knots)

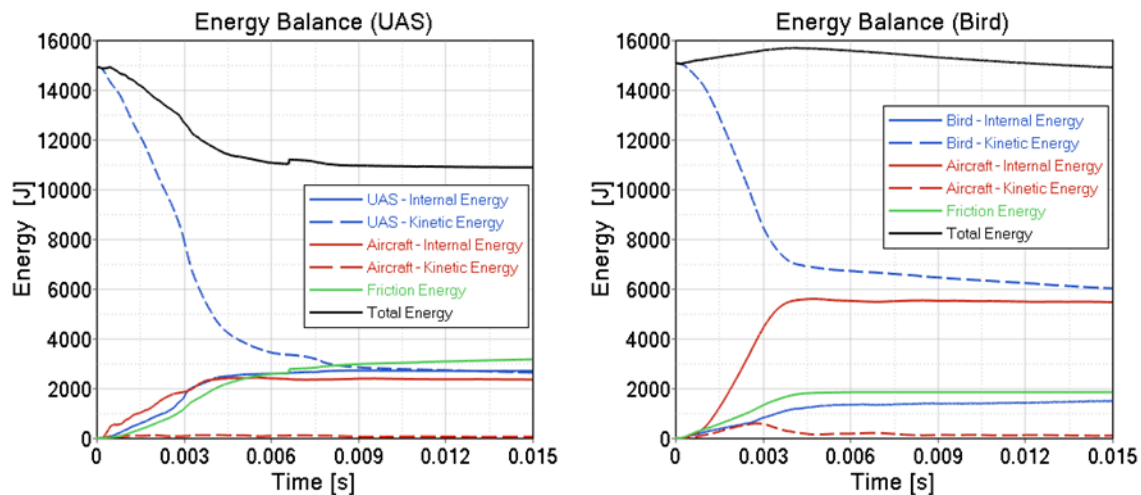


Figure 404. Comparison of the energy balance of the impact between a business jet wing and a 1.8 kg (4.0 lb) UAS/bird at 128.6 m/s (250 knots)

The impulse for the UAS was higher than that of the bird. From the energy balance comparison, it can be observed that the UAS absorbed considerably greater internal energy than the bird. Also, it is apparent that the residual kinetic energy of the bird after impact was greater than that of the UAS. This is an indication that the kinetic energy of the bird was deflected more efficiently than that of the UAS, for which most of the energy was absorbed in the impact.

F.2.4 Windshield

Impact simulations of a 1.8 kg (4.0 lb) UAS (case BFC1) and a 1.8 kg (4.0 lb) bird (case BB4C1) against a windshield are compared in terms of damage severity and kinematics. The initial conditions were based on the above UAS case which was identified as the most critical in the baseline

simulations (see Section 4.4.4.1). Figure 405 depicts the comparison of the kinematics of the event. Figure 406 shows the comparison of the damage caused to the windshield and surrounding structure.

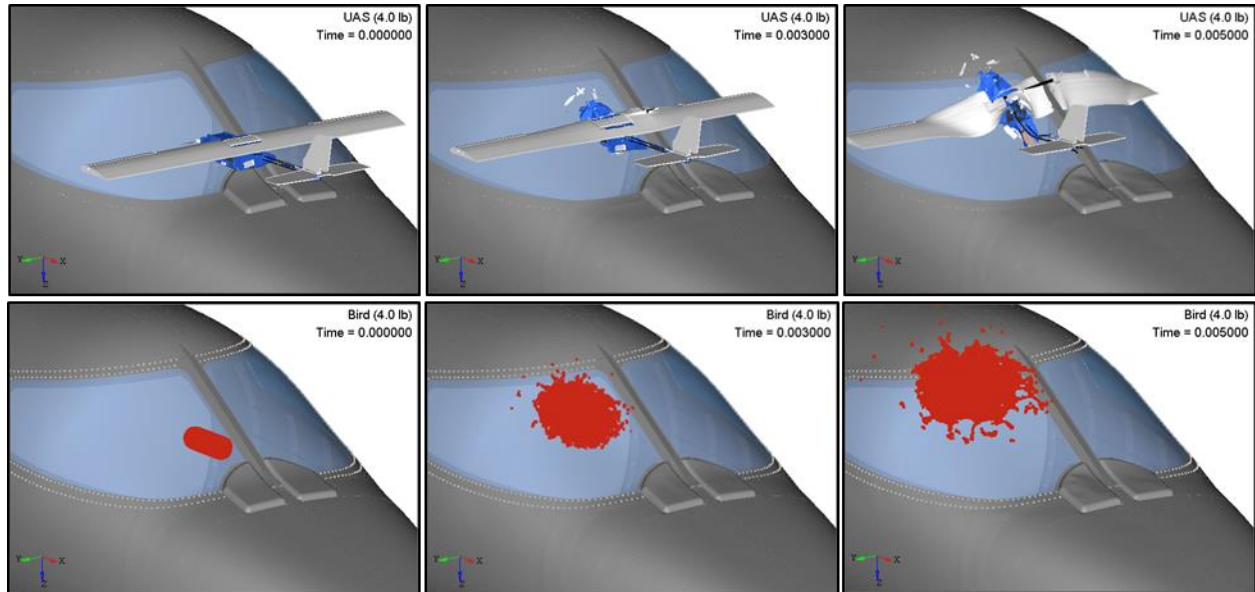


Figure 405. Comparison of the kinematics of impact between a business jet windshield and a 1.8 kg (4.0 lb) UAS/Bird at 128.6 m/s (250 knots)

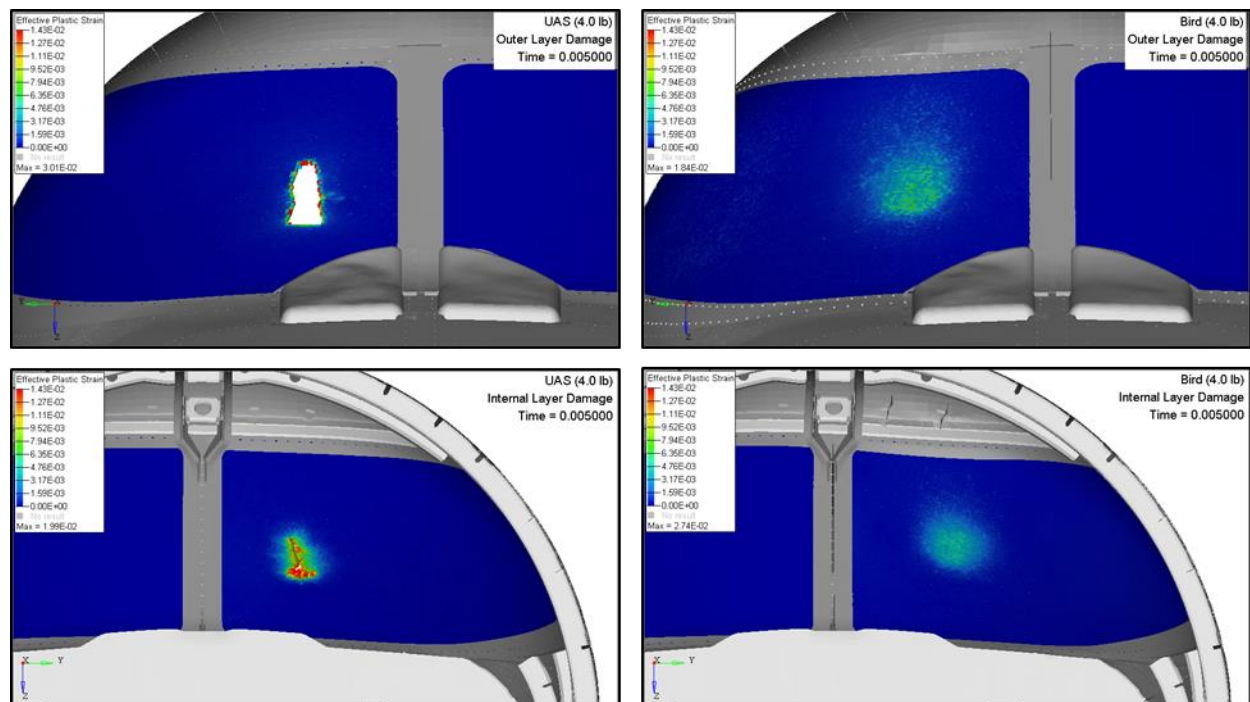


Figure 406. Comparison of external/internal damage sustained by a business jet windshield impacted with a 1.8 kg (4.0 lb) UAS/Bird at 128.6 m/s (250 knots)

The UAS damaged the windshield on the transparency, whereas the bird impacted the windshield and slid over it due to the windshield angle without causing noticeable permanent deformations to the transparency. It can also be seen in Figure 406 that amount of damage introduced into the windshield was considerably smaller for the case of bird than the UAS. Note that the top three plastic strain plots show only the outer layer of the windshield transparency and that the lower three plots show the layer which sustained the maximum plastic strain.

The damage introduced by the UAS is classified as Level 4 whereas the damage introduced by the bird is classified as Level 1. For this case, the UAS impact can be considered more severe than the equivalent bird strike in terms of damage.

Figure 407 shows the comparison for the contact force and impulse between the UAS/bird and windshield. Figure 408 shows the energy balance for the impact comparison.

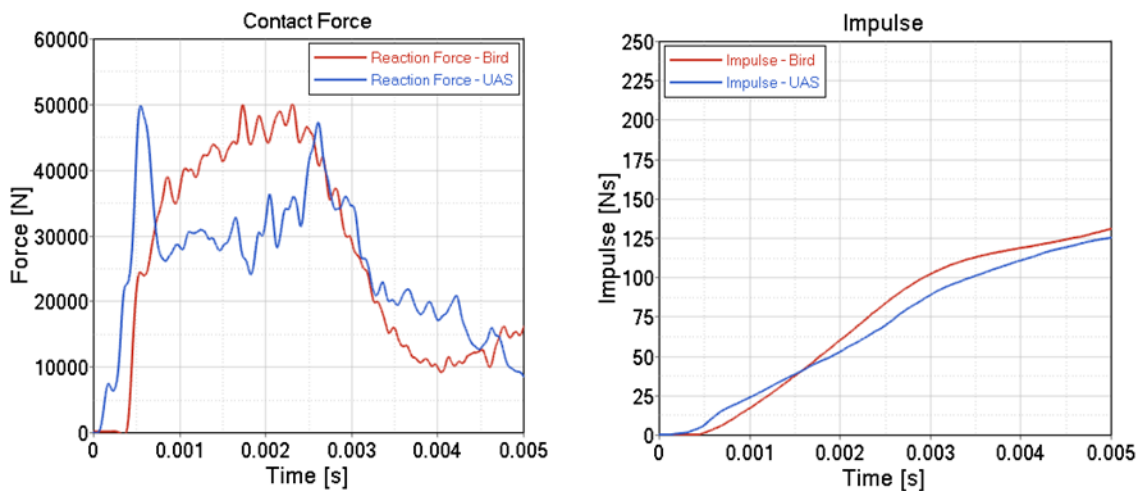


Figure 407. Comparison of the contact force and impulse of the impact between a business jet windshield and a 1.8 kg (4.0 lb) UAS/bird at 128.6 m/s (250 knots)

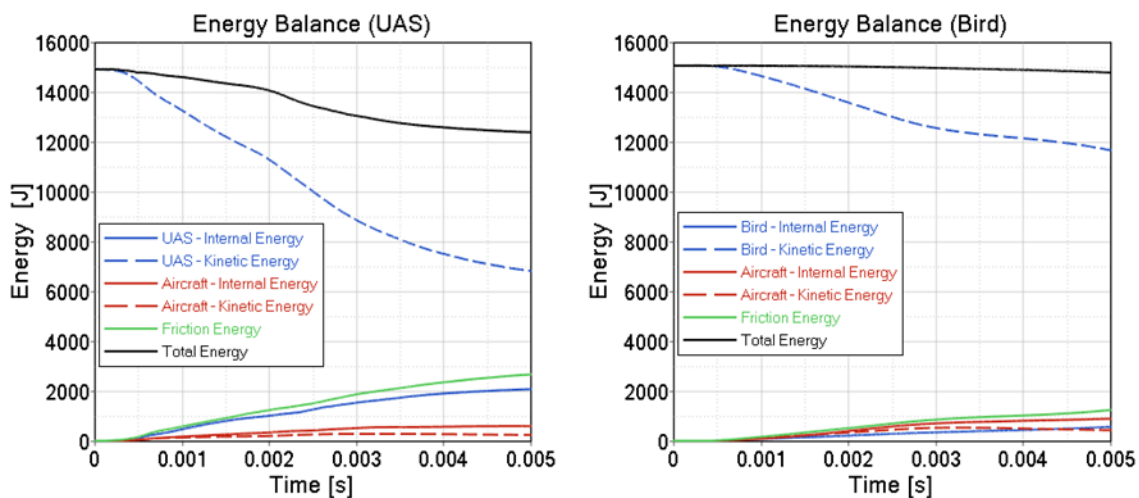


Figure 408. Comparison of the energy balance of the impact between a business jet windshield and a 1.8 kg (4.0 lb) UAS/bird at 128.6 m/s (250 knots)

The impulse for the bird was higher than that of the UAS. From the energy balance comparison, it can be observed that the UAS absorbed considerably greater internal energy than the bird. Also, it is apparent that the residual kinetic energy of the bird after impact was greater than that of the UAS. This is an indication that the kinetic energy of the bird was deflected more efficiently than that of the UAS, for which most of the energy was absorbed in the impact.

F.3 TRANSPORT JET – UAS VS. BIRD (8.0 LB)

F.3.1 Vertical Stabilizer

Impact simulations of a 3.6 kg (8.0 lb) UAS (case CFsV1) and a 3.6 kg (8.0 lb) bird (case CB8V1) against a vertical stabilizer are compared in terms of damage severity and kinematics. The initial conditions were based on the most critical case (CFV1) identified in the baseline simulations (see Section 4.3.1.1). Figure 409 depicts the comparison of the kinematics of the event. Figure 410 shows the comparison of the damage caused to the skin and the inner structure of the vertical stabilizer.

The UAS damaged the skin, the upper and lower ribs and the lightening hole above the impact location in the forward spar while the bird damaged the skin and forward spar to a lesser degree and just the upper rib. It can also be seen in Figure 410 that amount of damage introduced into the skin was considerably smaller for the case of bird than the UAS.

The damage introduced by the UAS is classified as Level 4, whereas the damage introduced by the bird is classified as Level 3. For this case, the UAS impact can be considered more severe than the equivalent bird strike in terms of damage.

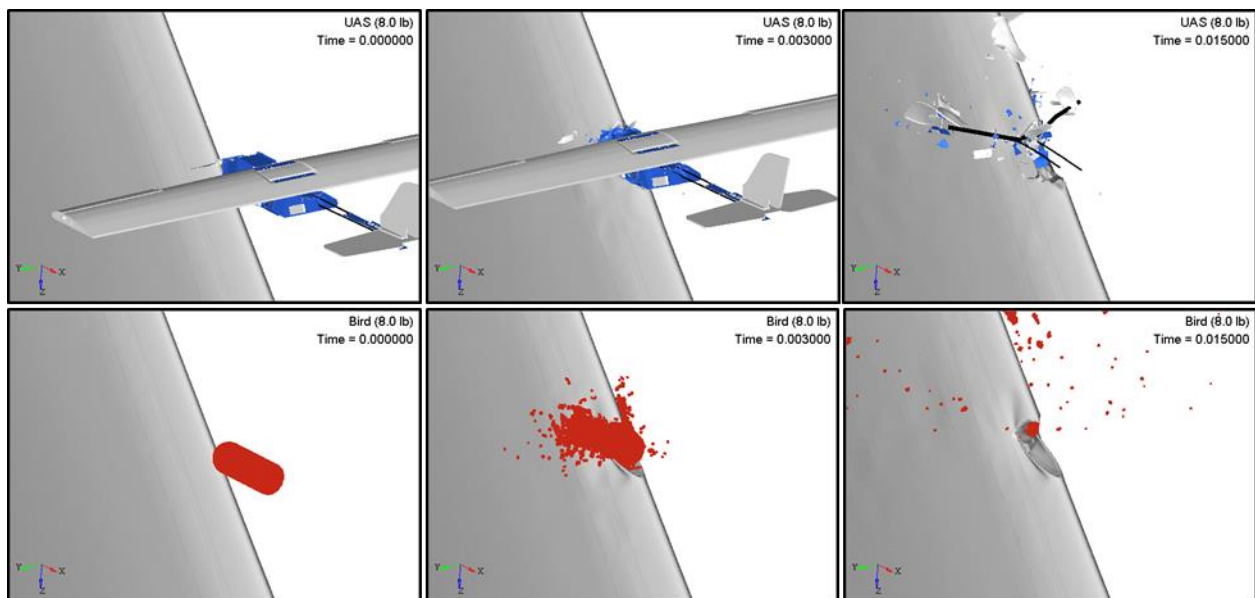


Figure 409. Comparison of the kinematics of impact between a commercial transport jet vertical stabilizer and a 3.6 kg (8.0 lb) UAS/Bird at 128.6 m/s (250 knots)

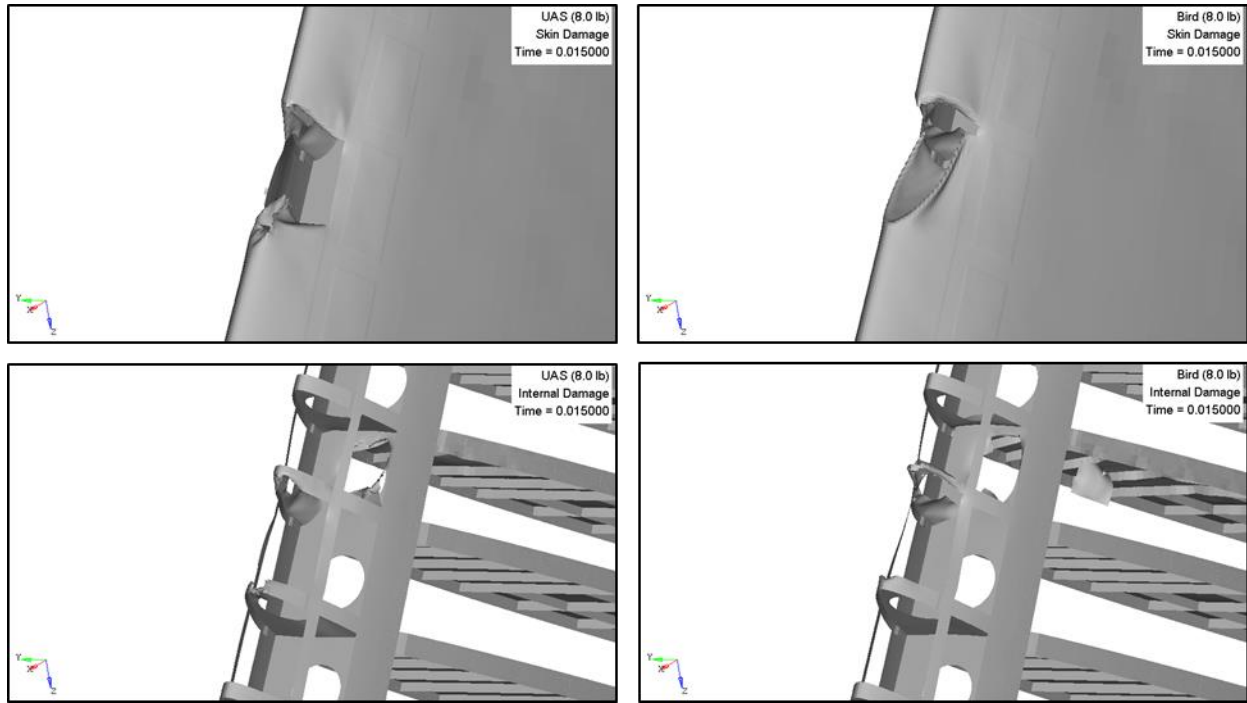


Figure 410. Comparison of external/internal damage sustained by a commercial transport jet vertical stabilizer impacted with a 3.6 kg (8.0 lb) UAS/Bird at 128.6 m/s (250 knots)

Figure 411 shows the comparison for the contact force and impulse between the UAS/bird and vertical stabilizer. Figure 412 shows the energy balance for the impact comparison.

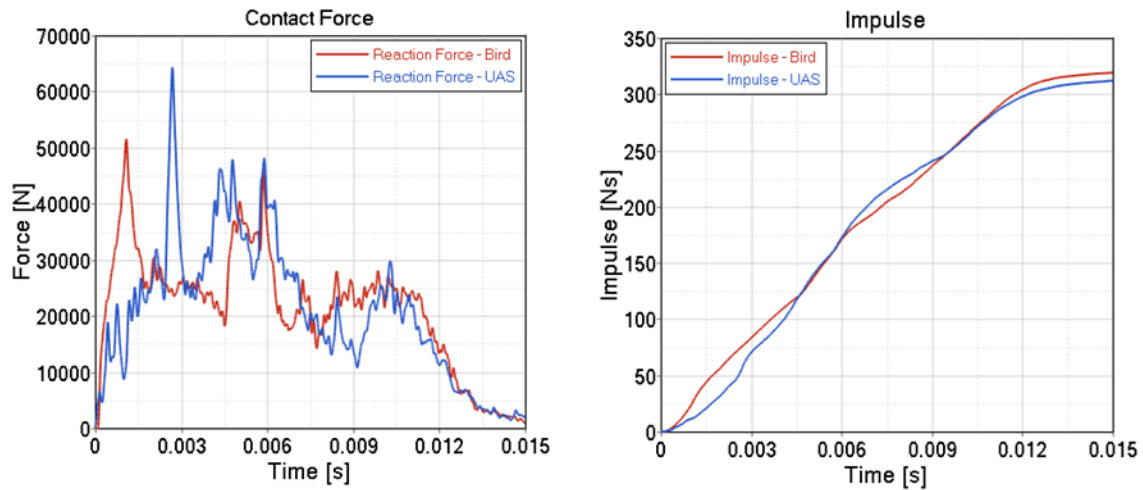


Figure 411. Comparison of the contact force and impulse of the impact between a commercial transport jet vertical stabilizer and a 3.6 kg (8.0 lb) UAS/bird at 128.6 m/s (250 knots)

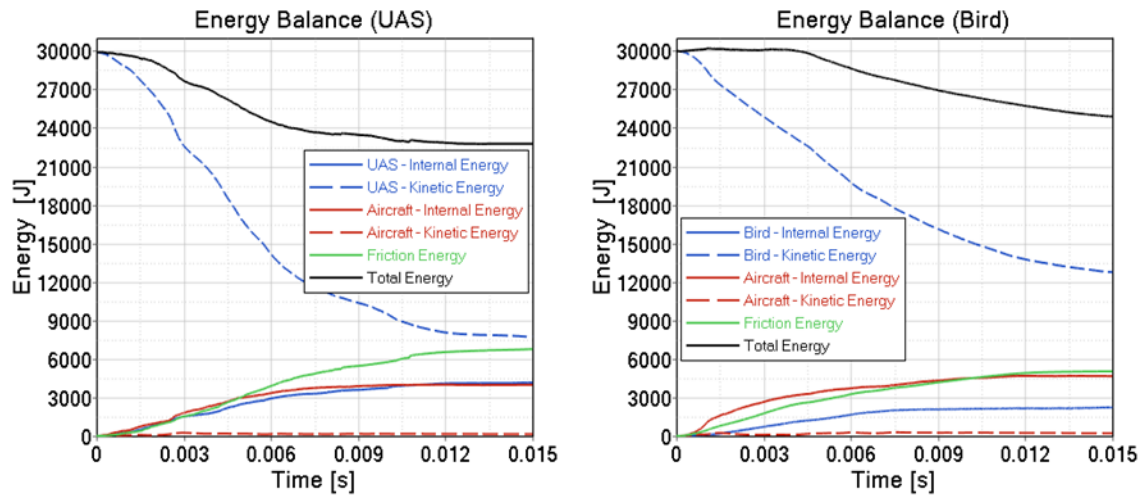


Figure 412. Comparison of the energy balance of the impact between a commercial transport jet vertical stabilizer and a 3.6 kg (8.0 lb) UAS/bird at 128.6 m/s (250 knots)

The impulse for both UAS and bird appear to be of similar magnitude. From the energy balance comparison, it can be observed that the UAS absorbed considerably greater internal energy than the bird. Also, it is apparent that the residual kinetic energy of the bird after impact was greater than that of the UAS. This is an indication that the kinetic energy of the bird was deflected more efficiently than that of the UAS, for which most of the energy was absorbed in the impact.

F.3.2 Horizontal Stabilizer

Impact simulations of a 3.6 kg (8.0 lb) UAS (case CFsH2) and a 3.6 kg (8.0 lb) bird (case CB8H2) against a horizontal stabilizer are compared in terms of damage severity and kinematics. The initial conditions were based on the most critical case (CFH2) identified in the baseline simulations (see Section 4.3.2.1). Figure 413 depicts the comparison of the kinematics of the event. Figure 414 shows the comparison of the damage caused to the skin and the inner structure of the horizontal stabilizer.

The UAS damaged the skin, the left nose rib and the sub-spar while the bird damaged the skin to a lesser degree and four nose ribs behind the skin. It can also be seen in Figure 414 that amount of damage introduced into the skin was considerably smaller for the case of bird than the UAS.

The damage introduced by the UAS is classified as Level 4 whereas the damage introduced by the bird is classified as Level 2. For this case, the UAS impact can be considered more severe than the equivalent bird strike in terms of damage.

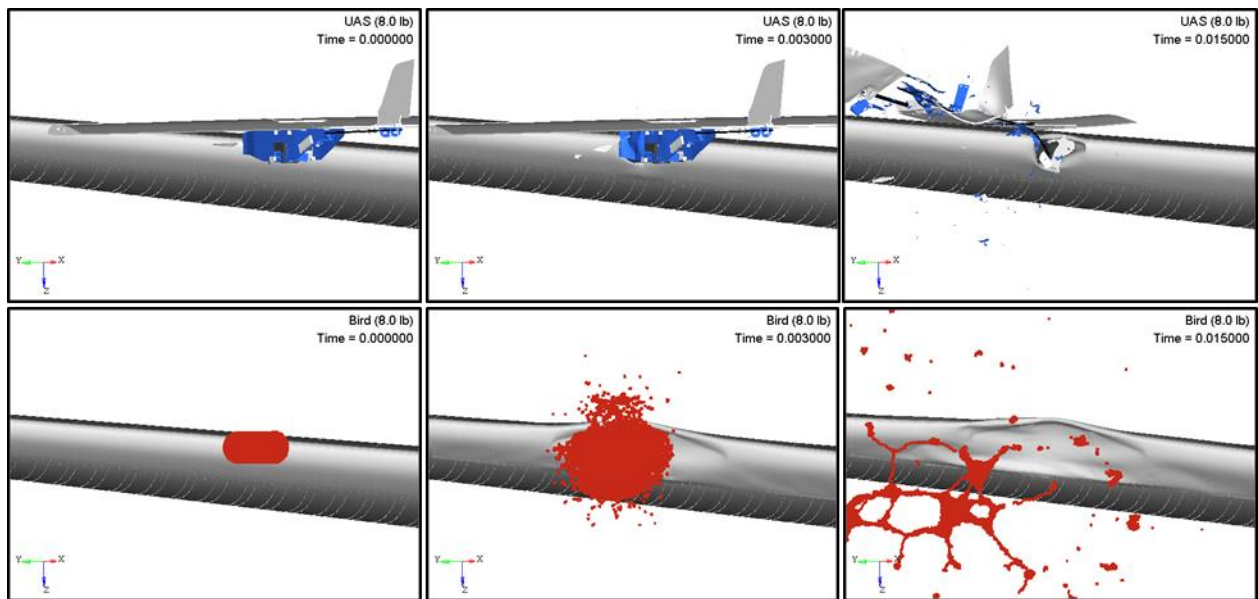


Figure 413. Comparison of the kinematics of impact between a commercial transport jet horizontal stabilizer and a 3.6 kg (8.0 lb) UAS/Bird at 128.6 m/s (250 knots)

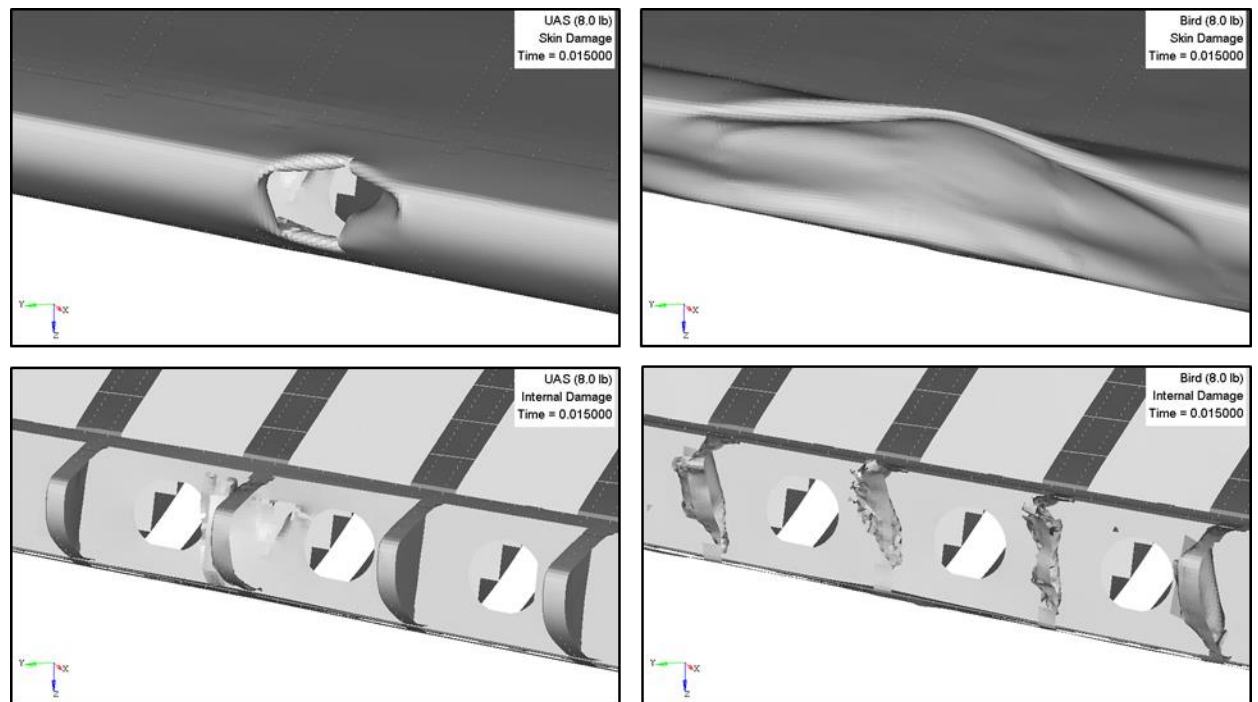


Figure 414. Comparison of external/internal damage sustained by a commercial transport jet horizontal stabilizer impacted with a 3.6 kg (8.0 lb) UAS/Bird at 128.6 m/s (250 knots)

Figure 415 shows the comparison for the contact force and impulse between the UAS/bird and horizontal stabilizer. Figure 416 shows the energy balance for the impact comparison.

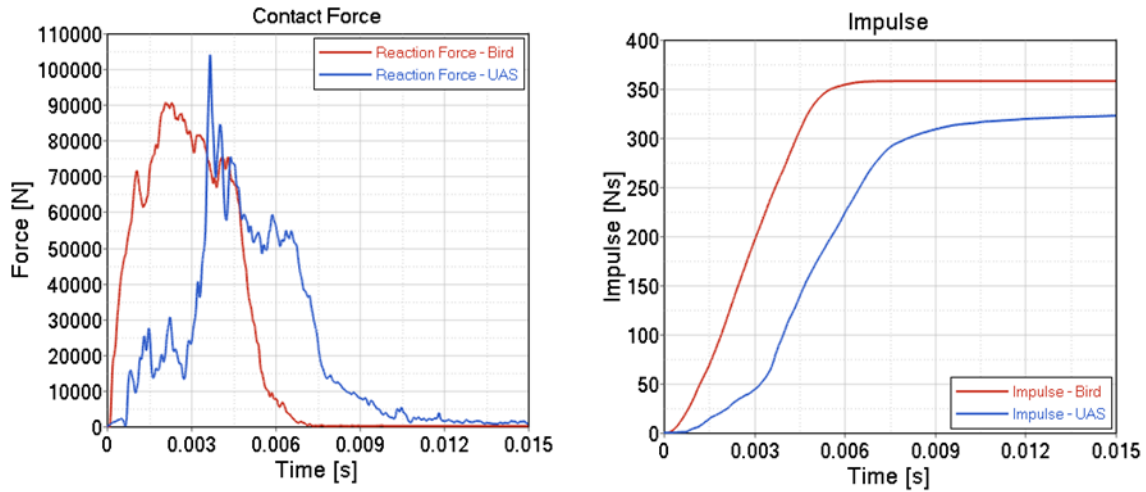


Figure 415. Comparison of the contact force and impulse of the impact between a commercial transport jet horizontal stabilizer and a 3.6 kg (8.0 lb) UAS/bird at 128.6 m/s (250 knots)

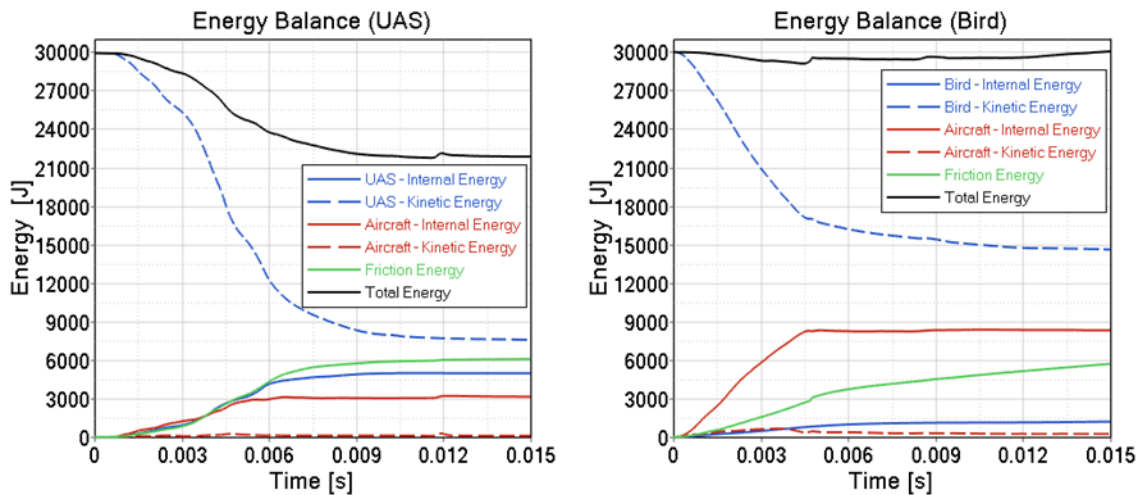


Figure 416. Comparison of the energy balance of the impact between a commercial transport jet horizontal stabilizer and a 3.6 kg (8.0 lb) UAS/bird at 128.6 m/s (250 knots)

The impulse for the bird was higher than that of the UAS. From the energy balance comparison, it can be observed that the UAS absorbed considerably greater internal energy than the bird. Also, it is apparent that the residual kinetic energy of the bird after impact was greater than that of the UAS. This is an indication that the kinetic energy of the bird was deflected more efficiently than that of the UAS, for which most of the energy was absorbed in the impact.

F.4 BUSINESS JET – UAS VS. BIRD (8.0 LB)

F.4.1 Vertical Stabilizer

Impact simulations of a 3.6 kg (8.0 lb) UAS (case BF_sV3) and a 3.6 kg (8.0 lb) bird (case BB8V3) against a vertical stabilizer are compared in terms of damage severity and kinematics. The initial conditions were based on the most critical case (BFV3) identified in the baseline simulations (see Section 4.4.1.1). Figure 417 depicts the comparison of the kinematics of the event. Figure 418 shows the comparison of the damage caused to the skin and the inner structure of the vertical stabilizer.

The UAS damaged the skin, the lightening hole in the front spar and the two fin tip ribs behind the spar, while the bird damaged the skin to a lesser degree, the front ribs and the front spar. It can also be seen in Figure 418 that amount of damage introduced into the skin was considerably smaller for the case of bird than the UAS.

The damage introduced by the UAS is classified as Level 4, whereas the damage introduced by the bird is classified as Level 2. For this case, the UAS impact can be considered more severe than the equivalent bird strike in terms of damage.

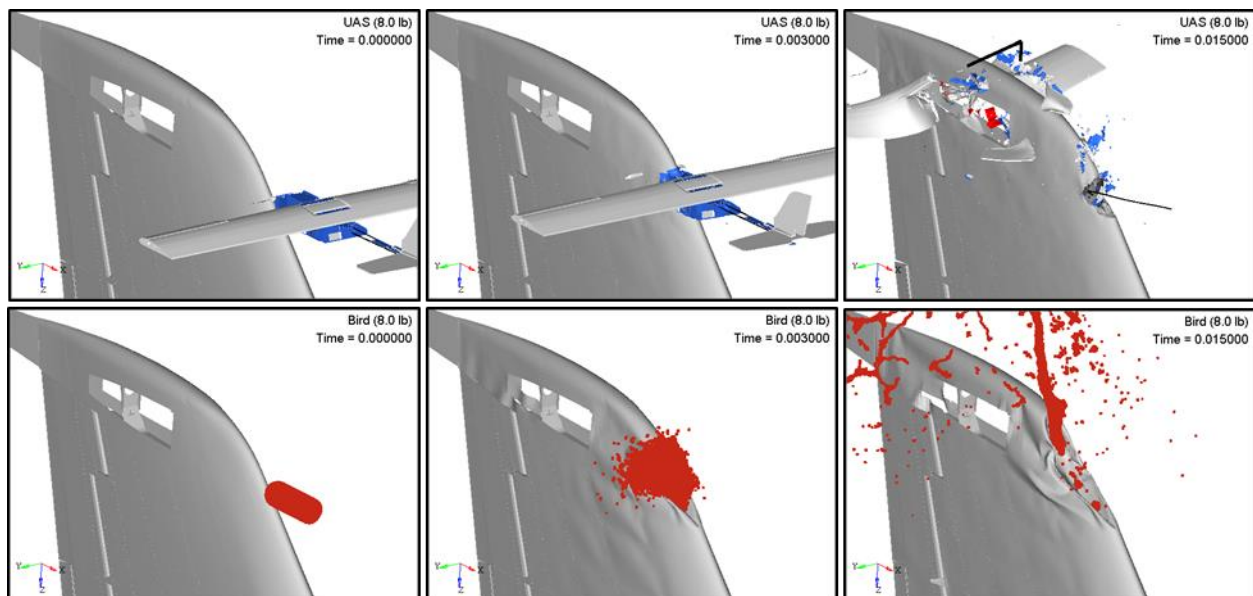


Figure 417. Comparison of the kinematics of impact between a business jet vertical stabilizer and a 3.6 kg (8.0 lb) UAS/Bird at 128.6 m/s (250 knots)

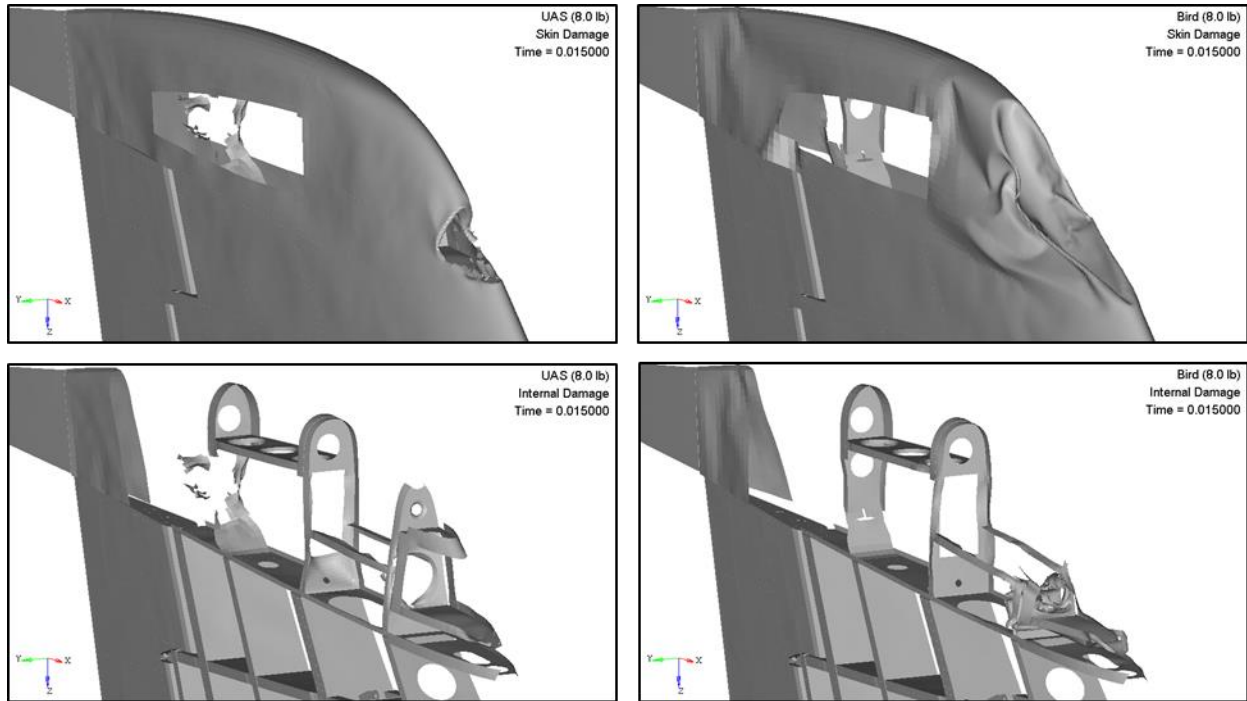


Figure 418. Comparison of external/internal damage sustained by a business jet vertical stabilizer impacted with a 3.6 kg (8.0 lb) UAS/Bird at 128.6 m/s (250 knots)

Figure 419 shows the comparison for the contact force and impulse between the UAS/bird and vertical stabilizer. Figure 420 shows the energy balance for the impact comparison. The impulse for the bird was higher than that of the UAS. From the energy balance comparison, it can be observed that the UAS absorbed considerably greater internal energy than the bird. Also, it is apparent that the residual kinetic energy of the bird after impact was greater than that of the UAS. This is an indication that the kinetic energy of the bird was deflected more efficiently than that of the UAS, for which most of the energy was absorbed in the impact.

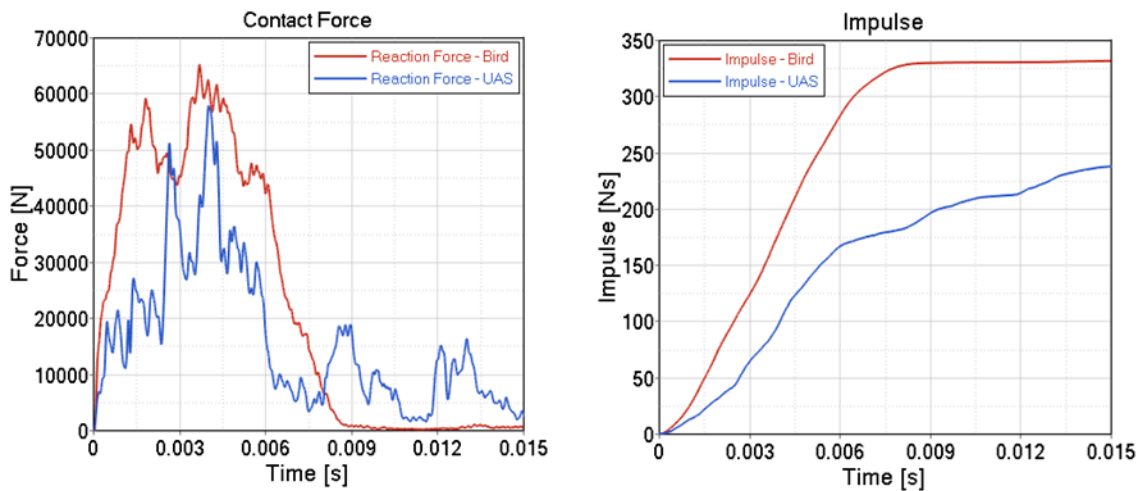


Figure 419. Comparison of the contact force and impulse of the impact between a business jet vertical stabilizer and a 3.6 kg (8.0 lb) UAS/bird at 128.6 m/s (250 knots)

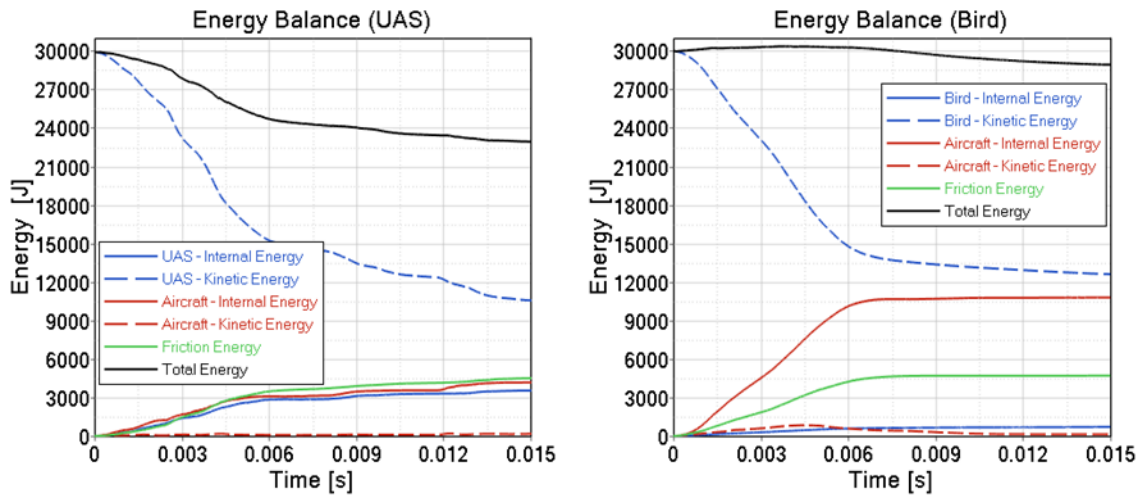


Figure 420. Comparison of the energy balance of the impact between a business jet vertical stabilizer and a 3.6 kg (8.0 lb) UAS/bird at 128.6 m/s (250 knots)

F.4.2 Horizontal Stabilizer

Impact simulations of a 3.6 kg (8.0 lb) UAS (case BF8H1) and a 3.6 kg (8.0 lb) bird (case BB8H1) against a horizontal stabilizer are compared in terms of damage severity and kinematics. The initial conditions were based on the most critical case (BFH1) identified in the baseline simulations (see Section 4.4.2.1). Figure 421 depicts the comparison of the kinematics of the event. Figure 422 shows the comparison of the damage caused to the skin and the inner structure of the horizontal stabilizer.

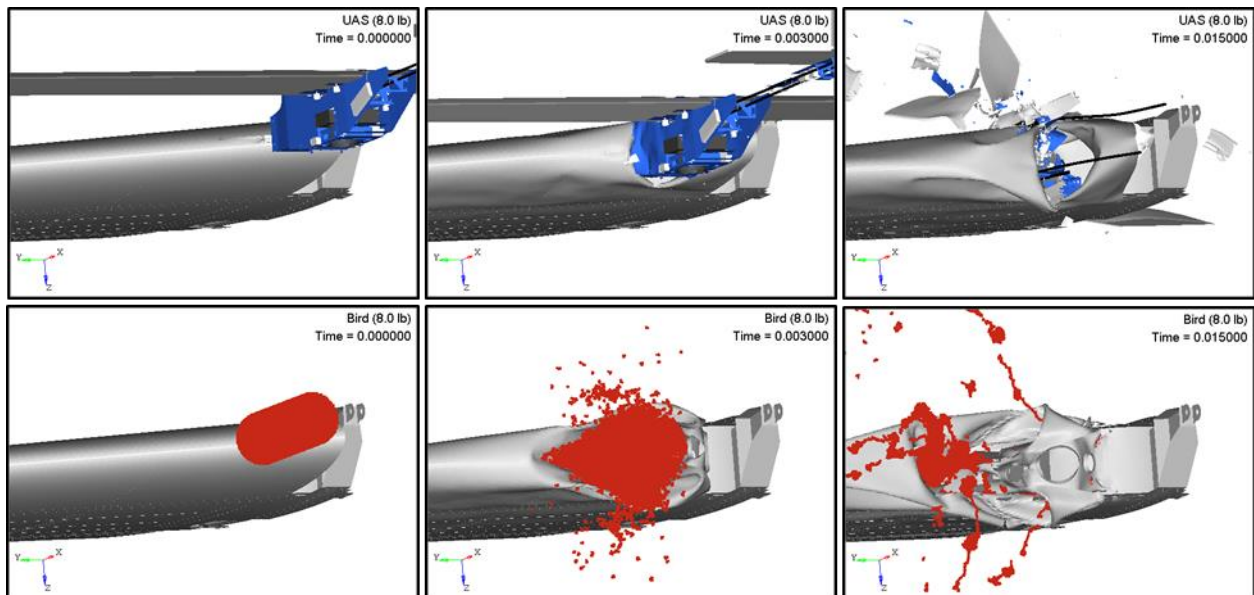


Figure 421. Comparison of the kinematics of impact between a business jet horizontal stabilizer and a 3.6 kg (8.0 lb) UAS/Bird at 128.6 m/s (250 knots)

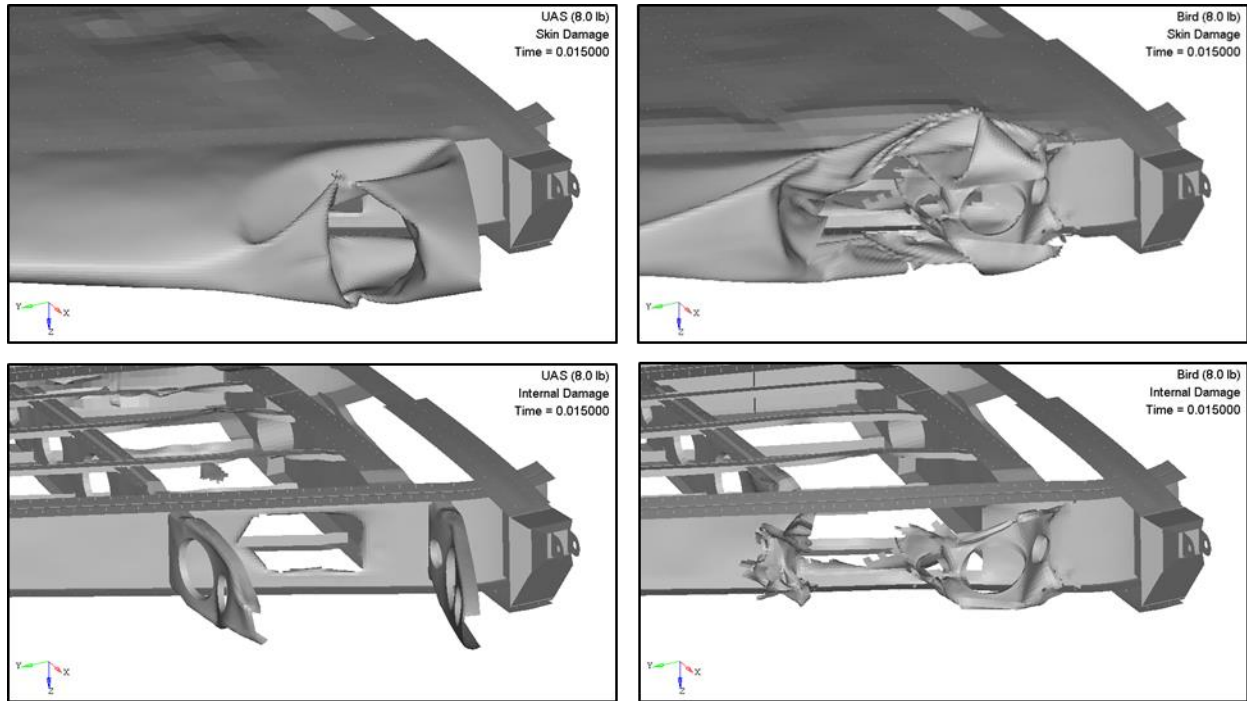


Figure 422. Comparison of external/internal damage sustained by a business jet horizontal stabilizer impacted with a 3.6 kg (8.0 lb) UAS/Bird at 128.6 m/s (250 knots)

The UAS damaged the skin, both the nose ribs and the front spar while the bird damaged the skin, both the nose ribs and the front spar to a higher degree. It can also be seen in Figure 422 that amount of damage introduced into the skin was of much greater magnitude for the bird. The damage introduced by both the UAS and the bird is classified as Level 4. For this case, the bird strike can be considered more severe than the equivalent UAS impact in terms of damage.

Figure 423 shows the comparison for the contact force and impulse between the UAS/bird and horizontal stabilizer. Figure 424 shows the energy balance for the impact comparison.

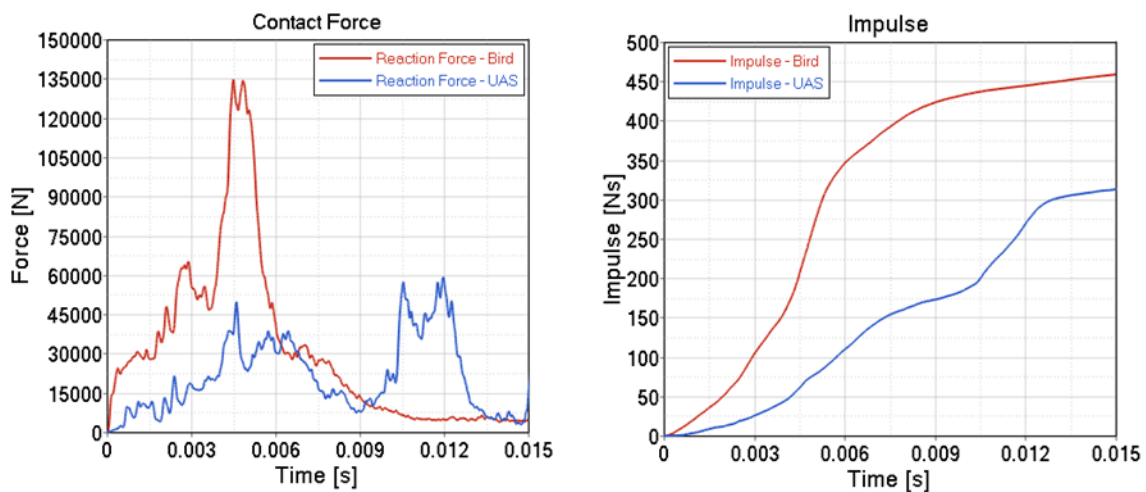


Figure 423. Comparison of the contact force and impulse of the impact between a business jet horizontal stabilizer and a 3.6 kg (8.0 lb) UAS/bird at 128.6 m/s (250 knots)

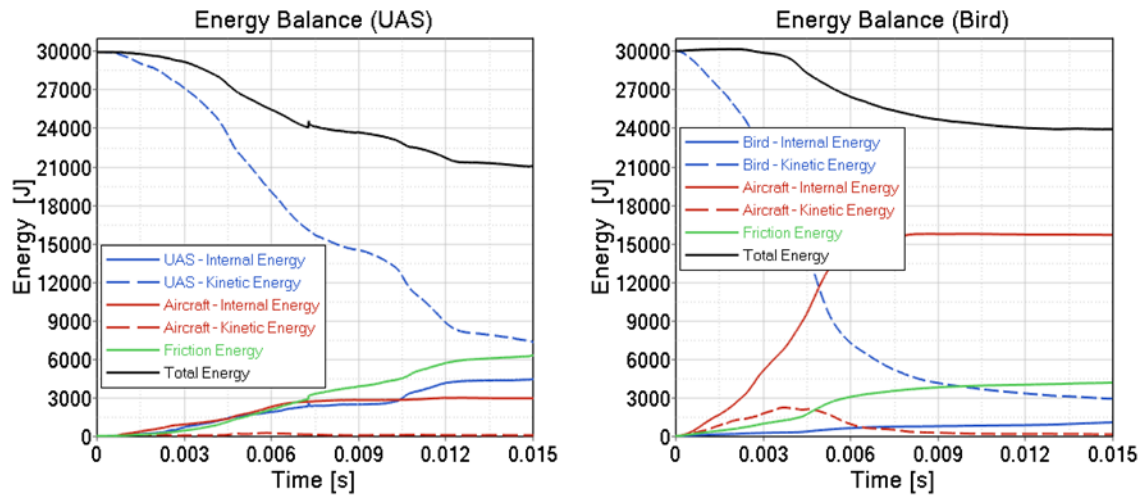


Figure 424. Comparison of the energy balance of the impact between a business jet horizontal stabilizer and a 3.6 kg (8.0 lb) UAS/bird at 128.6 m/s (250 knots)

The impulse for the bird was higher than that of the UAS. From the energy balance comparison, it can be observed that the UAS absorbed considerably greater internal energy than the bird. Also, it is apparent that the residual kinetic energy of the UAS after impact was greater than that of the bird. This is an indication that the kinetic energy of the UAS was deflected more efficiently than that of the bird, for which most of the energy was absorbed in the impact.

APPENDIX G – DATA PROCESSING METHODS

This appendix presents the methodology followed for the data processing of both physical testing and simulation for the test cases presented in Chapter 2. The procedure is presented with an example of how filtering was applied for a specific case. This same procedure was followed for all the plots in Chapter 2 in which it was indicated that the data had been filtered.

G.1 DATA PROCESSING EXAMPLE: COMPONENT LEVEL TEST 1 OF QUADCOPTER

This section presents a sample case for the strain gage channel 4 of battery test 1 of the quadcopter UAS, see section 2.4.4.6 of volume II [2]. The strain data acquired from the strain gages was sampled at 1 MHz. Similarly, the simulation set up to virtually replicate the test was also sampled at 1 MHz. Figure 425 shows a comparison of the raw data acquired for strain gage 4 during the simulation, and tests 5660, 5669, and 5670, respectively. It can be seen that for some cases the signal obtained became considerably noisy, therefore filtering was required to perceive a cleaner plot for comparison.

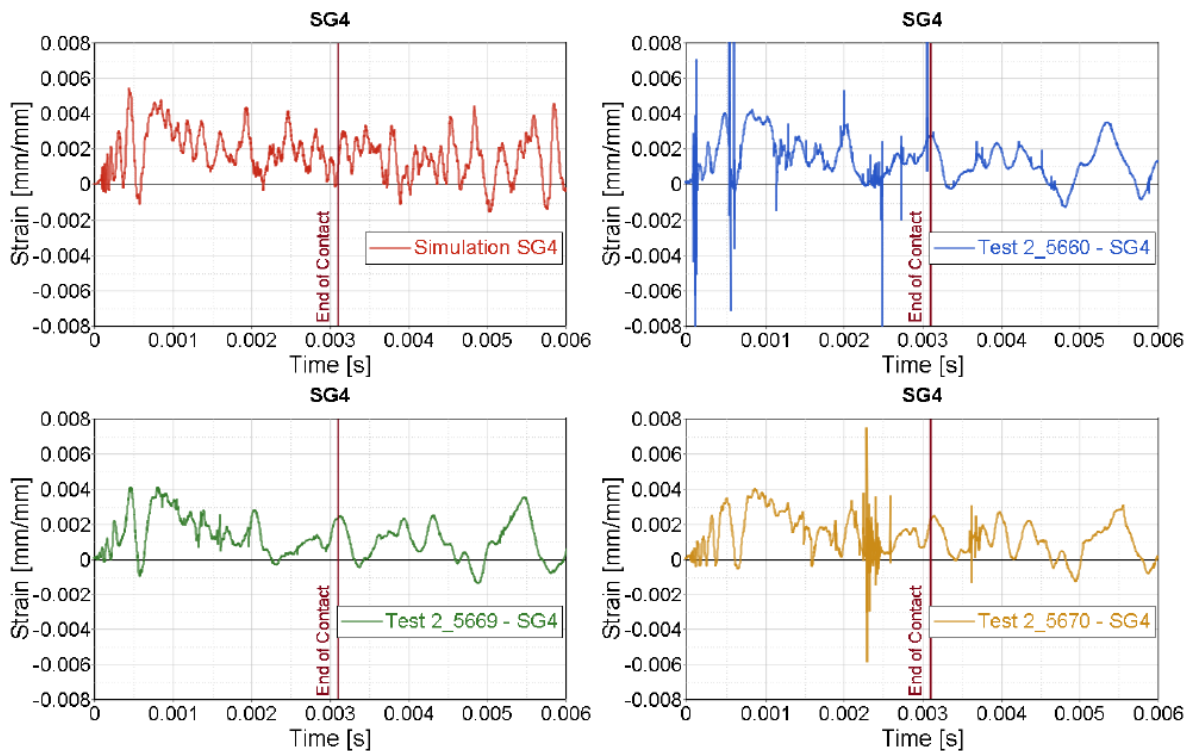


Figure 425. Quadcopter UAS component level test 1, strain gage 4, raw data.

To each of these signals, a low-pass filter of 15 kHz was applied to remove the high frequency noise present in the plots, without interfering with the strain oscillations. Altair Hypergraph software was used to process and filter the data. The filtered function selected was available in the software as an ‘ideal low-pass’ filter. More information about this filter can be found in the software’s manual.

Figure 426 presents the results of applying the filter to the noisy signal from Test 5660. Similarly, Figure 427 shows the results of filtering a not so noisy signal.

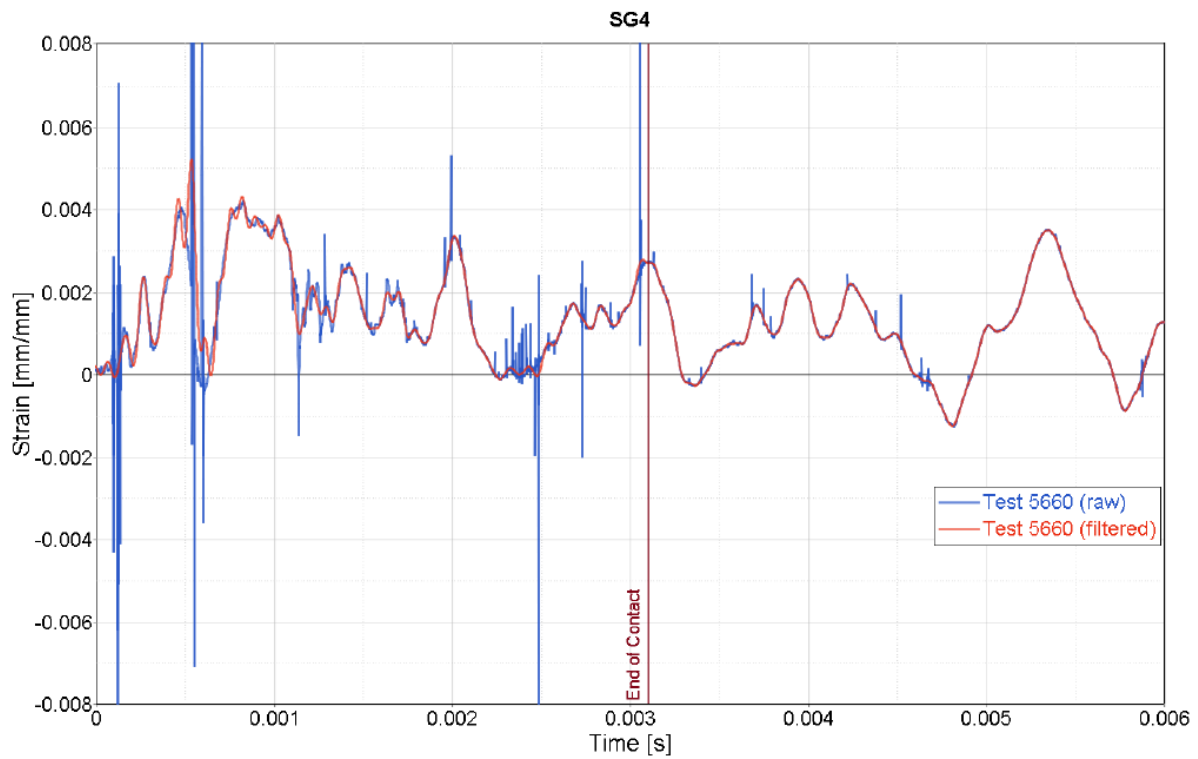


Figure 426. Quadcopter UAS component level test 1-5660, strain gage 4, comparison filtered/un-filtered.

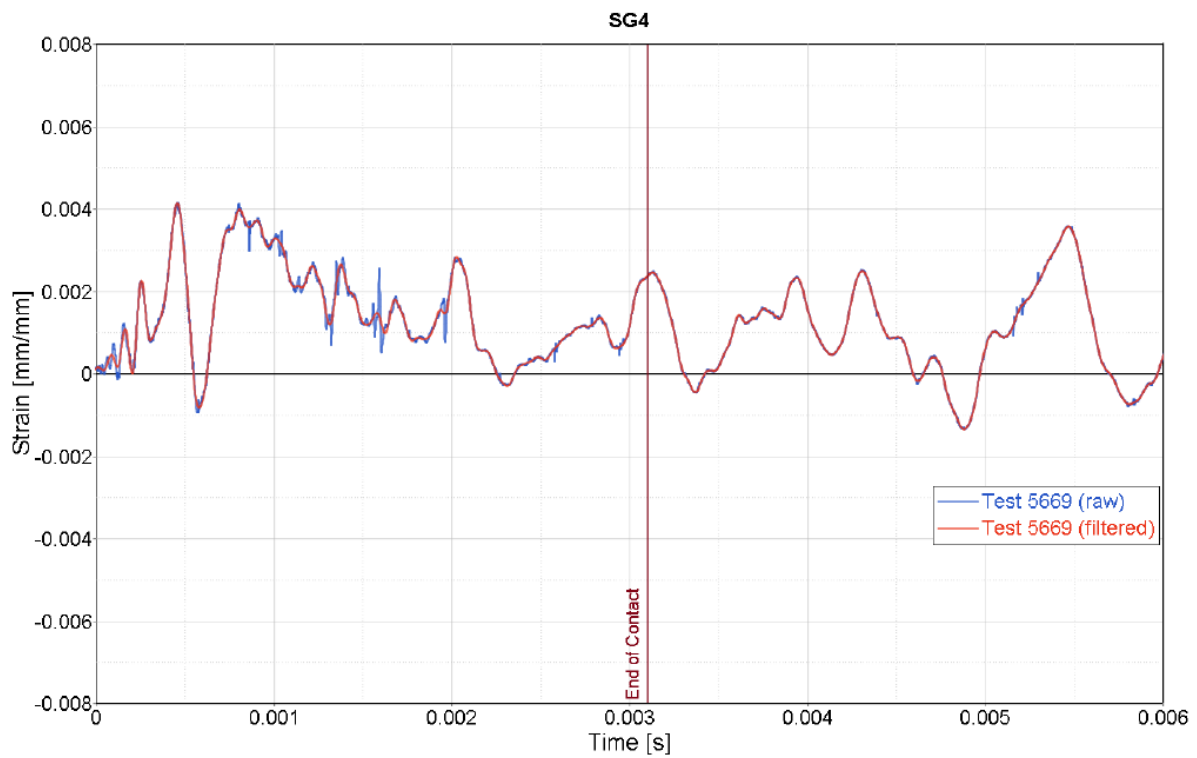


Figure 427. Quadcopter UAS component level test 1-5669, strain gage 4, comparison filtered/un-filtered

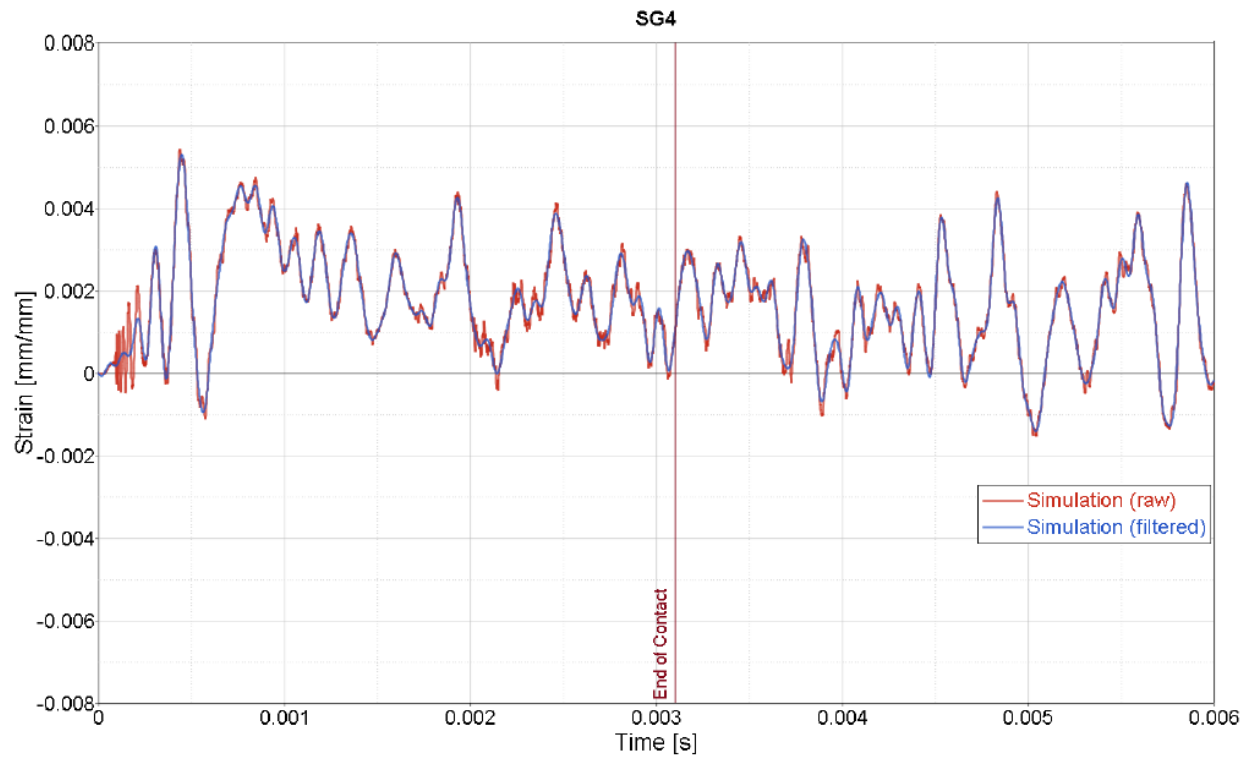


Figure 428. Quadcopter UAS component level test 1 simulation, strain gage 4, comparison filtered/unfiltered.